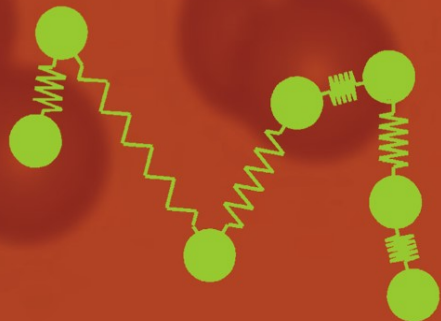


Gert Strobl

The Physics of Polymers

Concepts for Understanding
Their Structures and Behavior

Third Edition



 Springer

Gert Strobl

The Physics of Polymers

Gert Strobl

The Physics of Polymers

Concepts for Understanding
Their Structures and Behavior

Third Revised and Expanded Edition
With 295 Figures and 2 Tables

 Springer

Prof. Gert Strobl
Physikalisches Institut
Albert-Ludwigs-Universität
Hermann-Herder Str. 3
79104 Freiburg im Breisgau
Germany
e-mail: gert.strobl@physik.uni-freiburg.de

Library of Congress Control Number: 2006940708

ISBN 978-3-540-25278-8 Springer Berlin Heidelberg New York
DOI 10.1007/978-3-540-68411-4

This work is subject to copyright. All rights are reserved, whether the whole or part of the material is concerned, specifically the rights of translation, reprinting, reuse of illustrations, recitation, broadcasting, reproduction on microfilm or in any other way, and storage in data banks. Duplication of this publication or parts thereof is permitted only under the provisions of the German Copyright Law of September 9, 1965, in its current version, and permission for use must always be obtained from Springer. Violations are liable for prosecution under the German Copyright Law.

Springer is a part of Springer Science+Business Media
springer.com

© Springer-Verlag Berlin Heidelberg 2007

The use of general descriptive names, registered names, trademarks, etc. in this publication does not imply, even in the absence of a specific statement, that such names are exempt from the relevant protective laws and regulations and therefore free for general use.

Typesetting: Camera-ready by authors, LE- \TeX Jelonek, Schmidt & Vöckler GbR, Leipzig
Production: LE- \TeX Jelonek, Schmidt & Vöckler GbR, Leipzig
Cover Design: KünkelLopka, Heidelberg

Printed on acid-free paper 2/3100/YL 5 4 3 2 1 0

Preface

More than ten years have passed now since the first printing of this book, and I am happy to say that it is a success. Many thousands of volumes can today be found worldwide in libraries, laboratories of polymer science and private hands, with a special edition for China and an edition in Japanese. The book obviously filled a gap. After such a period the time had come for a revision and moderate expansion of the book's contents and I continuously worked on it during the last years. The basis of the new sections and chapters were again lectures given to students of physics and chemistry in Freiburg. Proceeding in this manner, the original 'pedagogical style' of the writing was continued. The results of the effort are presented here and they include some major changes:

- The electro-optically active conjugated polymers have attracted many scientists during the last decade and approach commercial uses as display materials. The newly written Chap. 7 deals with the physical basis of the electrooptic response and in addition discusses the spectacular electrical conduction properties of conjugated polymers created by doping.
- Quite peculiar properties are also shown by polyelectrolytes. They became popular in particular by their use as superabsorbers. Many researchers, both theoreticians and experimentalists, are fascinated by the ordering phenomena caused by the Coulomb forces. Polyelectrolyte properties are now discussed in different chapters of the book, in Sects. 3.3, 8.4.2 and 9.2.
- The basic understanding of melt crystallization, a classical field of polymer physics, has changed during the last decade; new experiments have provided novel insights. As a consequence, Chap. 5 was completely rewritten. It presents the new results in a selection of figures, formulates the deduced laws and also includes in Sect. 5.3.1 the – not yet generally accepted – 'multistage model' developed as an explanation of all the new observations.
- Chapter 10 also includes some substantial changes, again triggered by progress in understanding. Some principles governing shear deformation in semicrystalline polymers were revealed and enabled the construction of a mechanic-rheological model (Sect. 10.1).

In addition to these major changes, which resulted in an increase of the book volume by more than one hundred pages, many minor corrections and modifications have been made. Many of them are reactions to remarks from readers, and I would like to express here my high appreciation for the constructive criticism. I hope that it will continue, because it is a real help. There were also a few changes in the choice of symbols, necessitated by additional variables introduced in the new parts. The changed symbols appear in the updated Glossary in the Appendix.

When writing the new chapters I obtained advice by my renowned colleagues Prof. Heinz Bässler (Marburg), Prof. Jürgen Heinze (Freiburg), Prof. Manfred Schmidt (Mainz) and Prof. Stephan Förster (Hamburg), and I would like to express my gratitude to them here.

Last but not least, many thanks go to my secretary Christina Skorek. Without her most effective support in processing the TEX file and preparing all figures, the book with all its three editions would not have come into being.

Freiburg, November 2006

Gert Strobl

Preface to the First Edition

In our faculty, we offer to the graduate students in physics a course on ‘Condensed Matter Physics’ which goes beyond the usual lectures on solid state physics, by also including the physics of simple liquids, liquid crystals and polymers. While there is a large selection of textbooks on solid state physics and also a choice of excellent treatises on the physics of liquids and liquid crystals, a book on a comparable level covering the major parts of the physics of polymers apparently does not exist. The desire is to have a textbook on polymer physics which, ideally, would stand in line with the ‘Kittel’, the ‘Egelstaff’ and ‘de Gennes’ books on the physics of liquid crystals, to cite only some of the best known volumes. This book is a first attempt to comply with these needs and to fill the gap. Certainly the aim is high, too high to be reached with this first approach, but hopefully other polymer physicist will also take on the task in future and then do better, once a frame is set and a first trial exists.

For me personally, writing such a textbook was indeed highly valuable and a worthwhile experience. In a time when science has such a strong tendency for diversification, there is a great danger of losing contact even with the neighboring branches and simultaneously the ability to see and assess the relevance of one’s own activities. Students have this sensitivity and often have a better feeling about the importance of a topic. When teaching students as a lecturer, it is of primary importance always to provide the motivation and to make clear the role and relevance of a certain problem. Indeed, for me this amounts to a true check which helps me to discriminate between the major phenomena and secondary effects. Senior scientists with time tend to become acquainted with complicated, sometimes even artificial concepts; the young student, however, being confronted for the first time with an explanation, reacts naturally and distinguishes intuitively between reasonable, illuminating concepts and less attractive complicated ways of thinking. Hence, writing a textbook also means to put the state of the art of polymer physics to the test. If it is possible to present this field coherently and to explain convincingly the main properties with the aid of clear and appealing concepts, then it is in good shape. It is my impression, already gained in the lectures and now further

corroborated during writing, that this is the case. The level of understanding is quite satisfactory and compares well with the understanding of simple liquids or liquid crystals. Therefore, the goal to write a coherent textbook on polymer physics can be reached, I am only rather uncertain if I have succeeded in demonstrating it.

As I am not sufficiently familiar from own experience with all the topics treated in the various chapters I am certainly not in a position to eliminate all errors. Hopefully, the ones I have made, are only minor ones. In any case, I would be grateful for reactions and comments from readers and any indication of faults in the treatment. Some incorrect conclusions have already been eliminated, after comments by Professor M.H. Wagner (Stuttgart) and Dr. L. Könczöl (Freiburg), who were kind enough to go through Chaps. 7 and 8 and I wish to thank them here once again for their advice.

Even if all of us in the scientific community use the English language, for a non-native speaker, the writing of a book is a different matter. As I do not like to read something in bad German I guess that Anglo-American scientists must feel the same. I received help at the beginning of my writing from Dr. Sandra Gilmour, who was working at this time as a postdoctoral student in Freiburg, and would like to express my gratitude again. Then, after completion, the manuscript was thoroughly revised by the copy editor, but he remarked that 'the sentence structure is very German which often makes it sound strange to a native speaker'. So I can only hope that this does not amount to a problem in understanding and offer my apologies.

In the first version produced two years ago the manuscript was dictated immediately after given lectures. This is the reason for the 'pedagogical style' of the writing. The emphasis is on the various concepts which have successfully established the present-day understanding of polymer physics. The focus is on the major phenomena, both in the formation of structures and the behavior under forces applied externally, mainly mechanical ones. This implies that many further effects, although important in certain cases, remain untouched. Hence, this textbook does not represent a comprehensive treatise and, therefore, should be better considered as an 'interface', providing help to enter into the various fields of polymer science, emanating from a basis which shows the interrelations. The recommendations given under the 'Further Readings' at the end of each chapter, the selected works included as figures, and the bibliography supplied in the Appendix are meant to open the way for more detailed studies.

One active area of research is completely missing. These are the optical and electrical properties, with effects such as the high conductivity of doped conjugated polymers, electro-luminescence in polymeric light emitting diodes, or the ferro- and piezoelectricity of poly(vinylidene fluoride), to cite only a few examples. There is no good reason for this omission, only that I did not want to overload the book with another topic of different character which, besides, mostly employs concepts which are known from the physics of semi-conductors and low molar mass molecules.

As already mentioned, this book is primarily written for students of physics and physicists wishing to enter into polymer science for the first time. Interested macromolecular chemists and chemical engineers may also find it useful. The prerequisite for an understanding is not a special one, all that is needed is a background in phenomenological and statistical thermodynamics on the level of the respective courses in physical chemistry, together with the related mathematical knowledge.

Of course, I will be happy if the book finds many readers. It is a matter of fact that polymer physics is largely unknown to the majority of physicists. As a consequence, it is only rarely included in university courses on condensed matter behavior. This is difficult to comprehend considering the widespread uses of polymeric materials and in view of the appealing physical concepts developed for the description of their properties. It is therefore my wish that this book will contribute a little to change the present situation by helping to widen the physicists' general knowledge with a better understanding of the physics of polymers.

Freiburg, November 1995

Gert Strobl

Contents

1	Constitution and Architecture of Chains	1
2	Single Chain Conformations	15
2.1	Rotational Isomeric States	15
2.2	Helices	19
2.3	Coils	22
2.3.1	The Ideal Chain	26
2.3.2	The Expanded Chain	45
2.4	The Persistent Chain	55
2.5	The Ising Chain	59
3	Polymer Solutions	69
3.1	Dilute and Semidilute Solutions	70
3.1.1	Osmotic Pressure	71
3.2	Screening of Excluded Volume Forces	82
3.3	Polyelectrolyte Solutions	89
3.3.1	Condensation and Screening of Charges	89
3.3.2	Chain Stretching, Salt Effects and Interchain Ordering	95
3.3.3	Osmotic Pressure	100
4	Polymer Blends and Block Copolymers	105
4.1	The Flory–Huggins Treatment of Polymer Mixtures	106
4.1.1	Phase Diagrams: Upper and Lower Miscibility Gap	117
4.2	Phase Separation Mechanisms	122
4.3	Critical Fluctuations and Spinodal Decomposition	129
4.3.1	Critical Scattering	132
4.3.2	Decomposition Kinetics	143
4.4	Block Copolymer Phases	151
4.4.1	Layered Structures	155
4.4.2	Pretransitional Phenomena	157

5	The Semicrystalline State	165
5.1	Structure Characteristics	167
5.1.1	Morphological Elements	167
5.1.2	Structure Parameters	173
5.2	Kinetics of Crystallization and Melting	181
5.3	Laws for the Structure Development	190
5.3.1	The Multistage Model	199
5.4	Mechanisms of Secondary Crystallization	205
5.4.1	The Insertion Mode	208
5.4.2	Surface Crystallization and Melting	212
5.5	Crystallization from Oriented Melts	216
6	Mechanical and Dielectric Response	223
6.1	Response Functions	224
6.1.1	Viscoelasticity	224
6.1.2	Orientational Polarization	228
6.1.3	General Relationships	229
6.2	Relaxatory Modes	236
6.2.1	Single-Time Relaxation Process	237
6.2.2	Retardation and Relaxation Time Spectra	242
6.3	Specific Relaxation Processes and Flow Behavior	245
6.3.1	Local Processes	246
6.3.2	Glass–Rubber Transition and Melt Flow	250
6.3.3	The Glass Transition Temperature	269
6.3.4	Relaxation in Partially Crystalline Systems	277
7	Conjugated Polymers	287
7.1	Electrooptic Activity	289
7.1.1	Excitons and Free Charges	289
7.1.2	Electroluminescence	297
7.2	Effects of Doping	302
7.2.1	Electrical Conductivity	302
7.2.2	Magnetism and Reflectivity	306
8	Microscopic Dynamics	313
8.1	The Fluctuation-Dissipation Theorem	313
8.2	The Rouse Model	317
8.2.1	Stress Relaxation	325
8.2.2	The Dielectric Normal Mode	330
8.3	Entanglement Effects in Polymer Melts	333
8.3.1	The Reptation Model	338
8.4	Solution Viscosities	343
8.4.1	Neutral Polymers: Hydrodynamic Interaction	344
8.4.2	Polyelectrolytes: Coulomb Interaction	352

9	Non-Linear Mechanics	357
9.1	Rubber Elasticity	361
9.1.1	The Fixed Junction Model of Ideal Rubbers	364
9.1.2	The Cauchy Strain Tensor	371
9.1.3	Finger's Constitutive Equation	376
9.2	Swelling of Neutral and Electrolytic Gels	384
9.3	Non-Newtonian Melt Flow	390
9.3.1	Rheological Material Functions	391
9.3.2	The Lodge Liquid	398
9.3.3	The Stress-Optical Rule	404
10	Deformation, Yielding and Fracture	415
10.1	Shear Deformation in Semicrystalline Polymers	418
10.1.1	Critical Strains	418
10.1.2	Constituents of the Drawing Stress	426
10.1.3	The Mechanics of Neck Formation	429
10.1.4	Fibrillar State of Order	435
10.2	Crazing	444
10.3	Brittle Fracture	450
10.3.1	Linear Fracture Mechanics	453
10.3.2	The Slow Mode of Crack Growth	455
A	Scattering Experiments	463
A.1	Fundamentals	463
A.1.1	Basic Equations	464
A.1.2	Time-Resolved Scattering Experiments	468
A.2	Absolute Intensities	471
A.3	Low Angle Scattering Properties	474
A.3.1	Guinier's Law	474
A.3.2	Forward Scattering	476
A.4	Special Polymer Systems	477
A.4.1	Binary Mixtures and Block Copolymers	477
A.4.2	Two-Phase Layer Systems	484
B	Glossary of Symbols	493
C	Bibliography	501
	References	505
	Index	511

Constitution and Architecture of Chains

Polymers, also known as **macromolecules**, are built up of a large number of molecular units that are linked together by covalent bonds. Usually they represent organic compounds, containing carbon atoms together with hydrogen, oxygen, nitrogen, and halogens, etc. In this first chapter, we briefly survey the main characteristics of their chemical constitution and molecular architecture and introduce the notions employed for their description, using examples for the explanation.

Let us begin with a look at polyethylene (PE), which has a particularly simple structure. It is depicted in Fig. 1.1. The chemical repeat unit or **monomeric unit** building up the chain is the CH_2 -(methylene)group and their number determines the **degree of polymerization**, denoted by the symbol N . Macromolecules are generally obtained by a polymerization process starting from reactive low molar mass compounds. The name ‘polyethylene’ indicates that here the process is usually based on ethylene. Figure 1.2 shows, as a second example, the chemical composition of another common polymer, that of polystyrene (PS). Here phenyl groups are attached as **sidegroups** to the C–C **backbone chain**. Table 1.1 presents a selection of further conventional polymers, giving the chemical constitution of the repeat units and commonly used short forms. The majority (from polypropylene to polycarbonate) has a flexible backbone set-up of carbon atoms, in some cases in combination with some heteroatoms. The four polymers following in the listing (poly(ether ether ketone) to polyimide) are examples for polymers with a stiff backbone.

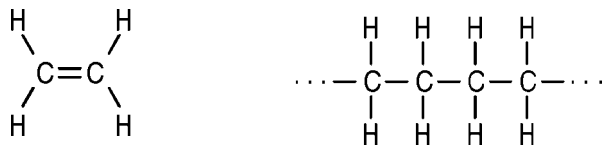


Fig. 1.1. Ethylene and polyethylene

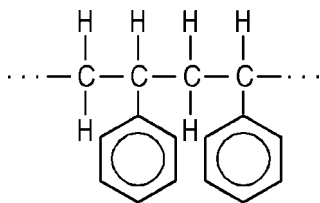


Fig. 1.2. Polystyrene

Rather than being carbon-based, the backbone chain can also be composed of silicon atoms, again together with other elements. The last two materials, poly(dimethylsiloxan) and poly(tetramethyl-p-silphenylene-siloxane) are corresponding examples.

All these polymers are electrically neutral. If chains are built up of monomers that contain an ionizable group, i.e., a group that can dissociate into a chain-fixed kation or anion and a mobile counter-ion bearing the opposite charge, a **polyelectrolyte** is obtained. Table 1.2 collects a few typical examples. The first three compounds are synthetic polymers, the other two samples are biopolymers; cellulose and starch in the form of derivatives which include ionizable substitutes.

Charges on a chain can also be created by doping processes. For **conjugated polymers**, i.e., chains with conjugated C–C double bonds, this is particularly easy. Even more importantly, the produced charges are mobile and thus provide electrical conductivity. Table 1.3 compiles some of these special materials.

Rather than leading to polymers with a unique degree of polymerization, reactions usually result in a mixture of macromolecules with various molar masses. Therefore, for a full characterization, the **molar mass distribution** function has to be determined, and this is usually accomplished by gel permeation chromatography. We choose the symbol M for the molar mass and introduce the distribution function $p(M)$ as a number density, adopting the definition that the product

$$p(M) dM$$

gives the fraction of polymers with molar masses in the range from M to $M + dM$. As a distribution function $p(M)$ must be normalized

$$\int_0^{\infty} p(M) dM = 1 . \quad (1.1)$$

The average molar mass follows by

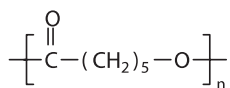
$$\overline{M}_n = \int_0^{\infty} p(M) M dM . \quad (1.2)$$

Table 1.1. A selection of conventional polymers

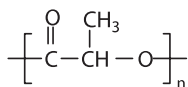
$\left[\text{CH}_2 - \underset{\text{CH}_3}{\text{CH}} \right]_n$	polypropylene PP
$\left[\text{CH}_2 - \underset{\text{CH}_3}{\overset{\text{CH}_3}{\text{C}}} \right]_n$	polyisobutylene PIB
$\left[\text{CH}_2 - \underset{\text{CH}_3}{\overset{\text{O}}{\parallel} \text{C} - \text{O} - \text{CH}_3} \right]_n$	poly(methylmethacrylate) PMMA
$\left[\text{CH}_2 - \underset{\text{H}}{\overset{\text{O} - \overset{\text{O}}{\parallel} \text{C} - \text{CH}_3}{\text{C}}} \right]_n$	poly(vinylacetate) PVAc
$\left[\text{CH}_2 - \underset{\text{O} - \text{CH}_3}{\text{CH}} \right]_n$	poly(vinylmethylether) PVME
$\left[\text{CH} = \text{CH} - \text{CH}_2 - \text{CH}_2 \right]_n$	polybutadiene PB
$\left[\underset{\text{CH}_3}{\text{C}} = \text{CH} - \text{CH}_2 - \text{CH}_2 \right]_n$	polyisoprene PI
$\left[\text{CH}_2 - \underset{\text{H}}{\overset{\text{Cl}}{\text{C}}} \right]_n$	poly(vinyl chloride) PVC

Table 1.1. A selection of conventional polymers (continued)

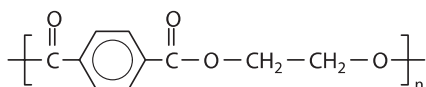
$\left[\text{CH}_2 - \underset{\text{Cl}}{\overset{\text{Cl}}{\text{C}}} \right]_n$	poly(vinylidene chloride) PVDC
$\left[\text{CH}_2 - \underset{\text{F}}{\overset{\text{F}}{\text{C}}} \right]_n$	poly(vinylidene fluoride) PVDF
$\left[\text{CF}_2 - \text{CF}_2 \right]_n$	poly(tetrafluoroethylene) PTFE
$\left[\underset{\text{CN}}{\text{CH}} - \text{CH}_2 \right]_n$	poly(acrylonitrile) PAN
$\left[\text{O} - \text{CH}_2 \right]_n$	poly(oxymethylene) POM
$\left[\text{O} - (\text{CH}_2)_2 \right]_n$	poly(ethyleneoxide) PEO
$\left[\underset{\text{H}}{\text{N}} - (\text{CH}_2)_6 - \underset{\text{H}}{\text{N}} - \overset{\text{O}}{\parallel} \text{C} - (\text{CH}_2)_4 - \overset{\text{O}}{\parallel} \text{C} \right]_n$	poly(hexamethylene adipamide) nylon 6,6
$\left[\overset{\text{O}}{\parallel} \text{C} - (\text{CH}_2)_5 - \underset{\text{H}}{\text{N}} \right]_n$	poly(ϵ -caprolactam) nylon 6
$\left[\text{CH}_2 - \underset{\text{C}_6\text{H}_5}{\overset{\text{CH}_3}{\text{C}}} \right]_n$	poly(α -methylstyrene)
$\left[\text{O} - \text{C}_6\text{H}_4 \right]_n$	poly(α -phenylene oxide) PPO

Table 1.1. A selection of conventional polymers (continued)

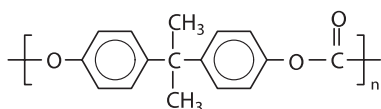
poly(ϵ -caprolactone)
P ϵ CL



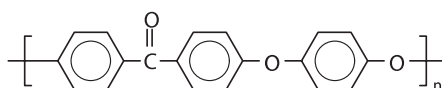
poly(L-lactic acid)
PLLA



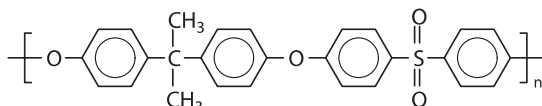
poly(ethylene terephthalate)
PET



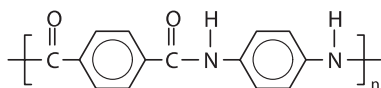
polycarbonate
PC



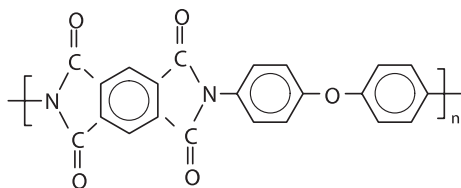
poly(ether ether ketone)
PEEK



polysulfone
PSF



poly(p-phenylene-
terephthalamide)
Kevlar



polyimide

Table 1.1. A selection of conventional polymers (continued)

$\left[\begin{array}{c} \text{CH}_3 \\ \\ \text{---Si---O---} \\ \\ \text{CH}_3 \end{array} \right]_n$	poly(dimethylsiloxan) PDMS
$\left[\begin{array}{c} \text{CH}_3 \\ \\ \text{---Si---} \\ \\ \text{CH}_3 \end{array} \text{---} \text{C}_6\text{H}_4 \text{---} \begin{array}{c} \text{CH}_3 \\ \\ \text{---Si---O---} \\ \\ \text{CH}_3 \end{array} \right]_n$	poly(tetramethyl-p-silphenylene-siloxane) TMPS

In this description, we treat M as a continuous variable although, strictly speaking, M changes in discrete steps, corresponding to the molar mass of the monomer. For the normally given high degrees of polymerization, this discrete character does not become apparent and can be ignored.

Instead of using the **number average** \overline{M}_n , the **weight average** of the molar mass, \overline{M}_w , may also be employed. \overline{M}_w is given by

$$\overline{M}_w = \frac{\int_0^{\infty} p(M)M \cdot M \, dM}{\int_0^{\infty} p(M)M \, dM} . \quad (1.3)$$

The origin of Eq. (1.3) is obvious. Just recognize that the function

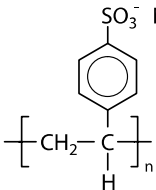
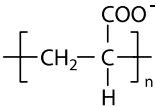
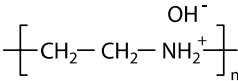
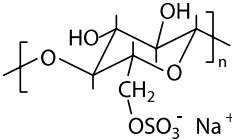
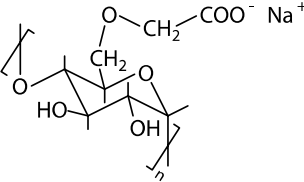
$$p'(M) = \frac{pM}{\int_0^{\infty} p(M)M \, dM} \quad (1.4)$$

describes the molar mass distribution in terms of weight fractions.

For molar mass distributions with a finite width \overline{M}_w is always larger than \overline{M}_n . The ratio of the two mean values is used to specify the width of the distribution. One introduces the **polydispersity coefficient** U defined as

$$U = \frac{\overline{M}_w}{\overline{M}_n} - 1 . \quad (1.5)$$

Table 1.2. A selection of polyelectrolytes

	<p>sodium poly(styrene sulfonate) NaPSS</p>
	<p>poly(acrylic acid) PAA</p>
	<p>poly(ethylene imine)</p>
	<p>sodium cellulose sulfate</p>
	<p>sodium carboxymethyl amylose</p>

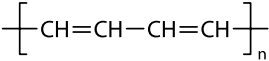
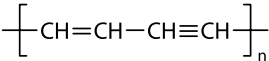
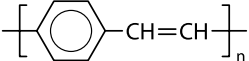

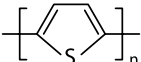
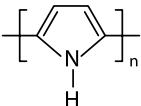
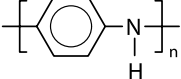
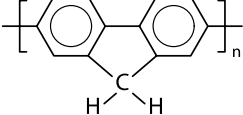
U does indeed measure the polydispersity, as it can be directly related to the variance of $p(M)$. We have

$$\begin{aligned}
 \langle \Delta M^2 \rangle &= \int_0^{\infty} p(M)(M - \overline{M}_n)^2 dM \\
 &= \int_0^{\infty} p(M)M^2 dM - \overline{M}_n^2
 \end{aligned}
 \tag{1.6}$$

or, according to Eq. (1.3),

$$\langle \Delta M^2 \rangle = \overline{M}_w \cdot \overline{M}_n - \overline{M}_n^2
 \tag{1.7}$$

Table 1.3. A selection of conjugated polymers

	polyacetylene PAC
	polydiacetylene PdAc
	poly(p-phenylenevinylene) PPhV
	poly(p-phenylene) PPh
	polythiophene PTh
	polypyrrole PPy
	polyaniline PAn
	polyfluorene

and therefore

$$\frac{\langle \Delta M^2 \rangle}{\overline{M}_n^2} = U . \quad (1.8)$$

U becomes zero only for a perfectly **monodisperse** sample, i.e., a sample with a uniform molar mass.

Molar mass distributions may vary greatly between different polymeric compounds. Distributions depend on the method of synthesis used in the polymerization process, and most methods belong to either of two general classes. In the first class of processes, known as **step polymerizations**, monomers react in such a way that groups are already linked together can be coupled

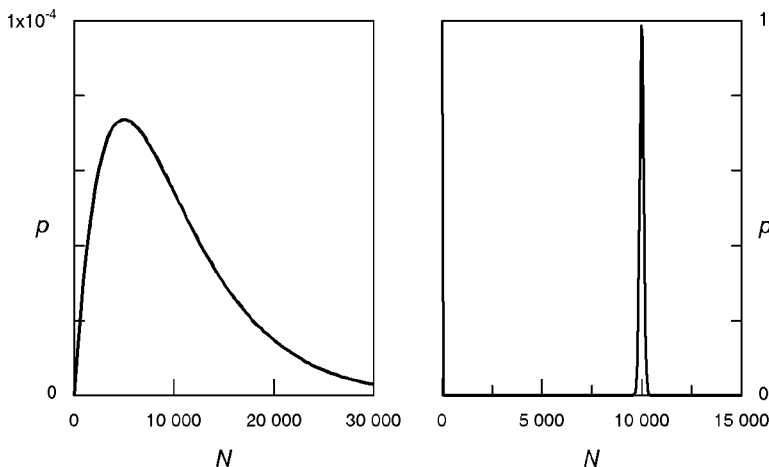


Fig. 1.3. Molar mass distributions of the Schulz–Zimm type for $\beta = 2$ (*left*) and of the Poisson type (*right*). Both correspond to the same number average degree of polymerization, $\bar{N}_n = 10^4$

with other groups. In the second class, called **chain polymerizations**, reactive centers that react only with monomers are created at the beginning and become shifted after the reaction to the new end of the chain, thus growing. Figure 1.3 shows, in an idealized form, distribution functions resulting from the two different synthetic routes. For step polymerizations, distributions are broad, and a good representation is often achieved by the **Schulz–Zimm distribution**. The latter is usually formulated in terms of the degree of polymerization rather than the molar mass and is given by the equation

$$p(N) = \frac{1}{\Gamma(\beta)} \left(\frac{\beta}{\bar{N}_n} \right)^\beta N^{\beta-1} \exp - \frac{\beta N}{\bar{N}_n}. \quad (1.9)$$

The function includes two parameters: β determines the shape and \bar{N}_n denotes the number average of the degree of polymerization; Γ is the gamma function. A straightforward evaluation shows that the polydispersity index U is given by

$$U = \frac{1}{\beta}.$$

Choosing β values of about two, Eq. (1.9) provides a good data fit in many practical cases.

Much narrower distributions can be obtained for chain polymerizations. Typical here is a Poisson distribution, given by

$$p(N) = \exp(-\bar{N}_n) \frac{(\bar{N}_n)^N}{\Gamma(N+1)} \approx \exp(-\bar{N}_n) \left(\frac{\bar{N}_n e}{N} \right)^N. \quad (1.10)$$

As only one parameter, \overline{N}_n , is included, U is no longer an independent variable. A straightforward calculation yields

$$U = \frac{1}{\overline{N}_n} . \quad (1.11)$$

The two distribution functions are presented in Fig. 1.3, choosing $\beta = 2$ for the Schulz-Zimm distribution and equal values of $\overline{N}_n (= 10^4)$ in both cases.

Properties of polymer systems are generally affected by the shape of $p(M)$. This dependence is of considerable technical importance, and variations of $p(M)$ may often be used to improve and optimize the performance of materials. These are specific questions, and in the following we shall mostly omit a discussion of them. For the sake of simplicity, sharp molar mass distributions will always be assumed, i.e., distributions like the one shown on the right-hand side of Fig. 1.3. The degree of polymerization, N , then becomes a well-defined quantity.

Coupling of the units in polyethylene is unambiguous. For polystyrene, however, this is no longer the case, because styrene is composed of two different groups, CH_2 and C_7H_6 . In principle, either group can be attached to the growing chain, but the energetically disfavored ‘head-to-head’ and ‘tail-to-tail’ couplings are, in fact, rare. Much more important is the choice in the possible placements of the phenyl group on either side of the C–C backbone. Variations may result in steric disorder along the chain. The notion used to describe steric order is **tacticity**. Polymers with a unique way of coupling the monomeric units are called **isotactic** and contrasted to those with an irregular steric structure, which are addressed as **atactic**. If the coupling varies, in a regular way, polymer chains are called **syndiotactic**. All three types are found for polystyrene, depending on the process chosen for the synthesis.

Polyethylene and polystyrene are built up of one type of monomeric unit only. This is not a necessity, and large variations in the chemical structure may be achieved by a combination of different monomers. The procedure is known as **copolymerization**. To give an example: Ethylene and propylene monomers can be copolymerized, which leads to ‘ethylene-propylene copolymers’. For the coupling of the two monomeric units in the chain two limiting cases exist. In the first, the coupling is statistical and determined by the probabilities of attachment of the two monomers on a growing chain. Chains of this type are called **statistical copolymers**. They can exhibit a short-range order with preferred sequences, and thus are different from a random mixing, but possess no order in the chemical composition over the long range. The second limiting case are **block copolymers**. These are obtained by coupling long macromolecular sequences of uniform composition, and depending on the number of sequences, di-, tri- or multiblock copolymers may be prepared. The structures of the two types are sketched in Fig. 1.4 with the ethylene-propylene system as an example.

The chains discussed so far all have a linear topology. There exists a large group of polymers with a different architecture and some of their typical forms

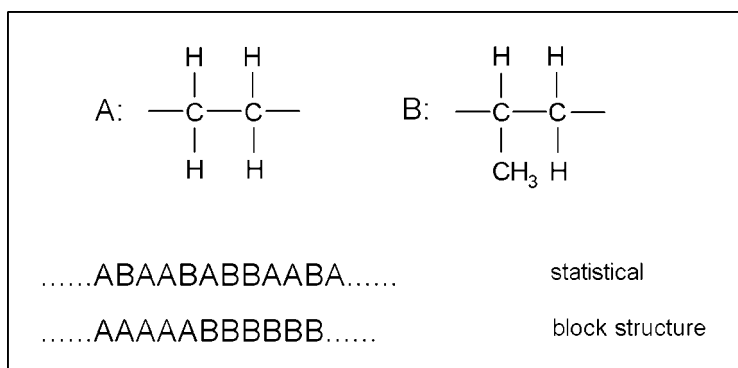


Fig. 1.4. Ethylene-propylene copolymers

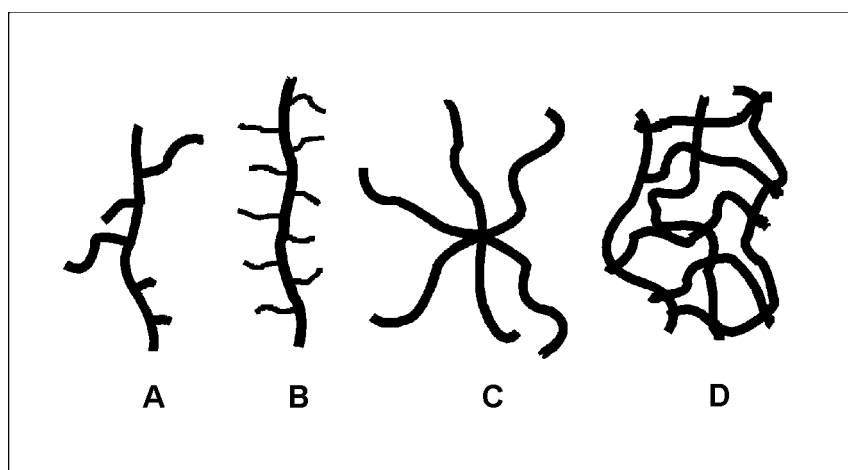


Fig. 1.5. Polymers with non-linear architectures: Polymer with short-chain and long-chain branches (A), polymer with grafted oligomer side chains (B), star polymer (C), network of cross-linked chains (D)

are sketched in Fig. 1.5. For example, a polymer may include **short-chain and long-chain branches** in a statistical distribution. A well-known representative of this architecture is ‘low density polyethylene’, which, as a result of the polymerization process, incorporates alkyl-branches of different length in a random fashion. Typical values for the branching ratio, i.e., the fraction of branched units, are of the order of several percent. If more extended **oligomer** chains are attached to a backbone chain with different composition, **grafted-chain** polymers are obtained. A quite exotic species are **star polymers**, where several polymer chains emanate from one common multifunctional center.

A qualitative change in properties is achieved by coupling all the polymer chains of a sample together, thereby building up a three-dimensional **network**. This is the basic structure of **rubbers**. In fact, a rubber represents one huge macromolecule of macroscopic dimensions, with properties depending on the cross-link density and the functionality of the junction units.

Finally, at the end of this short first chapter, let us briefly recall the manifold uses of polymers in daily life. First there are the solid polymeric materials in various forms, ‘commodity polymers’ for widespread applications, as well as speciality polymers for specific utilizations. In industry these are called **thermoplasts**, which expresses that they can be shaped and brought into forms of choice by thermomechanical treatments at elevated temperatures. The price to be paid for the advantage of using comparatively simple processing techniques is the temperature range limitation, which contrasts with the much larger application range of ceramics and metals. **Polymer fibers** comprise a second large class of materials and are mostly used for the production of textiles and woven products. Fibers are generally obtained by spinning processes carried out on the melt or concentrated solutions at elevated temperatures, which is followed by a fixing accomplished by rapid cooling. Again, the temperature range for uses is limited. If a fiber is heated to a too high temperature it shrinks. Rubbers, technically addressed as **elastomers**, constitute the third class of polymeric materials. Both synthetic and natural products are utilized. The essential step in rubber production is the cross-linking process. ‘Natural rubber’, for example, is obtained by heating cis-polyisoprene in the presence of sulfur. This **vulcanization process** creates cross-links between the polyisoprene chains, composed of short sequences of sulfur atoms. For high cross-link densities the large deformability characteristic of a rubber is lost, and one obtains stiff solids. This is known as the class of **duromers** or **thermosets**, also known as **resins**. Various adhesives based on the mixing of two reacting components belong to this class of polymers. The shapes of these compounds are rather stable and remain unaffected by heating, up to the point of chemical decomposition. Polyelectrolytes are also broadly used. The well-known **superabsorbers** are able to take up and bind large amounts of water after cross-linking. Conjugated polymers have been increasingly employed quite recently in technical applications such as **displays**, where they serve as active elements in light emitting diodes.

With the exception of natural rubber, cellulose and starch, all the above-mentioned polymers are synthetic products. Although this book deals with the properties of synthetic materials only, we have to be aware of the decisive role played by polymers in nature. The control of life processes is based on two polymer species, nucleic acids and proteins. The specific property of these polymers is that they form stable microscopic objects, mainly as the result of the action of intramolecular hydrogen bonds. The stable, specifically ordered surface of the proteins provides the high selectivity and catalytic potential used in biochemical reactions; selectivity and catalytic activity disappear when the globular molecular shape is destroyed at elevated temperatures or upon the

addition of an active chemical agent. The synthetic polymers discussed in this book do not possess the potential to form a unique molecular conformation as single chains and, therefore, do not show any biochemical activity.

The large variability in the chemical constitution and architecture of macromolecules opens a broad route to the preparation of materials with a wide spectrum of different properties. Chemistry, however, is not the only factor responsible for the actual behavior. It is a specific feature of polymers that one finds a particularly strong impact of the thermomechanical processes experienced during manufacture since these control the final formation of structures. An understanding of these processes is a necessary prerequisite for a successful utilization of polymers, and the promotion of knowledge to levels as high as possible therefore constitutes one of the main aims of polymer physics.

Further Reading

- F.W. Billmeyer: *Textbook on Polymer Science*, John Wiley & Sons, 1984
J.M.G. Cowie: *Polymers: Chemistry and Physics of Modern Materials*, CRC Press, 1991
P.J. Flory: *Principles of Polymer Chemistry*, Cornell University Press, 1953
P. Munk: *Introduction to Macromolecular Science*, John Wiley & Sons, 1989

Single Chain Conformations

Condensed matter is composed of strongly interacting molecules, and discussions of the bulk properties of low molar mass compounds therefore focus from the beginning on the role of the interaction forces between different molecules in establishing thermal equilibrium. In dealing with polymeric systems, one encounters a different situation. As each macromolecule possesses a huge number of internal degrees of freedom, the analysis of the properties of the individual polymer becomes an important first point of concern. It is obvious that the understanding of single chain behavior is a necessary prerequisite for treatments of aggregate properties, but in fact, it implies even more and in many cases leads to a major step forward. There are, of course, phenomena that are dominated by intermolecular forces, such as the phase behavior of binary polymer mixtures, the structures in polyelectrolyte solutions, or the flow properties of polymer melts. However, other important phenomena, in particular essential parts of the viscoelasticity, are much under the control of the dynamic properties of the individual molecules. It is therefore quite natural and also necessary to start an introduction into polymer physics with a discussion of the conformational states of single chains.

2.1 Rotational Isomeric States

Let us choose polyethylene as an example and consider its full steric structure. The latter is shown in Fig. 2.1. A polymer chain like polyethylene possesses a great internal flexibility and is able to change its conformation totally. Basically, the number of degrees of freedom of the chain is given by three times the number of atoms, but it is convenient to split them up into two different groups. A first group concerns changes in valence angles and bond lengths, because they occur during molecular vibrations with frequencies in the infrared range. These movements are limited and do not affect the overall form of the chain. The second group of motions is of a different character, in that they have the potential to alter the form. These are the rotations about the

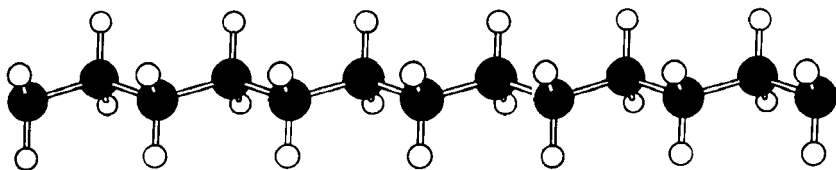


Fig. 2.1. The steric structure of PE. Rotations about the C–C bonds result in a change in the conformation

C–C bonds, which can convert the stretched chain of Fig. 2.1 into a coil and accomplish the transitions between all the different conformational states.

Clearly, in dealing with the conformational properties of a given polymer, only the latter group of degrees of freedom has to be considered. A discussion of the conformational states of a given macromolecule therefore first of all requires an analysis of the **bond rotation potentials**.

To begin with, we first go back to a related low molar mass molecule and consider the rotational potential of ethane. Here a rotation about the central C–C bond is possible, and one can anticipate the general form of the rotational potential. Interaction energies may be described as a superposition of a part that directly relates to the **rotational state** of the C–C bond and **non-bonded interactions** between the hydrogen atoms. The latter are for the given distances of repulsive nature. Figure 2.2 will help us to describe the situation. The staggered conformation of ethane, shown at the bottom on the right, corresponds to the minimum in the potential energy since it is associated with the largest distances between the hydrogens. Owing to the three-fold symmetry of the two methyl groups, the rotational potential $\tilde{u}(\varphi)$ (φ denotes the rotation angle) exhibits a 120° -periodicity. Therefore, in a first approximation, employing only the lowest order Fourier contribution, it can be described by

$$\tilde{u} = \tilde{u}_0(1 - \cos(3\varphi)) . \quad (2.1)$$

This rotational potential is indicated in the figure by the broken line and shows three energy minima with equal potential energies.

Next, we consider the rotational potential of butane. The replacement of one hydrogen atom by a methyl group for both carbon atoms removes the three-fold symmetry. As a consequence, the potential energy function $\tilde{u}(\varphi)$ gets a shape like that indicated by the continuous curve in Fig. 2.2. The minimum occurs for the staggered conformation depicted in the upper part on the right, where the distance between the two methyl groups is at the maximum. There still exist local minima in the potential energy at 120° and 240° , but now at an elevated level. The maximum of $\tilde{u}(\varphi)$ is expected for 180° , when the two methyl groups closely approach each other.

Particular terms are used to address the three energy minima. The conformational state with the lowest energy at $\varphi = 0^\circ$ is called the **trans**-conformation. The other two minima at 120° and 240° are called **gauche** and

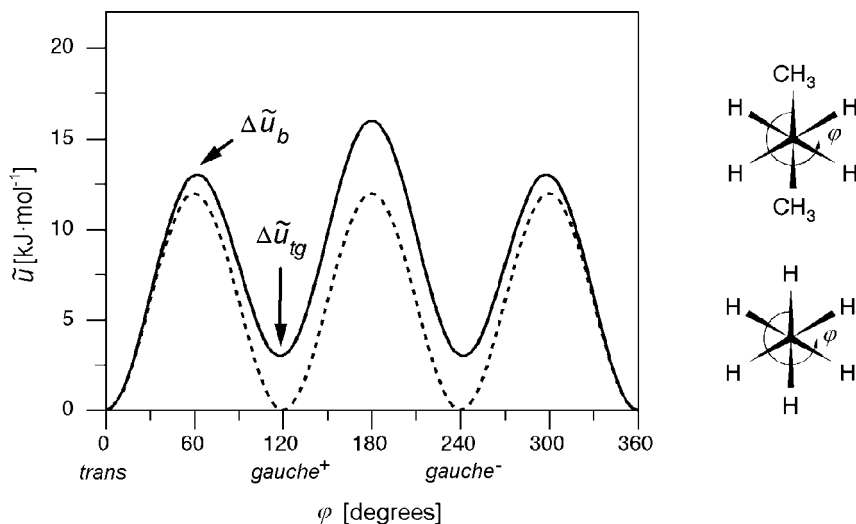


Fig. 2.2. Potential energies associated with the rotation of the central C–C bond for ethane (*broken line*) and butane (*continuous line*). The *sketches* show the two molecules in views along the C–C bond

are distinguished by adding a plus or minus sign. Note that in the trans-state the three C–C bonds of butane lie in one plane; the gauche-states are non-planar.

The internal dynamics of butane depends on the energy difference $\Delta\tilde{u}_{tg}$ between the trans-state and the gauche-state and the height of the barriers, $\Delta\tilde{u}_b$, between the local minima. One can envisage two limiting cases. For $\tilde{R}T \gg \Delta\tilde{u}_b$ (the symbol \tilde{R} stands for the perfect gas constant) rotations about the C–C bonds are quasi-free, and the details of $\tilde{u}(\varphi)$ with its minima and maxima become irrelevant. In the opposite case, $\tilde{R}T \ll \Delta\tilde{u}_{tg}$, the molecules settle down in the lowest energy state, i.e., in the trans-conformation, and only librate about the equilibrium position.

The prerequisite in order to be able to judge the actual situation, say at ambient temperature, is therefore a knowledge of the two energy differences $\Delta\tilde{u}_{tg}$ and $\Delta\tilde{u}_b$. These can be determined by spectroscopic and calorimetric experiments. $\Delta\tilde{u}_{tg}$ can be derived from temperature-dependent Raman scattering experiments, due to the vibrational spectra for the trans-state and the gauche-state being different. One selects two bands associated with the gauche-conformation or the trans-conformation, respectively, and measures their intensities, I_g and I_t , as a function of temperature. The ratio I_g/I_t changes with the populations of the two states, according to

$$\frac{I_g}{I_t} \propto \exp - \frac{\Delta\tilde{u}_{tg}}{\tilde{R}T} . \quad (2.2)$$

An Arrhenius plot of $\ln(I_g/I_t)$ versus $1/T$ thus yields $\Delta\tilde{u}_{tg}$. Experiments were performed on different n -alkanes and gave values in the range

$$\Delta\tilde{u}_{tg} \simeq 2-3 \text{ kJ mol}^{-1} .$$

The fraction ϕ_g of molecules in the two gauche-states follows from

$$\phi_g = \frac{2 \exp(-\Delta\tilde{u}_{tg}/\tilde{R}T)}{1 + 2 \exp(-\Delta\tilde{u}_{tg}/\tilde{R}T)} , \quad (2.3)$$

which leads to

$$\phi_g \simeq 0.5 .$$

Hence, trans-states and gauche-states are populated with similar probabilities.

The barrier height $\Delta\tilde{u}_b$ can be deduced, for example, from measurements of the heat capacity of ethane. It turns out that data can only be described if the internal degree of freedom associated with the C-C bond rotation is accounted for, in addition to the translational and rotational degrees of freedom of the whole molecule. A fit of the data yields $\Delta\tilde{u}_b$, with the result

$$\Delta\tilde{u}_b \simeq 12 \text{ kJ mol}^{-1} .$$

This is the barrier height for ethane. For butane, one expects somewhat larger values.

Looking at these results, we conclude that

$$\Delta\tilde{u}_b \gg \tilde{R}T \simeq \Delta\tilde{u}_{tg} .$$

Under these conditions, the internal dynamics of the butane molecule may be envisaged as follows. Most of the time, the molecule is in one of the three conformational states and just vibrates about the respective energy minimum. From time to time, the molecule collects sufficient thermal energy so that the barrier can be passed over and the conformation changes. As the transitions take place rapidly compared to the time of staying near a minimum, a sample of butane resembles a mixture of different rotational isomers. For each molecule there exist three **rotational isomeric states**. They are all accessible and populated according to the available thermal energy.

We now turn to polyethylene and discuss its case by starting from butane considering the effect of a replacement of the two methyl endgroups by longer chain sequences. The result is qualitatively clear. One expects modifications in the details of $\tilde{u}(\varphi)$, which also depend on the conformations of the two sequences. However, the overall form of the rotational potential energy of a given C-C bond will remain unchanged. There still exists an energy minimum for the trans-conformation and local minima for two gauche-states. Also the values of $\Delta\tilde{u}_{tg}$ and $\Delta\tilde{u}_b$ do not alter significantly. We may thus conclude that the conformation of polyethylene can again be described in terms

of rotational isomeric states and that there are still three rotational isomeric states per bond, corresponding to *trans*, *gauche*⁺ and *gauche*⁻. A polyethylene chain with a degree of polymerization N therefore possesses 3^N different conformational states. In order to address one specific conformation, the rotational isomeric states for all bonds have to be given. This may be done, for example, in the form

$$(\varphi_1, \varphi_2, \dots, \varphi_N), \quad (2.4)$$

whereby $\varphi_i \hat{=}$ *trans*, *gauche*⁺ or *gauche*⁻.

Two different situations are found in polymer systems and shall be dealt with separately. In the crystalline state, chains adopt unique conformations that represent helices with a straight axis. In the fluid state, on the other hand, all rotational isomeric states are populated, with probabilities determined by the temperature and the respective energies.

2.2 Helices

Polymers can form crystals, not like low molar mass substances under all circumstances, but for many species under the prerequisite that the cooling from the molten state occurs slowly enough to enable the necessary rearrangements of the chains. The building principle is obvious. As a basic requirement, chains must adopt a straight, perfectly ordered form. Then a lattice can be constructed by orienting the chains uniformly in one direction and packing them laterally in a regular manner. The thus-obtained lattice with three-dimensional order has the monomeric units as structure units. The specific property is the strong anisotropy in the binding forces, with valence forces in one direction and weak van der Waals forces in the two other directions.

Crystal lattices at low temperatures generally represent the structure with the minimum internal energy. For polymer crystals one expects that the main contribution be furnished by the intramolecular energies as determined by the bond rotations. Structure determinations in combination with energetic calculations, which have been carried out for several polymers, do indeed support this view. They indicate that the conformation adopted by a polymer in the crystalline phase equals, or comes very close to, the lowest energy rotational isomeric state of the single chain. Conditions are simple if the coupling between successive bonds is only weak. Then rotations take place independently and each bond settles down in the energy minimum.

To have equal conformations in all monomeric units is of course not a peculiarity of chains with independent bonds. In the general case, in the lowest energy state of a chain one also finds a uniform conformation of the monomers. What is the general structure that then emerges? It is important to recognize that this is of the helical type. To see and to illustrate this, we consider some examples.

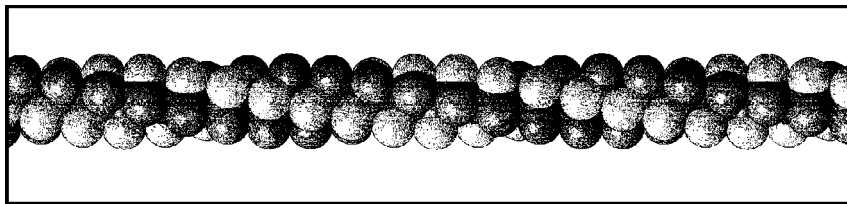


Fig. 2.3. PTFE in the crystalline state. The conformation corresponds to a 13/6-helix

We begin with polyethylene. Here, in order to have the energy minimum, all C–C bonds must be in the trans-state. Crystalline polyethylene thus adopts the **all-trans**-conformation, which is the structure shown in Fig. 2.1.

While polyethylene with its planar zig-zag structure is not a helix in the usual sense, poly(tetrafluoroethylene) (PTFE) in the crystalline state possesses the typical wound appearance. This chain is shown in Fig. 2.3. Poly(tetrafluoroethylene) is obtained from polyethylene by a replacement of all hydrogen atoms by fluorines. The reason for the resulting structure change is easy to see. The replacement of hydrogen atoms by the much larger fluorines increases the interaction energy between the CF_2 groups of second nearest neighbors. When we start off from an all-trans-form, a uniform twist of the chain diminishes the repulsive F–F interaction energies but, at the same time, the bond rotational energy increases. There exists an energy minimum at a finite torsion angle, $\varphi_{\min} = 16.5^\circ$.

Figure 2.4a presents as a further example a helix of poly(oxymethylene) (POM). It corresponds to an **all-gauche**-conformation. Different from poly(tetrafluoroethylene), here a trans-rotational isomeric state also exists, but it does not represent the energy minimum.

For some polymers, one does not observe a unique helical form but two or three different ones that possess very similar energies. Poly(oxymethylene) actually gives an example for such a **polymorphism**. Here one can also find the helix shown in Fig. 2.4b. It also represents an all-gauche-conformation, but the torsion angle, which was near 60° for the first modification, has now increased to 77° . Which of the two helices is formed depends on the crystallization conditions. In principle, at a given temperature, only one of the modifications can be stable, the other one being metastable. Annealing can induce a transformation to the stable state, but often this transformation is kinetically hindered, and then it may become difficult to identify the stable modification.

For the description of a given helix, we have a natural basis. One refers to the screw symmetry and just specifies the screw operation that maps the molecule onto itself. Screw operations comprise a turn about a certain angle, say $\Delta\zeta$, together with a simultaneous longitudinal shift, say Δz . These two values that describe the move from one monomer unit to the adjacent one constitute the **external helix parameters**. For polyethylene we have $\Delta\zeta =$

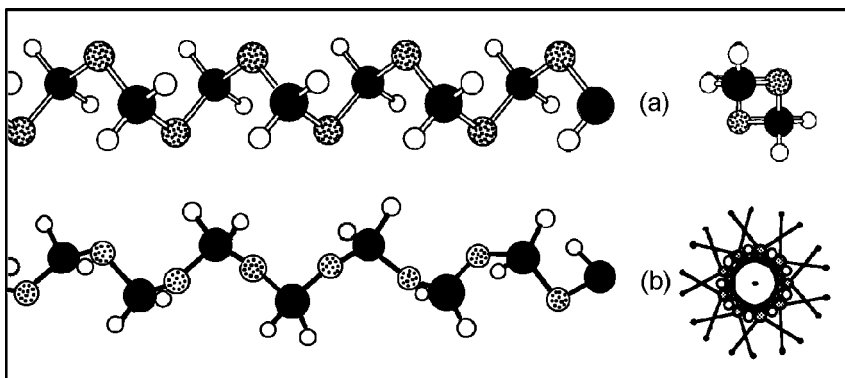


Fig. 2.4. Two different helices formed by POM: 2/1-helix (a) and 9/5-helix (b). Side views (*left*) and views along the helix axis (*right*)

180° and $\Delta z = 1.27 \text{ \AA}$, for poly(tetrafluoroethylene) $\Delta\zeta = 166^\circ$ and $\Delta z = 1.31 \text{ \AA}$, for the two polymorphic forms of poly(oxyethylene) $\Delta\zeta = 180^\circ$, $\Delta z = 1.78 \text{ \AA}$ and $\Delta\zeta = 200^\circ$, $\Delta z = 1.93 \text{ \AA}$, respectively. The external helix parameters are functions of the **internal helix parameters**, the latter being given by the bond rotational angles. The dependencies may be formulated on the basis of geometrical considerations, assuming constant values for both bond lengths and valence angles.

Several polymers form helices that are simple in the sense that $\Delta\zeta$ is a fraction of 360° , like 180° , 120° or 90° . These are called $m/1$ -helices, m giving the number of monomeric units arranged along one 360° -turn. Examples are polypropylene, polystyrene or poly-1-butene, which all form 3/1-helices. The all-trans-conformation of polyethylene and the all-gauche-conformation of poly(oxyethylene) correspond to 2/1-helices. The next general helical form is given by the m/n -helices. The name is meant to indicate that m monomeric units are equally distributed over n turns.

Particularly interesting is the observation that polymers with $n > 1$ often cannot be described as an m/n -helix with m and n being small numbers. Poly(tetrafluoroethylene) and the second form of poly(oxyethylene) represent such examples. The helix of poly(tetrafluoroethylene) is usually called a 13/6-helix, thereby indicating that 13 CF_2 units are distributed over six turns. This results in the measured value of $\Delta\zeta$ as

$$360^\circ \cdot 6 : 13 = 166^\circ .$$

Likewise, the second modification of poly(oxyethylene) also requires a non-simple notation for the description of the conformation, namely that of a 9/5-helix. If we recall the reason for the winding of chains, these results are not surprising. The helix conformation represents the minimum of the intramolecular energy and this may arise as a result of competing forces. The internal

helix parameters thus determined do not always have to be associated with a simple external helical structure.

Interestingly enough, measurements with higher accuracy showed that even the descriptions of the poly(tetrafluoroethylene) chain as a 13/6-helix and of the poly(oxymethylene) chain as a 9/5-helix are only approximations. Refinements of data necessitated a change in the characteristic ratio m/n towards higher numbers. In the case of poly(tetrafluoroethylene), the evaluation of electron diffraction data indicated a 473/219-helix. What does this mean? Indeed, these observations can be understood as indicating a qualitative structural change. Rather than accepting helix descriptions with large numbers n and m as representing exact structures, it might be more appropriate to assume that these helices possess no strict periodicity at all. This would mean that poly(tetrafluoroethylene) and poly(oxymethylene), in the crystalline state, both form **irrational helices**. As a consequence, the lattice lacks periodicity in one direction. We rather find, in the chain direction, two independent length scales, as given by the height Δz per monomeric unit and the height of one 360° -turn, respectively. Structures like this are generally addressed as **incommensurate**. They are also found in non-polymeric materials such as, for example, certain anorganic ferromagnetic compounds, where the positional and the magnetic order show different periodicities.

2.3 Coils

The huge number of rotational isomeric states that a polymer chain may adopt becomes effective in fluid phases. Polymers in solution or the melt change between the different states, and these are populated according to the laws of Boltzmann statistics. Because the large majority of conformations are coil-like, it is said that polymers in the fluid state represent **random coils**.

At first, one might think that any treatment of the properties of a polymer has to emanate from its microscopic chemical structure, since this determines the rotational isomeric states. One would then have to consider in detail the effects of bond lengths, bond angles, rotational potentials, the presence and length of sidegroups, etc. Treatments of this kind are necessarily specific and vary between different compounds. It is now a most important fact that one can omit the consideration of all these structural details in many discussions. Indeed, the dependence on the chemical constitution vanishes if structural properties are discussed for a lowered resolution, corresponding to length scales in the order of some nanometers. In such a coarse-grained picture, polymer chains become equivalent to each other and then also exhibit a common behavior.

Figure 2.5 shows a polymer coil as it might look like at limited resolution. We would observe a bent chain with a continuous appearance.

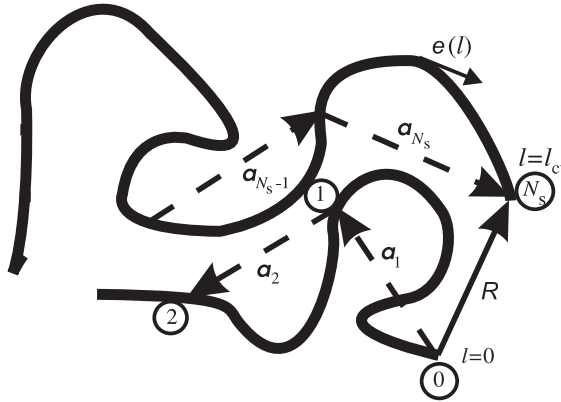


Fig. 2.5. Polymer chain in low resolution (contour length l_{ct} , local chain direction $\mathbf{e}(l)$) together with an associated chain of N_s freely jointed segments, connecting the junction points 0 to N_s

For its representation, we choose a curvilinear coordinate l , running from $l = 0$ at one end to $l = l_{\text{ct}}$ at the other end and describe the varying local chain direction by unit vectors $\mathbf{e}(l)$.

What can be said about such a chain? A first point of interest is the internal chain flexibility. Chains may be stiff, i.e., oppose strong bending, or also highly flexible, thus facilitating coiling. In searching for a parameter that provides a measure for the chain flexibility we can start from the **orientational correlation function**. This function, denoted K_{or} , describes the correlation between the chain directions at two points with a curvilinear distance Δl . It is defined as

$$K_{\text{or}}(\Delta l) = \langle \mathbf{e}(l) \mathbf{e}(l + \Delta l) \rangle. \quad (2.5)$$

Here and in the following, the brackets indicate an ensemble average that includes all chain conformations with their statistical weights. For homopolymers, K_{or} is independent of the position l , and we restrict our attention to this case. Figure 2.6 shows the general shape expected for K_{or} . Owing to the flexibility of the chain, orientational correlations must vanish for sufficiently large distances Δl . Therefore, K_{or} tends asymptotically to zero

$$K_{\text{or}}(\Delta l \rightarrow \infty) \rightarrow \langle \mathbf{e}(l) \rangle \langle \mathbf{e}(l + \Delta l) \rangle = 0. \quad (2.6)$$

We are looking for a parameter that measures the chain stiffness. As a suitable choice, one can take the integral width of K_{or} . This is known in the literature as the **persistence length**, and we denote it by l_{ps}

$$l_{\text{ps}} = \int_0^{\infty} K_{\text{or}}(\Delta l) d(\Delta l). \quad (2.7)$$

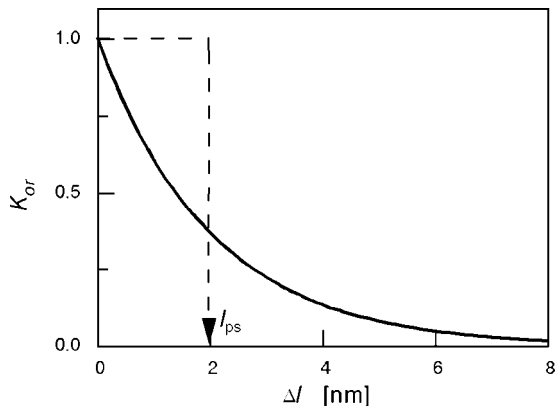


Fig. 2.6. Schematic representation of the orientational correlation function of a chain. The integral width determines the persistence length l_{ps}

The second, main point of concern are the global chain properties, as described by statistical means. More specifically, we inquire about the distribution of chain conformations. As has already been indicated, for the coarse-grained chain this problem can be solved immediately. Distribution functions may be directly deduced, with the aid of the following procedure. We split the chain into subchains of uniform length, this length being much larger than l_{ps} . Then, as indicated in Fig. 2.5, we associate with the chain a sequence of vectors

$$(\mathbf{a}_1, \mathbf{a}_2, \dots, \mathbf{a}_{N_s}),$$

which connect the junction points of the subchains. We thus have created a segment chain composed of N_s straight units. Now, rather than discussing the statistical properties of the continuously bent chain, we consider the distribution functions of the segment chain. Obviously, with regard to the global properties both agree with each other. Quantities of interest are the distribution functions for the vectors connecting any two junction points. One pair is of special interest, namely the two end points of the chain, being connected by the end-to-end distance vector \mathbf{R} . Regarding the given situation, the distribution function for \mathbf{R} can be directly formulated. As we have chosen the subchains large compared to the persistence length, successive steps \mathbf{a}_i of the segment chain show no orientational correlations. For this **freely jointed segments chain** we therefore have a situation that is formally identical with the case of the movement of a Brownian particle suspended in a liquid. The latter performs a diffusive motion set up by perfectly uncorrelated steps. So do the segments of the chain! The distribution function for the displacement of a Brownian particle is well-known. It equals a Gaussian function and this, therefore, also represents the solution of our polymer problem.

Hence, it appears at first that the system can be treated quite easily. However, this is not the full truth. On reconsidering the situation more carefully, we must recognize that an important point has been disregarded: The comparison with the Brownian motion is only allowed, if the volume of the monomer units is neglected since, in contrast to the diffusing Brownian particle, a chain of monomers with non-vanishing sizes cannot occupy a given location twice. What are the consequences? They are drastic indeed since the existence of an **excluded volume** alters the situation not just a little, but completely. For monomers of finite size, the stated equivalence between the polymer problem and the diffusion case is no longer valid. Since the excluded volume forces are effective between any two monomers at arbitrary distances along the chain and thus, are of long-range nature, this results in a qualitative change in behavior. It is intuitively clear that the excluded volume interaction must result in a chain expansion, but how can this effect be quantified? Up until 1972 this amounted to a major problem, but then it was solved in one step by de Gennes who noted that the problem is formally equivalent to a solvable problem in the physics of critical phenomena. With the basic solution on hand, excluded volume effects were analyzed further in experiments, theories and computer simulations. Studies led to a second important conclusion: It became clear that all **expanded chains** have properties in common, to be described by simple power laws.

Since all monomeric units have a finite size, at this point one might wonder if chains with Gaussian properties exist at all. In fact, they do exist in two cases. First, one finds solvents known as **theta solvents**, which produce conditions for the interaction between the monomeric units resulting in an effective vanishing of the excluded volume interactions. The second case is even more astonishing and may come as a real surprise: In the early years of polymer science Flory predicted on theoretical grounds that chains in the melt should behave as if the monomers have a zero volume. In fact, much later this was proven to be valid by utilizing neutron scattering.

Hence in summary, it can be stated that polymer chains possess, on length scales in the order of some nanometers, properties that are independent of the chemical structure. They may be grouped into two **universality classes** with common characteristic behaviors

- Gaussian or **ideal chains**, for vanishing excluded volume interactions,
- **expanded chains**, otherwise.

Strictly speaking, we have to restrict this statement somewhat. In fact, the prediction that all coils may be assigned to either of two universality classes holds only for very large molar masses, strictly in the limit $M \rightarrow \infty$. Real chains, in particular those with moderate molar masses, often exhibit intermediate structures representing mixed states where the chain character depends on the selected length scale. For example, chains can be expanded over their whole length but follow Gaussian statistics within parts, or, chains can resemble straight rods for low molar masses and turn into ideal coils for high molar

masses. The model of a **persistent chain** introduced later in this chapter deals with the latter case. Examples illustrating the first sketched behavior will also be presented.

2.3.1 The Ideal Chain

Let us now at first treat in more detail the ideal chains, on the basis of the introduced freely jointed segments model. We choose numbers, from 0 to N_s , for the junction points, as indicated in Fig. 2.5. The distance between the junction points i and j is given by

$$\mathbf{r}_{ij} = \sum_{l=i+1}^j \mathbf{a}_l, \quad (2.8)$$

and the end-to-end vector \mathbf{R} by

$$\mathbf{R} = \sum_{l=1}^{N_s} \mathbf{a}_l. \quad (2.9)$$

Of interest are the properties of the distribution function

$$p(\mathbf{R}) d^3 \mathbf{R},$$

which expresses the probability that the end-to-end vector points into the volume element $d^3 \mathbf{R}$ at a distance \mathbf{R} . The distribution function is isotropic, depending only on

$$R = |\mathbf{R}|$$

and is normalized

$$\int p(\mathbf{R}) d^3 \mathbf{R} = 1. \quad (2.10)$$

As explained above, $p(\mathbf{R})$ is identical with the distribution function for the displacement of a Brownian particle, after N_s uncorrelated steps. The latter is derived in many textbooks on statistical physics. It equals a Gaussian function with the explicit form

$$p(\mathbf{R}) = \left(\frac{3}{2\pi \langle R^2 \rangle} \right)^{3/2} \exp - \frac{3R^2}{2 \langle R^2 \rangle}. \quad (2.11)$$

Figure 2.7 depicts this functional dependence.

It is important to note that Eq. (2.11) includes only one parameter, namely the mean squared end-to-end distance $\langle R^2 \rangle$, related to $p(\mathbf{R})$ by

$$\langle R^2 \rangle = \int_{R=0}^{\infty} p(\mathbf{R}) R^2 4\pi R^2 dR. \quad (2.12)$$

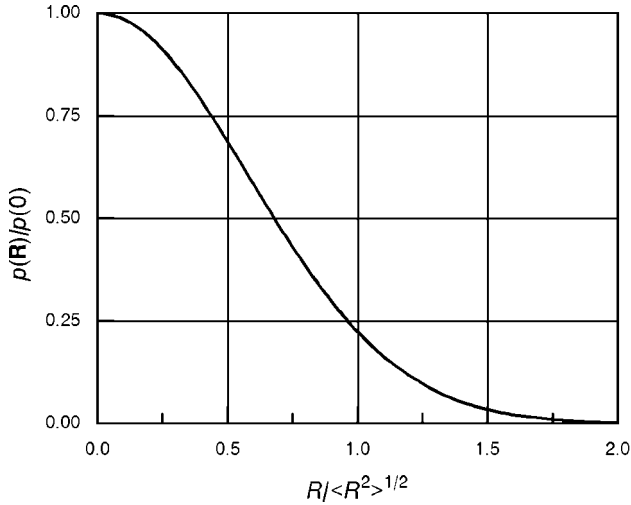


Fig. 2.7. Gaussian distribution function of the end-to-end distance vector \mathbf{R} of an ideal chain

$\langle R^2 \rangle$ can be directly calculated for our chain of freely jointed segments by

$$\langle R^2 \rangle = \left\langle \left(\sum_{l=1}^{N_s} \mathbf{a}_l \right)^2 \right\rangle = \left\langle \sum_{l,l'=1}^{N_s} \mathbf{a}_l \cdot \mathbf{a}_{l'} \right\rangle . \quad (2.13)$$

Since

$$\langle \mathbf{a}_l \cdot \mathbf{a}_{l'} \rangle = \langle |\mathbf{a}_l|^2 \rangle \delta_{ll'} , \quad (2.14)$$

we obtain

$$\langle R^2 \rangle = N_s \langle |\mathbf{a}_l|^2 \rangle . \quad (2.15)$$

When dealing with polymer chains, one requires a parameter for estimating the size of the volume that encloses a polymer chain in the fluid phase. A suitable measure is provided by the quantity R_0 , defined as

$$R_0 = \langle R^2 \rangle^{1/2} . \quad (2.16)$$

Furthermore, if we introduce a mean segment length a_s by

$$a_s = \langle |\mathbf{a}_l|^2 \rangle^{1/2} , \quad (2.17)$$

which agrees with the mean diameter of the subchains, as an important first result we obtain the relation between the size of a polymer and the segment number N_s , as

$$R_0 = a_s N_s^{1/2} . \quad (2.18)$$

Equivalent equations hold for the distribution functions of the internal distance vectors \mathbf{r}_{ij} between two junction points in the chain, which follow as

$$p(\mathbf{r}_{ij}) = \left(\frac{3}{2\pi \langle r_{ij}^2 \rangle} \right)^{3/2} \exp -\frac{3r_{ij}}{2\langle r_{ij}^2 \rangle}, \quad (2.19)$$

with

$$\langle r_{ij}^2 \rangle = |i - j| \langle |\mathbf{a}_l|^2 \rangle = |i - j| a_s^2. \quad (2.20)$$

The coarse-grained representation of a given polymer by the freely jointed segments model is not unambiguous. There is only the requirement to select the subchain so that its contour length is large compared to the persistence length l_{ps} . Different choices of subchains imply different values of N_s and a_s . All pairs of values, however, have to lead to the same value of R_0^2 . For two different choices, with parameters N_s, a_s and N'_s, a'_s , we have

$$N_s a_s^2 = R_0^2 = N'_s a_s'^2 \quad (2.21)$$

and, therefore,

$$\frac{N_s}{N'_s} = \frac{a_s'^2}{a_s^2}. \quad (2.22)$$

An identical equation holds for the number of segments, $N_s(i, j)$, between the points i, j in the chain. A change of the subchain size from a_s to a'_s has to be accompanied by changes of the segment numbers according to

$$\frac{N_s(i, j)}{N'_s(i, j)} = \frac{a_s'^2}{a_s^2}. \quad (2.23)$$

The possibility of a rescaling of the representative freely jointed chain, as formulated by these equations, expresses an important basic property of ideal polymer chains, namely their **self-similarity**. Self-similarity here means that independent of the chosen length scale, i.e., the resolution, an ideal chain always exhibits the same internal structure, one for which all internal distance vectors are distributed like Gaussian variables. A change of the length scale leaves the characteristics of this structure invariant.

Self-similarity is the basic property of **fractal objects** and ideal chains do indeed represent a nice example. The fractal dimension can be directly derived. If one proceeds n_s segmental steps, starting from a point in the interior of the chain, there results on average a displacement of the order of

$$r(n_s) \simeq a_s n_s^{1/2}. \quad (2.24)$$

In reverse, the number of monomers n contained in a sphere with radius r may be estimated as

$$n \propto n_s \propto r^2. \quad (2.25)$$

Hence, the fractal dimension d , being defined as the exponent in the general relation

$$n \propto r^\nu \quad (2.26)$$

between the mass of an object and its diameter, follows as

$$d = 2. \quad (2.27)$$

We see that the polymer chain occupying a region in three dimensions, fills this volume only partially, corresponding to a fractal dimension $d = 2$. As one consequence, the monomer density c_m in the volume of size R_0 occupied by a chain decreases with an increasing degree of polymerization, N , like

$$c_m(N) \simeq \frac{N}{R_0^3} \propto \frac{1}{N^{1/2}}. \quad (2.28)$$

It is important to recognize that self-similarity holds only for a finite range. Clearly, the upper bound is set by the size of the molecule, R_0 . On the other hand, there is a lower limit, which is given by the persistence length.

It is possible to remove the arbitrariness in the choice of the freely jointed segments model by imposing a second condition. For this purpose, the length of the real chain in the fully extended straight form, denoted R_{\max} , may be employed, and a second condition formulated as

$$R_{\max} = N_s a_s. \quad (2.29)$$

This implies that the model chain and the real chain agree not only in size, as assured by the equality

$$\langle R^2 \rangle = N_s a_s^2, \quad (2.30)$$

but also in the contour length. Both equations together yield a unique value for the segment length a_s , which is known as the **Kuhn length** a_K , and given by

$$a_s = a_K = \frac{\langle R^2 \rangle}{R_{\max}}. \quad (2.31)$$

Obviously, the Kuhn length characterizes the stiffness of a given polymer chain. Stiffer chains have larger values of a_K and for a perfectly stiff chain one obtains $a_K = R_{\max}$. One may anticipate and does indeed find a close correspondence between the persistence length and the Kuhn length, namely, as shown later (Eq. (2.128)),

$$a_K = 2l_{ps}.$$

A related parameter, called the **characteristic ratio**, was introduced by Flory and is defined as

$$C_\infty = \frac{\langle R^2 \rangle}{N a_b^2}. \quad (2.32)$$

Table 2.1. Characteristic ratios C_∞ of some selected polymers derived from viscosity measurements under theta conditions at the indicated temperatures (data from Flory [1])

Polymer	Solvent	T [°C]	C_∞
polyethylene	dodecanol-1	138	6.7
polystyrene (atactic)	cyclohexane	35	10.2
polypropylene (atactic)	cyclohexane	92	6.8
polyisobutylene	benzene	24	6.6
poly(vinylacetate) (atactic)	<i>i</i> -pentanone-hexane	25	8.9
poly(methylmethacrylate) (atactic)	various solvents	4–70	6.9
poly(oxyethylene)	aqueous K ₂ SO ₄	35	4.0
poly(dimethylsiloxane)	butanone	20	6.2

Here a_b^2 stands for the sum of the squares of the lengths of the backbone bonds of one monomeric unit

$$a_b^2 = \sum_i a_i^2 . \quad (2.33)$$

For low degrees of polymerization, this ratio is not a constant but varies with N . For large values of N , an asymptotic value is reached and the latter is referred to as C_∞ . In the hypothetical case of freely jointed bonds forming the chain backbone, C_∞ would equal unity, whereas for real polymers having fixed valence angles and restrictions in the rotations about the C–C bonds, the values are in the range of 4 to 12. As will be explained in a later section (Eq. (8.167)), viscosity measurements on polymers dissolved in theta solvents may be used for determination of C_∞ . Table 2.1 contains values of C_∞ for some selected polymers obtained by this method. Solvent and temperature are always indicated, since C_∞ may vary between different theta systems.

With the aid of C_∞ a **scaling law** can be formulated, which relates the size R_0 of a polymer to the degree of polymerization N . It reads as

$$R_0^2 = \langle R^2 \rangle = C_\infty a_b^2 N , \quad (2.34)$$

or

$$R_0 = a_0 N^{1/2} , \quad (2.35)$$

with

$$a_0 = a_b C_\infty^{1/2} . \quad (2.36)$$

Equation (2.35) tells us how R_0 scales with N : If we double N , then R_0 increases by a factor $2^{1/2}$. As we can see, scaling is a property of power law dependencies, and the scaling factor follows from the exponent.

Exact Distribution Function for Finite Chain Lengths

When we formulated Eq. (2.19) for the distribution function $p(\mathbf{R})$, we did this on the basis of the assumption that the random walk carried out by a chain of

freely jointed segments should be equivalent to the motion of a Brownian particle. We pointed out that the equivalence is lost in the presence of excluded volume forces; however, this is not the only possible deficiency in the treatment. Checking the properties for large values of R we find that the Gaussian function never vanishes and actually extends to infinity. For the model chain, on the other hand, an upper limit exists, and it is reached for

$$R = R_{\max} = N_s a_s . \quad (2.37)$$

At this point, the chain is completely stretched and cannot be extended further. It is possible to analyze the problem and to derive the exact distribution function for the end-to-end distance vector of a finite segment chain. The result may then be compared to the Gaussian function.

The distribution function $p(\mathbf{R})$ of a chain of N_s freely jointed segments with length a_s may be expressed as

$$p(\mathbf{R}) = \frac{1}{Z} \int_{\sum_l \mathbf{a}_l = \mathbf{R}} d^3 \mathbf{a}_1 \cdot d^3 \mathbf{a}_2 \dots d^3 \mathbf{a}_{N_s} , \quad (2.38)$$

where Z denotes the partition function

$$Z = \int_{\mathbf{a}_1} d^3 \mathbf{a}_1 \cdot \int_{\mathbf{a}_2} d^3 \mathbf{a}_2 \dots \int_{\mathbf{a}_{N_s}} d^3 \mathbf{a}_{N_s} = (4\pi a_s^2)^{N_s} . \quad (2.39)$$

The integral in Eq. (2.38) includes all chain conformations $\{\mathbf{a}_l\}$ leading to an end-to-end distance vector \mathbf{R} .

One can derive an exact expression for the Fourier transform of p

$$p(\mathbf{q}) = \int \exp(-i\mathbf{q}\mathbf{R}) p(\mathbf{R}) d^3 \mathbf{R} . \quad (2.40)$$

As the integration over all values of \mathbf{R} removes the bounds in the integral Eq. (2.38), all orientations of all segments become included, and $p(\mathbf{q})$ may be written as

$$\begin{aligned} p(\mathbf{q}) &= \frac{1}{(4\pi a_s^2)^{N_s}} \int_{\{\mathbf{a}_l\}} \exp\left(-i\mathbf{q} \sum_l \mathbf{a}_l\right) d^3 \mathbf{a}_1 d^3 \mathbf{a}_2 \dots d^3 \mathbf{a}_{N_s} \\ &= \frac{1}{(4\pi a_s^2)^{N_s}} \left(\int \exp(-i\mathbf{q}\mathbf{a}) d^3 \mathbf{a} \right)^{N_s} . \end{aligned} \quad (2.41)$$

The integral over all orientations of one segment can be evaluated. Adopting spherical coordinates for \mathbf{a} ($|\mathbf{a}| = a_s, \vartheta, \varphi$), with the axis ($\vartheta = 0$) oriented parallel to \mathbf{q} , we have

$$\begin{aligned}
\int \exp(-i\mathbf{q}\mathbf{a}) d^3\mathbf{a} &= a_s^2 \int_{\vartheta, \varphi} \exp(-iqa_s \cos \vartheta) \sin \vartheta d\vartheta d\varphi \\
&= a_s^2 2\pi \int_{x=\cos \vartheta=-1}^1 \exp(-ixqa_s) dx \\
&= \frac{a_s 4\pi}{q} \sin(qa_s) .
\end{aligned} \tag{2.42}$$

This leads us to an analytical expression for $p(\mathbf{q})$

$$p(\mathbf{q}) = \left(\frac{\sin(qa_s)}{qa_s} \right)^{N_s} . \tag{2.43}$$

The distribution function $p(\mathbf{R})$ follows as the reverse Fourier transform

$$p(\mathbf{R}) = \frac{1}{(2\pi)^3} \int \exp(i\mathbf{q}\mathbf{R}) \left(\frac{\sin(qa_s)}{qa_s} \right)^{N_s} d^3\mathbf{q} . \tag{2.44}$$

Equation (2.44) can be evaluated numerically, and Fig. 2.8 shows, as an example, the result of a calculation for $N_s = 5$, which corresponds to a rather short chain. It is compared to the Gaussian function for the same value of $\langle R^2 \rangle$ ($= N_s a_s^2 = R_{\max}^2 / N_s$). As we can see, both equations produce almost identical results for $R < R_{\max}$. In addition, the contributions of the Gaussian distribution function for $R > R_{\max}$ appear to be negligible.

We may conclude from this result that in treatments of polymer chains in the melt or in solutions in the absence of excluded volume forces, the use of the Gaussian distribution function is always permitted. However, there exist situations that require the application of the exact equation. Rubber

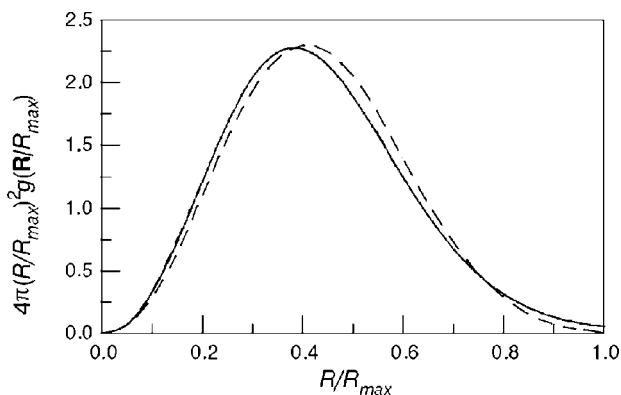


Fig. 2.8. Exact distribution function for the end-to-end distance vector of a chain of five freely jointed segments (*broken line*) compared to the Gaussian distribution function with the same value of $\langle R^2 \rangle$ (*continuous line*)

elasticity, or treatments of yielding properties of polymers are affected by the limits in extensibility given for finite chains. Here, the Gaussian approximation can be used for small deformations only, and dealing with large deformations necessitates an introduction of the exact expression.

The Brownian Chain

Here the question may arise as to which system the Gaussian distribution function Eq. (2.11) really belongs to. There is a formal answer: It is associated with a limiting configuration of a segment chain, having an infinite number of segments

$$N_s \longrightarrow \infty$$

and vanishing segment lengths a_s

$$a_s \longrightarrow 0 ,$$

both parameters being coupled, so that the mean squared end-to-end distance remains constant

$$N_s a_s^2 = R_0^2 = \text{const} .$$

This constitutes a purely mathematical procedure, resulting in a mathematical object rather than a real polymer chain. Note that the contour length of this object tends to infinity,

$$l_{\text{ct}} = N_s a_s = \frac{R_0^2}{a_s} \longrightarrow \infty \quad \text{for} \quad a_s \longrightarrow 0 , \quad (2.45)$$

and this property also emerges in the Gaussian distribution function.

The object we have thus created is usually addressed as the **Brownian chain**, and it is characterized by just one parameter, namely the mean squared end-to-end distance $\langle R^2 \rangle$. Although defined as a mathematical limiting structure, the Brownian chain may indeed serve as a representative of real polymer chains in a certain well-defined region, namely for length scales that are larger than the persistence length and smaller than the size R_0 of the chain. The Brownian chain correctly represents the fractal properties and differs from the real chain in that it extends these fractal properties down to zero distances.

In polymer theories, one even proceeds one step further and introduces the **infinite Brownian chain**, which is associated with the passage to the limit $\langle R^2 \rangle \rightarrow \infty$. By this procedure, the upper bound for the self-similarity is also removed, and we now have an object that is self-similar on all length scales. This is exactly the situation of physical systems at critical points. Hence, the infinite Brownian chain represents a perfect critical object and the consequences are far-reaching. Application of all the effective theoretical tools developed for the study of critical phenomena now also becomes possible for

polymer systems. In particular, scaling laws that tell us how certain structure properties scale with the degree of polymerization may be derived. As mentioned above, scaling laws always have the mathematical form of a power law, and we have already met one example in Eq. (2.35),

$$R_0 = a_0 N^{1/2} .$$

We derived this relation directly, by simple arguments, but it could have been assessed on general grounds as well, referring to fundamental properties of critical systems. On these grounds, scaling laws may be deduced for other properties and conditions, thereby proceeding much in the same manner as, for example, in discussions of the critical behavior of a ferromagnet near the Curie temperature.

We will leave this discussion now, as any further extension would definitely be outside our scope. Nevertheless, it may have become clear that the introduction of mathematical objects such as the infinite Brownian chain can be very helpful. Although they are not real, they may be employed with success as starting points for series expansions that lead us right back into the world of real polymer systems.

The Debye Structure Function

Much insight into the structure of polymer systems is provided by scattering experiments, and so we have to be concerned about the scattering properties of single ideal polymer chains. As we shall see, the associated scattering function can be formulated explicitly and then applied in the evaluation of experimental data. Our treatment is based on general relations of scattering theory, in particular on Eq. (A.21) given in the Appendix and readers who lack this knowledge should first study Sect. A.1.1 for a brief introduction.

Let us first consider the pair distribution function for the segments of a freely jointed chain. For N_s segments in a chain, this pair distribution function, $g_s(\mathbf{r})$, is given by

$$g_s(\mathbf{r}) = \frac{1}{N_s} \sum_{m=-(N_s-1)}^{N_s-1} (N_s - |m|) \left(\frac{3}{2\pi|m|a_s^2} \right)^{3/2} \exp\left(-\frac{3r^2}{2|m|a_s^2}\right) . \quad (2.46)$$

Here, $g_s(\mathbf{r})$ is obtained by a summation over all pairs of segments, whereby we identify their distances with those of the (lower) adjacent junction points (the contribution for $m = 0$ equals a δ -function). There exist $N_s - |m|$ pairs with a distance m and all these pairs have a common distribution function, as given by Eqs. (2.19) and (2.20). Approximating the sum by an integral

$$\sum_{m=-(N_s-1)}^{N_s-1} \longrightarrow \int_{m=-(N_s-1)}^{N_s-1} dm \approx 2 \int_{m=0}^{N_s} dm$$

and introducing the following substitutions:

$$u' = \frac{ma_s^2}{r^2} \quad u = \frac{N_s a_s^2}{r^2} = \frac{R_0^2}{r^2}, \quad (2.47)$$

one obtains

$$g_s(\mathbf{r}) = 2 \frac{N_s R_0}{R_0^3} \frac{1}{r} \int_{u'=0}^u \left(1 - \frac{u'}{u}\right) \left(\frac{3}{2\pi u'}\right)^{3/2} \exp -\frac{3}{2u'} du' \quad (2.48)$$

$$= \frac{N_s}{R_0^3} \tilde{g}_0 \left(\frac{r}{R_0}\right). \quad (2.49)$$

The pair distribution function for the monomers follows as

$$g(\mathbf{r}) = \frac{N}{N_s} g_s(\mathbf{r}), \quad (2.50)$$

giving

$$g(\mathbf{r}) = \frac{N}{R_0^3} \tilde{g}_0 \left(\frac{r}{R_0}\right). \quad (2.51)$$

According to this result, the pair distribution function of an ideal chain is given by a general function \tilde{g}_0 that depends on the dimensionless quantity r/R_0 . In this reduced representation all ideal chains become equivalent. Note that the integral value of \tilde{g}_0 is unity. Since

$$\int g d^3\mathbf{r} = N \quad (2.52)$$

we have

$$\int \tilde{g}_0 \left(\frac{r}{R_0}\right) d^3 \left(\frac{\mathbf{r}}{R_0}\right) = 1. \quad (2.53)$$

Quite characteristic is the behavior for $r/R_0 \ll 1$, i.e., for distances within the macromolecule. The integral in Eq. (2.48) may be replaced in this limit by its value for $u \rightarrow \infty$, and this leads to

$$g(\mathbf{r}) \propto \tilde{g}_0 \left(\frac{r}{R_0} \ll 1\right) \propto \frac{1}{r}. \quad (2.54)$$

Equation (2.54) expresses a power law behavior. In the last section we addressed the self-similar nature of ideal polymer chains. The power law exactly reflects this property, since the function $g(r) \propto 1/r$ maintains its shape if we alter the unit length employed in the description of \mathbf{r} .

Next we derive the structure function of an ideal chain. It can be measured in diluted states, i.e., for low average monomer densities

$$\langle c_m \rangle \approx 0. \quad (2.55)$$

Using Eq. (2.50), the general Eq. (A.21) becomes

$$S(\mathbf{q}) = \frac{N}{N_s} \int \exp(-i\mathbf{q}\mathbf{r}) g_s(\mathbf{r}) d^3\mathbf{r} . \quad (2.56)$$

If we take Eq. (2.46) and carry out the Fourier transformation for the Gaussian functions, we obtain

$$S(\mathbf{q}) = \frac{2N}{N_s^2} \int_{m=0}^{N_s} (N_s - m) \exp\left(-\frac{ma_s^2 q^2}{6}\right) dm . \quad (2.57)$$

Hereby, we again replaced the summation by an integration. The substitutions

$$v' = \frac{ma_s^2 q^2}{6} \quad v = \frac{N_s a_s^2 q^2}{6} = \frac{R_0^2 q^2}{6} \quad (2.58)$$

lead to

$$S(\mathbf{q}) = N \frac{2}{v} \int_{v'=0}^v \left(1 - \frac{v'}{v}\right) \exp(-v') dv' . \quad (2.59)$$

The integral can be evaluated and the result then is usually presented as

$$S(\mathbf{q}) = N S_D(q) \quad (2.60)$$

with

$$S_D\left(v = \frac{R_0^2 q^2}{6}\right) = \frac{2}{v^2} (\exp(-v) + v - 1) . \quad (2.61)$$

S_D is known as the **Debye structure function** of an ideal chain; a plot is shown in Fig. 2.9.

In correspondence to the pair distribution function, the Debye structure function can also be expressed in a reduced form, with v as a general variable. Both the equations for the pair distribution function and for the scattering law indicate that all ideal chains are similar to each other, differing only in the length scale as expressed by R_0 .

Some properties of S_D are noteworthy and furnish the basis for a straightforward analysis of experiments. First consider the limiting behavior for $v \rightarrow 0$, focussing on data near the origin of reciprocal space, i.e., in the range of small scattering angles. Series expansion of Eq. (2.61) gives

$$S_D(v \rightarrow 0) = 1 - \frac{v}{3} \dots \quad (2.62)$$

Experimental results are usually presented in plots of S^{-1} versus q^2 , corresponding to the equivalent formulation

$$S^{-1}(q^2) = N^{-1} \left(1 + q^2 \frac{R_0^2}{18} + \dots\right) . \quad (2.63)$$

Equation (2.63) exemplifies **Guinier's law**, which generally holds for scattering experiments on dilute colloidal systems. As explained in the Appendix,

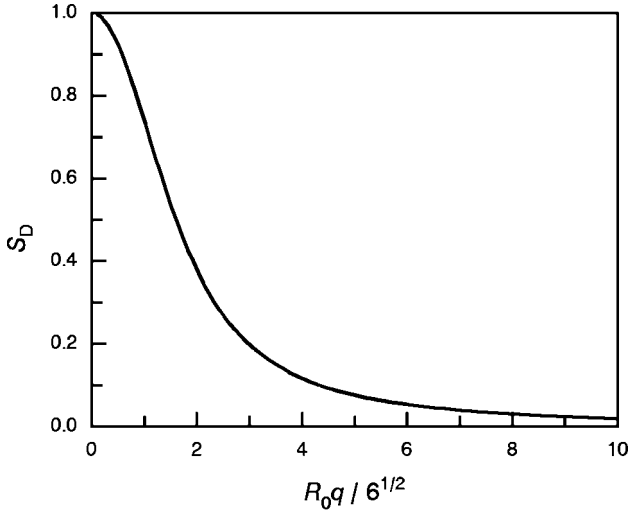


Fig. 2.9. Debye structure function of an ideal chain with size R_0

Sect. A.3.1, analysis of small angle scattering data enables the determination of the colloidal mass, here given by the molar mass or the degree of polymerization, and of the size of the colloid, here represented by R_0 . The general relation formulated by Eq. (A.71) in the Appendix

$$S(q^2) = N \left(1 - q^2 \frac{R_g^2}{3} + \dots \right)$$

or

$$S^{-1}(q^2) = N^{-1} \left(1 + q^2 \frac{R_g^2}{3} + \dots \right)$$

includes the **radius of gyration**, denoted R_g . For a chain of N monomers, R_g is defined as

$$R_g^2 = \frac{1}{N} \sum_{i=1}^N \langle |\mathbf{r}_i - \mathbf{r}_c|^2 \rangle$$

whereby \mathbf{r}_c denotes the location of the center of gravity

$$\mathbf{r}_c = \frac{1}{N} \sum_{i=1}^N \mathbf{r}_i .$$

As is also shown in the Appendix, this is equivalent to

$$R_g^2 = \frac{1}{2N^2} \sum_{i,j=1}^N \langle |\mathbf{r}_i - \mathbf{r}_j|^2 \rangle .$$

A comparison of Eqs. (2.63), (A.71) tells us that for an ideal chain we have

$$R_{g,0}^2 = \frac{R_0^2}{6} . \quad (2.64)$$

According to Eq. (2.61), the Debye structure function exhibits a characteristic asymptotic behavior

$$S_D(v \rightarrow \infty) = \frac{2}{v} = \frac{12}{q^2 R_0^2} . \quad (2.65)$$

Here we again find a power law, $S_D \propto 1/q^2$, and indeed, it just represents the Fourier transform of the previously discussed power law $g(r) \propto 1/r$.

Quite instructive is a plot of measured data in the form Sq^2 versus q , known as the **Kratky plot**. This is depicted schematically in Fig. 2.10. The plateau region, representing the part of the curve where $S_D \propto 1/q^2$, contains information about the internal structure of the chain. As the plateau value is given by

$$Sq^2(q^2 R_0^2 \gg 1) = \frac{12N}{R_0^2} \quad (2.66)$$

$$= \frac{12}{C_\infty a_b^2} . \quad (2.67)$$

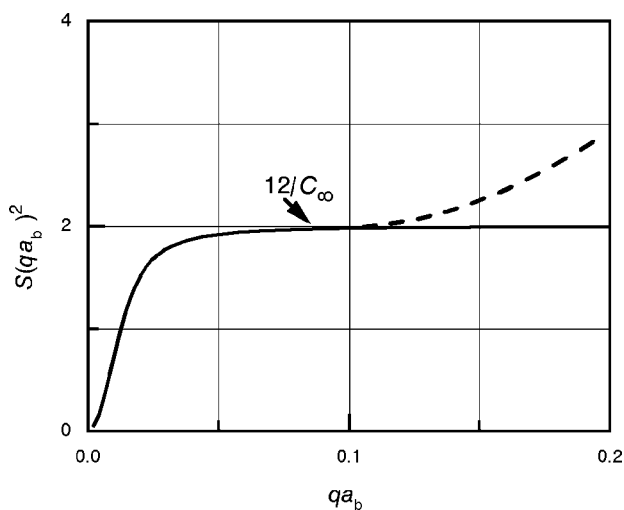


Fig. 2.10. Kratky plot of the scattering function of an ideal chain. The internal rigidity of the chain results in a change to a rod-like scattering at higher q 's

When applying Eq. (2.32), it can be used for a determination of the characteristic ratio C_∞ , which expresses an intrinsic, molar mass independent property.

The range of the self-similar internal structure ends when r approaches R_0 . Around $q \simeq 1/R_0$ the curve deviates from the plateau and decays to zero. As mentioned earlier, universal behavior is also limited towards small distances. Specific polymer properties emerge if one approaches distances in the order of the persistence length. For this reason, for polymers at higher q 's deviations from the Debye structure function show up, beginning around $q \simeq l_{ps}^{-1}$. As indicated in Fig. 2.10, one observes an increase in the slope and the structure function changes into that of a rod. It can be shown that the latter is generally given by

$$S_{\text{rod}} \propto \frac{1}{q} \quad (2.68)$$

and this implies

$$Sq^2 \propto q. \quad (2.69)$$

The point of cross-over from coil-like to rod-like scattering may be used for an estimation of the persistence length.

Theta Solutions and Polymer Melts

As proved by experiments, ideal chains are found in **theta solutions** and in the melt. It is possible to provide qualitative explanations for this peculiar behavior and we begin with the solutions.

For an explanation of what theta conditions in polymer solutions mean, it may help to recall the properties of real gases. For these systems the relation between pressure p , (molar) volume \tilde{v} and temperature can be represented by the van der Waals equation

$$\left(p + \frac{\tilde{a}}{\tilde{v}^2} \right) (\tilde{v} - \tilde{b}) = \tilde{R}T. \quad (2.70)$$

It includes two parameters, \tilde{a} and \tilde{b} , which account for attractive van der Waals forces and repulsive hard core interactions, respectively. There exists one temperature, called Boyle temperature, where the attractive and repulsive forces compensate each other, so that an apparent ideal gas behavior results. To locate this point a virial expansion in terms of the particle density $c_m = N_L/\tilde{v}$ (N_L : Avogadro-Loschmidt number) can be used, in the form

$$p = kT(c_m + A_2c_m^2 + A_3c_m^3 \dots). \quad (2.71)$$

The Boyle temperature is that point at which the second virial coefficient A_2 vanishes, so that second order corrections to the ideal equation of state do not exist. The virial expansion of the van der Waals equation is

$$\begin{aligned}
p\tilde{v} &= \tilde{R}T - \frac{\tilde{a}}{\tilde{v}} + \tilde{b}p + \mathcal{O}\left(\frac{1}{\tilde{v}^2}\right) \\
&= \tilde{R}T - \frac{\tilde{a}}{\tilde{v}} + \frac{\tilde{b}\tilde{R}T}{\tilde{v}} + \mathcal{O}\left(\frac{1}{\tilde{v}^2}\right) \\
&= \tilde{R}T \left(1 + \frac{1}{\tilde{v}} \left(\tilde{b} - \frac{\tilde{a}}{\tilde{R}T}\right)\right) + \mathcal{O}\left(\frac{1}{\tilde{v}^2}\right)
\end{aligned} \tag{2.72}$$

or, in terms of c_m ,

$$p = kT \left(c_m + c_m^2 \left(\frac{\tilde{b}}{N_L} - \frac{\tilde{a}}{N_L^2 kT} \right) + \dots \right). \tag{2.73}$$

Hence, the second virial coefficient is given by

$$A_2 = \frac{\tilde{b}}{N_L} - \frac{\tilde{a}}{N_L^2 kT} \tag{2.74}$$

and we obtain for the Boyle temperature, T_B , the result

$$T_B = \frac{\tilde{a}}{N_L k \tilde{b}} = \frac{\tilde{a}}{\tilde{R} \tilde{b}}. \tag{2.75}$$

Another formulation for A_2 and derivation of T_B follows from the general theory of real gases. A_2 may be directly deduced from the pair interaction potential between the gas molecules, $u(r)$, by

$$A_2 = \frac{1}{2} \int_{r=0}^{\infty} \left(1 - \exp -\frac{u(r)}{kT} \right) 4\pi r^2 dr. \tag{2.76}$$

Curve (a) in Fig. 2.11 gives an example of the form of $u(r)$ that results from the superposition of the repulsive hard core interaction, originating from Pauli's exclusion principle opposing an overlap of electron wave functions, and the attractive dispersive forces of the van der Waals type. At the Boyle temperature this integral vanishes.

An analogous situation is encountered in a theta solution, with the quantity of interest now being the effective interaction potential between two solute molecules, or in the polymer case, between two monomeric units. The curve (b) in Fig. 2.11 represents the situation in a good solvent, where the potential is repulsive at all distances. Each solute molecule is surrounded by a hydrate shell of solvent molecules and this shell has to be destroyed when two solute molecules or monomeric units are to approach each other. The situation in a poor solvent is different, due to there being a preference for solute-solute contacts. Here, the solute molecules effectively attract each other and repulsion occurs only at short distances, for the same reason as for the real gases, namely the presence of hard core interactions. For poor solvents, therefore, $u(r)$ has an appearance similar to the pair interaction potential in a van der Waals gas and a shape like curve (a) in Fig. 2.11.

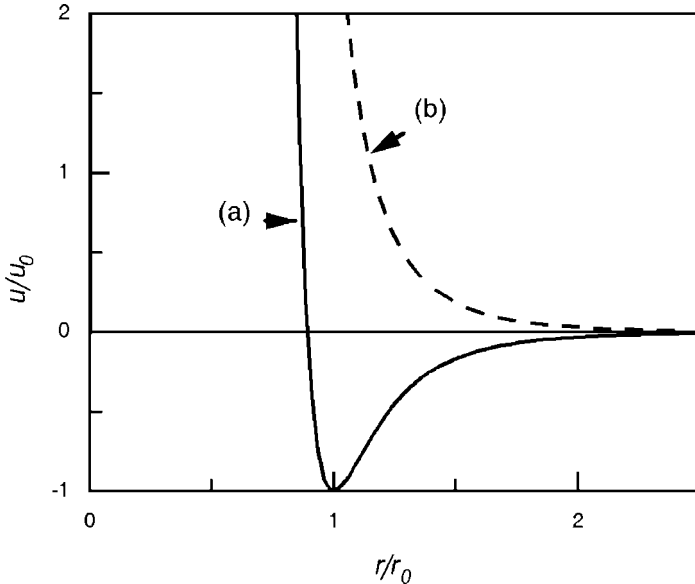


Fig. 2.11. Pair interaction potential for two monomers in a poor solvent (a) and in a good solvent (b). The potential (a) is also representative for a van der Waals gas

On dealing with solutions, the osmotic pressure Π rather than the pressure p becomes the quantity of interest. Its virial expansion may be written as

$$\Pi = kT(A_1 c_m + A_2 c_m^2 + A_3 c_m^3 + \dots), \quad (2.77)$$

where c_m now denotes the number density of monomers in the solution. If we identify $u(r)$ in Eq. (2.76) with the effective monomer–monomer interaction potential, we obtain the second virial coefficient for the osmotic pressure. We can now define what theta conditions mean: For a solution at the theta point, A_2 vanishes. A solution then becomes quasi-ideal; neither excluded volume interactions nor attractive forces emerge, since both compensate each other. Under this condition, monomers appear to have zero volumes and polymers exhibit ideal chain behavior.

Figure 2.12 presents measurements of osmotic pressures for solutions of polystyrene in cyclohexane, carried out under variation of the weight fraction of the dissolved polymer, $c_w \propto c_m$ and of the temperature. As can be seen, A_2 vanishes at 35°C , which therefore represents the theta point of this system. As indicated by the positive values of A_2 , for temperatures above 35°C the repulsive forces become dominant. On the other hand, we observe negative values of A_2 for $T < 35^\circ\text{C}$, indicative of the actual presence of effective attractive forces between the monomers. On further cooling, the attractive forces then lead to a separation of solvent and solute, and the sample becomes turbid.

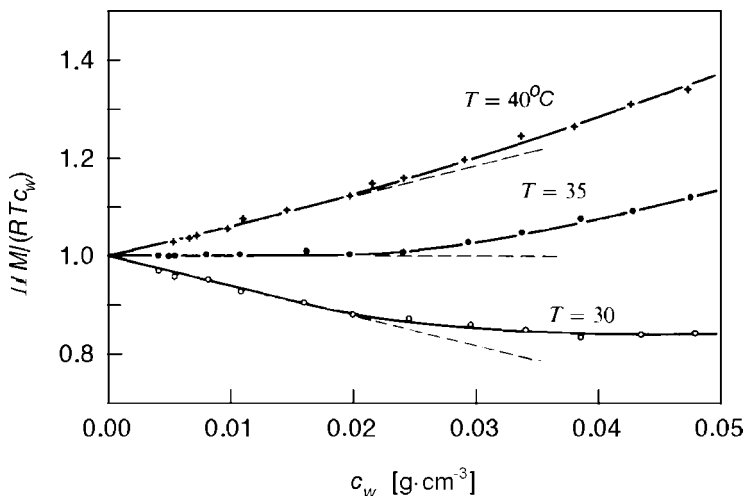


Fig. 2.12. Concentration and temperature dependence of the osmotic pressure measured for solutions of PS ($\bar{M}_n = 1.3 \times 10^5 \text{ g mol}^{-1}$) in cyclohexane. Data from Strazielle in [2]

Figure 2.13 shows the result of a light scattering experiment on the same system, a dilute solution of polystyrene ($\bar{M}_n = 8.79 \times 10^6 \text{ g mol}^{-1}$) in cyclohexane. The measurement was conducted exactly at the theta point. As we have learned, ideal chains scatter according to the Debye structure function, with the asymptotic limit $S_D \propto 1/q^2$. The data display the product

$$\Sigma(q)q^4 \propto S_D q^4 \propto \exp -\frac{R_0^2 q^2}{6} + \frac{R_0^2 q^2}{6} - 1$$

plotted versus q^2 . $\Sigma(q)$ is the **Rayleigh ratio** and K_1 represents the contrast factor for light; definitions and equations are given in the Appendix, in Eqs. (A.4), (A.50), and (A.51). The observed linear dependence at high q 's demonstrates that the chains in this system do indeed show ideal behavior.

Next, let us turn to the situation in a polymer melt. The arguments to be presented are even more qualitative than those given for the theta point, but they nevertheless address the basic features correctly. We consider the conditions experienced by one isolated polymer chain. The density distribution, averaged over all conformations of the macromolecule, has an appearance similar to the bell-shaped curve in Fig. 2.14. There is a central maximum followed by continuous decays. We begin with an ideal chain and then consider the changes introduced by the excluded volume forces. These create a potential energy, which is sensed by each monomer. In a simplified approximate treatment, this potential, denoted ψ_m^{ev} , may be represented by the expression

$$\psi_m^{\text{ev}} = kT v_e c_m. \quad (2.78)$$

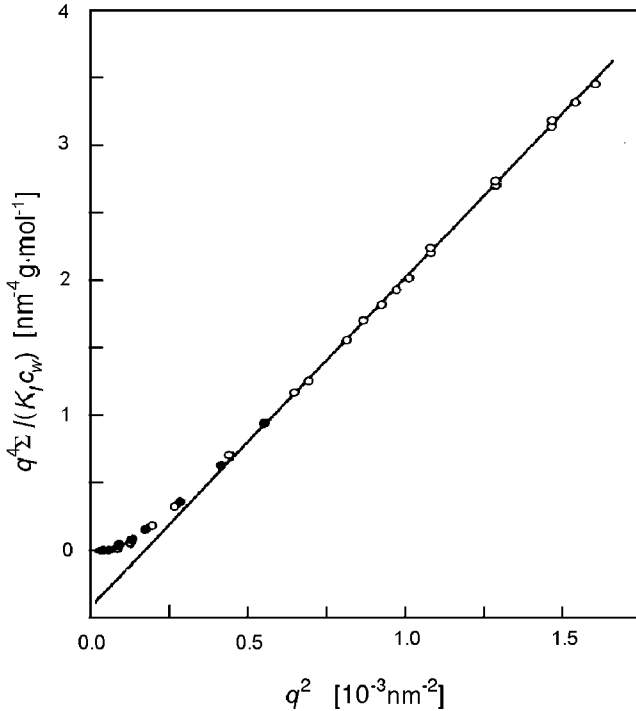


Fig. 2.13. Result of a light scattering experiment on a dilute solution of PS ($\overline{M}_n = 8.78 \times 10^6 \text{ g mol}^{-1}$) in cyclohexane, carried out under theta conditions ($T = 34.7^\circ \text{C}$). Data from Miyaki et al. [3]

This is an empirical equation of the **mean field** type, based on the assumption that ψ_m^{ev} should be proportional to the local density of monomers. The magnitude of the excluded volume interactions is described by the volume-like parameter v_e , with typical values of the order of $1 \text{ \AA}^3 - 1 \text{ nm}^3$. The factor kT is explicitly included, not only for dimensional reasons, but also in order to stress that excluded volume energies, like hard core interactions in general, are of entropic nature (entropic forces are always proportional to T , as is exemplified by the pressure exerted by an ideal gas, or the restoring force in an ideal rubber to be discussed in a later chapter). If the local potential experienced by a monomer is given by Eq. (2.78), then forces arise for all non-uniform density distributions. For the coil under discussion, forces in radial direction result since everywhere, with the exception of the center at $x = 0$, we have $dc_m/d|x| < 0$. The obvious consequence is an expansion of the chain.

Envisage now the situation given in the melt. In contrast to an isolated polymer molecule, the monomer concentration c_m here is constant. For the excluded volume force onto a monomer, it is irrelevant whether the contacting other monomers are parts of the same chain or of other chains. The determining quantity is the total concentration and the latter does not vary.

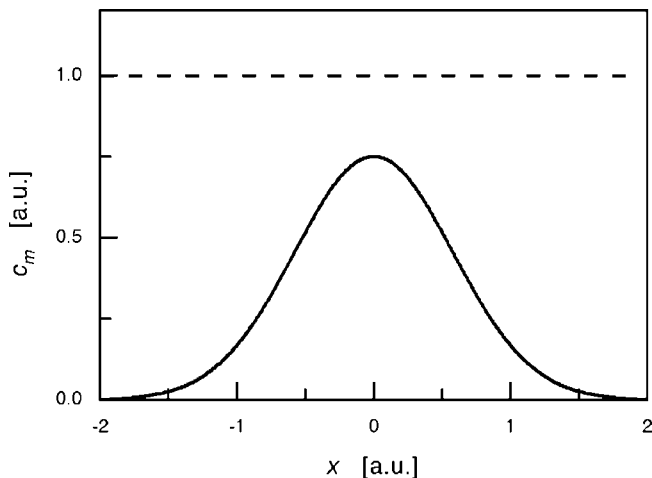


Fig. 2.14. Monomer density distribution for an individual chain along a line through the center and the constant overall density in a melt (*broken line*)

Hence, no forces arise and the polymer chain does not expand. In the literature one often finds a particular formulation for addressing this effect. As the concentration gradient given for an isolated chain is compensated for by the presence of monomers from the other chains, one says that the latter ones ‘screen’ the intramolecular excluded volume interactions. Here we leave it at this short remark. Further comments on this picture and the origin of the saying will follow at a later stage when we discuss the properties of semidilute solutions.

Neutron scattering experiments allowed this prediction for melts to be verified. There is no way to investigate the conformation of single chains in a melt by conventional scattering experiments, since a melt just represents a densely packed ensemble of monomers which shows some short-range order. In order to make single chains visible, one has to label them, i.e., supply them with contrast, so that they stand out from the background produced by the majority chains. Choosing neutrons for the scattering experiment, there is a preparatory technique to achieve this aim. Experiments can make use of the fact that neutrons possess different cross-sections for protons and deuterons. On the other hand, substitution of hydrogens by deuterium for part of the chains in a sample leaves the interaction forces and thus the chain conformations essentially unchanged (minor effects exist, but in melts they appear to be negligible). Thus, for a determination of the single chain conformation in a melt, a dilute solution of deuterated chains in a protonated matrix (or reversely, of protonated chains in a deuterated matrix) can be prepared and investigated by neutron scattering. Figure 2.15 presents the results of one of the first experiments, carried out on a solution of poly(methyl methacrylate) (PMMA) in deuterated PMMA.

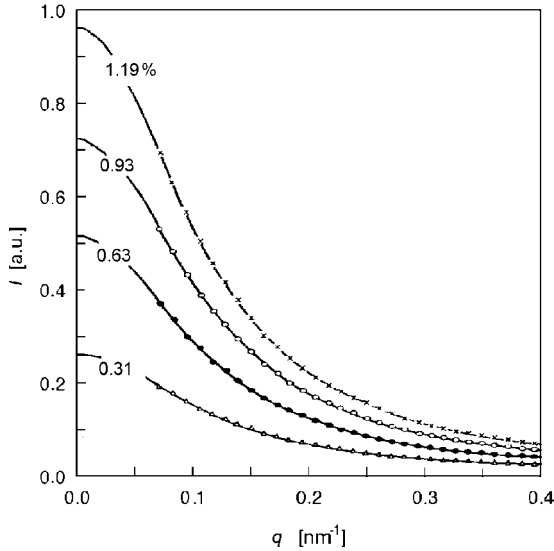


Fig. 2.15. Scattering curves obtained in a neutron scattering experiment on solutions of PMMA (mol fractions as indicated) in d-PMMA. Data from Kirste et al. [4]

The continuous lines, which give perfect data fits, represent Debye structure functions (with minor corrections to account for polydispersity effects), thus proving the ideal behavior of chains. In addition, intensities were found to be proportional to the weight fraction of deuterated chains

$$I(q) \propto c_w S_D(q) . \quad (2.79)$$

As will be discussed in the next chapter, exactly this proportionality is indicative for a vanishing second virial coefficient. Hence, deuterated chains dissolved in a normal melt of the same polymer represent a theta system, fully equivalent to a theta solution with a low molar mass liquid. Therefore, as this second criterion is also fulfilled, we have unambiguous evidence of the existence of ideal chains in melts.

2.3.2 The Expanded Chain

Expanded chains are found in dilute solution in good solvents. The effective interaction energy between two monomers is always repulsive here and, as a consequence, chains become expanded. Expansion will come to an end at some finite value since it is associated with a decreasing conformational entropy. The reason for this decrease is easily seen by noting that the number of accessible rotational isomeric states decreases with increasing chain extension. The decrease produces a retracting force, which balances the repulsive excluded volume forces at equilibrium.

The formal problem treated by polymer theory in the analysis of excluded volume effects is the analysis of the properties of **self-avoiding random walks**. As already mentioned, it is not possible to come to a satisfactory solution if one takes an ideal random walk as a starting point and then introduces the excluded volume forces as a perturbation. Since excluded volume forces are effective between any pair of monomers, for arbitrary distances Δl along the chain, they are of long-range nature and as a consequence ideal chains and expanded chains become qualitatively different. The distribution function for the end-to-end vector and, in particular, the scaling law, which relates the size of the volume occupied by a polymer with its degree of polymerization, differ qualitatively from Eqs. (2.11) and (2.35) which are valid for ideal chains. Derivations are due to des Cloiseaux and de Gennes. Solutions were obtained using field theoretical techniques and renormalization group methods and here we just cite the results.

The distribution function $p(\mathbf{R})$ has a general shape as indicated in Fig. 2.16. When compared to the properties of ideal chains there is first a change in the asymptotic behavior at large R . It is now given by

$$p(|\mathbf{R}| \rightarrow \infty) \propto \exp - \left(\frac{R}{R_F} \right)^{5/2} \quad (2.80)$$

rather than by $p \propto \exp[-3R^2/(2R_0^2)]$. An even more drastic modification occurs around $R = 0$. Whereas ideal chains there reach the maximum, expanded chains show a steep decrease down to zero, indicating that a return of a self-

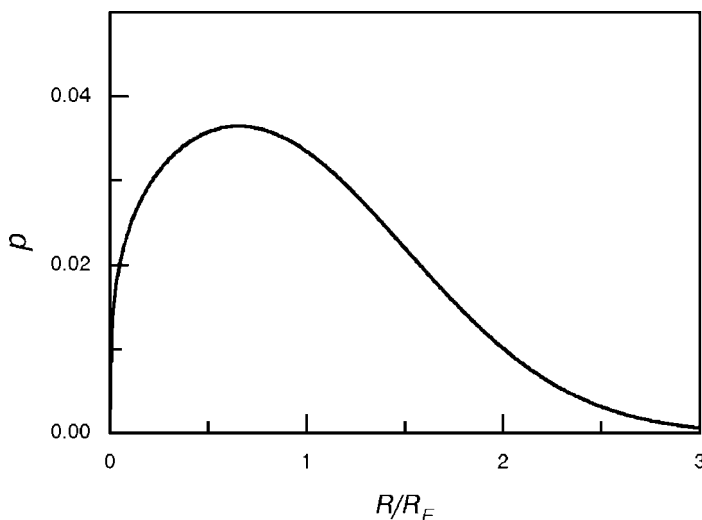


Fig. 2.16. Distribution function for the end-to-end vector of an expanded chain in the asymptotic limit of large degrees of polymerization (R_F : size of the chain)

avoiding random walk to its starting point is highly improbable. The shape near the origin equals the power law

$$p(|\mathbf{R}| \rightarrow 0) \propto \left(\frac{R}{R_F} \right)^{0.275} . \quad (2.81)$$

The described distribution function refers to the asymptotic limit of large degrees of polymerization. It is important to note that, as for ideal chains, $p(\mathbf{R})$ includes one parameter only, now the quantity R_F , called **Flory radius** in the literature. R_F is a measure for the diameter of the volume that encloses an expanded polymer chain, with the identical definition as for ideal chains

$$R_F = \langle R^2 \rangle^{1/2} . \quad (2.82)$$

Of central importance for the discussion of the properties of expanded chains is the relation between R_F and the degree of polymerization N . It is given by the scaling law

$$R_F = a_F N^{3/5} . \quad (2.83)$$

The value of the exponent, $\nu = 3/5$, expresses the difference to the ideal chains, where $\nu = 1/2$. Strictly speaking, $\nu = 0.6$ is not the exact value, as the calculation by renormalization group methods gives $\nu = 0.588$, but for the description of experimental results the rounded value is accurate enough. The second parameter included in the equation, a_F , denotes the effective length per monomer. It depends on the microstructure of the chain, i.e., on bond lengths, volume angles and the rotational angles of the isomeric states, and, in particular, on the strength of the excluded volume force.

Although the rigorous solution was not presented until 1972, Flory offered arguments in support of the scaling law Eq. (2.83) already much earlier. The point of concern is the equilibrium conformation of a chain, being the result of a balance between repulsive excluded volume forces and retracting forces arising from the decreasing conformational entropy. Above, with Eq. (2.78), we have already introduced Flory's expression for the potential produced by the excluded volume forces,

$$\psi_m^{\text{ev}} = kT v_e c_m .$$

ψ_m^{ev} describes, in a mean field approximation, the potential experienced by a monomer as a result of the interaction with the other monomers in its neighborhood. Consequently, we may represent the contribution of the excluded volume interactions to the free energy density by

$$\frac{\Delta \mathcal{F}^{\text{ev}}}{\Delta \mathcal{V}} = \frac{c_m \psi_m^{\text{ev}}}{2} = \frac{kT v_e c_m^2}{2} \quad (2.84)$$

whereby the division by 2 eliminates the twofold counting of each pair of monomers. The excluded volume contribution to the free energy of one chain,

denoted f_p^{ev} , is obtained by an integration over the occupied volume, hereby calculating the average over all conformations

$$f_p^{\text{ev}} = \frac{1}{2} \int kT v_e \langle c_m^2(\mathbf{r}) \rangle d^3\mathbf{r}. \quad (2.85)$$

In the mean field treatment one approximates the square average $\langle c_m^2 \rangle$ by $\langle c_m \rangle^2$. If we choose for the description of the mean local density $\langle c_m(\mathbf{r}) \rangle$ a Gaussian function, with a radius of gyration R_g and the maximum at the center of gravity \mathbf{r}_c

$$\langle c_m(\mathbf{r}) \rangle = N \left(\frac{3}{2\pi R_g} \right)^{3/2} \exp -\frac{3|\mathbf{r} - \mathbf{r}_c|^2}{2R_g^2}, \quad (2.86)$$

we obtain

$$\begin{aligned} f_p^{\text{ev}} &= \frac{kT}{2} v_e N^2 \left(\frac{3}{4\pi R_g^2} \right)^{3/2} \left(\frac{6}{2\pi R_g^2} \right)^{3/2} \int \exp -\frac{6|\mathbf{r} - \mathbf{r}_c|^2}{2R_g^2} d^3\mathbf{r} \\ &= \frac{kT}{2} v_e N^2 \left(\frac{3}{4\pi R_g^2} \right)^{3/2}. \end{aligned} \quad (2.87)$$

As we are interested in the change of f_p^{ev} following from an expansion, we choose the ideal state with vanishing excluded volume forces, where $R_g = R_{g,0}$ and $R_0^2 = a_0^2 N$, as our reference and write

$$f_p^{\text{ev}} = \frac{kT}{2} v_e \left(\frac{3}{4\pi} \right)^{3/2} \frac{R_0^4}{a_0^4} \frac{1}{R_{g,0}^3} \left(\frac{R_{g,0}}{R_g} \right)^3, \quad (2.88)$$

or, by replacement of R_g with R assuming $R \propto R_g$ and applying Eq. (2.64)

$$f_p^{\text{ev}} = \frac{kT}{2} v_e \left(\frac{18}{4\pi} \right)^{3/2} \frac{R_0}{a_0^4} \left(\frac{R_0}{R} \right)^3. \quad (2.89)$$

Now we introduce a parameter 'z', defined as

$$z = \left(\frac{3}{2\pi} \right)^{3/2} \frac{v_e}{a_0^4} R_0 \quad (2.90)$$

and express f_p^{ev} as

$$f_p^{\text{ev}} = \frac{kT}{2} 3^{3/2} z \left(\frac{R_0}{R} \right)^3. \quad (2.91)$$

The parameter z is dimensionless and according to Eq. (2.91) determines the excluded volume energy associated with a single chain.

Next, we require a formula for the second part of the free energy, f_p^s , the one originating from the conformational entropy. The following expression appears suitable:

$$f_p^s = \beta kT \left(\left(\frac{R_0}{R} \right)^2 + \left(\frac{R}{R_0} \right)^2 \right). \quad (2.92)$$

This is an empirical equation that accounts for the fact that for ideal chains, i.e., vanishing excluded volume interactions, the coil size in thermal equilibrium equals R_0 ; β is a dimensionless coefficient of order unity. The first term gives the repulsion experienced on squeezing a polymer chain, the second term represents the retracting force built up on a coil expansion. As only the second term appears to be relevant for the case under discussion, we ignore the first term and write

$$f_p^s \approx \beta kT \left(\frac{R}{R_0} \right)^2. \quad (2.93)$$

Combining the expressions for the two contributions yields the free energy of a chain as a function of R

$$f_p \left(\frac{R}{R_0} \right) = f_p^{\text{ev}} + f_p^s = \frac{kT}{2} 3^{3/2} z \left(\frac{R_0}{R} \right)^3 + \beta kT \left(\frac{R}{R_0} \right)^2. \quad (2.94)$$

We now calculate the equilibrium value of R at the minimum of the free energy, where

$$\frac{df_p}{d(R/R_0)} = 0. \quad (2.95)$$

This leads us to

$$z \left(\frac{R_0}{R} \right)^4 \simeq \left(\frac{R}{R_0} \right) \quad (2.96)$$

and to the equation

$$R \simeq R_0 z^{1/5} \simeq \left(\frac{v_e}{a_0^4} \right)^{1/5} R_0^{6/5} = (v_e a_0^2)^{1/5} N^{3/5}. \quad (2.97)$$

This is Flory's result. We identify R with the Flory radius R_F and write

$$R_F = a_F N^{3/5} \quad (2.98)$$

with

$$a_F \simeq (v_e a_0^2)^{1/5}. \quad (2.99)$$

Here and generally we use the symbol ' \simeq ' in all 'order of magnitude equations' that correctly include all variables but omit the exact numerical front factor.

As we can see, Flory's simple mean field treatment leads to the same result as the exact analysis by renormalization group methods. In fact, this comes as a real surprise because there is no good reason to expect that a mean field treatment, which in principle is not allowed for a single chain in view of the pronounced concentration variations, would give the correct result. However, it does, and so it appears that different faults in the treatment mutually cancel out.

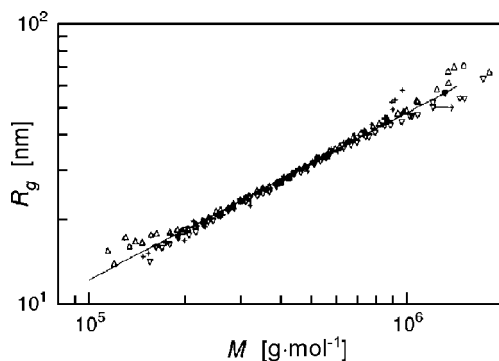


Fig. 2.17. Relation between the radius of gyration R_g and the molar mass M , observed in light scattering experiments on dilute solutions of PS in toluene. The *continuous straight line* corresponds to the scaling law Eq. (2.83). Data from Wintermantel et al. [5]

The scaling law Eq. (2.83) is indeed in full accord with experiments and Fig. 2.17 presents an example. It shows the results of light scattering experiments on dilute solutions of polystyrene in toluene. These can be used for determining the radius of gyration $R_g \propto R_F$ and the molar mass $M \propto N$. Both parameters follow from a measurement of the scattering intensity in the low angle range, by applying Guinier's law Eq. (A.71). The straight line in Fig. 2.17 agrees exactly with the scaling law Eq. (2.83). The set of data was obtained in only two runs on two polydisperse samples. In the measurements, a fractionation of the samples by gel permeation chromatography was combined with a simultaneous registration of low angle light scattering curves.

From the scaling law Eq. (2.83) it is possible to deduce the fractal dimension of expanded chains, as well as characteristic properties of the pair distribution function and the structure function. The fractal dimension d follows from the same argument as applied above for the ideal chains, by estimating the average number of monomers included in a sphere of radius r which is now given by

$$n(r) \propto r^{5/3} . \quad (2.100)$$

This power law implies that we have

$$d = 5/3 . \quad (2.101)$$

The pair distribution function in the chain interior may be derived similarly. For a given pair distribution function $g(\mathbf{r})$ the average number of monomers in a sphere of radius r can be calculated in general by

$$n(r) = \int_{r'=0}^r g(\mathbf{r}') 4\pi r'^2 dr' . \quad (2.102)$$

On the other hand, we know that

$$n(r) \simeq \left(\frac{r}{a_F} \right)^{5/3}. \quad (2.103)$$

Equating the two expressions and taking the first derivatives on both sides gives

$$g(\mathbf{r})r^2 \propto r^{2/3}, \quad (2.104)$$

hence

$$g(\mathbf{r}) \propto r^{-4/3}. \quad (2.105)$$

Equation (2.105) describes the pair distribution function for distances that lie within the chain interior, i.e., for $r < R_F$. Note the difference to the respective relation for ideal chains, $g(\mathbf{r}) \propto r^{-1}$ (Eq. (2.54)).

More detailed considerations show that, as in the case of the ideal chains, the pair distribution function of expanded chains may also be presented in a reduced general form

$$g(\mathbf{r}) = \frac{N}{R_F^3} \tilde{g}_F \left(\frac{r}{R_F} \right). \quad (2.106)$$

Again one parameter only, R_F , enters into this expression and \tilde{g}_F is a general function. Fourier transformation of the pair distribution function gives the structure function $S_F(\mathbf{q})$:

$$S_F(\mathbf{q}) = \frac{N}{R_F^3} \int \exp(-i\mathbf{q}\mathbf{r}) \tilde{g}_F d^3\mathbf{r}. \quad (2.107)$$

A straightforward evaluation of the integral yields, for the asymptotic behavior at large q 's in an inverse correspondence to Eq. (2.105), the power law

$$S_F(\mathbf{q}) \propto q^{-5/3}. \quad (2.108)$$

Note that the fractal dimension $d = 5/3$ shows up directly in the asymptotically valid power law. Recall that this was also found for the ideal chains, where we had $S_D \propto q^{-2}$. Indeed, we meet here a general relationship: Scattering laws measured for fractal objects exhibit the fractal dimension directly in the asymptotic exponent

$$S(q) \propto q^{-d}. \quad (2.109)$$

Figure 2.18 exemplifies the predicted behavior and depicts the neutron scattering curve measured for a dilute solution of polystyrene in CS_2 , which is a good solvent. The plot of I^{-1} versus $q^{5/3}$ gives a straight line, in agreement with Eq. (2.108).

In fact, such a result, with the power law characteristic for expanded chains extending over the full q -range of the measurement, is not always found, but only for very high molar masses and a really good solvent. The range, where

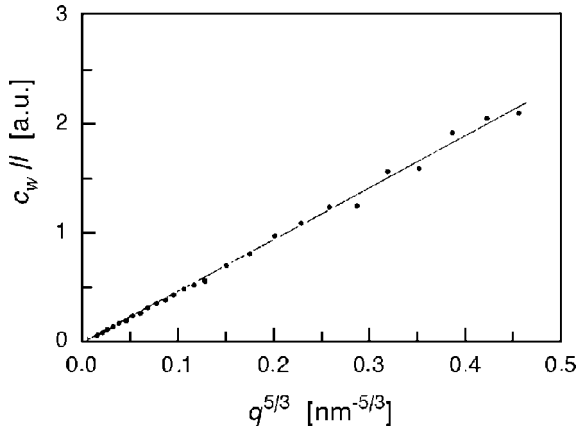


Fig. 2.18. Intensities obtained in a neutron scattering experiment on dilute solutions of (deuterated) PS ($\overline{M}_w = 1.1 \times 10^6 \text{ g mol}^{-1}$) in CS_2 ($c_w = 10^{-3} \text{ g cm}^{-3}$). The straight line corresponds to the scattering law characteristic for expanded chains. Data from Farnoux [6]

Eqs. (2.105), (2.108) apply, is in general limited. There is first an upper limit for r and correspondingly a lower limit for q , being given by the size of the chain; the validity of Eq. (2.108) ends on approaching $q \simeq 1/R_F$. Near $q = 0$, the structure function depends only on the degree of polymerization and the radius of gyration of the expanded chain, as described by Guinier's law. The relation between R_g and R_F differs slightly from the respective relation valid for ideal chains, Eq. (2.64). Computer simulations suggest a relation of the form

$$R_{g,F}^2 = \frac{R_F^2}{6.66}. \quad (2.110)$$

Of particular interest are the observations in neutron scattering experiments on solutions of polystyrene in cyclohexane presented in Fig. 2.19. These findings point to a second limitation for the power laws Eqs. (2.105) and (2.108), now towards small distances r , corresponding to high values of q . Curves enable us to follow the changes in the internal chain structure. They are introduced if starting from an ideal conformation at the theta point ($T = 35^\circ\text{C}$) by increasing the temperature. The excluded volume interaction is 'switched on', and then becomes further intensified. We see that, in the q -range of the experiment up to temperatures of about 50°C , chains remain ideal, as is demonstrated by the scattering law $I^{-1} \propto q^2$. Then, at higher temperatures deviations from ideal behavior become apparent on the low q side and indicate a cross-over to the scattering behavior of an expanded chain, $I^{-1} \propto q^{5/3} < q^2$. This is a most interesting observation, as it tells us that the chain structure actually becomes dependent on the length scale: While the structure is still ideal for short distances, for larger distances we find the properties of expanded chains. In other words, the fractal dimension of the

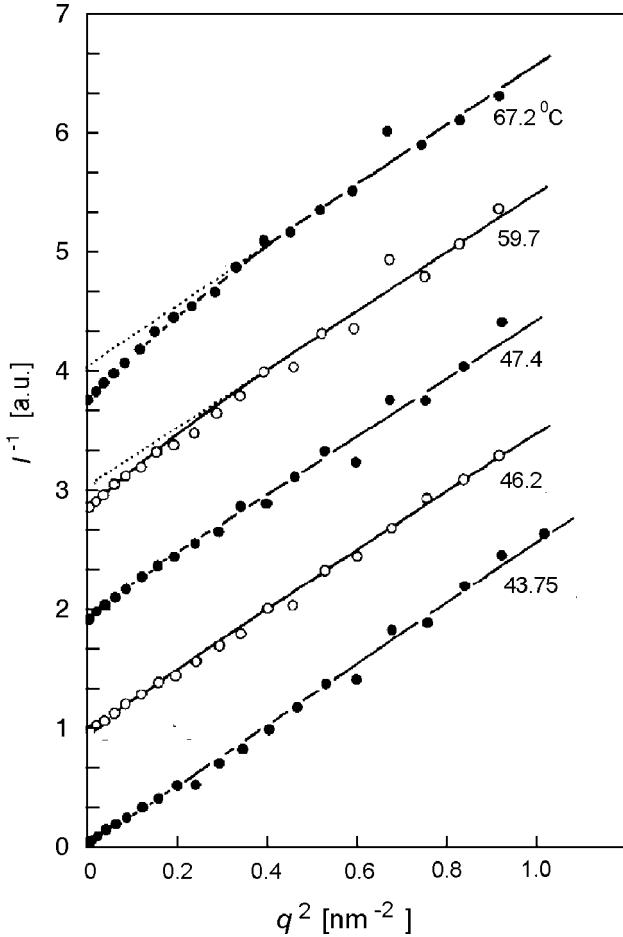


Fig. 2.19. Neutron scattering intensities $I(q)$ measured for dilute solutions of PS in cyclohexane ($\overline{M}_w = 3.8 \times 10^6 \text{ g mol}^{-1}$; $qR \gg 1$) at the indicated temperatures above the theta point ($T = 35^\circ\text{C}$). The *straight lines* correspond to the scattering law of ideal chains (subsequent curves are shifted upwards by constant amounts). Data from Farnoux et al. [7]

chain here depends on the resolution; for low resolutions $d = 5/3$, for high resolutions $d = 2$. The cross-over occurs at a certain distance, in the literature called **thermic correlation length**. Its value, ξ_t , can be derived from the value of q where the change takes place in the scattering curve, by $\xi_t \simeq 1/q$. Obviously ξ_t must be determined by the excluded volume forces, i.e., by the parameter v_e , with ξ_t shifting to lower values on increasing v_e .

The functional dependence $\xi_t(v_e)$ may be derived using simple scaling arguments. The experimental observation suggests modeling a chain with non-vanishing excluded volume interactions as indicated in Fig. 2.20. Here, the

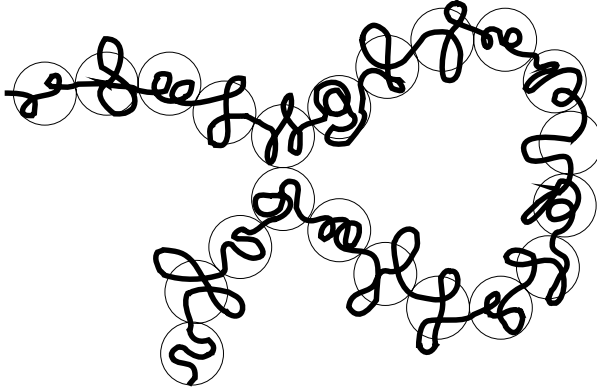


Fig. 2.20. Model of a composite chain with different fractal dimensions for $r < \xi_t$ ($d = 2$) and $r > \xi_t$ ($d = 5/3$). The cross-over distance corresponds to the size of the pearls

polymer is represented by a chain of N_{su} subunits with size ξ_t , each subunit being composed of n_{su} monomers. We have

$$N = N_{\text{su}} n_{\text{su}} . \tag{2.111}$$

Since within each subunit, chain sequences exhibit ideal behavior, we can write

$$\xi_t^2 = a_0^2 n_{\text{su}} . \tag{2.112}$$

Excluded volume interactions become effective for distances larger than ξ_t . We may account for this behavior in the model by assuming that the subunits cannot interpenetrate each other. The chain of subunits then displays the properties of an expanded chain, and we express its size with the aid of the scaling law Eq. (2.83), identifying a_F with ξ_t and N with N_{su} :

$$R_F \simeq \xi_t N_{\text{su}}^{3/5} . \tag{2.113}$$

This leads us to

$$R_F^{5/3} \simeq \xi_t^{5/3} \frac{N}{n_{\text{su}}} \tag{2.114}$$

and, in combination with Eq. (2.112), to

$$R_F^{5/3} = \xi_t^{5/3} \frac{a_0^2}{\xi_t^2} N = \frac{a_0^2}{\xi_t^{1/3}} N . \tag{2.115}$$

On the other hand, we may apply the scaling law Eq. (2.83) for expanded chains also directly, together with Eq. (2.99)

$$R_F^{5/3} = a_F^{5/3} N = v_e^{1/3} a_0^{2/3} N . \tag{2.116}$$

A comparison shows us

$$\xi_t \simeq \frac{a_0^4}{v_e}. \quad (2.117)$$

Thus, we have a reciprocal relation between ξ_t and v_e .

We previously introduced the dimensionless parameter z as (Eq. (2.90))

$$z = \left(\frac{3}{2\pi} \right)^{3/2} \frac{v_e}{a_0^4} R_0.$$

Making use of Eq. (2.117), we realize what z actually means. We obtain

$$z \simeq \frac{R_0}{\xi_t} = \frac{a_0 N^{1/2}}{a_0 n_{\text{su}}^{1/2}} = (N_{\text{su}})^{1/2} \quad (2.118)$$

and thus may conclude that z^2 gives the number of subunits of the model chain.

Above, it was pointed out that samples with ideal behavior are well represented by the asymptotic limit given by the Brownian chain, provided that the number of segments is large enough. An analogous property is found for expanded chains. Here, a mathematical object also exists, which furnishes a good representation of real chains. It is constructed in an analogous manner by carrying out a passage to the limit $N \rightarrow \infty$, $a_F \rightarrow 0$, $\xi_t \rightarrow 0$, thereby keeping R_F constant. This mathematical object, which is a continuous curve with infinite contour length like the Brownian chain, was named **Kuhnian chain** by Janninck and des Cloiseaux. It constitutes an object with a fractal dimension $d = 5/3$ for all distances $r \ll R_F$, down to $r \rightarrow 0$. Polymers in good solvents are well represented by the Kuhnian chain provided that the number of subunits is large, i.e., $z \gg 1$.

It is always useful to check for the number of independent parameters. For the Brownian chain there is only one parameter, namely R_0 . For the expanded chain in general, we find two parameters, R_F and ξ_t , but in the Kuhnian limit $\xi_t \rightarrow 0$ we return again to the simple one parameter case.

2.4 The Persistent Chain

The ideal and the expanded chain were both introduced as chains composed of freely jointed segments, under the prerequisite $a_s \gg l_{\text{ps}}$. For distances Δl along the chain with $\Delta l \leq l_{\text{ps}}$ the coil models can no longer be applied, since the local chain stiffness then leads to rod-like properties. The model of the **persistent chain**, also known as the ‘worm-like chain’ or the ‘Kratky–Porod chain’ is able to describe this change. It can be used in particular in treatments of chains with a high backbone rigidity, i.e., a high value of l_{ps} , and, moreover, when dealing with polyelectrolytes where the repulsive Coulomb forces acting between ionized groups result in a stiffening.

The basic structure of the persistent chain has, indeed, already been introduced in Fig. 2.5 at the beginning of Sect. 2.3. It shows a chain with varying curvature being represented by a curve of length l_{ct} , which possesses at each point a well-defined tangent vector, $\mathbf{e}(l)$. In order to describe the chain structure, statistics was employed and the orientational correlation function $K_{\text{or}}(\Delta l)$ introduced by Eq. (2.5)

$$K_{\text{or}}(\Delta l) = \langle \mathbf{e}(l)\mathbf{e}(l + \Delta l) \rangle .$$

The persistent chain model is obtained by an obvious choice for K_{or} , namely the exponential function

$$K_{\text{or}}(\Delta l) = \exp -\frac{\Delta l}{l_{\text{ps}}} . \quad (2.119)$$

The persistence length is included as the characteristic parameter and is equal to the integral width of K_{or} (Eq. (2.7)). A basic property of K_{or} is

$$K_{\text{or}}(\Delta l_1 + \Delta l_2) = K_{\text{or}}(\Delta l_1)K_{\text{or}}(\Delta l_2) , \quad (2.120)$$

which means that bending motions of adjacent chain parts are not correlated.

It is possible to directly derive for the thus established model the mean squared end-to-end distance $\langle R^2 \rangle$. We write

$$\mathbf{R} = \int_0^{l_{\text{ct}}} \mathbf{e}(l') dl' \quad (2.121)$$

and obtain

$$\langle \mathbf{R} \cdot \mathbf{R} \rangle = \int_{l'=0}^{l_{\text{ct}}} \int_{l''=0}^{l_{\text{ct}}} \langle \mathbf{e}(l')\mathbf{e}(l'') \rangle dl' dl'' \quad (2.122)$$

$$= 2 \int_{\Delta l=0}^{l_{\text{ct}}} K_{\text{or}}(\Delta l)(l_{\text{ct}} - \Delta l) d\Delta l \quad (2.123)$$

$$= 2 \int_{\Delta l=0}^{l_{\text{ct}}} \exp\left(-\frac{\Delta l}{l_{\text{ps}}}\right) (l_{\text{ct}} - \Delta l) d\Delta l . \quad (2.124)$$

The evaluation of the integral is straightforward and yields

$$\langle R^2 \rangle = 2l_{\text{ps}}l_{\text{ct}} - 2l_{\text{ps}}^2 \left(1 - \exp -\frac{l_{\text{ct}}}{l_{\text{ps}}}\right) . \quad (2.125)$$

We have two limiting cases: First, for $l_{\text{ct}} \gg l_{\text{p}}$ we obtain

$$\langle R^2 \rangle = 2l_{\text{ps}}l_{\text{ct}} . \quad (2.126)$$

Since $l_{ct} \propto N$, we find here, as expected, the scaling law of an ideal chain. The Kuhn segment length a_K of an ideal chain was introduced in Eqs. (2.29) and (2.30), (Eq. (2.31))

$$\langle R^2 \rangle = a_K l_{ct} \quad (2.127)$$

if we identify l_{ct} with the length R_{\max} of the straight, fully extended chain. A comparison gives the relation

$$2l_{ps} = a_K \quad (2.128)$$

between the persistence length and the length of the Kuhn segment. The other limit, that of a stiff rod, is found for $l_{ct} \ll l_{ps}$. A power law expansion of the exponential function in Eq. (2.125) yields

$$\langle R^2 \rangle = l_{ct}^2. \quad (2.129)$$

Equation (2.125) thus describes the transition from rod-like properties to a coil structure. Here the equation refers to chains with varying length l_{ct} , but, when replacing l_{ct} by Δl and $\langle R^2 \rangle$ by $\langle r_{ij}^2 \rangle$, it can also be applied to one given chain to express the changing inner structure.

How does the persistence length change with the temperature? An answer follows from a statistical mechanical treatment of the bending motion of a long thin rod. The given mechanical property is its stiffness, which can be specified by a **bending modulus** E_b . Consider now a short piece of length Δl within this rod as is sketched in Fig. 2.21. Imagine that starting from the straight conformation plotted on the left bending is carried out, keeping the lower end

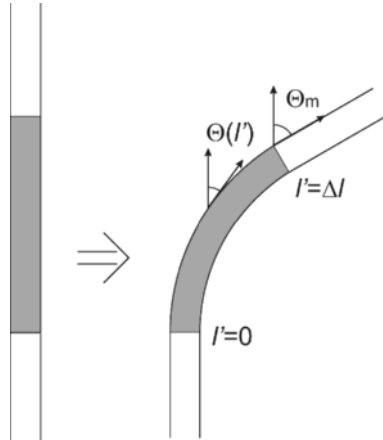


Fig. 2.21. Bending of a section with length Δl within a thin rod: The direction θ of the tangent vector \mathbf{e} changes linearly between 0 and θ_m

fixed and turning the upper end by an angle θ_m . In mechanical equilibrium θ changes linearly,

$$\theta(l) = \frac{\theta_m}{\Delta l} l, \quad (2.130)$$

within this section, i.e., a circular form with a constant curvature develops. Using E_b , the local bending energy per unit length is given by

$$\frac{du}{dl} = \frac{E_b}{2} \frac{de}{dl} \frac{de}{dl} \quad (2.131)$$

$$= \frac{E_b}{2} \left(\frac{d\theta}{dl} \right)^2. \quad (2.132)$$

The total energy stored in the curved section of length Δl is therefore

$$\Delta u = \frac{E_b}{2} \left(\frac{\theta_m}{\Delta l} \right)^2 \Delta l. \quad (2.133)$$

At a temperature T the mean energy uptake is given by

$$kT = \langle \Delta u \rangle = \frac{E_b}{2} \frac{\langle \theta_m^2 \rangle}{\Delta l}, \quad (2.134)$$

which leads to

$$\frac{\langle \theta_m^2 \rangle}{2} = \frac{kT \Delta l}{E_b}. \quad (2.135)$$

The orientational correlation function specifies the magnitude of the bending motion. We have

$$K_{\text{or}}(\Delta l) = \langle \mathbf{e}(l) \mathbf{e}(l + \Delta l) \rangle = \langle \cos \theta_m \rangle \approx 1 - \frac{\langle \theta_m^2 \rangle}{2} = 1 - \frac{kT \Delta l}{E_b}. \quad (2.136)$$

Using the power law expansion of the exponential function,

$$K_{\text{or}}(\Delta l) \approx 1 - \frac{\Delta l}{l_{\text{ps}}}, \quad (2.137)$$

we obtain by comparison

$$l_{\text{ps}} = \frac{E_b}{kT}. \quad (2.138)$$

Hence, the persistence length is proportional to the bending modulus and decreases with increasing temperature. In the case of polyelectrolyte chains in solution, the bending modulus relates to both, the inner stiffness of the chain as given by the properties of the chain backbone and to the Coulomb repulsive forces between the chain-fixed ions. Note that the stiffness introduced and expressed by the parameter l_{ps} expands the chain only over finite distances. As demonstrated by Eq. (2.126) no long-ranged expansion results because it is produced by the excluded volume effect. Persistent chains still belong to the universality class of ideal chains.

Different from the ideal chain description, the persistent chain model is not only able to deal with short chains, but also addresses the effect of temperature. Another model, which will be introduced as the ‘Ising chain’ in the next section, accomplishes these tasks in an even more detailed, rather perfect manner.

2.5 The Ising Chain

A discussion of the properties of a polymer chain only on the basis of the global scaling laws or with the aid of Eqs. (2.125) and (2.138) would be incomplete. The description of specific properties of a given polymer molecule, as for example its internal energy or entropy, requires a different approach. For this purpose, one needs a treatment that takes the energetics of the chain into account. As was explained at the beginning of this chapter, chain conformations may be described microscopically in terms of the accessible rotational isomeric states. Now we shall see that this representation of a polymer corresponds exactly to the one-dimensional Ising model, also known as the **Ising chain**, which is an important concept in general statistical mechanics. As the tools for the treatment of Ising chains are well-known, Birshtein and Ptitsyn, and Flory adapted the Ising model to the polymer problem. This adaptation addressed in the literature as the **rotational isomeric state (RIS) model**, opens a straightforward way to calculate the thermodynamic functions and the specific structural properties of a given polymer chain.

The general Ising chain is set up by an array of interacting particles, with each particle being able to change between a certain number of different states. In the simplest case, interactions are restricted to adjacent pairs. Then the total energy of the chain equals the sum of the interaction energies between neighbors and for n particles is given by

$$u = \sum_{i=2}^n u(\varphi_{i-1}, \varphi_i). \quad (2.139)$$

Here φ_i denotes the state of particle i and $u(\varphi_{i-1}, \varphi_i)$ is the pair interaction energy.

The relation to a polymer chain becomes clear when one considers that the energy of one conformational state is a function of the rotational isomeric states of all N_b backbone bonds. The latter correspond to the ‘particles’ of the Ising chain. Conditions would be trivial if all bonds were energetically independent, since then the chain energy would be equal to N_b times the mean energy of a single bond. In reality, however, adjacent bonds may well affect each other. This is nicely exemplified by polyethylene, where the ‘pentane effect’, indicated in Fig. 2.22, becomes effective. The depicted conformation represents the sequence gauche⁺-gauche⁻, and pentane is the shortest n -alkane, for which this sequence may be built up. As we see, a sharp fold

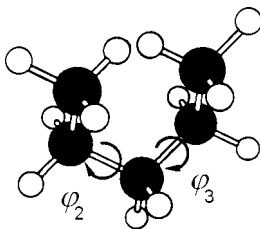


Fig. 2.22. The conformation of pentane associated with a sequence $\varphi_2 \hat{=} \text{gauche}^+$, $\varphi_3 \hat{=} \text{gauche}^-$. A sharp fold with elevated energy is formed

is formed, and it is clear that this requires more energy than is necessary to form two independent gauche-states. Since the Ising model deals with energies depending on the states of both partners in a pair, it can take this situation into account.

The main task in the computation of thermodynamic functions is the calculation of the partition function, denoted Z . In our case, its basic form can be formulated directly, as

$$Z = \sum_{\{\varphi_i\}} \exp -\frac{u\{\varphi_i\}}{kT} . \quad (2.140)$$

The summation includes all conformational states, here shortly designated by $\{\varphi_i\}$, each state being determined by specifying the conformations of all bonds

$$\{\varphi_i\} \hat{=} (\varphi_1, \varphi_2, \dots, \varphi_{N_b}) .$$

The energy for each conformational state of the chain follows from Eq. (2.139).

Knowing the partition function, we can employ general laws of thermodynamics in order to deduce the free energy per polymer chain, using

$$f_p = -kT \ln Z , \quad (2.141)$$

the entropy per chain, by

$$s_p = -\frac{\partial f_p}{\partial T} , \quad (2.142)$$

and the internal energy per polymer, by

$$e_p = f_p + T s_p . \quad (2.143)$$

The partition function Z can be evaluated in straightforward manner. We write

$$\begin{aligned} Z &= \sum_{\varphi_2} \cdots \sum_{\varphi_{N_b-1}} \exp \left(-\frac{1}{kT} \sum_{i=2}^{N_b} u(\varphi_{i-1}, \varphi_i) \right) \\ &= \sum_{\varphi_2} \cdots \sum_{\varphi_{N_b-1}} \prod_{i=2}^{N_b} \exp \left(-\frac{1}{kT} u(\varphi_{i-1}, \varphi_i) \right) , \end{aligned} \quad (2.144)$$

or, introducing the **statistical weights**

$$t(\varphi_{i-1}, \varphi_i) = \exp\left(-\frac{1}{kT}u(\varphi_{i-1}, \varphi_i)\right) \quad (2.145)$$

briefly

$$Z = \sum_{\varphi_2} \cdots \sum_{\varphi_{N_b-1}} \prod_{i=2}^{N_b} t(\varphi_{i-1}, \varphi_i). \quad (2.146)$$

To explain further, let us select polyethylene as an example. Here, for the three states per bond, nine different values t_{ij} exist. We collect them in a matrix \mathbf{T}

$$\mathbf{T} = \begin{pmatrix} 1 & w_0 & w_0 \\ 1 & w_0 & w_1 w_0 \\ 1 & w_1 w_0 & w_0 \end{pmatrix}. \quad (2.147)$$

Thereby we attribute to the different rotational isomeric states the following indices

$$\text{trans} \hat{=} 1, \quad \text{gauche}^+ \hat{=} 2, \quad \text{gauche}^- \hat{=} 3.$$

The matrix includes two parameters, denoted w_0 and w_1 . To understand the matrix structure, imagine that a specific conformation is formed by subsequently arranging all bonds, emanating from the lowest energy state all-trans. We start at $i = 2$ and then proceed up to the end, $i = N_b - 1$ (the step to the last bond, $i = N_b$, can be omitted, since for this bond without a further neighbor no energy contribution arises). The coefficients of the matrix give the statistical weights associated with each step:

1. Since no energy is required if the trans-state is maintained, we have

$$u(i, 1) = 0 \rightarrow t_{i1} = 1.$$

2. Formation of a gauche⁺-state after a trans- or gauche⁺-state requires an energy Δu_{tg} and thus carries a statistical weight

$$w_0 = \exp -\Delta u_{tg}/kT < 1. \quad (2.148)$$

3. Increased energies of formation are associated with the ‘hairpin-bend’-conformations gauche⁺-gauche⁻ and gauche⁻-gauche⁺, resulting in lowered statistical weights, as expressed by the product $w_1 w_0$ with

$$w_1 < 1.$$

The evaluation of the partition function

$$\begin{aligned} Z &= \sum_{\varphi_2} t(\varphi_t, \varphi_2) \cdot \sum_{\varphi_3} t(\varphi_2, \varphi_3) \cdots \sum_{\varphi_{N_b-2}} t(\varphi_{N_b-3}, \varphi_{N_b-2}) \\ &\cdot \sum_{\varphi_{N_b-1}} t(\varphi_{N_b-2}, \varphi_{N_b-1}) t(\varphi_{N_b-1}, \varphi_t) \end{aligned} \quad (2.149)$$

can be rationalized using matrix multiplication rules. We can repeatedly apply the general summation rule

$$\sum_l t_{il}t_{lj} = (\mathbf{T}^2)_{ij} \quad (2.150)$$

for successive reductions:

$$\begin{aligned} Z &= \sum_{\varphi_2} t(\varphi_t, \varphi_2) \cdot \sum_{\varphi_3} t(\varphi_2, \varphi_3) \cdots \sum_{\varphi_{N_b-2}} t(\varphi_{N_b-3}, \varphi_{N_b-2}) \cdot (\mathbf{T}^2)_{\varphi_{N_b-2}, \varphi_t} \\ &= \sum_{\varphi_2} t(\varphi_t, \varphi_2) \cdot \sum_{\varphi_3} t(\varphi_2, \varphi_3) \cdots \sum_{\varphi_{N_b-3}} t(\varphi_{N_b-4}, \varphi_{N_b-3}) \cdot (\mathbf{T}^3)_{\varphi_{N_b-3}, \varphi_t} \\ &\quad \cdot \\ &\quad \cdot \\ &= (\mathbf{T}^{N_b-2})_{11} . \end{aligned} \quad (2.151)$$

Hence, Z can be obtained by calculating the power $(N_b - 2)$ of \mathbf{T} and extracting the 11-coefficient. The task of calculating the power $(N_b - 2)$ of \mathbf{T} can be much simplified if \mathbf{T} is first transformed into a diagonal form. This can be achieved as usual by solving the set of homogeneous linear equations

$$\sum_j T_{ij}A_j = \lambda A_i , \quad (2.152)$$

i.e., evaluating the determinant

$$|\mathbf{T} - \lambda \mathbf{1}| = 0 . \quad (2.153)$$

There are three eigenvalues, λ_1, λ_2 and λ_3 , and they set up a diagonal matrix $\mathbf{\Lambda}$. The matrix \mathbf{A} that transforms \mathbf{T} into $\mathbf{\Lambda}$

$$\mathbf{\Lambda} = \mathbf{A}^{-1}\mathbf{T}\mathbf{A} \quad (2.154)$$

is composed of the three eigenvectors, $(A_{1,j}), (A_{2,j}), (A_{3,j})$. With the aid of $\mathbf{\Lambda}$, the matrix multiplication becomes very simple

$$\begin{aligned} \mathbf{T}^{N_b-2} &= (\mathbf{A}\mathbf{\Lambda}\mathbf{A}^{-1})^{N_b-2} \\ &= \mathbf{A}\mathbf{\Lambda}\mathbf{A}^{-1}\mathbf{A}\mathbf{\Lambda}\mathbf{A}^{-1} \cdots \mathbf{A}\mathbf{\Lambda}\mathbf{A}^{-1} \\ &= \mathbf{A}\mathbf{\Lambda}^{N_b-2}\mathbf{A}^{-1} . \end{aligned} \quad (2.155)$$

We employ this equation and obtain an explicit expression for the partition function Z

$$Z = A_{11}(A^{-1})_{11}\lambda_1^{N_b-2} + A_{12}(A^{-1})_{21}\lambda_2^{N_b-2} + A_{13}(A^{-1})_{31}\lambda_3^{N_b-2} . \quad (2.156)$$

Usually all three eigenvalues are different and one, say λ_1 , is the largest

$$\lambda_1 > \lambda_2, \lambda_3 .$$

Since N_b is huge, the partition function is well approximated by

$$Z \approx A_{11}(A^{-1})_{11}\lambda_1^{N_b-2} . \quad (2.157)$$

The free energy then follows as

$$f_p = -kT \left((N_b - 2) \ln \lambda_1 + \ln (A_{11}A_{11}^{-1}) \right) . \quad (2.158)$$

For a polymer, where $N_b \gg 1$, we can ignore the constant second term. This leads us to a simple expression for the free energy per bond

$$\frac{f_p}{N_b} = -kT \ln \lambda_1 . \quad (2.159)$$

The entropy and the internal energy per bond follow as

$$\frac{s_p}{N_b} = k \ln \lambda_1 + \frac{kT}{\lambda_1} \frac{\partial \lambda_1}{\partial T} \quad (2.160)$$

and

$$\frac{e_p}{N_b} = \frac{f_p}{N_b} + T \frac{s_p}{N_b} . \quad (2.161)$$

As we can see, in the framework of the RIS model it is a simple matter of deriving the thermodynamic functions for a given polymer chain, the only requirement being a knowledge of the matrix \mathbf{T} of the statistical weights.

Let us carry out the calculation for polyethylene. The determinant equation to be solved is

$$\begin{vmatrix} 1 - \lambda & w_0 & w_0 \\ 1 & w_0 - \lambda & w_0 w_1 \\ 1 & w_0 w_1 & w_0 - \lambda \end{vmatrix} = 0 . \quad (2.162)$$

This is a third order equation, but an evaluation shows that it factorizes, having the form

$$(w_0 - \lambda - w_0 w_1)[\lambda^2 - \lambda(w_0 + w_0 w_1 + 1) + w_0(w_1 - 1)] = 0 . \quad (2.163)$$

Therefore, the solutions can be given analytically. The three eigenvalues are

$$\begin{aligned} \lambda_{1/2} &= \frac{1}{2} \left[(w_0 + w_0 w_1 + 1) \pm \sqrt{(w_0 + w_0 w_1 + 1)^2 + 4w_0(1 - w_1)} \right] \\ \lambda_3 &= w_0(1 - w_1) . \end{aligned} \quad (2.164)$$

As is obvious, the largest eigenvalue is λ_1 .

It is instructive to consider the numerical results for polyethylene in a computation for its melting point, $T_f = 415$ K. For the energy required to form a gauche-state after a trans-state we choose the value $\Delta \tilde{u}_{tg} = 2$ kJ mol⁻¹ (see

Sect. 2.1) and obtain $w_0 = 0.56$. The second statistical weight that is needed, the product $w_0 w_1$, has so far not been experimentally determined. Estimates for the related energy of the hairpin-bend states have been obtained by potential energy calculations, using empirical expressions for the non-bonded interaction energies. Values in the range of 7 kJ mol^{-1} are thus indicated, corresponding to a statistical weight $w_0 w_1 = 0.13$. With these values the following results are obtained for the thermodynamic functions, expressed per mol of CH_2 -units:

$$\begin{aligned}\tilde{f} &= N_{\text{L}} f_{\text{p}} / N_{\text{b}} = -2.28 \text{ kJ mol}^{-1}, \\ \tilde{s} &= N_{\text{L}} s_{\text{p}} / N_{\text{b}} = 8.25 \text{ J K}^{-1} \text{ mol}^{-1}, \\ \tilde{e} &= N_{\text{L}} e_{\text{p}} / N_{\text{b}} = 1.14 \text{ kJ mol}^{-1}.\end{aligned}$$

It is interesting to compare these results with the measured heat of fusion and the entropy of fusion

$$\begin{aligned}\Delta \tilde{h}_{\text{f}} &= 4.10 \text{ kJ mol}^{-1}, \\ \Delta \tilde{s}_{\text{f}} &= \Delta \tilde{h}_{\text{m}}^{\text{f}} / T_{\text{f}} = 9.9 \text{ J K}^{-1} \text{ mol}^{-1}.\end{aligned}$$

We notice that the experimental heat of fusion, $\Delta \tilde{h}_{\text{f}}$, is much larger than can be accounted for by the change in the intramolecular conformational energy, as given by \tilde{e} . Hence, the major part of the heat of fusion seems to be related to a change in the intermolecular energy, i.e., to the increase in the specific volume (which amounts to 15%). With regard to the change in entropy, the conclusions are different. Here the major part is indeed contributed by the change of the conformation from the all-trans state into the coiled form, with only the smaller rest being due to the increase in free volume.

In Sect. 2.1 we carried out a first estimate of the fraction of trans-states and gauche-states in polyethylene. In this estimate, independence of the rotational isomeric states of different bonds was implicitly assumed. We now may check for the modification introduced by the pentane effect, because the Ising model also provides us with equations for the fractions of the different pairs of conformational states. We rewrite the partition function

$$Z = \sum_{\{\varphi_i\}} t(\varphi_1, \varphi_2) \dots t(\varphi_{N_{\text{b}}-2}, \varphi_{N_{\text{b}}})$$

and choose a special form that collects all conformations with l pairs of type (i, j) . These pairs produce a factor t_{ij}^l . We extract this factor and denote the remainder $\Omega(i, j; l)$

$$Z = \sum_{l=0}^{N_{\text{b}}-1} (t_{ij})^l \dots \Omega(i, j; l). \quad (2.165)$$

The probability for one specific conformation, $p\{\varphi_i\}$, is given by

$$p\{\varphi_i\} = \frac{\exp(-u\{\varphi_i\}/kT)}{Z}. \quad (2.166)$$

We first derive the probability $p(i, j; l)$ that l pairs of type (i, j) occur in the chain. The necessary summation over the corresponding states of the chain is already implied in our formulation, and we can write

$$p(i, j; l) = \frac{t_{ij}^l \Omega(i, j, l)}{Z}. \quad (2.167)$$

From this result it follows that the average number of pairs (i, j) , denoted $\langle n_{ij} \rangle$, is given by

$$\langle n_{ij} \rangle = \sum_{l=0}^{N_b-1} l \frac{t_{ij}^l \Omega(i, j, l)}{Z}. \quad (2.168)$$

or, using the above relations, by

$$\langle n_{ij} \rangle = \frac{t_{ij}}{Z} \frac{\partial Z}{\partial t_{ij}} = \frac{\partial \ln Z}{\partial \ln t_{ij}} = (N_b - 1) \frac{\partial \ln \lambda_1}{\partial \ln t_{ij}}. \quad (2.169)$$

The probability for a sequence (i, j) in adjacent bonds, denoted ϕ_{ij} , is

$$\phi_{ij} = \frac{\langle n_{ij} \rangle}{N_b - 1} = \frac{\partial \ln \lambda_1}{\partial \ln t_{ij}}. \quad (2.170)$$

Insertion of the statistical weights w_0 and $w_0 w_1$ yields

$$\begin{aligned} \phi_{tt} &= 0.29, \\ \phi_{g^+t} &= \phi_{tg^+} = \phi_{g^-t} = \phi_{tg^-} = 0.14, \\ \phi_{g^+g^+} &= \phi_{g^-g^-} = 0.06, \\ \phi_{g^+g^-} &= \phi_{g^-g^+} = 0.015. \end{aligned}$$

The pentane effect shows up quite clearly, as the fraction of pairs with sequences gauche⁺-gauche⁻ and gauche⁻-gauche⁺ is rather low.

Finally, the fractions of trans- and gauche-conformational states in the polyethylene chains are obtained by

$$\phi_i = \sum_j \phi_{ij}, \quad (2.171)$$

resulting in

$$\begin{aligned} \phi_t &= 0.60, \\ \phi_{g^+} &= \phi_{g^-} = 0.20. \end{aligned}$$

As expected, compared to the estimate based on the assumption of independent rotational isomeric states, the fraction of trans-states is increased.

The RIS model also enables a computation of the characteristic ratio C_∞ to be made, if the stereochemical properties of the chain are included into the considerations. The calculations are more tedious but, using the algebraic

properties of matrices, they can still be carried out in straightforward manner. As it turns out, the experimental value for polyethylene, $C_\infty = 6.7$, is reproduced for reasonable assumptions about the molecular parameters, namely a C–C–C valence angle of 112° and gauche-rotational angles $\varphi_{g^+} = 127.5^\circ$ and $\varphi_{g^-} = 232.5^\circ$.

One may even advance one step further and calculate structure factors of specific chains numerically, for a comparison with the results of scattering experiments. Figure 2.23 presents, as an example, neutron scattering data of polycarbonate obtained for mixtures of deuterated and protonated species. The experiment covers a large range of q 's, and results are represented in the form of a Kratky plot.

We observe a plateau, characteristic for ideal chains, and then a rise at higher q 's, for distances shorter than the persistence length where the microscopic chain structure takes over control. The peculiar shape of the curve in this range reflects specific properties of polycarbonate and indeed, these can be reproduced by calculations on the basis of the RIS model. The continuous curve represents the theoretical results, and even if the agreement is not perfect, it describes the main characteristics qualitatively correctly.

Calculations based on the RIS model now exist for the majority of common polymers, thus providing a quantitative representation of the energetic and structural properties of single macromolecules. The prerequisite is a knowledge about the energies $u(\varphi_{i-1}, \varphi_i)$ associated with the different pairs of conformational states. Information about these values has improved steadily with the number of carefully analyzed experiments. Clearly, the model does not account for the excluded volume interaction, but it provides a microscopic understanding for all situations with ideal chain behavior.

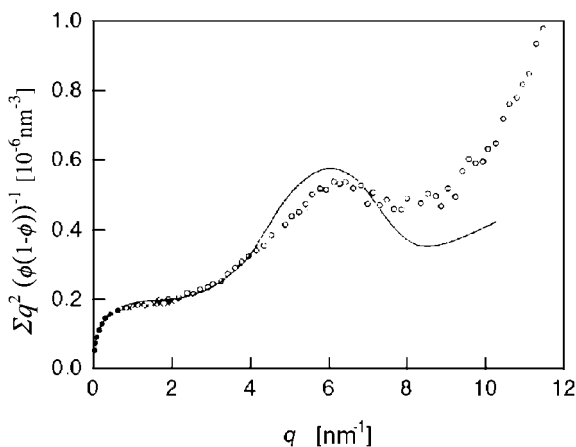


Fig. 2.23. Neutron scattering experiment on mixtures of PC and d-PC. The *continuous curve* has been calculated on the basis of the RIS model. Data from Gawrisch et al. [8]

Further Reading

- R.H. Boyd, P.J. Phillips: *The Science of Polymer Molecules*, Cambridge University Press, 1993
- P.J. Flory: *Statistical Mechanics of Chain Molecules*, John Wiley & Sons, 1969
- P.-G. de Gennes: *Scaling Concepts in Polymer Physics*, Cornell University Press, 1979
- A.Y. Grosberg, A.R. Khokhlov: *Statistical Physics of Macromolecules*, AIP Press, 1994
- W.L. Mattice, U.W. Suter: *Conformational Theory of Large Molecules – The Rotational Isomeric State Model in Macromolecular Systems*, Wiley & Sons, 1994
- H. Tadokoro: *Structure of Crystalline Polymers*, John Wiley & Sons, 1979

Polymer Solutions

After having considered the structural behavior of single chains we turn now to the collective properties of polymers in bulk phases and in the next two chapters we discuss liquid states of order. Liquid polymers are in thermal equilibrium, so that statistical thermodynamics can be applied. At first view one might think that theoretical analysis presents a formidable problem since each polymer may interact with many other chains. This multitude of interactions can, of course, create a complex situation; however, cases also exist where conditions allow for a facilitated treatment. Important representatives for simpler behavior are melts and liquid **polymer mixtures** and the basic reason is easy to see. As here each monomer encounters, on average, the same surroundings, the chain as a whole experiences a mean field, thus fulfilling the requirements for an application of a well-established theoretical scheme, the **mean field treatment**. We shall deal with this approach in Chap. 4 when we discuss the properties of polymer mixtures. Chapter 4 includes in Sect. 4.4 also a brief introduction into the properties of **block copolymers**, which can also be treated by mean field theories. Block copolymers are obtained by chemically coupling two different polymer chains. In addition to a homogeneous melt with short-range ordering, also lattices with long-range order are observed, and the transformation shows some of the properties of second order phase transitions. **Polymer solutions**, on the other hand, cannot be treated under the mean field assumptions. Take expanded chains in dilute solution, for example. Here, we find considerable variations in the monomer density, in the solution altogether and also within each chain where we have a maximum at the center, followed by decays to the edges. Here replacement of the spatially varying interaction energy density by a mean value, corresponding to an equal interaction of each monomer with a constant mean field, is not allowed. In the previous chapter, when discussing expanded chains, we indicated how theory can comply with such a situation, scaling arguments and renormalization group treatments providing solutions. It was another great achievement of the French school around des Cloiseaux and de Gennes to show that this treatment can be further

extended to deal also with situations where chains begin to overlap. This became known as the regime of semidilute solutions, and in this chapter we shall present some major results in order to provide a first basic understanding.

The situation changes completely when the dissolved chains are polyelectrolytes rather than electrically neutral macromolecules. **Polyelectrolytes** in a, usually aqueous, – solution dissociate in polyions with fixed positive or negative charges and mobile counter-ions. The arising Coulomb forces are much stronger than the van der Waals forces and result in quite unusual solution properties.

3.1 Dilute and Semidilute Solutions

Polymer chains in dilute solutions are isolated and interact with each other only during brief times of encounter. Increasing the polymer concentration in a solvent leads to a change at a certain stage. As is schematically indicated in Fig. 3.1, a limit is reached when the polymer molecules become closely packed because then they begin to interpenetrate.

The monomer concentration at this limit can be estimated by regarding that for close-packed polymers this concentration must agree with the mean concentration in a single chain. For expanded chains we find for the critical concentration at the **overlap limit**, c_m^* , the expression

$$c_m^* \simeq \frac{N}{R_F^3}. \quad (3.1)$$

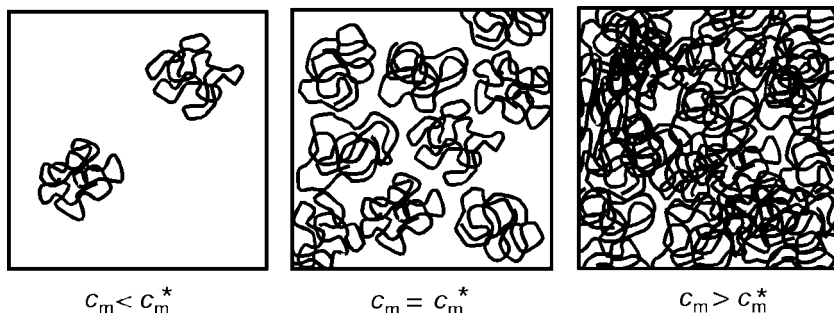


Fig. 3.1. Polymer solution: Dilute regime ($c_m < c_m^*$) and semidilute regime with overlapping chains ($c_m > c_m^*$). The cross-over occurs for $c_m = c_m^*$ when the volumes occupied by the individual chains just cover the sample volume

Since we need a unique expression for the further treatments, we replace the above estimate by an exact equation and write, per definition

$$c_m^* = \frac{N}{R_F^3} . \quad (3.2)$$

It is interesting to check how the location of c_m^* changes with the degree of polymerization. For a good solvent, the scaling law Eq. (2.83) applies and we have

$$c_m^* = \frac{N}{a_F^3 N^{9/5}} = \frac{1}{a_F^3 N^{4/5}} . \quad (3.3)$$

The volume fraction ϕ of polymers in a solution is generally

$$\phi = v_m c_m , \quad (3.4)$$

where v_m designates the monomer volume. The volume fraction ϕ^* associated with the critical concentration is therefore

$$\phi^* = v_m c_m^* = \frac{v_m}{a_F^3 N^{4/5}} . \quad (3.5)$$

Since a_F is always much larger than the actual length of a monomer, we have

$$\frac{v_m}{a_F^3} < 1$$

and therefore

$$\phi^* < N^{-4/5} . \quad (3.6)$$

We learn from this estimate that for a typical polymer, say with $N \simeq 10^4$, interpenetration of chains already begins at volume fractions below 0.001. In order to have dilute conditions, polymer volume fractions have to be really low, below 10^{-4} . On the other hand, solutions with polymer volume fractions in the order of 10^{-3} – 10^{-1} , which can still be considered as low, are already clearly affected by the chain interpenetration. To set this special class of solutions apart from both the dilute and the concentrated solutions a new name was introduced: They are called **semidilute**.

3.1.1 Osmotic Pressure

In discussions of solution behavior, the osmotic pressure Π becomes a property of primary interest. Π depends on the temperature and the concentration of the solute. In this section we will discuss the form of this dependence and begin with considering dilute polymer solutions.

As for low molar mass solutes, a virial expansion can also be used for polymers to give Π in the limiting range of low concentrations

$$\Pi = kT (A_1 c_m + A_2 c_m^2 + \dots) . \quad (3.7)$$

This is a series expansion in powers of the solute concentration and the A_i 's are the i -th **virial coefficients**. For an ideal solution of low molar mass molecules all higher order virial coefficients beginning with the second virial coefficient A_2 vanish, and furthermore we have

$$A_1 = 1 . \quad (3.8)$$

The dependence $\Pi(c_m)$ then agrees exactly with the pressure-concentration dependence of an ideal gas. For dissolved polymers the first virial coefficient is not unity but given by

$$A_1 = 1/N . \quad (3.9)$$

The reason for the change is easily seen. Remember that the osmotic pressure is a colligative property. It is exerted by the translational motion of the centers of mass of the polymers only, not being affected by the internal degrees of freedom of the chains. This implies that, for polymer solutions, the polymer density

$$c_p = \frac{c_m}{N} \quad (3.10)$$

rather than the monomer density controls quantity for the osmotic pressure. The virial expansion therefore has to be expressed as

$$\begin{aligned} \frac{\Pi}{kT} &= \frac{c_m}{N} + A_2 c_m^2 + \dots \\ &= \frac{c_m}{N} (1 + N A_2 c_m + \dots) . \end{aligned} \quad (3.11)$$

Equation (3.11) is the virial expansion valid for a dilute polymer solution. One may also interpret the second order term. It describes an increase in osmotic pressure due to the contacts between the dissolved polymer molecules, which occur with a probability proportional to $c_p^2 \propto c_m^2$.

For experimental studies, another form is more convenient, where the number density of monomers, c_m , is replaced by the mass concentration c_w , using

$$c_w = \frac{c_m}{N_L} M_m ; \quad (3.12)$$

M_m describes the molar mass of a monomer. In addition, one introduces a modified second virial coefficient, \tilde{A}_2 , defined as

$$\tilde{A}_2 = \frac{N_L A_2}{M_m^2} . \quad (3.13)$$

Equation (3.11) can then be rewritten as

$$\frac{\Pi}{\tilde{R}T} = c_w \left(\frac{1}{M} + \tilde{A}_2 c_w + \dots \right) . \quad (3.14)$$

Figure 3.2 presents a typical experimental result. It shows the dependence of the osmotic pressure on c_w for a series of poly(α -methylstyrenes), with

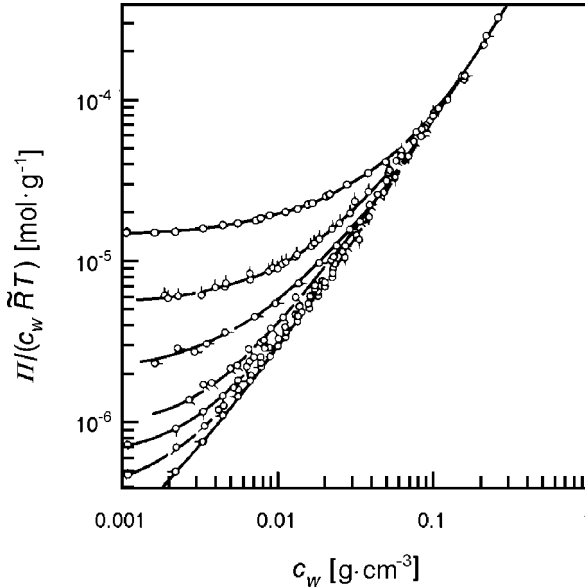


Fig. 3.2. Osmotic pressures measured for samples of poly(α -methylstyrene) dissolved in toluene (25 °C). Molar masses vary between $M = 7 \times 10^4 \text{ g mol}^{-1}$ (uppermost curve) and $M = 7.47 \times 10^6 \text{ g mol}^{-1}$ (lowest curve). Data taken from Noda et al. [9]

different molar masses, dissolved in toluene. First, it is noted that the limiting values $c_w \rightarrow 0$ change with the molar mass. Actually, they agree with the relation

$$\lim_{c_w \rightarrow 0} \frac{\Pi}{\tilde{R}T c_w} = \frac{1}{M}. \quad (3.15)$$

Secondly, since $\Pi/\tilde{R}T c_w$ increases with c_w , we have evidence for a non-vanishing positive second virial coefficient as it is indicative for a good solvent. The third observation is that, in the limit of high concentrations, the molar mass dependence of Π vanishes. This occurs when the polymer chains interpenetrate each other and an entanglement network builds up. The observation tells us that, once the entanglement network has formed, the single chain properties become irrelevant.

An especially interesting result is presented in Fig. 3.3, which deals with the same set of data here plotted in a special form. We make use of c_w^* , the polymer weight fraction at the overlap limit and replace c_w by a dimensionless reduced variable x , called the **overlap ratio**

$$x = \frac{c_w}{c_w^*} = \frac{c_m}{c_m^*}. \quad (3.16)$$

c_m^* or c_w^* follow from Eq. (3.2) when R_F is determined by light scattering or, as will be explained below, also directly from A_2 . Along the ordinate, the

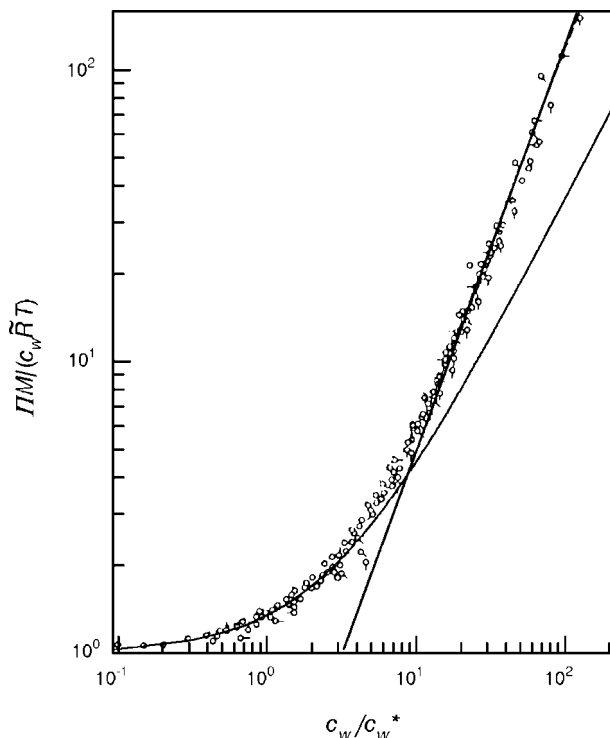


Fig. 3.3. Data of Fig. 3.2, presented in a plot of the reduced osmotic pressure versus the overlap ratio. The *continuous lines* correspond to the theoretical results Eqs. (3.26), (3.41)

expression $\Pi M / (\tilde{R} T c_w)$ is plotted. For this **reduced osmotic pressure** we have a common limit for $c_w \rightarrow 0$, independent of M

$$\lim_{c_w \rightarrow 0} \frac{\Pi M}{\tilde{R} T c_w} = 1. \quad (3.17)$$

The result of this redrawing procedure is quite remarkable: The curves for all samples coincide.

The conclusions that can be drawn from these observations are far-reaching and important. Polymers in solution interact with each other and details of this interaction become apparent in the concentration dependence of the osmotic pressure. The results presented in Figs. 3.2 and 3.3 strongly suggest that the interaction obeys general laws that are valid for all polymers and solvents.

Let us consider the given situation and search for an equation for the osmotic pressure. First we have to inquire about the independent variables in the system. In the case of a dilute solution, we have three of them apart from the trivial T . To specify the single chain properties, we must know the Flory

radius R_F and the thermic correlation length ξ_t or the parameter z . The third variable is the number density of polymers c_p . The question arises whether there are any more parameters that have to be accounted for when leaving the dilute range and coming into the regime of the semidilute solutions. The answer is no for physical reasons: We encounter only one class of interactions throughout, the excluded volume forces, which do not differentiate between monomers within a chain and on different chains. Their effect is implied in the values of R_F and z . As the cross-over to the semidilute regime does not bring in any new forces, there is also no further parameter. This remains true as long as the monomer concentration in the solution is sufficiently low so that one has to account for binary interactions only. At higher concentrations, where ternary interactions become progressively important; the situation changes.

Having identified the independent variables, we can formulate the following functional dependence for Π :

$$\frac{\Pi}{kT} = c_p F(R_F, \xi_t, c_p) . \quad (3.18)$$

F is a universal function with properties to be discussed. With the extraction of the factor c_p , we fix the limit $F(c_p \rightarrow 0)$. As we expect ideal properties for $c_p \rightarrow 0$, we have

$$F(c_p \rightarrow 0) = 1 . \quad (3.19)$$

The experimental result depicted in Fig. 3.3 provides us with a hint with regard to the form of F . It suggests that R_F and c_p are included in a coupled manner, namely as the product $c_p R_F^3$, which is identical with the overlap ratio

$$x = \frac{c_m}{c_m^*} = c_p R_F^3 . \quad (3.20)$$

We therefore write, and this was first proposed by des Cloiseaux,

$$\frac{\Pi}{kT} = c_p F_{II}(x, z) . \quad (3.21)$$

Here ξ_t is substituted by z .

For low concentrations, we can use a series expansion in powers of x for the function F_{II}

$$F_{II} = 1 + h(z)x + \dots \quad (3.22)$$

Since chains become ideal for $z \rightarrow 0$, i.e., $\xi_t \rightarrow \infty$, we must have

$$h(z = 0) = 0 . \quad (3.23)$$

On the other hand, one can carry out the passage to the Kuhnian limit $z \rightarrow \infty$ as realized in good solvents. Theory shows that there is a well-defined limiting value, $h(z \rightarrow \infty)$ and a corresponding limiting function, which now depends on x only

$$F_{II}(x, z \rightarrow \infty) = F_{II}(x) .$$

If we employ this limiting function, we obtain a general equation for the osmotic pressure exerted by polymers in good solvents

$$\frac{\Pi}{kTc_p} = \frac{\Pi M}{RTc_w} = F_{II} \left(x = \frac{c_w}{c_w^*} \right). \quad (3.24)$$

According to the derivation, Eq. (3.24) is valid for both dilute and semidilute solutions. We now understand the experimental curve in Fig. 3.3: It exactly represents the universal function $F_{II}(x)$.

The value of the expansion coefficient in Eq. (3.22) in the Kuhnian limit, $h(z \rightarrow \infty)$, can be calculated using renormalization group methods, with the result

$$h(z \rightarrow \infty) = 0.353. \quad (3.25)$$

A check is displayed in Fig. 3.3, by inclusion of the curve corresponding to

$$F(x) = 1 + 0.353x. \quad (3.26)$$

A comparison shows an excellent agreement with the data for $x < 2$.

Discussion of Eq. (3.21) enables some direct conclusions. First, consider the dilute case, $x \ll 1$, where the virial expansion is valid. We write for $F_{II}(x, z)$

$$F_{II}(x, z) = 1 + h(z)x + \dots \quad (3.27)$$

A comparison of Eqs. (3.21), (3.27) and Eq. (3.11) gives a relation between the concentration at chain overlap c_m^* and the second virial coefficient A_2 :

$$c_m^* = \frac{h(z)}{NA_2}. \quad (3.28)$$

The use of Eq. (3.2) yields

$$A_2 = \frac{h(z)R_F^3}{N^2}. \quad (3.29)$$

The last equation relates the second virial coefficient to the Flory radius and the degree of polymerization of the chains.

It is instructive to introduce this relation in Eq. (3.11), also replacing c_m by the polymer density c_p . We obtain

$$\frac{\Pi}{kT} = c_p + h(z)R_F^3 \cdot c_p^2 + \dots \quad (3.30)$$

Equation (3.30) formulates an interesting result. It reveals that the increase in the osmotic pressure over the ideal behavior, as described in lowest order by the second term on the right-hand side, may be understood as being caused by repulsive hard core interactions between the polymer chains that occupy volumes in the order of $h(z)R_F^3$. To see this, just compare Eq. (3.30) with Eq. (2.73), which is valid for a van der Waals gas. For a gas with hardcore

interactions only, i.e., $\tilde{a} = 0$, the second virial coefficient equals the excluded volume per molecule \tilde{b}/N_L . Therefore, we may attribute the same meaning to the equivalent coefficient in Eq. (3.30). Our result thus indicates that polymer chains in solution behave like hard spheres, with the radius of the sphere depending on R_F and additionally on z , i.e., on the solvent quality. For good solvents, in the Kuhnian limit $h(z \rightarrow \infty) = 0.353$, the radius is similar to R_F .

This strong repulsion is understandable since an overlap between two coils produces many contacts between the monomers. We can estimate the related energy, utilizing Eq. (2.78). For monomer density distributions $c_m(\mathbf{r} - \mathbf{r}_{c,i})$ about the centers of gravity $\mathbf{r}_{c,1}$ and $\mathbf{r}_{c,2}$ of two polymers, it is given by

$$f_{pp}^{ev}(\mathbf{r}_{c,1}, \mathbf{r}_{c,2}) = kTv_e \int \langle c_m(\mathbf{r} - \mathbf{r}_{c,1})c_m(\mathbf{r} - \mathbf{r}_{c,2}) \rangle d^3\mathbf{r} . \quad (3.31)$$

Assuming Gaussian density distributions, in the limit of a complete overlap, $\mathbf{r}_{c,1} = \mathbf{r}_{c,2}$, we obtain an expression identical to the internal excluded volume interaction energy Eq. (2.91), apart from a factor 1/2. Omitting the numerical prefactor of order unity we write

$$f_{pp}^{ev}(\mathbf{r}_{c,1} = \mathbf{r}_{c,2}) \simeq kTz \left(\frac{R_0}{R_F} \right)^3 . \quad (3.32)$$

This has to be compared with the mean kinetic energies associated with the translational motion of the centers of mass

$$\langle u_{kin} \rangle = \frac{3}{2}kT . \quad (3.33)$$

Even for an only partial overlap, to a degree β , we have

$$\frac{\langle u_{kin} \rangle}{f_{pp}^{ev}} \simeq \frac{1}{\beta z} \ll 1 \quad (3.34)$$

if, as is the case for good solvents and standard degrees of polymerization

$$z = N_{su}^{1/2} \gg 1 . \quad (3.35)$$

As a consequence, in a dilute solution of expanded chains, interpenetration of two polymer molecules is largely suppressed so that they do indeed resemble hard spheres.

Equation (3.29) enables a prediction of the molar mass dependence of A_2 . For good solvents we again may set $h(z) = h(z \rightarrow \infty) = 0.353$, then obtaining

$$\begin{aligned} A_2 &= 0.353 \frac{R_F^3}{N^2} \\ &= 0.353 \frac{a_F^3 N^{9/5}}{N^2} = 0.353 a_F^3 N^{-1/5} . \end{aligned} \quad (3.36)$$

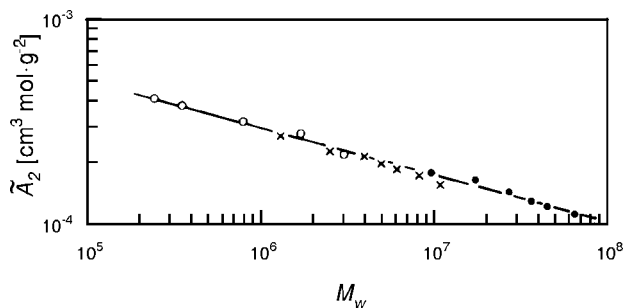


Fig. 3.4. Molar mass dependence of the second virial coefficient, obtained for solutions of fractions of PS in benzene. Data from Cotton [10]

Figure 3.4 presents experimental results, obtained for solutions of fractions of polystyrene (PS) in benzene. They do, in fact, agree with the power law $\tilde{A}_2 \propto A_2 \propto N^{-1/5} \propto M^{-1/5}$.

Next we consider the other limit, $x \gg 1$, associated with an entangled semidilute solution far above the overlap threshold. Here, the degree of polymerization N must become irrelevant, as is also demonstrated by the data in Fig. 3.2. For des Cloiseaux's expression (Eq. (3.21)) this condition implies a stringent requirement, since N is included in both the factor c_p and F_{II}

$$\frac{\Pi}{kT} = \frac{c_m}{N} F_{II}(x, z) . \quad (3.37)$$

The dependence on N contributed by c_p can only be eliminated if F_{II} asymptotically shows an appropriate power law behavior. Assuming

$$F_{II}(x, z) \propto x^\mu \quad (3.38)$$

and therefore

$$F_{II}(x, z) \propto c_m^\mu \frac{R_F^{3\mu}}{N^\mu} \propto c_m^\mu N^{4\mu/5} , \quad (3.39)$$

we obtain

$$\frac{\Pi}{kT} \propto c_m^{\mu+1} N^{(4\mu/5)-1} . \quad (3.40)$$

The exponent of N has to vanish and this occurs for $\mu = 5/4$. By introduction of this value, we obtain the concentration dependence of the osmotic pressure in the semidilute regime

$$\frac{\Pi}{kT} \propto c_m^{9/4} . \quad (3.41)$$

Figures 3.2 and 3.3 confirm this prediction. The slope of the continuous straight lines drawn through the data in the limit of high concentrations exactly corresponds to Eq. (3.41). Note the qualitative difference to the dilute regime, where $\Pi \propto c_m^2$. We conclude that the entanglements further enhance the osmotic pressure.

The Zimm Diagram

Light scattering experiments permit further checks of the theoretical predictions since they can be used for a determination of both the osmotic compressibility and the second virial coefficient. As explained in Sect. A.3.2 of the Appendix, a general equation in scattering theory relates the osmotic compressibility $(\partial c_m / \partial \Pi)_T$ to the scattering in the forward direction (Eq. (A.81))

$$S(q=0) = kT \left(\frac{\partial c_m}{\partial \Pi} \right)_T .$$

Taking the reciprocal expressions on both sides gives

$$S^{-1}(q=0) = \frac{1}{kT} \left(\frac{\partial \Pi}{\partial c_m} \right)_T . \quad (3.42)$$

$(\partial \Pi / \partial c_m)_T$ represents the **osmotic modulus**.

This relation is very useful. First, we can employ the virial expansion Eq. (3.11), valid in the dilute range for a calculation of the osmotic modulus. The result is

$$S^{-1}(q=0, c_m \rightarrow 0) = \frac{1}{N} + 2A_2 c_m . \quad (3.43)$$

In a second step, Eq. (3.43) can be combined with Guinier's law (Eq. (A.71)) for dilute solutions. The latter relates the curvature at $q=0$ to the radius of gyration of the polymer, by

$$S(q \rightarrow 0, c_m \rightarrow 0) = N \left(1 - \frac{R_g^2 q^2}{3} + \dots \right) .$$

Again taking the reciprocals, we have

$$S^{-1}(q \rightarrow 0, c_m \rightarrow 0) = N^{-1} \left(1 + \frac{R_g^2 q^2}{3} + \dots \right) . \quad (3.44)$$

The combination is achieved by writing the reciprocal scattering function as a product of both expressions

$$S^{-1}(q \rightarrow 0, c_m \rightarrow 0) = \frac{1}{N} \left(1 + \frac{R_g^2 q^2}{3} + \dots \right) (1 + 2A_2 N c_m + \dots) . \quad (3.45)$$

Equation (3.45) correctly describes the dependence of S^{-1} on q and c_m within the limit of small values of both parameters and is well-known as the basis of **Zimm plots**. To make use of the equation, scattering experiments on polymer solutions (these are mostly carried out by light) have to be conducted under variation of both the scattering angle and the concentration. Extrapolation

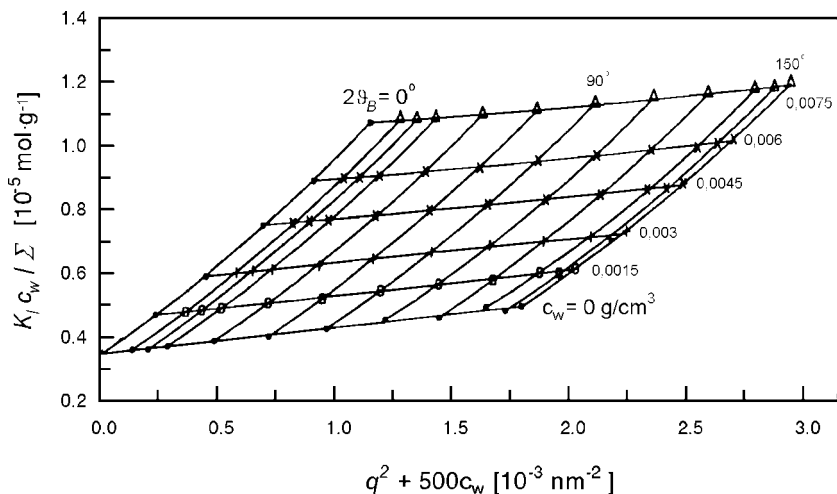


Fig. 3.5. Light scattering experiments on solutions of PS ($M = 2.8 \times 10^5 \text{ g mol}^{-1}$) in toluene at 25°C . Results are presented in a Zimm plot, enabling an extrapolation to $c_w = 0$ and $q = 0$. Data from Lechner et al. [11]

of q and c_m to zero then permits a determination of three parameters of the polymer to be made. One can deduce the radius of gyration R_g , the degree of polymerization N and the second virial coefficient A_2 .

The extrapolations are carried out in peculiar manner. Figure 3.5 shows, as an example, data obtained for a dilute solution of polystyrene in toluene. The reciprocal of the scattering function is plotted as a function of the sum $q^2 + \beta c_w$, where β is a conveniently chosen constant. If we were to utilize Eq. (3.45), then the slopes dS^{-1}/dq and dS^{-1}/dc_m of the two lines at the origin would give $R_g^2/3$ and $2A_2$; the limiting value $S^{-1}(q = 0, c_m = 0)$ would furnish N . Actually, in experiments directly measurable quantities such as the Raleigh ratio Σ and the mass concentration c_w are usually employed, rather than S and c_m . Corresponding substitutions can be carried out in Eq. (3.45), which is then converted to

$$\frac{c_w K_1}{\Sigma} = \left(1 + \frac{R_g^2 q^2}{3} + \dots \right) \left(\frac{1}{M} + 2\tilde{A}_2 c_w + \dots \right) \quad (3.46)$$

with

$$K_1 = 4\pi^2 n^2 \left(\frac{dn}{dc_w} \right)^2 / (N_L \lambda_0^4) .$$

Here n denotes the index of refraction and λ_0 is the wavelength in a vacuum (see the Appendix, Eqs. (A.50)(A.51)). One obtains the modified second virial coefficient \tilde{A}_2 defined by Eq. (3.13).

Equation (A.81) also permits us to check the osmotic pressure equation deeper in the semidilute regime. Introduction of Eq. (3.21) gives

$$\begin{aligned} S^{-1}(q=0, c_m) &= \frac{d}{dc_m} \left(\frac{c_m}{N} F_{II}(x, z) \right) \\ &= \frac{1}{N} F_{II}(x, z) + \frac{c_m}{N} \frac{1}{c_m^*} \frac{\partial F_{II}}{\partial x}(x, z). \end{aligned} \quad (3.47)$$

For good solvents as represented by the Kuhnian limit $z \rightarrow \infty$, we obtain

$$S^{-1}(q=0, c_m) = \frac{1}{N} \left(F_{II}(x) + x \frac{\partial}{\partial x} F_{II}(x) \right) = \frac{1}{N} F'_{II}(x). \quad (3.48)$$

Here, $F'_{II}(x)$ denotes another general function. Hence, one expects to find a unique curve when plotting $NS^{-1}(q=0)$ versus x . Light scattering experiments have been carried out for various polymer solutions and they indeed confirm this prediction. Figure 3.6 gives an experimental result in a slightly modified representation. As an alternative to the overlap ratio x one may also use the quantity x' defined as

$$x' = A_2 N c_m. \quad (3.49)$$

According to Eq. (3.28), x' is proportional to x

$$x' = h(z=0)x = 0.353x. \quad (3.50)$$

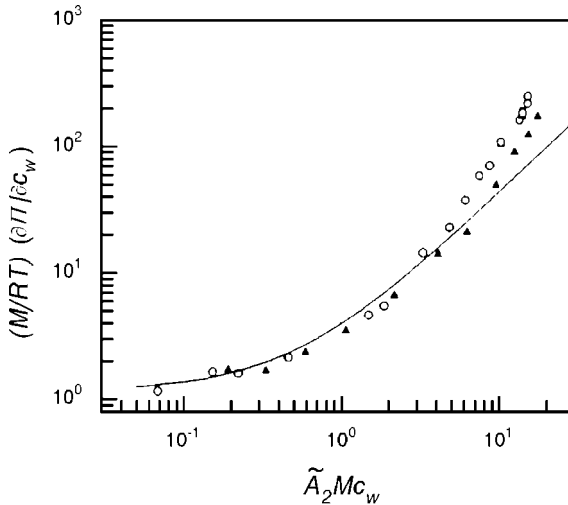


Fig. 3.6. Reduced osmotic moduli of two fractions of PS ($M = 2.3 \times 10^4$ and 4.7×10^4 g mol $^{-1}$) dissolved in toluene, as derived from light scattering experiments. In the dilute and semidilute range results agree with the theoretical prediction as given by the *continuous curve* [12]

Using the mass concentration c_w , the molar mass M and the modified second virial coefficient \tilde{A}_2 rather than c_m , N and A_2 leaves the plotted variables unchanged, since

$$NS^{-1}(q=0) = N \frac{1}{kT} \frac{\partial \Pi}{\partial c_m} = M \frac{1}{\tilde{R}T} \frac{\partial \Pi}{\partial c_w} \quad (3.51)$$

and

$$x' = A_2 N c_m = \tilde{A}_2 M c_w . \quad (3.52)$$

The presented arguments provide information on the limiting behavior of the osmotic modulus only, for $x \ll 1$ and $x \gg 1$. It is possible to derive the full shape of the curve encompassing the dilute regime, the cross-over region, and the semidilute range, using renormalization group methods. Figure 3.6 includes a theoretically deduced curve and demonstrates good agreement with the experimental results. Deviations show up at higher concentrations, thereby pointing at the limitations of the treatment. As has already been mentioned, at higher concentrations it is no longer sufficient to consider only binary interactions and we must also include higher order contributions. The situation then becomes much more involved and it appears that universality is lost.

3.2 Screening of Excluded Volume Forces

In the previous chapter, we considered the structures of single chains in the dilute regime. Now we may inquire how these become altered in semidilute solutions. Discussions can be based on the pair distribution function of the individual chains, thereby focussing on the structure of single chains in states where chains overlap and interpenetrate. We choose for this intramolecular pair correlation function a symbol with a hat, $\hat{g}(\mathbf{r})$, to distinguish it from the general pair distribution function $g(\mathbf{r})$, which includes monomers from all chains.

For $\hat{g}(\mathbf{r})$, we can assess the behavior for both limits, dilute solutions and the melt. As explained earlier in Sect. 2.3.2, we find for isolated expanded chains $\hat{g} \propto r^{-4/3}$, for distances in the range $\xi_t < r < R_F$. On the other hand, one observes in the melt ideal chain behavior, i.e., $\hat{g} \propto 1/r$, for $r < R_0$. Therefore, a change has to occur and indeed, it is possible to describe it in qualitative terms. Explanations were first provided by Edwards in a theory that envisages a **screening effect**. The view is that, similar to the screening of the long-range Coulomb forces in electrolytes caused by the presence of mobile ions as described by the Debye–Hückel theory (see the next section), the long-range excluded volume forces acting within an isolated chain are screened if monomers of other polymer molecules interfere. We have already addressed this effect from a different point of view when discussing the chain structure in melts referring to Fig. 2.14. There we argued that the presence of foreign monomers reduces and finally completely removes the concentration gradient

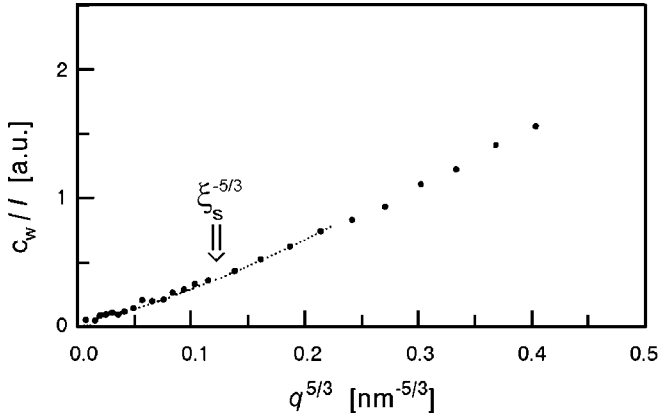


Fig. 3.7. Result of a neutron scattering experiment on a semidilute solution of a mixture of deuterated and protonated PS ($\overline{M}_w = 1.1 \times 10^6 \text{ g mol}^{-1}$) in CS_2 ($c_w = 0.15 \text{ g cm}^{-3}$). Intensities reflect the structure factor of individual chains. The cross-over from the scattering of an expanded chain to that of an ideal chain at $q^{5/3} \simeq \xi_s^{-5/3}$ is indicated. Data from Farnoux [6]

of the monomers belonging to one chain, thus blocking the chain expansion. In Edwards' treatment this process formally corresponds to a screening, put into effect by the contacts with foreign monomers.

In entangled solutions screening becomes effective at a characteristic distance called the **screening length** and denoted ξ_s . Figure 3.7 provides an experimental example of the evidence. We see the scattering intensity measured for a semidilute solution of polystyrene in CS_2 , in a plot of I^{-1} versus $q^{5/3}$. We are interested in the single chain structure factor in the semidilute solution, as given by the Fourier-transform of \hat{g}

$$\hat{S}(\mathbf{q}) = \int \exp(-i\mathbf{q}\mathbf{r})\hat{g}(\mathbf{r})d^3\mathbf{r}. \quad (3.53)$$

$\hat{S}(\mathbf{q})$ can be measured if the dissolved polystyrene includes a small fraction of deuterated molecules. Due to the large difference in the scattering length of protons and deuterium, the deuterated chains dominate the scattering pattern, which then indeed may be described as

$$I(\mathbf{q}) \propto \hat{S}(\mathbf{q}). \quad (3.54)$$

For a dilute solution, one observes the scattering function of expanded chains, $I \propto q^{-5/3}$, which corresponds to the straight line shown previously in Fig. 2.18. Now we notice a change at low scattering vectors q , indicative of a cross-over from the scattering behavior of an expanded chain to that of an ideal one, with $I^{-1} \propto q^2 = (q^{5/3})^{6/5}$. The cross-over occurs around a certain q , related to ξ_s by $q \simeq \xi_s^{-1}$.

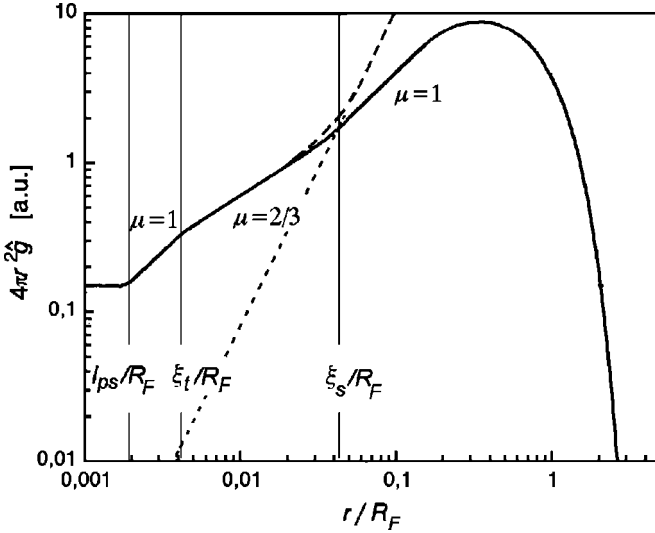


Fig. 3.8. Pair distribution function of an individual chain in a semidilute solution, exhibiting different regions with specific power laws $4\pi r^2 \hat{g} \propto (r/R_F)^\mu$. R_F denotes the Flory radius in the dilute state. The *dotted line* gives the function $4\pi r^2 \langle c_m \rangle$. The *dashed line* indicates the pair distribution function for all monomers, $4\pi r^2 \hat{g}$, which deviates from $4\pi r^2 \hat{g}$ for $r > \xi_s$

Combining all the information collected so far, for the single chain pair distribution function in a semidilute solution we can predict an overall shape as indicated in Fig. 3.8. For the presentation we choose a plot of $4\pi r^2 \hat{g}(r)$ versus r . The curve is a composite of different functions in four ranges, with cross-overs at the persistence length l_{ps} , the thermic correlation length ξ_t and the screening length ξ_s . Up to $r \simeq \xi_s$ we find the properties of the expanded chain, which

- resembles a rigid rod for $r < l_{ps}$, with $4\pi r^2 \hat{g} = \text{const}$,
- at first exhibits ideal behavior, in the range $l_{ps} < r < \xi_t$ ($4\pi r^2 \hat{g} \propto r$),
- and then shows excluded volume effects as indicated by the scaling law

$$\hat{g} \propto r^{-4/3} \longrightarrow 4\pi r^2 \hat{g} \propto r^{2/3} .$$

This pertains up to the cross-over at $r \simeq \xi_s$ where we again enter into an ideal regime

$$4\pi r^2 \hat{g} \propto r .$$

The final range is determined by the size of the chain.

With the knowledge about the single chain pair distribution function, one can also predict the general shape of the pair distribution function for all

monomers, $g(\mathbf{r})$. The behavior of $g(\mathbf{r})$ in the limits of small and large distances is obvious. Since for small distances r correlations are mostly of intramolecular nature, we there have $g \approx \hat{g}$. On the other hand, we have a non-vanishing asymptotic value for large distances r , given by $g = \langle c_m \rangle$. Indeed, with the aid of the screening length, we may express the behavior more accurately as

$$g(\mathbf{r}) \approx \hat{g}(\mathbf{r}) \quad \text{for } r \ll \xi_s \quad (3.55)$$

and

$$g(\mathbf{r}) \approx \langle c_m \rangle \quad \text{for } r \gg \xi_s . \quad (3.56)$$

Why the change from the one to the other limit must take place around ξ_s is intuitively clear. ξ_s essentially corresponds to the distance between entanglement points, as these are the points where monomers interact with other chains, which is the cause for the alteration of the chain structure. In the literature, ξ_s is therefore often addressed as **mesh-size**, in order to emphasize that it can also be interpreted as the diameter of the meshes of the entanglement network built up by the chains in a semidilute solution. It is furthermore plausible to assume that ξ_s approximately equals the distance r , where $\hat{g}(r)$ comes down to values in the order of the mean monomer density in the sample

$$\hat{g}(\xi_s) \simeq \langle c_m \rangle , \quad (3.57)$$

since this condition implies similar weights of intramolecular and intermolecular contributions to $g(\mathbf{r})$. Figure 3.8 also shows these properties. $4\pi r^2 g$ is indicated by a dashed line that deviates from $4\pi r^2 \hat{g}$ at $r \simeq \xi_s$. The plot also includes the function $4\pi r^2 \langle c_m \rangle$, given by the straight dotted line. It crosses $4\pi r^2 \hat{g}$ at $r \simeq \xi_s$.

While studies of \hat{g} require neutron scattering experiments on partially deuterated samples, information on $g(\mathbf{r})$ can be obtained by standard X-ray (or neutron) scattering experiments on normal solutions. Measurements yield the screening length ξ_s , using a simple straightforward procedure, which may be explained as follows. Generally the structure function for a polymer solution is given by Eq. (A.25), which is valid for all isotropic systems (see the Appendix, Sect. A.1.1)

$$S(q) = \int_{r=0}^{\infty} \frac{\sin(qr)}{qr} 4\pi r^2 (g(r) - \langle c_m \rangle) dr .$$

For the small angle range we may use a series expansion in powers of q ,

$$S(q) = \int_{r=0}^{\infty} \left(1 - \frac{1}{3} q^2 r^2 + \dots \right) 4\pi r^2 (g(r) - \langle c_m \rangle) dr , \quad (3.58)$$

which yields for the curvature at $q = 0$

$$\frac{d^2 S}{dq^2} = -\frac{2}{3} \int_{r=0}^{\infty} r^2 4\pi r^2 (g(r) - \langle c_m \rangle) dr . \quad (3.59)$$

We can represent this result by writing

$$\frac{d^2 S}{dq^2} = -2\xi^2 S(0) , \quad (3.60)$$

introducing a parameter ξ . According to the definition, ξ^2 is one third of the second moment of the function $4\pi r^2(g(r) - \langle c_m \rangle)$; ξ is therefore a measure for the width of this function. On the other hand, a look at Fig. 3.8 shows us that this width essentially agrees with the screening length. Hence, we may identify ξ with ξ_s . So far, there has been no precise definition of ξ_s ; Eq. (3.60) provides us with one.

Based on Eq. (3.60), $S(q)$ may now be represented in the small angle range by

$$S(q) = S(0)(1 - \xi_s^2 q^2 + \dots) \quad (3.61)$$

or, using the reciprocal function, by

$$S^{-1}(q) = S(0)(1 + \xi_s^2 q^2 + \dots) . \quad (3.62)$$

Figure 3.9 presents experimental results obtained from small angle X-ray scattering (SAXS) experiments on semidilute solutions of polystyrene in toluene, choosing three different concentrations. They agree with Eq. (3.62) and enable a determination of the concentration dependence of ξ_s to be made.

One can predict this dependence for the semidilute range, again using scaling arguments. We anticipate that in a good solvent we have only one relevant parameter, namely the overlap ratio x and write

$$\xi_s = R_F F_{\xi_s}(x) . \quad (3.63)$$

The parameter R_F is included as a prefactor, in order to set the length scale. The limiting value of F_{ξ_s} for $x \rightarrow 0$ is necessarily unity

$$F_{\xi_s}(x \rightarrow 0) = 1 . \quad (3.64)$$

Within the semidilute range we expect power law behavior again

$$F_{\xi_s}(x \rightarrow \infty) \propto x^\mu . \quad (3.65)$$

In this range, where the chains overlap strongly, ξ_s has to be independent of N and this can only be accomplished by a power law in connection with an appropriate exponent. Application of Eqs. (2.83) and (3.3) leads to

$$\xi_s \propto N^{3/5} N^{4\mu/5} c_w^\mu . \quad (3.66)$$

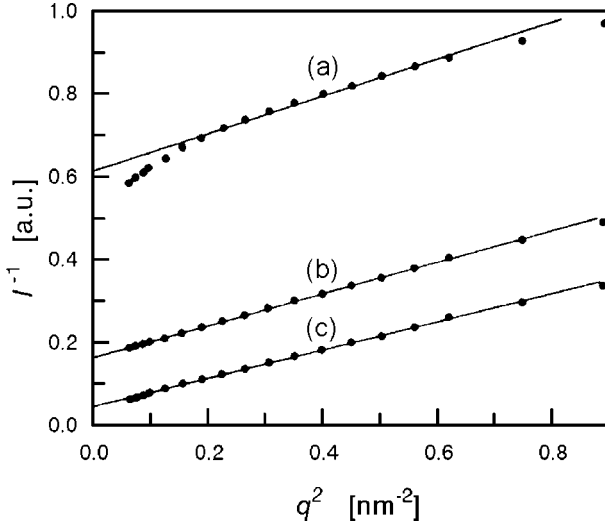


Fig. 3.9. Solutions of PS ($M = 5 \times 10^4 \text{ g mol}^{-1}$) in toluene, with mass concentrations $c_w = 0.0105$ (a), 0.0953 (b) and 0.229 g cm^{-3} (c). Intensities measured by SAXS. Data from Hamada et al. [13]

Independence of ξ_s with regard to N requires that

$$\mu = -3/4 . \tag{3.67}$$

Hence, we obtain

$$\xi_s \simeq R_F \left(\frac{c_w}{c_w^*} \right)^{-3/4} . \tag{3.68}$$

Figure 3.10 depicts the concentration dependence of the screening length for the same system as presented in Fig. 3.9. The decrease, as observed for higher concentrations, agrees exactly with the scaling law Eq. (3.68).

Similar arguments may be used to derive the concentration dependence of the mean squared end-to-end distance of a chain. If we start with an expanded chain in a dilute solution, we expect a shrinkage back to the size of an ideal chain when screening becomes effective on increasing the concentration. We assume a dependence

$$\langle R^2 \rangle^{1/2} = R_F F_R(x) \tag{3.69}$$

with

$$F_R(x \rightarrow 0) = 1 . \tag{3.70}$$

For higher concentrations in the semidilute regime we again expect a power law

$$F_R(x \rightarrow \infty) \propto x^\mu , \tag{3.71}$$

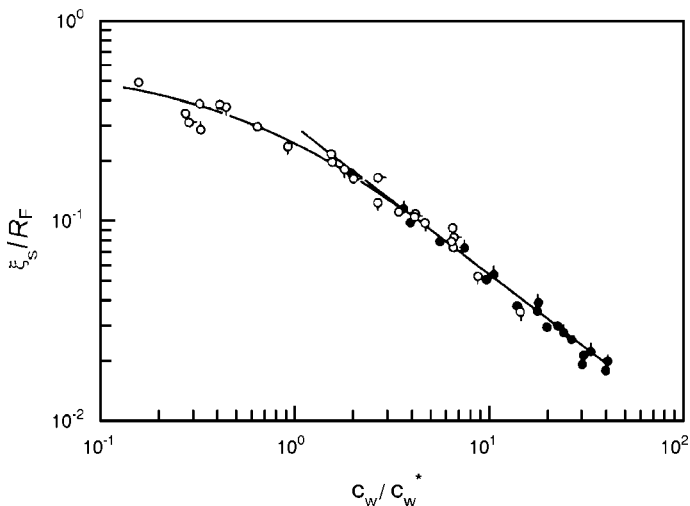


Fig. 3.10. The same system as in Fig. 3.9. Values derived for the concentration dependence of the screening length ξ_s . Data from Hamada et al. [13]

thereby obtaining

$$\langle R^2 \rangle^{1/2} \propto N^{3/5} c_w^\mu N^{4\mu/5} . \quad (3.72)$$

On the other hand, since chains behave ideally for distances that are large compared to the screening length, we have

$$\langle R^2 \rangle^{1/2} \propto N^{1/2} . \quad (3.73)$$

A comparison yields the exponent, with the value

$$\mu = -1/8 . \quad (3.74)$$

Hence, we can formulate the equation for the dependence of the coil diameter on the degree of polymerization and the concentration

$$\langle R^2 \rangle^{1/2} \propto N^{1/2} c_w^{-1/8} . \quad (3.75)$$

This is proved to be valid by the results shown in Fig. 3.11. They were obtained in neutron scattering experiments on solutions of a mixture of protonated and deuterated polystyrenes in CS_2 .

Considering these results, we now see how the change from the expanded chains in dilute solutions to the ideal chains in a melt is accomplished: With increasing concentration the screening length decreases continuously and if it comes down to the thermic correlation length ξ_t all excluded volume effects have disappeared. Simultaneously the chain size shrinks, from the Flory radius R_F in the dilute solution down to the radius R_0 of the Gaussian chains in the melt.

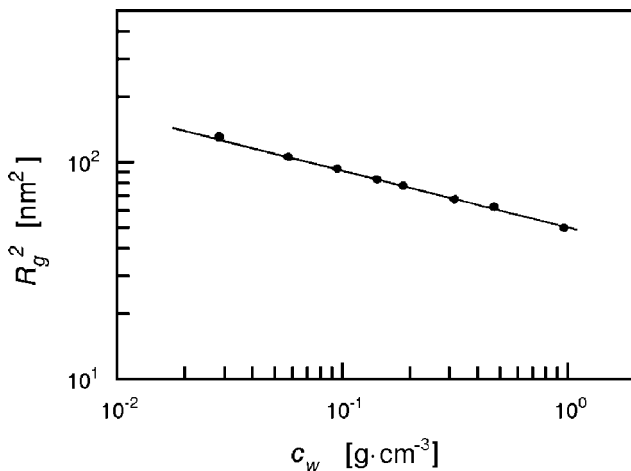


Fig. 3.11. PS ($M = 1.14 \times 10^5 \text{ g mol}^{-1}$) dissolved in CS_2 . Shrinkage of the radius of gyration with increasing polymer concentration. Data from Daoud et al. [14]

3.3 Polyelectrolyte Solutions

The solutions dealt with so far contained electrically neutral, i.e., non-charged polymers. Polyelectrolytes are built up of monomeric units that include an ionizable group, i.e., a group that can dissociate in aqueous surroundings into a **chain-fixed kation or anion** and a **mobile counter-ion** bearing the opposite charge. Some typical examples were already given in Table 1.2. Charges are the origin of Coulomb forces. These are much stronger than van der Waals forces and can thus act over longer distances. Their presence changes the conditions in a qualitative manner and lead to unusual solution properties. In particular:

- The chain stretching caused by the repulsive Coulomb forces is accompanied by a regular distribution of the chains in the solvent with concentration dependent equilibrium distances.
- Given the presence of mobile counter-ions, the osmotic pressure, which is extremely low in solutions of neutral polymers, again takes on the much higher values of low molar mass systems.

In this section, we discuss these properties and begin with the explanation of two basic effects.

3.3.1 Condensation and Screening of Charges

One might think at first that on dissolving a polyelectrolyte chain all counter-ions diffuse away and distribute themselves homogeneously in the solvent. As a consequence, the chain would get fully stretched in a reaction to the

repulsive Coulomb forces between the chain-fixed charges. In fact, this does not happen. This is due to two effects that change the conditions:

- In a polyelectrolyte with ionizable groups at short distances along the chain, for example, in every monomeric unit, strong attractive forces on the counter-ions arise that prevent them from diffusing away. Part of them is kept as a **condensate** in the immediate neighborhood of the **polyion** so that the effective charge density is reduced. It then appears as if units with an elementary charge occur only at distances ξ_B along the chain that are larger than the monomeric length. This characteristic minimum distance is known as the **Bjerrum length**.
- Existing chain-fixed charges often do not create in full the associated Coulomb force, but become **screened** by a shell of counter-ions. This formation of a cloud of opposite charges is found in all electrolytes, polyions and low molar mass ions, and results in a practical disappearance of the Coulomb forces at distances above a certain length. This length ξ_D , known as the **Debye length**, also describes the size of the charge compensating cloud. It varies with the ionic strength given by the total concentration of mobile ions.

Charge Condensation on Rod-like Polyions

Consider a single rod-like chain with radius r_0 , which includes monovalent kations at regular distances l_{io} , i.e., possesses a linear charge density e/l_{io} . If it is brought in a solvent with a dielectric coefficient ε it develops an electric field. The corresponding potential V follows from an application of basic laws of electrostatics as

$$V = \frac{e}{2\pi\varepsilon\varepsilon_0 l_{io}} \ln \frac{r}{r_0}, \quad (3.76)$$

where e and ε_0 denote the elementary charge and the electric constant, respectively. The potential has cylindrical symmetry and r denotes the distance from the chain axes. Imagine that a single monovalent anion is placed in the neighborhood of the chain. Will it move towards the chain under the attractive electrostatic force or, possessing the kinetic energy $3kT/2$, diffuse away?

In order to deal with this question, the cell structure shown in Fig. 3.12 is set up. A series of cylindrical cells i with inner radii r_i and a constant thickness Δr surrounds the rod. We consider the probability of an occupation of cell i . The electrostatic energy of the anion in cell i is

$$u_i = -eV(r_i). \quad (3.77)$$

The entropy associated with the motion within the cell amounts to

$$s_i = k \ln \frac{2\pi r_i \Delta r}{r_0^2} + \text{const} = k \ln \frac{r_i}{r_0} + \text{const}. \quad (3.78)$$

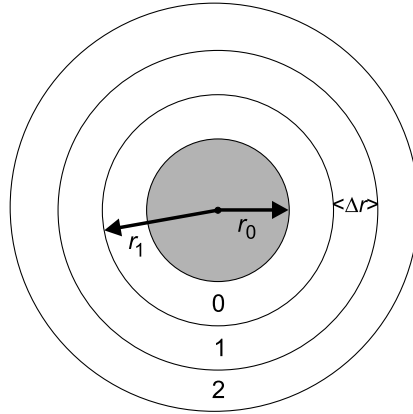


Fig. 3.12. A rod-like polyeon with radius r_0 and its neighborhood subdivided into cylindrical cells with inner radius r_i and thickness Δr

The free energy is therefore

$$f_i = u_i - T s_i = \left(\frac{e^2}{2\pi\epsilon\epsilon_0 l_{io}} - kT \right) \ln \frac{r_i}{r_0} + \text{const} \quad (3.79)$$

$$= kT(\beta - 1) \ln \frac{r_i}{r_0} + \text{const} \quad (3.80)$$

with

$$\beta = \frac{e^2}{2\pi\epsilon\epsilon_0 l_{io} kT}. \quad (3.81)$$

If there are many non-interacting anions, the number n_i of anions in cell i at a temperature T follows from Boltzmann statistics as

$$n_i \propto \exp \frac{-f_i}{kT} = \left(\frac{r_i}{r_0} \right)^{1-\beta}. \quad (3.82)$$

Referring to the number of anions in the cell at the chain surface ($i = 0$) one obtains

$$\frac{n_i}{n_0} = \left(\frac{r_i}{r_0} \right)^{1-\beta}. \quad (3.83)$$

The occupation probability for cell 0 is given by

$$p_0 = \frac{1}{\sum_{i=0}^{\infty} \frac{n_i}{n_0}}. \quad (3.84)$$

In the calculation we replace the sum by an integral and write

$$\sum_{i=0}^{\infty} \frac{n_i}{n_0} \approx \int_0^{\infty} x^{1-\beta} dx \quad (3.85)$$

with

$$x = \frac{r_i}{r_0}. \quad (3.86)$$

For $\beta \leq 2$ the integral diverges and consequently p_0 vanishes. Under these conditions the anions will not stay at the chain surface. The situation changes for $\beta > 2$. The integral then remains finite and the probability p_0 shows a non-vanishing value. We thus find a critical value for β

$$\beta = 2 = \frac{e^2}{2\pi\epsilon\epsilon_0 l_{io} kT}. \quad (3.87)$$

What is the consequence? The result indicates the existence of a critical distance along the chain, l_{io} , with the value

$$l_{io} = \frac{e^2}{4\pi\epsilon\epsilon_0 kT} = \xi_B. \quad (3.88)$$

ξ_B is known as the Bjerrum length and has, according to our considerations, the following meaning: If the distance between neighboring charges on the rod is larger than ξ_B , all the counter-ions will diffuse away. If it is smaller, a certain fraction stays in the immediate neighborhood of the rod surface.

We have obtained a clear answer to our question, however, the actual situation is more complex. What we have considered is the behavior of a system of mobile independent anions in the fixed electrical field generated by the polycation, whereas, in reality, the anions interact with each other or, in other words, modify the field. Dealing with a system of many interacting anions is difficult. There exists no exact analytical solution; however, one can make use of a good approximate treatment. The problem to be solved is the common determination of both the spatially varying charge density, denoted $\rho_e(\mathbf{r})$, and the varying electrostatic potential $V(\mathbf{r})$, under the boundary conditions set by the existing fixed kations on the rod. For a given charge density distribution, the electrostatic potential follows from a solution of the Poisson equation

$$\Delta V(\mathbf{r}) = -\frac{\rho_e(\mathbf{r})}{\epsilon_0\epsilon}. \quad (3.89)$$

Reversely, $V(\mathbf{r})$ determines the charge density distribution. Applying Boltzmann statistics, we write

$$\rho_e(\mathbf{r}) \propto (-e) \exp -\frac{(-e)V}{kT}, \quad (3.90)$$

whereby, different from our first considerations, the electrostatic potential now also accounts for the presence of the anions. With the second equation the system is closed and solutions can be obtained by numerical evaluations. Calculations lead to the following results. Firstly, the previous conclusion is confirmed: For $l_{io} > \xi_B$ all counter-ions diffuse away from the polyion,

which then creates the electrostatic potential given by Eq. (3.76). A new result follows for $l_{io} < \xi_B$. We concluded that then part of the counter-ions remains near the rod. The calculations show that the effective charge density left on the rod after the condensation of a certain fraction of anions exactly amounts to e/ξ_B . Hence, independent of the actual value of l_{io} it always appears, as if charges are only placed at distances ξ_B .

What happens if the chain is not perfectly stiff but shows some curvature, which is the reality? Essentially, the answer is: As long as the Bjerrum length is small compared to the persistence length, over which the chain can be regarded as stiff, the behavior does not change.

The Debye–Hückel Theory of Charge Screening

The cations in an electrolyte are preferentially surrounded by shells of anions and vice-versa. As a consequence, the electrostatic potential created by a single charge is modified. While an isolated positive elementary charge generates in an electrically neutral solvent with a dielectric constant ε a potential

$$V(r) = \frac{e}{4\pi\varepsilon_0\varepsilon r}, \quad (3.91)$$

the presence of the multitude of anions and cations in the electrolyte solution screens this potential and turns the spatial dependence into

$$V(r) = \frac{e}{4\pi\varepsilon_0\varepsilon r} \exp -\frac{r}{\xi_D}. \quad (3.92)$$

The modification of the dependence implies that the Coulomb force originating from a kation practically disappears at distances r above the **Debye screening length** ξ_D . The effect was explained for the first time in 1923 in the famous theory developed by Debye and Hückel, and we briefly sketch its content. The explanation refers at first to low molar mass electrolytes, but the results can be transferred to polyelectrolyte solutions.

The problem that we have to treat is similar to the one discussed in the preceding chapter: One has to determine in common the interrelated functions $V(r)$ and $\rho_e(r)$, i.e., the electrostatic potential and the charge distribution, now for a fixed kation in an electrolytic surrounding. We consider the case of a system of monovalent ions. If a charge distribution is given, the resulting potential can be calculated by solving the **Poisson equation** in the form valid for an isotropic system,

$$\frac{1}{r^2} \frac{d}{dr} \left(r^2 \frac{d}{dr} \right) V(r) = -\frac{\rho_e(r)}{\varepsilon_0\varepsilon}. \quad (3.93)$$

The inclusion of the dielectric constant ε allows the polarization properties of the solvent to be taken into account.

In reverse, a given varying potential $V(r)$ determines the charge distribution $\rho_e(r)$. The **Debye–Hückel theory** uses Boltzmann statistics and writes

for the local number densities of the cations and anions, denoted $c_+(r)$ and $c_-(r)$,

$$c_+(r) = \bar{c}_+ \exp -\frac{eV(r)}{kT} \quad (3.94)$$

$$c_-(r) = \bar{c}_- \exp \frac{eV(r)}{kT} . \quad (3.95)$$

Here it is assumed that for the vanishing potential at large distances from the central kation, the densities \bar{c}_+ and \bar{c}_- are found, whereby $\bar{c}_+ = \bar{c}_-$. The total charge density $\rho_e(r)$ follows as

$$\rho_e(r) = e\bar{c}_+ \exp -\frac{eV(r)}{kT} - e\bar{c}_- \exp \frac{eV(r)}{kT} . \quad (3.96)$$

If the kinetic energy is large compared to the potential energy, i.e.,

$$\frac{eV}{kT} \ll 1 , \quad (3.97)$$

a linear approximation can be used, which leads to

$$\rho_e(r) \approx -2e\bar{c}_+ \frac{eV(r)}{kT} . \quad (3.98)$$

Employing Eq. (3.96) or the linear form Eq. (3.98) together with Eq. (3.93) implies treating a system of interacting particles as a system of individual particles in a potential field that is collectively produced by all the particles together. In this molecular field the particles then move independently from each other. Actually, this treatment is an approximation, but an often used one, known as **molecular field** approximation. Here it yields a qualitatively correct, good result.

The next step in the solution is the elimination of $\rho_e(r)$ from Eqs. (3.93) and (3.98), which leads to

$$\frac{1}{r^2} \frac{d}{dr} \left(r^2 \frac{d}{dr} \right) V(r) = \frac{1}{\xi_D^2} V(r) . \quad (3.99)$$

This differential equation is known as the **Poisson–Boltzmann equation**. It includes only one coefficient, namely

$$\xi_D = \left(\frac{\varepsilon_0 \varepsilon kT}{2\bar{c}_+ e^2} \right)^{1/2} , \quad (3.100)$$

and as we shall see, ξ_D has the properties of the already introduced Debye length. Performing the analogous steps in the more general case of an electrolyte of arbitrary composition, with number densities \bar{c}_i of ions with charges $\pm z_i e$, gives

$$\xi_D = \left(\frac{\varepsilon_0 \varepsilon kT}{I_{io}} \right)^{1/2} , \quad (3.101)$$

where

$$I_{\text{io}} = \sum_i \bar{c}_i z_i^2 e^2 \quad (3.102)$$

is referred to as the **ionic strength**.

The Poisson–Boltzmann equation can be exactly solved, and the general solution is

$$V(r) = \frac{\beta_1}{r} \exp -\frac{r}{\xi_D} + \frac{\beta_2}{r} \exp \frac{r}{\xi_D} . \quad (3.103)$$

This can be verified by inserting Eq. (3.103) back into Eq. (3.99). The obvious requirement $V(r \rightarrow \infty) = 0$ implies that β_2 must be zero, leading to

$$V(r) = \frac{\beta_1}{r} \exp -\frac{r}{\xi_D} . \quad (3.104)$$

The physical meaning of the result is immediately recognized: The accumulation of oppositely charged ions in the vicinity of an ion leads to such a **screening effect** that its Coulomb field is weakened and finally vanishes at distances above ξ_D . On raising the ion strength, screening sets in at ever-decreasing distances. ξ_D also describes the extension of the **ion cloud** around the central ion, as can be deduced from Eqs. (3.98) and (3.104).

In the immediate vicinity of the central ion, i.e., for $r \ll \xi_D$, the Coulomb potential is not screened and therefore fully active. This allows the determination of the integration constant c_1 . The final solution for the discussed case of a monovalent kation is

$$V(r) = \frac{e}{4\pi\epsilon_0\epsilon} \exp -\frac{r}{\xi_D} . \quad (3.105)$$

It is obvious that such a charge screening is also found in polyelectrolyte solutions. There, it affects in particular the repulsive electrostatic forces acting between the fixed charges of the polyions. These become screened by all mobile ions, i.e., the counter-ions and, if present, further low molar mass ions. The size of the shielding cloud of mobile ions around the charges on the polyion is again given by the Debye length and is determined by the ionic strength.

Given a sufficiently high salt concentration in the system, the screening can be so strong that the polyelectrolyte chains completely lose their peculiar properties and show a similar behavior as neutral polymer chains. This change occurs when at a sufficiently high salt concentration the Debye length drops below the Bjerrum length, which sets the minimum distance between effective charges on a chain.

3.3.2 Chain Stretching, Salt Effects and Interchain Ordering

Single neutral polymers in a highly dilute solution have coiled conformations with sizes as described by the scaling laws Eq. (2.35) and (2.83) for a theta solvent and a good solvent, respectively,

$$R = a_0 N^{1/2} ,$$

$$R = a_F N^{3/5} .$$

What is the conformation of a polyelectrolyte chain in a solvent with a dielectric coefficient ε , again in the case of a very high dilution? Let us assume that it has $\phi_{\text{io}}N$ ionized groups regularly distributed along the chain with distances l_{io} , and furthermore $l_{\text{io}} > \xi_{\text{B}}$. Then all the counter-ions will diffuse away and their concentration in the solution be negligible. Under these conditions no screening occurs and the Coulomb forces between the chain-fixed charges develop their full power. It can be easily demonstrated that chains in such a system become stretched, i.e., have an end-to-end distance proportional to the degree of polymerization

$$R \propto N . \quad (3.106)$$

To show this, we ask about the balance between the Coulomb repulsion that expands the chain and the entropic rubber elastic forces acting in opposite direction. For an estimate of the total electrostatic energy stored in a chain with a diameter of the order R , we write

$$f_{\text{p}}^{\text{e}} \simeq \frac{1}{4\pi\varepsilon_0\varepsilon} \frac{e^2}{R} (N\phi_{\text{io}})^2 = \frac{kT\xi_{\text{B}}}{R} (N\phi_{\text{io}})^2 . \quad (3.107)$$

The expression implies that Coulomb interaction energies of the order $e^2/(4\pi\varepsilon_0\varepsilon R)$ arise from the repulsive interaction between the $(N\phi_{\text{io}})^2$ ion pairs in the chain. On the other hand, rubber-elastic entropic forces for a polymer chain with an end-to-end distance R lead to an increase of the free energy to a value

$$f_{\text{p}}^{\text{s}} \simeq \frac{kT}{Na_0^2} R^2 \quad (3.108)$$

(compare Eq. (2.93)). The equilibrium value of R follows from

$$\frac{d}{dR} (f_{\text{p}}^{\text{e}} + f_{\text{p}}^{\text{s}}) = 0 = -\frac{kT\xi_{\text{B}}}{R^2} (N\phi_{\text{io}})^2 + \frac{2kTR}{Na_0^2} . \quad (3.109)$$

We obtain

$$R^3 \simeq N^3 \xi_{\text{B}} a_0^2 \phi_{\text{io}}^2 , \quad (3.110)$$

i.e., $R \propto N$ as is indicative for a stretched chain conformation.

Note that the chain is not completely stretched. The ratio between R and the contour length Na_0 of the chain amounts to

$$\frac{R}{Na_0} = \left(\frac{\xi_{\text{B}} \phi_{\text{io}}^2}{a_0} \right)^{1/3} . \quad (3.111)$$

Since the charge distance along the chain, $l_{io} = a_0/\phi_{io}$, is always larger than ξ_B , we find

$$\frac{R}{Na_0} < 1. \quad (3.112)$$

The conformation of an isolated polyelectrolyte chain can be envisaged as a stretched object set up of coiled subunits. A coiled subunit forms for a sequence of n monomeric units for which the electrostatic energy arising from the inner repulsive forces, f^e , equals the thermal energy, i.e.,

$$kT \simeq f^e.$$

For an ideal coil, Eq. (3.107) can be applied again, together with $R = a_0n^{1/2}$, yielding

$$kT \simeq \frac{kT\xi_B}{n^{1/2}a_0}(n\phi_{io})^2. \quad (3.113)$$

The number of monomers in the subunit is therefore

$$n^{3/2} \propto \frac{a_0}{\phi_{io}^2\xi_B}. \quad (3.114)$$

A straight sequence of subunits will then have the length

$$R = \frac{N}{n}a_0n^{1/2} \propto N\xi_B^{1/3}a_0^{2/3}\phi_{io}^{2/3}, \quad (3.115)$$

and this exactly agrees with Eq. (3.110). According to Eq. (3.114) the size of the subunits depends on ϕ_{io} only. Hence, for weakly charged polyelectrolyte chains, where ϕ_{io} is small, the subunits can be quite large.

The arguments presented to show that isolated polyelectrolyte chains are stretched are straightforward, but the experimental verification is difficult. Scattering experiments, which is the main technique for determining the size of dissolved polymers, reach their sensitivity limits before the chains get linearly stretched, which requires extremely high dilutions. They can, however, be applied to study the effect of an **addition of salt** at still low, but not ultra-low, polyelectrolyte concentrations. Since the Coulomb forces then become screened, chains shrink in size. Figure 3.13 presents as an example results of light scattering experiments carried out for a dilute solution of poly(vinylpyridium)bromide.

Addition of NaBr here causes a continuous decrease of the radius of gyration R_g .

One approach for discussing this effect is based on the properties of the persistent chain introduced in Sect. 2.4. As was already mentioned there, when this model is applied to polyelectrolytes, the bending modulus, E_b , relates to both, the inner stiffness of the chain as given by the constitution of the chain backbone and the repulsive Coulomb forces between the chain-fixed charges. The latter depend on the distance l_{io} of the charges along the chain, which is always larger than ξ_B and on the Debye length. With the increase in the

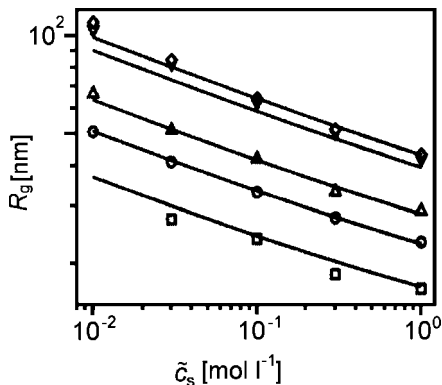


Fig. 3.13. Poly(vinylpyridium)bromide with different molar masses ($\overline{M}_w = 1.68 \times 10^5 - 8.8 \times 10^5 \text{ g mol}^{-1}$) in aqueous solution: Variation of the radius of gyration with the concentration of added NaBr as determined by light scattering. From Volk et al. [15]

ionic strength achieved by the added salt, the Debye length and, therefore, the electrostatic contribution to E_b decrease. For a perfect agreement between theory and experiment – as was reached with the continuous lines in the figure, which nicely reproduce the results – the excluded volume forces between chain segments, which are not included in the persistent chain model, also have to be accounted for. Actually, the electrostatic forces not only enlarge E_b , but give also an additional contribution to the magnitude of the excluded volume effect.

What happens when, beginning with a highly diluted solution with stretched chains, the polyelectrolyte concentration is increased? With the polyion concentration the counter-ion concentration also increases and therefore again the ionic strength. As a consequence, the Debye length decreases and screening effects show up. For a larger range of concentrations one finds conditions with

$$R \gg \xi_D \gg l_{io} (\geq \xi_B) .$$

Under these circumstances chains are coiled, whereby they can be ideal or expanded depending on the quality of the solvent and the concentration. Scattering experiments carried out for such solutions demonstrate that a structure forms; the ordering of the chains in the solution is higher than in an equivalent solution of neutral polymers. The signature of the order is the appearance of a rather sharp peak in the scattering curve and Fig. 3.14 presents a typical example.

Applying Bragg's law on the peak location, a characteristic distance, d , can be derived. It varies with the concentration of the polyelectrolyte in a systematic manner as

$$d \propto c_m^{-1/2} ,$$

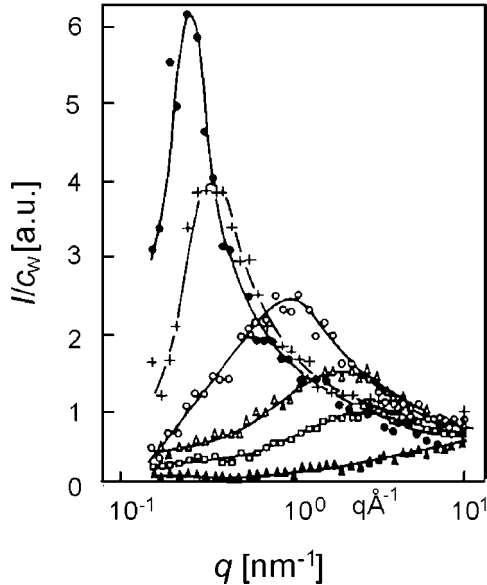


Fig. 3.14. Small angle neutron scattering curves obtained for salt-free aqueous solutions of NaPSS ($\overline{M}_w = 3.54 \times 10^5 \text{ g mol}^{-1}$). The polymer concentration varies between $1.0 \times 10^{-5} \text{ g l}^{-1}$ (*filled circles*) and $2.3 \times 10^{-4} \text{ g l}^{-1}$ (*filled triangles*). From Nierlich et al. [16]

as is shown in Fig. 3.15. The dependence is indicative for a parallel packing of rods, at least locally in the 10 nm to 100 nm range.

What is the meaning of this distance d ? The average volume per chain-fixed charge is of the order $l_{io}d^2$. In a homogeneous solution the chains will be equally distributed in the sample volume, which implies

$$l_{io}d^2 \simeq \frac{1}{c_m \phi_{io}} . \quad (3.116)$$

The term $c_m \phi_{io}$ describes both, the concentration of the chain-fixed ions as well as that of the counter-ions and therefore determines the ionic strength, as

$$I_{io} = e^2 c_m \phi_{io} . \quad (3.117)$$

According to Eq. (3.101) the Debye length is given by

$$\xi_D = \left(\frac{\varepsilon_0 \varepsilon k T}{I_{io}} \right)^{1/2} , \quad (3.118)$$

or, introducing the Bjerrum length by Eq. (3.88), by

$$\xi_D = \left(\frac{e^2}{4\pi \xi_B I_{io}} \right)^{1/2} . \quad (3.119)$$

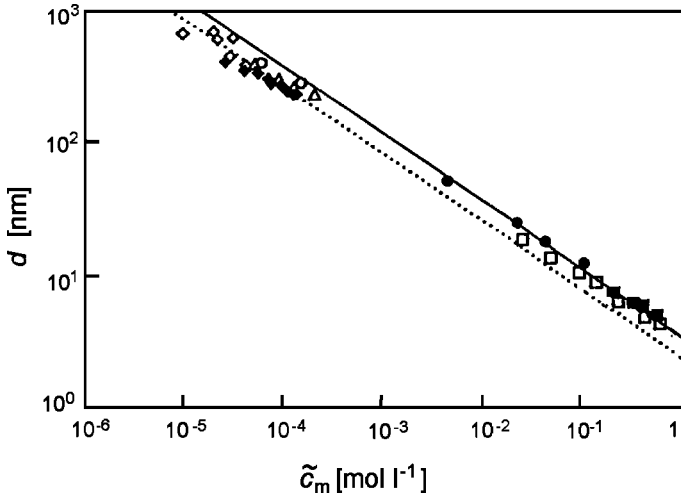


Fig. 3.15. Concentration dependence of the distance d derived from the peak location in scattering curves measured for various NaPSS solutions. From Förster and Schmidt [17]

With Eq. (3.117) we write

$$\xi_D = \left(\frac{1}{4\pi\xi_B c_m \phi_{io}} \right)^{1/2}, \quad (3.120)$$

and with Eq. (3.116) we finally obtain

$$\xi_D \simeq \left(\frac{l_{io} d^2}{\xi_B} \right)^{1/2}. \quad (3.121)$$

This is an interesting result. For a strong electrolyte with $l_{io} \simeq \xi_B$ due to the charge condensation there follows

$$d \simeq \xi_D. \quad (3.122)$$

Hence, in this often encountered case the interchange distance equals the Debye length. For weak electrolytes with $l_{io} > \xi_B$ the distance d is smaller than the Debye length, $d < \xi_D$.

3.3.3 Osmotic Pressure

Osmotic pressures are measured for solutions in a cell with two compartments that are separated by a semipermeable membrane. They arise if the dissolved molecules are only contained in one compartment and cannot pass the membrane. The osmotic pressure depends on the number density of the dissolved

molecules only, irrespective of their size. Therefore, for solutions of neutral, i.e., non-dissociating polymers it is extremely low and in the dilute limit given by

$$\Pi = kT \frac{c_m}{N},$$

whereby c_m/N describes the number density of polymers. For polyelectrolytes the behavior changes completely. The mobile counter-ions now produce an osmotic pressure similar to that in a low molar mass solution. The reason for this change is easily seen: Even if their small size would allow a passage through the semipermeable membrane, the counter-ions will not leave the compartment with the solution because the strong electrostatic forces preserve a global charge neutrality. Since the polyions cannot leave their compartment due to their size, the counter-ions are kept there as well, and so become fully active in the production of the osmotic pressure. For a dilute polyelectrolyte solution it is therefore given by

$$\frac{\Pi}{kT} = \frac{c_m}{N} + \phi_{\text{io}} c_m. \quad (3.123)$$

The second term due to the counter-ions dominates by far, i.e.,

$$\frac{\Pi}{kT} \approx \phi_{\text{io}} c_m. \quad (3.124)$$

Writing this expression it is assumed that the distance of ionizable groups along the chain is larger than $l_{\text{io}} > \xi_B$, so that no counter-ion condensation occurs.

What happens if salt is now added to the system? Figure 3.16 gives the answer with an experimental result. For a salt-free NaPSS solution one finds a behavior in agreement with Eq. (3.124) (the slope in the log-log representation actually indicates an increase with a power of 9/8 rather than 1 and there exist attempts to interpret this small deviation). The second, much steeper line refers to a solution where NaCl was added in a concentration of $10^{-2} \text{ mol l}^{-1}$. This concentration dependence now exactly agrees with that observed for neutral polymers, namely, according to Eq. (3.41),

$$\frac{\Pi}{kT} \propto c_m^{9/4}.$$

How can the observation be understood? The ionic strength supplied by the salt can lead to a complete screening of the chain-fixed charges, then, when $\xi_D < l_{\text{io}}$ Na- and Cl-ions freely pass through the semipermeable membrane and are found in both compartments. However, since charge neutrality is preserved on both sides, an equal number of positive and negative salt ions must pass through the membrane in each direction. Why are the counter-ions of the polyion no longer active under these circumstances? The answer was

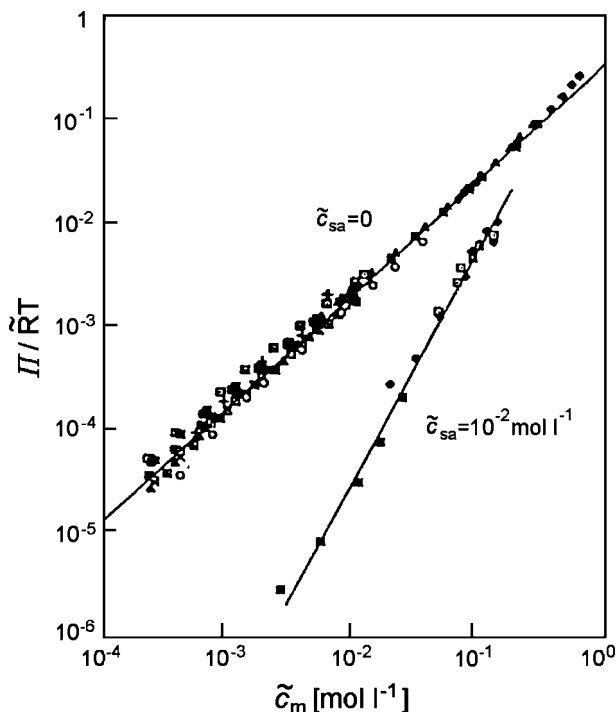


Fig. 3.16. Concentration dependence of the osmotic pressure measured for aqueous solutions of NaPSS with and without added NaCl. From Wang and Bloomfield [18]

given long ago, in a work by Donnan in 1911. Consider a positively charged polyion and counter-ions that are identical with the negatively charged ions of the salt. Let c'_- be their concentration in the polymer compartment and c'_+ the concentration of the mobile positive salt ions in the same compartment. The other part of the cell contains dissolved salt only, with ion concentrations c''_+ and c''_- . Charge neutrality requires for the polymer side

$$c'_- = c'_+ + c_m \phi_{io} , \quad (3.125)$$

there are more negative than positive mobile ions, and for the other side

$$c''_- = c''_+ = c_{sa} ; \quad (3.126)$$

c_{sa} is here introduced as the number density of salt molecules in the polymer free compartment. Even if the degree of dissociation of the salt molecules is very close to one, there still exist some non-dissociated molecules. Their concentration, denoted c_{+-} , is equal on both sides since they can pass freely through the membrane. The dissociation-association equilibria fulfill the equation

$$c'_{+-} = c''_{+-} \quad (3.127)$$

$$\frac{c_+'' c_-''}{c_{+-}} = \text{const} = \frac{c_+' c_-'}{c_{+-}}, \quad (3.128)$$

hence

$$c_+' c_-' = c_+'' c_-'' = c_{\text{sa}}^2. \quad (3.129)$$

Equation (3.125) can be rewritten as

$$(c_-' - c_+')^2 = (c_m \phi_{\text{io}})^2. \quad (3.130)$$

A multiplication of Eq. (3.129) by a factor 4, followed by an addition to Eq. (3.130), yields

$$(c_-' + c_+')^2 = 4c_{\text{sa}}^2 + (c_m \phi_{\text{io}})^2. \quad (3.131)$$

The concentration difference between the mobile ions in the two compartments Δc_{io} is given by

$$\Delta c_{\text{io}} = c_-' - c_+' - 2c_{\text{sa}} \quad (3.132)$$

and therefore amounts to

$$\Delta c_{\text{io}} = (4c_{\text{sa}}^2 + c_m^2 \phi_{\text{io}}^2)^{1/2} - 2c_{\text{sa}}. \quad (3.133)$$

This is the quantity we searched for, because Δc_{io} determines the osmotic pressure. In the absence of salt, $c_{\text{sa}} = 0$, we have

$$\Delta c_{\text{io}} = c_m \phi_{\text{io}}, \quad (3.134)$$

i.e., the difference arises from the counter-ions of the polyion only. On the other hand, for high salt concentrations

$$c_m \phi_{\text{io}} \ll c_{\text{sa}}$$

a series expansion of the square root expression yields

$$\Delta c_{\text{io}} \approx \frac{c_m^2 \phi_{\text{io}}^2}{4c_{\text{sa}}}. \quad (3.135)$$

The associated osmotic pressure is obtained by replacing the term $\phi_{\text{io}} c_m$ in Eq. (3.123) by Δc_{io} , leading to

$$\frac{\Pi}{kT} = \frac{c_m}{N} + \frac{\phi_{\text{io}}^2}{4c_{\text{sa}}} c_m^2. \quad (3.136)$$

The second term in Eq. (3.123), which is linear in c_m , is exchanged for a term that is quadratic in c_m . The associated coefficient

$$A_2^{\text{Do}} = \frac{\phi_{\text{io}}^2}{4c_{\text{sa}}} \quad (3.137)$$

formally represents a second order virial coefficient, and is known as the **Donnan contribution** to A_2 .

Equation (3.136) implies that the osmotic pressure of a salt containing solution approaches in the limit of low polyelectrolyte concentrations the value found for neutral polymers

$$\lim_{c_m \rightarrow 0} \frac{\Pi}{kTc_m} = \frac{1}{N}. \quad (3.138)$$

Hence, after an addition of salt, osmotic pressure measurements can again be used for a determination of the degree of polymerization.

Our considerations qualitatively explain the results of Fig. 3.16: The dissolution of salt in addition to the polyelectrolyte suppresses the osmotic pressure contribution by the counter-ions and transforms the stiffened polyelectrolyte chain into a much more flexible quasi-neutral chain. In the absence of these polyelectrolyte characteristics, one recovers the behavior of neutral systems and, therefore, in the semidilute range the associated scaling law Eq. (3.41). Equation (3.136) correctly describes the general tendencies, but is not an accurate expression. First, in view of the complex structures in polyelectrolytes with shell formations and screening effects, equilibria have to be expressed in terms of activities rather than concentrations. Furthermore, the Donnan expression is not the only contribution to the second virial coefficient. There exists another part, ΔA_2 , which accounts as usually for excluded volume effects, the quality of the solvent and the peculiar ordering phenomena found in polyelectrolyte solutions. Therefore, in general, one has to write

$$\frac{\Pi}{kT} = \frac{c_m}{N} + A_2^{\text{Do}} c_m^2 + \Delta A_2 c_m^2, \quad (3.139)$$

thus dealing with two contributions to the second virial coefficient.

Further Reading

- J. des Cloizeaux, G. Jannink: *Polymers in Solution: Their Modelling and Structure*, Oxford Science Publishers, 1990
- H. Dautzenberg, W. Jaeger, J. Kötz, B. Philipp, Ch. Seidel, D. Stscherbina: *Polyelectrolytes*, Carl Hanser, 1994
- M. Doi, S.F. Edwards: *The Theory of Polymer Dynamics*, Clarendon Press, 1986
- S. Förster, M. Schmidt: *Polyelectrolytes in Solution*, Advances in Polymer Science, Vol. 120, Springer, 1995
- A.Y. Grosberg, A.R. Khokhlov: *Statistical Physics of Macromolecules*, AIP Press, 1994
- M. Schmidt (Ed.): *Polyelectrolytes with Defined Molecular Architectures*, Springer, 2004

Polymer Blends and Block Copolymers

A large part of applications oriented research is devoted to the study of polymer blends, since mixing opens a route for a combination of different properties. Take, for example, the mechanical performance of polymeric products. In many cases one is searching for materials that combine high stiffness with resistance to fracture. For the majority of common polymers these two requirements cannot be realized simultaneously, because an increase in stiffness, i.e., the elastic moduli, is usually associated with samples becoming more brittle and decreasing in strength. Using mixtures offers a chance to achieve good results for both properties. High-impact polystyrene, a mixture of polystyrene and polybutadiene, represents a prominent example. Whereas polystyrene is stiff but brittle, a blending with rubbers furnishes a tough material that still retains a satisfactory stiffness. Here mixing results in a two-phase structure with rubber particles of spherical shape being incorporated in the matrix of polystyrene. Materials are tough, if fracture energies are high due to yield processes preceding the ultimate failure, and these become initiated at the surfaces of the rubber spheres where stresses are intensified. On the other hand, inclusion of rubber particles in the polystyrene matrix results in only a moderate reduction in stiffness. Hence, the blending yields a material with properties that in many situations are superior to pure polystyrene. There are other cases, where an improvement of the mechanical properties is achieved by a homogeneous mixture of two polymers, rather than a two-phase structure. A well-known example is again given by polystyrene when blended with poly(phenyleneoxide). In this case, a homogeneous phase is formed and as it turns out in mechanical tests, it also exhibits a satisfactory toughness together with a high elastic modulus.

It is generally very difficult or even impossible to predict the mechanical properties of a mixture; however, this is only the second step. The first problem is an understanding of the mixing properties, i.e., a knowledge of under which conditions two polymeric compounds will form either a homogeneous phase or a two-phase structure. In the latter case, it is important to see how structures develop and how this can be controlled. This section deals

with these topics. We shall first discuss the thermodynamics of mixing of two polymers and derive equations that can be used for the setting-up of phase diagrams. Subsequently we shall be concerned with the kinetics of unmixing and here, in particular, with a special mode known as spinodal decomposition.

4.1 The Flory–Huggins Treatment of Polymer Mixtures

Flory and Huggins devised a general scheme that enables one to deal with the mixing properties of a pair of polymers. It provides a basic understanding of the occurrence of different types of phase diagrams, in dependence on temperature and the molar masses.

The mixing properties of two components may generally be discussed by considering the change in the Gibbs free energy. Figure 4.1 addresses the situation and introduces the relevant thermodynamic variables. Let us assume that we have \tilde{n}_A moles of polymer A, contained in a volume \mathcal{V}_A and \tilde{n}_B moles of polymer B, contained in a volume \mathcal{V}_B . Mixing may be initiated by removing the boundary between the two compartments, so that both components can expand to the full volume of size $\mathcal{V} = \mathcal{V}_A + \mathcal{V}_B$. In order to find out whether a mixing would indeed occur, the change in the Gibbs free energy has to be considered. This change, called the **Gibbs free energy of mixing** and denoted $\Delta\mathcal{G}_{\text{mix}}$, is given by

$$\Delta\mathcal{G}_{\text{mix}} = \mathcal{G}_{AB} - (\mathcal{G}_A + \mathcal{G}_B), \quad (4.1)$$

where \mathcal{G}_A , \mathcal{G}_B and \mathcal{G}_{AB} denote the Gibbs free energies of the compounds A and B in separate states and the mixed state, respectively. Employing the Gibbs, rather than the Helmholtz, free energy allows one to also include volume changes in the treatment, which may accompany a mixing at constant pressure. However, since the related term $p\Delta\mathcal{V}$ is always negligible, this is only a formal remark.

The **Flory–Huggins treatment** represents $\Delta\mathcal{G}_{\text{mix}}$ as a sum of two contributions

$$\Delta\mathcal{G}_{\text{mix}} = -T\Delta\mathcal{S}_t + \Delta\mathcal{G}_{\text{loc}}, \quad (4.2)$$

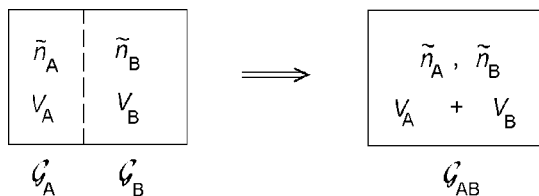


Fig. 4.1. Variables used in the description of the process of mixing of two polymers, denoted A and B

which describe the two main aspects of the mixing process. Firstly, mixing leads to an increase of the entropy associated with the motion of the centers of mass of all polymer molecules, and secondly, it may change the local interactions and motions of the monomers. We call the latter part $\Delta\mathcal{G}_{\text{loc}}$ and the increase in the **translational entropy** $\Delta\mathcal{S}_t$. $\Delta\mathcal{S}_t$ and the related decrease $-T\Delta\mathcal{S}_t$ in the Gibbs free energy always favor a mixing. $\Delta\mathcal{G}_{\text{loc}}$, on the other hand, may act favorably or unfavorably, depending on the character of the monomer–monomer pair interactions. In most cases, and, as can be verified, for van der Waals interactions generally, attractive energies between equal monomers are stronger than those between unlike pairs. This behavior implies $\Delta\mathcal{G}_{\text{loc}} > 0$ and therefore opposes a mixing. As a free energy, $\Delta\mathcal{G}_{\text{loc}}$ also accounts for changes in the entropy due to local effects. For example, a shrinkage or an expansion of the total volume on mixing results in a change in the number of configurations available for local motions of the monomeric units, hence in a change of entropy to be included in $\Delta\mathcal{G}_{\text{loc}}$.

The decomposition of $\Delta\mathcal{G}_{\text{mix}}$ in these two contributions points to the two main aspects of the mixing process, but this alone would not be of much value. What is needed for actual use are explicit expressions for $\Delta\mathcal{S}_t$ and $\Delta\mathcal{G}_{\text{loc}}$, so that the sum of the two contributions can be calculated. The Flory–Huggins treatment is based on approximate equations for both parts. We formulate them first and then discuss their origins and the implications. The equations have the following forms:

1. The increase in the translational entropy is described by

$$\frac{\Delta\mathcal{S}_t}{\tilde{R}} = \tilde{n}_A \ln \frac{\mathcal{V}}{\mathcal{V}_A} + \tilde{n}_B \ln \frac{\mathcal{V}}{\mathcal{V}_B}. \quad (4.3)$$

Introducing the volume fractions ϕ_A and ϕ_B of the two components in the mixture, given by

$$\phi_A = \frac{\mathcal{V}_A}{\mathcal{V}} \quad \text{and} \quad \phi_B = \frac{\mathcal{V}_B}{\mathcal{V}}, \quad (4.4)$$

$\Delta\mathcal{S}_t$ can be written as

$$\frac{\Delta\mathcal{S}_t}{\tilde{R}} = -\tilde{n}_A \ln \phi_A - \tilde{n}_B \ln \phi_B. \quad (4.5)$$

2. The change in the local interactions is expressed by the equation

$$\Delta\mathcal{G}_{\text{loc}} = \tilde{R}T \frac{\mathcal{V}}{\tilde{v}_c} \chi \phi_A \phi_B. \quad (4.6)$$

It includes two parameters. The less important one is \tilde{v}_c , denoting the (molar) volume of a reference unit common to both polymers. Principally it can be chosen arbitrarily, but usually it is identified with the volume occupied by one of the monomeric units. The decisive factor is the **Flory–Huggins parameter** χ . It is dimensionless and determines in empirical manner the change in the local free energy per reference unit.

What is the physical background of these expressions? There are numerous discussions in the literature, mainly based on Flory's and Huggins' original derivations. As the full treatment lies outside our scope, we here present only a simplified view, which nevertheless may aid in providing a basic understanding. The view emanates from a **molecular** or **mean field** description. We consider the actual system of interpenetrating interacting chains, which comprise the fluid mixture as being equivalent to a system of independent chains that interact with a common uniform mean field set up by the many chain system as a whole. The interaction of a given chain with all other chains, as represented in an integral form by the mean field, has two effects. The first one was discussed earlier: The contacts with other chains screen the intramolecular excluded volume interactions, thus leading to ideal chain behavior. The Flory–Huggins treatment assumes that this effect is maintained in a mixture, with unchanged conformational distributions. The second effect was already mentioned in the introduction to this chapter. Being in contact with a large number of other chains, a given chain in a binary mixture effectively integrates over the varying monomer–monomer interactions and thus probes their average value. The change in the monomer–monomer interactions following from a mixing may therefore be expressed as change of the mean field, with uniform values for all units of the A-chains and B-chains, respectively.

Equations (4.5) and (4.6) are in agreement with this picture, as can be easily verified. In order to formulate the increase in the translational entropy for \tilde{n}_A moles of independent A-chains, expanding from an initial volume \mathcal{V}_A to a final volume \mathcal{V} , and \tilde{n}_B moles of B-chains, expanding from \mathcal{V}_B to \mathcal{V} , we may just apply the standard equations used for perfect gases, and these lead exactly to Eq. (4.5). As the single chain conformational distributions should not change on mixing, we have no further contribution to the entropy (Flory addressed in his original treatment Eq. (4.5) correspondingly as the change in the total configurational entropy, rather than associating it with the center of mass motions only).

Regarding the expression for $\Delta\mathcal{G}_{\text{loc}}$, we may first note that Eq. (4.6) represents the simplest formula which fulfills the requirement that $\Delta\mathcal{G}_{\text{loc}}$ must vanish for $\phi_A \rightarrow 0$ and $\phi_B \rightarrow 0$. More about the background may be learned if we consider the change in the interaction energy following from a transfer of an A-chain from the separated state into the mixture. Each chain probes the average value of the varying contact energies with the adjacent foreign monomers, and the increase in the potential energy per reference unit may be written as

$$\frac{z_{\text{eff}}}{2}\phi_B kT\chi'.$$

Here, the effective coordination number z_{eff} gives the number of nearest neighbors (in reference units) on other chains, and a division by 2 is necessary to avoid a double count of the pair contacts. An increase in the local Gibbs free energy only results if an AB-pair is formed and this occurs with a probability

equal to the volume fraction of the B's, ϕ_B . The product $kT\chi'$ is meant to specify this energy increase by employing a dimensionless parameter χ' . For the potential experienced by the units of the B-chains in the mixture we write correspondingly

$$\frac{z_{\text{eff}}}{2} \phi_A kT\chi'$$

with the identical parameter χ' . To obtain $\Delta\mathcal{G}_{\text{loc}}$, which refers to the total system, we have to add the contributions of all A-chains and B-chains, weighted according to the respective fraction. This leads us to

$$\begin{aligned} \Delta\mathcal{G}_{\text{loc}} &= \frac{\mathcal{V}}{\tilde{v}_c} N_L \frac{z_{\text{eff}}}{2} (\phi_A \phi_B + \phi_B \phi_A) kT\chi' \\ &= \tilde{R}T \frac{\mathcal{V}}{\tilde{v}_c} \phi_A \phi_B z_{\text{eff}} \chi'. \end{aligned} \quad (4.7)$$

The prefactor $\mathcal{V}N_L/\tilde{v}_c$ gives the number of reference units in the system. As we can see, Eq. (4.7) is equivalent to Eq. (4.6) if we set

$$\chi = z_{\text{eff}} \chi'. \quad (4.8)$$

Originally the χ -parameter was introduced to account for the contact energies only. However, its meaning can be generalized and in fact, this is necessary. Experiments indicate that $\Delta\mathcal{G}_{\text{loc}}$ often includes an entropic part, so that we have in general

$$\Delta\mathcal{G}_{\text{loc}} = \Delta\mathcal{H}_{\text{mix}} - T\Delta\mathcal{S}_{\text{loc}}. \quad (4.9)$$

The enthalpic part $\Delta\mathcal{H}_{\text{mix}}$ shows up in the heat of mixing, which is positive for endothermic and negative for exothermic systems. As has already been mentioned, the entropic part $\Delta\mathcal{S}_{\text{loc}}$ is usually due to changes in the number of available local conformations.

A particular concept employed in the original works must also be commented on, since it is still important. In the theoretical developments, Flory used a **lattice model**, constructed as drawn schematically in Fig. 4.2.

The A-units and B-units of the two polymer species both have the same volume v_c and occupy the cells of a regular lattice with coordination number z . It is assumed that the interaction energies are purely enthalpic and effective between nearest neighbors only. Excess contributions $kT\chi'$, which add to the interaction energies in the separated state, arise for all pairs of unlike monomers. The parameter $\chi = (z - 2)\chi'$ was devised to deal with this model and therefore depends on the size of the cell. Flory evaluated this model with the tools of statistical thermodynamics. Using approximations, he arrived at Eqs. (4.5) and (4.6).

Although a modeling of a liquid polymer mixture on a lattice may at first look rather artificial, it makes sense because it retains the important aspects of both the entropic and enthalpic parts of $\Delta\mathcal{G}_{\text{mix}}$. In recent years, lattice

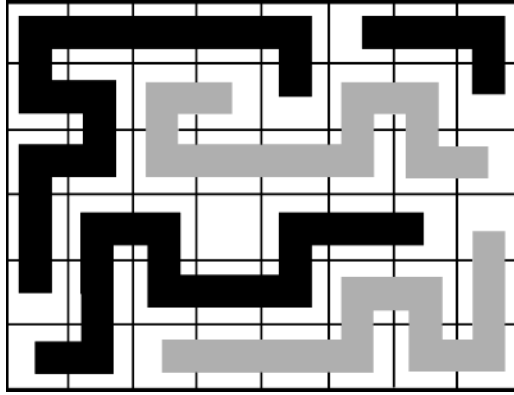


Fig. 4.2. Lattice model of a polymer mixture. Structure units of equal size setting up the two species of polymers occupy a regular lattice

models have gained a renewed importance as a concept that is suitable for computer simulations. Numerical investigations make it possible to check and assess the validity range of the Flory–Huggins treatment. In fact, limitations exist and, as analytical calculations are difficult, simulations are very helpful and important. We shall present one example in a later section.

Application of the two expressions for $\Delta\mathcal{S}_t$ and $\Delta\mathcal{G}_{loc}$, Eqs. (4.5) and (4.6), results in the Flory–Huggins formulation for the Gibbs free energy of mixing of polymer blends

$$\Delta\mathcal{G}_{mix} = \tilde{R}T(\tilde{n}_A \ln \phi_A + \tilde{n}_B \ln \phi_B + \tilde{n}_c \phi_A \phi_B \chi) \quad (4.10)$$

$$= \tilde{R}T\mathcal{V} \left(\frac{\phi_A}{\tilde{v}_A} \ln \phi_A + \frac{\phi_B}{\tilde{v}_B} \ln \phi_B + \frac{\chi}{\tilde{v}_c} \phi_A \phi_B \right) \quad (4.11)$$

$$= \tilde{R}T\tilde{n}_c \left(\frac{\phi_A}{N_A} \ln \phi_A + \frac{\phi_B}{N_B} \ln \phi_B + \chi \phi_A \phi_B \right). \quad (4.12)$$

Here, we have introduced the molar volumes of the polymers, \tilde{v}_A and \tilde{v}_B , using

$$\tilde{n}_A = \mathcal{V} \frac{\phi_A}{\tilde{v}_A} \quad \text{and} \quad \tilde{n}_B = \mathcal{V} \frac{\phi_B}{\tilde{v}_B}, \quad (4.13)$$

and the molar number of the reference units

$$\tilde{n}_c = \frac{\mathcal{V}}{\tilde{v}_c}. \quad (4.14)$$

The second equation follows when we replace the molar volumes by the degrees of polymerization expressed in terms of the numbers of structure units. If we choose the same volume, equal to the reference volume \tilde{v}_c , for both the A-structure and B-structure units we have

$$N_A = \frac{\tilde{v}_A}{\tilde{v}_c} \quad \text{and} \quad N_B = \frac{\tilde{v}_B}{\tilde{v}_c}. \quad (4.15)$$

ϕ_A and ϕ_B add up to unity,

$$\phi_A + \phi_B = 1. \quad (4.16)$$

The **Flory–Huggins equation** (4.11) or (4.12) is famous and widely used. It sets the basis from which the majority of discussions of the properties of polymer mixtures emanates.

Starting from $\Delta\mathcal{G}_{\text{mix}}$, the entropy of mixing, $\Delta\mathcal{S}_{\text{mix}}$, follows as

$$\begin{aligned} \Delta\mathcal{S}_{\text{mix}} &= -\frac{\partial\Delta\mathcal{G}_{\text{mix}}}{\partial T} \\ &= -\tilde{R}\mathcal{V} \left(\frac{\phi_A}{\tilde{v}_A} \ln \phi_A + \frac{\phi_B}{\tilde{v}_B} \ln \phi_B + \frac{\phi_A\phi_B}{\tilde{v}_c} \frac{\partial(\chi T)}{\partial T} \right) \end{aligned} \quad (4.17)$$

and the enthalpy of mixing, $\Delta\mathcal{H}_{\text{mix}}$, as

$$\Delta\mathcal{H}_{\text{mix}} = \Delta\mathcal{G}_{\text{mix}} + T\Delta\mathcal{S}_{\text{mix}} = \tilde{R}T \frac{\mathcal{V}}{\tilde{v}_c} \phi_A\phi_B \left(\chi - \frac{\partial(\chi T)}{\partial T} \right). \quad (4.18)$$

These expressions show that the χ -parameter includes an entropic contribution given by

$$\chi_S = \frac{\partial}{\partial T}(\chi T) \quad (4.19)$$

and an enthalpic part

$$\chi_{\mathcal{H}} = \chi - \frac{\partial(\chi T)}{\partial T} = -T \frac{\partial\chi}{\partial T}, \quad (4.20)$$

both setting up χ as

$$\chi = \chi_{\mathcal{H}} + \chi_S. \quad (4.21)$$

Equation (4.19) indicates that for purely enthalpic local interactions, χ must have a temperature dependence

$$\chi \propto \frac{1}{T}. \quad (4.22)$$

In this case, the increase in entropy is associated with the translational entropy only,

$$\Delta\mathcal{S}_{\text{mix}} = \Delta\mathcal{S}_t, \quad (4.23)$$

and the heat of mixing is given by

$$\Delta\mathcal{H}_{\text{mix}} = \tilde{R}T \frac{\mathcal{V}}{\tilde{v}_c} \chi \phi_A \phi_B = \tilde{R}T \tilde{n}_c \chi \phi_A \phi_B. \quad (4.24)$$

The Flory–Huggins equation provides the basis for a general discussion of the miscibility properties of a pair of polymers. As we shall see, this can be achieved in a transparent manner and leads to clear conclusions. To start with, we recall that as a necessary requirement mixing must be accompanied

by a decrease of the Gibbs free energy. For liquid mixtures of low molar mass molecules this is mainly achieved by the large increase in the translational entropy. For these systems the increase in ΔS_t can accomplish miscibility even in the case of unfavorable AB-interaction energies, i.e., for mixtures with an endothermal heat of mixing. In polymers we find a qualitatively different situation. The Flory–Huggins equation teaches us that for polymer mixtures the increase in the translational entropy ΔS_t is extremely small and vanishes in the limit of infinite molar mass, i.e., $\tilde{v}_A, \tilde{v}_B \rightarrow \infty$. The consequences are obvious:

- Positive values of χ necessarily lead to incompatibility. Since the entropic part, χ_S , appears to be mostly positive, one may also state that no polymer mixtures exist with a positive heat of mixing.
- If the χ -parameter is negative, then mixing takes place.

The reason for this behavior becomes clear if we regard miscibility as the result of a competition between the osmotic pressure emerging from the translational motion of the polymers and the forces acting between the monomers. The osmotic pressure, which always favors miscibility, depends on the polymer density c_p , whereas the change in the free energy density associated with the interactions between unlike monomers – it can be positive or negative – is a function of the monomer density c_m . Since $c_p/c_m = 1/N$, the osmotic pressure part is extremely small compared to the effect of the monomer–monomer interactions. Hence, mutual compatibility of two polymers, i.e., their potential to form a homogeneous mixture, is almost exclusively determined by the local interactions. Endothermal conditions are the rule between two different polymers, exothermal conditions are the exception. Hence, the majority of pairs of polymers cannot form homogeneous mixtures. Compatibility is only found if there are special interactions between the A-monomers and the B-monomers as they may arise in the form of dipole–dipole forces, hydrogen bonds or special donor–acceptor interactions.

All these conclusions refer to the limit of large degrees of polymerization. It is important to see that the Flory–Huggins equation permits one to consider how the compatibility changes if the degrees of polymerization are reduced and become moderate or small. For the sake of simplicity, for a discussion we choose the case of a symmetric mixture with equal degrees of polymerization for both components, i.e.,

$$N_A = N_B = N \quad (4.25)$$

Using

$$\frac{\tilde{n}_c}{N} = \tilde{n}_A + \tilde{n}_B \quad (4.26)$$

we obtain

$$\Delta \mathcal{G}_{\text{mix}} = \tilde{R}T(\tilde{n}_A + \tilde{n}_B)(\phi_A \ln \phi_A + \phi_B \ln \phi_B + \chi N \phi_A \phi_B). \quad (4.27)$$

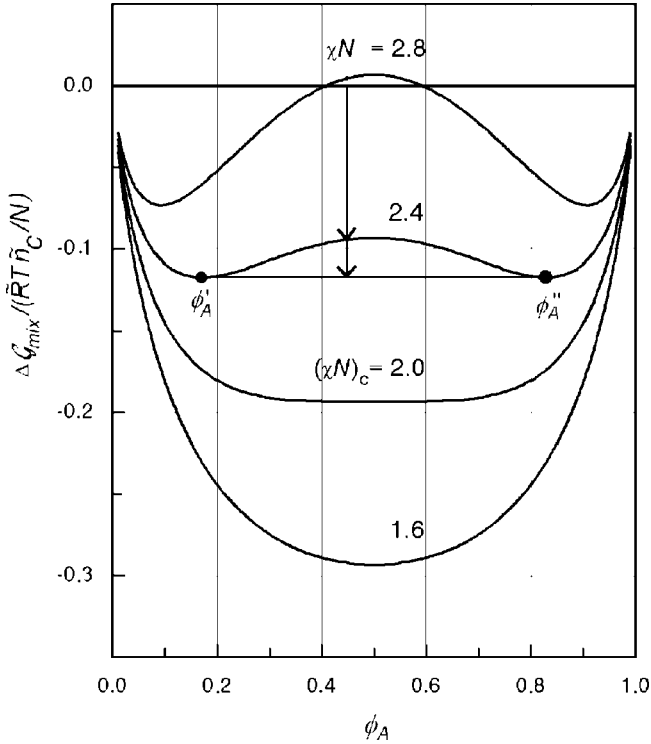


Fig. 4.3. Gibbs free energy of mixing of a symmetric binary polymer mixture ($N_A = N_B = N$), as described by the Flory–Huggins equation

Note that there is only one relevant parameter, namely the product $N\chi$. The dependence of $\Delta\mathcal{G}_{\text{mix}}$ on ϕ_A is shown in Fig. 4.3, as computed for different values of χN .

A discussion of these curves enables us to reach some direct conclusions. For vanishing χ , one has negative values of $\Delta\mathcal{G}_{\text{mix}}$ for all ϕ_A , with a minimum at $\phi_A = 0.5$. In this case, we have perfect miscibility caused by the small entropic forces related with $\Delta\mathcal{S}_t$. For negative values of χN , we have a further decrease of $\Delta\mathcal{G}_{\text{mix}}$ and therefore also perfect miscibility.

A change in behavior is observed for positive values of χN . The curves alter their shape and for parameters χN above a critical value

$$(\chi N) > (\chi N)_c$$

a maximum rather than a minimum emerges at $\phi_A = 0.5$. This change leads us into a different situation. Even if $\Delta\mathcal{G}_{\text{mix}}$ is always negative, there a homogeneous mixture does not always form. To understand the new conditions consider, for example, the curve for $\chi N = 2.4$ and a blend with $\phi_A = 0.45$. There the two arrows are drawn. The first arrow indicates that a homogeneous mixing of A and B would lead to a decrease in the Gibbs free energy,

when compared to two separate one component phases. However, as shown by the second arrow, the Gibbs free energy can be further reduced, if again a two-phase structure is formed, now being composed of two mixed phases, with compositions ϕ'_A and ϕ''_A . The specific feature in the selected curve responsible for this peculiar behavior is the occurrence of the two minima at ϕ'_A and ϕ''_A , as these enable the further decrease of the Gibbs free energy. For which values of ϕ_A can this decrease be achieved? Not for all values, because there is an obvious restriction: The overall volume fraction of the A-chains has to be in the range

$$\phi'_A \leq \phi_A \leq \phi''_A .$$

Outside this central range, for $\phi_A < \phi'_A$ and $\phi_A > \phi''_A$, a separation into the two-phases with the minimum Gibbs free energies is impossible and one homogeneous phase is formed. For a given ϕ_A we can calculate the fractions ϕ_1, ϕ_2 of the two coexisting mixed phases. As we have

$$\phi_A = \phi_1 \cdot \phi'_A + (1 - \phi_1)\phi''_A , \quad (4.28)$$

we find

$$\phi_1 = \frac{\phi''_A - \phi_A}{\phi''_A - \phi'_A} \quad (4.29)$$

and

$$\phi_2 = 1 - \phi_1 = \frac{\phi_A - \phi'_A}{\phi''_A - \phi'_A} . \quad (4.30)$$

Hence in conclusion, for curves $\Delta\mathcal{G}_{\text{mix}}(\phi_A)$, which exhibit two minima and a maximum in-between, mixing properties depend on the value of ϕ_A . Miscibility is found for low and high values of ϕ_A only, and in the central region there is a **miscibility gap**.

One can determine the critical value of χN that separates the range of perfect mixing, i.e., compatibility through all compositions, from the range with a miscibility gap. Clearly, for the critical value of χN , the curvature at $\phi_A = 0.5$ must vanish,

$$\frac{\partial^2 \Delta\mathcal{G}_{\text{mix}}(\phi_A = 0.5)}{\partial \phi_A^2} = 0 . \quad (4.31)$$

The first derivative of $\Delta\mathcal{G}_{\text{mix}}$ is given by

$$\frac{1}{(\tilde{n}_A + \tilde{n}_B)\tilde{R}T} \frac{\partial \Delta\mathcal{G}_{\text{mix}}}{\partial \phi_A} = \ln \phi_A + 1 - \ln(1 - \phi_A) - 1 + \chi N(1 - 2\phi_A) \quad (4.32)$$

and the second derivative by

$$\frac{1}{(\tilde{n}_A + \tilde{n}_B)\tilde{R}T} \frac{\partial^2 \Delta\mathcal{G}_{\text{mix}}}{\partial \phi_A^2} = \frac{1}{\phi_A} + \frac{1}{1 - \phi_A} - 2\chi N . \quad (4.33)$$

The critical value is

$$\chi N = 2. \quad (4.34)$$

Hence, we expect full compatibility for

$$\chi < \chi_c = \frac{2}{N} \quad (4.35)$$

and a miscibility gap for

$$\chi > \chi_c. \quad (4.36)$$

Equations (4.35) and (4.36) describe the effect of the molar mass on the compatibility of a pair of polymers. In the limit $N \rightarrow \infty$ we have

$$\chi_c \rightarrow 0.$$

This agrees with our previous conclusion that for positive values of χ polymers of average and high molar mass do not mix at all.

The properties of symmetric polymer mixtures are summarized in the phase diagram shown in Fig. 4.4. It depicts the two regions associated with homogeneous and two-phase structures in a plot that uses the sample composition as expressed by the volume fraction ϕ_A and the parameter χN as variables. The boundary between the one phase and the two-phase region is called **binodal**. It is determined by the compositions ϕ'_A and ϕ''_A of the equi-

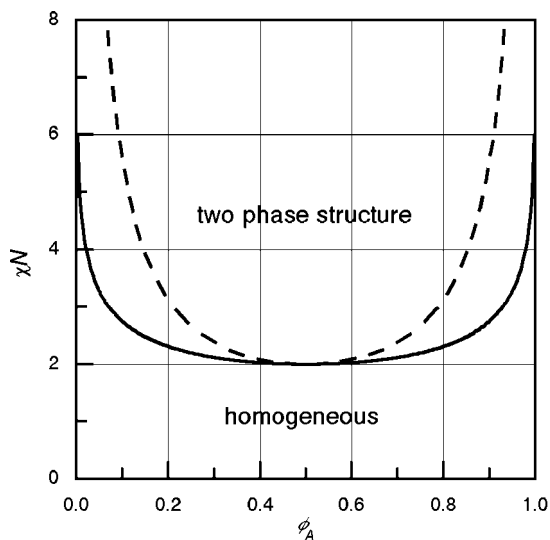


Fig. 4.4. Phase diagram of a symmetric polymer mixture ($N_A = N_B = N$). In addition to the binodal (*continuous line*) the spinodal is shown (*broken line*)

librium phases with minimum Gibbs free energies in the miscibility gap. ϕ'_A and ϕ''_A follow for a given value of χN from

$$\frac{\partial \Delta \mathcal{G}_{\text{mix}}}{\partial \phi_A} = 0. \quad (4.37)$$

Using Eq. (4.32) we obtain an analytical expression for the binodal:

$$\chi N = \frac{1}{1 - 2\phi'_A} \ln \frac{1 - \phi_A}{\phi_A}. \quad (4.38)$$

The derived phase diagram is universal in the sense that it is valid for all symmetric polymer mixtures. It indicates a miscibility gap for $\chi N > 2$ and enables us to make a determination of χN in this range if the compositions of the two coexisting phases are known.

For mixtures of polymers with different degrees of polymerization, i.e., $N_A \neq N_B$, the phase diagram loses its symmetrical shape. Figure 4.5 depicts $\Delta \mathcal{G}_{\text{mix}}(\phi_A)$ for a mixture with $N_B = 4N_A$, as computed on the basis of the Flory–Huggins equation. Straightforward analysis shows that, in this general case, the critical value of χ is given by

$$\chi_c = \frac{1}{2} \left(\frac{1}{\sqrt{N_A}} + \frac{1}{\sqrt{N_B}} \right)^2. \quad (4.39)$$

The critical point where the miscibility gap begins is located at

$$\phi_{A,c} = \frac{\sqrt{N_B}}{\sqrt{N_A} + \sqrt{N_B}}. \quad (4.40)$$

The points along the binodal can be determined by the construction of the common tangent as indicated in the figure. The explanation for this procedure is simple. We refer here to the two arrows drawn at $\phi_A = 0.45$ and the curve calculated for $\chi N_A = 1.550$. First, consider the change in $\Delta \mathcal{G}_{\text{mix}}$ if starting-off from separate states, two arbitrary mixed phases with composition ϕ_A^* and ϕ_A^{**} are formed. $\Delta \mathcal{G}_{\text{mix}}$ is given by the point at $\phi_A = 0.45$ on the straight line that connects $\Delta \mathcal{G}_{\text{mix}}(\phi_A^*)$ and $\Delta \mathcal{G}_{\text{mix}}(\phi_A^{**})$. This is seen when we first write down the obvious linear relation

$$\Delta \mathcal{G}_{\text{mix}}(\phi_A) = \phi_1 \Delta \mathcal{G}_{\text{mix}}(\phi_A^*) + \phi_2 \Delta \mathcal{G}_{\text{mix}}(\phi_A^{**}), \quad (4.41)$$

where ϕ_1 and ϕ_2 denote the volume fractions of the two mixed phases. Recalling that ϕ_1 and ϕ_2 are given by Eqs. (4.29) and (4.30), we obtain the expression

$$\Delta \mathcal{G}_{\text{mix}}(\phi_A) = \frac{\phi_A^{**} - \phi_A}{\phi_A^{**} - \phi_A^*} \Delta \mathcal{G}_{\text{mix}}(\phi_A^*) + \frac{\phi_A - \phi_A^*}{\phi_A^{**} - \phi_A^*} \Delta \mathcal{G}_{\text{mix}}(\phi_A^{**}), \quad (4.42)$$

which indeed describes a straight line connecting $\Delta \mathcal{G}_{\text{mix}}(\phi_A^*)$ and $\Delta \mathcal{G}_{\text{mix}}(\phi_A^{**})$. So far, the choice of ϕ_A^* and ϕ_A^{**} has been arbitrary, but we know that on

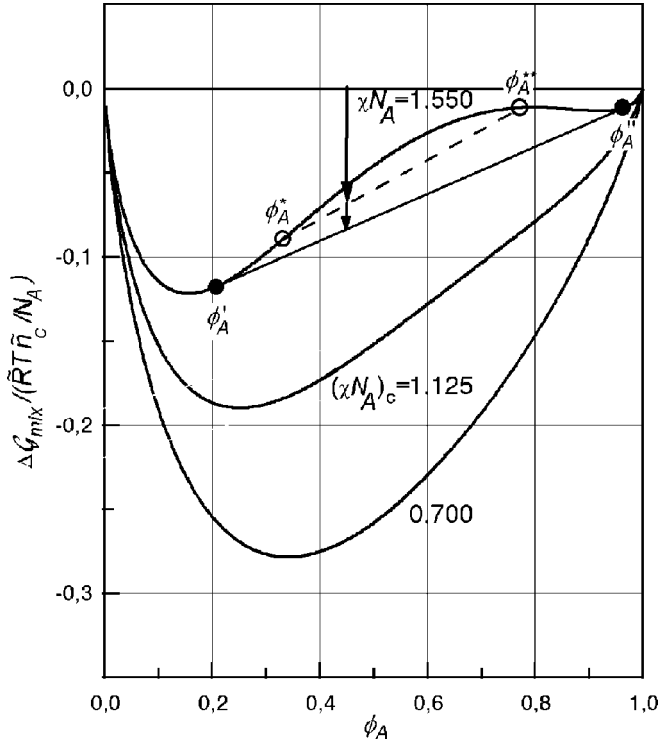


Fig. 4.5. Gibbs free energy of mixing of an asymmetric polymer mixture with $N_B = 4N_A$, calculated for the indicated values of χN_A . The points of contact with the common tangent, located at ϕ'_A and ϕ''_A , determine the compositions of the equilibrium phases on the binodal. The critical values are $(\chi N_A)_c = 9/8$ and $\phi_c = 2/3$

separating into two mixed phases, the system seeks to maximize the gain in Gibbs free energy. The common tangent represents that connecting line between any pair of points on the curve which is at the lowest possible level. A transition to this line therefore gives the largest possible change ΔG_{mix} . It is associated with the formation of two phases with compositions ϕ'_A and ϕ''_A , as given by the points of contact with the common tangent. The binodal is set up by these points and a determination may be based on the described geometrical procedure.

4.1.1 Phase Diagrams: Upper and Lower Miscibility Gap

Phase diagrams of polymer blends under atmospheric pressure are usually presented in terms of the variables ϕ_A and T . Emanating from the discussed universal phase diagram in terms of χ and ϕ_A these can be obtained by introducing the temperature dependence of the Flory–Huggins parameter into the consideration. This function $\chi(T)$ then solely determines the appearance. For

different types of temperature dependencies $\chi(T)$, different classes of phase diagrams emerge and we shall discuss them in this section.

Let us first consider an endothermal polymer mixture with negligible entropic contributions to the local Gibbs free energy, i.e., a system with $\chi = \chi_H > 0$. Here the temperature dependence of χ is given by Eq. (4.22)

$$\chi \propto \frac{1}{T}.$$

The consequences for the phase behavior are evident. Perfect miscibility can principally exist at high temperatures, provided that the molar mass of the components are low enough. The increase of χ with decreasing temperature necessarily results in a termination of this region and the formation of a miscibility gap, found when $\chi > \chi_c$. For a symmetric mixture we obtained $\chi_c = 2/N$ (Eq. (4.36)). If χ_c is reached at a temperature T_c , we can write

$$\chi = \frac{2}{N} \frac{T_c}{T}. \quad (4.43)$$

The resulting phase diagram is shown in Fig. 4.6, together with the temperature dependence of χ . The binodal follows from Eq. (4.38), as

$$\frac{T}{T_c} = \frac{2(1 - 2\phi_A)}{\ln((1 - \phi_A)/\phi_A)}. \quad (4.44)$$

It marks the boundary between the homogeneous state at high temperatures and the two-phase region at low temperatures.

Upon cooling a homogeneous mixture, phase separation at first sets in for samples with the **critical composition**, $\phi_A = 0.5$, at the temperature T_c . For the other samples demixing occurs at lower temperatures, as described by the binodal. We observe here a **lower miscibility gap**. A second name is also

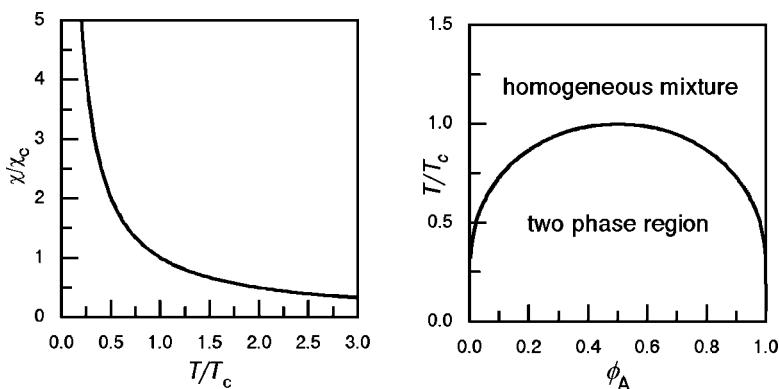


Fig. 4.6. Endothermal symmetrical mixture with a constant heat of mixing. Temperature dependence of the Flory–Huggins parameter (*left*) and phase diagram showing a lower miscibility gap (*right*)

used in the literature: T_c is called the **upper critical dissolution temperature**, shortly abbreviated UCDDT. The latter name refers to the structural changes induced when coming from the two-phase region, where one observes a dissolution and merging of the two phases.

Experiments show that exothermal polymer blends sometimes have an **upper miscibility gap**, i.e., one which is open towards high temperatures. One may wonder why a mixture that is homogeneous at ambient temperature separates in two phases upon heating, and we shall have to think about possible physical mechanisms. At first, however, we discuss the formal prerequisites. On the right-hand side of Fig. 4.7 there are phase diagrams of symmetric polymer mixtures that display an upper miscibility gap. The various depicted binodals are associated with different molar mass. The curved binodals relate to polymers with low or moderate molar masses. For high molar mass, the phase boundary becomes a horizontal line and phase separation then occurs for $\chi \geq 0$ independent of ϕ_A . The latter result agrees with the general criterion for phase separations in polymer systems with high molar masses. It is therefore not particular to the symmetric system, but would be obtained in the general case, $N_A \neq N_B$, as well.

The temperature dependencies $\chi(T)$ that lead to these diagrams are shown on the left-hand side of Fig. 4.7. Their main common property is a change of the Flory–Huggins parameter from negative to positive values. The crossing of the zero line takes place at a certain temperature, denoted T_0 . Coming from low temperatures, unmixing sets in for $T = T_c$ with

$$N\chi(T_c) = 2.$$

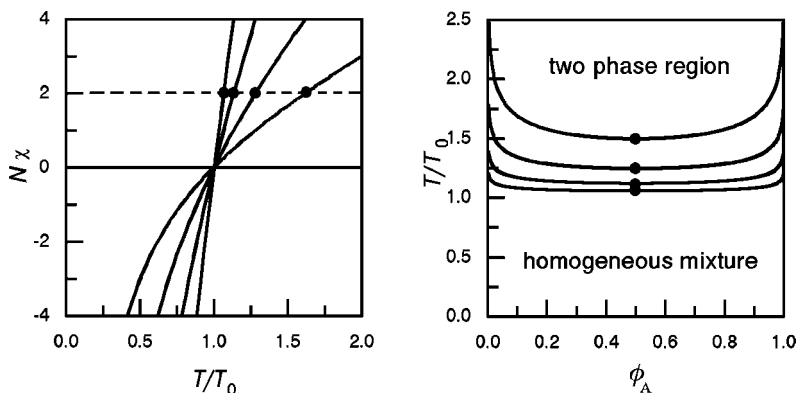


Fig. 4.7. Phase diagram of an exothermal symmetric polymer mixture with an upper miscibility gap. The binodals correspond to the different functions $N\chi(T)$ shown on the left, associated with an increase in the molar mass by factors 2, 4 and 8. Critical points are determined by $N\chi(T_c/T_0) = 2$, as indicated by the filled points in the drawings

In the limit of high degrees of polymerization we have $\chi(T_c) \rightarrow 0$ and therefore $T_c \rightarrow T_0$. We see that the prerequisite for an upper miscibility gap, or a **lower critical solution temperature**, abbreviated as LCST, as it is alternatively called, is a negative value of χ at low temperatures, followed by an increase to values above zero.

One can envisage two different mechanisms as possible explanations for such a behavior. First, there can be a competition between attractive forces between specific groups incorporated in the two polymers on one side and repulsive interactions between the remaining units on the other side. In copolymer systems with pairs of specific comonomers that are capable of forming stable bonds these conditions may arise. With increasing temperature the fraction of closed bonds decreases and the repulsive forces finally dominate. For such a system, χ may indeed be negative for low temperatures and positive for high ones.

The second conceivable mechanism has already been mentioned. Sometimes it is observed that a homogeneous mixing of two polymers results in a volume shrinkage. The related decrease in the free volume available for local motions of the monomers may lead to a reduced number of available conformations and hence a lowering of the entropy. The effect usually increases with temperature and finally overcompensates the initially dominating attractive interactions.

For mixtures of polymers with low molar mass there is also the possibility that both a lower and an upper miscibility gap appear. In this case, χ crosses the critical value χ_c twice, first during a decrease in the low temperature range and then, after passing through a minimum, during the subsequent increase at higher temperatures. Such a temperature dependence reflects the presence of both a decreasing endothermal contribution and an increasing entropic part.

As we can see, the Flory–Huggins treatment is able to account for the various general shapes of existing phase diagrams. This does not mean, however, that one can reproduce measured phase diagrams in a quantitative manner. To comply strictly with the Flory–Huggins theory, the representation of measured binodals has to be accomplished with one temperature-dependent function $\chi(T)$ only. As a matter of fact, this is rarely the case. Nevertheless, data can be formally described if one allows for a ϕ_A -dependence of χ . As long as the variations remain small, one can consider the deviations as perturbations and still feel safe on the grounds of the Flory–Huggins treatment. For some systems, however, the variations with ϕ_A are large. Then the basis is lost and the meaning of χ becomes rather unclear. Even then the Flory–Huggins equation is sometimes employed but only as a means to carry out interpolations and extrapolations and to relate different sets of data. That deviations arise is not unexpected. The mean field treatment, on which the Flory–Huggins theory is founded, is only an approximation with varying quality.

Let us look at two examples.

Figure 4.8 presents phase diagrams of mixtures of different polystyrenes with polybutadiene (PB), all of them with moderate to low molar mass

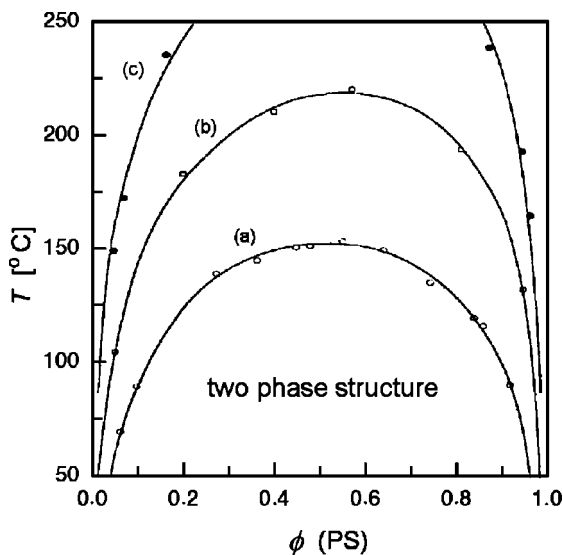


Fig. 4.8. Phase diagrams for different PS/PB-mixtures, exhibiting lower miscibility gaps. (a) $M(\text{PS}) = 2250 \text{ g mol}^{-1}$, $M(\text{PB}) = 2350 \text{ g mol}^{-1}$; (b) $M(\text{PS}) = 3500 \text{ g mol}^{-1}$, $M(\text{PB}) = 2350 \text{ g mol}^{-1}$; (c) $M(\text{PS}) = 5200 \text{ g mol}^{-1}$, $M(\text{PB}) = 2350 \text{ g mol}^{-1}$. Data from Roe and Zin [19]

($M = 2000\text{--}4000 \text{ g mol}^{-1}$). The temperature points on the curves are measured **cloud points**. As samples are transparent in the homogeneous phase and become turbid when demixing starts, the cloudiness can be used for a determination of the binodal. For an accurate detection one can use measurements of the intensity of scattered or transmitted light. Here, we are dealing with an endothermal system that exhibits a lower miscibility gap. Note that T_c , as given by the highest point of each curve, decreases with decreasing molar mass in accordance with the theoretical prediction. The curves, which provide a satisfactory data fit, were obtained on the basis of the Flory–Huggins theory assuming a weakly ϕ_A -dependent χ .

As a second example, Fig. 4.9 shows a phase diagram obtained for mixtures of polystyrene and poly(vinylmethylether) (PVME). Here, one observes that homogeneous mixtures are obtained in the temperature range below 100°C and that there is an upper miscibility gap. The phase diagram depicted in the figure was obtained for polymers with molar mass $M(\text{PS}) = 2 \times 10^5 \text{ g mol}^{-1}$, $M(\text{PVME}) = 4.7 \times 10^4 \text{ g mol}^{-1}$. For molar mass in this range the contribution of the translational entropy becomes very small indeed and mixing properties are mostly controlled by χ . The curved appearance of the binodal, which contrasts with the result of the model calculation in Fig. 4.7 where we obtained a nearly horizontal line for polymers, is indicative of a pronounced compositional dependence of χ . This represents a case where the Flory–Huggins treatment does not provide a comprehensive description. Interactions in this

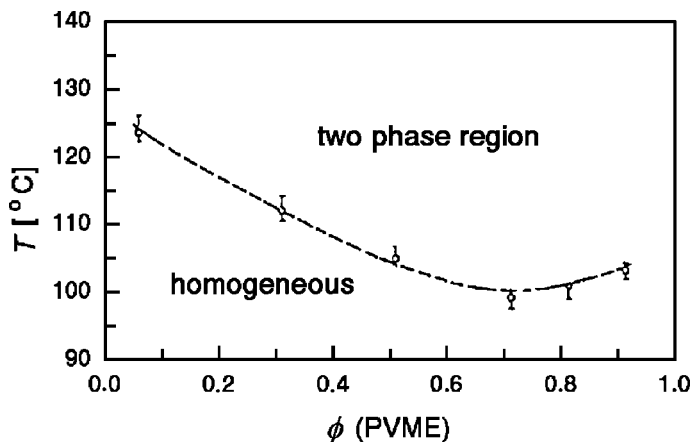


Fig. 4.9. Phase diagram of mixtures of PS ($M = 2 \times 10^5 \text{ g mol}^{-1}$) and PVME ($M = 4.7 \times 10^4 \text{ g mol}^{-1}$), showing an upper miscibility gap. Data from Hashimoto et al. [20]

mixture are of a complex nature and apparently change with the sample composition, so that it becomes impossible to represent them by only one constant.

4.2 Phase Separation Mechanisms

As we have seen, binary polymer mixtures can vary in structure with temperature, forming either a homogeneous phase or in a miscibility gap a two-phase structure. We now have to discuss the processes that are effective during a change, i.e., the mechanisms of phase separation.

Phase separation is induced, when a sample is transferred from the one phase region into a miscibility gap. Usually, this is accomplished by a change in temperature, upward or downward depending on the system under study. The evolution of the two-phase structure subsequent to a temperature jump can often be continuously monitored and resolved in real-time, owing to the high viscosity of polymers, which slows down the rate of unmixing. If necessary for detailed studies, the process may also be stopped at any stage by quenching samples to temperatures below the glass transition. Suitable methods for observations are light microscopy or scattering experiments.

Figure 4.10 presents as an example two micrographs obtained with a light microscope using an interference technique, showing two-phase structures observed for mixtures of polystyrene and partially brominated polystyrene (PBr_xS), with both species having equal degrees of polymerization ($N = 200$). The two components show perfect miscibility at temperatures above 220 °C and a miscibility gap below this temperature. Here phase separation was induced by a temperature jump from 230 °C to 200 °C, for two mixtures of

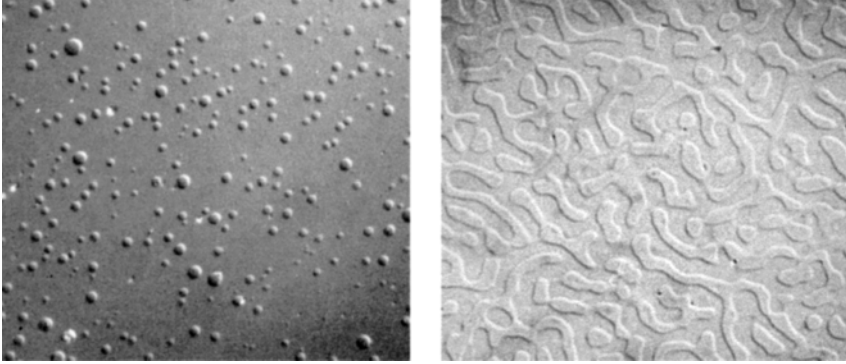


Fig. 4.10. Structure patterns emerging during phase separation in PS/PBr_xS-mixtures. *left*: Pattern indicating phase separation by nucleation and growth ($\phi(\text{PS}) = 0.8$); *right*: Pattern suggesting phase separation by spinodal decomposition ($\phi(\text{PS}) = 0.5$) [21]

different composition, $\phi(\text{PS}) = 0.8$ and $\phi(\text{PS}) = 0.5$. We observe two structure patterns that do not only vary in length scale, but differ in the general characteristics: The picture on the left shows spherical precipitates in a matrix, whereas the pattern on the right exhibits interpenetrating continuously extending domains. The diverse evidence suggests that different mechanisms were effective during phase separation. Structures with spherical precipitates are indicative of **nucleation and growth** and the pattern with two structurally equivalent interpenetrating phases reflects a **spinodal decomposition**. In fact, this example is quite typical and is representative of the results of investigations on various polymer mixtures. The finding is that structure evolution in the early stages of unmixing is generally controlled by either of these two mechanisms.

The cause for the occurrence of two different modes of phase separation becomes revealed when we consider the shape of the curve $\Delta\mathcal{G}_{\text{mix}}(\phi_A)$. As ϕ_A is the only independent variable, in the following we will omit the subscript A, i.e., replace ϕ_A by the shorter symbol ϕ . The upper part of Fig. 4.11 depicts functions $\Delta\mathcal{G}_{\text{mix}}(\phi)$ computed for three different values of χ , which belong to the one phase region (χ_i), the two-phase region (χ_f) and the critical point (χ_c). The lower part of the figure gives the phase diagram, with the positions of χ_i , χ_f and χ_c being indicated. The arrows ‘1’ and ‘2’ indicate two jumps that transfer a polymer mixture from the homogeneous phase into the two-phase region.

Immediately after the jump, the structure is still homogeneous but, of course, no longer stable. What is different in the two cases, is the character of the instability. The difference shows up when we consider the consequences of a spontaneous local concentration fluctuation, as it could be thermally induced directly after the jump. Figure 4.12 represents such a fluctuation

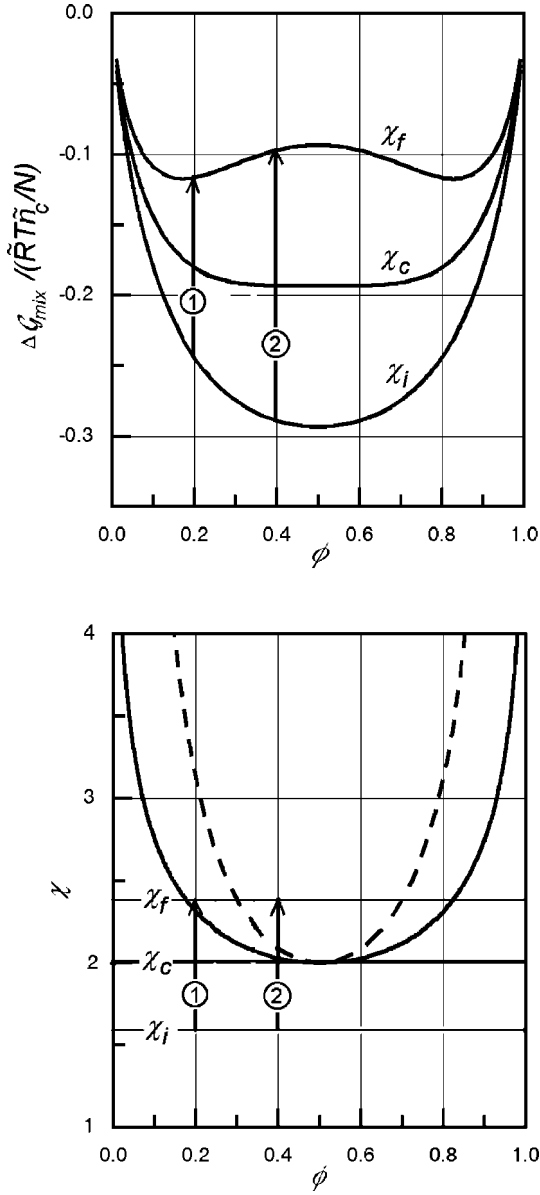


Fig. 4.11. Temperature jumps that transfer a symmetric binary polymer mixture from the homogeneous state into the two-phase region. Depending upon the location in the two-phase region, phase separation occurs either by nucleation and growth ('1') or by spinodal decomposition ('2')

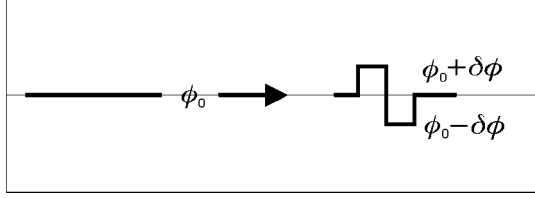


Fig. 4.12. Local concentration fluctuation

schematically, being set up by an increase $\delta\phi$ in the concentration of A-chains in one half of a small volume $d^3\mathbf{r}$ and a corresponding decrease in the other half. The fluctuation leads to a change in the Gibbs free energy, described as

$$\delta\mathcal{G} = \frac{1}{2}(g(\phi_0 + \delta\phi) + g(\phi_0 - \delta\phi))d^3\mathbf{r} - g(\phi_0)d^3\mathbf{r}. \quad (4.45)$$

Here, we have introduced the free energy density, i.e., the Gibbs free energy per unit volume, denoted $g(\phi)$. Series expansion of $g(\phi)$ up to the second order in ϕ for $\delta\mathcal{G}$ yields the expression

$$\delta\mathcal{G} = \frac{1}{2} \frac{\partial^2 g}{\partial \phi^2}(\phi_0) \delta\phi^2 d^3\mathbf{r}. \quad (4.46)$$

We calculate $\partial^2 g / \partial \phi^2$ with the aid of the Flory–Huggins equation, i.e., write

$$\frac{\partial^2 g}{\partial \phi^2} = \frac{1}{\mathcal{V}} \frac{\partial^2 \Delta\mathcal{G}_{\text{mix}}}{\partial \phi^2} \quad (4.47)$$

with $\Delta\mathcal{G}_{\text{mix}}$ given by Eq. (4.11). Then the change $\delta\mathcal{G}$ associated with the local fluctuation is

$$\delta\mathcal{G} = \frac{1}{2} \frac{1}{\mathcal{V}} \frac{\partial^2 \Delta\mathcal{G}_{\text{mix}}}{\partial \phi^2}(\phi_0) \delta\phi^2 d^3\mathbf{r}. \quad (4.48)$$

This is a most interesting result. It tells us that, depending on the sign of the curvature $\partial^2 \Delta\mathcal{G}_{\text{mix}} / \partial \phi^2$, the fluctuation may either lead to an increase, or a decrease in the Gibbs free energy. In stable states, there always has to be an increase to ensure that a spontaneous local association of monomers A disintegrates again. This situation is found for jump ‘1’. It leads to a situation where the structure is still stable with regard to spontaneous concentration fluctuations provided that they remain sufficiently small. Jump ‘2’ represents a qualitatively different case. Since the curvature here is negative, the Gibbs free energy decreases immediately, even for an infinitesimally small fluctuation, and no restoring force arises. On the contrary, there is a tendency for further growth of the fluctuation amplitude. Hence, by the temperature jump ‘2’ an initial structure is prepared, which is perfectly unstable.

It is exactly the latter situation which results in a spinodal decomposition. The process is sketched at the bottom of Fig. 4.13. The drawing indicates

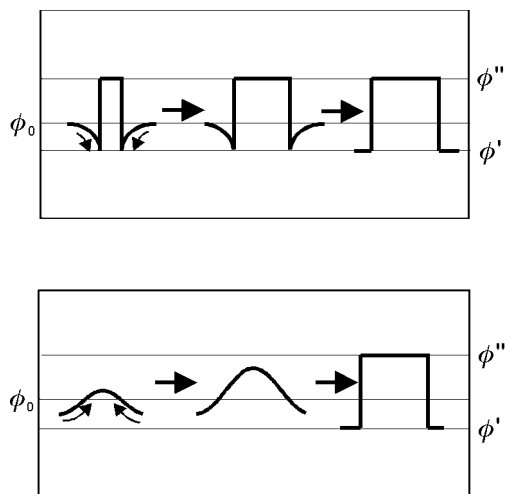


Fig. 4.13. Mechanisms of phase separation: Nucleation and growth (*top*) and spinodal decomposition (*bottom*). The *curved small arrows* indicate the direction of the diffusive motion of the A-chains

that a spinodal decomposition implies a continuous growth of the amplitude of a concentration fluctuation, starting from infinitesimal values and ensuing up to the final state of two equilibrium phases with compositions ϕ' and ϕ'' . The principles governing this process have been studied in numerous investigations and clarified to a large extent. We shall discuss its properties in detail in the next section. At this point, we leave it with one short remark with reference to the figure. There the arrows indicate the directions of flow of the A-chains. The normal situation is found for nucleation and growth, where the flow is directed as usual, towards decreasing concentrations of the A-chains. In spinodal decompositions, the flow direction is reversed. The A-chains diffuse towards higher concentrations, which formally corresponds to a negative diffusion coefficient.

The upper half of the figure shows the process that starts subsequent to the temperature jump '1'. As small fluctuations decay again, the only way to achieve a gain in the Gibbs free energy is a large fluctuation, which directly leads to the formation of a nucleus of the new equilibrium phase with composition ϕ'' . After it has formed it can increase in size. Growth is accomplished by regular diffusion of the chains since there exists, as indicated in the drawing, a zone with a reduced ϕ at the surface of the particle that attracts a stream of A-chains.

The process of nucleation and growth is not peculiar to polymers, but observed in many materials and we consider it only briefly. The specific point making up the difference to the case of a spinodal decomposition is the existence of an activation barrier. The reason for its occurrence is easily recog-

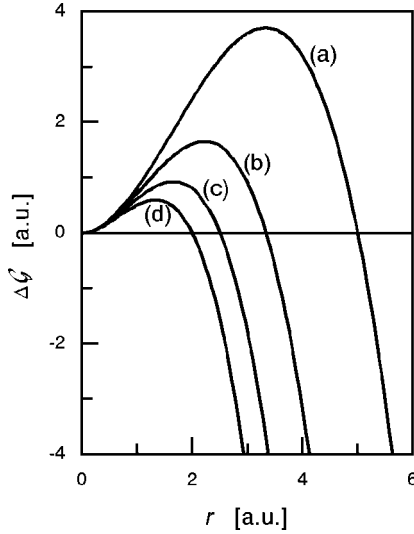


Fig. 4.14. Activation barrier encountered during formation of a spherical nucleus. Curves (a)–(d) correspond to a sequence 2:3:4:5 of values for $\Delta g/\sigma_{\text{if}}$

nized. Figure 4.14 shows the change of the Gibbs free energy, $\Delta\mathcal{G}$, following from the formation of a spherical precipitate of the new equilibrium phase.

$\Delta\mathcal{G}$ depends on the radius r of the precipitate, as described by the equation

$$\Delta\mathcal{G}(r) = -\frac{4\pi}{3}r^3\Delta g + 4\pi r^2\sigma_{\text{if}} \quad (4.49)$$

with

$$\Delta g = g(\phi_0) - g(\phi'') . \quad (4.50)$$

Equation (4.49) emanates from the view that $\Delta\mathcal{G}$ is set up by two contributions, one being related to the gain in the bulk Gibbs free energy of the precipitate, the other to the effect of the interface between particle and matrix. This interface is associated with an excess free energy and the symbol σ_{if} stands for the excess free energy per unit area.

Since the building up of the interface causes an increase in the free energy, a barrier $\Delta\mathcal{G}_b$ develops, which first has to be overcome before growth can set in. The passage over this barrier constitutes the nucleation step. Representing an activated process, it occurs with a rate given by the Arrhenius equation,

$$\nu_{\text{nuc}} \propto \exp -\frac{\Delta\mathcal{G}_b}{kT} , \quad (4.51)$$

whereby $\Delta\mathcal{G}_b$ is the barrier height

$$\Delta\mathcal{G}_b = \frac{16\pi}{3} \frac{\sigma_{\text{if}}^3}{(\Delta g)^2} . \quad (4.52)$$

Equation (4.52) follows from Eq. (4.49) when searching for the maximum. $\Delta\mathcal{G}_b$ increases with decreasing distance from the binodal where we have $\Delta g = 0$. The change is illustrated by the curves in Fig. 4.14, which were calculated for different values of the ratio $\Delta g/\sigma_{if}$. We learn from this behavior that, in order to achieve reasonable rates, nucleation requires a certain degree of supercooling (or overheating, if there is an upper miscibility gap).

Nucleation and growth occurs if the unmixing is induced at a temperature near the binodal, where the system is still stable with regard to small concentration fluctuations. Further away from the binodal this restricted **metastability** is lost and spinodal decomposition sets in. Transition from one growth regime to another occurs in the range of the **spinodal**, which is defined as the locus of those points in the phase diagram where the stabilizing restoring forces vanish. According to the previous arguments this occurs for

$$\frac{\partial^2 \Delta\mathcal{G}_{\text{mix}}}{\partial\phi^2} = 0. \quad (4.53)$$

Equation (4.53) determines a certain value χ for each ϕ and for the resulting spinodal curve we choose the designation $\chi_{\text{sp}}(\phi)$. In the case of a symmetric mixture with a degree of polymerization N for both species, we can use Eq. (4.33) for a determination. The spinodal follows as

$$\chi_{\text{sp}} = \frac{1}{2N\phi_A(1-\phi_A)}. \quad (4.54)$$

It is this line that is included in Figs. 4.4 and 4.11. For $N_A \neq N_B$ we start from Eq. (4.11) and obtain

$$\frac{\partial^2 \Delta\mathcal{G}_{\text{mix}}}{\partial\phi^2} \propto \frac{1}{N_A\phi} + \frac{1}{N_B(1-\phi)} + \frac{\partial^2}{\partial\phi^2} \chi\phi(1-\phi). \quad (4.55)$$

In this case, the spinodal is given by the function

$$2\chi_{\text{sp}} = \frac{1}{N_A\phi} + \frac{1}{N_B(1-\phi)}. \quad (4.56)$$

As was mentioned earlier, reality in polymer mixtures often differs from the Flory–Huggins model in that a ϕ -dependent χ is required. Then we have to write for the equation of the spinodal

$$\frac{1}{N_A\phi} + \frac{1}{N_B(1-\phi)} = -\frac{\partial^2}{\partial\phi^2} (\chi(\phi)\phi(1-\phi)) = 2\Lambda. \quad (4.57)$$

Here we have introduced another function, Λ , which is related to χ by

$$\Lambda = \chi - (1-2\phi)\frac{\partial\chi}{\partial\phi} - \frac{1}{2}\phi(1-\phi)\frac{\partial^2\chi}{\partial\phi^2}. \quad (4.58)$$

We see that the situation has now become more involved. As we shall learn in the next section, rather than χ , A follows from an experimental determination of the spinodal.

It might appear at first that the spinodal marks a sharp transition between two growth regimes, but this is not true. Activation barriers for the nucleation are continuously lowered when approaching the spinodal and thus may lose their effectiveness already prior to the crossing. As a consequence, the transition from the nucleation and growth regime to the region of spinodal decompositions is actually diffuse and there is no way to employ it for an accurate determination of the spinodal. There is, however, another effect for which the spinodal is significant and well-defined: The distance from the spinodal controls the concentration fluctuations in the homogeneous phase. The next section deals in detail with this interesting relationship.

4.3 Critical Fluctuations and Spinodal Decomposition

The critical point of a polymer mixture, as given by the critical temperature T_c jointly with the critical composition ϕ_c , is the locus of a **second order phase transition**. Second order phase transitions have general properties that are found independent of the particular system; this may be a ferromagnetic or ferroelectric solid near its Curie temperature, a gas near the critical point, or, as in our case, a mixture. As one general law, the approach of a critical point is always accompanied by a strong increase of the local fluctuations of the **order parameter** associated with the transition. For our mixture, the order parameter is given by the composition, as specified, for example, by the volume fraction of A-chains. So far, we have been concerned with the overall concentrations of the A- and B-chains in the sample only. On microscopic scales, concentrations are not uniform but show fluctuations about the mean value, owing to the action of random thermal forces. According to the general scenario of critical phase transitions, one expects a steep growth of these fluctuations on approaching T_c .

The most convenient technique for a verification are scattering experiments, as these probe the fluctuations directly. Figure 4.15 presents, as an example, results obtained by neutron scattering for a mixture of (deuterated) polystyrene and poly(vinylmethylether). As was mentioned earlier, this system shows an upper miscibility gap (Fig. 4.9). Measurements were carried out for a mixture with the critical composition at a series of temperatures in the one phase region. The figure depicts the reciprocals of the scattering intensities in plots versus q^2 . We notice that approaching the critical point indeed leads to an overall increase of the intensities, with the strongest growth being found for the scattering in the forward direction $q \rightarrow 0$. The temperature dependence of the forward scattering is shown on the right hand side, in a plot of $S^{-1}(q \rightarrow 0)$ against $1/T$. Data indicate a divergence, and its location determines the critical temperature. Here we find $T_c = 131.8^\circ\text{C}$.

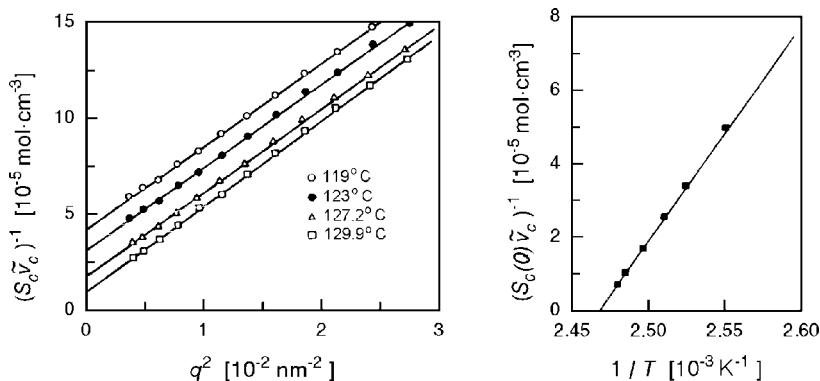


Fig. 4.15. Results of neutron scattering experiments on a (0.13:0.87)-mixture of d-PS ($M = 3.8 \times 10^5 \text{ g mol}^{-1}$) and PVME ($M = 6.4 \times 10^4 \text{ g mol}^{-1}$). S_c denotes the scattering function Eq. (4.79) referring to structure units with a molar volume \tilde{v}_c . Intensities increase on approaching the critical point (*left*). Extrapolation of $S(q \rightarrow 0)$ to the point of divergence yields the critical temperature (*right*). Data from Schwahn et al. [22]

When the phase boundary is crossed through the critical point, a spinodal decomposition is initiated, and it can be followed by time-dependent scattering experiments. Figure 4.16 shows the evolution of the scattering function during the first stages, subsequent to a rapid change from an initial temperature T_{in} two degrees below T_c , to $T_{\text{fi}} = 134.1^\circ\text{C}$, located 2.3°C above. Beginning at zero time with the equilibrium structure factor associated with the temperature T_{in} in the homogeneous phase, a peak emerges and grows in intensity.

Figure 4.17 presents, as a second example, a further experiment on mixtures of polystyrene and poly(vinylmethylether), now carried out by time dependent light scattering experiments (this sample had a lower critical temperature, probably due to differences in behavior between normal and deuterated polystyrene). Experiments encompass a larger time range and probe the scattering at the small q 's reached when using light. Again one observes the development of a peak, and it also stays at first at a constant position. Here, we can see that during the later stages it shifts to lower scattering angles.

This appearance of a peak which grows in intensity, initially at a fixed position and then shifting to lower scattering angles, can in fact be considered as indicative of a spinodal decomposition. One can say that the peak reflects the occurrence of wave-like modulations of the local blend composition, with a dominance of particular wavelengths. Furthermore, the intensity increase indicates a continuous amplitude growth. This, indeed, is exactly the process sketched at the bottom of Fig. 4.13.

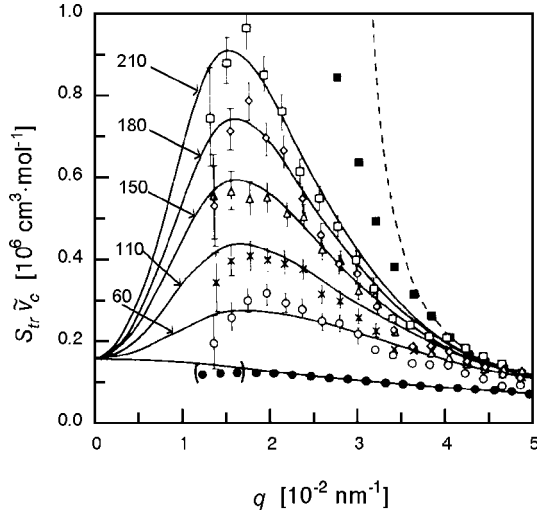


Fig. 4.16. The same system as in Fig. 4.15. Transient scattering functions $S_{tr}(q, t)$ measured after a temperature jump from $T_{in} = 130\text{ }^\circ\text{C}$ (one phase region) to $T_{fi} = 134.1\text{ }^\circ\text{C}$ (two-phase region). Times of evolution are indicated (in seconds) [22]

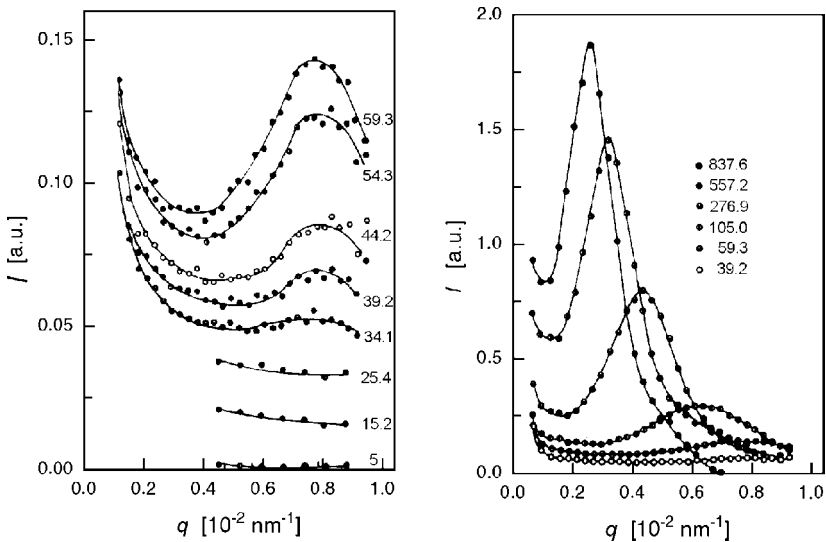


Fig. 4.17. Time dependent light scattering experiments, conducted on a (0.3:0.7)-mixture of PS ($M = 1.5 \times 10^5\text{ g mol}^{-1}$) and PVME ($M = 4.6 \times 10^4\text{ g mol}^{-1}$) subsequent to a rapid transfer from a temperature in the region of homogeneous states to the temperature $T_{fi} = 101\text{ }^\circ\text{C}$ located in the two-phase region. Numbers give the time passed after the jump (in seconds). Data from Hashimoto et al. [23]

All these findings, the steep growth of the concentration fluctuations in the homogeneous phase near the critical point, as well as the kinetics of spinodal decomposition with its strong preference for certain wavelengths, can be treated in a common theory. It was originally developed by Cahn, Hilliard, and Cook, in order to treat unmixing phenomena in metallic alloys and anorganic glasses, and then adjusted by de Gennes and Binder to the polymer case. Polymers actually represent systems that exhibit these phenomena in a particularly clear form and thus allow a verification of the theories. In the following three subsections, which concern the critical scattering as observed in the homogeneous phase, the initial stages of spinodal decomposition and the late stage kinetics, some main results will be presented.

4.3.1 Critical Scattering

Here we consider the concentration fluctuations in the homogeneous phase and also the manner in which these are reflected in measured scattering functions.

How can one deal with the fluctuations? At first view it might appear that the Flory–Huggins treatment does not give any help. Accounting for all microscopic states, the Flory–Huggins expression for the Gibbs free energy includes also the overall effect of all the concentration fluctuations in a mixture. The overall effect, however, is not our point of concern. We wish to grasp a *single* fluctuation state, as given by a certain distribution of the A's specified by a function $\phi(\mathbf{r})$ and determine its statistical weight. What we need for this purpose is a knowledge about a *constrained* Gibbs free energy, namely that associated with a single fluctuation state only.

To solve our problem we use a trick that was originally employed by Kadanoff in an analysis of the critical behavior of ferromagnets. Envisage a division of the sample volume in a large number of cubic ‘blocks’, with volumes v_B that, although being very small, still allow the use of thermodynamic laws; block sizes in the order of 10–100 nm³ seem appropriate for this purpose. For this grained system, the description of a certain fluctuation state is accomplished by giving the concentrations ϕ_i of all blocks i . The (constrained) free energy of a thus characterized fluctuation state can be written down, proceeding in three steps. As we may apply the Flory–Huggins equation for each block separately, we first write a sum

$$\mathcal{G}(\{\phi_i\}) = \sum_i v_B g(\phi_i). \quad (4.59)$$

Here, g stands for the free energy density of the mixture

$$g(\phi) = \phi g_A + (1 - \phi) g_B + \tilde{R}T \left[\frac{\phi}{\tilde{v}_A} \ln \phi + \frac{(1 - \phi)}{\tilde{v}_B} \ln(1 - \phi) + \frac{\chi}{\tilde{v}_c} \phi(1 - \phi) \right], \quad (4.60)$$

g_A and g_B denoting the free energy densities of the one component phases. Being in close contact, neighboring blocks, interact with each other across the interfaces and we have to inquire about the related interfacial energy. We know that it must vanish for equal concentrations and increase with the concentration difference, independent of the direction of change. The simplest expression with such properties is the quadratic term

$$\beta(\phi_i - \phi_j)^2,$$

where ϕ_i, ϕ_j are the concentrations in the adjacent blocks. It includes a coefficient β that determines the strength of the interaction. We add this term to the first sum and write

$$\mathcal{G}(\{\phi_i\}) = \sum_i v_B g(\phi_i) + \sum_{ij} \beta(\phi_i - \phi_j)^2. \quad (4.61)$$

Finally, replacing the summation by an integral, we obtain

$$\mathcal{G}(\phi(\mathbf{r})) = \int (g(\phi(\mathbf{r})) + \beta'(\nabla\phi)^2) d^3\mathbf{r} \quad (4.62)$$

with $\beta' = \beta v_B^{-1/3}$. With this result we have solved our problem. Equation (4.62) describes in an approximate, empirical manner the free energy to be attributed to a given fluctuation state $\phi(\mathbf{r})$. It is known in the literature as **Ginzburg–Landau functional** and is widely applied in treatments of various kinds of fluctuations.

The equation can be further simplified if a linearization approximation is used. Clearly the state with a uniform concentration,

$$\phi(\mathbf{r}) = \text{const} = \phi,$$

has the lowest free energy, \mathcal{G}_{\min} . For considering the change in the Gibbs free energy

$$\delta\mathcal{G} = \mathcal{G} - \mathcal{G}_{\min}$$

as it results from a fluctuation

$$\delta\phi(\mathbf{r}) = \phi(\mathbf{r}) - \phi$$

we may use a series expansion of $g(\delta\phi)$ up to the second order

$$\delta\mathcal{G} = \int_{\mathcal{V}} (\delta g(\delta\phi(\mathbf{r})) + \beta'(\nabla\delta\phi)^2) d^3\mathbf{r} \quad (4.63)$$

$$= \frac{\partial g}{\partial \phi} \int_{\mathcal{V}} \delta\phi d^3\mathbf{r} + \frac{1}{2} \frac{\partial^2 g}{\partial \phi^2} \int_{\mathcal{V}} (\delta\phi)^2 d^3\mathbf{r} + \beta' \int_{\mathcal{V}} (\nabla\delta\phi)^2 d^3\mathbf{r}. \quad (4.64)$$

Conservation of the masses of the two species implies

$$\int_{\mathcal{V}} \delta\phi d^3\mathbf{r} = 0, \quad (4.65)$$

and we only have to calculate the second derivative of g . This leads to

$$\delta\mathcal{G} = \frac{\tilde{R}T}{2} \left(\frac{1}{\tilde{v}_A\phi} + \frac{1}{\tilde{v}_B(1-\phi)} - \frac{2\chi}{\tilde{v}_c} \right) \int_{\mathcal{V}} (\delta\phi)^2 d^3\mathbf{r} + \beta' \int_{\mathcal{V}} (\nabla\delta\phi)^2 d^3\mathbf{r}. \quad (4.66)$$

This is a useful result. It relates the Gibbs free energy of a given fluctuation state to two parameters only, namely the integral or mean values of $(\delta\phi)^2$ and $(\nabla\delta\phi)^2$.

We now turn to scattering experiments. They may generally be regarded as carrying out a Fourier analysis, in our case a Fourier analysis of the concentration fluctuations in the mixture. We therefore represent $\delta\phi(\mathbf{r})$ as a sum of wave-like modulations with amplitudes $\phi_{\mathbf{k}}$

$$\delta\phi(\mathbf{r}) = \mathcal{V}^{-1/2} \sum_{\mathbf{k}} \exp(i\mathbf{k}\mathbf{r})\phi_{\mathbf{k}}. \quad (4.67)$$

For a finite sample volume \mathcal{V} , the sum includes a sequence of discrete values of \mathbf{k} (see Eq. (A.117)). When writing a Fourier series in terms of exponential functions, the amplitudes $\phi_{\mathbf{k}}$ are complex numbers

$$\phi_{\mathbf{k}} = |\phi_{\mathbf{k}}| \exp(i\varphi_{\mathbf{k}})$$

with a modulus $|\phi_{\mathbf{k}}|$ and a phase $\varphi_{\mathbf{k}}$. Since $\delta\phi(\mathbf{r})$ is a real quantity, we have

$$\phi_{-\mathbf{k}} = \phi_{\mathbf{k}}^* \quad (4.68)$$

and therefore

$$|\phi_{\mathbf{k}}| = |\phi_{-\mathbf{k}}|. \quad (4.69)$$

When we introduce the Fourier series into the integral of Eq. (4.66), we obtain

$$\int_{\mathcal{V}} (\delta\phi)^2 d^3\mathbf{r} = \mathcal{V}^{-1} \sum_{\mathbf{k}, \mathbf{k}'} \phi_{\mathbf{k}}\phi_{\mathbf{k}'} \int_{\mathcal{V}} \exp[i(\mathbf{k}\mathbf{r} + \mathbf{k}'\mathbf{r})] d^3\mathbf{r}. \quad (4.70)$$

Since

$$\int_{\mathcal{V}} \exp[i(\mathbf{k} + \mathbf{k}')\mathbf{r}] d^3\mathbf{r} = \mathcal{V}\delta_{\mathbf{k}, -\mathbf{k}'} \quad (4.71)$$

we can write

$$\int_{\mathcal{V}} (\delta\phi)^2 d^3\mathbf{r} = \sum_{\mathbf{k}} \phi_{\mathbf{k}}\phi_{-\mathbf{k}} = \sum_{\mathbf{k}} |\phi_{\mathbf{k}}|^2. \quad (4.72)$$

For the gradient term we obtain in similar manner

$$\int_{\mathcal{V}} (\nabla \delta \phi)^2 d^3 \mathbf{r} = \sum_{\mathbf{k}} (i\mathbf{k}) \cdot (-i\mathbf{k}) \phi_{\mathbf{k}} \phi_{-\mathbf{k}} = \sum_{\mathbf{k}} |\mathbf{k}|^2 |\phi_{\mathbf{k}}|^2. \quad (4.73)$$

Introducing Eqs. (4.72), (4.73) into Eq. (4.66), we obtain

$$\delta \mathcal{G} = \frac{\tilde{R}T}{2} \sum_{\mathbf{k}} \left(\frac{1}{\tilde{v}_A \phi} + \frac{1}{\tilde{v}_B (1 - \phi)} - \frac{2\chi}{\tilde{v}_c} + \beta'' |\mathbf{k}|^2 \right) |\phi_{\mathbf{k}}|^2. \quad (4.74)$$

The coupling constant $\beta'' = 2\beta'(\tilde{R}T)^{-1}$ is unknown at this point of the discussion, but later on we shall learn more about it.

As we can see, the Fourier transformation leads to a decoupling. Whereas, in direct space, we have a short-ranged coupling between fluctuations at different positions as expressed by the gradient term in Eq. (4.66), different Fourier amplitudes $\phi_{\mathbf{k}}$ contribute separately to $\delta \mathcal{G}$, thus being perfectly independent. Hence, the wave-like modulations of the concentration may be regarded as the basic **modes** of the system, which can be excited independently from each other. The general dynamics of the concentration fluctuations in a polymer mixture is described as a superposition of all these modes, each mode being characterized by a certain wavevector.

Having an expression for the free energy increase associated with the excitation of the mode \mathbf{k} , one can calculate its mean squared amplitude in thermal equilibrium $\langle |\phi_{\mathbf{k}}|^2 \rangle$. It follows from Boltzmann statistics as

$$\langle |\phi_{\mathbf{k}}|^2 \rangle = \int |\phi_{\mathbf{k}}|^2 \exp -\frac{\delta \mathcal{G}(\phi_{\mathbf{k}})}{kT} \delta |\phi_{\mathbf{k}}| \Big/ \int \exp -\frac{\delta \mathcal{G}(\phi_{\mathbf{k}})}{kT} \delta |\phi_{\mathbf{k}}|. \quad (4.75)$$

Evaluation of the integrals yields

$$\langle |\phi_{\mathbf{k}}|^2 \rangle = N_L^{-1} \left(\frac{1}{\tilde{v}_A \phi} + \frac{1}{\tilde{v}_B (1 - \phi)} - \frac{2\chi}{\tilde{v}_c} + \beta'' |\mathbf{k}|^2 \right)^{-1}. \quad (4.76)$$

The result includes a singularity that comes up if the denominator equals zero. It tells us that finite concentration fluctuations can exist only under the condition

$$\frac{1}{\tilde{v}_A \phi} + \frac{1}{\tilde{v}_B (1 - \phi)} - \frac{2\chi}{\tilde{v}_c} + \beta'' |\mathbf{k}|^2 > 0. \quad (4.77)$$

Regarding Eq. (4.56), this is equivalent to

$$\chi_{\text{sp}} - \chi + \frac{\tilde{v}_c}{2} \beta'' |\mathbf{k}|^2 > 0. \quad (4.78)$$

As we can see, in the limit $k \rightarrow 0$, the stability criterion of the Flory–Huggins theory, $\chi < \chi_{\text{sp}}$, is recovered. For finite values of k , the criterion becomes modified.

Next, we relate the calculated fluctuations amplitudes to the scattering function obtained in X-ray or light scattering experiments. Discussions are usually based on a scattering function that refers to the reference volume common for both species, v_c , or in the language of the lattice models, on a scattering function that refers to the cells of the lattice. It is denoted as S_c and defined as

$$S_c(\mathbf{q}) = \frac{1}{\mathcal{N}_c} \langle |C(\mathbf{q})|^2 \rangle. \quad (4.79)$$

$C(\mathbf{q})$ is the scattering amplitude and \mathcal{N}_c stands for the total number of A-units and B-units in the sample. The scattering function $S_c(\mathbf{q})$ can be directly related to the mean squared amplitudes of the fluctuations $\langle |\phi_{\mathbf{k}}|^2 \rangle$. As is shown in Sect. A.4.1 in the Appendix, the relation is

$$S_c(\mathbf{q}) = \frac{1}{v_c} \langle |\phi_{\mathbf{k}=\mathbf{q}}|^2 \rangle. \quad (4.80)$$

Making use of Eq. (4.76), we obtain the scattering function of a polymer mixture. It is given by the following equation:

$$S_c(\mathbf{q}) = \left(\frac{1}{N_A \phi} + \frac{1}{N_B(1-\phi)} - 2\chi + \tilde{v}_c \beta'' q^2 \right)^{-1}. \quad (4.81)$$

The result allows a reconsideration of the open question about the functional form of the coupling coefficient β'' . Insight results from a view on the limiting properties of the scattering function for low concentrations of the polymers A and B, respectively. For the discussion it is advantageous to change to the reciprocal of the scattering function, since this leads to a separation of the contributions of the A's and B's

$$\frac{1}{S_c} = \frac{1}{N_A \phi} + \frac{1}{N_B(1-\phi)} - 2\chi + \tilde{v}_c \beta'' q^2. \quad (4.82)$$

First consider the limit $\phi \rightarrow 0$. When A is the minority species, present only in low concentration, our equation gives

$$\frac{1}{S_c} \rightarrow \frac{1}{\phi N_A} + \tilde{v}_c \beta'' q^2. \quad (4.83)$$

On the other hand, for this case, the exact form of S_c is known. Since in melts polymer chains are ideal, S_c is given by the Debye structure function (Eqs. (2.60) and (2.61)), multiplied by the volume fraction ϕ in order to account for the dilution

$$S_c = \phi N_A S_D(R_A^2 q^2). \quad (4.84)$$

Using the series expansion Eq. (2.63) we may write

$$\frac{1}{S_c} \approx \frac{1}{N_A \phi} \left(1 + \frac{R_A^2 q^2}{18} \right). \quad (4.85)$$

Equivalently, when choosing polymer B as the diluted species, our equation leads to

$$\frac{1}{S_c} \rightarrow \frac{1}{(1-\phi)N_B} + \tilde{v}_c \beta'' q^2, \quad (4.86)$$

whereas the complete expression is

$$\frac{1}{S_c} = \frac{1}{(1-\phi)N_B S_D(R_B^2 q^2)} \quad (4.87)$$

$$\approx \frac{1}{N_B(1-\phi)} \left(1 + \frac{R_B^2 q^2}{18} \right). \quad (4.88)$$

A comparison of Eq. (4.83) with Eq. (4.85) and Eq. (4.86) with Eq. (4.88) gives us an explicit expression for the coupling constant β'' : Equations agree for

$$\beta'' = \frac{1}{\tilde{v}_c} \frac{R_A^2}{18N_A\phi} + \frac{1}{\tilde{v}_c} \frac{R_B^2}{18N_B(1-\phi)}. \quad (4.89)$$

Inserting this expression into Eq. (4.82), we obtain as the final result

$$\frac{1}{S_c} = \frac{1}{\phi N_A} \left(1 + \frac{R_A^2 q^2}{18} \right) + \frac{1}{(1-\phi)N_B} \left(1 + \frac{R_B^2 q^2}{18} \right) - 2\chi. \quad (4.90)$$

Is this really correct? Considering the simple Ginzburg–Landau functional, Eq. (4.62), which we chose as our starting point, this is a legitimate question and indeed the comparisons with the known limiting behaviors for $\phi \rightarrow 0$ and $(1-\phi) \rightarrow 0$ point at limitations. Full agreement in these limits is only reached for $R_A^2 q^2 \ll 1$, $R_B^2 q^2 \ll 1$.

One might suspect that these limitations can be removed by an obvious extension of Eq. (4.90). It is possible to construct a scattering function that is correct for the known limits without being restricted to low q 's. Evidently this is accomplished by the equation

$$\frac{1}{S_c} = \frac{1}{\phi N_A S_D(R_A^2 q^2)} + \frac{1}{(1-\phi)N_B S_D(R_B^2 q^2)} - 2\chi. \quad (4.91)$$

In fact, Eq. (4.91) represents the correct result. It can be obtained with the aid of a theoretical method superior to the Ginzburg–Landau treatment known as the **random phase approximation**. The interested reader finds the derivation in the Appendix, Sect. A.4.1.

The use of Eq. (4.91) enables us to make an evaluation of scattering experiments, in particular

- a determination of the Flory–Huggins parameter χ and the coil sizes R_A, R_B ;
- a determination of the spinodal, based on the temperature dependence of the concentration fluctuations in the homogeneous phase.

We reduce the discussion again to the case of symmetric polymer mixtures with

$$N_A = N_B = N$$

and apply Eq. (4.90), now in the form

$$\begin{aligned} \frac{1}{S_c} &= \frac{1}{N} \frac{1}{\phi(1-\phi)} + \frac{q^2}{18N} \left(\frac{R_A^2}{\phi} + \frac{R_B^2}{1-\phi} \right) - 2\chi \\ &= \frac{1}{N} \frac{1}{\phi(1-\phi)} + \frac{1}{N\phi(1-\phi)} \frac{q^2}{18} R_\phi^2 - 2\chi. \end{aligned} \quad (4.92)$$

In the last equation we have introduced a ϕ -dependent average over the coil radii, R_ϕ , defined as

$$R_\phi^2 = (1-\phi)R_A^2 + \phi R_B^2. \quad (4.93)$$

Applying Eq. (4.54), we may also write

$$\frac{1}{S_c} = 2(\chi_{\text{sp}} - \chi) + 2\chi_{\text{sp}} \frac{R_\phi^2}{18} q^2. \quad (4.94)$$

Equation (4.94) enables us to make a determination of χ and R_ϕ for a (symmetric) polymer mixture. Figure 4.18 presents, as an example, results of small angle X-ray scattering experiments, carried out on mixtures of polystyrene and partially brominated polystyrene (PBr_xS, with $x = 0.17$). Data are represented by a plot S_c^{-1} versus q^2 , as suggested by Eq. (4.94). The difference in slopes indicates a change of R_ϕ with the composition, telling us that the coil sizes of polystyrene and the partially brominated polystyrene are different (analysis of the data yielded $R(\text{PS}) = 32 \text{ \AA}$, $R(\text{PBr}_x\text{S}) = 39 \text{ \AA}$). The bottom part of Fig. 4.18 presents the values derived for χ , together with χ_{sp} according to Eq. (4.54). Results show that χ is not a constant, although the changes are comparatively small. Strictly speaking, the measurement yields Λ (Eq. (4.58)) rather than χ , but the difference seems negligible.

An understanding of the microscopic origin of the observed ϕ -dependence on theoretical grounds is difficult and this is a situation where computer simulations can be quite helpful. In fact, computations for a lattice model have led to qualitatively similar results, as demonstrated by the curves depicted in Fig. 4.19. These curves all exhibit the slight curvature of the experimental curves. A second result of the simulations is particularly noteworthy. Computer simulations can be used for general checks of the assumptions of the Flory–Huggins model, which cannot be accomplished in an easy manner by analytical considerations. In the example, computations were carried out for a simple cubic lattice. In order to reduce the ‘equilibration time’ in the computer, as given by the number of steps necessary to reach the equilibrium when starting from an arbitrary configuration, 20% of the lattice sites were

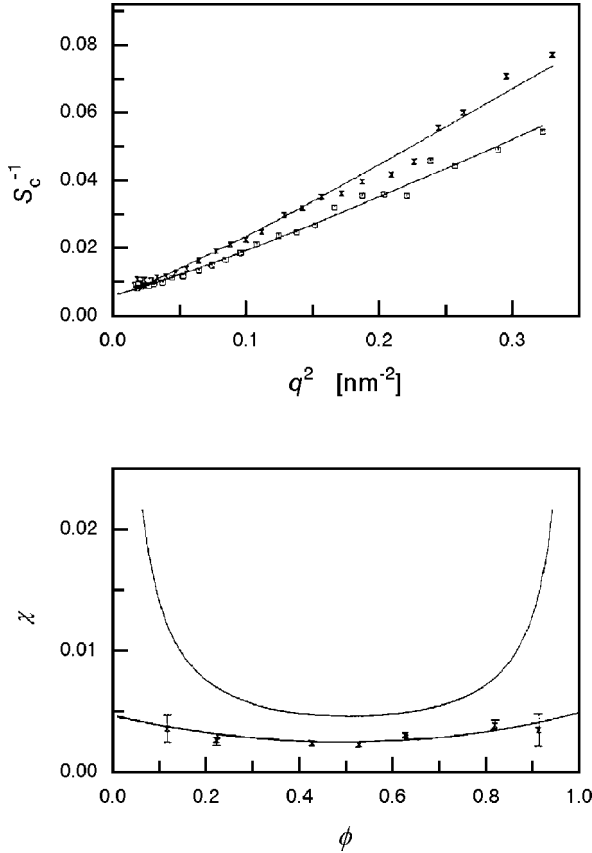


Fig. 4.18. Results of SAXS experiments on mixtures of PS and PBr_xS , both species having equal degrees of polymerization ($N = 430$). Scattering functions for $\phi(\text{PS}) = 0.42$ and 0.62 (*top*) and derived function $\chi(\phi)$ (*bottom*). The *upper* curve in the lower figure represents χ_{sp} [24]

left empty. Calculations were carried out for different values of χ' . We discussed the predictions of the Flory–Huggins model and expect from it, for a dense system, the relation Eq. (4.8)

$$(\Delta =) \chi = z_{\text{eff}} \chi' . \tag{4.95}$$

The simulation yielded consistently lower values, i.e.,

$$\Delta < z_{\text{eff}} \chi' . \tag{4.96}$$

There is first a trivial reason, given by the presence of the vacancies that reduce the interaction energy, but this contributes only a factor of about 0.8. The observed difference is definitely larger and this points at deficiencies

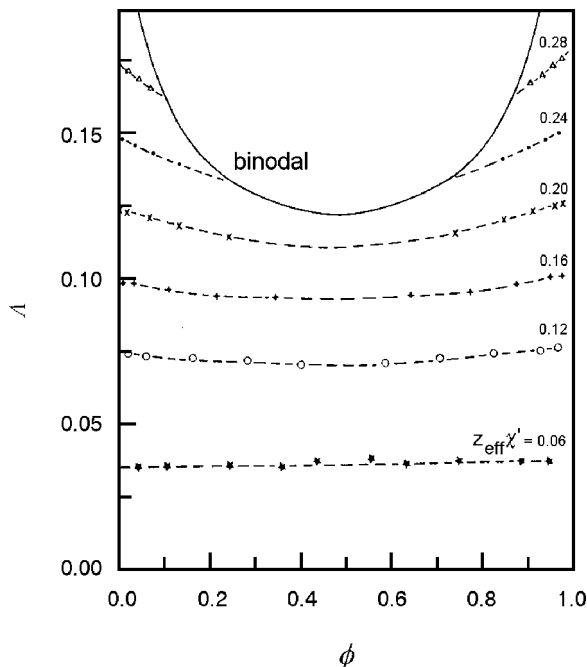


Fig. 4.19. Results obtained in a Monte-Carlo simulation for a lattice model of a polymer mixture ($N_A = N_B = 16$; simple cubic lattice, i.e., $z_{\text{eff}} = 4$; 80% of the lattice are occupied by the chains). Calculation of the function $\Lambda(\phi)$ for different values of $z_{\text{eff}}\chi'$ ($\phi = \phi_A/(\phi_A + \phi_B)$ is the relative concentration of A-chains). Calculation by Sariban and Binder [25]

of the mean field approximation in the description of this model system. Obviously, the number of AB-contacts is smaller than expected under the assumption of a random distribution of the chains. A closer inspection of the data indicated an enhanced number of intramolecular contacts and also some intermolecular short-range order. Hence, the simulation tells us, as a general kind of warning, that one should be careful in interpreting measured χ -parameters. There can always be perturbing effects. Shortcomings of the Flory–Huggins treatment show up in particular if the molar masses are low. Some effects emerge only for such systems, an important one being the short-range ordering mentioned above. Short-range order effects can only arise if the distances over which the concentration fluctuations are correlated are larger than or similar to the chain size. Conversely, for chains with sufficiently high degrees of polymerization, short-range order effects are ruled out; chains actually average over all local concentration fluctuations and experience the mean value of the contact energies only. In our case, both the experiment and the simulation refer to moderate or even low degrees of polymerization and the qualitative comparison appears justified.

Next, let us return once again to Fig. 4.15, which shows temperature dependent measurements on mixtures of deuterio-polystyrene and poly(vinylmethyl-ether). Now, we can recognize the theoretical basis of the chosen representation S^{-1} versus q^2 , namely as corresponding to Eq. (4.91). A change in temperature with the resulting change in χ leads to a parallel shift of the curve $S^{-1}(q^2)$. The right part of the figure shows the limiting value $S^{-1}(q \rightarrow 0)$ as a function of temperature, directly expressing the T -dependence of χ according to

$$\frac{1}{S_c(q \rightarrow 0)\tilde{v}_c} = \frac{2(\chi_{\text{sp}} - \chi)}{\tilde{v}_c}. \quad (4.97)$$

For $\chi(T)$ the observed straight line indicates a linear dependence

$$\chi_{\text{sp}} - \chi \propto T^{-1} - T_{\text{sp}}^{-1}. \quad (4.98)$$

If we wish to account for both upper and lower miscibility gaps, we may write in linear approximation

$$\chi_{\text{sp}} - \chi \propto |T - T_{\text{sp}}| \quad (4.99)$$

and thus expect a temperature dependence

$$S^{-1}(0) \propto |T - T_{\text{sp}}|. \quad (4.100)$$

The data in Fig. 4.15 were obtained for a mixture with the critical concentration and here the extrapolation to the point where $S_c(0)$ diverges yielded the critical temperature. We can now also see the procedure to be used for a determination of the complete spinodal. One has to carry out temperature-dependent measurements for a series of mixtures, which cover the whole range of compositions. Extrapolations on the basis of Eq. (4.100), i.e., a continuation of the temperature-dependent $S_c^{-1}(0)$ down to zero, yields the spinodal $T_{\text{sp}}(\phi)$, as represented in a (ϕ, T) -phase diagram. Figure 4.20 shows, as an example, a respective set of data that was obtained in another neutron scattering study on mixtures of deuterated polystyrene and poly(vinylmethyl-ether). The linear relation Eq. (4.100) appears verified and the corresponding extrapolations then yield the spinodal depicted in the lower half of the figure.

The concentration fluctuations in a mixture are spatially correlated, with the degree of coupling decreasing with the distance. We may inquire about the **correlation length** of the fluctuations, i.e., the maximum distance over which correlations remain essential. The answer follows from the scattering function. Rewriting Eq. (4.94), we obtain for the small angle range a curve with Lorentzian shape,

$$S_c = \frac{1}{2(\chi_{\text{sp}} - \chi)} \frac{1}{1 + \xi_\phi^2 q^2}. \quad (4.101)$$

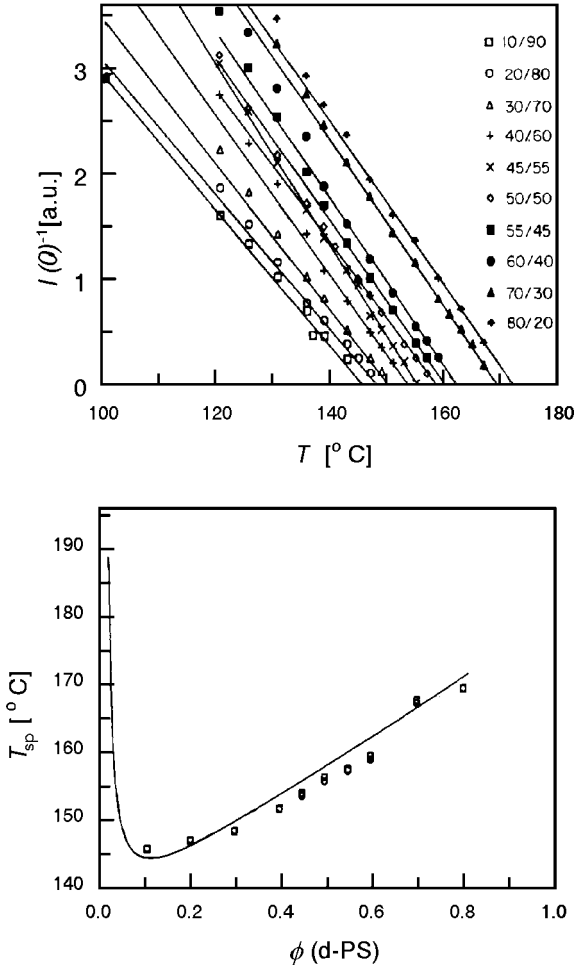


Fig. 4.20. Spinodal of a mixture of d-PS ($M = 5.93 \times 10^5 \text{ g mol}^{-1}$) and PVME ($M = 1.1 \times 10^6 \text{ g mol}^{-1}$) (*bottom*) as derived from the temperature dependence of neutron scattering intensities in forward direction (*top*). Data from Han et al. [26]

The parameter ξ_ϕ^2 is given by

$$\xi_\phi^2 = \frac{\chi_{sp} R_\phi^2}{18(\chi_{sp} - \chi)}. \quad (4.102)$$

ξ_ϕ represents the correlation length, as is revealed by a Fourier transformation of S_c . It yields the correlation function for the concentration fluctuations in direct space

$$\langle \delta\phi(0)\delta\phi(\mathbf{r}) \rangle \propto \int \exp(i\mathbf{q}\mathbf{r}) S_c(\mathbf{q}) d^3\mathbf{q} \quad (4.103)$$

(if an explanation is necessary, look at the derivation of Eq. (A.17) in the Appendix). The evaluation is straightforward and leads to

$$\langle \delta\phi(0)\delta\phi(\mathbf{r}) \rangle \propto \frac{1}{r} \exp -\frac{r}{\xi_\phi} . \quad (4.104)$$

As we can see, ξ_ϕ indeed describes the spatial extension of the correlations.

In all second order phase transitions, the correlation length of the fluctuations of the order parameter diverges at the critical point. We also find this behavior in our system, when making use of Eq. (4.100). For the temperature dependence of ξ_ϕ we obtain the power law

$$\xi_\phi \propto (\chi_{\text{sp}} - \chi)^{-1/2} \propto |T - T_{\text{sp}}|^{-1/2} . \quad (4.105)$$

If an experiment is conducted for the critical composition ϕ_c , then one observes the divergence of ξ_ϕ . For concentrations different from ϕ_c , the increase of ξ_ϕ stops when the binodal is reached.

4.3.2 Decomposition Kinetics

After having crossed the spinodal, either through the critical point or somewhere else by a rapid quench that passes quickly through the nucleation and growth range, unmixing sets in by the mechanism known as spinodal decomposition. Measurements like the ones presented in Figs. 4.16 and 4.17 allow detailed investigations. The experiments yield the time-dependent **transient scattering function**, which we denote as $S_{\text{tr}}(q, t)$.

Theory has succeeded to derive an **equation of motion** for $S_{\text{tr}}(q, t)$, which can be used for an analysis of the kinetics of structure evolution in the early stages of development. It has the following form:

$$\frac{dS_{\text{tr}}(q, t)}{dt} = -\Gamma(q)(S_{\text{tr}}(q, t) - S_c(q)) . \quad (4.106)$$

S_c is defined by Eq. (4.91) and $\Gamma(q)$ is a rate constant, determined by

$$\Gamma(q) = 2q^2\lambda(q)S_c^{-1}(q) . \quad (4.107)$$

λ is a function that relates to the single chain dynamics in the mixture.

A derivation of this equation lies outside our scope, so that we can only consider briefly its background and some implications. First of all, note that Eq. (4.106) has the typical form of a first order relaxation equation, as it is generally used to describe irreversible processes that bring a system from an initial non-equilibrium state back to equilibrium. Therefore, if rather than crossing the spinodal, the temperature jump is carried out within the one phase region, causing a transition of the structure into a new state with higher or lower concentration fluctuations, then the applicability of the equation is unquestionable. Indeed, Eq. (4.106) is meant to cover this ‘normal’ case as

well. S_c then represents the structure factor associated with the new equilibrium state. The different factors included in the equation for the relaxation rate Γ are all conceivable. A quadratic term in q always shows up for particle flows based on diffusive motions and these have to take place if a concentration wave is to alter its amplitude. Its background is of a twofold nature and easily seen. Firstly, according to Fick's law, flow velocities are proportional to concentration gradients and thus proportional to q . Secondly, with increasing wavelength, particles have to go over correspondingly larger distances and this produces a second factor q . Both effects together give the characteristic q^2 . The origin of the factor S_c^{-1} is revealed by a look at Eqs. (4.74) and (4.82). Equation (4.74) is formally equivalent to the energy (u)-displacement (x) relation of a harmonic oscillator

$$u = \frac{1}{2}ax^2. \quad (4.108)$$

We therefore may also address the factor in Eq. (4.74), which corresponds to a as a 'stiffness coefficient', now related to the formation of a concentration wave. Interestingly enough, exactly this stiffness coefficient shows up again in Eq. (4.82) for S_c^{-1} , apart from a trivial factor $\tilde{R}T/\tilde{v}_c$. As S_c^{-1} is determined by this factor only, it can replace the stiffness coefficient in equations. Clearly, the latter affects the relaxation rate and therefore has to be part of any equation for Γ . Since our system shows close similarities to an overdamped harmonic oscillator, both having the same equation of motion, we can also understand the linear dependence of Γ on S_c^{-1} . Hence in conclusion, for temperature jumps within the one phase region, Eq. (4.106) looks perfectly reasonable. It may appear less obvious that its validity is maintained if temperature jumps transfer the system into the two-phase region so that spinodal decomposition sets in. One could argue that, in view of the continuous character of critical phase transitions, one could expect the same kinetic equations to hold on both sides of the phase boundary, but a direct proof is certainly necessary and is indeed provided by the theoretical treatments.

A change occurs in the meaning of S_c . For temperatures in the two-phase region, S_c can no longer be identified with an equilibrium structure function. Nevertheless, its definition by Eq. (4.91) is maintained. This implies that S_c shows negative values at low q 's, being positive only for high q 's. Here we are dealing with a **virtual structure function**, which is not a measurable quantity but defined by an extrapolation procedure. In order to obtain S_c , one has to determine the temperature dependence of χ in the homogeneous phase, introduce it into Eq. (4.91) and use this equation also for temperatures in the two-phase region.

The specific character of the spinodal decomposition can now be understood as being a consequence of the peculiar q -dependence of the rate constant Γ . Figure 4.21 presents results of a calculation applying Eq. (4.107). For q 's below a critical value q_c , S_c^{-1} and therefore $\Gamma(q)$ take on negative values. A negative value of Γ indicates an amplitude growth, instead of the usual

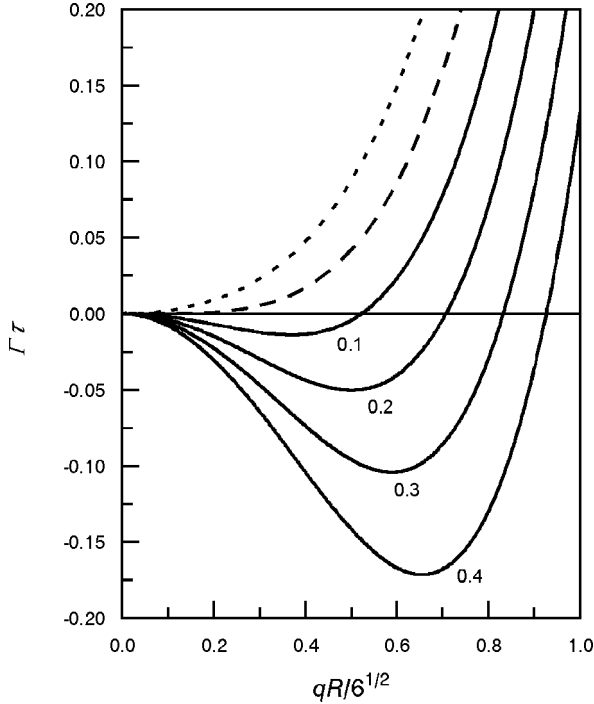


Fig. 4.21. Rate constants Γ determining the time-dependent changes of the structure function of a symmetric polymer mixture ($R_A = R_B = R$) after a temperature jump from the homogeneous phase ($\chi < \chi_{\text{sp}}$) into the two-phase region ($\chi > \chi_{\text{sp}}$) (*continuous lines*). Curves correspond to different distances from the spinodal, $(\chi - \chi_{\text{sp}})/\chi_{\text{sp}} = 0.1-0.4$ and were obtained applying Eqs. (4.107), (4.91) ($\tau = NR^2\phi(1-\phi)/6\lambda(0)$). The *dashed line* gives the rate constants at the spinodal, the *dotted line* those associated with a temperature jump within the one phase region to $\chi/\chi_{\text{sp}} = 0.9$

decay. The main feature in the curve is the maximum in the growth rate, $-\Gamma$, at a certain value q_{max} somewhere in the range

$$0 < q_{\text{max}} < q_c .$$

Structure evolution is controlled by the concentration waves with wavevectors around q_{max} . These constitute the dominant modes of structure formation and determine the length scale of the pattern during the early stages of development. Figure 4.21 also indicates the temperature dependence of q_{max} and the largest associated growth rate. We see that the approach of the spinodal in the two-phase region is accompanied by a decrease of q_{max} . Straightforward analysis shows that the decrease obeys the power law

$$q_{\text{max}} \propto (\chi - \chi_{\text{sp}})^{1/2} \propto |T_{\text{sp}} - T|^{1/2} . \quad (4.109)$$

Simultaneously, a slowing down of the growth rate occurs according to

$$-\Gamma(q_{\max}) \propto -q_{\max}^2 S_c^{-1}(q_{\max}) . \quad (4.110)$$

Employing Eq. (4.94) we obtain

$$-\Gamma(q_{\max}) \propto -q_{\max}^2 \left((\chi_{\text{sp}} - \chi) + \chi_{\text{sp}} \frac{R_\phi^2}{18} q_{\max}^2 \right) \propto |T_{\text{sp}} - T|^2 . \quad (4.111)$$

This **critical slowing down** also shows up on the other side of the phase boundary, when for a critical mixture the critical temperature is approached from the one phase region. The kinetic parameter of interest, to be used on both sides, is the **collective diffusion coefficient**, D_{coll} , defined as

$$D_{\text{coll}} = \lim(q \rightarrow 0) \frac{\Gamma(q)}{2q^2} , \quad (4.112)$$

and it is given by

$$D_{\text{coll}} = \lambda(0) S_c(0)^{-1} . \quad (4.113)$$

The attribute ‘collective’ is used in order to distinguish this parameter from the **self-diffusion coefficient** of the individual chains, which relates to the single chain dynamics as expressed by λ only, and therefore shows no critical slowing down. We see that D_{coll} takes on positive and negative values, crossing zero at the spinodal

$$D_{\text{coll}} \propto \chi_{\text{sp}} - \chi \propto \pm |T - T_{\text{sp}}| . \quad (4.114)$$

Equation (4.106) can be solved exactly and the solution is

$$S_{\text{tr}}(q, t) = S_c(q) + (S_{\text{tr}}(q, 0) - S_c(q)) \exp[-\Gamma(q)t] . \quad (4.115)$$

Figure 4.22 presents the results of model calculations performed on the basis of this equation. We find that a spinodal decomposition leads to an intensity increase for all q 's, with a maximum at a certain q_{\max} . Growing in intensity, the peak stays at a fixed position. In the long time limit we observe an exponential law

$$S_{\text{tr}}(q_{\max}) \propto \exp(-\Gamma t) . \quad (4.116)$$

As we can see, the model calculations reproduce the main features of the experimental observations during the initial stages of spinodal decompositions. In fact, the equations can be applied for a representation of experimental data and we refer here once again to the measurement presented in Fig. 4.16. Figure 4.23 shows a plot on the left-hand side according to

$$\ln \frac{S_{\text{tr}}(q, t) - S_c(q)}{S_{\text{tr}}(q, 0) - S_c(q)} = \ln \frac{\Delta S(q, t)}{\Delta S(q, 0)} = -\Gamma(q)t . \quad (4.117)$$

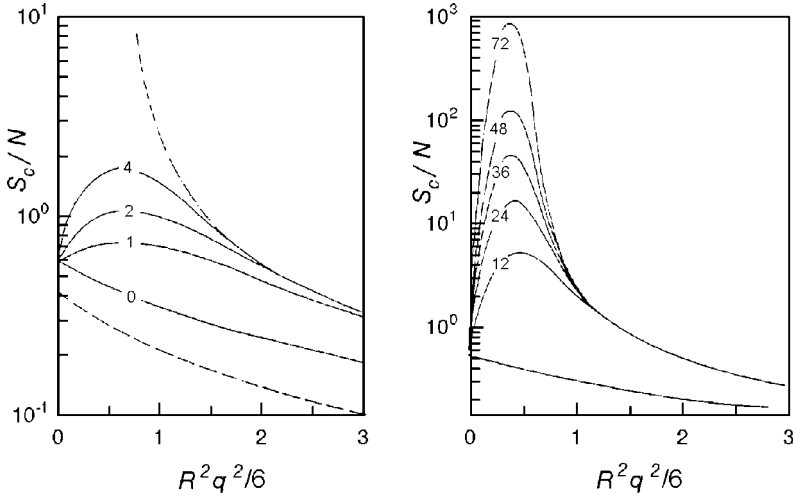


Fig. 4.22. Spinodal decomposition initiated by a jump from the one phase region ($N\chi = 1$) to the two-phase region ($N\chi = 2.5$). Model calculation for a symmetric polymer blend ($N_A = N_B = N, R_A = R_B = R$) on the basis of Eqs. (4.115), (4.107), (4.91). The numbers represent units of time [27]

The virtual structure function $S_c(q)$ has been constructed by a linear extrapolation of the equilibrium values in the homogeneous region shown in Fig. 4.15; the change from positive to negative values occurs for $q_c = 2.9 \times 10^{-2} \text{ nm}^{-1}$. For all q 's we find exponential time dependencies in agreement with Eq. (4.115). The derived rate constants Γ are given by the lowest curve (134.1°C) on the right-hand side. One has negative values for $q < q_c$ and in this range a maximum in the growth rate. In addition, the right-hand figure includes the results of two other experiments, one conducted at $T = 133^\circ\text{C}$, even closer to T_c , and the other at $T = 131.85^\circ\text{C}$, which is in the one phase region. One observes a shift of q_{max} towards zero for $T \rightarrow T_c$ and on both sides of T_c a critical slowing down for $D_{\text{coll}} \propto d^2\Gamma/dq^2(q=0)$, which is in full agreement with the theoretical predictions.

Late Stage Kinetics

The described initial stages of spinodal decomposition constitute the entrance process, thereby setting the basic structure characteristics and the primary length and time scales. They represent a first part only, coming to an end when the concentration waves produce, in summary, variations $\delta\phi$, which already approach the concentrations of the two equilibrium phases. Then the exponential increase of the amplitudes cannot continue further and the kinetics must change. A first natural effect is a retardation of the growth rate, and a second is a shift of q_{max} towards lower values. An example for this generally observed behavior was presented in Fig. 4.17 with the light scattering curves

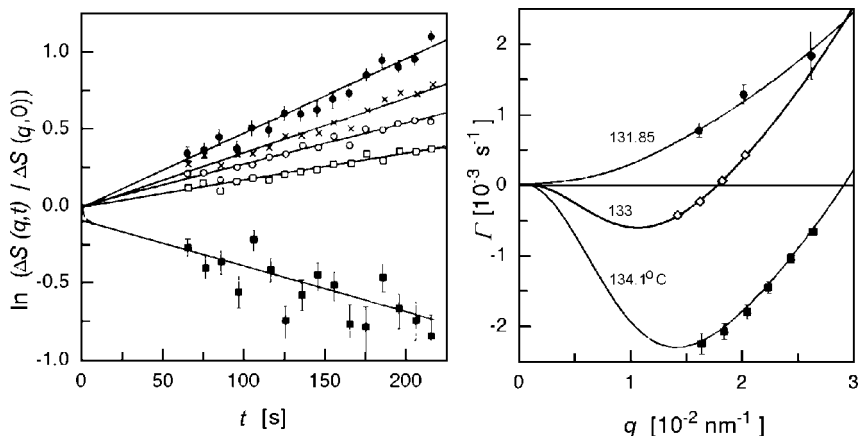


Fig. 4.23. Same system as in Figs. 4.15 and 4.16 [22]. Plot demonstrating an exponential time dependence of the transient scattering intensities at $T = 134.1 \text{ }^\circ\text{C}$ for different q 's (1.79×10^{-2} ; 2.2×10^{-2} ; 2.4×10^{-2} ; 2.6×10^{-2} ; $3.62 \times 10^{-2} \text{ nm}^{-1}$) (left). Derived rate constants $\Gamma(q)$ for growth ($\Gamma < 0$) or decay ($\Gamma > 0$), together with the results of equivalent experiments for $T = 133 \text{ }^\circ\text{C}$ ($> T_c = 131.9 \text{ }^\circ\text{C}$) and $T = 131.85 \text{ }^\circ\text{C}$ ($< T_c$) (right)

obtained for a polystyrene/poly(vinylmethylether) mixture. Theory has dealt with these first changes by a generalization of the linear equations valid for the initial stages and accounting for the saturation effects introduced by the bounds. Treatments are rather involved and we cannot present them here. Interestingly enough, after this second period, there follows a third part where behavior again becomes simpler. This is the regime of the **late stage kinetics** and we will briefly describe some major observations in this section.

The micrograph on the right-hand side of Fig. 4.10 was obtained during this late stage of structure evolution and represents an instructive example. The interconnected domains are set up by the two equilibrium phases. The interfaces are well-established and it can be assumed that their microscopic structure, as described by the concentration profile of the transition zone, has also reached the equilibrium form. Further observations for the same system, a mixture of polystyrene and partially brominated polystyrene, are included in Fig. 4.24. The three micrographs were obtained at somewhat earlier times. Although the observed structures are finer and therefore less well-resolved, it seems clear that they are identical in their general character. What we see here is a coarsening process and, importantly, the observations suggest that all these transient structures which are passed through during the late stages of unmixing are similar to each other and differ only in length scale. It is possible to check for the suspected similarity by light scattering experiments. Figure 4.25 depicts, as an example, scattering curves obtained for a mixture of polybutadiene (PB) and polyisoprene (PI).

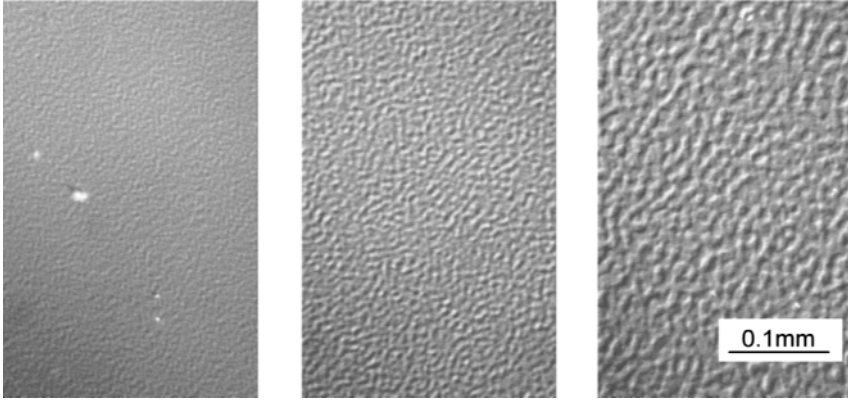


Fig. 4.24. Structure development during the late stages of spinodal decomposition observed for a PS/PBr_xS-(1:1) mixture. Micrographs were obtained during annealing at 200 °C ($< T_c = 220$ °C) for 1 min (*left*), 3 min (*center*) and 10 min (*right*) [21]

Here a spinodal decomposition can be initiated by a temperature jump into an upper miscibility gap. Similarity implies that in a representation with reduced variables, plotting $\log(I/I_{\max})$ versus $\log(q/q_{\max})$, curves measured at different times must become identical. As we can see, this is indeed true. We notice in addition that even the structures observed at different temperatures are similar to each other. We thus have a most simple situation that allows us to describe the kinetics of unmixing by the time dependence of just one parameter. Possible choices are either q_{\max}^{-1} , representing a typical length in the structure, or the interfacial area per unit volume, denoted by O_{12} . In fact, both quantities are related. Two-phase systems in general have two primary structure parameters, namely the volume fraction of one phase, ϕ , and O_{12} . As explained in Sect. A.4.2 in the Appendix, from ϕ and O_{12} one can derive a characteristic length of the structure, l_c , as

$$l_c = \frac{2\phi(1-\phi)}{O_{12}} \quad (4.118)$$

(see Eq. (A.161)). l_c and q_{\max}^{-1} have equal orders of magnitude and are proportional to each other

$$l_c = \text{const } q_{\max}^{-1}, \quad (4.119)$$

the proportionality constant depending on the structure type. Clearly, when the formation of the equilibrium phases is completed for the first time, ϕ is fixed and does not change any more. Hence from this point on, throughout the late stages of unmixing, one must find a strict inverse proportionality between l_c or q_{\max}^{-1} and O_{12} . O_{12} can be directly derived from the scattering curve us-

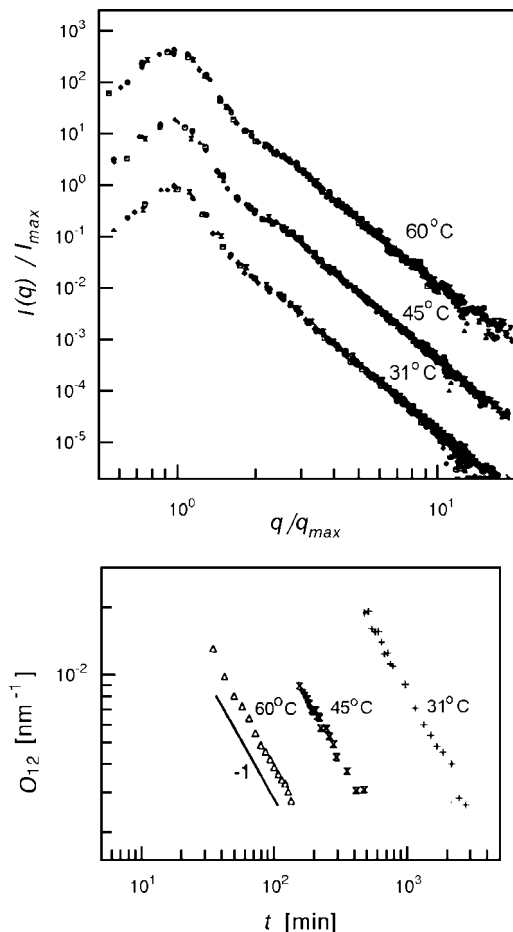


Fig. 4.25. Light scattering curves obtained for a PB ($M = 5.8 \times 10^5 \text{ g mol}^{-1}$)/PI ($M = 1 \times 10^5 \text{ g mol}^{-1}$)-(1:1) mixture during the late stage of spinodal decomposition at the indicated temperatures (*top*; curves for 45°C and 60°C are shifted by constant amounts in vertical direction). Each curve contains measurements for different times and these superpose exactly. Time dependence of the interfacial area per unit volume, O_{12} , in agreement with a power law $O_{12} \propto t^{-1}$, as indicated by the straight line with slope -1 (*bottom*). Data from Takenaka and Hashimoto [28]

ing **Porod's law** (Eq. (A.159)), which states that the scattering function of a two-phase system generally shows an asymptotic behavior according to the power law

$$S(q \rightarrow \infty) \propto \frac{O_{12}}{q^4}. \quad (4.120)$$

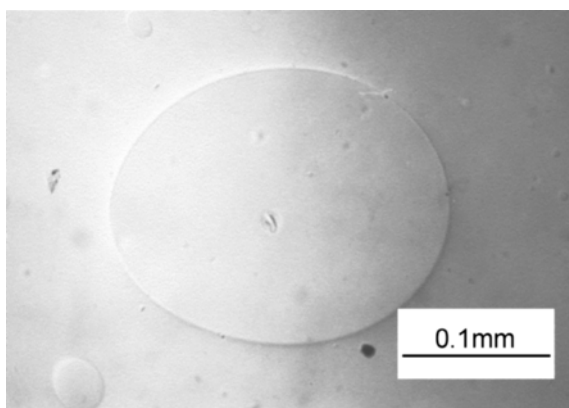


Fig. 4.26. Macroscopic domains in a two-phase PS/PBr_xS-(1:1) mixture, formed after 2 h of annealing [21]

The curves in Fig. 4.25 are in agreement with this law, which can therefore be employed for a determination of O_{12} . The time dependence of O_{12} is given in the lower half of Fig. 4.25. Results indicate a decrease of O_{12} inverse to t ,

$$O_{12} \propto t^{-1} . \quad (4.121)$$

Here, we cannot discuss the theories developed for the late stage kinetics, but the physical background must be mentioned, since it is basically different from the initial stages discussed above. Whereas the kinetics in the initial stages is based on diffusive processes only, the late stages are controlled by convective flow. The driving force originates from the excess free energy of the interfaces. The natural tendency is a reduction of O_{12} and this is achieved by a merging of smaller domains into larger ones.

The latter mechanism remains effective up to the end; however, the structure characteristics must finally change as the similarity property cannot be maintained. The very end is a macroscopic phase separation, as shown, for example, in Fig. 4.26 and clearly, the final structure is always of the same type independent of whether phase separation has started by spinodal decomposition or by nucleation and growth.

4.4 Block Copolymer Phases

If two different polymeric species are coupled together by chemical links, one obtains block copolymers. These materials possess peculiar properties and we will consider them in this section.

In the discussion of the behavior of binary polymer mixtures, we learned that, in the majority of cases, they separate into two phases. As the linkages in block copolymers inhibit such a macroscopic phase separation, one may

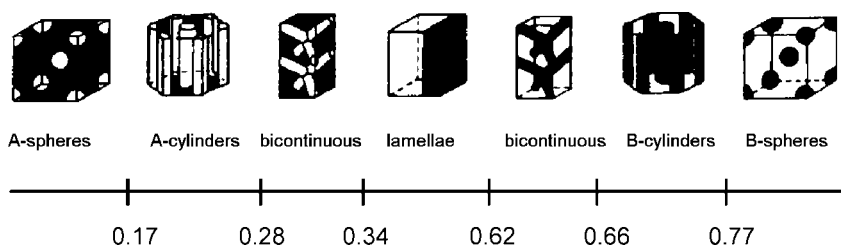


Fig. 4.27. Different classes of microphase separated structures in block copolymers, as exemplified by PS-*block*-PI. The *numbers* give the phase boundaries in terms of the volume fraction of the PS blocks. Figure taken from a review article by Bates and Frederickson [29]

wonder how these systems react under comparable conditions. Figure 4.27 gives the answer with a drawing: The A's and B's still segregate but the domains have only mesoscopic dimensions corresponding to the sizes of the single blocks. In addition, as all domains have a uniform size, they can be arranged in regular manner. As a result ordered mesoscopic lattices emerge. In the figure it is also indicated that this **microphase separation** leads to different classes of structures in dependence on the ratio between the degrees of polymerization of the A's and B's. For $N_A \ll N_B$ spherical inclusions of A in a B-matrix are formed and they set up a body-centered cubic lattice. For larger values N_A , but still $N_A < N_B$, the A-domains have a cylindrical shape and are arranged in a hexagonal lattice. Layered lattices form under essentially symmetrical conditions, i.e., $N_A \approx N_B$. Then, for $N_A > N_B$, the phases are inverted and the A-blocks now constitute the matrix.

In addition to these lattices composed of spheres, cylinders and layers, periodic structures occur under special conditions where both phases are continuous and interpenetrate each other. These bicontinuous **gyroid** structures exist only in a narrow range of values N_A/N_B , between the regimes of the cylindrical and lamellar structures and, as it appears, only when the repulsion forces between the A's and the B's are not too strong. To be sure, the figure depicts the structures observed for polystyrene-*block*-polyisoprene, but these are quite typical. Spherical, cylindrical and layer-like domains are generally observed in all block copolymers. Less is known about how general the bicontinuous special types like the gyroid lattices are.

The majority of synthesized compounds are **di-block copolymers** composed of one A-chain and one B-chain; however, tri-blocks and multiblocks, comprising an arbitrary number of A-chains and B-chains, can be prepared as well. One can also proceed one step further and build up multiblocks that incorporate more than two species, thus again increasing the variability. The question may arise as to whether all these modifications result in novel structures. In fact, this is not the case. The findings give the impression that at least all block copolymers composed of two species exhibit qualitatively sim-

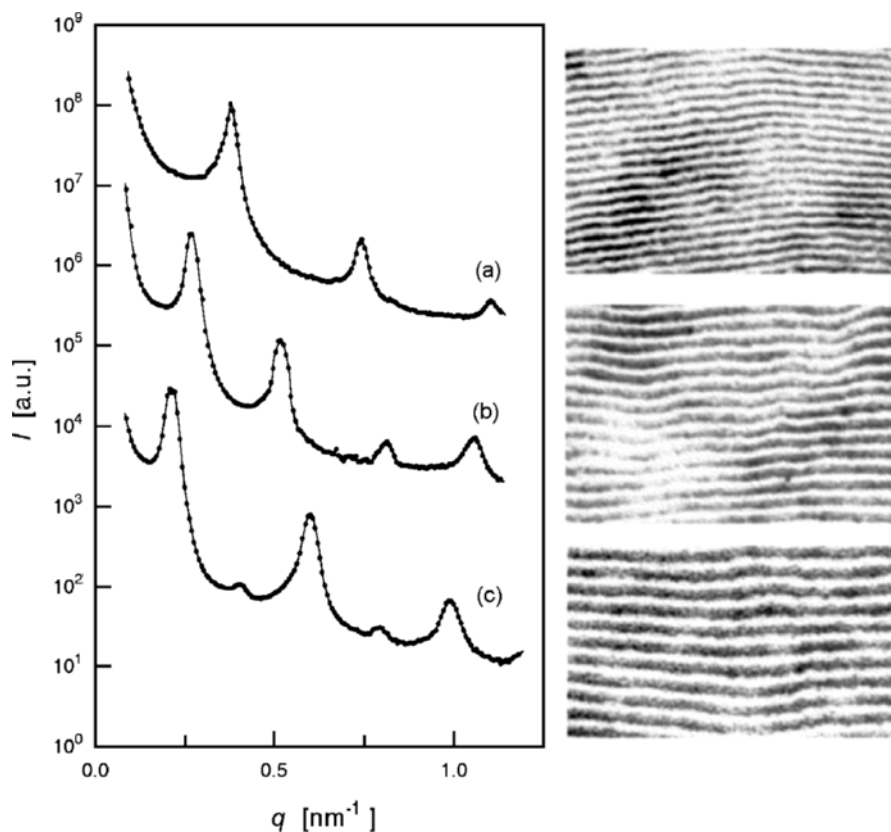


Fig. 4.28. SAXS curves measured for a series of PS-*block*-PI with different molar masses in the microphase separated state: (a) $M = 2.1 \times 10^4 \text{ g mol}^{-1}$, $\phi(\text{PS}) = 0.53$; (b) $M = 3.1 \times 10^4 \text{ g mol}^{-1}$, $\phi(\text{PS}) = 0.40$; (c) $M = 4.9 \times 10^4 \text{ g mol}^{-1}$, $\phi(\text{PS}) = 0.45$ (*left*). Transmission electron micrographs obtained using ultra-thin sections of specimen stained with OsO_4 (*right*). Structures belong to the layer regime. Data from Hashimoto et al. [30]

ilar phase behaviors. Changes then occur for ternary systems. For the latter, the observed structures still possess periodic orders, but the lattices are more complex. Here, we shall only be concerned with the simplest systems, the di-block copolymers.

Suitable methods for an analysis of block copolymer structures are electron microscopy and small angle X-ray scattering (SAXS) experiments. Figure 4.28 gives an example and on the left-hand side presents scattering curves obtained for a series of polystyrene-*block*-polyisoprenes where both blocks had similar molar mass. Structures belong to the layer regime and one correspondingly observes series of equidistant Bragg reflections. The right-hand side depicts micrographs obtained for the same samples in an electron microscope using

ultra-thin sections of specimens where the polyisoprene blocks were stained with OsO_4 . The layered structure is clearly visible and one notices an increase of the layer thicknesses with the molar masses of the blocks.

In binary polymer mixtures, under favorable conditions one finds homogeneous phases. They either arise if the forces between unlike monomers are attractive or, generally, if the molar masses are sufficiently low. Block copolymers behave similarly and can also have a homogeneous phase. It actually has a larger stability range than the corresponding binary mixture. Recall that for a symmetric mixture ($N_A = N_B$) the two-phase region begins at (Eq. (4.35))

$$(\chi N_A)_c = 2 .$$

If a symmetric di-block copolymer is formed from the same A- and B-chains, the transition between the homogeneous phase and the microphase separated state takes place at a higher χ , namely for

$$(\chi N_A)_c \approx 5 . \quad (4.122)$$

The complete phase diagram of a block copolymer is displayed in Fig. 4.29 in a schematic representation. Variables are the volume fraction of the A-blocks

$$\phi_A = \frac{N_A}{N_A + N_B} \quad (4.123)$$

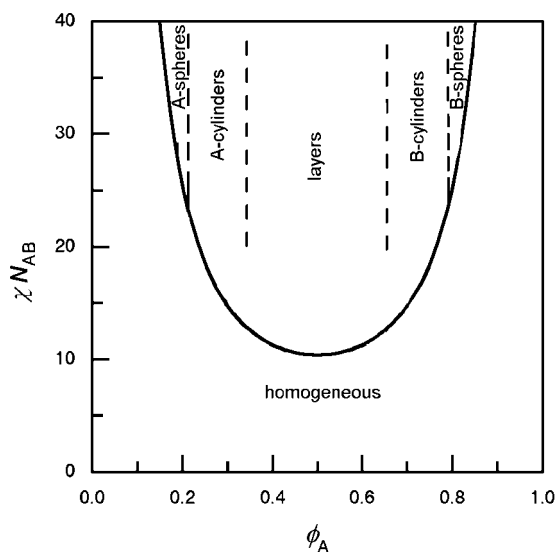


Fig. 4.29. Phase diagram of a di-block copolymer in a schematic representation. The curve describes the points of transition between the homogeneous phase and the microphase separated states. The ordered states are split into different classes as indicated by the *dashed boundary lines*. They are only shown here for the region of higher values of χN_{AB} away from the phase transition line

and the product χN_{AB} , where N_{AB} describes the total degree of polymerization

$$N_{AB} = N_A + N_B .$$

The transition line separating the homogeneous phase from the various microphase separated structures has an appearance similar to the binodal of a polymer mixture. There is, however, a basic difference: In the block copolymer case, we are dealing with a one component system rather than a binary mixture. The line therefore relates to a phase transition rather than to a miscibility gap. It should also be noted that, in contrast to the binodal of a mixture, the transition line tells us nothing about the internal composition of the microphases. In principle, these could be mixed states; however, with the exception of situations near the transition line, compositions are mostly close to pure A- or B-states. The schematic drawing indicates only the structures arising under the conditions of a **strong segregation**, $\chi N_{AB} \gg 10$, where solely lattices of spheres, cylinders and layers are found. The situation for a **weak segregation** with χN_{AB} just above the critical value is more complicated. Here, also the bicontinuous structures are found and subtle features decide about their stability relative to the three major forms.

4.4.1 Layered Structures

Each of the ordered structures represents under the respective conditions the state with the lowest Gibbs free energy. Calculations of the Gibbs free energies and comparisons between the various lattices and the homogeneous phase can therefore provide an understanding of the phase diagram. In addition, they make it possible to determine the structure parameters.

Theoretical analyses were carried out by Meier and Helfand. A full presentation lies outside our possibilities but in order to gain at least an impression of the approaches, we will pick out the layered structures as an example and discuss the equilibrium conditions. The main result will be a power law that formulates the dependence of the layer thicknesses on the degree of polymerization of the blocks.

If we think about the structural changes that accompany a transition from the homogeneous phase to an ordered layer structure, we find three contributions to the change in the Gibbs free energy

$$\Delta g_p = \Delta h_p - T\Delta s_{p,if} - T\Delta s_{p,conf} . \quad (4.124)$$

There is a change in enthalpy, a change in entropy following from the arrangement of the junction points along the interfaces and another change in entropy resulting from altered chain conformations. We write the equation in terms of quantities referring to one di-block polymer.

The driving force for the transitions comes from the enthalpic part. In the usual case of unfavorable AB-interactions, i.e., $\chi > 0$, there is a gain

in enthalpy on unmixing. We assume a maximum gain, achieved when we have a random distribution of the monomers in the homogeneous phase and a perfect segregation in the lamellar phase. Then the enthalpy change per polymer, Δh_p , is given by

$$\Delta h_p = -kT\chi N_{AB}\phi_A(1 - \phi_A) + \Delta h_{p,\text{if}} . \quad (4.125)$$

The first term follows directly from Eq. (4.24). The second term, $\Delta h_{p,\text{if}}$, accounts for an excess enthalpy that is contributed by the interfaces. To see the background, bear in mind that interfaces always possess a finite thickness, typically in the order of one to several nm. Within this transition layer the A's and B's remain mixed, which leads to an increase in enthalpy proportional to χ and to the number of structure units in the transition layer. Let the thickness of the transition layer be d_t and the interface area per polymer o_p , then we may write

$$\Delta h_{p,\text{if}} \simeq kT\chi \frac{o_p d_t}{v_c} . \quad (4.126)$$

v_c again is the volume of the structure unit, commonly chosen for both the A- and B-chains.

The two entropic parts both work in the opposite direction. There is first the loss in entropy, which results from the confinement of the junction points, being localized in the transition layer. For a layered phase with layer thicknesses d_A and d_B , and therefore a period

$$d_{AB} = d_A + d_B , \quad (4.127)$$

$\Delta s_{p,\text{if}}$ may be estimated using a standard equation of statistical thermodynamics

$$\Delta s_{p,\text{if}} \simeq k \ln \frac{d_t}{d_A + d_B} . \quad (4.128)$$

The second entropic contribution, $\Delta s_{p,\text{conf}}$, accounts for a decrease in entropy, which follows from a change in the chain conformations. The Gaussian conformational distribution found in the homogeneous phase cannot be maintained in the microphase separated state. Formation of a layer structure leads, for steric reasons, necessarily to a chain stretching, which in turn results in a loss in entropy. For a qualitative description we employ the previous Eq. (2.93),

$$\Delta s_{p,\text{conf}} \simeq -k \left(\frac{R}{R_0} \right)^2 , \quad (4.129)$$

where R and R_0 are now the end-to-end distances of the block copolymer in the layered and the homogeneous phase, respectively. Assuming that chain sizes and layer spacings are linearly related, by

$$R = \beta d_{AB} , \quad (4.130)$$

the equation converts into

$$\Delta s_{\text{p,conf}} \simeq -k\beta^2 \left(\frac{d_{\text{AB}}}{R_0} \right)^2. \quad (4.131)$$

We can now search for the equilibrium. First note that o_{p} and d_{AB} are related by the obvious equation

$$o_{\text{p}} d_{\text{AB}} = N_{\text{AB}} v_{\text{c}}. \quad (4.132)$$

We therefore have only one independent variable, for example o_{p} . Using all the above expressions, we obtain for the change in the Gibbs free enthalpy

$$\frac{1}{kT} \Delta g_{\text{p}} = -\chi N_{\text{AB}} \phi_{\text{A}} (1 - \phi_{\text{A}}) + \chi o_{\text{p}} d_{\text{t}} v_{\text{c}}^{-1} + \ln \frac{d_{\text{t}}}{d_{\text{AB}}} + \beta^2 \left(\frac{d_{\text{AB}}}{R_0} \right)^2. \quad (4.133)$$

If we neglect the slowly varying logarithmic term, we obtain for the derivative

$$\frac{1}{kT} \frac{d\Delta g_{\text{p}}}{do_{\text{p}}} = \chi \frac{d_{\text{t}}}{v_{\text{c}}} - 2\beta^2 \frac{N_{\text{AB}}^2 v_{\text{c}}^2}{R_0^2} \frac{1}{o_{\text{p}}^3}. \quad (4.134)$$

The equilibrium value of o_{p} follows as

$$o_{\text{p}}^3 \propto 2 \frac{v_{\text{c}}^3}{R_0^2 d_{\text{t}} \chi} N_{\text{AB}}^2. \quad (4.135)$$

With

$$R_0^2 \propto v_{\text{c}}^{2/3} N_{\text{AB}} \quad (4.136)$$

we find

$$o_{\text{p}}^3 \propto \frac{v_{\text{c}}^{7/3}}{d_{\text{t}} \chi} N_{\text{AB}}. \quad (4.137)$$

Replacement of o_{p} by d_{AB} gives us the searched-for result

$$d_{\text{AB}}^3 = \frac{N_{\text{AB}}^3 v_{\text{c}}^3}{o_{\text{p}}^3} \propto \chi d_{\text{t}} v_{\text{c}}^{2/3} N_{\text{AB}}^2. \quad (4.138)$$

How does this result compare with experiments? Figure 4.30 depicts the data obtained for the samples of Fig. 4.28. Indeed, the agreement is perfect. The slope of the line in the double logarithmic plot exactly equals the predicted exponent $2/3$.

4.4.2 Pretransitional Phenomena

A characteristic property of polymer mixtures in the homogeneous phase is the increase of the concentration fluctuations associated with an approaching of the point of unmixing. A similar behavior is found for the homogeneous phase of block copolymers and a first example is given in Fig. 4.31. The figure

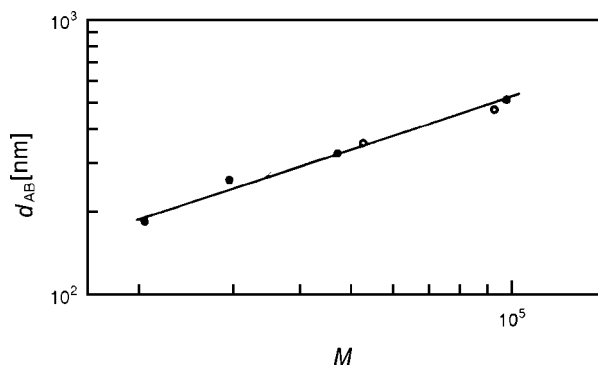


Fig. 4.30. Set of samples of Fig. 4.28. Molecular weight dependence of the layer spacing d_{AB}

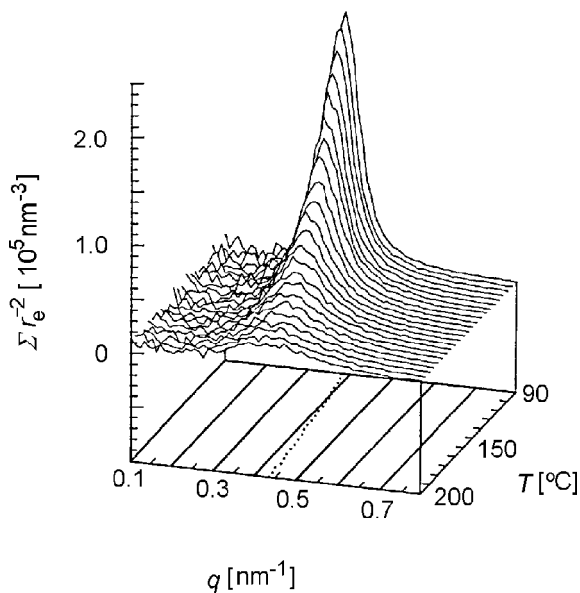


Fig. 4.31. SAXS curves measured for a polystyrene-*block*-polyisoprene ($M = 1.64 \times 10^4 \text{ g mol}^{-1}$, $\phi(\text{PS}) = 0.22$) in the homogeneous phase. The *dotted line* on the base indicates the temperature dependence of the peak position [31]

shows scattering functions measured for a PS-*block*-PI under variation of the temperature. The temperature of the transition to the microphase separated state is located around 85°C , just outside the temperature range of the plot. The curves exhibit a peak, with an intensity that strongly increases when the temperature moves towards the transition point.

The feature in common with the polymer mixtures is the intensity increase; however, we can also see a characteristic difference: The maximum of

the scattering intensity and the largest increase are now found for a finite scattering vector q_{\max} , rather than at $q = 0$. As scattering curves display the squared amplitudes of wave-like concentration fluctuations, the observation tells us that concentration fluctuations with wavevectors in the range $|\mathbf{k}| \approx q_{\max}$ are always large compared to all the others and show a particularly strong increase on approaching the phase transition. What do these observations mean? Clearly, they remind us of the pretransitional phenomena observed for second order phase transitions. There, the approach of the transition point is always associated with an unusual increase of certain fluctuations. Hence as it appears, one also finds properties in the homogeneous phase that have much in common with the behavior of critical systems, not only for polymer mixtures, but also for block copolymers.

The general shape of the scattering curve, showing a maximum at some q_{\max} and going to zero for $q \rightarrow 0$ is conceivable. As explained in Sect. A.3.2 of the Appendix, the forward scattering, $S(q \rightarrow 0)$, always relates to the fluctuation of the number of particles in a fixed macroscopic volume. In our case, this refers to both the A's and the B's. The strict coupling between A- and B-chains in the block copolymers completely suppresses number fluctuations on length scales that are large compared to the size of the block copolymer. The limiting behavior of the scattering function, $S(q \rightarrow 0) \rightarrow 0$, reflects just this fact. On the other hand, for large q 's, scattering of a block copolymer and of the corresponding polymer mixture composed of the decoupled blocks, must be identical because here only the internal correlations within the A- and B-chains are of importance. As a consequence, asymptotically the scattering law of ideal chains, $S(q) \propto 1/q^2$, shows up again. Hence, one expects an increase in the scattering intensity coming down from large q 's and when emanating from $q = 0$ as well. Both increases together produce a peak, located at a certain finite q_{\max} .

The increase of the intensity with decreasing temperature reflects a growing tendency for associations of the junction points accompanied by some short-ranged segregation. As long as this tendency is not too strong, this could possibly occur without affecting the chain conformations, i.e., chains could still maintain Gaussian properties. If one adopts this view, then the scattering function can be calculated explicitly. Leibler and others derived the following expression for the scattering function per structure unit S_c :

$$\frac{1}{S_c(q)} = \frac{1}{S_c^0(q)} - 2\chi \quad (4.139)$$

with $S_c^0(q)$, the scattering function in the athermal case, given by

$$\begin{aligned} S_c^0(q) N_{AB} S_D(R_0^2 q^2) &= \phi(1 - \phi) N_A N_B S_D(R_A^2 q^2) S_D(R_B^2 q^2) \\ &\quad - \frac{1}{4} [N_{AB} S_D(R_0^2 q^2) - \phi N_A S_D(R_A^2 q^2) \\ &\quad - (1 - \phi) N_B S_D(R_B^2 q^2)]^2 . \end{aligned} \quad (4.140)$$

R_0^2 denotes the mean squared end-to-end distance of the block copolymer, given by

$$R_0^2 = R_A^2 + R_B^2 . \quad (4.141)$$

With regard to the effect of χ , Eq. (4.139) is equivalent to Eq. (4.91). Indeed, the physical background of both equations is similar and they are obtained in an equal manner by an application of the random phase approximation (RPA). The interested reader can find the derivation in Sect. A.4.1 in the Appendix.

Importantly, Eq. (4.139) describes the effect of χ directly. It becomes very clear if one plots the inverse scattering function. Then changes in χ result in parallel shifts of the curves only. Figure 4.32 depicts the results of model calculations for a block copolymer with a volume fraction of polystyrene blocks of $\phi = 0.22$, in correspondence to the sample of Fig. 4.31. The curves were obtained for the indicated values of the product χN_{AB} .

Obviously the calculations represent the main features correctly: They yield a peak at a certain q_{\max} , which grows in intensity with increasing χ , i.e., with decreasing temperature. The important result comes up for $\chi N_{AB} = 21.4$. For this value we find a diverging intensity at the position of the peak, $S(q_{\max}) \rightarrow \infty$. This is exactly the signature of a critical point. We thus realize that the RPA equation formulates a critical transition with a continuous passage from the homogeneous to the ordered phase. When dealing with critical phenomena, it is always important to see the order parameter. Here it is

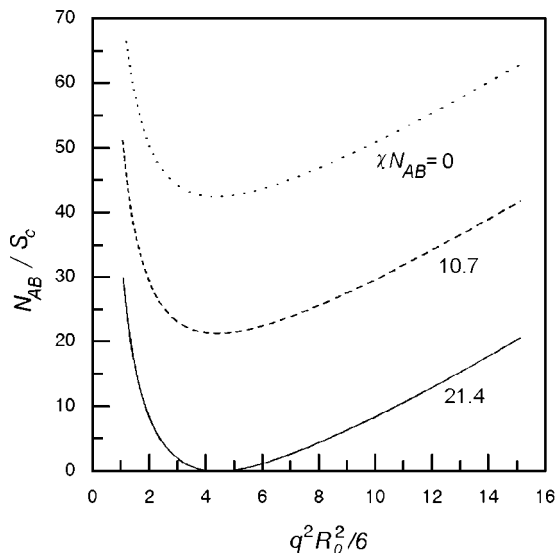


Fig. 4.32. Theoretical scattering functions of a block copolymer with $\phi = 0.22$, calculated for the indicated values of χN_{AB}

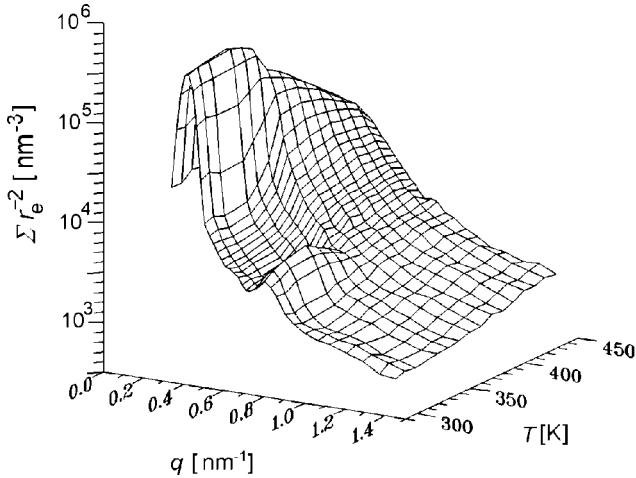


Fig. 4.33. SAXS curves measured for a PS-*block*-PI ($\phi(\text{PS}) = 0.44$, $M = 1.64 \times 10^4 \text{ g mol}^{-1}$) in the temperature range of the microphase separation. The transition occurs at $T_t = 362 \text{ K}$. Data from Stühn et al. [32]

of a peculiar nature. According to the observations it is associated with the amplitudes of the concentration waves with $|\mathbf{k}| = q_{\text{max}}$.

For $\phi = 0.22$, the critical point is reached for $N_{\text{AB}}\chi = 21.4$. With the aid of the RPA result, Eq. (4.140), one can calculate the critical values for all ϕ 's. In particular, for a symmetric block copolymer one obtains

$$\chi N_{\text{AB}} = 10.4 .$$

This is the lowest possible value and the one mentioned in Eq. (4.122).

In polymer mixtures, one calls the curve of points in the phase diagram, where $S(q = 0)$ apparently diverges, the spinodal. One can use the same notion for block copolymers and determine this curve in an equal manner by a linear extrapolation of scattering data measured in the homogeneous phase. We again denote this spinodal by $T_{\text{sp}}(\phi)$.

Regarding all these findings, one could speculate that the microphase separation might take place as a critical phase transition in the strict sense, at least for block copolymers with the critical composition associated with the lowest transition temperature. In fact, experiments that pass over the phase transition show that this is not true and they also point to other limitations of the RPA treatment. Figure 4.33 presents scattering curves obtained for a polystyrene-*block*-polyisoprene near to the critical composition ($\phi(\text{PS}) = 0.44$) in a temperature run through the transition point. As we can see, the transition is not continuous up to the end but is associated with the sudden appearance of two Bragg reflections. Hence, although the global behavior is dominated by the steady growth of the concentration fluctuations

typical for a critical behavior, finally there is a discontinuous step, which converts this transition into one of **weakly first order**.

There exists another weak point in the RPA equation. As a basic assumption, it implies that chains in the homogeneous phase maintain Gaussian statistical properties up to the transition point. The reality is different and this is not at all surprising: An increasing tendency for an association of the junction points also necessarily induces a stretching of chains, for the same steric reasons that in the microphase separated state lead to the specific power law Eq. (4.138). This tendency is shown by the data presented in Fig. 4.33 and, even more clearly, by the results depicted in Fig. 4.31. In both cases, q_{\max} shifts to smaller values with decreasing temperature, as is indicative for chain stretching.

The details of the transition are interesting. Figure 4.34 depicts the temperature dependence of the inverse peak intensity $I^{-1}(q_{\max})$.

Equation (4.139) predicts a dependence

$$S(q_{\max})^{-1} \propto \chi_{\text{sp}} - \chi, \quad (4.142)$$

or, assuming a purely enthalpic χ with $\chi \propto 1/T$ (Eq. (4.22)),

$$S(q_{\max})^{-1} \propto T_{\text{sp}}^{-1} - T^{-1}. \quad (4.143)$$

The findings, however, are different. We can see that the data follow a linear law only for temperatures further away from the transition point and then

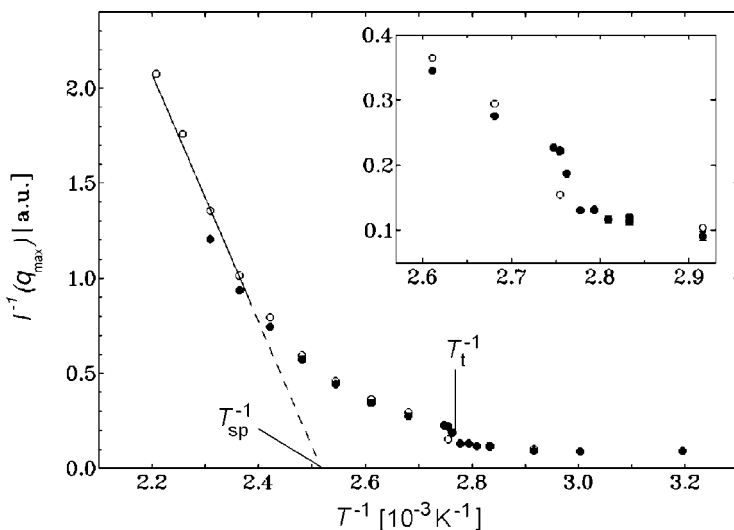


Fig. 4.34. Measurements shown in Fig. 4.33: Temperature dependence of the reciprocal peak intensity, showing deviations from the RPA predictions. The linear extrapolation determines the spinodal temperature

deviate towards higher values. The transition is retarded and does not take place until a temperature 35 K below the spinodal point is reached. According to theoretical explanations, which we cannot further elaborate on here, the phenomenon is due to a lowering of the Gibbs free energy, caused by the temporary short-range order associated with the fluctuations. The short-range order implies local segregations and thus a reduction of the number of AB-contacts, which in turn lowers the Gibbs free energy. We came across this effect earlier in the discussion of the causes of the energy lowering observed in computer simulations of low molar mass mixtures. Remember that there the effect exists only for low enough molar masses, since for high molar masses a short-range ordering becomes impossible. The same prerequisite holds for block copolymers and this is also formulated by the theories.

The short-range ordering is even more pronounced for asymmetric block-copolymers with $\phi_A \ll \phi_B$, which form in the microphase separated state

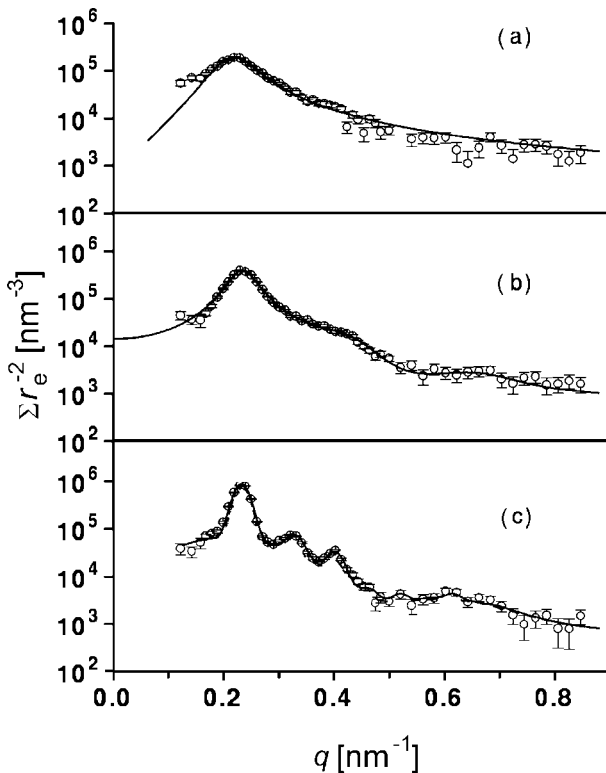


Fig. 4.35. PS-block-PI ($\phi(\text{PS}) = 0.11$): (a) Scattering curves referring to the homogeneously disordered state ($T = 458$ K), (b) the state of liquid-like order between spherical domains ($T = 413$ K), and (c) the bcc ordered state ($T = 318$ K). The *continuous lines* are fits of structural models for the different states of order. From Schwab and Stühn [33]

a bcc-lattice of spheres. The fluctuation-affected temperature range between T_{sp} and T_t is even larger and the short-range ordering here shows up quite clearly in the scattering curves. Figure 4.35(b) presents as an example the scattering curve obtained for polystyrene-*block*-polyisoprene ($\phi(\text{PS}) = 0.11$) at $T = 413 \text{ K}$ ($T_{sp} = 450 \text{ K}$, $T_t = 393 \text{ K}$) in a comparison with scattering curves measured above T_{sp} in the homogeneous phase (a) and in the microphase separated state respectively (c). Curve (c) shows the Bragg reflections of a bcc-lattice and the data points in (a) are perfectly reproduced by the RPA equation. Interestingly, the data points in (b) are well-represented by a curve calculated for the scattering of hard spheres with liquid-like ordering; the continuous line drawn through the data points was obtained using the Perkus–Yevick theory, which deals with such liquids. Hence, the ordering during cooling of this block copolymer proceeds in two steps, beginning with the formation of spherical domains that are then placed at the positions of a lattice. The second step takes place when the repulsive interaction reaches a critical value.

Further Reading

- K. Binder: *Spinodal Decomposition* in P. Haasen (Ed.): *Material Science and Technology*, Vol. 5 *Phase Transitions in Materials*, VCH Publishers, 1991
- P.J. Flory: *Principles of Polymer Chemistry*, Cornell University Press, 1953
- P.-G. de Gennes: *Scaling Concepts in Polymer Physics*, Cornell University Press, 1979
- I. Goodman: *Developments in Block Copolymers*, Vol. 1, Applied Science Publishers, 1982
- I. Goodman: *Developments in Block Copolymers*, Vol. 2, Applied Science Publishers, 1985
- I. Hamley: *Block Copolymers*, Oxford University Press, 1999
- T. Hashimoto: *Structure Formation in Polymer Systems by Spinodal Decomposition* in R.M. Ottenbrite, L.A. Utracki, S. Inoue (Eds.): *Current Topics in Polymer Science*, Vol. 2, Hanser, 1987
- D.R. Paul, S. Newman (Eds.): *Polymer Blends*, Vols. 1 and 2, Academic Press, 1978

The Semicrystalline State

At first it may seem questionable that polymers can set up a crystal at all, but after thinking about it a little it becomes clear how this can be accomplished. In principle, a periodic structure in three dimensions is obtained by choosing identical helical conformations for all polymers, orienting the helical axes of all chains parallel to each other and then packing the chains laterally in a regular manner. The scheme is applicable for all polymers, provided that they have a linear architecture and a regular chemical constitution. Hence, we may conclude that polymers have the potential to crystallize. As we shall see, they indeed form crystals, however, this occurs in a peculiar way.

For an understanding of the peculiarities, it is helpful to begin with a look at the crystallization behavior of simpler but related systems, namely that of **oligomers**. Oligomers are chain molecules of lower molar mass, prominent examples being the n -alkanes (C_nH_{2n+2}) or the perfluoro- n -alkanes (C_nF_{2n+2}). In contrast to polymers that always show a certain distribution in the molar mass of the chains, oligomers represent sharp fractions with a uniform molar mass. Oligomers readily crystallize and the crystal structures of various compounds have been determined by standard methods of X-ray crystallography. The results indicate that common principles exist in the composition of crystals; Fig. 5.1 depicts them in a schematic drawing: Crystals are composed of **stacked layers**, each layer being assembled of chain molecules with identical helical conformations. The endgroups of the molecules set up and occupy the **interfaces**. Oligomer molecules in the melt take on coiled conformations, just like polymers. In order to form a crystal, these chains have to be straightened and separated from each other and then attached in helical form onto the growing lateral crystal surface.

Can this building principle be transferred to polymers? At first, one cannot see any reason why it should not be employed for polymers in the same way, in case we have sharp fractions. For a polymer with uniform molar mass, the same type of crystal, composed of extended straight chains with the endgroups assembled in planar interfaces, could be formed in principle and it would again represent the equilibrium state with the lowest free energy. How-

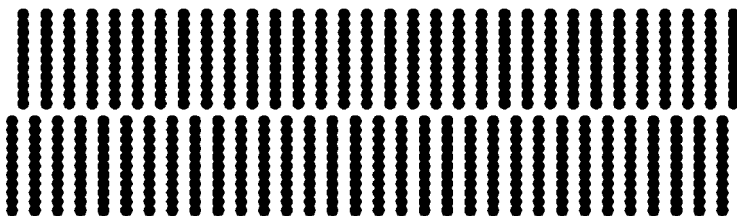


Fig. 5.1. Structure of an oligomer crystal. Schematic drawing showing two layers

ever, a serious problem now arises, quite independently of the unrealistic assumption of a uniform molar mass. Starting from a melt of coiled, mutually interpenetrating macromolecules it is just impossible to reach this ideal crystalline state. The required complete disentangling would need a too long time as it is associated with an extremely high entropic activation barrier. What happens instead? The way in which polymer systems react under these conditions is that cooling a melt below the equilibrium melting point produces structures that are only crystalline in parts. One observes layer-like crystallites that are separated by disordered regions, thus setting up a **lamellar two-phase structure**. That the crystallites formed have the shape of layers is not surprising considering the principles governing the crystallization of oligomers. There, the formation of the interfaces can be regarded as a natural way to deal with the endgroups, which cannot be incorporated into the single layers. Similarly, polymer crystallization requires that the entanglements present in the melt be dealt with and disposed of, as the large majority of them cannot be resolved and eliminated within the given time. Adopting this view, we can address the basic mechanism leading to the formation of two-phase structures in crystallizable polymer systems as a **separation process**. Crystallization occurs together with a preceding unmixing, whereby sequences that can be stretched and incorporated into a growing crystal are separated from chain parts near entanglements that can only be removed and shifted into the **amorphous regions**. To be sure, not only entanglements constitute the non-crystallizable chain parts, but endgroups, chemical perturbations like co-units and short chain branches, or stereo defects that oppose a transformation into the regular helical form as well. They all become accumulated in the amorphous parts of a **partially crystalline** or **semicrystalline** polymer.

In the previous chapter, we discussed liquid polymer systems. These exist in specific states selected by the laws of equilibrium thermodynamics. The rules that control structure formation during crystallization are different and this is an important point: Structure formation is here governed by **kinetic criteria** rather than by equilibrium thermodynamics. What does this mean? Indeed, here we encounter a new criterion: The structure that develops at a given temperature is that with the **maximum rate of development** rather than that with the lowest free energy. As a consequence, treatment of

the crystallization behavior of polymers requires considerations about pathways and kinetics of the transition. Thermodynamics is still necessary for the description of the driving forces, but it now constitutes only a partial aspect of the problem; time and efficiency come into play as decisive factors.

5.1 Structure Characteristics

Being kinetically controlled, structures of partially crystalline samples are always strongly affected by the processing and show a memory of the thermal history, i.e. temperatures and times of crystallization, cooling rates, etc. A first requirement for the analysis are experiments enabling a characterization of the evolving structures. In this section, we will deal with some of the applied techniques and main observations.

5.1.1 Morphological Elements

Semicrystalline polymers exhibit different characteristic features on different length scales. Proceeding from low to high resolutions, we begin with the morphological elements in the μm – mm range, as observed in a **polarizing optical microscope**. Figure 5.2 gives a typical example. It shows optical micrographs obtained for a sample of poly(L-lactic acid) (PLLA) that has been cooled from the melt to a temperature where crystallization occurs. We observe spherical objects, so-called **spherulites**, which appear somewhere in the view field and then grow in size. Correspondingly, the process is addressed as a crystallization by **nucleation and growth** of spherulites. Inspection shows that the spherulites usually grow with a constant rate up to the point where they touch each other. For two spherulites that were nucleated at the same time, the area of contact is planar, if starting times are different, the boundary is bent. Finally, the whole volume is covered by bound spherulites. Their final sizes depend on the nucleation density and can vary over a large range, from several 100 nm up to some cm.

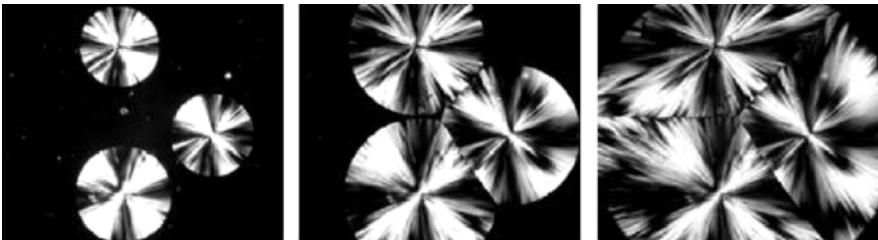


Fig. 5.2. Growing spherulites observed during the crystallization of PLLA in an optical microscope (polarized light, crossed nicols) (by Cho, FMF, Universität Freiburg, 2006)

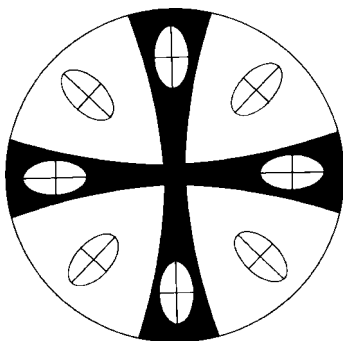


Fig. 5.3. Ordering of the indicatrices in a spherulite and the resulting Maltese cross extinction pattern as observed between cross nicols. The orientation of the Maltese cross coincides with the directions of polarizer and analyzer

Spherulites are optically anisotropic objects. As in the example of Fig. 5.2, in many cases one observes a **Maltese cross** between crossed nicols. The appearance of a Maltese cross is indicative of a specific arrangement of the optical indicatrices and Fig. 5.3 represents the type of order. The basic property is a systematic variation of the orientation of the indicatrices. As indicated in the drawing, one of the axes is directed at each point along the radius vector. The cause of the birefringence is obvious: It originates from the optical anisotropy of the stretched polymer chains in the crystallites. Findings directly tell us that the chains in the crystallites must be oriented either parallel or perpendicular to the spherulite radius. In fact, a closer examination based on a determination of the sign of the birefringence shows that the chain orientation is always perpendicular to the radius vector.

The optical observations cannot resolve the crystalline-amorphous structure. Observation of the crystallites requires methods that provide an analysis in the 10–100 nm range. **Electron microscopy** (EM) and **atomic force microscopy** (AFM) are particularly suited for this purpose. Figure 5.4 shows as one example the surface of a partially crystalline polyethylene (PE), as it becomes reproduced in the electron microscope when using a carbon film replica technique. The picture of the surface resembles a landscape with many terraces. These obviously result from cuts through stacks of laterally extended, slightly curved crystalline lamellae, which have thicknesses in the order of 10 nm.

Figure 5.5 presents as another example the AFM image of the surface of a crystallized sample of poly(L-lactic acid). Using the **tapping technique**, during the scan the vibrating AFM tip probes the varying local viscoelastic properties. The curved edges of stacked flat lying lamellar crystallites are clearly apparent.

More insight into the internal structure of the stacks of lamellae follows from electron microscopic studies on ultra-thin slices if these are stained.

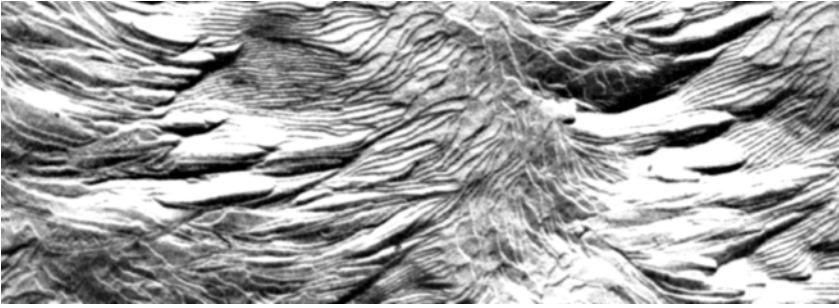


Fig. 5.4. EM image of a carbon film replica of a surface of PE. Picture obtained by Eppe and Fischer [34]

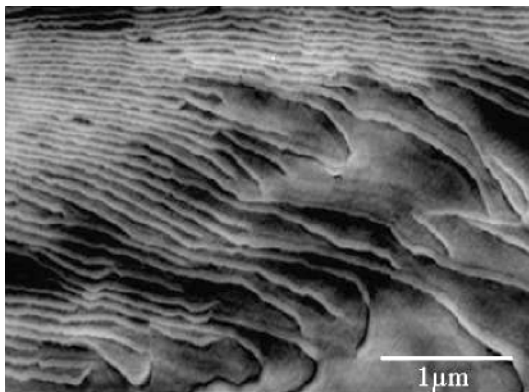


Fig. 5.5. AFM tapping mode image of the surface of a sample of PLLA (obtained by Cho, FMF, Universität Freiburg, 2006)

Figure 5.6 shows a typical picture of polyethylene being stained by OsO_4 . Because it is rejected by the crystallites, the staining agent only enters the disordered regions. The image is due to the different absorption of the electron beam, which is high in the Os-containing amorphous regions and low for the crystallites. The white lines therefore correspond to layer-like polyethylene crystallites, which are separated by amorphous regions given by the dark parts. More accurately, only those crystallites are observed that happen to be oriented with their surface perpendicular to the slice surfaces so that the electron can pass through with minor absorption.

The presented three micrographs are typical and they indeed exemplify the basic structural principle in the morphology of semicrystalline polymers: These are built up as a two-phase structure, and are composed of layer-like crystallites that are separated by amorphous regions.

If we now regard both, the essentially planar structure in the 10 nm range and the isotropic spherulites observed in the μm range, we may wonder, how these two can fit together. Figure 5.7 shows how this is accomplished and how

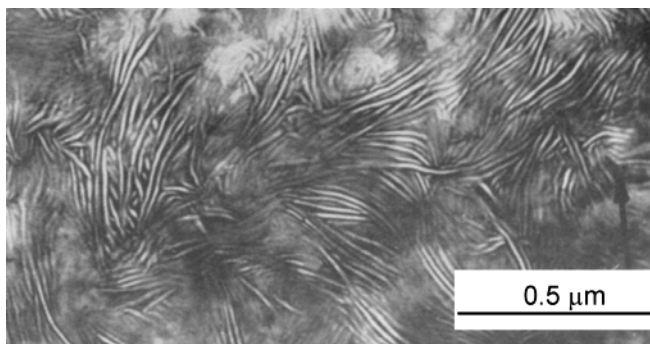


Fig. 5.6. Ultra-thin slice of a PE sample stained with OsO_4 . Electron micrograph obtained by Kanig [35]

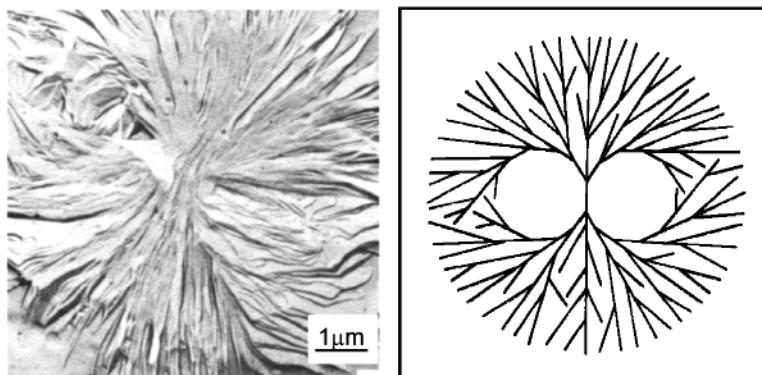


Fig. 5.7. Central sheaf-like part observed at an early stage of development of a spherulite of iPS. Electron micrograph obtained by Vaughan and Bassett [36] (*left*). Schematic drawing showing branching and splaying in the fully developed spherulite (*right*)

the stacks of layers set up and fill the space of the spherulites. The left-hand side depicts an electron micrograph of the center of a spherulite of isotactic polystyrene (iPS) at an early stage of development. The center is sheaf-like and formed by an aggregate of layers. On further growth, more layers are created and finally a stable spherical growth surface is established.

The right-hand side of Fig. 5.7 shows the principle that has to be obeyed during growth. In order to keep the increasing surface of the spherulite filled with layers, **branching** and **splaying** is a necessary requirement. The orientational distribution of the crystallites within a developed spherulite, that is to say the internal **texture**, is well-determined. Away from the central sheaf-like region the surface normal of the crystalline layers is always directed perpendicular to the radius vector. As we deduced from the birefringence properties

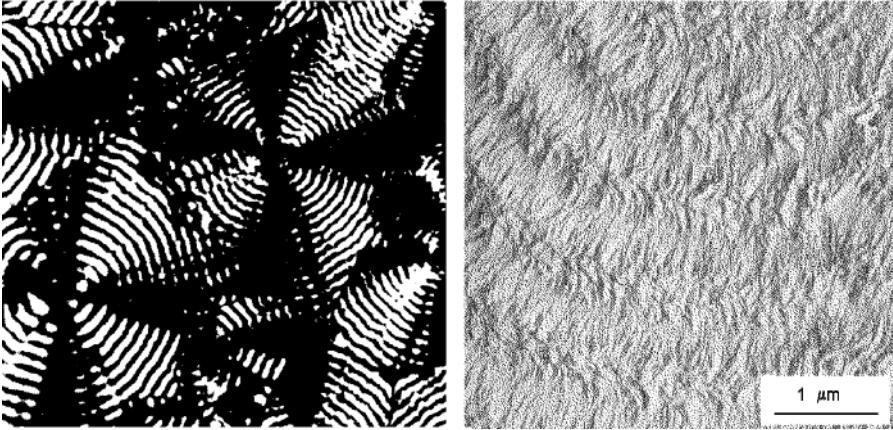


Fig. 5.8. Banded spherulites of PE. Optical micrographs showing a regular sequence of concentric rings (polarized light, crossed nicols; *left*) and electron micrographs of a surface that cuts through a spherulite (obtained by Vaughan and Bassett [36]; *right*)

of the spherulites, the same holds for the direction of the crystalline chains. Chain direction and surface normal must not be identical, but the enclosed angle is usually small.

Quite often, **banded spherulites** are observed. Figure 5.8 presents such a case, as given again by a sample of polyethylene. As shown by the optical micrograph on the left, here, in addition to the Maltese cross, one finds light extinctions along circles in a periodic manner. The observation indicates a regular rotation of the chain direction and the layer normal about the radius vector. This is confirmed by electron microscopic investigations, for example, the micrograph shown on the right-hand side. Both experiments tell us that, on μm length scales, the crystallites are twisted and that this occurs strictly periodically. The coherence of this texture throughout the whole spherulite is astonishing; the orientations of all crystallites are well-determined and thus exactly correlated.

The crystalline lamellae have a **granular substructure**. Evidence is provided by the widths of the $hk0$ -Bragg reflections in wide angle X-ray scattering (WAXS) patterns, which give the inverse of the coherence length along the normal onto the respective lattice plane (see Eq. (5.23)). For polymers, reflections are much broader than in the case of low molar mass crystals and generally indicate coherence lengths of several to some tens of nanometers only. This small coherence length is to be identified with the extension of crystal blocks that compose the lamella. They show up directly in electron micrographs when a staining agent penetrates into the block boundaries. Figure 5.9 presents as an example electron micrographs obtained for a sample of

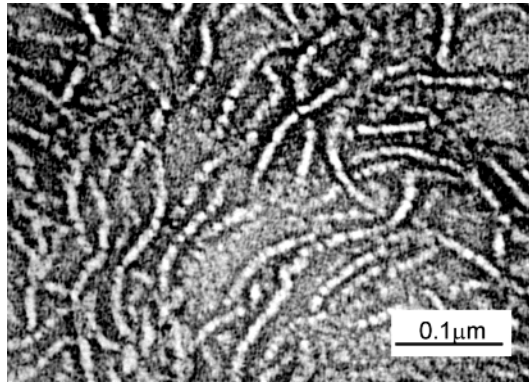


Fig. 5.9. Sample of LDPE with a crystallinity $\phi_c \approx 0.5$. EM micrographs of a stained ultra-thin section obtained by Michler [37]. Crystallites are composed of mosaic blocks

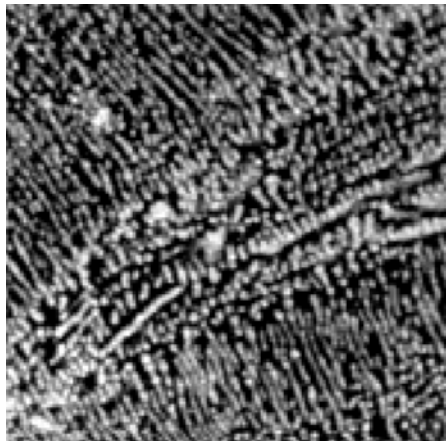


Fig. 5.10. Sample of iPP: AFM tapping mode image showing a granular substructure of the edge-on oriented crystal lamellae (1 μm scan). From Magonov et al. [38]

polyethylene (of low density, LDPE). The granular structure is clearly apparent, and as we can see, the lateral extension of the blocks is comparable to the crystallite thickness.

There are cases in which the granular substructure is also seen in AFM tapping mode images. The example presented in Fig. 5.10 was obtained for a sample of isotactic polypropylene (iPP).

The blocky substructure is fundamental for the deformation properties of semicrystalline polymers. A main yielding mechanism is block sliding, which sets in in a cooperative manner at the yield point (see Figs. 10.13 and 10.14 in Sect. 10.1). The strain-controlled, comparatively simple deformation properties of semicrystalline polymers are mainly based on the many degrees of

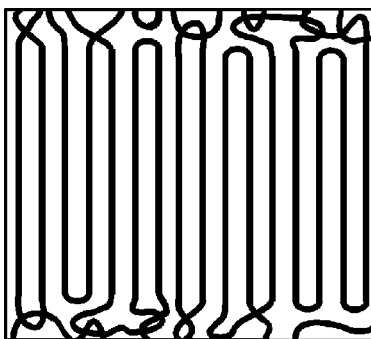


Fig. 5.11. Surface regions of a crystal in a semicrystalline polymer

freedom offered by block sliding; internally stiff crystal layers would cause a quite different, much more complex deformation behavior.

How do the chain conformation and the packing change in the transition from the crystal into the surrounding melt? The sketch in Fig. 5.11 presents a view known as the **switchboard model**. When a crystal develops, entanglements are shifted to the surface and loops that bring some of the chains back into the crystal form. In the literature, this interface is addressed as the **fold surface** of the crystal, because it can be anticipated that it includes a higher number of sharp folds. These reduce effectively the **chain flux** given by the number of chains passing through a unit area. Since the crossing of an area parallel to the fold surface is perpendicular within the crystal but mostly oblique in the melt, the chain flux has to be reduced. Computer simulations show that this reduction does not take place abruptly but extends over a certain transition zone.

5.1.2 Structure Parameters

The polymer crystalline state is composed of chains in that helical conformation which corresponds to the minimum of the intramolecular conformational energy. The interaction energy between neighboring chains determines the packing mode but leaves the chain conformation unchanged. The crystallographic lattice structure follows from both the helix conformation and the packing. Figure 5.12 presents as an example the structure of the unit cell of polyethylene. Two chains with all-trans conformation pass through the cell, with their C–C planes in nearly perpendicular orientation. One unit-cell then includes two C_2H_4 groups.

Structure analysis for polymer crystallites, i.e., the determination of the edge lengths and angles of the unit cell and of the positions of all atoms therein, is carried out as for low molar mass compounds first of all by X-ray scattering experiments. The conventional straightforward methods of X-ray structure analysis, however, cannot be applied since these require single crystals, which

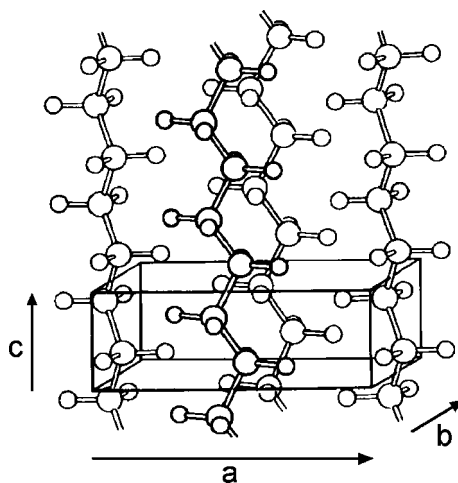


Fig. 5.12. Unit cell of PE crystallites: Orthorhombic symmetry, $a = 7.42 \text{ \AA}$, $b = 4.95 \text{ \AA}$, $c = 2.55 \text{ \AA}$. Each cell is occupied by two C_2H_4 groups. Structure determination by Bunn [39]

are unavailable for polymers. As the best choice under the given conditions, analysis then is based on the evaluation of scattering patterns obtained for fibers. In fibers or oriented films, crystallites can exhibit a high degree of orientation, with a virtually uniform direction for one of the crystallographic axes. Figure 5.13 shows, as an example, the X-ray scattering pattern obtained for an uniaxially oriented film of poly(tetrafluoroethylene) (PTFE).

Bragg reflections in such a **fiber diagram** are generally arranged along **layer-lines** that are oriented perpendicular to the drawing direction. The latter coincides with the chain direction in the crystallites. To carry out a structure analysis, all reflections have to be assigned to lattice planes, i.e., associated with the respective Miller indices. Although the assignment is facilitated when using fiber diagrams rather than an isotropic scattering pattern, it is usually not straightforwardly accomplished and then requires trial-and-error methods.

Even if one solves the indexing problem and then proceeds with the analysis by an evaluation of measured reflection intensities, one cannot expect to achieve an accuracy in the crystal structure data that would be comparable to those of low molar mass compounds. This is not only a result of the lack of single crystals, but also represents a principal property: In small crystallites, as they are found in partially crystalline polymers, lattice constants can be affected by their size. Furthermore, disorder is more frequently found as in low molar mass systems, in particular, in the region near the fold surface.

A semicrystalline polymeric solid has a certain degree of crystallization. There are two slightly different choices for the definition of this **crystallinity** and the selection depends on the method of determination. Consider, for ex-

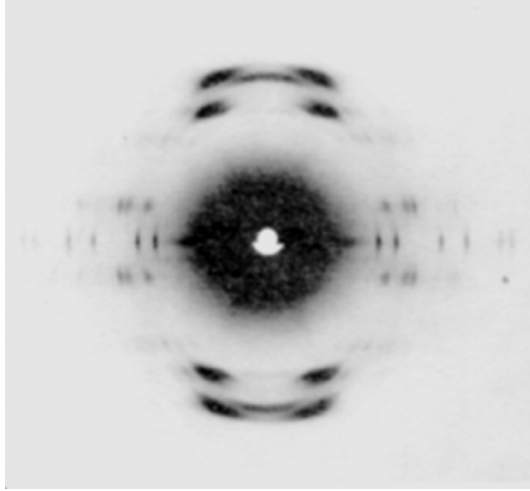


Fig. 5.13. Fiber diagram obtained for a sample of PTFE with uniaial orientation in an X-ray scattering experiment at 15 °C [40]

ample, a measurement of the density of a sample. For a two-phase structure the total mass is given by

$$\mathcal{V}\rho = \mathcal{V}_a\rho_a + \mathcal{V}_c\rho_c . \quad (5.1)$$

Here, \mathcal{V}_a and \mathcal{V}_c denote the volumes occupied by the amorphous and the crystalline parts and \mathcal{V} is the total volume; ρ_a , ρ_c and ρ give the respective densities. As one possibility, the crystallinity ϕ_c can be identified with the **volume fraction** of the crystalline material, i.e.,

$$\phi_c = \frac{\mathcal{V}_c}{\mathcal{V}} . \quad (5.2)$$

Using Eq. (5.1) ϕ_c follows as

$$\phi_c = \frac{\rho - \rho_a}{\rho_c - \rho_a} . \quad (5.3)$$

In order to apply Eq. (5.3), the densities of the crystalline and the amorphous phase have to be known. There is no problem with ρ_c , as this can be derived from the lattice constants. The determination of ρ_a is less direct. Usually it is obtained by an extrapolation of the values measured in the melt, with the assumption of a constant expansion coefficient.

The most often used method for a determination of the crystallinity is a measurement of the heat of fusion, $\Delta\mathcal{H}_f$, of a sample. This leads us to the other possibility, namely to use the **weight fraction** of the crystalline material. It follows from $\Delta\mathcal{H}_f$ as

$$\phi_c = \frac{\Delta\mathcal{H}_f}{\Delta\mathcal{H}_f(\phi_c = 1)} . \quad (5.4)$$

The prerequisite is a knowledge of the heat of fusion of a fully crystalline sample $\Delta\mathcal{H}_f$ ($\phi_c = 1$). Since a fully crystalline sample normally cannot be prepared, extrapolation methods have to be used. If a homogeneous series of oligomers is available, then one can measure their heats of fusion and subsequently carry out an extrapolation to the limit of an infinite molar mass, either empirically, or better, on the basis of a theoretical expression. Another feasible procedure is a combination of calorimetric and density measurements for samples with different crystallinity, i.e., a measurement of $\Delta\mathcal{H}_f$ as a function of the density. Then a series of data can be extrapolated to $\rho = \rho_c$. Equation (5.4) neglects the effect of the crystallite surfaces. As will be discussed later in this chapter, the surface free energy results in a decrease in the melting points and also somewhat reduces the heat of fusion. These effects can be accounted for, but in practice they are mostly ignored.

Crystallinity values should not be regarded as quantities of high accuracy, for various reasons. They are introduced assuming a two-phase structure with well-defined properties of the single phases. Actually this is not strictly true, as properties of both the crystallites and the amorphous regions may vary between different samples, or even within a sample, and the transition is not sharp. Therefore, when comparing crystallinity values from different measurements, one should always be aware of possible slight variations, in addition to the necessary distinction between volume and weight based values.

Representing a bulk property, the crystallinity tells us nothing about the characteristic lengths of the partially crystalline structure. Approximate values can be taken from the electron micrographs but, in order to obtain accurate data, X-ray scattering experiments have to be used. As typical length scales of partially crystalline structures are in the order of 10 nm, the associated scattering curves are found in the small angle range. Figure 5.14 shows as an example some scattering functions $\Sigma(q)$ (see Eqs. (A.3) and (A.4) in the Appendix) measured for a sample of polyethylene. Data were obtained for a series of different temperatures, beginning at the temperature of crystallization coming from the melt of 125 °C and continuing down to 31 °C during a stepwise cooling. The general shape of the curves corresponds to the morphological features appearing in the electron micrographs. The stacks of layer-like crystallites show a periodicity, although not in the sense of a strict long-range order. This quasi-periodicity, named **long spacing**, becomes reflected in the peak. By applying Bragg's law one can derive from the peak position q_{\max} the long spacing d_{ac} :

$$d_{\text{ac}} = \frac{2\pi}{q_{\max}} . \quad (5.5)$$

The temperature-dependent changes in the intensity and in the shape of the scattering curves in the figure are due to both changes in the electron densities of the crystallites and the amorphous regions as well as continuous modifications in the structure to be discussed later in this chapter.

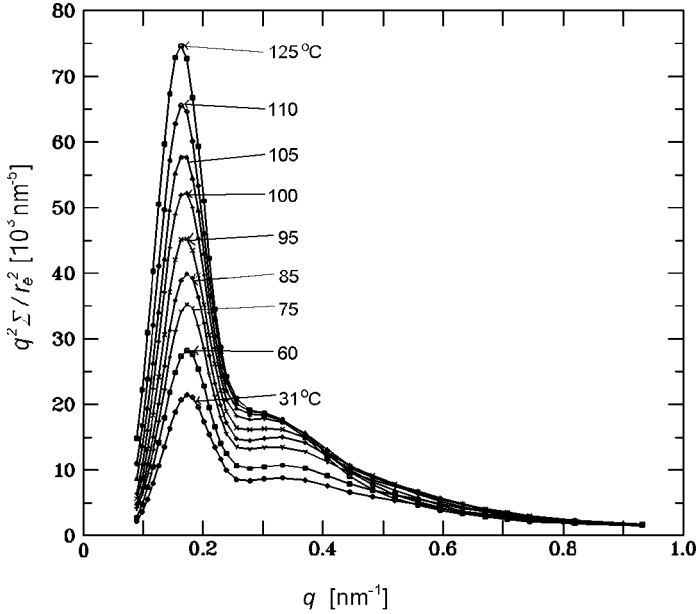


Fig. 5.14. SAXS curves measured for a sample of PE after completion of a crystallization at 125 °C and at the indicated temperatures during a subsequent cooling [41], [42]

As explained in detail in Sect. A.4.2 in the Appendix, it is possible to evaluate the **small angle X-ray scattering** (SAXS) curves in greater detail. A Fourier transformation of the scattering function $\Sigma(q)$ yields the **electron density correlation function**

$$K(z) = \langle (c_e(0) - \langle c_e \rangle) \cdot (c_e(z) - \langle c_e \rangle) \rangle. \quad (5.6)$$

Here $c_e(z)$ denotes the electron density distribution along the stack normal. $K(z)$ possesses peculiar properties that can be directly used for a structure characterization. They are given on the left-hand side of Fig. 5.15 in a schematic drawing.

Included are:

- the **inner surface** O_{ac} , i.e., the area of interface between crystalline and amorphous regions (per unit volume);
- the **electron density difference** between the crystalline and amorphous parts $\Delta c_e = c_{e,c} - c_{e,a}$;
- the long spacing d_{ac} ;
- depending on the crystallinity, either the thickness d_c of the crystallites (for $\phi_c < 0.5$) or the thickness of the disordered regions d_a (for $\phi_c > 0.5$).

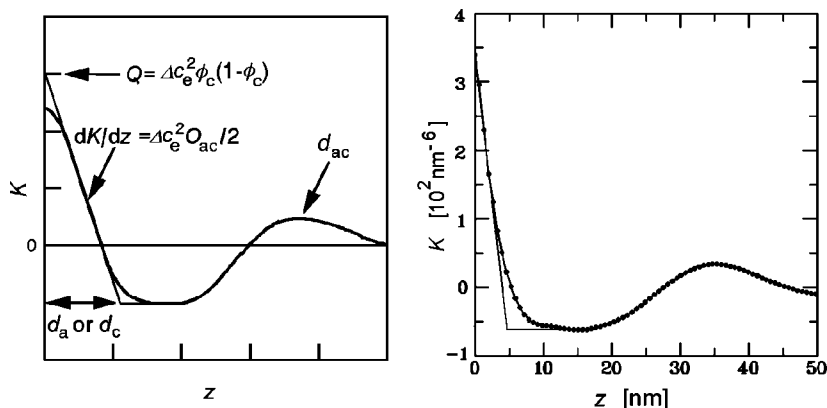


Fig. 5.15. Schematic drawing showing the basic properties of the electron density correlation function $K(z)$ associated with a stack of crystalline and amorphous layers (*left*). $K(z)$ derived from the scattering curve of PE for 31 °C in Fig. 5.14, giving $\phi_c = 0.85$, $O_{ac} = 0.065 \text{ nm}^{-1}$, $d_a = 4.6 \text{ nm}$, $\Delta c_e = 52 \text{ nm}^{-3}$, $d_{ac} = 34 \text{ nm}$ (*right*)

On the right-hand side of Fig. 5.15, the correlation function deduced from one of the scattering curves in Fig. 5.14 is presented as an example. The derived parameters have typical values.

Evaluation of the small angle X-ray scattering curves assumes a two-phase structure. This is not strictly valid as the interfaces are not sharp; the presence of the crystallites affects the surrounding melt. The limited resolving power of small angle X-ray scattering experiments does not allow detection of these changes. These show up when techniques that probe mobilities and the conformational statistics of the chain molecules rather than densities are used, the most prominent ones being Raman and NMR spectroscopy. Here, we consider two examples: a Raman spectroscopic experiment on polyethylene and an NMR experiment on poly(ϵ -caprolactone)(P ϵ CL).

The **Raman spectrum** of a polymer is sensitive to the chain conformation since the latter determines the vibrational properties. One expects characteristic differences between a crystalline sequence with a unique regular helical conformation and the wide distribution of different conformations typical for a melt. Figure 5.16 displays spectra measured for polyethylene, in part (a) the spectrum of a crystal, measured for a specially prepared sample of ‘extended chain’ polyethylene with a crystallinity close to 100%, and in part (b) the spectrum of the melt. The third spectrum (part (c)) was obtained for a partially crystalline sample. The spectrum of the crystal shows sharp bands because restrictive selection rules apply; in order to be Raman active, all monomers have to move in-phase. This contrasts with the disordered liquid state, where in the absence of a structural symmetry, selection rules are relaxed and the Raman bands are broadened. On first view, the spectrum of the semicrystalline sample looks like a superposition of the elementary spectra (a) and (b); however,

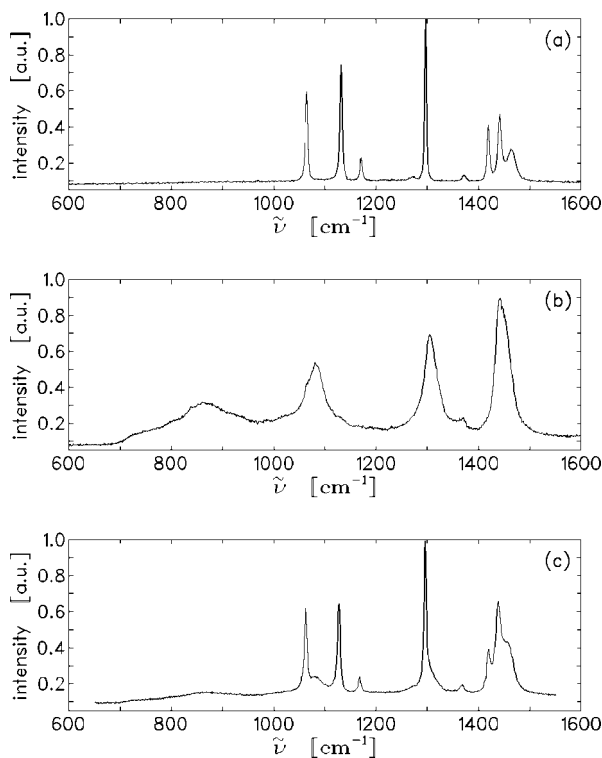


Fig. 5.16. Raman spectra measured for different states of order of PE: extended chain sample with a crystallinity close to 100% (a); melt (b); partially crystalline sample (c) [43]

a closer look shows significant deviations. The spectral range between 1400 and 1500 cm^{-1} is assigned to the CH_2 scissor vibrations with a deformation of the H-C-H valence angle. In the crystalline state two C_2H_4 groups occupy a unit cell (Fig. 5.12). As a result the scissor vibration splits into a doublet, corresponding to the frequency difference between in-phase and anti-phase vibrations of the two groups. The two sharp lines located at 1416 and 1440 cm^{-1} represent this doublet. In the crystalline sample they have equal intensities, but in the semicrystalline state this is no longer found. The findings can be interpreted as being indicative of the occurrence of regions in a semicrystalline sample where chain sequences are still in the all-trans conformation but not packed in an orthorhombic unit cell. Then the splitting disappears and only the band at 1440 cm^{-1} remains, as can be derived from the spectrum of the triclinic modification of n -alkanes with only one chain per unit cell. Superposition results in the observed enhancement of the 1440 cm^{-1} band. The Raman spectrum of a partially crystalline sample thus includes more contributions than just one corresponding to the orthorhombic crystalline state and

a second one corresponding to the pure melt. It appears that this third contribution originates from regions that, although being disordered, still include an enhanced fraction of all-trans sequences. The transition region between crystals and the melt may well have such properties. A decomposition of a given spectrum in three parts can be straightforwardly accomplished and yields the respective fractions. In the case of the example given in Fig. 5.16c, obtained for a polyethylene with high molar mass ($M > 10^6 \text{ g mol}^{-1}$), the following values were obtained:

- orthorhombic crystalline phase 66%,
- transition zones 13%,
- melt-like amorphous phase 21%.

Generally speaking, **nuclear magnetic resonance spectroscopy** (NMR) provides information on the local state of order and the molecular dynamics in a solid or liquid by probing it with spin carrying nuclei. Protons (^1H), deuterium (^2H) and the carbon isotope ^{13}C (the major carbon isotope ^{12}C has zero spin) are particularly suited for studies. There is a large variety of NMR experiments, distinguished by the way the spins are excited and the manner in which the resulting magnetization is further modified and probed. One of the basic experiments are measurements of the decay of the transverse magnetization produced by 90° pulse, known as **free induction decay** (FID). They can be used for studies of semicrystalline polymers, in particular applied in investigations of the crystallization kinetics. As a typical example Fig. 5.17 reproduces on the left-hand side a set of ^1H FID curves, $A(t)$, registered during the crystallization of poly(ϵ -caprolactone) at 50°C .

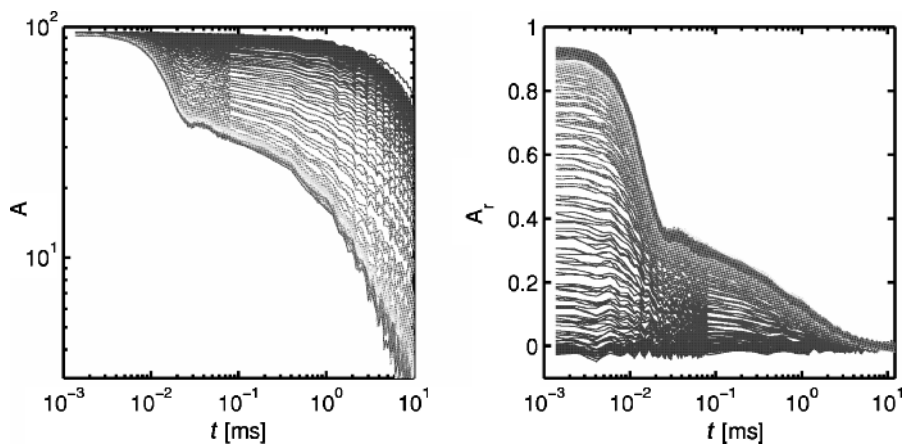


Fig. 5.17. P ϵ CL, crystallization at 51°C studied by time-dependent ^1H NMR. Measured FIDs $A(t)$ (*left*) and extracted component $A_r(t)$ associated with protons with reduced mobility (*right*) [44]

The uppermost curves are those obtained at the beginning when the sample is still in the molten state and the lowest curves are those measured at the end when the crystallization process is completed. One observes a continuous change in the curve shape. The main feature is the development of a first rapid decay of the FID amplitude completed at about $30\ \mu\text{s}$. The decay is to be associated with protons in the crystallites that experience strong dipole–dipole interactions. The FID measurement ends at around 0.5 s; then the amplitude of the FID signal has dropped to vanishingly small values. The log–log representation of the FIDs shows that in the asymptotic limit of long decay times one always finds the signal of the melt, reduced in intensity. The reduction factor directly yields the mass fraction of protons that are still in melt-like surroundings. The signal that remains after a subtraction of the melt-like component, denoted by $A_r(t)$, is to be assigned to all protons that have changed their local mobility, i.e., both those included in the crystals and those in amorphous regions in the vicinity of crystal surfaces. The right-hand side of Fig. 5.17 shows these signals throughout the crystallization process. Splitting them up into contributions from the crystallites and a remaining part yields the respective weight fractions. Here, the following values were obtained at the end of the crystallization process:

- The melt-like fraction drops to 10%,
- the amorphous component with a reduced mobility ends at 35%,
- and the crystalline part amounts to 55%.

5.2 Kinetics of Crystallization and Melting

When a low molar mass fluid is cooled, it crystallizes immediately when the equilibrium melting point is reached. A polymer melt behaves differently. Crystallization starts only at a considerable supercooling, at first slowly and then accelerating on further decreasing the temperature. Under practical circumstances the solidification process thus extends over a large temperature range. Samples crystallized in this manner have a non-uniform inner structure and cannot be used for basic studies. Necessary for this are crystallization experiments under isothermal conditions, for crystallization temperatures that cover the whole range of temperatures from near the equilibrium melting point to the glass transition temperature. The times required for the crystallization varies therein in a characteristic manner; Fig. 5.18 presents some examples. It shows the temperature dependencies of the spherulite growth rates of *i*-polystyrene, poly(ϵ -caprolactam) (nylon6) and poly(tetramethyl-*p*-silpheylylene siloxane) (TMPS). We observe a maximum for all three polymers, with rapid drops on both sides towards the melting points at high temperatures and the glass transition at low temperatures.

In order to characterize the crystallization properties of a given polymer system, experiments have to be carried out with the objective to determine

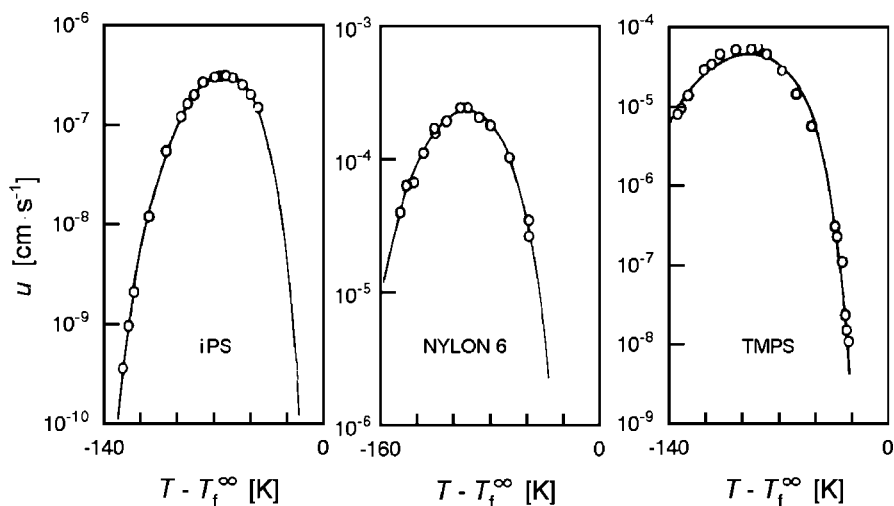


Fig. 5.18. Temperature dependence of the radial growth rate u of spherulites of iPS (*left*), nylon6 (*center*) and TMPS (*right*). Data from different authors taken from [45]

the parameters of the developing structure, i.e., the crystal thickness, the long spacing, or the crystallinity, in dependence on the crystallization temperature. Polymers of the same basic type may vary in their chemical regularity, they often include stereo defects or co-units, or in the molar mass. It is important to know the influence of these factors on the crystallization behavior.

As in low molar mass systems crystal formation in a polymer melt starts with a **nucleation** step. Thermal fluctuations form in the melt **embryos**, i.e., particles with an enhanced inner order. If the size of an embryo surpasses a critical value it turns into the **nucleus** of a growing crystal; smaller embryos disappear again. It is possible to directly observe this process with an atomic force microscope, as is shown in Fig. 5.19 for a crystallizing polyether (short name BA-C8, the material crystallizes slowly at room temperature). The encircled dot in the left-hand picture is a nucleus that subsequently develops into a single lamellar crystallite.

Nucleation is a bulk property to be described by a rate, τ_{nuc}^{-1} , per unit volume. Experiments on ensembles of μm sized melt droplets allow a determination when the **nucleation time** τ_{nuc} is much longer than the time required by the expanding crystallite to cover the whole droplet. Figure 5.20 shows results of such an experiment conducted for poly(ethylene oxide) (PEO). As expected for a bulk property, the observations on ensembles of droplets with various volumes \mathcal{V} show that

$$\tau_{\text{nuc}} \propto \mathcal{V}^{-1}. \quad (5.7)$$

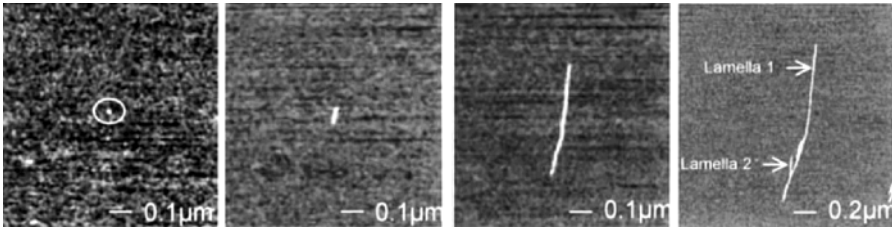


Fig. 5.19. BA-C8 crystallizing at 22 °C. AFM tapping mode phase images of a nucleus (*left*), one growing primary lamella and the development of branches (*right*). From Chan et al. [46]. Copyright (2002) American Chemical Society

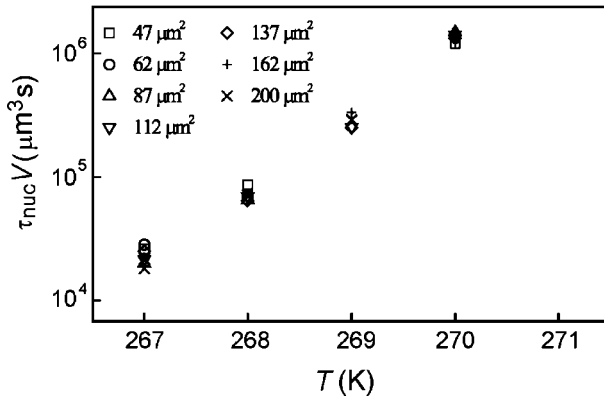


Fig. 5.20. Nucleation times τ_{nuc} observed for PEO droplets of various sizes (base areas) in the temperature range 267–270 K. From Massa and Dalnoki-Veress [47]

Data indicate as a further characteristic feature that τ_{nuc} changes exponentially with temperature. This finding demonstrates that the nucleation step is an activated process associated with a free energy barrier to be surmounted.

As can be seen in the further images of Fig. 5.19, the growing lamella keeps a constant thickness. Crystal growth takes place in the lateral direction only, i.e., it is two-dimensional. There is no growth in chain direction perpendicular to the layer surface. A widening in this direction is, however, achieved by splaying processes and these are necessary for setting up a spherulite. The right-hand image of Fig. 5.19 shows the development of a first branch out of the primary lamella, found here when the lamellar crystallite has reached a length of about 1 μm . The result of a repetition of branching shows up in Fig. 5.21. The object shown is on the way to ending up as a spherulite. As a characteristic feature it keeps a pair of ‘eyes’ at the center.

The figures under consideration concern the nucleation out of a homogeneous, pure melt; however, this is not the usual case. Under practical conditions, nucleation mostly starts on the surface of low molar mass particles, which come into the sample either uncontrolled, or deliberately as **nucleat-**

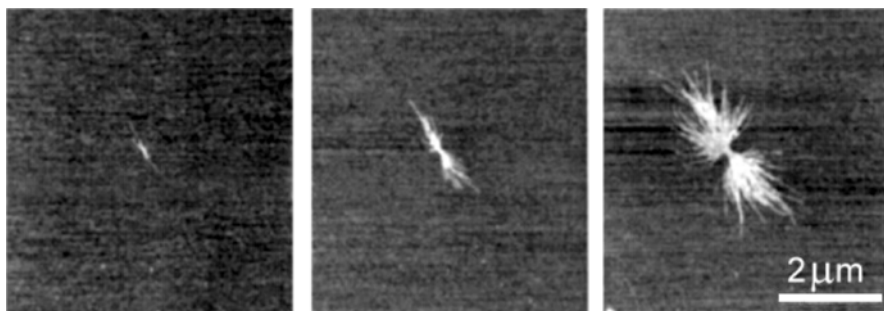


Fig. 5.21. In-situ AFM recording of crystallizing BA-C8 (at 22 °C). AFM tapping mode images of a homogeneously nucleated growing spherulite obtained at different times. From Li et al. [48]. Copyright (2003) Elsevier Science Ltd

ing agents. The addition of nucleating agents is a measure of considerable technical importance. It helps to diminish the supercooling at the onset of crystallization during cooling, as a result of a strong reduction of the surface free energy of the nucleus. If spherulites start from some heterogeneity by **heterogeneous nucleation** a different growth pattern is observed; an example is given in Fig. 5.22.

Here, many lamellar crystallites develop simultaneously, emanating from the surface of the heterogeneity. As a consequence, the growing object shows a quasi-spherical symmetry from the very beginning which differs from the initial anisotropy associated with a homogeneous nucleation.

If the branching rate is low, building up of a spherulite becomes a sequential process where some rapidly growing **dominant lamellae** at first set up a frame that is subsequently filled by slower growing **subsidiary lamellae**. Atomic force microscopy enables an observation of the sequential building up in real time. Figure 5.23 presents as an example a series of images obtained during an isothermal crystallization of polyethylene at a temperature of 133 °C. The picture on the left-hand side shows a few lamellae that have advanced with a very rapid growth. As shown by further pictures this is followed by a retarded in-filling growth. The growth speed of the latter is obviously much slower. In spite of the retardation in their development subsidiary crystallites have the same thickness as the preceding dominant lamellae. After completion of the crystallization the two sorts can no longer be distinguished.

Whether spherulites grow, for high splaying rates, with a completed inner structure or in a sequential manner, subsidiary crystallites being filled-in later, can be deduced from **crystallization isotherms**, which can be recorded by various tools, the most popular ones being calorimetry, wide angle and small angle X-ray scattering and dilatometry. If different tools are commonly used, either simultaneously or one after the other in a comparison, it is possible to discriminate between different factors acting together in the crystalliza-

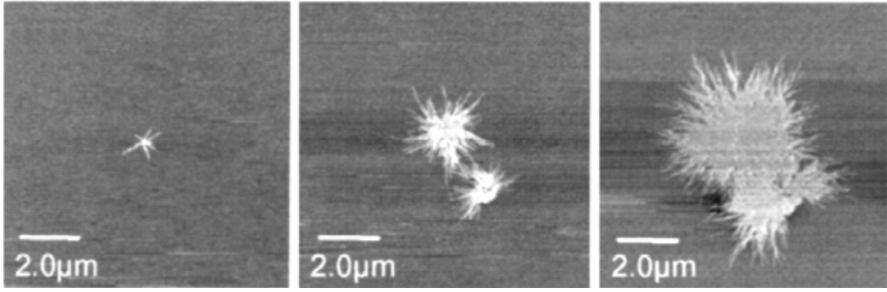


Fig. 5.22. In-situ AFM recording of crystallizing BA-C8 (22 °C). Tapping mode images of a heterogeneously nucleated growing spherulite obtained at different times. From Li et al. [48]. Copyright (2003) Elsevier Science Ltd

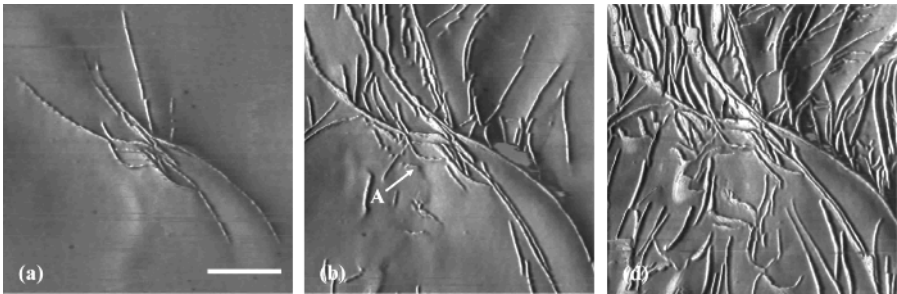


Fig. 5.23. PE, crystallized at 133 °C: AFM tapping mode phase images obtained after different times of development (*scale bar*: 1 μm). From Hobbs [49]. Copyright (2003) Springer

tion process. Figure 5.24 presents crystallization isotherms of a syndiotactic polypropylene (sPP) obtained by SAXS and dilatometry.

The appropriate parameter used in SAXS studies of crystallization kinetics is the **Porod coefficient** P defined as (Eq. (A.160))

$$P = \frac{1}{8\pi^3} (\Delta c_e)^2 O_{ac} . \quad (5.8)$$

P is determined by the inner surface, O_{ac} , and the electron density difference, Δc_e . Multiplication with the crystal thickness, d_c , leads to

$$Pd_c = \frac{1}{4\pi^3} (\Delta c_e)^2 \phi_c \quad (5.9)$$

and thus to a property that includes the crystallinity ϕ_c . On the other hand, dilatometry yields the change in the specific volume, δv , or the change in the global density, $\delta\rho$. They can also be related to Δc_e and ϕ_c by

$$\delta v \propto \delta\rho \propto \Delta c_e \phi_c . \quad (5.10)$$

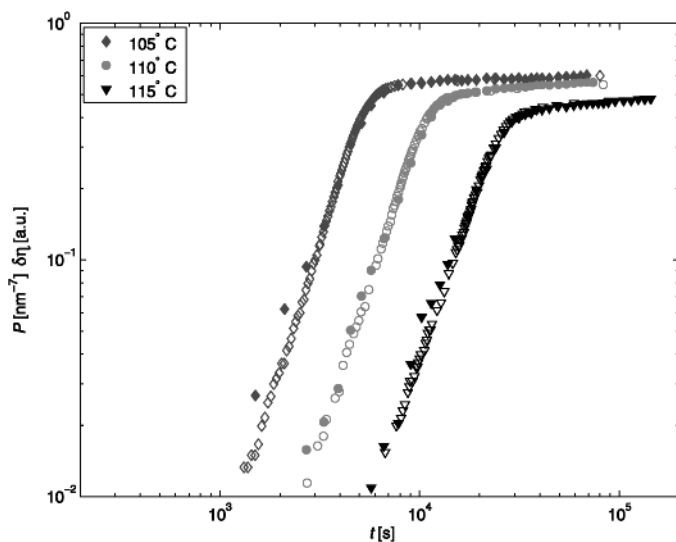


Fig. 5.24. sPP: Crystallization isotherms as given by the time dependence of P (from SAXS, *filled symbols*) and of the density change $\delta\rho$ (from dilatometry, *open symbols*). The initial slope indicates a kinetic power law $P \propto \delta\rho \propto t^3$ [50]

Figure 5.24 uses a log–log plot in the representation of the time dependencies $P(t)$ and $\delta\rho(t)$. The power law for the initial development of the crystallinity can be derived from the initial slope as

$$\phi_c \propto t^3 . \quad (5.11)$$

This is the functional dependence expected for a growth with constant growth rate of spherulites with a constant inner structure. The agreement in the kinetics recorded in terms of P and in terms of $\delta\rho$ implies that the density in the growing lamellar crystallites does not change. The different functional dependencies of $\delta\rho$ and P on Δc_e , linear and quadratic ones, respectively, would result in different isotherms for P and $\delta\rho$ if Δc_e would vary in time.

As it turns out, the full time dependence is well-represented by the **Avrami equation**

$$\phi_c(t) \propto 1 - \exp -(zt)^\beta \quad (5.12)$$

with $\beta = 3$. The Avrami equation was originally obtained by statistical geometrical considerations dealing with the problem of how a sample volume gets covered by growing objects of a certain shape. Thereby it is assumed that these start at random points, either all at once or at random times. It is the objective of the Avrami treatment to relate the ‘Avrami exponent’ β and the rate coefficient z to the shape of the particles, their growth rate, and the time distribution of the nucleation events. The coefficient $\beta = 3$ indicates

growth of a constant number density of spheres (c_s) with a constant rate (u), which leads to

$$z \propto c_s^{1/3} u. \quad (5.13)$$

This is the situation given for the system of Fig. 5.24.

Figure 5.25 depicts isotherms that were obtained in simultaneous small and wide angle X-ray scattering (SWAXS) experiments, carried out for a polyethylene-co-octene with 14% per weight of octene co-units (PEcO14). The time dependence of the product Pd_c is compared with the time dependence of the intensity of the 110-Bragg reflection, I_B . Both series of isotherms coincide. Hence, Δc_e is again a constant, i.e., the development of crystallinity is based on the growth of lamellar crystallites with a constant density. The power law found for the initial stages of crystallinity development is $Pd_c \propto I_B \propto t^\nu$ with $\nu = 1.4-1.6$. Such a result indicates that the crystallinity development is dominated by an in-filling process rather than a growth of spherulites with a completed inner structure. An open frame of dominant lamellae here developed very rapidly in a first step and the main part of the crystallization process is then the creation of subsidiary lamellae.

Figures 5.24 and 5.25 contain measurements at different crystallization temperatures and indicate a specific temperature dependence of the crystallization time. The shifts of the isotherms with temperature correspond to the law

$$\Delta \log \tau \propto \Delta T. \quad (5.14)$$

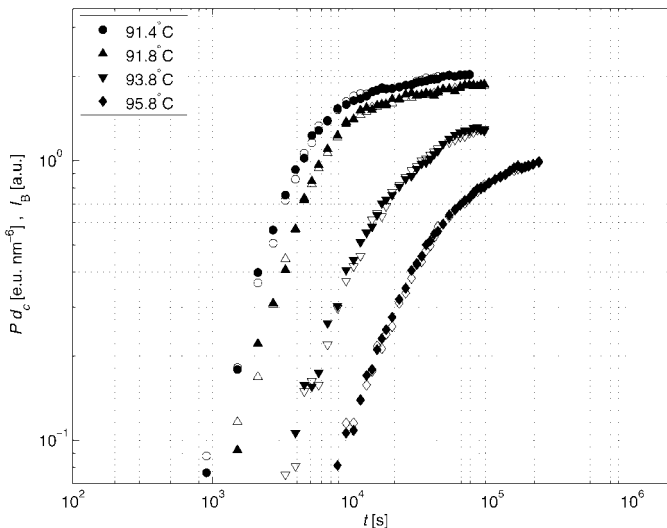


Fig. 5.25. SWAXS experiments on PEcO14: Crystallization isotherms as given by the time dependence of the product Pd_c (open symbols) and by the change of the intensity of the 110-reflection I_B (filled symbols). The initial slopes indicate a kinetic power law $Pd_c \propto I_B \propto t^\nu$ with $\nu = 1.4-1.6$ [51]

Here τ denotes some characteristic time of the crystallization process, for example, that at which half of the final crystallinity is reached. The exponential change of τ with temperature tells that, as in the nucleation step, crystal growth is associated with an **activation barrier**. For polyethylene, where τ changes by a decade within 4 K, this barrier is lower and more temperature sensitive than in s-polypropylene, where a shift in the crystallization temperature of 15 K is necessary for a comparable change. There are different views in the literature about the nature of this barrier; one possible explanation is given later in Sect. 5.3.1.

The uniformity in the thickness of the lamellar crystallites, which generally results if crystallization processes are conducted isothermally, does not imply a uniform **stability**. In a subsequent heating process melting still extends over a broad temperature range. Part of the stability variations can be associated with the sequential building up of the spherulites; subsidiary lamellae always melt prior to the dominant crystallites although both have equal thicknesses. The lowering of the stability of the subsidiary crystallites is due to the constraints encountered when they form in between the already present dominant crystallites. Figure 5.26 presents corresponding observations in a **differential scanning calorimeter** (DSC), an instrument which measures the heat flow into a sample during heating, cooling or under isothermal conditions, for an octene copolymer of s-polypropylene (sP(PcO15)).

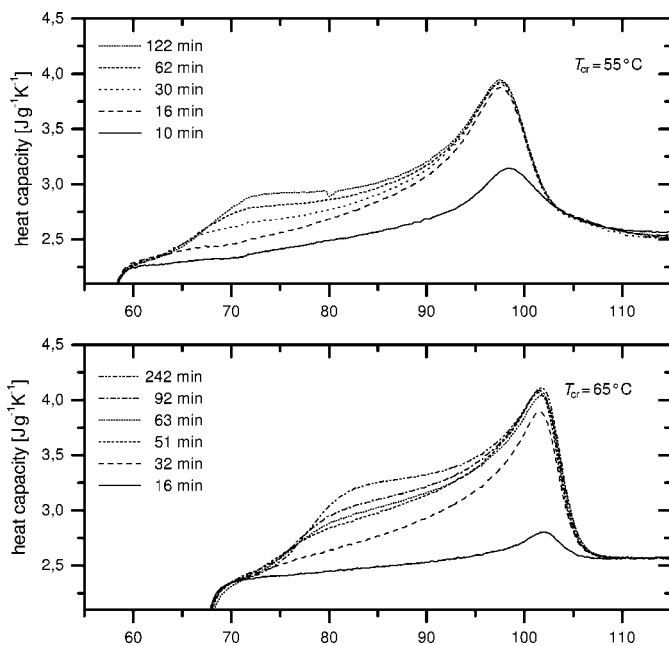


Fig. 5.26. sP(PcO15): DSC melting curves obtained after different times of an isothermal crystallization at 55 °C and 65 °C [52]

The sample was isothermally crystallized at two temperatures, under variation of the time of crystallization. The structures developed during the preset times were probed by heating scans. It is evident that the crystals developed first all possess a high melting point, i.e., the highest possible stability, whereas the later formed crystals melt much earlier, i.e., have a lower stability. Accompanying SAXS experiments showed a larger crystal thickness for the higher crystallization temperature, which led to a higher final melting point, but no thickening during the heating.

A constant crystal thickness during heating is not always observed. A different scenario is found when the crystallization is conducted on the low temperature side of the crystallization range. Then the crystal thickness increases immediately when the heating begins and reorganization processes continue up to the final melting point. This final melting point is independent of the initial crystallization temperature. Figure 5.27 shows as an example the DSC melting curves of s-polypropylene for various crystallization temperatures and Fig. 5.28 depicts the changes of the crystal thickness and the long spacing during the heating subsequent to a crystallization at 25 °C. The final melting point is constantly at 145 °C. The ongoing **recrystallization processes** do not show up in the DSC curves, i.e., they do not change the crystallinity.

Polymers are often modified by introducing co-units into the chain in a statistical distribution. Figure 5.29 shows the consequence for the melting properties, exemplified for poly(L-lactic acid) and related statistical copolymers that include $x\%$ of mesomonomers (P(LcMx)LA). The figure presents the DSC heating curves measured for the different samples subsequent to an isothermal crystallization at 80 °C. We see that the melting temperature shifts to lower values with increasing co-unit content and this is accompanied by a drop in the heat of fusion, hence, the crystallinity.

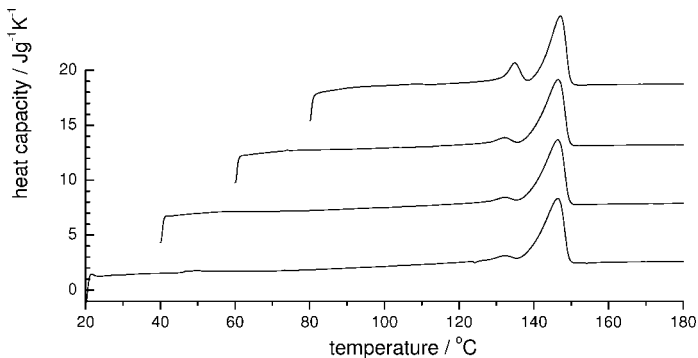


Fig. 5.27. sPP, crystallized at various temperatures followed by a heating to the melt: DSC curves obtained with a heating rate of 10 K/min [53]

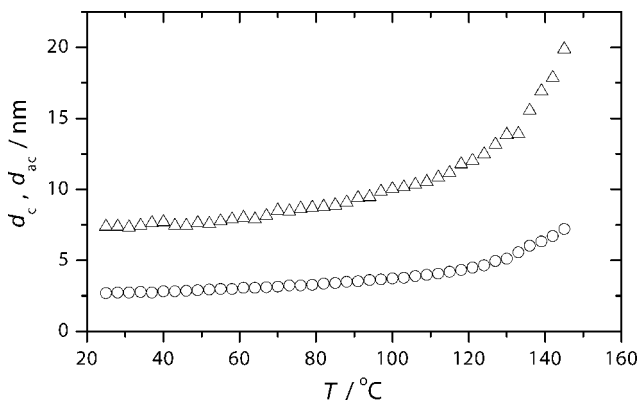


Fig. 5.28. sPP, crystallized at 25 °C and heated up to the melt: Temperature dependencies of crystal thickness d_c (circles) and long spacing d_{ac} (triangles) [53]

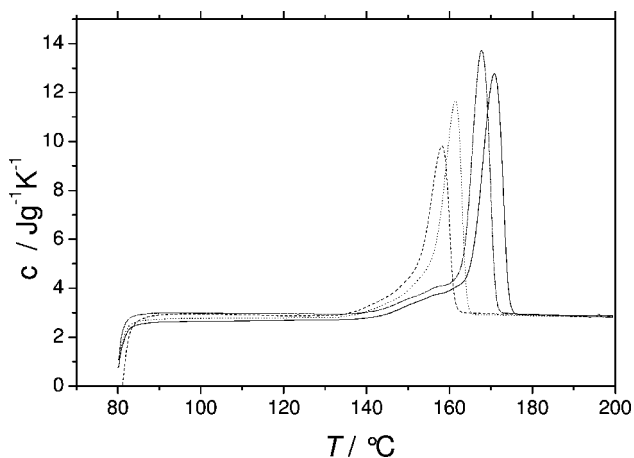


Fig. 5.29. PLLA, P(LcM1)LA (*dash-dotted*), P(LcM3)LA (*dotted*), P(LcM5)LA (*dashed*): DSC heating curves obtained after an isothermal crystallization at 130 °C. Heck and Siegenführ, Physikalisches Institut, Universität Freiburg, 2006

5.3 Laws for the Structure Development

Crystallization and melting of polymers is controlled by a number of laws. These concern

- the variation of the main structural parameters d_c, d_{ac}, ϕ_c with the crystallization temperature;
- the dependence of melting points on the crystal thickness;
- the structural changes during recrystallization processes; and
- the temperature dependence of growth rates.

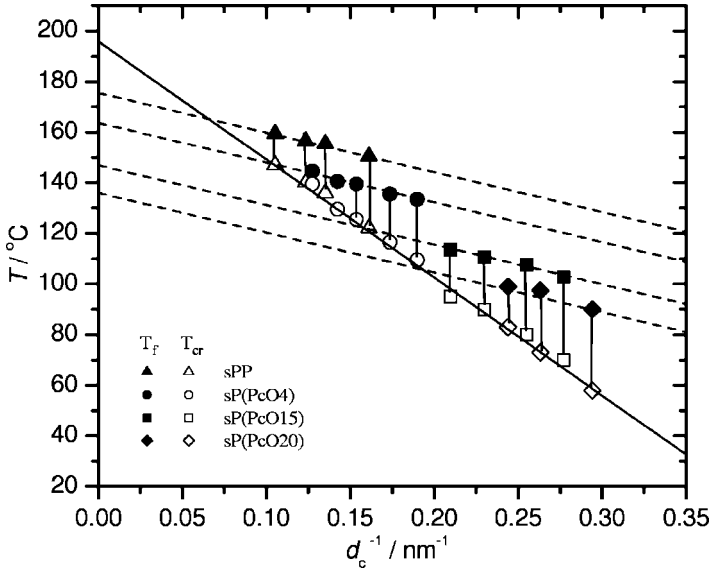


Fig. 5.30. sPP and sP(PcOx), x: % per weight of octene-units: Unique crystallization line (through open symbols) and a series of melting lines (through filled symbols) [52]

A knowledge of effects of the molar mass or, for statistical copolymers, of the co-unit content, is also of importance. Some of these relationships are remarkably simple, as demonstrated by the following examples.

Figure 5.30 collects data obtained by temperature-dependent SAXS experiments conducted on s-polypropylene and some derived octene-copolymers. The samples were crystallized at various temperatures T_{cr} and then heated up to the molten state. From the SAXS curves the crystal thicknesses d_c were deduced, both at T_{cr} and at the melting point T_f . The figure presents the inverse thickness values d_c^{-1} as a function of T_{cr} using open symbols, and as measured at T_f , with filled symbols. Here heating from T_{cr} to T_f did not change the thickness, as is indicated by the vertical connecting lines.

The relationships between T_f and d_c^{-1} for the different samples, given by the series of dashed lines, can be described by the **Gibbs–Thomson equation**. It expresses the melting point depression resulting from the finite size of the crystallites, proceeding as follows. For Gibbs free energies g_a and g_c of a monomer in the melt and in an infinite perfect crystal, respectively, and an excess free energy σ_e to be attributed to each of the two monomeric units located at the surfaces, the equilibrium condition at the melting point of crystallites composed of sequences of n monomers, $T_f(n)$, becomes

$$g_c n + 2\sigma_e = g_a n . \quad (5.15)$$

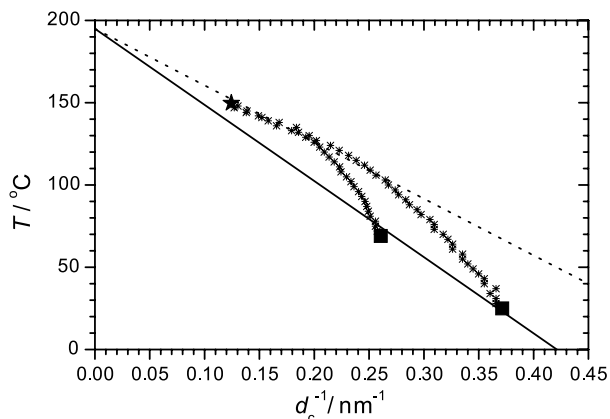


Fig. 5.31. sPP crystallized at 25 °C and 70 °C followed by heating: Inverse crystal thicknesses at the beginning (*filled squares*), during recrystallization and at final melting (*star*). The crystallization line from Fig. 5.30 and the line controlling recrystallization (*dots*) [53]

The equation can be combined with a linear approximation for the difference $g_a - g_c$:

$$g_a - g_c \approx \Delta s_f (T_f^\infty - T) = \frac{\Delta h_f}{T_f^\infty} (T_f^\infty - T). \quad (5.16)$$

Here Δs_f and Δh_f denote the entropy and the heat of fusion per monomer, respectively, and T_f^∞ represents the **equilibrium melting point** associated with a sample of macroscopic size. This gives

$$T_f(n) = T_f^\infty - \frac{2\sigma_e T_f^\infty}{\Delta h_f} \frac{1}{n}. \quad (5.17)$$

Equation (5.17) is known as the Gibbs–Thomson equation and describes the melting point depression resulting from the finite size of the crystallites in one direction. It is valid under the given conditions, where crystallization and melting occur on the lateral crystal face only, through the attachment or removal of a complete sequence. The results in Fig. 5.30 agree with Eq. (5.17). Plots of T_f versus $d_c^{-1} \propto n^{-1}$ indeed produce straight **melting lines**. An extrapolation to $d_c^{-1} \rightarrow 0$ yields the respective equilibrium melting point for each sample. The melting lines shift to lower temperatures when co-units are introduced; the higher the co-unit content is the larger is the shift. This corresponds to the melting point depression in low molar mass systems when a solute is present, as described by Raoult’s law.

The relationship between the crystallization temperature T and d_c^{-1} is different. The data points of all copolymers are commonly allocated on a unique **crystallization line**, i.e., d_c is simply determined by the equation

$$d_c^{-1} = C_c (T_c^\infty - T). \quad (5.18)$$

The temperature T_c^∞ ($= 195^\circ\text{C}$) is above all the equilibrium melting points T_f^∞ of the different samples. Crystallization line and melting lines cross each other, and Eq. (5.18) holds for each sample up to the respective point of intersection. Higher temperatures are rarely reached under practical circumstances. However, it is known that the dependence of the crystal thickness on the crystallization temperature then changes so that d_c^{-1} always remains below the melting line value.

As mentioned above, heating a sample after a crystallization in the low temperature region of the crystallization range is accompanied by continuous recrystallization processes up to the final melting. Figure 5.31 shows the crystal thickness data of s-polypropylene from Fig. 5.28, now in a plot of d_c^{-1} versus T , together with a second data set measured for a crystallization temperature of 70°C . It also includes the crystallization line of s-polypropylene as given in Fig. 5.30. The figure shows the **recrystallization line** as a further feature. When this line is reached after some initial changes it controls for all crystallization temperatures, and as it turns out also commonly for all samples, the further variation of d_c^{-1} up to the point of final melting. The recrystallization line is given by the equation

$$d_c^{-1} = C_r(T_c^\infty - T). \quad (5.19)$$

It again includes T_c^∞ (here 195°C) as the limiting temperature, but has another slope than the crystallization line ($C_r < C_c$). The final melting, indicated by a star, occurs at that temperature where the recrystallization line intersects the melting line.

Figure 5.32 presents as a second example the results of analogous experiments carried out for poly(ϵ -caprolactone)(P ϵ CL). One again finds a linear relationship between d_c^{-1} and the crystallization temperature; the crystallization line here starts from $T_c^\infty = 135^\circ\text{C}$ and another linear relationship between melting points and d_c^{-1} in agreement with the Gibbs–Thomson law; extrapolation yields an equilibrium melting point $T_f^\infty = 99^\circ\text{C}$. Samples crystallized below 42°C all melt at 58°C after a recrystallization process, for higher crystallization temperatures thicknesses remain constant until final melting.

s-Polypropylene and poly(ϵ -caprolactone) represent typical examples. In fact, crystallization, recrystallization and melting of bulk polymers can always be discussed in the framework of a generally applicable scheme. This is given in Fig. 5.33, with data referring to s-polypropylene and its related statistical copolymers. Described by a d_c^{-1}/T -diagram, the scheme always contains three lines:

- a crystallization line representing the relationship between the crystallization temperature and the inverse crystal thickness d_c^{-1} , as given by Eq. (5.18);
- a recrystallization line that controls the course of recrystallization processes, given by Eq. (5.19), and

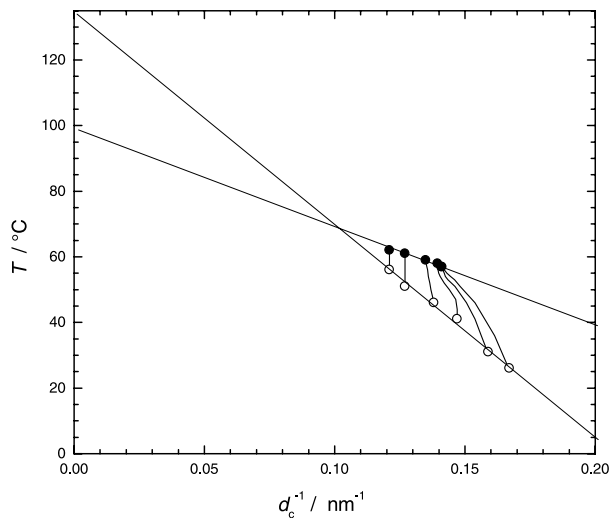


Fig. 5.32. P ϵ CL: Crystallization line ($T_c^\infty = 135^\circ\text{C}$) and melting line ($T_f^\infty = 98^\circ\text{C}$) [54]

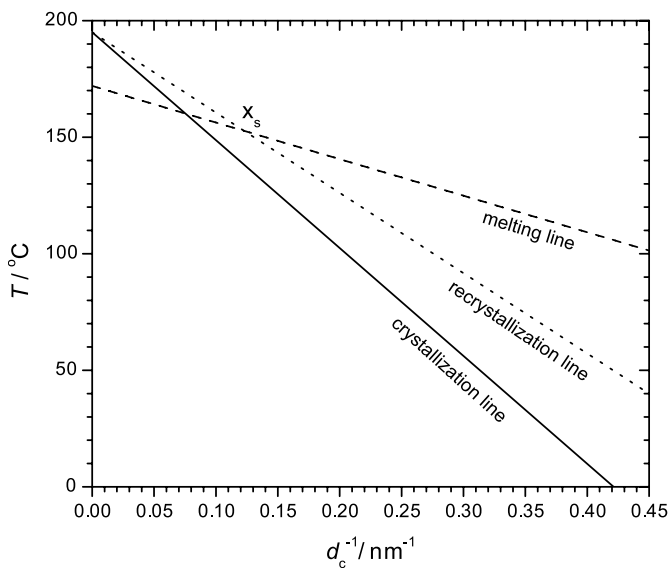


Fig. 5.33. A general scheme treating crystallization, recrystallization and melting of s-polypropylene: Common crystallization line, common recrystallization line, sample-dependent melting line (here for the sample of Fig. 5.31)

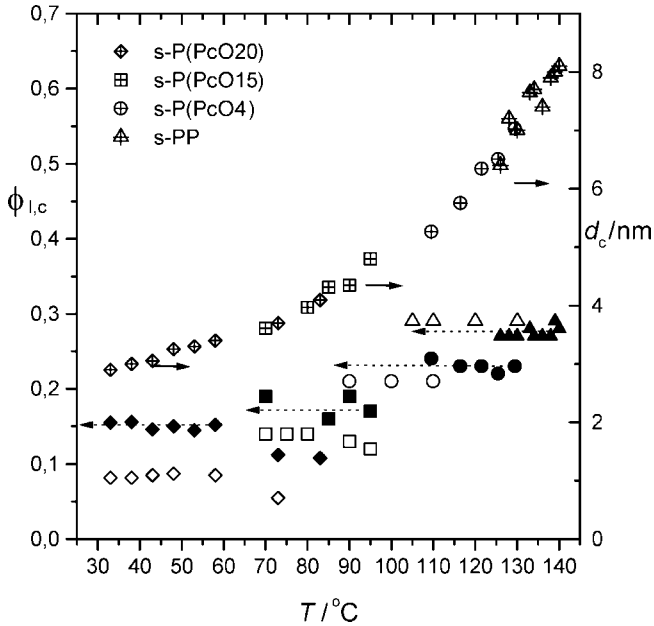


Fig. 5.34. Crystallinities of sPP and sP(PcOx) after crystallizations at different temperatures: Crystallinity ϕ_c derived from the DSC heat of fusion (*open symbols*) and linear crystallinity ϕ_l determined by SAXS (*filled symbols*). Temperature dependence of d_c (*right axis*) [54]

- a melting line on which all final melting points T_f are located; according to the Gibbs–Thomson equation it is given by

$$d_c^{-1} = C_f(T_f^\infty - T_f). \quad (5.20)$$

The crystallization line and the recrystallization line are sample-invariant, i.e., they are not affected by the tacticity or the co-unit content. The melting line, on the other hand, shifts to lower temperatures when the chemical disorder in the chain increases; its slope remains constant. Melting line and recrystallization line intersect each other at a certain temperature and a certain value d_c^{-1} . This point of intersection, denoted by X_s in Fig. 5.33, marks the end of recrystallization processes. If the initial value of the crystal thickness is above the thickness value at X_s no recrystallization occurs, the sample just melts. If the initial thickness is below the critical value recrystallization processes precede the melting. Whenever the recrystallization line is reached during heating, d_c^{-1} varies from thereon guided by this line, up to the temperature at X_s where the crystals melt. This temperature of final melting varies between different samples according to the location of X_s .

The crystal thickness and also the long spacing change with the crystallization temperature, but the crystallinity as determined after completion

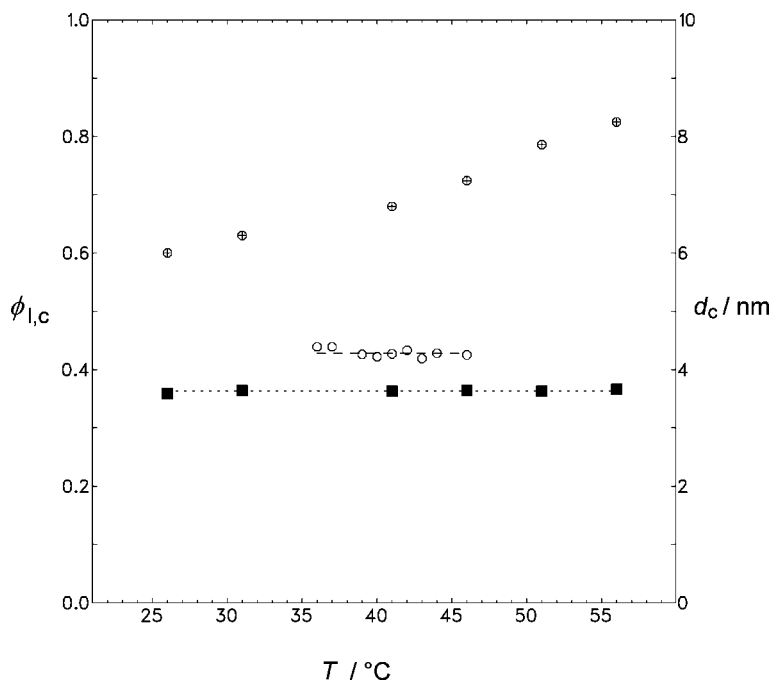


Fig. 5.35. Crystallinities of PeCL after crystallizations at different temperatures T : Weight fraction crystallinity ϕ_c derived from the DSC signal (*open symbols*) and linear crystallinity ϕ_1 determined by SAXS (*filled symbols*). Temperature dependence of d_c (*crossed symbols*, right axis) [54]

of the isothermal crystallization remains constant over a wide temperature range. Figures 5.34 and 5.35, referring again to a set of s-polypropylenes and copolymers and to poly(ϵ -caprolactone), show, together with d_c -data, the temperature dependence of the SAXS based **linear crystallinity**

$$\phi_1 = \frac{d_c}{d_{ac}} \quad (5.21)$$

and of the crystallinity derived from the heat of fusion. As can be seen, crystallinities are constant for each sample and they decrease with increasing co-unit content.

What is the effect of the molar mass on the semicrystalline structure? Figure 5.36 presents a characteristic result: An increase in the molar mass leads to an increase of the amorphous layer thickness d_a , but d_c is unaffected, depending only on the crystallization temperature. A data evaluation shows that the long spacing $d_{ac} = d_a + d_c$ is comparable to R_0 , the size of the chain in the melt

$$d_{ac} \simeq R_0 \propto \sqrt{M}. \quad (5.22)$$

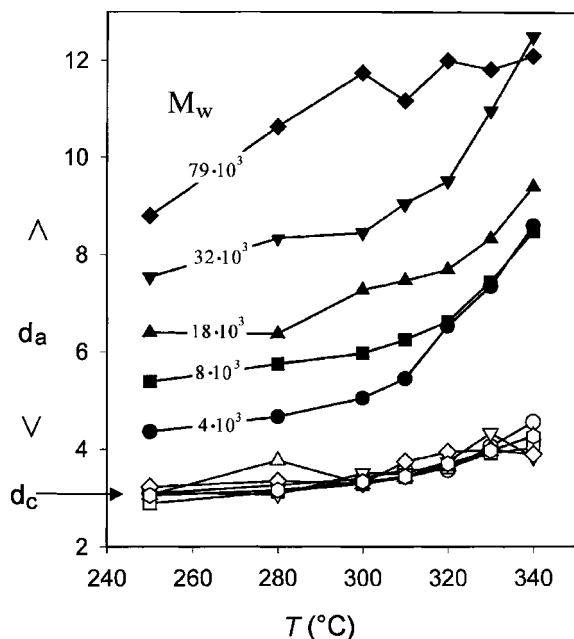


Fig. 5.36. Fractions of PEEK, crystallized at various temperatures T : Temperature dependence of the thicknesses of crystallites (d_c) and amorphous intercrystalline layers (d_a) for different molar masses. From Dosière et al. [55]

The relation indicates that a chain that has already been included with one or more sequences in a crystallite will usually not be incorporated into another one; adjacent crystallites are then kept at a distance of the order of the coil diameter.

As was mentioned earlier, the lamellar crystallites possess a blocky substructure. **Block diameters** can generally be derived from linewidths of $hk0$ -reflections in WAXS patterns, Δq_{hk0} , by application of the **Scherrer equation**

$$D_{hk0} = \frac{2\pi}{\Delta q_{hk0}} \quad (5.23)$$

(q is the scattering vector, see Eq. (A.3), Δq_{hk0} denotes the integral linewidth). Figure 5.37 presents the diameters thus obtained, again for a set of different s-polypropylenes with copolymers. The given lengths were derived from the linewidth of the 200-reflection, i.e., they refer to the direction perpendicular to the 200-lattice planes. As can be seen, all points $D_{200}^{-1}(T)$ are allocated on one common line. When continued, this line again ends at $T_c^\infty = 195^\circ\text{C}$, like the crystallization line of s-polypropylene (which is also included in the figure).

Growth rates vary only within a small temperature interval according to Eq. (5.14), which holds for a practically constant activation barrier.

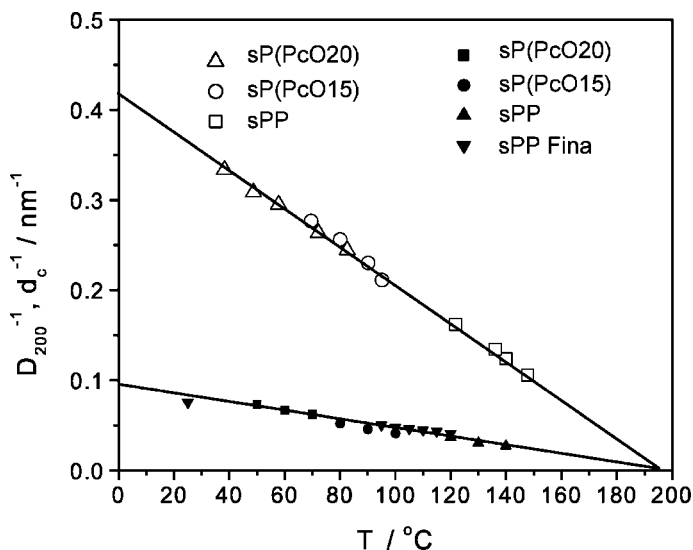


Fig. 5.37. Different samples of sPP (sPP, sP(PcOx) and the commercial sPP Fina) crystallized at various temperatures T : Crystallization line d_c^{-1} versus T determined by SAXS (*open symbols*) and inverse lateral coherence lengths D_{200}^{-1} derived from the linewidth of the 200-reflection (*filled symbols*) [56]

Figure 5.38 covers a larger interval for poly(ϵ -caprolactone) and shows the spherulite growth rate u as determined in a polarizing optical microscope. u is in the nm/s-range and the bending of the $\log u$ versus T curve indicates a changing activation barrier. The line representing the experimental data is given by the expression

$$u = u_0 \exp \left(-\frac{T_A}{T - T_V} \right) \cdot \exp \left(-\frac{T_G}{T_{zg} - T} \right). \quad (5.24)$$

The second exponential factor with parameters T_G and T_{zg} is dominant in the temperature range of the experiment. T_{zg} is the **zero growth temperature**; according to Eq. (5.24) u goes to zero, i.e., the barrier height divergences on approaching T_{zg} . A comparison with Fig. 5.32 shows that T_{zg} ($= 77^\circ\text{C}$) is 22°C below the equilibrium melting point of poly(ϵ -caprolactone).

The first exponential factor with parameters T_V and T_A only has a minor influence on the data in Fig. 5.38 but shows up clearly in the overall temperature dependence of u down to the glass transition temperature as illustrated by the three examples in Fig. 5.18. It describes the steep decrease on the low temperature side caused by the slowing down of the segmental mobility in the melt when approaching the glass transition. We will concern ourselves with this slowing down in later chapters, in particular in Sect. 6.3.2, and here only cite a main result. In the melt, chain segments experience frictional forces emanating from contacting adjacent segments and these increase

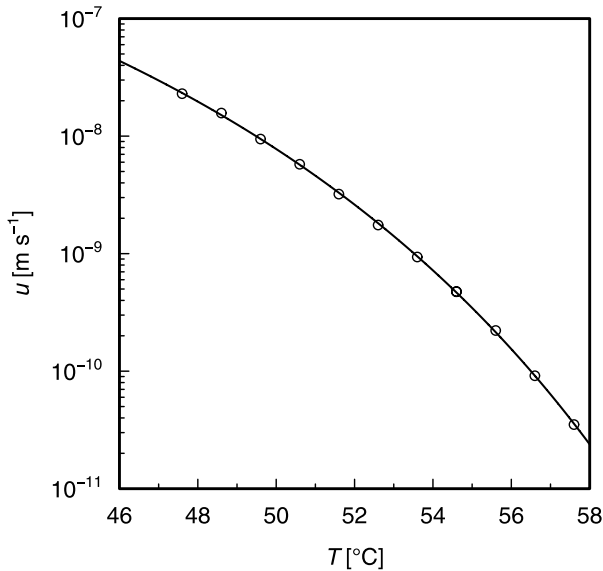


Fig. 5.38. Temperature dependence of the radial growth rate of spherulites of PeCL as measured in a polarizing microscope. Representation by Eq. (5.24) with $T_A = 1350$ K, $T_V = -110$ °C and $T_G = 443$ K; the zero growth temperature is $T_{zg} = (77 \pm 1)$ °C [57]

progressively on cooling. This increase is well-described by the Vogel–Fulcher equation (Eq. (6.126)) as

$$\zeta \propto \exp \frac{T_A}{T - T_V} . \quad (5.25)$$

ζ is the **segmental frictional coefficient** and its inverse determines the segmental mobility that affects u . T_V , the Vogel temperature is located 30–70 °C below the glass transition temperature and T_A is an activation temperature, with typical values in the range of 1000–2000 K. According to Eq. (5.24) similar functional dependencies exist on both the low temperature and the high temperature side, but for different physical reasons. The given examples are representative. Experiments on various crystallizable polymer systems have shown that Eq. (5.24) always provides a satisfactory description of the growth rate data.

5.3.1 The Multistage Model

What is the physical background of the linear dependencies showing up in the T/d_c^{-1} -diagram of Fig. 5.33, i.e., the meaning of the crystallization and the recrystallization lines? First of all, the difference between the crystallization and the melting lines demonstrates that different laws control crystallization and melting in bulk polymers. Here, crystallization and melting are not reverse

processes. While melting is based on a direct transfer of chain sequences from lateral crystal faces into the melt, formation of crystals obviously follows another route. Characteristic features are the independence of d_c of the tacticity or the co-unit content and the control of d_c by a temperature, T_c^∞ , which is different from the equilibrium melting point. They indicate that the pathway includes a transient phase with a structure intermediate between crystal and melt.

Figure 5.39 depicts a possible pathway within a multistage model. A thin layer with a **mesomorphic** inner structure forms between the lateral crystal face and the melt, stabilized by epitaxial forces. All the stereo defects and co-units are already rejected on its front. A high inner mobility allows a spontaneous thickening of the layer up to a critical value where the core region crystallizes under formation of a block. In a last step the surface region of this block, at first still disordered, perfects, which leads to a further stabilization.

The thermodynamic conditions under which such a mesomorphic phase can interfere and affect the crystallization process are described in Fig. 5.40. The schematic plot shows the difference of the chemical potential (per monomer) to that of the melt ('a') for both the crystalline phase (label 'c') and the mesomorphic phase ('m'):

$$\begin{aligned}\Delta g_{ac} &= g_c - g_a, \\ \Delta g_{am} &= g_m - g_a.\end{aligned}\quad (5.26)$$

Coming from high temperatures the chemical potential of the crystalline phase drops below the value of the melt when crossing the equilibrium melting point, now denoted T_{ac}^∞ . The mesomorphic phase requires a lower temperature, T_{am}^∞ , to fall with its chemical potential below that of the melt. The plot also includes a temperature T_{mc}^∞ . It represents the temperature of a virtual transition, namely that between the mesomorphic phase and the crystalline phase. The transition temperatures have the order $T_{mc}^\infty > T_{ac}^\infty > T_{am}^\infty$. Since the chemical potential of the crystal is always below that of the mesomorphic phase,

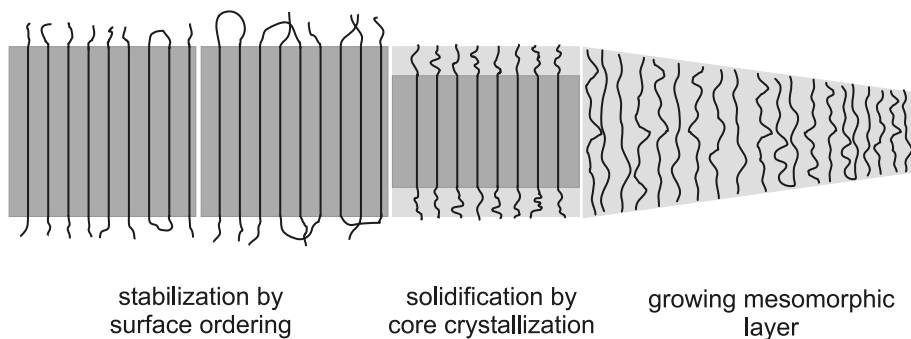


Fig. 5.39. Multistage model: A possible pathway followed in the growth of polymer crystallites

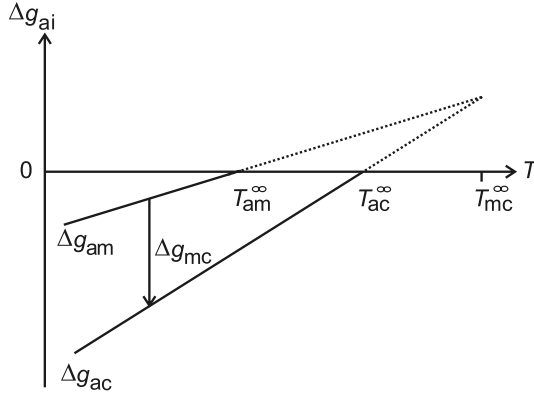


Fig. 5.40. Thermodynamic conditions assumed for crystallizing polymers: Temperature dependencies of the chemical potentials of the mesomorphic phase and the crystalline phase. The potentials are referred to the chemical potential of the melt and denoted by Δg_{am} and Δg_{ac}

the mesomorphic phase is only metastable for macroscopic systems. However, for small objects with sizes in the nm range, stabilities can be inverted. Due to their usually lower surface free energy thin mesomorphic layers can have a lower Gibbs free energy than a crystallite with the same thickness.

Thermodynamics relates the three transition temperatures T_{am}^∞ , T_{ac}^∞ , T_{mc}^∞ to the heats of transition $\Delta h_{ca} = h_a - h_c$ and $\Delta h_{ma} = h_a - h_m$. Since the slopes of Δg_{am} and Δg_{ac} are given by the entropy changes $\Delta s_{ma} = s_a - s_m$ and $\Delta s_{ca} = s_a - s_c$, respectively, one can write

$$(T_{mc}^\infty - T_{ac}^\infty)\Delta s_{ca} = (T_{mc}^\infty - T_{am}^\infty)\Delta s_{ma} , \tag{5.27}$$

and therefore one obtains

$$\frac{\Delta h_{ma}}{\Delta h_{ca}} \approx \frac{\Delta s_{ma}}{\Delta s_{ca}} = \frac{T_{mc}^\infty - T_{ac}^\infty}{T_{mc}^\infty - T_{am}^\infty} . \tag{5.28}$$

It is possible to construct a thermodynamic scheme that shows the features of Fig. 5.33, i.e., a crystallization line, a recrystallization line, both being unaffected by co-units and stereo-defects, and a melting line. It deals with four different phases:

- the amorphous melt and
- the mesomorphic layers (labeled ‘m’), and two limiting forms of the block-like crystallites, namely
- native crystals (labeled ‘c_n’) and
- stabilized crystals (labeled ‘c_s’).

The scheme is displayed in Fig. 5.41 and delineates the **stability ranges** and **transition lines** for these phases.

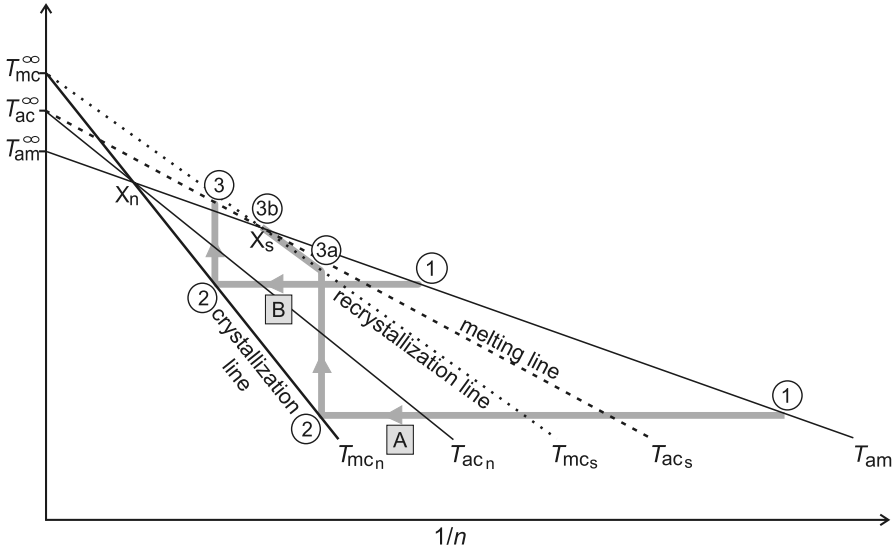


Fig. 5.41. (T/n^{-1}) -phase diagram for polymer layers in a melt (label a) dealing with three phases: mesomorphic (m), native crystalline (c_n) and stabilized crystalline (c_s). Lines of size-dependent phase transitions. Two routes for an isothermal crystallization followed by heating: A (low crystallization temperatures) and B (high crystallization temperatures)

The variables in this phase diagram are as in Fig. 5.33: the temperature and the inverse crystal thickness. The thickness is given by the number n of structure units in a stem, i.e., $n = d_c/\Delta z$ with Δz denoting the stem length increment per structure unit. The transition lines are denoted by $T_{mc_n}, T_{ac_n}, T_{mc_s}, T_{ac_s}, T_{am}$, all to be understood as functions of n^{-1} . They represent equilibria determined by thermodynamics. T_{ac_s} is identical with the Gibbs–Thomson melting line and therefore given by Eq. (5.17)

$$T_{ac}^{\infty} - T \approx \frac{2\sigma_{ac_s} T_{ac}^{\infty}}{\Delta h_{ca}} \frac{1}{n} \tag{5.29}$$

(T_f^{∞} is renamed in T_{ac}^{∞} , Δh_f in Δh_{ca} and σ_e in σ_{ac_s}). Proceeding in an analogous manner in the derivation of expressions for the other size-dependent phase transitions, one obtains for T_{mc_n} the equation

$$T_{mc}^{\infty} - T \approx \frac{(2\sigma_{ac_n} - 2\sigma_{am})T_{mc}^{\infty}}{\Delta h_{cm}} \frac{1}{n} \tag{5.30}$$

and for T_{mc_s} the equation

$$T_{mc}^{\infty} - T \approx \frac{(2\sigma_{ac_s} - 2\sigma_{am})T_{mc}^{\infty}}{\Delta h_{cm}} \frac{1}{n} . \tag{5.31}$$

σ_{am} and σ_{ac_n} denote respective surface free energies. The line T_{am} refers to the transition between the melt and the mesomorphic layer and is correspondingly described by

$$T_{\text{am}}^{\infty} - T \approx \frac{2\sigma_{\text{am}}T_{\text{am}}^{\infty}}{\Delta h_{\text{ma}}} \frac{1}{n}. \quad (5.32)$$

The line begins at the temperature T_{am}^{∞} .

The scheme identifies

- T_{mc_n} with the crystallization line, i.e., the experimental relationship Eq. (5.18) with Eq. (5.30);
- T_{mc_s} with the recrystallization line, i.e., Eq. (5.19) with the theoretical expression Eq. (5.31).

This implies in particular that T_c^{∞} , the controlling temperature for the crystal thickness, is set equal to the transition temperature T_{mc}^{∞} .

Of particular importance are the **triple points** X_n and X_s . At X_n both mesomorphic layers and native crystals have the same Gibbs free energy as the melt, at X_s this equality holds for the stabilized crystallites. The positions of X_n and X_s control what happens during an isothermal crystallization followed by heating. In agreement with the experiments the scheme predicts two different scenarios. In the figure they are exemplified by the routes A and B, respectively. Route B, realized by crystallizations at high temperatures, is as follows: At the point of entry, labeled ‘1’, chains are attached from the melt onto the front of a mesomorphic layer with minimum thickness. The layer spontaneously thickens until the transition line T_{mc_n} is reached at point ‘2’, where native crystals form immediately. The subsequently following stabilization transforms them into a lower free energy state and the triple point is shifted to X_s . On heating crystallites remain stable up to the transition line T_{ac_s} associated with a melting of the crystal. Route A (low crystallization temperatures) is different. The beginning is the same, i.e., a start at point 1 with an attachment of chain sequences onto a spontaneously thickening mesomorphic layer, then, on reaching T_{mc_n} , the formation of native crystals followed by a stabilization. When heating the stabilized crystals they at first remain stable. Then, the transition line T_{mc_s} is crossed which relates to a transformation into the mesomorphic state instead of melting. The consequence for a further heating is a continuous recrystallization mediated by the mesophase ((3a) to (3b)). This ends at the triple point X_s where the crystal melts.

What is the nature of the temperature-dependent activation barrier showing up in the second exponential factor in Eq. (5.24) determining the growth rate? In particular, what is the meaning of the zero growth temperature T_{zg} ? The model described in this section includes a possible answer. The series of steps sketched in Fig. 5.39 involves several activation barriers. The first step, attachment of a chain sequence on the growth front of the mesomorphic layer, may be dominant, and observations support this supposition. Before a sequence that lies coiled in the melt is incorporated into the growing mesomorphic layer, it has to be ‘activated’ by a transfer into an overall straightened

form as required for an attachment. Different from the crystal, the mesomorphic layer thereby allows for a variety of conformations. The straightening has to reach at least the length given by the initial thickness of the mesomorphic layer. The number of monomers in such a sequence, n^* , is determined by Eq. (5.32) as

$$n^* = \frac{2\sigma_{\text{am}}T_{\text{am}}^{\infty}}{\Delta h_{\text{ma}}} \frac{1}{T_{\text{am}}^{\infty} - T} . \quad (5.33)$$

Since the straightening leads to a decrease in entropy that is proportional to the sequence length, it introduces an entropic activation barrier

$$-\frac{\Delta S}{k} \propto n^* . \quad (5.34)$$

Transition of the barrier takes place with a probability

$$\exp \frac{\Delta S}{k} = \exp -\frac{\text{const}}{T_{\text{am}}^{\infty} - T} . \quad (5.35)$$

If T_{zg} is identified with T_{am}^{∞} , this agrees with the experimental result as given by Eq. (5.24). Hence, it is the distance to T_{am}^{∞} that controls the growth rate of polymer crystallites in the high temperature range.

Application of the scheme to experimental results, as given by the crystallization, melting and recrystallization lines of a system, the zero growth temperature as well as measured heats of fusion, yields the thermodynamic parameters included in the equilibrium relationships. Figure 5.42 shows once

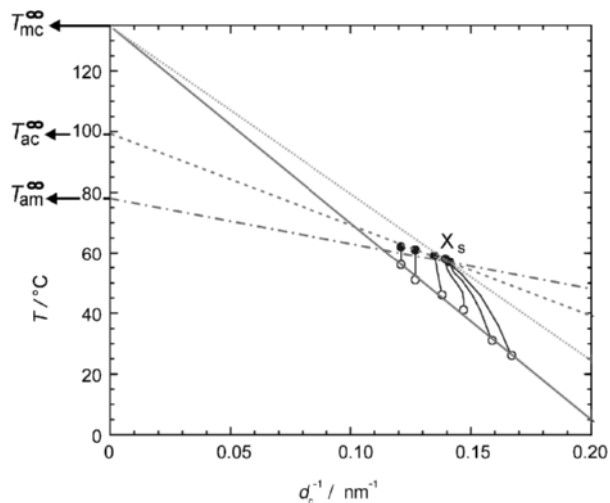


Fig. 5.42. PeCL: Crystallization line, recrystallization line (*dots*) and melting line (*dashes*) determined by SAXS, zero growth temperature T_{am}^{∞} (from Fig. 5.38) and $a \Rightarrow m$ transition line (*dash-dots*)

Table 5.1. P ϵ CL: Thermodynamic data derived from the experiments

T_{mc}^{∞} °C	T_{ac}^{∞} °C	T_{am}^{∞} °C	Δh_{ca} kJ mol C ₆ H ₁₀ O ₂	Δh_{ma} kJ mol C ₆ H ₁₀ O ₂	σ_{acn} kJ mol	σ_{acs} kJ mol	σ_{am} kJ mol
135	99	77	17.9	10.5	9.9	8.5	2.5

again the data of poly(ϵ -caprolactone) from Fig. 5.32, now complemented by the recrystallization line and the $a \Rightarrow m$ transition line. The latter is fixed by T_{am}^{∞} ($= T_{zg}$) and the location of X_s . The data derived from the figure are shown in Table 5.1. The heat of fusion $\Delta h_{ca} = 17.9$ kJ/mol C₆H₁₀O₂ is taken from the literature. The heat of transition $\Delta h_{ma} = 10.5$ kJ/mol C₆H₁₀O₂ follows from Eq. (5.28) and the three surface free energies are deduced from the slopes of the respective transition lines. Data indicate that the mesophase is more crystal-like than melt-like.

5.4 Mechanisms of Secondary Crystallization

One might think at first that the formation of the semicrystalline structure is essentially completed when the crystallization at the first chosen temperature is finished. This is not the case. Crystallization continues on cooling to room temperature, proceeding by two different modes of **secondary crystallization**.

Especially broad crystallization and melting ranges are observed for polymers that include a small amount of non-crystallizable co-units, such as short-chain branches or chemically different monomers. Figure 5.43 presents two melting curves of a commercial polyethylene that has about 3% of short chain branches. The melting process was here followed by calorimetry and in a parallel experiment also by a measurement of the thermal expansion coefficient β using a dilatometer. This particular sample had first been crystallized by a step-wise cooling, being kept for extended times at a series of discrete temperatures. The melting curve is very broad and exhibits a fine-structure that obviously keeps a memory of this special thermal history.

Figure 5.44 displays as a second example the results of a Raman spectroscopic experiment on a linear polyethylene. Spectra were measured in the ranges of the CC stretching and CH₂ twisting vibrations at different temperatures during cooling. Pronounced changes are observed and the results of the data evaluation are given in the bottom figure. One notices a continuous decrease of the melt-like fraction, an increase of the crystalline fraction, and an essentially constant value for the fraction of methylene units in the transition zone.

Detailed insight into the nature of such secondary crystallization processes comes from small angle X-ray scattering experiments. In Fig. 5.14 a series of SAXS curves was presented for a sample of linear polyethylene at the end

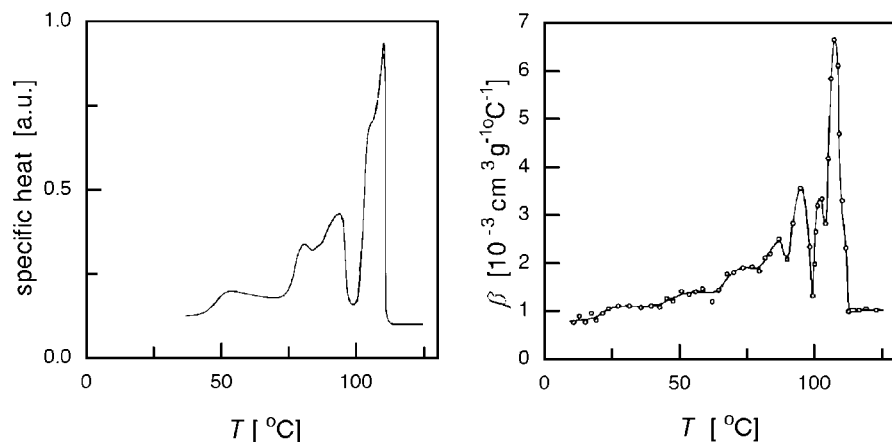


Fig. 5.43. Melting curves of a sample of branched PE crystallized by stepwise cooling (melt at $115\text{ }^{\circ}\text{C} \rightarrow 100\text{ }^{\circ}\text{C} \rightarrow 75\text{ }^{\circ}\text{C} \rightarrow 50\text{ }^{\circ}\text{C} \rightarrow 25\text{ }^{\circ}\text{C}$), obtained in measurements of the specific heat using a DSC (*left*) and of the expansion coefficient β , registered in a dilatometer (*right*) [58]

of an isothermal crystallization at $125\text{ }^{\circ}\text{C}$ and at several temperatures during a subsequent cooling. This is now complemented in Fig. 5.45 by the derived electron density correlation functions.

Pronounced changes are observed and the analysis of the shapes of $K(z)$ indicates how the semicrystalline structure changes during cooling. Insights are provided by a look at the **self-correlation triangle** with maximum at the origin. As indicated in the schematic drawing on the left-hand side of Fig. 5.15, the width of its base gives the thickness of the amorphous layers. Obviously, this thickness decreases continuously during cooling. The correlation functions $K(z)$ were evaluated and in the left column Fig. 5.46 presents plots of the derived structure parameters.

The crystallinity, reaching 75% after the primary crystallization, increases further during cooling by another 10% and this is associated with a decrease in the thickness of the amorphous layers to half of its original value. The interface area O_{ac} is much less affected by the structure change and remains constant below $100\text{ }^{\circ}\text{C}$. The column of plots on the right-hand side collects the results of an analogous SAXS experiment, now conducted on the sample of Fig. 5.43, the polyethylene with short chain branches. One finds a different behavior: The primary crystallization process yields only a crystallinity of 15%, which then goes up by another 35% during cooling. Here, secondary crystallization produces the larger part of crystals.

Results like these enable structural interpretations to be made. The observations on the branched polyethylene indicate the formation of additional crystallites during cooling. These become successively inserted into the original stack built up during the initial isothermal crystallization. On the other

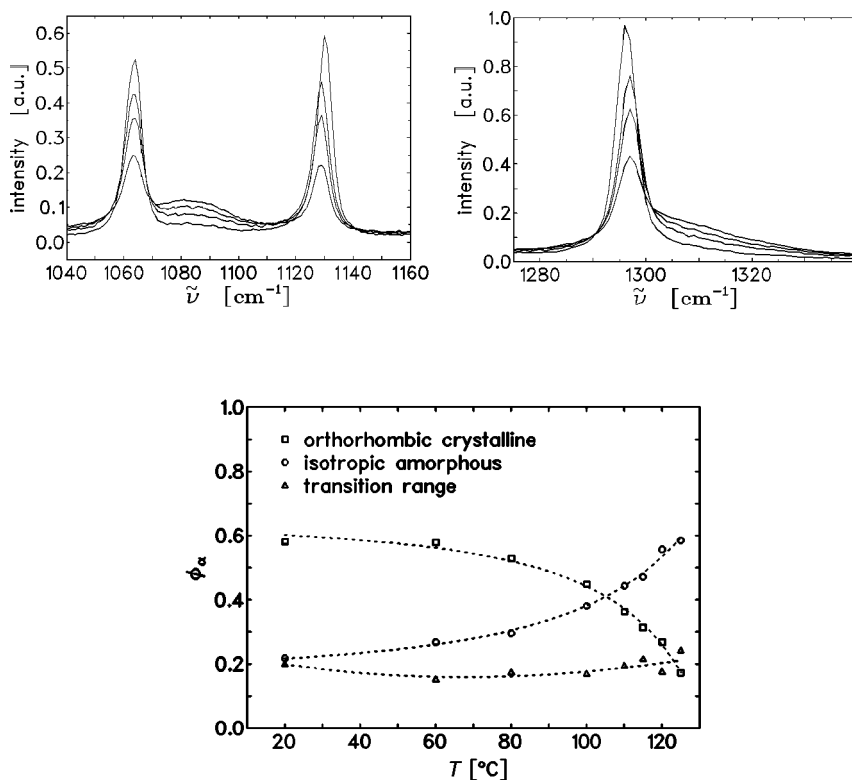


Fig. 5.44. Raman spectra measured for a sample of PE ($M \geq 10^6 \text{ g mol}^{-1}$) in the frequency ranges of the CC stretching vibrations (*top left*) and the CH₂ twisting vibrations (*top right*). Spectra were registered after completion of an isothermal crystallization at 126 °C and then successively at 115 °C, 100 °C and 25 °C. Fractions of methylene units in the orthorhombic-crystalline, amorphous and intermediate phases, as derived from a decomposition of the spectra (*bottom*) [43]

hand, the mechanism dominating the behavior in linear polyethylene is a continuous shift of the interface towards the amorphous regions corresponding to a surface crystallization process. Both processes have in common that they reduce the mean thickness of the amorphous layers but they accomplish this in different manner. Observations show that both processes are largely reversible. They both emanate from the primary structure built up during the first crystallization and leave this structure, as given by the positions of the primary crystallites, unchanged. The next parts of this section concern these two processes, known as the **insertion mode** of secondary crystallization and **surface crystallization and melting**.

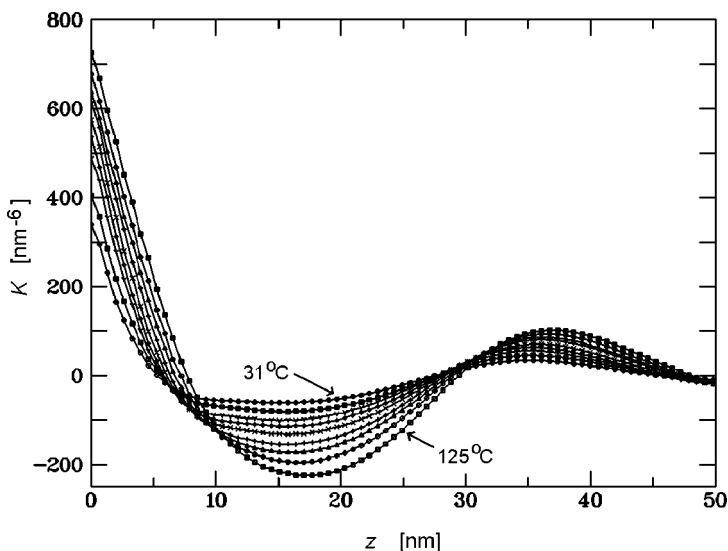


Fig. 5.45. Same sample as Fig. 5.14. Electron density correlation functions $K(z)$ derived from the scattering curves [42]

5.4.1 The Insertion Mode

Using an electron microscope, it is possible to look at the structure that exists at the end of the primary isothermal crystallization at elevated temperatures and to compare it with the final state reached after cooling the sample down to room temperature. Figure 5.47 presents two micrographs showing the structure of a polyethylene with short chain branches at 100°C and at ambient temperature. The images were obtained for thin sections where the crystallites show up as white lines as in Fig. 5.6. The difference in the morphologies for the two temperatures is evident. The partially crystalline structure at 100°C (right-hand image) is composed of crystallites with large lateral extensions and uniform thickness. At room temperature this uniformity is lost. As is apparent, many thin lamellae have formed in between the primary crystallites.

The observation suggests a structural development by the mechanism sketched in Fig. 5.48. The left-hand side shows what happens during the lateral growth of a single crystallite. Growth is associated with the transport to the surface of all non-crystallizable chain parts, such as short chain branches, end groups, and entanglements. As a consequence, a zone is created which has an enhanced concentration (c_B) of non-crystallizable units. Together with the crystallite this zone sets up a region with thickness d_{\min} that cannot be entered by any other growing crystalline lamella. As a result, after completion of the primary crystallization at T_0 , distances between the centers of adjacent crystallites will vary between d_{\min} as the lower and $d_{\max} \approx 2d_{\min}$ as an upper limit; if a distance is larger than $2d_{\min}$, another crystallite will grow in between. The

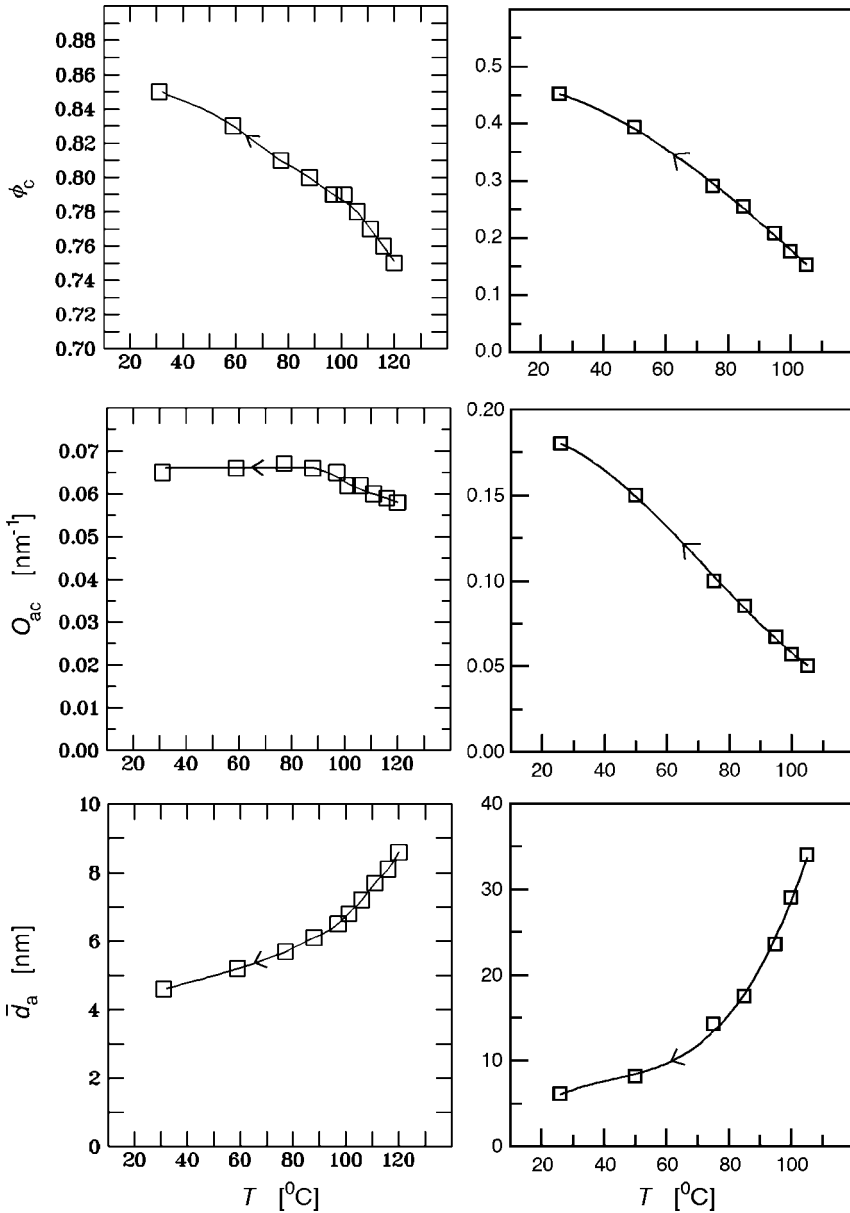


Fig. 5.46. Changes of the crystallinity ϕ_c , the interface area per unit volume O_{ac} and the mean thickness of the amorphous layers \bar{d}_a during cooling of samples of linear PE (left column) and branched PE (right column), as derived from SAXS experiments and density measurements [41], [59]

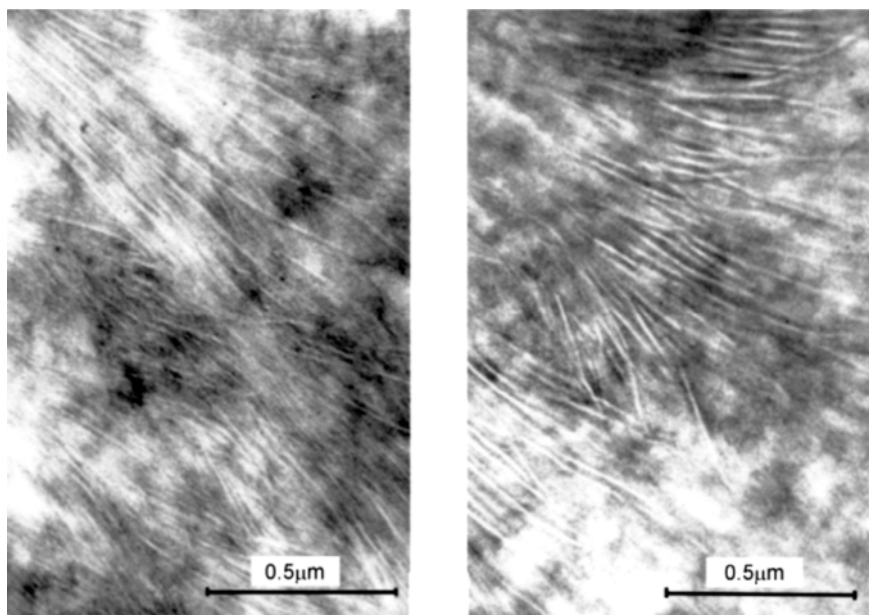


Fig. 5.47. Electron micrographs showing the structures of a PE with short chain branches after an isothermal crystallization at 100 °C (*right*) and a subsequent cooling to room temperature (*left*). Images were obtained on thin sections stained with OsO_4 [59]

sketch on the right-hand side describes what happens during cooling: Additional crystallites are inserted into the primary stack. At the first temperature, T_1 , they appear only in the thickest amorphous regions. On cooling to the next temperature, T_2 , crystallization proceeds into the next thinner amorphous layers and on further cooling into even thinner ones. With decreasing temperature, the crystal thickness decreases as well. The variable controlling the temperature at which a crystallite forms within a given amorphous layer is the concentration of non-crystallizable units therein. Their presence leads to a growth rate reduction, shifting the crystallization to lower temperatures.

The central point in the scheme is the non-uniform distribution of the non-crystallizable units in the primary stack, being higher in the thinner and lower in the thicker amorphous layers. The necessary prerequisite for this is a suppression of any transport of non-crystallizable units through the crystallites, so that the difference in concentrations is maintained and an equilibration prevented. For branched polyethylene this condition is obviously fulfilled, which appears reasonable considering the size of the short-chain branches.

The additional crystallites that form during cooling do not need a separate nucleation step. Figure 5.49 shows the difference in crystallization kinetics between the primary isothermal crystallization and the subsequent secondary crystallization steps. The time dependence of the density for the primary

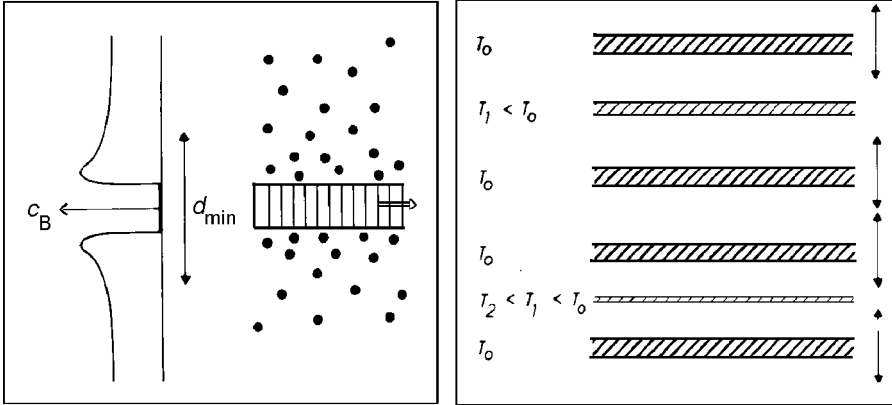


Fig. 5.48. Consecutive building up of a stack of crystallites during cooling via the insertion mechanism. Formation of a crystallite generates a zone of thickness d_{min} that cannot be entered by other crystallites (*left*). Primary crystallization at T_0 produces a stack of crystallites with varying distances d_{ac} in the range $d_{min} < d_{ac} < 2d_{min}$. On cooling to T_1 and T_2 further lamellae become successively inserted, their thicknesses decreasing together with the temperature (*right*)

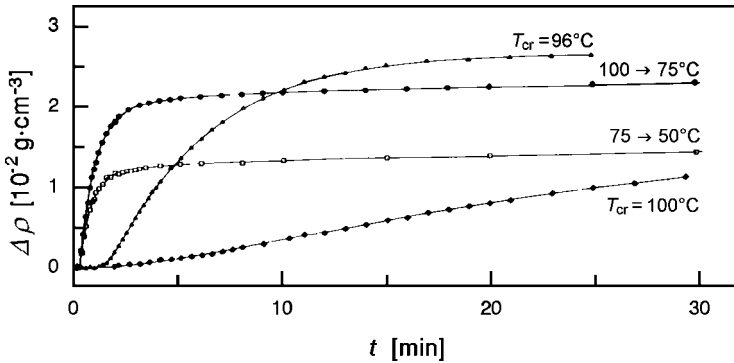


Fig. 5.49. Crystallization isotherms observed in density measurements on a PE sample with short chain branches. Note the difference in shape between the primary crystallizations at 100°C or 96°C and the subsequent crystallizations on stepwise cooling from 100°C to 75°C and 50°C [58]

crystallization shows a sigmoidal shape. In contrast, in the subsequent crystallization, the maximum crystallization rate is found at the beginning. An explanation is indicated in Fig. 5.50. Crystallites are often slightly tilted with respect to each other. In this situation a gradient in the concentration of non-crystallizable units is built up. The consequences are obvious: A lamella growing at a given temperature, say T_0 , in between two tilted crystallites practically stops at first at a certain point and then continues growth on fur-

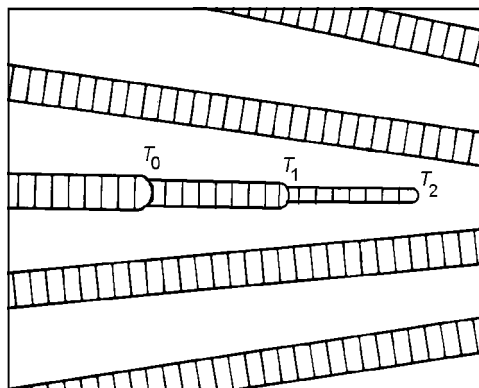


Fig. 5.50. Growth of a lamella in between two tilted crystallites. At the primary temperature T_0 growth practically stops at a certain point and then proceeds upon cooling to T_1 and T_2 , accompanied by a thinning

ther cooling to T_1 and T_2 . From step to step, the thickness of the crystallite becomes successively smaller.

5.4.2 Surface Crystallization and Melting

By indicating a continuous shift of the interfaces, the results of the SAXS experiments on linear polyethylene given in the left column of Fig. 5.46 suggest the occurrence of a surface crystallization and melting process. Corroborating evidence comes from the Raman-spectroscopic findings depicted in Fig. 5.44. There we see that in spite of pronounced changes in the crystallinity the fraction of material in the transition zones is largely constant, which is indicative for an unchanged interfacial area as expected for a surface melting process. Figure 5.51 shows a sketch of this peculiar mode of crystallization. A change of temperature is accompanied by a continuous shift of the interface, on cooling towards the amorphous regions and on heating towards the crystallites.

The existence of this process demonstrates that the structure of the amorphous intercrystalline layers in a semicrystalline polymer is different from a polymer melt. The reason can be easily seen: All the chain sequences are fixed with their ends in the crystallites and, furthermore, the concentration of entanglements is enhanced. As a consequence, the mean chemical potential of the units is higher than in a melt and varies with the layer thickness. The direction of change is obvious. The numbers of entanglements and points of chain entry into the crystallites are constant. The motional restrictions thus become diminished if the layer thickness increases, which implies a decrease in the chemical potential. Under such conditions each change in temperature leads to a new local equilibrium between crystallites and amorphous regions, via a surface crystallization or melting process.

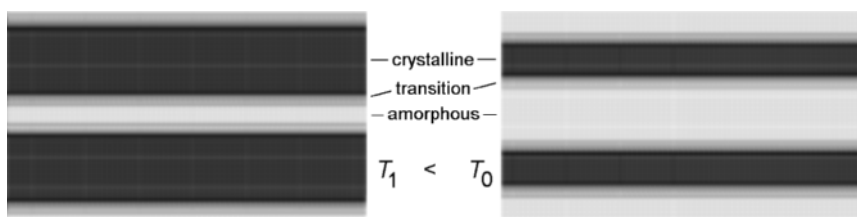


Fig. 5.51. Schematics of the process of surface crystallization and melting

The continuously renewed equilibration has a prerequisite: A shift of the interface necessitates a rearrangement of the chains in the crystallites, which can only be accomplished if the chains possess sufficient mobility within the crystals. For polyethylene this condition is fulfilled, a longitudinal mobility being provided by the α -process (see Fig. 6.28). Direct evidence comes from a NMR experiment on polyethylene using a resonance of ^{13}C . The resonance frequency differs between the crystalline and the amorphous phase; in terms of the ppm-units used in NMR spectroscopy (frequency shifts are expressed in ‘parts per million’ referring to the resonance frequency of a standard substance), the resonance of the crystallites is found at 32.5 ppm and the signal of the amorphous parts at 30.5 ppm. The shift can only be observed if the much larger shifts due to the magnetic interactions between all the spins in the sample are completely removed. This can be accomplished by a rapid rotation of the sample about the ‘magic angle’ $\theta = 54.7^\circ$ (θ is the angle enclosed by the magnetic field and the rotation axis). The experiment considered uses this technique and is called a **magic angle spinning ^{13}C two-dimensional exchange** (MAS ^{13}C 2d) experiment. It is possible to explain its information content in broad outlines.

Figure 5.52 shows the results of measurements at two different temperatures, 363 K and 373 K. Functions that depend on two variables, $p(\omega_1, \omega_2)$, are represented in two-dimensional plots with level-line plots as inserts. A certain ‘mixing time’ t_m belongs to each curve. The functions $p(\omega_1, \omega_2)$ represent the probability that a ^{13}C nucleus, which was at a position with a resonance frequency ω_1 at zero time, changes within a time t_m to a position with a resonance frequency ω_2 . In the figures we observe four peaks, two large ones, designated ‘a’ and ‘c’, located on the diagonal $\omega_1 = \omega_2$ and two smaller ones, ‘ac’ and ‘ca’, found in off-diagonal positions. Contributions to the diagonal peaks originate from those ^{13}C nuclei that either remained within the crystalline phase ($\omega_1 = \omega_2 = 32.5$ ppm) or within the amorphous phase ($\omega_1 = \omega_2 = 30.5$ ppm). The two off-diagonal peaks relate to shifted monomers, which moved from the crystalline to the amorphous phase ($\omega_1 = 32.5, \omega_2 = 30.5$) or in reverse direction ($\omega_1 = 30.5, \omega_2 = 32.5$). A comparison of the two results in Fig. 5.52 indicates that the amount of exchange increases with time and temperature.

The experiment demonstrates that a motional mechanism is active, which produces the exchange. It appears reasonable to assume that a longitudinal

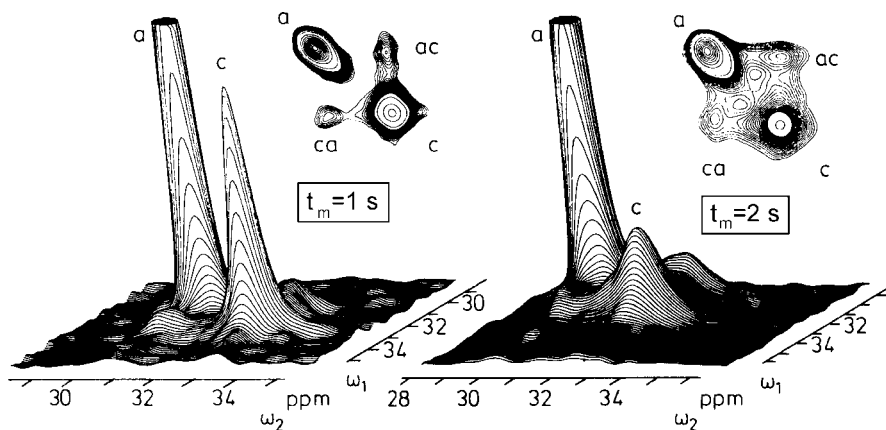


Fig. 5.52. MAS ^{13}C 2d exchange spectra measured for a sample of PE ($M = 4 \times 10^6 \text{ g mol}^{-1}$) at 363 K (*left*) and 373 K (*right*). Work reported by Schmidt-Rohr and Spiess [60]

transport is mediated by diffusing conformational defects, such as a local chain twist by 180° . A large set of data obtained under variation of t_m and the temperature was evaluated and yielded the rate of a displacement over the length of one CH_2 unit. Figure 5.53 shows the temperature dependence of this jump rate. It obeys an Arrhenius law with an activation energy $\tilde{A} = 105 \text{ kJ mol}^{-1}$.

A second observation in Fig. 5.52 is also noteworthy. There are non-vanishing values of $p(\omega_1, \omega_2)$ between the peak ‘c’ and the off-diagonal peaks ‘ac’ and ‘ca’. This is just the range where contributions of the transition zones are expected, when units are passing through during a change from the crystallite into the amorphous phase. The monomers only remain for a short time in this region, then diffuse away, either into the crystallite or towards the center of the amorphous zones.

Temperature modulated differential scanning calorimetry (TMDSC) and heat wave spectroscopy (HWS) are particularly suited to study a reversible process like surface crystallization and melting. They extract heat flows associated with reversible structure changes and separate them from latent heats of fusion and crystallization. Experiments probe the reaction of a sample onto an imposed oscillating temperature

$$T(t) = \bar{T} + \delta T \exp(-i\omega t), \quad (5.36)$$

whereby the mean temperature \bar{T} is kept constant. The programmed temperature induces an oscillating, in general phase-shifted heat flow

$$\dot{Q}(t) = \bar{\dot{Q}} + \delta \dot{Q} \exp(-i\omega t). \quad (5.37)$$

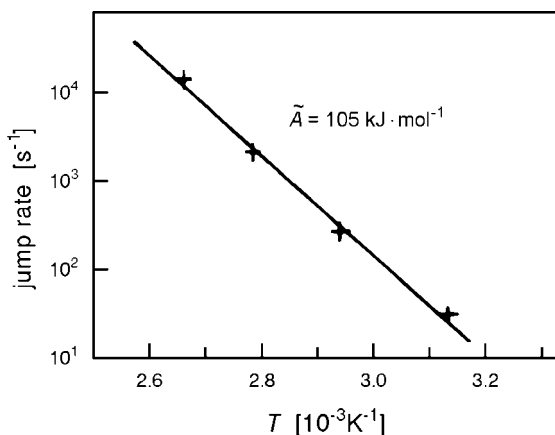


Fig. 5.53. Rate of jumps over one CH_2 unit performed by the crystalline sequences in PE. Result of the NMR experiment of Fig. 5.52 [60]

The **dynamic heat capacity** of the sample, $C(\omega)$, expresses the ratio between the amplitudes of the heat flow and the heating rate

$$\frac{dT}{dt} = -i\omega\delta T \exp(-i\omega t) \quad (5.38)$$

as

$$C(\omega) = \frac{\delta\dot{Q}}{-i\omega\delta T}. \quad (5.39)$$

The normally used **dynamic specific heat** $c(\omega)$ as given by the heat capacity per unit mass is in general a complex, frequency-dependent quantity of the form

$$c(\omega) = c'(\omega) + ic''(\omega) = |c(\omega)| \exp(i\varphi(\omega)). \quad (5.40)$$

Surface crystallization and melting shows up in the dynamic heat capacity with a contribution that varies with the modulation frequency. Figure 5.54 reproduces results obtained for polyethylene choosing various modulation frequencies between 8×10^{-3} Hz and 0.4 Hz. The frequency dependence of the signal amplitude indicates the time scale of the process. The results demonstrate that surface melting and crystallization takes place with rates within this range. For a frequency of 0.04 Hz the signal amplitude is reduced to half its original value, which means that 25 s is here the characteristic time associated with surface crystallization and melting. This time depends on the temperature and here refers to 130 °C.

One may wonder if surface crystallization and melting represents a widespread phenomenon, since similar conditions as in polyethylene are also found for many other polymers. As it appears this is not the case. Positive evidence so far is restricted to polyethylene and poly(ethylene oxide). Surface crystallization and melting being the exception, the insertion mode is the rule and

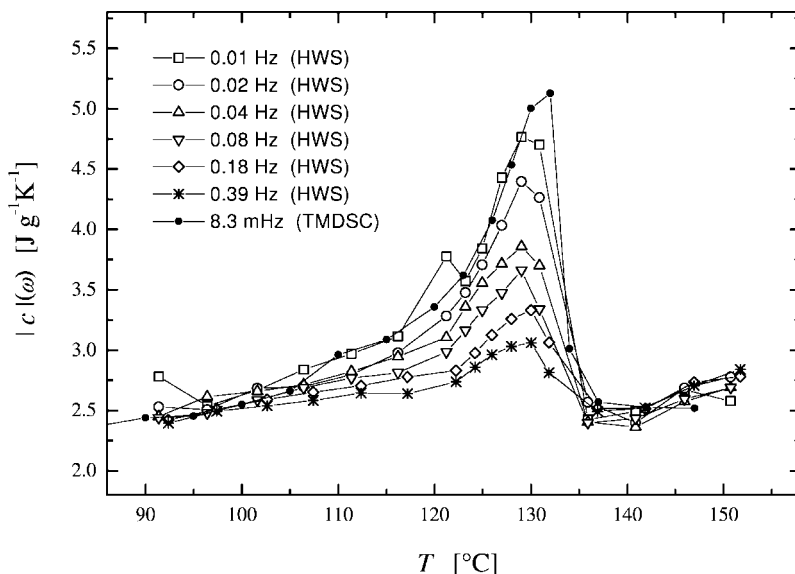


Fig. 5.54. PE studied by TMDSC and HWS: Temperature dependence of the modulus of the dynamic specific heat measured for various frequencies [61]

mainly responsible for the generally observed secondary crystallization. As it does not require a mobile crystalline phase, it can always occur.

5.5 Crystallization from Oriented Melts

Polymeric materials are usually processed from the melt state. In common operations such as injection molding, film blowing or fiber spinning the melt is subject to extensive shear flow before it solidifies on cooling. The orientation of the chain sequences in flow fields affects the crystallization properties. Times of crystallization are reduced, crystal textures become anisotropic and non-uniform, and morphologies can change completely in qualitative manner. A wealth of experience concerning correlations between processing parameters, inner structure and resulting mechanical properties of bodies of polymeric resins has been collected, but this must be supported by a knowledge of the basic phenomena that control **flow enhanced crystallization**. In order to achieve this knowledge experiments have to be carried out under well-defined conditions of flow impact. Some of these, having clear results, are presented in this section.

An appropriate procedure is the application of a short shear pulse on a sample confined by two parallel plates, which is then followed by an observation of the evolving structure. The pulse time can be kept short compared to the crystallization time. Experiments then extract the effect of flow on the

initial stages of the crystallization process, i.e., in particular, on the nucleation. The micrograph shown in Fig. 5.55 was obtained in a polarizing optical microscope (crossed nicols) for a sample of i-polypropylene (iPP) that crystallized at 141 °C. The shear pulse at the beginning with a duration of 12 s produced a flow field with a maximum shear stress $\sigma_{zx} = 0.06$ MPa at the two plate surfaces; σ_{zx} linearly decreases towards the interior and vanishes in the center. The micrograph depicts the structure in a microtomed section through the layer in a view onto the flow direction, i.e., the zx -plane. Bright **skin** regions with a thickness of 55 μm appear at both surfaces, which have a homogeneous, strong birefringence. The inner **core** region contains spherulites whose size rises towards the central region. The large spherulites near the center developed only during a subsequent cooling; a quiescent melt crystallizes at 141 °C only very slowly. From the picture two conclusions can be drawn:

- If a threshold value of the stress (here $\sigma_{zx} = 0.047$ MPa) is surmounted, a uniformly oriented structure forms rather than spherulites.
- Shear stresses below the threshold enhance the density of nuclei resulting in spherulites. The density rises from the low value of the quiescent melt up to a maximum reached at the threshold.

Other experiments show that effects not only relate to the magnitude of the shearing stress but also to the pulse duration, i.e., to the applied mechanical work. In the experiment of Fig. 5.56 the kinetics of crystallization of i-polypropylene initiated by pulses with various shearing times was monitored by turbidity measurements. The developing crystals scatter light and thus attenuate the intensity I of a beam passing through the sample; curves show the time-dependent attenuation coefficient $I(t)/I(0)$. Crystallization times, as

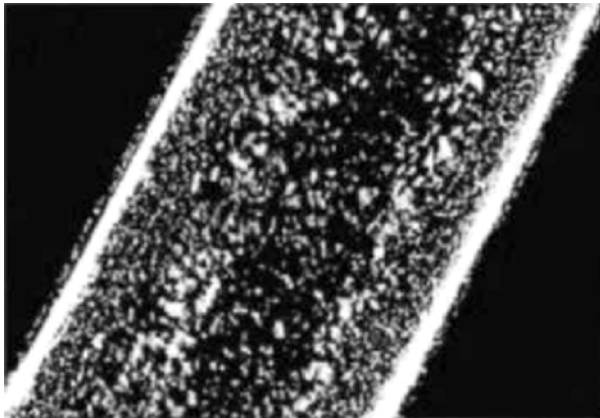


Fig. 5.55. iPP, crystallized at 141 °C after a shear pulse (duration 12 s) with a stress $\sigma_{zx} = 0.06$ MPa at the confining plates. Optical micrograph showing the structure in the zx -plane after cooling to room temperature (polarizer and analyzer are $\pm 45^\circ$ to the flow direction). From Kornfield et al. [62]

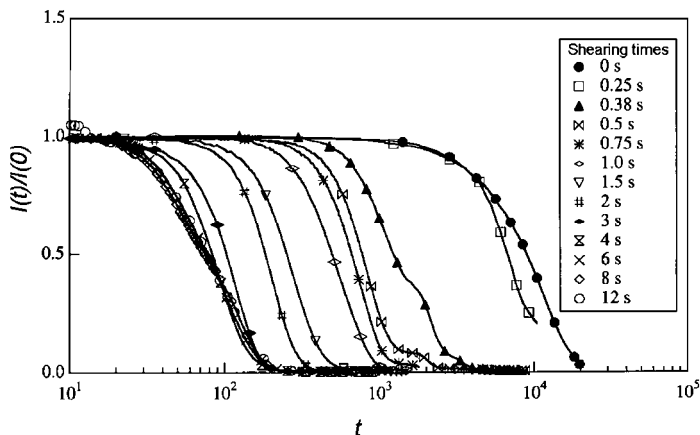


Fig. 5.56. iPP, sample between two glass slides, crystallization at 141°C initiated by shearing pulses ($\sigma_{zx} = 0.06\text{ MPa}$ at slide) with various durations. Kinetics of the crystallization is monitored by a measurement of the light attenuation coefficient $I(t)/I(0)$. From Kornfeld et al. [62]

given, for example, by the time at which the attenuation coefficient drops by 50%, decrease by two orders of magnitude when comparing quiescent conditions with an initiation by shear pulses with times of more than 5 s. According to Eq. (5.13) this implies an increase in the number density of spherulites by a factor 10^6 . The nucleation density varies non-linearly with the shearing time and saturates at about 5 s.

The nonlinearity is also seen in the experimental results presented in Fig. 5.57. Nucleation densities c_{nuc} in i-polypropylene were again determined after shearing pulses of different lengths producing different amounts of shear Δe_{zx} , now also at various temperatures. The dependence of c_{nuc} on the mechanical work $\sigma_{zx}\Delta e_{zx}$ can be represented by a power law with an exponent varying between 3 and 4. As apparent, all lines converge at high values of the applied work.

What does the structure of the skin layer, which is uniformly highly oriented, look like? Figures 5.58, 5.59, and 5.60 give typical examples for its nature. The image in Fig. 5.58 was obtained for polyethylene with an AFM. Orientation in the surface region of a melt film was achieved by dragging a razor blade. The contact with the blade also somewhat cooled the melt so that it started to crystallize. Scanning was carried out after completion of the crystallization process at room temperature. In the image many stacked lamellae are seen edge-on, as well as three parallel thin microfibrils oriented along the direction of dragging. Chains have identical orientations in the fibrils and the lamellae thus produce the uniform strong birefringence of this peculiar structure. The images in Figs. 5.59 and 5.60, obtained with the aid

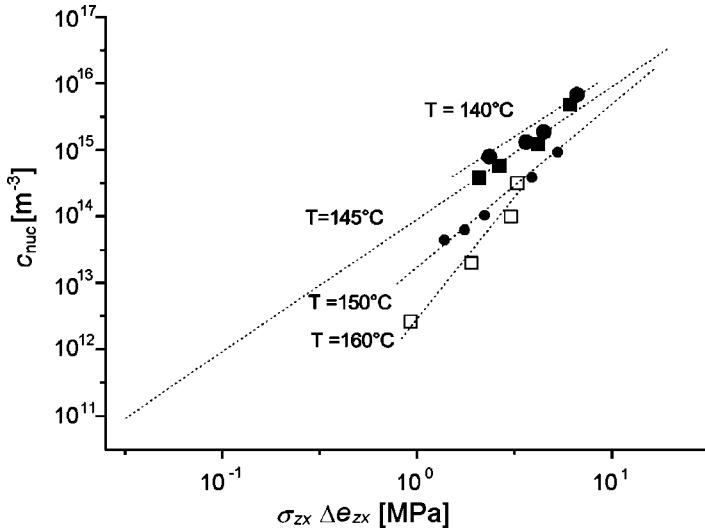


Fig. 5.57. iPP, crystallization at the given temperatures subsequent to shearing pulses of different length (Δe_{zx} : shear displacement, σ_{zx} : shearing stress): Density of nuclei c_{nuc} . From Janeschitz-Kriegl [63]

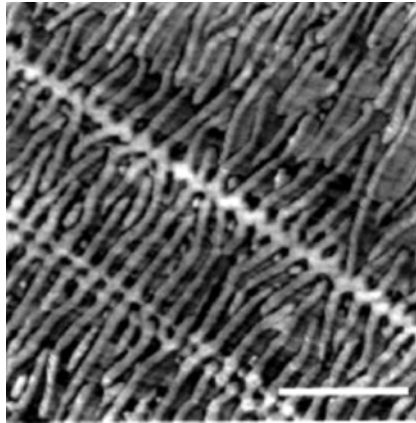


Fig. 5.58. AFM image depicting a PE shish kebab structure (*scale bar: 300 nm*). The surface of a melt film was sheared and cooled with a dragged razor blade thus inducing a crystallization in the oriented state. From Hobbs et al. [64]

of an electron microscope for a drawn ultra-thin film of i-polystyrene (iPS), indicate how this structure forms.

The first step is the nucleation and rapid growth of a microfibril with a thickness in the nm-range. This fibril then serves as nucleus for the row of lamellae growing in perpendicular direction. Figure 5.59 presents an early stage of the lamellar growth and Fig. 5.60 a late stage where neighboring

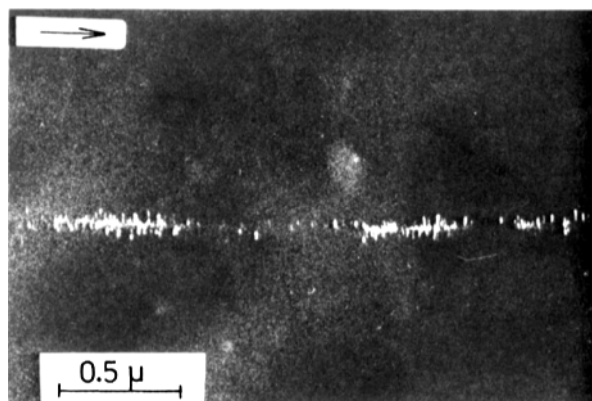


Fig. 5.59. EM micrograph of a thin film of iPS strained at 240°C and cooled with a rate of 10^2 K s^{-1} to room temperature. A shish kebab at an early stage of development is seen. From Petermann and Gleiter [65]

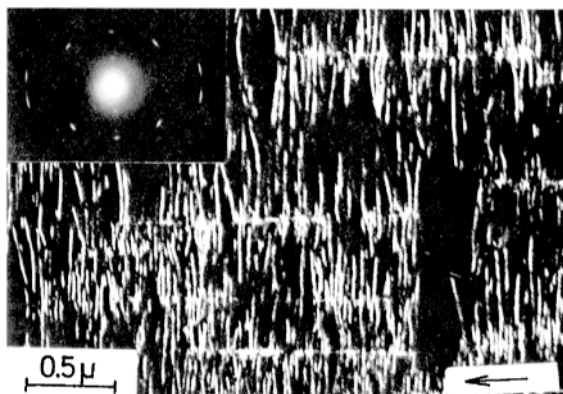


Fig. 5.60. iPS strained at 240°C and slowly cooled to room temperature (1 K s^{-1}): Interdigitating fully developed shish kebab. The electron scattering pattern in the *insert* is indicative for a uniform chain orientation in all crystallites. From Petermann and Gleiter [65]

lamellar stacks interdigitate. **Shish kebab** is the name commonly used for this morphology; ‘shish’ for the primary fibrillar crystal and ‘kebab’ for the lamellar crystallites nucleated by the shish.

The lamellar crystallites grow according to the same laws that are valid for the crystals in the spherulites. Since the nucleation sites are all along a microfibril a row of crystallites with a uniform chain orientation results. The splaying typical for growing spherulites is suppressed; there exists a stack of parallel lamellae from the very beginning. The new phenomenon are the microfibrils and they form in peculiar manner. If the degree of chain orientation in

a melt surpasses a certain threshold, a new type of nucleus appears, initiating a growth in longitudinal, i.e., chain direction, which is opposite to the lamellar crystallites that grow laterally. This longitudinal growth is very rapid, much more rapid than the lateral growth of the ‘kebabs’ and has specific properties: (i) The nucleus is always oriented in flow direction, but the growing fibril does not necessarily proceed along the flow lines. It can also enter non-oriented regions of the melt and continue the growth straightforwardly, or change the direction of growth on approaching some obstacle. Figure 5.61 shows the EM image of a shish kebab grown in an oriented thin film of i-polystyrene. The film was placed on a microscope grid, and the grid together with the adhering film was deformed in the temperature range where shish kebabs form (225–250 °C). The image, which was obtained after a quench to room temperature, shows a bending of the shish by nearly 90° on approaching a bar of the grid. As is apparent, it is first of all the growing microfibril itself that creates a localized strain field at its tip, which aligns the chains in the melt along its direction. In this sense, one finds here a **self-supported growth** process.

(ii) If the fibril growth is stopped by cooling, a reheating does not take up the longitudinal growth again, which again contrasts the properties of transverse growth of lamellar crystals. The strain at the tip has relaxed and does not come back.

(iii) The growth speed of the fibrils increases with increasing temperature; hence, it is seemingly controlled by rheological properties rather than a supercooling. Figure 5.62 shows the result of an experiment in which the shish formation was followed via the developing birefringence Δn . The initial rise of Δn relates to the chain stretching in the melt; the next, much stronger rise is caused by the developing shishes. Shishes obviously develop more rapidly at higher temperatures. As is apparent, the chain alignment near the tip of the growing fibril is facilitated at higher temperatures.

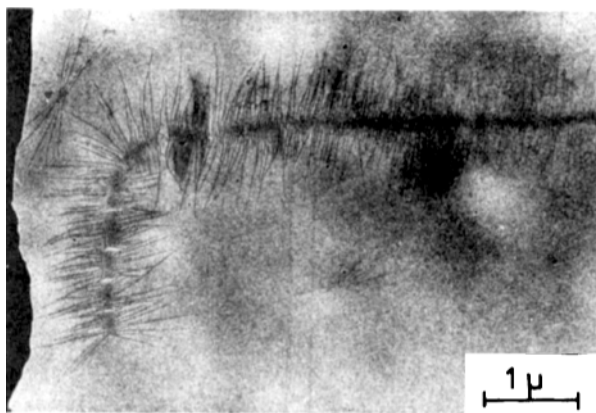


Fig. 5.61. EM image of a shish kebab grown in an oriented thin film of iPS. The *black edge on the left-hand side* is a bar of a microscope grid. From Petermann et al. [66]

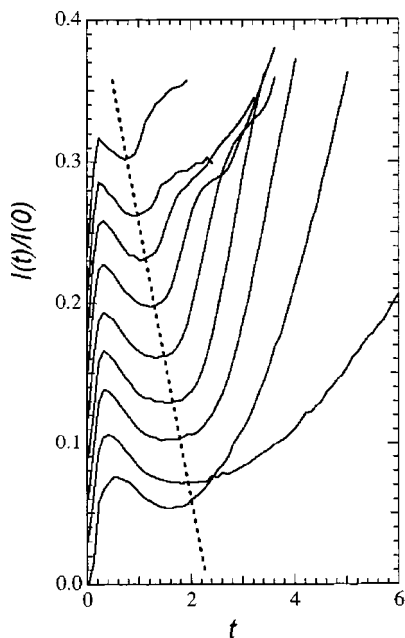


Fig. 5.62. iPP, development of shish kebabs in a strained melt followed by measurements of the light intensity after the passage of a beam through a sample (crossed polarizers). The direction of strain is 45° against the crossed polarizers. From Kornfield et al. [62]

Further Reading

- G. Allegra (Ed.): *Interfaces and Mesophases in Polymer Crystallization*, Advances in Polymer Science 180, 181, 191, Springer, 2005
- P. Barham: *Crystallization and Morphology of Semicrystalline Polymers* in R.W. Cahn, P. Haasen, E.J. Kramer, E.L. Thomas (Eds.): *Materials Science and Technology*, Vol. 12 *Structure and Properties of Polymers*, VCH Publishers, 1993
- E.W. Fischer: *Investigation of the Crystallization Process of Polymers by Means of Neutron Scattering* in L.A. Kleintjens, P.J. Lemstra (Eds.): *Integration of Fundamental Polymer Science and Technology*, Elsevier, 1886
- A. Keller: *Chain-folded Crystallisation of Polymers From Discovery to Present Day: A Personalised Journey* in R.G. Chambers, J.E. Enderby, A. Keller, A.R. Lang, J.W. Steeds (Eds.): *Sir Charles Frank, An Eightieth Birthday Tribute*, Adam Hilger, 1991
- L. Mandelkern: *Crystallization of Polymers*, Cambridge University Press, 2002
- J.-U. Sommer, G. Reiter (Eds.): *Polymer Crystallization*, Lecture Notes in Physics 606, Springer 2003
- B. Wunderlich: *Macromolecular Physics*, Vols. 1, 2, 3, Academic Press, 1973

Mechanical and Dielectric Response

In the large majority of present day uses of polymeric materials the focus is on their mechanical performance. Properties are of a peculiar nature since polymer melts are different from low molar mass liquids and polymer solids differ from conventional crystalline solids. While the latter usually represent perfectly elastic bodies and low molar mass liquids develop viscous forces only, bulk polymers combine elastic and viscous properties in both the fluid and the solid state. Therefore, they are generally addressed as **viscoelastic** and, in fact, polymers are the main representatives of this special class of materials.

Viscoelastic behavior does not just mean a superposition of independent viscous and elastic forces, but in addition it includes a new phenomenon known as **anelasticity**, where both become coupled. It becomes apparent in the observation that part of the deformation, although being reversible, requires a certain time to become established when a load is applied.

The contributions of perfect elasticity, anelasticity, and viscous flow to the total mechanical response of a sample possess different weights for different polymers and, in particular, they vary greatly with temperature. This strong temperature dependence represents another characteristic property of polymeric materials and contrasts with the much less sensitive behavior of metals or ceramics. As a consequence of the changes, the temperature range for a certain application of a polymer is limited. The most important limitation results from the **glass transition**, where the elasticity and strength shown by a glassy solid are lost and the polymer becomes melt-like or, if it is cross-linked, turns into a rubber. In addition, there are other transitions in the sense of further, usually weaker changes in the mechanical properties occurring within a narrow temperature range and they sometimes induce undesired effects. It is clear that, for the use of a polymeric compound, one requires a good knowledge of all these processes. Since this pattern is complex, analysis necessitates special measures in both the experimental methods of characterization and the theoretical descriptions.

Different fields are concerned and they all need their own approaches:

- The properties under moderate loads, where deformations and velocities of viscous flow remain small;
- the case of large reversible deformations realized in rubbers and the rheological properties of polymer melts at higher strain rates, both representing non-linear behavior;
- and, finally, of special importance for applications, large deformations, yielding and fracture.

We shall treat the first topic in this chapter and subsequently, in Chaps. 9 and 10, large deformations, non-linear flow and the **ultimate properties** of yield and break.

In electrical applications, polymers are often used as isolators. Since it is then important to be informed about possible electric losses, one needs to know their dielectric properties in dependence on frequency and temperature. As we shall see, a description of the response of dielectric materials to applied time-dependent electric fields is formally equivalent to the treatment of time-dependent mechanical responses. Therefore, we shall discuss both together in this chapter. There also exist electrically conductive polymers, namely polymers with conjugated double bonds after a doping process. Their properties will be treated separately in the next chapter.

6.1 Response Functions

If a mechanical or an electric field is applied to a polymer sample and remains sufficiently small, then the reaction, as given by the deformation and the polarization, respectively, can be described by linear equations. We shall first deal with the linear viscoelasticity, which can be specified by various mechanical response functions, and then with the linear dielectric behavior, as characterized by the time-dependent or frequency-dependent dielectric function.

6.1.1 Viscoelasticity

A direct simple method to study the viscoelastic properties of a given sample is the **creep experiment**. This is carried out by instantaneously applying a constant force, which is then followed by a measurement of the resulting deformation as a function of time.

Figure 6.1 schematically indicates a possible result, referring to the case where an uniaxial tensile load is applied, which then leads to an elongation ΔL_z . In general, it will be found that the **creep curve** represents a superposition of three contributions:

- a perfectly elastic, i.e., instantaneous response;
- a retarded elastic deformation, i.e., an anelastic part; and
- viscous flow.

The first two contributions are reversible, the last one is irreversible.

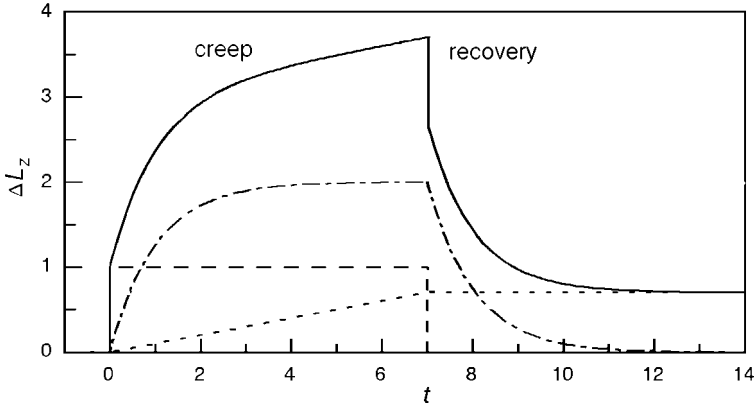


Fig. 6.1. Creep curve of a polymer sample under tension (schematic). The elongation ΔL_z induced by a constant force applied at zero time is set up by a superposition of an instantaneous elastic response (*dashed line*), a retarded anelastic part (*dash-dot line*), and viscous flow (*dotted line*). An irreversible elongation is retained after an unloading and the completion of the recovery process

It is of interest to determine separately the reversible and irreversible parts, and this can be accomplished in an easy manner by removing the load from the sample and monitoring the subsequent **recovery** process. As indicated in Fig. 6.1, this first leads to an immediate shortening, which is then followed by a retarded further length reduction; only the irreversible part, caused by the viscous flow, remains.

If the force applied is sufficiently small, then one finds that the creep curve, $\Delta L_z(t)$, becomes proportional to the force. In this **linear viscoelastic range** one can use the ratio between the time-dependent elongation and the force for a description of the response. For a sample under tension the **tensile creep compliance** $D(t)$ is introduced as

$$D(t) = \frac{e_{zz}(t)}{\sigma_{zz}^0}. \quad (6.1)$$

Here $e_{zz}(t)$ denotes the time-dependent longitudinal strain

$$e_{zz}(t) = \frac{\Delta L_z}{L_z}, \quad (6.2)$$

where L_z is the original sample length; σ_{zz}^0 stands for the constant tensile stress applied at zero time (as usual, the first subscript indicates the normal vector of the face acted upon and the second one gives the direction of the stress component). It is important to recognize that $D(t)$ provides, in principle, a complete characterization of the tensile properties of a given sample. Practical measurements are, of course, limited because registration cannot start before a certain minimum and extend over a certain maximum time.

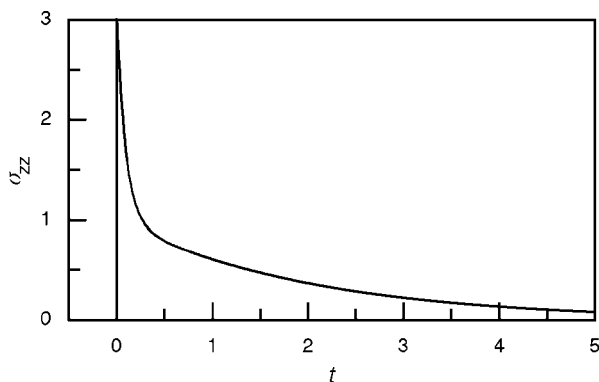


Fig. 6.2. Stress relaxation curve (schematic)

A second method in mechanical tests is the **stress relaxation experiment**. Here, a certain constant strain is instantaneously imposed on a sample and the stress induced by this procedure is measured as a function of time. Figure 6.2 schematically shows the possible shape of a stress relaxation curve for an uniaxially deformed sample. The tensile stress has its maximum directly after the deformation act and then it decays. Anelastic components first produce a downward step. If the sample can flow, the stress will further decrease and finally vanish completely. The result of such an experiment can be described by the **time-dependent tensile modulus** $E(t)$, defined as

$$E(t) = \frac{\sigma_{zz}(t)}{e_{zz}^0} , \quad (6.3)$$

whereby e_{zz}^0 denotes the imposed longitudinal strain.

The third method used is **dynamic-mechanical experiments**. In these measurements, samples are exposed to a periodically varying stress field, for example, to a tensile stress

$$\sigma_{zz}(t) = \sigma_{zz}^0 \exp(-i\omega t) . \quad (6.4)$$

The resulting time-dependent longitudinal strain, $e_{zz}(t)$, is indicated in Fig. 6.3. It varies with the frequency of the stress, but shows in general a phase-lag. Therefore, for the strain we write

$$e_{zz}(t) = e_{zz}^0 \exp(i\varphi) \exp(-i\omega t) . \quad (6.5)$$

A full description of the relation between $\sigma_{zz}(t)$ and $e_{zz}(t)$ is provided by the complex **dynamic tensile compliance** $D(\omega)$, defined as

$$D(\omega) = \frac{e_{zz}(t)}{\sigma_{zz}(t)} = \frac{e_{zz}^0 \exp(i\varphi)}{\sigma_{zz}^0} = D' + iD'' . \quad (6.6)$$

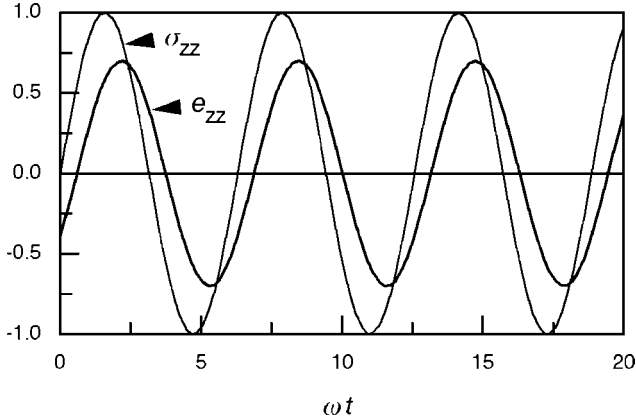


Fig. 6.3. Time dependence of stress (σ_{zz}) and strain (e_{zz}) in a dynamic-mechanical experiment (schematic)

We write the dynamic compliance as a function $D(\omega)$ because it generally varies with the frequency. To completely characterize the viscoelastic tensile properties of a given sample, one is indeed required to know the complete functional dependence.

As an alternative, one can also employ the complex **dynamic tensile modulus** $E(\omega)$, defined as

$$E(\omega) = \frac{\sigma_{zz}(t)}{e_{zz}(t)} = \frac{1}{D(\omega)} = E' - iE'' . \quad (6.7)$$

The different choices for the sign in front of the imaginary parts D'' and E'' represent a convention and result in positive values for both. The signs are reversed if the oscillation is described as $\sigma_{zz}(t) \propto \exp(i\omega t)$ rather than by Eq. (6.4).

Analogous experiments can be carried out for other kinds of mechanical loading. Of particular importance are measurements for **simple shear**, which determine the relation between the shear strain e_{zx} , giving the displacement along x per unit distance normal to the shear plane $z = \text{const}$, and the shear stress σ_{zx} , as given by the force per unit area, acting on the shear plane along x . Shear properties of samples are described by

- the **shear compliance**

$$J(t) = \frac{e_{zx}(t)}{\sigma_{zx}^0} , \quad (6.8)$$

- the **time-dependent shear modulus**

$$G(t) = \frac{\sigma_{zx}(t)}{e_{zx}^0} , \quad (6.9)$$

- the **dynamic shear compliance**

$$J(\omega) = \frac{e_{zx}^0}{\sigma_{zx}^0} \exp(i\varphi), \quad (6.10)$$

and

- the **dynamic shear modulus**

$$G(\omega) = \frac{\sigma_{zx}^0}{e_{zx}^0} \exp(-i\varphi). \quad (6.11)$$

As has already been mentioned, a dynamic-mechanical measurement at one frequency does not possess the same information content as creep or stress relaxation experiments, and in order to achieve equivalence, these measurements have to be carried out under variation of ω over a sufficiently large range. Commercially available mechanical spectrometers usually scan a range of three to four orders of magnitude. As this is still limited, one might suspect at first that the information content is reduced compared to the time-dependent experiments. However, as it turns out, if measurements are combined with temperature variations, one can also achieve a satisfactory overall characterization. We shall come back to this point for an explanation below.

Having introduced three different methods for a characterization of viscoelastic properties, one may wonder whether the results are interrelated. This is indeed the case, but before entering into this matter, we look at dielectric measurements.

6.1.2 Orientational Polarization

Application of an electric field \mathbf{E} on a non-conducting sample leads to a polarization \mathbf{P} . In electrostatics this process is described by the linear relation

$$\mathbf{P} = \varepsilon_0(\varepsilon - 1)\mathbf{E}. \quad (6.12)$$

Employing the dielectric displacement vector \mathbf{D} , one can write equivalently

$$\mathbf{D} = \varepsilon_0\mathbf{E} + \mathbf{P} = \varepsilon_0\varepsilon\mathbf{E}. \quad (6.13)$$

In both equations the response is given by the dielectric function ε .

If the experiment is carried out with a constant field \mathbf{E}_0 being switched on at zero time, one finds in general a time-dependent polarization $\mathbf{P}(t)$, set up of an instantaneous part \mathbf{P}_u and a retarded part \mathbf{P}_{or}

$$\mathbf{P}(t) = \mathbf{P}_u + \mathbf{P}_{or}(t). \quad (6.14)$$

One describes this result with the aid of a time-dependent dielectric function $\varepsilon(t)$, as

$$\mathbf{P}(t) = \varepsilon_0(\varepsilon(t) - 1)\mathbf{E}_0 \quad (6.15)$$

or, split up into the two contributions, by

$$\mathbf{P}(t) = \varepsilon_0(\varepsilon_u - 1)\mathbf{E}_0 + \varepsilon_0\Delta\varepsilon(t)\mathbf{E}_0 . \quad (6.16)$$

The immediately reacting part, \mathbf{P}_u , is due to the shift of the electron clouds and the deformation of the molecular skeletons occurring within times corresponding to frequencies in the UV-range and the IR-range, respectively. The retarded part, \mathbf{P}_{or} , arises for polar molecular fluids and originates from the orientation of the permanent dipoles.

More common than using dc-fields is the use of ac-fields for the characterization of dielectric properties of samples. On applying a sinusoidally varying field, represented in complex notation as

$$\mathbf{E}(t) = \mathbf{E}_0 \exp(-i\omega t) , \quad (6.17)$$

there results, in general, a time-dependent polarization

$$\mathbf{P}(t) = \mathbf{P}_0 \exp(i\varphi) \exp(-i\omega t) . \quad (6.18)$$

The angle φ denotes a possible phase-lag. For a description of the relation between the polarization and the field, one can again choose, as in the analogous case of the dynamic-mechanical experiment, their complex ratio, known as **complex dielectric susceptibility**. Rather than the latter, we will use the closely related **complex dielectric function** $\varepsilon(\omega)$, defined as

$$\varepsilon(\omega) = \frac{\mathbf{D}(t)}{\mathbf{E}(t)} = \varepsilon_0 + \frac{P_0}{E_0} \exp(i\varphi) . \quad (6.19)$$

$\varepsilon(\omega)$ splits up into a real and an imaginary part

$$\varepsilon(\omega) = \varepsilon'(\omega) + i\varepsilon''(\omega) . \quad (6.20)$$

6.1.3 General Relationships

It may have already been noticed that all the described experiments correspond to a common basic scheme. There is a force or field, represented here by the stress or the electric field, which leads to a 'displacement', as given by the strain or the polarization. In all the cases considered, the force and the resulting displacement are related by a linear equation. Hence, we deal throughout with **linear responses**. Clearly, many other effects exist that also represent linear responses. There are reactions on still other kinds of mechanical loading but also on the applications of other fields, as for example, a magnetic field \mathbf{B} , which induces a magnetization \mathbf{M} .

There is a second characteristic property that all cases have in common. One always deals with a pair of energy conjugated variables, that is to say, the

displacement caused by the field results in work. More specifically, if a field ψ gives rise to a displacement dx , then the work per unit volume is

$$\frac{d\mathcal{W}}{\mathcal{V}} = \psi dx . \quad (6.21)$$

This holds for the tensile load where

$$\frac{d\mathcal{W}}{\mathcal{V}} = \sigma_{zz} de_{zz} = D\sigma_{zz} d\sigma_{zz} , \quad (6.22)$$

for the applied shear stress where

$$\frac{d\mathcal{W}}{\mathcal{V}} = \sigma_{zx} de_{zx} = J\sigma_{zx} d\sigma_{zx} , \quad (6.23)$$

and also for the dielectric experiment when we identify dx with the change of the dielectric displacement vector, hence

$$\frac{d\mathcal{W}}{\mathcal{V}} = \mathbf{E} d\mathbf{D} . \quad (6.24)$$

So far, we have discussed the response of systems only for forces with special time dependencies. The creep compliance describes the reaction on a force that is switched on at zero time and then remains constant; the dynamic compliance specifies the response on a sinusoidally varying stress. What happens in the general case, when an arbitrary time-dependent force $\psi(t)$ is applied? There is a specific function that enables us to deal with this general situation, sometimes called the **primary response function**. It is introduced by considering the effect of an infinitely short pulse, as represented by

$$\psi(t) = \psi_0 \delta(t) \quad (6.25)$$

where $\delta(t)$ is the delta function. The primary response function, denoted by $\mu(t)$, describes the time-dependent displacement $x(t)$ caused by this pulse as

$$x(t) = \psi_0 \mu(t) . \quad (6.26)$$

It is instructive to look at some typical examples as sketched in Fig. 6.4. A damped harmonic oscillator reacts to a pulse by starting an oscillation with exponentially decaying amplitudes, and this is shown in part (a). The effect on a perfectly viscous body is quite different since it just becomes plastically deformed and then maintains the new shape (b). Part (c) shows the reaction of a perfectly elastic sample, i.e., a Hookean solid, which is only deformed during the short time of the pulse. Finally, part (d) represents the reaction of an overdamped oscillator or **relaxator** exhibiting an exponential decay.

The primary response function indeed enables us generally to formulate the displacement resulting from an arbitrary time-dependent force. It is given by

$$x(t) = \int_{-\infty}^t \mu(t-t') \psi(t') dt' . \quad (6.27)$$

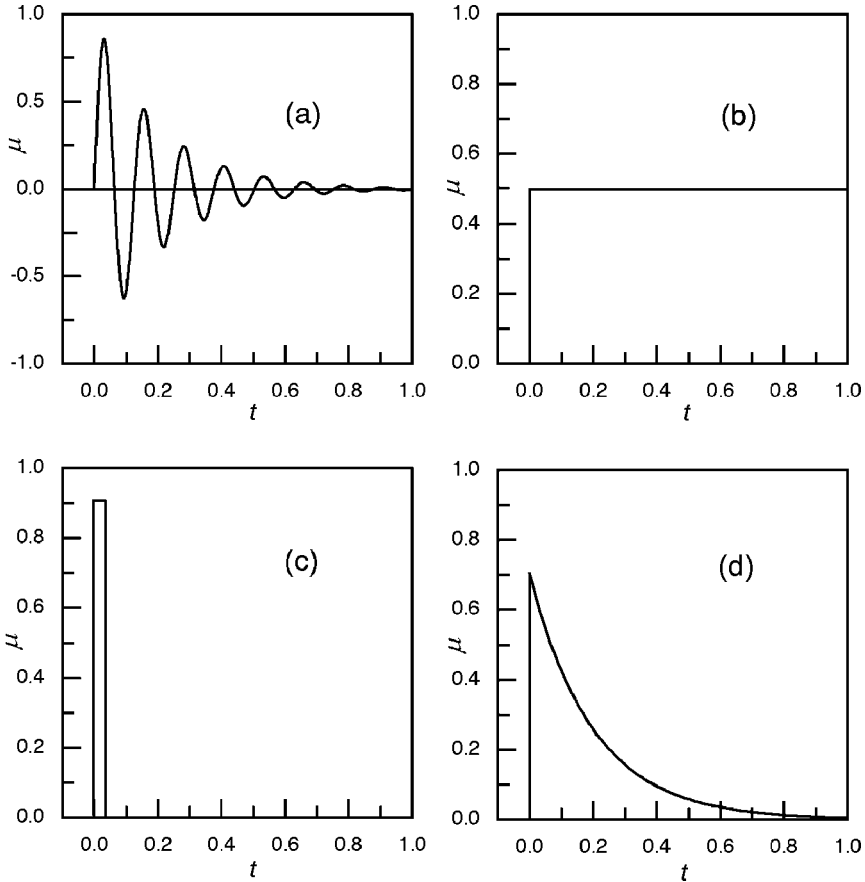


Fig. 6.4. Primary response function of a damped harmonic oscillator (a), a perfectly viscous body (b), a Hookean solid (c), and a simple relaxatory system (d)

The physical background of Eq. (6.27) is easily seen. The integral relation just follows from the two basic properties of linear systems, namely the causality principle and the validity of the superposition principle:

- Causality requires that the displacement at a given time can only depend on the forces in the past and this finds its expression in the limits chosen for the integral.
- Employing the superposition principle, an arbitrary time-dependent force can first be divided into a sequence of pulses with adjusted heights and then the total reaction can be represented as a sum over the responses to all the pulses. The integral expresses exactly this procedure.

Emanating from Eq. (6.27), one can derive the interrelations between the various response functions. We formulate them in terms of the general variables

x and ψ and consider, as a first example, the displacement $x(t)$ resulting from a force with amplitude ψ_0 switched on at zero time. Equation (6.27) yields directly

$$x(t) = \int_0^t \mu(t-t')\psi_0 dt' . \quad (6.28)$$

As for the creep experiment, the result can also generally be described with the aid of the ratio

$$\frac{x(t)}{\psi_0} = \alpha(t) . \quad (6.29)$$

The name used for this function $\alpha(t)$ is **time-dependent susceptibility**. We obtain

$$\alpha(t) = \int_0^t \mu(t-t') dt' = \int_0^t \mu(t'') dt'' . \quad (6.30)$$

Taking the derivative on both sides gives the relation between $\mu(t)$ and $\alpha(t)$:

$$\mu(t) = \frac{d\alpha}{dt}(t) . \quad (6.31)$$

Second, consider the stress relaxation experiment. In terms of the general variables it is to be described as

$$x_0 = \int_0^t \mu(t-t')\psi(t') dt' , \quad (6.32)$$

where x_0 denotes the imposed displacement. We introduce a **general time-dependent modulus** $a(t)$ as

$$a(t) = \frac{\psi(t)}{x_0} . \quad (6.33)$$

$a(t)$ and $\mu(t)$ are related by the integral equation

$$1 = \int_0^t \mu(t-t')a(t') dt' . \quad (6.34)$$

If we eliminate $\mu(t)$ from this equation with the aid of Eq. (6.31), we find the interrelation between the time-dependent susceptibility and the time-dependent modulus

$$1 = \int_0^t \frac{d\alpha}{dt}(t-t')a(t') dt' . \quad (6.35)$$

An important equation is obtained, if we take Eq. (6.31), introduce it into Eq. (6.27),

$$x(t) = - \int_{-\infty}^t \frac{d\alpha}{dt'}(t-t')\psi(t') dt' , \quad (6.36)$$

and then carry out a partial integration, leading to

$$x(t) = \int_{-\infty}^t \alpha(t-t') d\psi(t') . \quad (6.37)$$

Rather than beginning with Eq. (6.27), in the polymer literature, Eq. (6.37) is often used as the basis. It is then understood as the mathematical formulation of the **Boltzmann superposition principle**, which states that each loading step makes an independent contribution to the final deformation and that the latter then follows by simple addition. This is exactly the physical meaning of the integral. The contributions are described in the integral. As we can see, the after-effect of each step is a creep curve, starting with the step and being weighted by the step height.

Rather than considering the displacement $x(t)$ in dependence on the forces in the past, $\psi(t' < t)$, one can ask conversely for the functional dependence of the force $\psi(t)$ on the previous displacements $x(t' < t)$. The solution is obvious: We just have to exchange the susceptibility $\alpha(t-t')$ against the generalized time-dependent modulus $a(t-t')$ and represent $\psi(t)$ as a sum of relaxation curves:

$$\psi(t) = \int_{-\infty}^t a(t-t') dx(t') . \quad (6.38)$$

This is the alternative form of the Boltzmann superposition principle and it is of importance in particular in rheological treatments.

Let us finally come to the dynamic experiments, where an oscillatory force

$$\psi(t) = \psi_0 \exp(-i\omega t) \quad (6.39)$$

is applied. It results in a displacement, to be written in general as

$$x(t) = x_0 \exp(i\varphi) \exp(-i\omega t) . \quad (6.40)$$

Employing Eq. (6.27), this relation corresponds to

$$x_0 \exp(i\varphi) \exp(-i\omega t) = \int_{-\infty}^t \mu(t-t') \psi_0 \exp(-i\omega t') dt' . \quad (6.41)$$

The complex amplitude ratio

$$\frac{x_0 \exp(i\varphi)}{\psi_0} = \alpha(\omega) \quad (6.42)$$

describes the result of a dynamic experiment. $\alpha(\omega)$ is called **general dynamic susceptibility**, and we obtain for it

$$\alpha(\omega) = \int_{-\infty}^t \mu(t-t') \exp[i\omega(t-t')] dt' . \quad (6.43)$$

With the substitution

$$t - t' = t''$$

we can write

$$\alpha(\omega) = \int_0^\infty \mu(t'') \exp(i\omega t'') dt'' = \int_{-\infty}^\infty \mu(t'') \exp(i\omega t'') dt'' , \quad (6.44)$$

taking into account that $\mu(t'' < 0) = 0$. As we can see, the primary response function, $\mu(t)$ and the dynamic susceptibility, $\alpha(\omega)$ correspond to a pair of Fourier transforms.

The dynamic susceptibility is in general a complex quantity

$$\alpha(\omega) = \alpha'(\omega) + i\alpha''(\omega) . \quad (6.45)$$

Actually, the real part $\alpha'(\omega)$ and the imaginary part $\alpha''(\omega)$ are not independent, but related by the **Kramers–Kronig dispersion relations**. These have the following forms:

$$\alpha'(\omega_0) = \frac{1}{\pi} \text{P} \int_{-\infty}^\infty \frac{\alpha''(\omega)}{\omega - \omega_0} d\omega \quad (6.46)$$

$$\alpha''(\omega_0) = -\frac{1}{\pi} \text{P} \int_{-\infty}^\infty \frac{\alpha'(\omega)}{\omega - \omega_0} d\omega . \quad (6.47)$$

The relations include a special type of integral, the **Cauchy integral**, which eliminates the singularity at $\omega = \omega_0$. In the case of Eq. (6.46), it is defined by

$$\text{P} \int_{-\infty}^\infty \frac{\alpha''(\omega)}{\omega - \omega_0} d\omega = \lim_{\delta \rightarrow 0} \left[\int_{-\infty}^{\omega_0 - \delta} \frac{\alpha''}{\omega - \omega_0} d\omega + \int_{\omega_0 + \delta}^\infty \frac{\alpha''}{\omega - \omega_0} d\omega \right] , \quad (6.48)$$

and equivalently for Eq. (6.47). According to this expression, ω_0 is approached in a synchronized manner from both sides. Then the positive and negative divergent values compensate each other and the singularity does not emerge. A derivation of the Kramers–Kronig relations can be found in many textbooks on statistical mechanics. Here, we leave it with one remark concerning their physical origin: The relations can be regarded as a consequence of the causality principle, since the derivation makes use of one condition only, namely that $\mu(t'')$ vanishes for $t'' < 0$.

It is important that we now discuss the work resulting from the movement under the action of the force. A most useful and simple result is obtained for the dynamic experiments. Here the force

$$\psi(t) = \psi_0 \exp(-i\omega t) \quad (6.49)$$

produces a displacement

$$x(t) = \alpha(\omega)\psi(t) = (\alpha' + i\alpha'')\psi(t) . \quad (6.50)$$

For a calculation of the work one has to use the true values $\psi(t)$ and $x(t)$, which follow from the complex notation by an extraction of the real part. We therefore write

$$\psi(t) = \psi_0 \cos(\omega t) \quad (6.51)$$

and

$$x(t) = \alpha' \psi_0 \cos(\omega t) + \alpha'' \psi_0 \sin(\omega t) . \quad (6.52)$$

The power is given by

$$\frac{1}{\mathcal{V}} \frac{d\mathcal{W}}{dt} = \psi \frac{dx}{dt} = -\frac{\psi_0^2}{2} \omega \alpha' \sin(2\omega t) + \psi_0^2 \omega \alpha'' \cos^2(\omega t) . \quad (6.53)$$

There are two contributions, one proportional to α' and the other proportional to α'' . These two contributions just represent two different aspects of the work. The first contribution varies periodically between positive and negative values, which indicates an energy exchange between the driving part and the driven system. Obviously this first term is associated with an energy that during one half-period is stored in the driven system and during the successive half-period then is completely returned.

The second contribution is qualitatively different, as it yields a non-vanishing positive value in the time average

$$\frac{1}{\mathcal{V}} \overline{\frac{d\mathcal{W}}{dt}} = \frac{1}{2} \psi_0^2 \omega \alpha''(\omega) . \quad (6.54)$$

Hence, work is expended on the driven system. If the sample is kept under isothermal conditions, the internal energy \mathcal{E} does not change, i.e.,

$$\overline{\frac{d\mathcal{E}}{dt}} = 0 . \quad (6.55)$$

Since generally, according to the first law of thermodynamics, we have

$$d\mathcal{E} = d\mathcal{W} + d\mathcal{Q} , \quad (6.56)$$

we find

$$\overline{\frac{d\mathcal{W}}{dt}} = -\overline{\frac{d\mathcal{Q}}{dt}} . \quad (6.57)$$

This means that the power is dissipated, i.e., returned by the system in the form of heat.

We see that the susceptibility separates the elastic part and the viscous dissipative part of the work expended on the system. They show up in the real part $\alpha'(\omega)$ and the imaginary part $\alpha''(\omega)$, respectively. It is important to note that the two parts are not independent even if they represent quite different physical properties. In fact, they are related by the Kramers–Kronig relations, Eqs. (6.46) and (6.47).

We finish this section by mentioning another frequently used quantity, known as the **loss tangent**. It is defined as

$$\tan \delta(\omega) = \frac{\alpha''(\omega)}{\alpha'(\omega)}. \quad (6.58)$$

According to the definition, $\tan \delta(\omega)$ describes the ratio between the dissipated and the reversibly exchanged work.

6.2 Relaxatory Modes

Orientational polarization, as it is found in polar liquids, provides a good example for explaining the physical background of reversible retarded responses. First consider the natural state without a field. Here we have no polarization and this arises from distributing the orientations of the polar units in the sample isotropically. If an electric field is now applied, the orientational distribution changes. Since dipole orientations in the field direction are preferred, the distribution function becomes anisotropic. As a consequence we find a non-vanishing value for the orientational polarization \mathbf{P}_{or} .

For systems, where the coupling between the polar units is so weak that they can reorient largely independently from each other, \mathbf{P}_{or} can be calculated in simple manner. It then just emerges from the competition between the interaction energy of the dipoles with the electric field and the kinetic energy of the molecular rotation. The calculation is carried out in many textbooks on physical chemistry and the result reads, in an approximate form,

$$\mathbf{P}_{\text{or}} \simeq c_{\text{m}} \frac{|\mathbf{p}|^2 |\mathbf{E}|}{3kT}. \quad (6.59)$$

\mathbf{p} is the dipole moment of the reorienting units and c_{m} gives their number density.

Establishment of the new equilibrium subsequent to a sudden application of an electric field requires a finite time. To see the origin of the retardation, envisage the rotational dynamics in the fluid. Owing to the strongly varying intermolecular forces, the dipole carrying units cannot rotate freely, but rather show a statistical kind of motion. For independent units, this motion may be described as a **rotational diffusion**, that is to say, it equals a succession of uncorrelated angular steps. The diffusive motion leads to a complete reorientation within a certain time, say τ . In fact, τ is the only parameter required to characterize completely the state of rotational motion in a system of independent units. Therefore, it sets the time scale for generally all changes in the orientational distribution function. Hence, in particular, it also determines the time needed to attain the new equilibrium set by a changed electric field.

What is the microscopic background of the retarded mechanical responses? As we have learned, one can envisage a polymeric fluid as an ensemble of ma-

cromolecules that change between the various conformational states. The populations of the different states are determined by the laws of Boltzmann statistics. If a mechanical field is now applied, a change in the population numbers is induced. For example, consider a rubber to which a tensile stress is imposed. Clearly, now all conformations that are accompanied by an extension along the direction of stress are preferred. The repopulation of the conformational states and the resulting increase in the sample length require a finite time, which must correspond to the time scale of the conformational transitions.

Compared to the dielectric response first considered, the mechanical reaction is more complex. Dielectric relaxation in a system of independent polar units originates from their individual reorientational motions. In the mechanical relaxation of a rubber we find a different situation. Here, we are dealing with transitions between the different conformations of a chain and not with individual movements of single groups. Rather than having one process only, in this case, a large number of different **modes** exist, and these may vary over a wide range in the characteristic times. As a consequence, the sample's response showing up in the time-dependent change of its length subsequent to the application of the tensile stress cannot be associated with a single time constant only, but is of a complex nature.

There is also a simple situation equivalent to the dipole reorientations in mechanical behavior. In glassy polymers, large-scale conformational changes are inhibited but the possibility of localized conformational transitions remains. These can be observed, for example, for polymers with side-groups. In the next section, an example will be presented where the side-groups of a polymer chain possess just two conformational states. Application of stress here leads to a change in the respective occupation numbers and the redistribution occurs within a time as given by the rate of jumps between the two states. Macroscopically, a detectable change in the shape of the loaded sample results, which can be related to a single characteristic time only.

In all the examples discussed, we are concerned with the passage from a non-equilibrium situation, created by the sudden imposition of an external field, to the new equilibrium. The change is accompanied and driven by a decrease in the free energy. Using mechanistic terms one could say that a system that at first, when having an enhanced free energy, is 'strained', 'relaxes' while going to the equilibrium. Correspondingly, all these retarded transitions into a new equilibrium are generally addressed as **relaxation processes**. The name includes even more, namely the underlying microscopic motions as well. The notion 'relaxation' thus has a broad meaning in the literature, and is not at all restricted to the first introduced stress relaxation experiment, which just represents one special case.

6.2.1 Single-Time Relaxation Process

As we have seen, the time dependence of a macroscopic relaxation process always reflects the underlying microscopic dynamics. We may now proceed

and look for kinetical equations that correctly describe the time dependence of the observed retarded responses.

There is an obvious choice for the simple case when only a single characteristic time is included. It goes back to Debye, who proposed it in a famous work on the dielectric properties of polar liquids, based on a statistical mechanical theory. We formulate the equation for the above-mentioned simple mechanical relaxation process, associated with transitions between two conformational states only, and consider a creep experiment under shear stress. The equation has the following form:

$$\frac{de_{zx}}{dt} = -\frac{1}{\tau} (e_{zx}(t) - \Delta J \sigma_{zx}^0) . \quad (6.60)$$

It represents a linear differential equation of the first order, implying the assumption that, for a system in non-equilibrium, relaxation takes place with a rate that increases linearly with the distance from the equilibrium state. This is not a specific kind of expression devised to deal exclusively with our problem. Equivalent equations are broadly used in thermodynamics to describe the kinetics of all sorts of irreversible processes. Importantly, the equation includes one time constant only, the **relaxation time** τ .

A further parameter, ΔJ , here determines the equilibrium value of the anelastic contribution to the shear strain following from an applied stress σ_{zx}^0 . The equilibrium value is given by the product $\Delta J \sigma_{zx}^0$. In accordance with the physical meaning, ΔJ is called the **relaxation strength**. This is, in fact, a general name also used for the analogous parameters in other relaxation processes. They all have in common that they determine the magnitude of the effect, as given, for example, by a contribution to the strain, the stress or the polarization.

The solution of the relaxation equation for the creep experiment, i.e., a step-like application of a stress σ_{zx}^0 at zero time, can be written down directly. It is given by

$$e_{zx}(t) = \Delta J \sigma_{zx}^0 \left(1 - \exp\left(-\frac{t}{\tau}\right) \right) . \quad (6.61)$$

This is indeed a correct representation of the creep curve observed for a single-time relaxation process. The physical properties of the process are included in the two parameters ΔJ and τ . The latter agrees with the transition rates between the two conformational states. It is more difficult to predict and thus to interpret the relaxation strength. As is intuitively clear, the prerequisite for an alteration of the population numbers under an applied shear stress is a change in the ‘shape’ of the active unit, as only then can a change in the energy arise. To formulate this interaction energy for a unit as represented by a whole monomer or only the side-group can, however, be difficult; much more difficult than the case considered above of the interaction of a dipole with an electric field. It is therefore not surprising that calculations of me-

chanical relaxation strengths on microscopic grounds are rare and quantitative interpretations of measured values an exception.

The **relaxation equation** (6.60) is not restricted in use to step-like changes in the external conditions, but also holds if the equilibrium value $\Delta J\sigma_{zx}$ is not a constant and changes with time. In particular, it can be employed to treat dynamic-mechanical experiments. As is clear, applying an oscillatory shear stress

$$\sigma_{zx}(t) = \sigma_{zx}^0 \exp(-i\omega t) \quad (6.62)$$

means to impose an oscillatory variation for the characterization of dielectric properties of samples for the equilibrium strain, $\Delta J\sigma_{zx}(t)$. If we introduce it into the relaxation equation, we obtain

$$\frac{de_{zx}}{dt} = -\frac{1}{\tau} (e_{zx}(t) - \Delta J\sigma_{zx}^0 \exp(-i\omega t)) . \quad (6.63)$$

An oscillatory stress results in an oscillatory strain as given by Eq. (6.10),

$$e_{zx}(t) = \sigma_{zx}^0 J(\omega) \exp(-i\omega t) . \quad (6.64)$$

If we take this solution, introduce it into Eq. (6.63) and take away the common exponential factor from both sides, we obtain the dynamic compliance. It is given by

$$J(\omega) = \frac{\Delta J}{1 - i\omega\tau} . \quad (6.65)$$

The dynamic compliance of the single-time relaxation process, in the literature also addressed as the **Debye process**, thus has a simple form, being a function of the product $\omega\tau$ and ΔJ only. Separation into the real and the imaginary part yields

$$J(\omega) = J' + iJ'' = \frac{\Delta J}{1 + \omega^2\tau^2} + i\frac{\Delta J\omega\tau}{1 + \omega^2\tau^2} . \quad (6.66)$$

Figure 6.5 depicts J' and J'' using a logarithmic scale for the variable $\omega\tau$. The use of a logarithmic scale is not only convenient, regarding that experiments usually cover several orders of magnitude, but also has the advantage that the curves then exhibit characteristic symmetries. The imaginary part, which describes the loss, forms a symmetric bell-shaped curve with maximum at $\omega\tau = 1$. If J'' is written in the form

$$J'' = \frac{\Delta J}{10^{-\log(\omega\tau)} + 10^{\log(\omega\tau)}} , \quad (6.67)$$

the symmetry is obvious.

The real part shows a steep decrease in the range of the loss maximum and its physical cause is easily revealed. If the mechanical field applied has a frequency that is small compared to the transition rates in the system, establishment of thermal equilibrium is rapid compared to the period of the

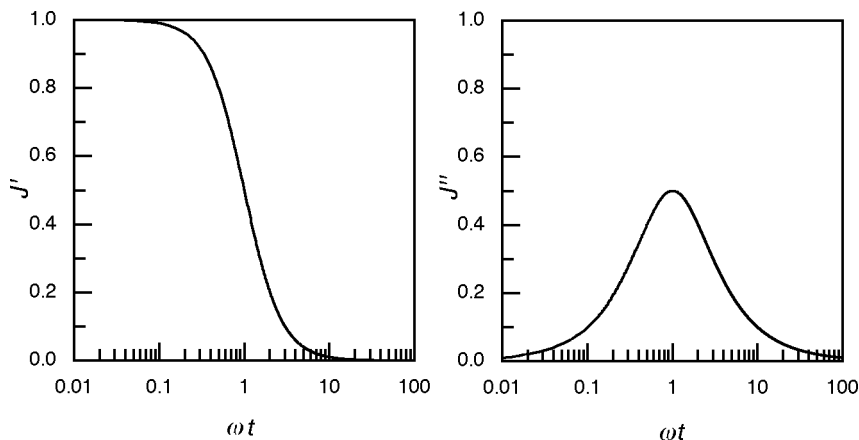


Fig. 6.5. Real part (*left*) and imaginary part (*right*) of the dynamic compliance associated with a mechanical Debye process

field and the system can always remain in equilibrium. Hence, we encounter quasistatic conditions and observe the full relaxation strength. At the other limit, when the frequencies of the field applied are large compared to the transition rates, equilibrium cannot be established and the system reacts to the average strain only, which is zero. The crossover from one to the other regime only occurs in the range $\omega\tau \simeq 1$.

The maximum in J'' and the steepest descent of J' are located at the same frequency. Furthermore, the area under the loss curve and the relaxation strength ΔJ are proportional to each other. Integration gives the following relation:

$$\int_{-\infty}^{\infty} J'' d \log(\omega\tau) = \frac{\pi}{2 \ln 10} \Delta J. \quad (6.68)$$

In fact, these properties are not specific to the Debye process, but have a deeper basis, which extends their validity. According to the Kramers–Kronig relations, J' and J'' are mutually dependent and closer inspection of the equations reveals that it is impossible, in principle, to have a loss without a simultaneous change in J' . Both effects are coupled, the reason being, as mentioned above, the validity of the causality principle.

The loss curve has a characteristic width, the total width at half height amounting to 1.2 decades. Compared to the loss at the resonance frequency of an oscillating system, the loss curve of the Debye process is much broader. In fact, a halfwidth of 1.2 decades presents the lower limit for all loss curves found in relaxing systems. Loss curves that are narrower are therefore indicative of the presence of oscillatory contributions, or more generally speaking, indicate effects of moments of inertia.

A simple check whether a measured dynamic compliance or a dielectric function agrees with a Debye process is provided by the **Cole–Cole plot**. Let

we illustrate it with a dielectric single-time relaxation process. If we choose an expression analogous to Eq. (6.66) for the dipolar polarization and also take into account the instantaneous electronic polarization with a dielectric constant ε_u , the dielectric function $\varepsilon(\omega)$ shows the form

$$\varepsilon = \varepsilon_u + \frac{\Delta\varepsilon}{1 + \omega^2\tau^2} + i \frac{\omega\tau\Delta\varepsilon}{1 + \omega^2\tau^2}. \quad (6.69)$$

When for all values of $\omega\tau$ the associated pairs $\varepsilon'(\omega\tau)$ and $\varepsilon''(\omega\tau)$ are plotted in a plane as shown in Fig. 6.6, a semicircle is obtained. The circle begins for $\omega\tau = 0$ at $\varepsilon' = \varepsilon_u + \Delta\varepsilon$ and ends for $\omega\tau \rightarrow \infty$ at $\varepsilon' = \varepsilon_u$. The proof for the circular form of the Cole–Cole plot is straightforward, as we can write

$$\begin{aligned} \left[\varepsilon' - \left(\varepsilon_u + \frac{\Delta\varepsilon}{2} \right) \right]^2 + (\varepsilon'')^2 &= \left[\frac{2\varepsilon' - 2\varepsilon_u - \Delta\varepsilon}{2} \right]^2 + (\varepsilon'')^2 \\ &= \left[\frac{2\Delta\varepsilon - \Delta\varepsilon(1 + \omega^2\tau^2)}{2(1 + \omega^2\tau^2)} \right]^2 + \frac{\Delta\varepsilon^2\omega^2\tau^2}{(1 + \omega^2\tau^2)^2} \\ &= \frac{\Delta\varepsilon^2(1 + \omega^2\tau^2)^2}{4(1 + \omega^2\tau^2)^2} = \frac{\Delta\varepsilon^2}{4}. \end{aligned} \quad (6.70)$$

Figure 6.6 presents, as examples, results of dielectric studies on certain rod-like molecules, shortly designated as ‘C₆C₃’, which carry a longitudinal electric dipole. The Cole–Cole plot on the left-hand side represents measurements in the liquid phase of this low molar mass compound. Points are arranged along a semicircle, as is indicative of a Debye process. The data given on the right-hand side were obtained for a polymer, which has the C₆C₃-rods attached as side-groups onto a polysiloxane backbone. Obviously, the coupling modifies the rotational kinetics so that it no longer equals a Debye process. Here a satisfactory representation of data is achieved by the use of an empirical function, with the form

$$\varepsilon(\omega) = \frac{\Delta\varepsilon}{1 + (-i\omega\tau)^\beta}. \quad (6.71)$$

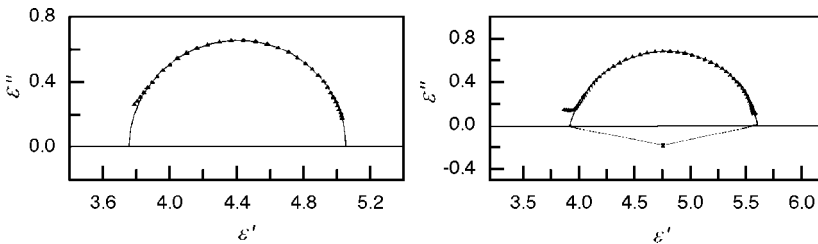


Fig. 6.6. Cole–Cole plots of dielectric data obtained for a dipole carrying a rod-like molecule of low molar mass (*left*) and a polysiloxane with these molecules attached as side-groups (*right*) [67]

It is known in the literature as the **Cole–Cole function**, and with β it includes an additional parameter. The more the value of β differs from unity, the more pronounced the deviations from a single-time relaxation. In the example, we have $\beta = 0.92$.

6.2.2 Retardation and Relaxation Time Spectra

Having established the properties of the single-time relaxation process, we now also have a means of representing a more complex behavior. This can be accomplished by applying the superposition principle, which must always hold in systems controlled by linear equations. Considering shear properties again, we write for a dynamic compliance $J(\omega)$ with general shape a sum of Debye processes with relaxation times τ_l and relaxation strengths ΔJ_l

$$J(\omega) = J_u + \sum_l \frac{\Delta J_l}{1 - i\omega\tau_l}. \quad (6.72)$$

Often it is more appropriate to employ a representation in integral form

$$J(\omega) = J_u + \int \frac{1}{1 - i\omega\tau} L_J(\log \tau) d \log \tau. \quad (6.73)$$

The characteristic function in this integral that specifies the relaxation properties of the system is $L_J(\log \tau)$, called the **retardation time spectrum** of the shear compliance J .

An identical function can be used in order to describe the result of a creep experiment on the system. One only has to substitute the dynamic compliance of the Debye process by the associated elementary creep function, as given by Eq. (6.61). This leads to

$$J(t) = J_u \Theta(t) + \int \left(1 - \exp\left(-\frac{t}{\tau}\right) \right) L_J(\log \tau) d \log \tau. \quad (6.74)$$

The immediate reaction with amplitude J_u is here represented by the Heaviside function $\Theta(t)$, which is unity for $t > 0$ and zero for $t < 0$.

The superposition approach may first look as a purely formal one, but a physical basis also exists, valid for many of the cases of interest. We are mostly dealing with the kinetics of transitions between the different conformational states. Motions include both local changes and cooperative movements of many monomers up to the full length of a chain. It appears reasonable to assume that the resulting total dynamics can be described as a superposition of a large number of independent **relaxatory modes**, each one representing a single-time relaxation process. In fact, theories like the Rouse model or the reptation model, to be discussed in the next chapter, lend support to this mode picture, which therefore may well be regarded as a notion suitable for general considerations.

Alternative to the shear compliances, $J(t)$ and $J(\omega)$, one can also use for the description of the properties under shear the shear moduli, $G(t)$ and $G(\omega)$. As we shall find, this can drastically change the values of the relaxation times. Let us first consider a single Debye process, now in combination with a superposed perfectly elastic part and calculate the associated dynamic modulus. We have

$$J(\omega) = J_u + \frac{\Delta J}{1 - i\omega\tau}, \quad (6.75)$$

and therefore

$$\begin{aligned} G(\omega) &= \frac{1}{J(\omega)} = \frac{1 - i\omega\tau}{J_u(1 - i\omega\tau) + \Delta J} \\ &= \frac{1}{J_u} \frac{J_u - i\omega\tau J_u + \Delta J - \Delta J}{J_u + \Delta J - i\omega\tau J_u} \\ &= \frac{1}{J_u} - \frac{\Delta J}{J_u J_r} \frac{1}{1 - i\omega\hat{\tau}}. \end{aligned} \quad (6.76)$$

Here J_r is defined as

$$J_r = J_u + \Delta J, \quad (6.77)$$

and $\hat{\tau}$ denotes another time constant, defined as

$$\hat{\tau} = \tau \frac{J_u}{J_r}. \quad (6.78)$$

The subscripts ‘r’ and ‘u’ stand for the attributes ‘relaxed’ and ‘unrelaxed’, respectively. We can also introduce the ‘relaxed’ and ‘unrelaxed’ limiting values of the shear modulus, by

$$G_r = \frac{1}{J_r}, \quad (6.79)$$

$$G_u = \frac{1}{J_u}, \quad (6.80)$$

and the change of G , giving the relaxation strength, by

$$\Delta G = G_u - G_r. \quad (6.81)$$

Using these parameters, the dynamic modulus obtains the simple form

$$G(\omega) = G_u - \frac{\Delta G}{1 - i\omega\hat{\tau}}. \quad (6.82)$$

The important point in this result is that, compared to the dynamic compliance, the characteristic time has changed. This change from τ to $\hat{\tau}$ can be quite large. For example, the relaxation processes that are responsible for the glass transition transfer a polymer sample from the glassy to the rubbery state, which means a change in the compliance by four orders of magnitude. This large change then shows up correspondingly in the ratio between τ and $\hat{\tau}$.

Rather than representing the viscoelastic properties of a given sample in the form of Eq. (6.73), i.e., by a superposition of Debye processes, which are specified by ΔJ_l and τ_l , one can perform an analogous procedure based on single-time relaxation processes specified by ΔG_l and $\hat{\tau}_l$. We then write in the integral form

$$G(\omega) = G_u - \int \frac{1}{1 - i\omega\hat{\tau}} H_G(\log \hat{\tau}) d \log \hat{\tau} . \quad (6.83)$$

It now includes the characteristic function $H_G(\log \hat{\tau})$, which obviously differs from $L_J(\log \tau)$. $H_G(\log \hat{\tau})$ is called the **relaxation time spectrum** of G .

The corresponding expression for the time-dependent modulus is

$$G(t) = G_r + \int \exp\left(-\frac{t}{\hat{\tau}}\right) H_G(\log \hat{\tau}) d \log \hat{\tau} . \quad (6.84)$$

In order to show that this is true, we have to prove that the time-dependent modulus for the Debye process does indeed equal the exponential function $\exp-(t/\hat{\tau})$. For the proof, we first calculate the primary response function, $\mu(t)$, by use of Eq. (6.31):

$$\mu(t) = \frac{dJ}{dt} = \frac{\Delta J}{\tau} \exp\left(-\frac{t}{\tau}\right) + J_u \delta(t) . \quad (6.85)$$

Then we apply Eq. (6.34)

$$1 = \frac{\Delta J}{\tau} \int_0^t \exp\left(-\frac{t-t'}{\tau}\right) G(t') dt' + J_u \int_0^t \delta(t-t') G(t') dt' . \quad (6.86)$$

This leads to

$$\exp\left(\frac{t}{\tau}\right) = \frac{\Delta J}{\tau} \int_0^t \exp\left(\frac{t'}{\tau}\right) G(t') dt' + J_u \exp\left(\frac{t}{\tau}\right) G(t) . \quad (6.87)$$

Taking on both sides the time derivative and dividing by $\tau^{-1} \exp(t/\tau)$ yields

$$1 = \Delta J G(t) + J_u G(t) + \tau J_u \frac{dG}{dt} . \quad (6.88)$$

Differentiating for a second time gives the equation

$$0 = J_r \frac{dG}{dt} + \tau J_u \frac{d^2 G}{dt^2} . \quad (6.89)$$

This is solved by

$$G(t) = G_r + \Delta G \exp\left(-\frac{t}{\hat{\tau}}\right) \quad (6.90)$$

for

$$0 = -\frac{J_r}{\hat{\tau}} + \tau J_u \frac{1}{(\hat{\tau})^2} \quad (6.91)$$

or

$$\hat{\tau} = \tau \frac{J_u}{J_r}, \quad (6.92)$$

in agreement with Eq. (6.78). Equations (6.90) and (6.92) confirm that Eq. (6.84) is correct.

Relaxation or retardation time spectra like $H_G(\log \hat{\tau})$ or $L_J(\log \tau)$ can always be used for a representation of measured data although its derivation from experimentally obtained modulus functions or compliance functions can be difficult. The inversion of one of the integral equations, Eqs. (6.73), (6.74), (6.83) or (6.84), belongs to a class of problems called 'ill-posed'. Here small fluctuations in the data, which cannot be avoided, become greatly magnified by the mathematical solution algorithm, thus leading to large variations in the derived quantities. Modern mathematical procedures can provide help, by allowing us to include in the solution any additional knowledge about the spectral functions. If they can be applied, situations improve and calculated spectra may then possess a satisfactory accuracy.

In this section, the focus was on the difference in the characteristic times observed in measurements of compliances or moduli, respectively. In the explanation, we had to use two different symbols, the notation τ for the **retardation time** and $\hat{\tau}$ for the **relaxation time**. In what follows we shall not persist in this differentiation and write τ generally, for all kinds of characteristic times observed in experiments.

6.3 Specific Relaxation Processes and Flow Behavior

After the introduction of the various interrelated response functions and basic concepts like the Debye process and the derived spectral representations in the second part of this chapter we now come to the description and discussion of actual polymer behavior. In fact, relaxation processes play a dominant role and result in a complex pattern of temperature-dependent and frequency-dependent properties.

We already have a general picture suitable for considerations. As has been emphasized, dealing with fluid polymers means dealing with an ensemble of chains that can exist in a manifold of different conformational states. Thermal equilibrium is a dynamical situation where chains change between these states activated by thermal energies. The microscopic dynamics shows up in the macroscopic experiments. Relaxation rates observed in certain mechanical or dielectrical measurements equal the rates of transitions within a certain group of conformations.

The rates of conformational transitions of a chain encompass an enormously wide range. Local rearrangements including only a few adjacent monomers are usually rapid and take place with rates similar to those in ordinary liquids. Conformational changes of more extended sequences require much longer times. In particular, relaxatory modes associated with the chain

as a whole show a pronounced dependence on the molar mass, as relaxation then has to propagate over larger and larger distances. Flow behavior is governed by these sluggish modes and therefore sets up the **terminal region**, i.e., the long time end, of the spectrum of relaxations.

The rates of the relaxatory modes in a sample do not cover the whole spectral range homogeneously, but usually one observes a separation into several zones where relaxation rates are accumulated. Each zone belongs to a group of processes with similar roots. It has become a convention to designate these different groups by Greek letters, α , β and γ , and to use the symbol α for the process with the lowest transition rates showing up at the highest temperature. On the other hand, the symbol γ is used for the processes observed at the low temperature end and this means those with the highest transition rates.

In the remaining part of this chapter, we discuss the properties of some major groups of relaxation processes in polymers as there are

- local processes, to be observed in the glassy state;
- cooperative processes in longer chain sequences that provide the basis for the elasticity of rubbers and the viscoelasticity of polymer melts;
- chain diffusion, which controls the flow behavior; and
- specific processes in partially crystalline states, associated with coupled motions of sequences in the crystallites and the amorphous regions.

6.3.1 Local Processes

Figure 6.7 shows the results of a dynamic shear experiment carried out on poly(cyclohexyl methacrylate) (PCHMA) in the glassy state. One observes a relaxation process that produces a loss maximum just in the frequency range of the mechanical spectrometer. With increasing temperature the position of the loss maximum shifts to higher values.

Considering the chemical constitution of PCHMA, there is an obvious assignment for this ‘ γ -process’: It reflects the flip-motion between the chair-conformation and the boat-conformation of the cyclohexane sidegroup. Since this process changes the shape of the sidegroup, it couples to the applied shear field. The assignment is corroborated by the observation that this process shows up whenever a cyclohexyl group is attached to a polymer chain. The relaxation rates were similar for all samples investigated, as expected for a mode with local character.

Figure 6.8 shows the temperature dependence of the relaxation rate in an Arrhenius-plot. The data were obtained in several experiments on polyacrylates and poly(methylacrylates) with pendant cyclohexyl groups. The linearity of the plot is indicative of an activated process, the relaxation time being given by the Arrhenius law

$$\tau = \tau_0 \exp \frac{\tilde{A}}{RT} . \quad (6.93)$$

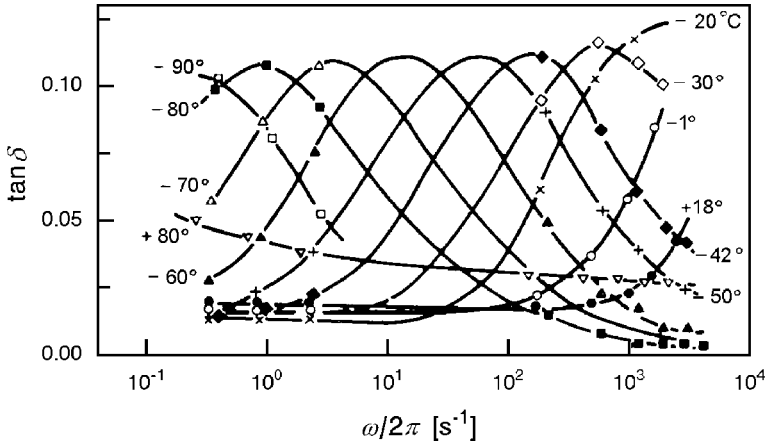


Fig. 6.7. Frequency dependence of the mechanical loss tangent measured for PCHMA at the indicated temperatures (after Heijboer [68])

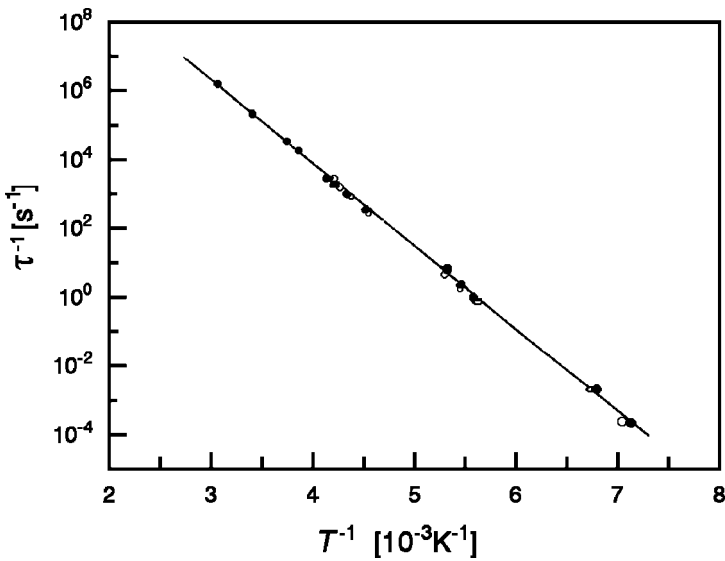


Fig. 6.8. Temperature dependence of the relaxation rates of the γ -process in polyacrylates (*open symbols*) and poly(methacrylates) (*filled symbols*) with pendant cyclohexyl groups. Data from Heijboer [69]

The relaxation rate τ^{-1} equals the rate of transitions between the two conformational states. The observed activation energy, $\tilde{A} = 47 \text{ kJ mol}^{-1}$, therefore has to be identified with the height of the energy barrier that has to be passed over during a change.

A remarkable fact to be noted in Fig. 6.7 is the constancy in the peak amplitude and the shape of the loss curves when varying the temperature. This behavior, in combination with the regular temperature shift according to Arrhenius' law, opens the way for an alternative experimental procedure. Rather than carrying out frequency-dependent measurements at one temperature, loss curves may also be registered by temperature-dependent measurements at constant frequency. Figure 6.9 presents such measurements, and as can be seen, they provide equivalent information. The relationship between the relaxation rate and the temperature follows equally from both measurements by a registration of the loss maxima.

In the combination of frequency-dependent and temperature-dependent measurements, one can even go one step further, thereby establishing an important general procedure. For groups of relaxation processes that encompass a broader time range, it often happens that the experimentally limited frequency range of the experimental device is not large enough to include the curves completely. Measurements carried out at a sequence of different temperatures can provide the missing information. As indicated by our example, different parts of the loss curve are placed into the accessible frequency window on changing the temperature. This property can now be used to set up the complete loss curve by a synthesis. The sections obtained at the different temperatures can be coupled together by carrying out appropriate shifts along the $\log \omega$ -axis, thus ending up in one continuous curve.

What is applied here is known in the literature as the **time-temperature superposition principle**. The result of the synthesis is called a **master curve**. For a thermally activated Debye process, the basis of the principle is

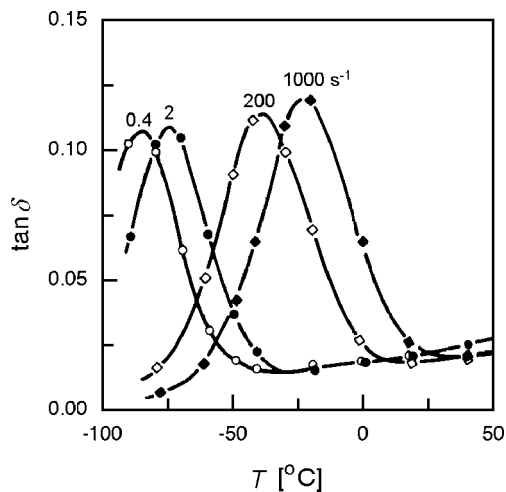


Fig. 6.9. Temperature dependent measurements of the loss tangent of the γ -process of PCHMA for several fixed frequencies $\omega/2\pi$ (after Heijboer [68])

easily seen. According to Eq. (6.65), the dynamic compliance and the dynamic modulus are here functions of the product $\omega\tau$, or equivalently, of $\log(\omega\tau)$. If we also use Eq. (6.93), we may then represent the compliance as a function of a sum of terms

$$J(\log \omega\tau) = J \left(\log \omega + \log \tau_0 + \frac{\tilde{A}}{RT} \log e \right). \quad (6.94)$$

The expression tells us that there are two ways of achieving a change in J , namely either by a shift in $\log \omega$, or by a shift in T^{-1} . The effects of frequency and temperature thus appear as superposed, and Eq. (6.94) informs us about the correspondences.

As a prerequisite for the construction of a master curve, the shape of the loss curve must remain constant under temperature variations. For the system under discussion, this is obviously fulfilled. Measured curves coincide after appropriate shifts along the $\log \omega$ -axis, as is shown in Fig. 6.10 for the real and imaginary part of the dynamic shear modulus. The example represents an ideal case, and here there is also no need for a synthesis of the curves from parts. In many other cases, however, construction of the master curve is the only means of exploring a group of relaxation processes in total. Even

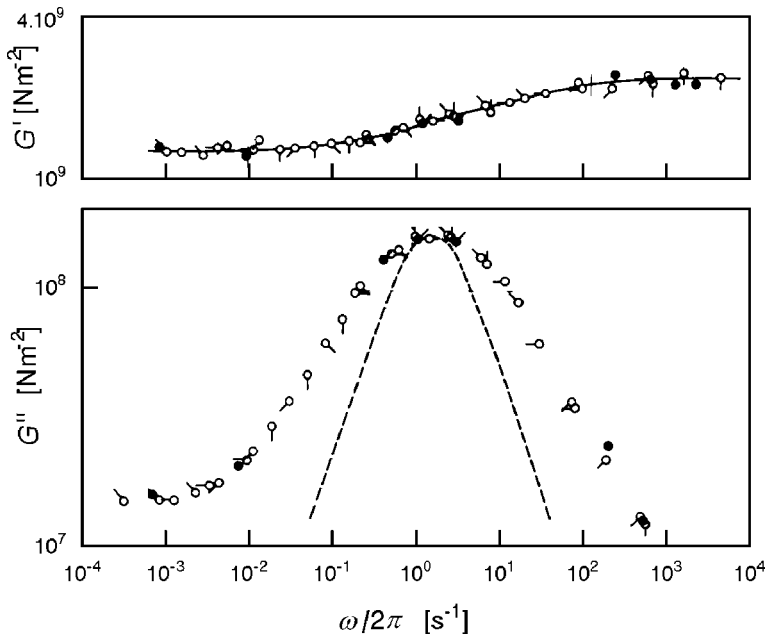


Fig. 6.10. Real and imaginary part of the dynamic shear modulus in the range of the γ -process of PCHMA, synthesized as a master curve using measurements at various temperatures. Curves represent the viscoelastic behavior at -80°C . The dashed curve indicates a perfect Debye process. Data from Heijboer [69]

if one is not sure whether curve shapes are really temperature-independent, construction of a master curve remains useful as it can always provide a rough overall view, which is good for qualitative purposes.

Figure 6.10 shows also a comparison with the Debye process. We notice that the γ -process of the cyclohexyl groups does not agree with a single-time relaxation process, but exhibits some broadening. This may be caused by a coupling between adjacent sidegroups, as a conformational change in one sidegroup may well affect the neighbors. More specifically, the jump rate may depend on the conformations of the neighbors, which then would lead to a distribution of relaxation times, as is indicated by the broadened loss spectrum.

6.3.2 Glass–Rubber Transition and Melt Flow

Figure 6.11 presents creep curves, registered for a sample of polystyrene under shear stress at various temperatures between $-268\text{ }^{\circ}\text{C}$ and $296.5\text{ }^{\circ}\text{C}$. We observe a creep compliance that encompasses the enormously broad range of nine orders of magnitude. At the lowest temperatures, the mechanical properties are those of a glass. At the other limit, the high temperature end, the behavior is dominated by viscous flow as indicated by the characteristic linear increase of J with time. The transition from the solid-like to the liquid-like behavior occurs continuously, and importantly, obviously in a systematic manner. Indeed, the way curves change with temperature indicates that again time-temperature superposition is obeyed. Temperature variations result in shifts of the creep compliance along the $\log t$ -axis, apparently without essential modifications in shape. The consequence is the same as for the just discussed local processes: On varying the temperature, different parts of $J(t)$ show up in the time-window of the experiment, and they can be reassembled to form a master curve. Applying this procedure yields the overall creep curve and it evidently has a shape as indicated schematically in Fig. 6.12. We can estimate the encompassed total time range by roughly summing up the time ranges of the sections included and find an enormous extension of about 20 orders of magnitude.

$J(t)$ has a characteristic shape composed of several parts. Subsequent to the glassy range with a solid-like compliance in the order of $10^{-9}\text{ N}^{-1}\text{ m}^2$, an additional anelastic deformation emerges and eventually leads to a shear compliance in the order of $10^{-5}\text{ N}^{-1}\text{ m}^2$. The latter value is typical for a rubber. For a certain time a plateau is maintained but then there finally follows a steady linear increase of J , as is indicative for viscous flow. The displayed creep curve of polystyrene is not a peculiar one and may be regarded as representative for all amorphous, i.e., noncrystalline polymers. One always finds these four parts in

- a glassy region;
- the glass–rubber transition, often also called the ‘ α -process’,

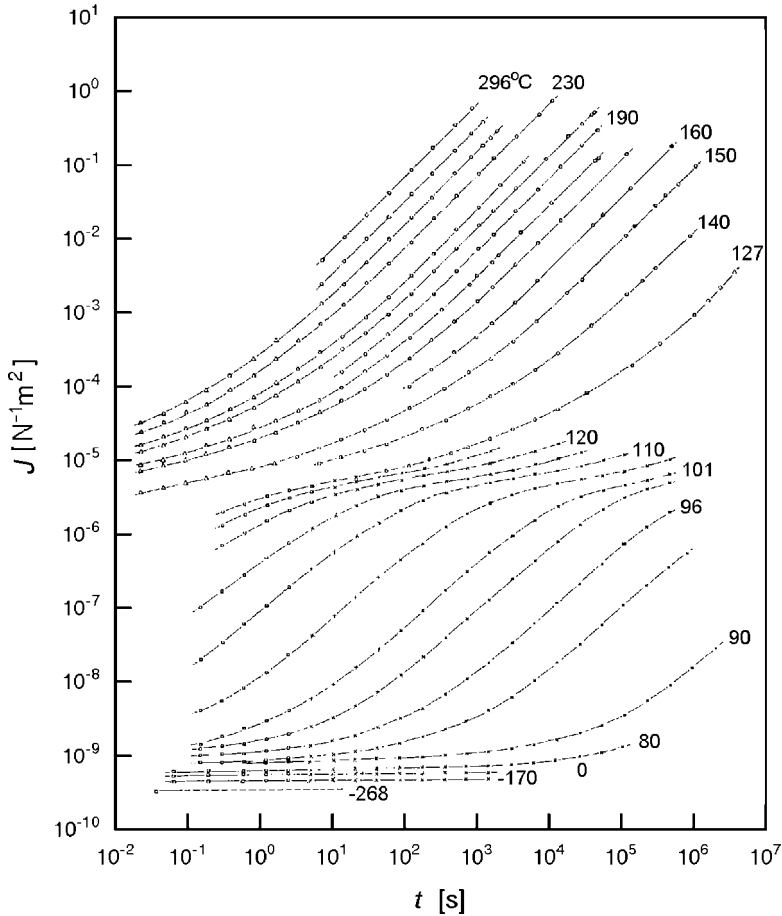


Fig. 6.11. Creep compliance of PS ($\overline{M}_w = 3.85 \times 10^5 \text{ g mol}^{-1}$), as measured at the indicated temperatures. Data from Schwarzl [70]

- a rubber–elastic plateau; and
- the terminal flow range.

These are the basic ingredients determining the mechanical properties of amorphous polymers and we now discuss them in a brief overview.

A first important conclusion can be drawn immediately; it concerns the nature of the main part, the glass–rubber transition. As we find a systematic shift of the time range of the transition with temperature, it is obvious that we are dealing here with a purely kinetical phenomenon rather than with a structural transition like the melting process or a solid–solid phase change. Curves demonstrate that whether a sample reacts like a glass or a rubber is just a question of time. Temperature enters only indirectly, in that it determines the characteristic time that separates glassy from rubbery behavior.

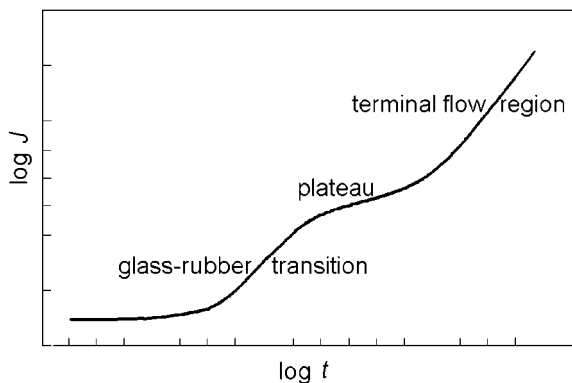


Fig. 6.12. General shape of the complete creep curve of PS, as suggested by the appearance of the different parts shown in Fig. 6.11

In Chap. 9, we will discuss the properties of rubbers. These are networks, composed of chemically cross-linked macromolecules. Owing to the weak restoring forces, application of stress here induces a deformation that is very large compared to solids. The observation of a plateau in the creep compliance at a height comparable to the compliance of rubbers indicates that a polymer melt actually resembles a temporary network. This behavior expresses a major property specific for polymeric liquids: These include chain entanglements, i.e., constraints for the motion arising from the chain connectivity, which act like cross-links. Different from true cross-links of chemical nature, entanglements are only effective for a limited time during which they are able to suppress flow. This time becomes apparent in the creep curve as the end of the plateau region.

Subsequent to the plateau, flow sets in. As is intuitively clear, the time needed for the chain disentangling increases with the molar mass and this shows up in a corresponding broadening of the plateau. Results of dynamic-mechanical experiments on polystyrene, presented later in Fig. 6.16, exemplify the behavior. The data also indicate a lower limit: When decreasing the molar mass one reaches a point, where the plateau vanishes. Then the glass-rubber transition and the terminal flow region merge together. Absence of the plateau means the absence of an entanglement network. The observation tells us that entanglement effects only exist above a certain minimum molar mass. For each polymer one finds for that a characteristic value, known as the **molar mass at the entanglement limit**.

The measurements at high temperatures in Fig. 6.11 indicate a viscous flow with a constant creep rate, determined by a viscosity η_0

$$\frac{dJ}{dt} \propto \frac{1}{\eta_0}. \quad (6.95)$$

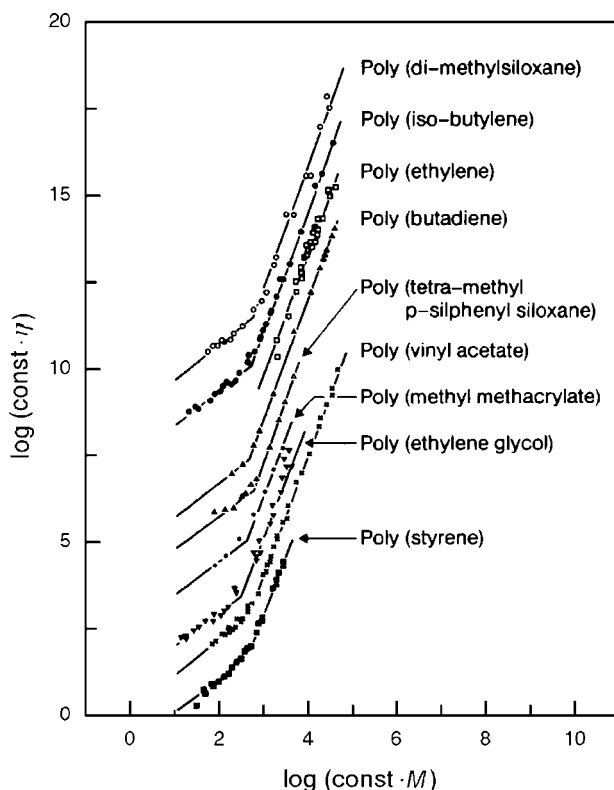


Fig. 6.13. Molecular weight dependence of the viscosity as observed for the indicated polymers. For better comparison curves are suitably shifted in horizontal and vertical directions. Data from Berry and Fox [71]

As the flow velocity relates to the disentangling time, this also holds for the melt viscosity. Indeed, η_0 and the disentangling time for entangled melts show the same dependence on the molar mass. Figure 6.13 collects the results of viscosity measurements for various polymers. As should be noted, a power law behavior

$$\eta_0 \propto M^\nu \quad (6.96)$$

is generally observed. One finds two regions, with different values of the exponent ν and a cross-over at a **critical molar mass** M_c . For molar masses below M_c one has $\nu = 1$; above M_c one observes $\nu \approx 3.2-3.6$. If viscosity measurements are further extended, up to the range of ultra-high molar masses, one finally observes an exponent $\nu = 3$. Figure 6.14 presents such measurements for 1,4-polyisoprene (PI), for molar masses up to $\overline{M}_w = 3 \times 10^6 \text{ g mol}^{-1}$.

Importantly, as is also shown by Fig. 6.16, the two parts of the mechanical response separated by the rubber-elastic plateau differ in their molar mass dependence. In contrast to the terminal flow region, the glass-rubber transi-

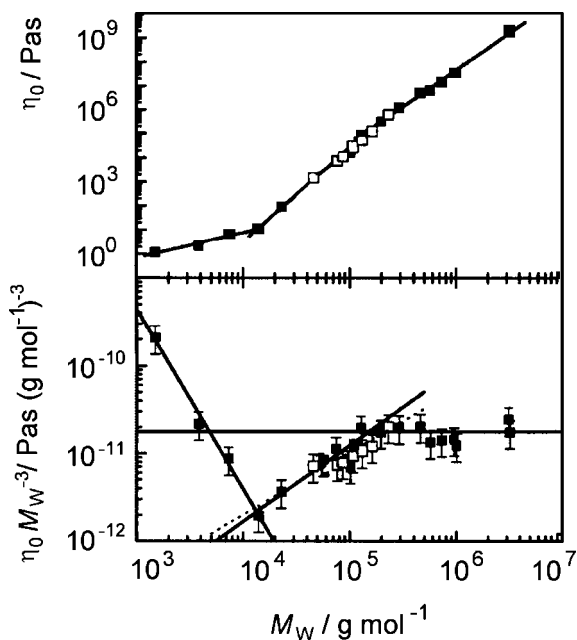


Fig. 6.14. Molar mass dependence of the zero shear rate viscosity of PI. The *lower figure* indicates for $\overline{M}_w > 2 \times 10^5 \text{ g mol}^{-1}$ a power law $\eta_0 \propto \overline{M}_w^3$. The critical molar mass as determined by the location of the break is $M_c = 1.3 \times 10^4 \text{ g mol}^{-1}$. From Pyckhout-Hintzen et al. [72]

tion remains largely unaffected by the molar mass. The findings teach us that chain equilibration in reaction to an applied field takes place as a two-step process with a finite delay time in between. In the first step, equilibration by relaxatory modes only includes chain sequences up to a certain length, which is determined by the distance between the entanglements. As this distance is independent of M , this holds likewise for the characteristic time of this first step. Further relaxation is postponed until a chain extricates itself from the **tube** formed by the other surrounding molecules and this process is of course strongly affected by the molar mass.

As explained in the first part of this chapter, the viscoelastic properties of polymers may also be studied by stress relaxation experiments or dynamic mechanical measurements. Since all response functions are interrelated, the mentioned ingredients of the mechanical behavior of amorphous polymers show up in the other experiments as well. To give an example, Fig. 6.15 displays the time-dependent tensile modulus registered for polyisobutylene (PIB). Measurements were again conducted for a series of temperatures. As expected, data show the glass–rubber transition (for temperatures in the range 190–220 K), followed by a plateau (around 230 K) and finally the onset of flow. The right-hand side presents the composite master curve, set up by shifting

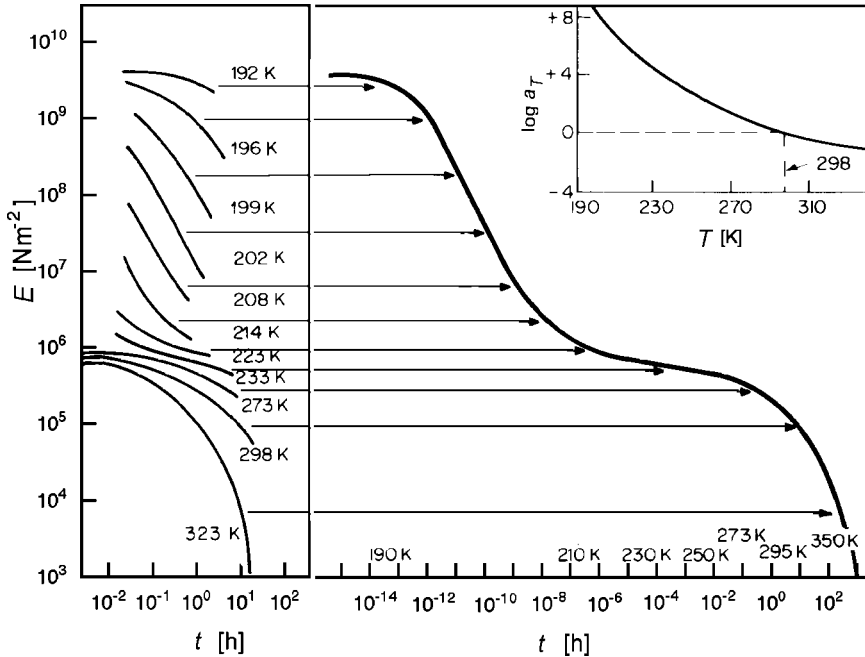


Fig. 6.15. Time-dependent tensile modulus of PIB. Measurements at the indicated temperatures (*left*) and master curve, constructed for a reference temperature $T = 298$ K (*right*). The *insert* displays the applied shifts. Data from Castiff and Tobolsky [73]

the partial curves as indicated by the arrows. The shifts along the $\log t$ -axis, which have to be carried out when going from the master curve to the measured parts, are displayed in the insert. In the construction of the master curve the time-dependent modulus obtained at 298 K was kept fixed, while all other curves were displaced. The shift factor, denoted $\log a_T$, is zero at this reference temperature. The result represents the complete time-dependent shear modulus at the reference temperature. Comparable to the creep compliance in Fig. 6.12, this tensile modulus again encompasses a huge range of about 20 orders of magnitude in time.

Regarding the large number of conformational changes that must take place if a rubber is to be extended, the glass–rubber transition cannot equal a single-time relaxation process and this is shown by the curve shapes. To describe $E(t)$, empirical equations that often provide good data fits exist. A first one is concerned with the beginning of the transition range. It is known as the **Kohlrausch–Williams–Watts (KWW) function** and has the form of a **stretched exponential function**

$$E(t) \propto \exp - \left(\frac{t}{\tau} \right)^\beta . \quad (6.97)$$

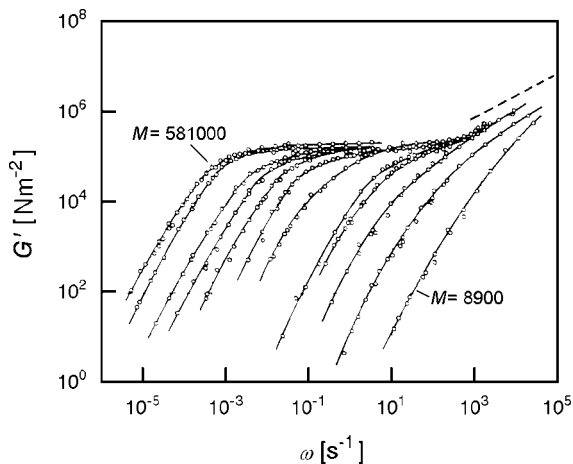


Fig. 6.16. Storage shear moduli measured for a series of fractions of PS with different molar masses in the range $M = 8.9 \times 10^3$ to 5.81×10^5 g mol $^{-1}$. The *dashed line in the upper right corner* indicates the slope corresponding to the power law Eq. (8.82) derived for the Rouse model of the glass transition. Data from Onogi et al. [74]

The KWW function employs two parameters: τ sets the time scale and β determines the extension in time of the decay process. For values $\beta < 1$ a broadening results, as is always observed for the glass–rubber transition. Typical values are in the order $\beta \simeq 0.5$. The KWW function holds only at the beginning, i.e., in the short-time range of the glass–rubber transition. Subsequently, there often follows a power law

$$E(t) \propto t^{-\nu}. \quad (6.98)$$

Experimentally it is indicated by a linear range in the center, when using a log–log plot. Typical values of the exponent are $\nu \simeq 0.5$.

Figure 6.16 presents, as a third example, results of dynamic-mechanical measurements. They were obtained for a series of monodisperse polystyrenes, i.e., fractions with sharp molar masses. The curves depict the frequency dependence of the storage shear modulus, $G'(\omega)$. As we note, the order of appearance of the viscous flow and the α -process is reversed when compared to the time-dependent measurements. The flow-dominated long-time behavior emerges first at low frequencies, whereas an investigation of the rubber–glass transition requires measurements at the high frequency end. The plateau appears in between. Its width varies systematically with the molar mass, as has already been mentioned and discussed. There is no plateau at all for the sample with the lowest molar mass ($M = 8.9 \times 10^3$ g mol $^{-1}$), but after its first appearance, it widens progressively with further increasing molar masses.

Low Frequency Properties of Polymer Melts

Also of interest in Fig. 6.16 is the finding that the shapes of curves in the terminal region remain similar to each other for all molar masses. More specifically, within the limit of low frequencies, a constant slope emerges, indicating a power law $G'(\omega) \propto \omega^2$. It is possible to explain this asymptotic behavior and to relate it to the properties of flowing polymer melts.

For a Newtonian low molar mass liquid, knowledge of the viscosity is fully sufficient for the calculation of flow patterns. Is this also true for polymeric liquids? The answer is no under all possible circumstances. Simple situations are encountered, for example, in dynamical tests within the limit of low frequencies or for slow steady state shears and even in these cases, one has to include one more material parameter in the description. This is the **recoverable shear compliance**, usually denoted by J_e^0 and it specifies the amount of recoil observed in a creep recovery experiment when the load is removed. J_e^0 relates to the elastic and anelastic parts in the deformation and has to be accounted for in all calculations. Experiments show that, at first, for $M < M_c$, J_e^0 increases linearly with the molar mass and then reaches a constant value that essentially agrees with the plateau value of the shear compliance.

At higher strain rates more complications arise. There the viscosity is no longer constant and shows a decrease with increasing rate, which is commonly addressed as **shear-thinning**. We will discuss this effect and related phenomena in Chap. 9 when dealing with non-linear behavior. In this section, the focus is on the limiting properties at low shear rates, as expressed by the **zero shear rate viscosity**, η_0 , and the recoverable shear compliance at zero shear rate, J_e^0 .

Our concern is to find out how the characteristic material parameters η_0 and J_e^0 are included in the various response functions. To begin with, consider a perfectly viscous system in a dynamic-mechanical experiment. Here the dynamic shear compliance is given by

$$J = i \frac{1}{\eta_0 \omega} . \quad (6.99)$$

This is seen when introducing the time dependencies

$$\begin{aligned} \sigma_{zx} &= \sigma_{zx}^0 \exp(-i\omega t) , \\ e_{zx} &= J \sigma_{zx}^0 \exp(-i\omega t) \end{aligned}$$

into the basic equation for Newtonian liquids

$$\sigma_{zx} = \eta_0 \frac{de_{zx}}{dt} , \quad (6.100)$$

which results in

$$\sigma_{zx}^0 \exp(-i\omega t) = -\eta_0 i \omega J \sigma_{zx}^0 \exp(-i\omega t) . \quad (6.101)$$

In a polymer melt, the viscous properties of Newtonian liquids combine with elastic forces. The latter contribute a real part to the dynamic shear compliance, to be identified with J_e^0 :

$$J'(\omega \rightarrow 0) = J_e^0 . \quad (6.102)$$

Combining Eqs. (6.99) and (6.102) gives the dynamic shear compliance of polymeric fluids in the limit of low frequencies

$$J(\omega \rightarrow 0) = J_e^0 + i \frac{1}{\eta_0 \omega} . \quad (6.103)$$

As we can see, η_0 and J_e^0 show up directly and separately, in the limiting behavior of J' and J'' .

The dynamic shear modulus follows as

$$\begin{aligned} G(\omega \rightarrow 0) &= \frac{1}{J(\omega \rightarrow 0)} = \frac{\eta_0 \omega}{\eta_0 \omega J_e^0 + i} \\ &= \frac{\eta_0^2 \omega^2 J_e^0 - i \eta_0 \omega}{(\eta_0 \omega J_e^0)^2 + 1} , \end{aligned} \quad (6.104)$$

giving

$$G'(\omega \rightarrow 0) = J_e^0 \eta_0^2 \omega^2 \quad (6.105)$$

in agreement with Fig. 6.16, and

$$G''(\omega \rightarrow 0) = \eta_0 \omega . \quad (6.106)$$

We thus find characteristic power laws also for the storage and the loss modulus that again include J_e^0 and η_0 in a well-defined way.

One may wonder if η_0 and J_e^0 can also be deduced from the time-dependent response functions, as for example, from $G(t)$. Indeed, direct relationships exist, expressed by the two equations

$$\eta_0 = \int_0^{\infty} G(t) dt \quad (6.107)$$

and

$$J_e^0 \eta_0^2 = \int_0^{\infty} G(t) t dt . \quad (6.108)$$

The first relation follows immediately from Boltzmann's superposition principle in the form of Eq. (6.38) when applied to the case of a deformation with constant shear rate $\dot{\epsilon}_{zx}$. We have

$$(dx \hat{=}) de_{zx} = \dot{\epsilon}_{zx} dt \quad (6.109)$$

and thus

$$(\psi \hat{=}) \sigma_{zx} = \dot{e}_{zx} \int_{t'=-\infty}^t G(t-t') dt' = \dot{e}_{zx} \int_{t''=0}^{\infty} G(t'') dt'' . \quad (6.110)$$

Since per definition

$$\sigma_{zx} = \eta_0 \dot{e}_{zx} ,$$

we find

$$\eta_0 = \int_{t=0}^{\infty} G(t) dt .$$

To derive the second equation, we consider a dynamic-mechanical experiment and treat it again on the basis of Boltzmann's superposition principle, writing

$$\sigma_{zx} = \int_{t'=-\infty}^t G(t-t') \dot{e}_{zx}(t') dt' . \quad (6.111)$$

Introducing

$$e_{zx}(t) = e_{zx}^0 \exp(-i\omega t) \quad (6.112)$$

and

$$\sigma_{zx}(t) = G(\omega) e_{zx}(t) \quad (6.113)$$

we obtain

$$G(\omega) = - \int_{t''=0}^{\infty} G(t'') i\omega \exp(i\omega t'') dt'' , \quad (6.114)$$

setting $t'' = t - t'$. In the limit $\omega \rightarrow 0$ we use the series expansion

$$G(\omega \rightarrow 0) = \int_{t''=0}^{\infty} G(t'') (-i\omega + \omega^2 t'' + \dots) dt'' , \quad (6.115)$$

giving

$$G'(\omega \rightarrow 0) = \omega^2 \int_{t=0}^{\infty} G(t) t dt . \quad (6.116)$$

A comparison with Eq. (6.105) yields Eq. (6.108).

Combination of Eqs. (6.107) and (6.108) can be used for estimating the average time of stress decay subsequent to a sudden shear deformation of a melt. We introduce this time, denoted by $\bar{\tau}$, as

$$\bar{\tau} = \frac{\int_{t=0}^{\infty} G(t)t dt}{\int_{t=0}^{\infty} G(t) dt}, \quad (6.117)$$

and then obtain simply

$$\bar{\tau} = J_e^0 \eta_0. \quad (6.118)$$

Equation (6.118) for the mean viscoelastic relaxation time may be applied for both non-entangled and entangled melts and yields different results for the two cases. For non-entangled melts, i.e., $M < M_c$, we have $J_e^0 \propto M$ and $\eta_0 \propto M$, hence

$$\bar{\tau} \propto M^2. \quad (6.119)$$

For molar masses above the entanglement limit, i.e., $M > M_c$, one finds $J_e^0 = \text{const}$ and $\eta_0 \propto M^\nu$ with $\nu = 3-3.6$, therefore,

$$\bar{\tau} \propto \eta_0 \propto M^\nu \text{ with } \nu = 3-3.6. \quad (6.120)$$

Vogel–Fulcher Law and the WLF Equation

We turn now to another point and consider the temperature dependence. Recall that the data indicate the validity of time-temperature or frequency-temperature superposition. This has an important implication: The findings show that the processes comprising the terminal flow region and the glass–rubber transition change with temperature in the same manner. Particularly suited for the description of this common temperature dependence is the shift parameter $\log a_T$. We introduced it in connection with the construction of the master curves, but it also has a well-defined physical meaning. This becomes revealed when we look at the equations valid in the terminal range, Eqs. (6.105) and (6.106). It is to be noted that ω and η_0 enter into the expressions for the dynamic modulus and the dynamic compliance not separately, but only as a product. As temperature only affects η_0 , we conclude that a_T and η_0 must be proportional quantities. The exact relationship follows when taking into account that shift parameters always relate to a certain reference temperature. Let this reference temperature be T_0 . Then a_T is given by

$$a_T = \frac{\eta_0(T)}{\eta_0(T_0)}. \quad (6.121)$$

With the aid of a_T we can express response functions at any temperature in terms of the respective response function at T_0 . Explicitly, for the dynamical shear modulus, the following relation holds:

$$G(T, \omega) = G(T_0, a_T \omega), \quad (6.122)$$

or for a logarithmic frequency scale

$$G(T, \log \omega) = G(T_0, \log \omega + \log a_T) . \quad (6.123)$$

In correspondence to this, we write for the time-dependent shear modulus

$$G(T, t) = G\left(T_0, \frac{t}{a_T}\right) , \quad (6.124)$$

or

$$G(T, \log t) = G(T_0, \log t - \log a_T) . \quad (6.125)$$

The uniform temperature dependence implies a joint rescaling of the relaxation times of all modes in both the glass transition range and the terminal flow region, and one may wonder how this might arise. One should be aware that these modes vary greatly in their spatial extensions, which begin with the length of a Kuhn segment and go up to the size of the whole chain, and also vary in character, as they include intramolecular motions as well as diffusive movements of the whole chain, and nevertheless, all modes behave uniformly. There seems to be only one possible conclusion: The temperature dependence must be a property of the individual segments. Since all modes are based on the motion of segments, their mobility affects each mode alike. There is a notion that suitably expresses this property and this is the **segmental frictional coefficient**. We will introduce it in the next chapter, in the treatment of microscopic dynamics. For the moment, it is sufficient to say that frictional forces that act in identical manner on all the segments exist. They uniformly control the kinetics of all the relaxatory modes of the chains. The common temperature dependence of all relaxatory modes in the α -transition range and the terminal zone, and thus of the viscosity, just reflects that of the segmental frictional force.

Equation (6.121) relates a_T to the temperature dependence of the viscosity. Numerous experiments were carried out to measure this function. They led to a specific result. As it turns out, for the majority of polymer systems, $\eta_0(T)$ is well-represented by an empirical equation known as the **Vogel–Fulcher law**. It has the form

$$\eta_0(T) = B \exp \frac{T_A}{T - T_V} . \quad (6.126)$$

In addition to the prefactor B two parameters are included, namely the **activation temperature** T_A and the **Vogel temperature** T_V . The introduction of the latter makes up the difference to Arrhenius' law.

The function $\eta_0(T)$, as formulated by the Vogel–Fulcher law, includes a singularity at $T = T_V$. However, whether the viscosity really diverges if T approaches T_V cannot be checked by any experiment. Measurements of viscosities always come to an end about 50 K above T_V , because η_0 is then already very large, reaching values in the order of 10^{13} poise. Notwithstanding the fact that the point of divergence is out of reach, validity of the Vogel–Fulcher equation is well-established since effects of a finite Vogel temperature

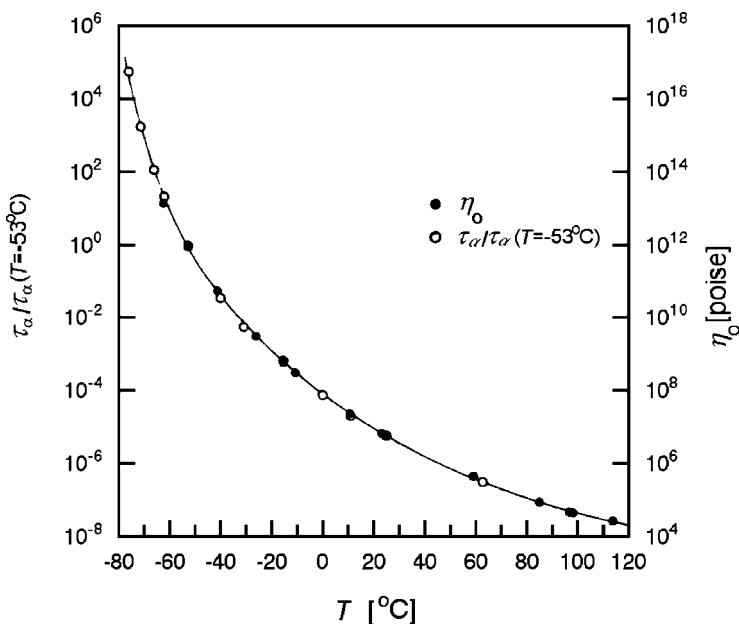


Fig. 6.17. Temperature dependencies of the viscosity η_0 of PIB (*open symbols, right axis*) and of the relaxation time of the α -process τ_α (*filled symbols, left axis*). Both correspond to a Vogel–Fulcher function (*continuous line*). Data from Plazek et al. [75]

are clearly observable also in the range of accessible temperatures. There, the function $\eta_0(T)$ exhibits a characteristic curvature that distinguishes it from Arrhenius behavior. Figure 6.17 depicts, as an example, results obtained for polyisobutylene (PIB). An increase to high values of η_0 is observed at low temperatures and it can be described by a Vogel–Fulcher function, as given by the continuous line. The figure also includes the temperature dependence of the characteristic time τ_α of the glass–rubber transition. It is given by

$$\tau_\alpha = \tau_0 \exp \frac{T_A}{T - T_V} \quad (6.127)$$

with the same values for T_A and T_V as in Eq. (6.126).

Having an equation for the temperature dependence of the viscosity, we may also formulate the shift factor $\log a_T$. Equations (6.126) and (6.121) yield

$$\begin{aligned} \log a_T &= \log e T_A \left(\frac{1}{T - T_V} - \frac{1}{T_0 - T_V} \right) \\ &= \log e (-T_A) \frac{T - T_0}{(T_0 - T_V)(T - T_V)} \\ &= \log e \frac{(-T_A)}{T_0 - T_V} \frac{T - T_0}{T - T_0 + (T_0 - T_V)}. \end{aligned} \quad (6.128)$$

This is usually expressed as

$$\log a_T = -C_1 \frac{T - T_0}{T - T_0 + C_2}, \quad (6.129)$$

introducing two parameters, C_1 and C_2 , defined as

$$C_1 = \log e \frac{T_A}{T_0 - T_V} \quad \text{and} \quad C_2 = T_0 - T_V. \quad (6.130)$$

Equation (6.129) was postulated by Williams, Landel and Ferry and is well-known in the literature under the abbreviated name **WLF equation**.

When master curves are constructed one chooses in most cases the glass transition temperature T_g as reference temperature. T_g is obtained by a standard calorimetric or volumetric measurement, as explained in Sect. 6.3.3. It is found that, for this choice of T_0 , the parameters C_1 and C_2 of the WLF equation have values which are bound to certain ranges, namely

$$C_1 = 14 - 18, \\ C_2 = (30 - 70) \text{ K}.$$

The values of C_2 indicate that T_V is located (30–70) K below T_g .

The Dielectric α -Process and the Normal Mode

The two groups of relaxatory modes that in mechanical relaxation experiments lead to the α -transition and the final viscous flow also emerge in the dielectric response.

Figure 6.18 presents, as a first example, the frequency dependencies of the real and imaginary part of the dielectric constant, obtained for poly(vinylacetate) (PVA) at the indicated temperatures. One observes a strong relaxation process.

Figure 6.19 displays the temperature dependence of the relaxation rate, as derived from the maxima of the loss curves. For a comparison it also includes the temperature dependencies of the loss maxima of the mechanical α -process, as observed in measurements of either $J''(\omega)$ or $G''(\omega)$. As we can see, the dielectric relaxation rates are located intermediately between the rates obtained in the mechanical experiments and, importantly, all three temperature dependencies are similar, the rates differing only by constant factors. The assignment of this dielectric relaxation process is therefore obvious: It originates from the same group of processes as the mechanical α -process and thus is to be addressed as the dielectric α -process.

There are other polymers that in addition show the chain disentangling associated with the flow transition. An example is given by *cis*-polyisoprene (PIP). Figure 6.20 depicts the dielectric loss ε'' in a three-dimensional representation of the functional dependence on frequency and temperature. Two

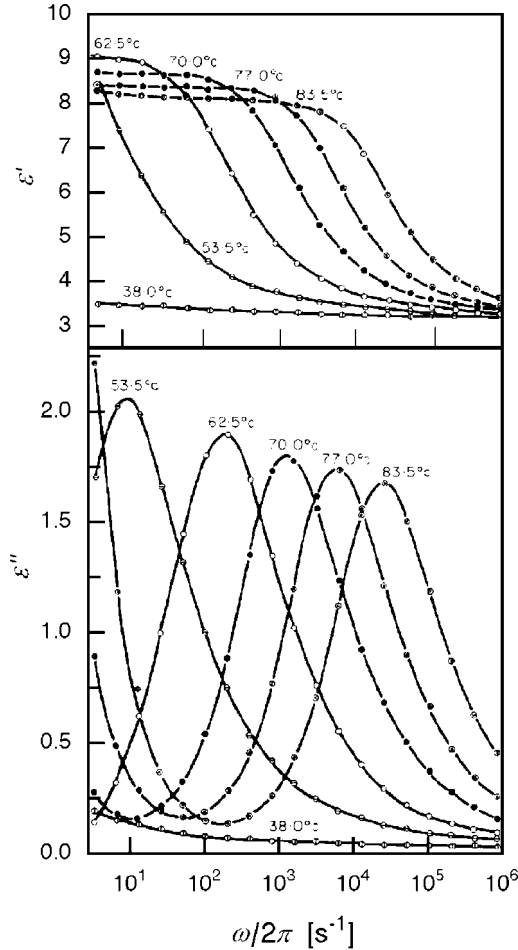


Fig. 6.18. Dielectric α -process in PVA. Data from Ishida et al. [76]

relaxation processes show up. The one with the higher frequency again represents the α -process, the other is called the **normal mode**, for reasons to be seen below.

To learn more about the two processes, it is instructive to check for the molar mass dependencies. In fact, one here finds a characteristic difference. The results of studies on a set of samples with different molar mass are displayed in Fig. 6.21. We observe that the α -process is molar mass independent, whereas the normal mode shows pronounced changes. Figure 6.22 depicts these changes in a plot of the relaxation time τ of the normal mode in dependence on the molar mass. Data demonstrate the validity of a power law,

$$\tau \propto M^\nu,$$

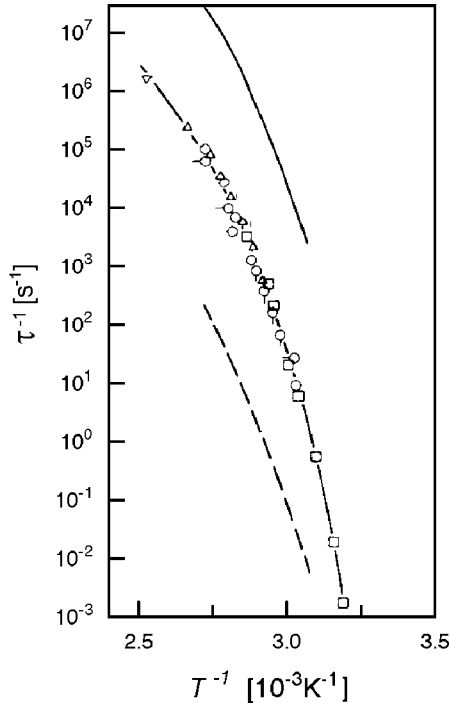


Fig. 6.19. Frequency–temperature locations of the dielectric loss maxima (*open symbols*) of PVA, compared to the maxima of G'' (*continuous line*) and J'' (*broken line*) observed in mechanical experiments. Collection of data published in [77]

with two different values for the exponent,

$$\nu = 3.7 \quad \text{for} \quad M > 10^4 \text{ g mol}^{-1}$$

and

$$\nu = 2 \quad \text{for} \quad M < 10^4 \text{ g mol}^{-1} .$$

The cross-over from one to the other regime shows up as a sharp bend in the curve.

We have already met such a molar mass dependence in Eqs. (6.119) and (6.120), when formulating the average viscoelastic relaxation time $\bar{\tau}$ of polymer melts. Roughly speaking, $\bar{\tau}$ gives the time required by a chain for a complete conformational reorganization. This also implies a full reorientation of the end-to-end distance vector of the chain. This is exactly this motion that shows up in the dielectric normal mode.

The question arises as to why *cis*-polyisoprene, different from poly(vinylacetate), shows the chain reorientation in its dielectric spectrum. The reason becomes clear when we look at the chemical constitution of polyisoprene, and

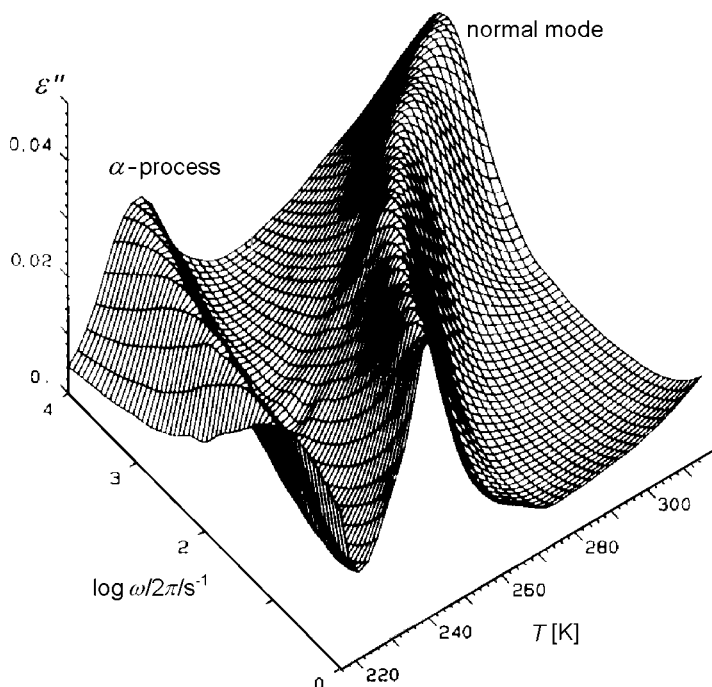


Fig. 6.20. Frequency dependence and temperature dependence of the dielectric loss in *cis*-PIP ($M = 1.2 \times 10^4 \text{ g mol}^{-1}$), indicating the activity of two groups of relaxatory modes. Spectra obtained by Boese and Kremer [78]

focus in particular on the associated dipole moments. Figure 6.23 displays the chemical structure. The main point is that isoprene monomers are polar units that possess a longitudinal component $p_{||}$ of the dipole moment, which always points in the same direction along the chain. As a consequence, the longitudinal components of the dipoles of all monomers become added up along the contour, giving a sum proportional to the end-to-end distance vector \mathbf{R} . In the dielectric spectrum the kinetics of this total dipole of the chain is observable, hence also the chain reorientation as described by the time dependence $\mathbf{R}(t)$.

The peculiar name ‘normal mode’ needs a comment. As will be explained in detail in the next chapter, chain dynamics in melts may be described with the aid of two theoretical models known as the Rouse model and the reptation model. In the framework of these treatments chain kinetics is represented as a superposition of statistically independent **relaxatory normal modes**. As it turns out, the dielectric normal mode is associated with the mode with the longest relaxation time. For non-entangled melts this is the lowest order Rouse mode; for entangled melts, it is the lowest order reptation mode.

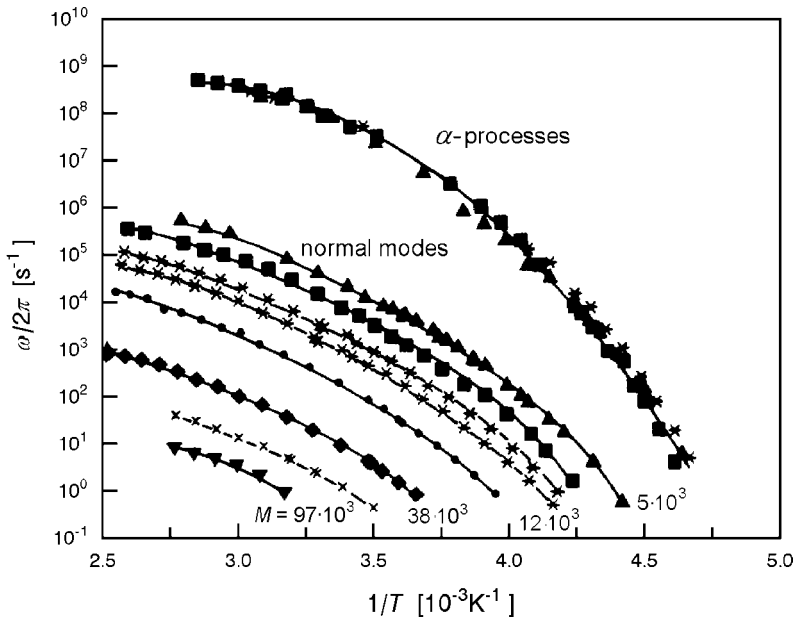


Fig. 6.21. Temperature dependence of the relaxation rates of the dielectric α -process and the normal mode, observed for samples of *cis*-PIP with different molar mass (four values are indicated). The *solid lines* are fits based on the WLF equation. Data from Boese and Kremer [78]

In addition to the longitudinal component of the dipole per monomer, there is also a transverse part. As the reorientation of the transverse component requires only local changes in the conformation, it can take place much more rapidly than the spatially extended normal mode. Hence, a qualitative change in the kinetics occurs and indeed, it is this movement that shows up in the α -process. Both the α -process and the normal mode obey the Vogel–Fulcher law, in full analogy to the common behavior of the α -process and the terminal relaxation in mechanics.

It is possible to write down approximate expressions for the relaxation strengths $\Delta\varepsilon$ of the two processes. As a chain may be described as a sequence of freely jointed segments, we can just make use of Eqs. (6.16) and (6.59), and introduce for the α -process and the normal mode the transverse and the longitudinal component of the dipole moment, respectively. The relaxation strength of the α -process then follows as

$$\varepsilon_0 \Delta\varepsilon_\alpha \simeq c_s \frac{\langle (p_\perp^s)^2 \rangle}{3kT} . \tag{6.131}$$

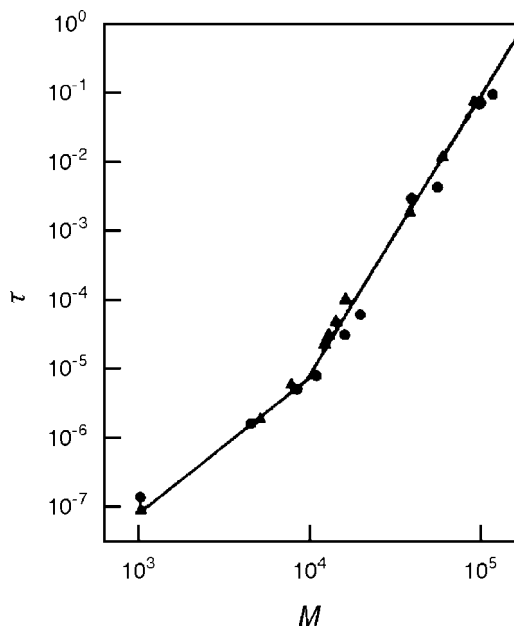


Fig. 6.22. Molecular weight dependence of the relaxation time of the dielectric normal mode in *cis*-PIP. Data from Boese and Kremer [78]

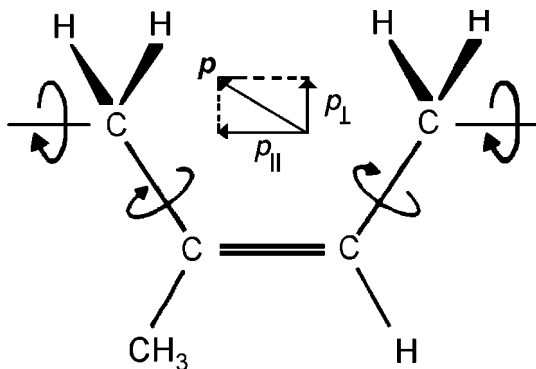


Fig. 6.23. Stereochemical constitution of a monomer unit of *cis*-PIP. The electric dipole moment, split into a longitudinal and a transverse component, is indicated

Here, p_{\perp}^s is the transverse dipole moment per segment, and c_s gives the number density of segments. The brackets indicate an averaging over all rotational isomeric states of one segment. The relaxation strength of the normal mode follows equivalently, by introduction of the mean longitudinal dipole moment per segment

$$\epsilon_0 \Delta \epsilon_{\text{nm}} \simeq c_s \frac{\langle (p_{\parallel}^s)^2 \rangle}{3kT}. \quad (6.132)$$

Neither the α -process nor the normal mode equal a single-time relaxation process. A good representation of data is often achieved by the use of the empirical **Havriliak–Negami equation**, which has the form

$$\varepsilon - \varepsilon_u = \frac{\Delta\varepsilon}{(1 + (-i\omega\tau)^{\beta_1})^{\beta_2}}. \quad (6.133)$$

This function is a formal generalization of the single-time relaxation function, achieved by an inclusion of two additional parameters, β_1 and β_2 (for $\beta_2 = 1$ it equals the Cole–Cole function mentioned earlier). These determine the asymptotic behavior, β_1 on the low frequency side, since

$$\beta_1 \approx \frac{d \log \varepsilon''}{d \log \omega} \quad \text{for } \omega\tau \ll 1, \quad (6.134)$$

and the product $\beta_1\beta_2$ on the high frequency side, since

$$\beta_1\beta_2 = -\frac{d \log \varepsilon''}{d \log \omega} \quad \text{for } \omega\tau \gg 1. \quad (6.135)$$

Obviously β_2 determines the curve asymmetry. It is needed for the data representation because the observed curves $\varepsilon''(\omega)$ generally exhibit a larger broadening on the high frequency side. Typical values are $\beta_1 \simeq 0.5$, $\beta_2 \simeq 0.7$ for the α -process and $\beta_1 \simeq 1$, $\beta_2 = 0.4$ for the normal mode.

Equations (6.131) and (6.133) together provide a description of the dielectric α -transition, with the assumption that dipoles of different segments reorient independently. In fact, this is only true at larger distances from the glass transition temperature. On approaching T_g deviations show up. Figure 6.24 shows the temperature dependence of the relaxation strength of poly(vinylacetate) and one observes a pronounced increase. The behavior indicates increasing correlations between the motions of the transverse dipoles, not only along one chain, but possibly also between adjacent segments on different chains.

6.3.3 The Glass Transition Temperature

The mechanical experiments clearly demonstrate that the transition from the glassy to the liquid state is a purely kinetical phenomenon. Whether the compliance of a sample is small as in a glass, or large as for a rubber, depends only on the measuring time or the applied frequency. The reasons were discussed above. Rubber elasticity originates from the activity of the α -modes, a major group of relaxation processes in polymer fluids. The establishment of the deformation subsequent to the application of a load requires a certain time, given by the time scale of the α -modes. If the load varies too rapidly, the deformation cannot follow and the sample reacts like a glass. We also discussed the effect of temperature and found, as a main property of the α -modes, that relaxation times change according to the Vogel–Fulcher law. The progressive

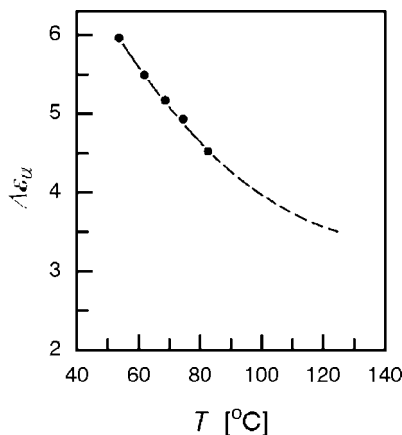


Fig. 6.24. Temperature dependence of the relaxation strength $\Delta\epsilon_\alpha$ of the dielectric α -process in PVA. Data from Ishida et al. [76]

increase of the relaxation times on cooling implied by this law finally leads to a freezing of the α -modes within a comparatively small temperature range. If they are frozen, we have a glass.

We thus find glass-like reactions for both sufficiently high frequencies and sufficiently low temperatures; but are the two situations really comparable? The answer is, yes and no, depending on the point of view. Yes, because both situations have in common that the α -modes cannot equilibrate. No, if we consider the thermodynamic state of order. In the first case, we are dealing with a system in thermal equilibrium and study its reaction on perturbations; in the second situation, however, the system has become non-ergodic, i.e., thermal equilibrium is only partially established. A major part of the internal degrees of freedom, as represented by the α -modes, cannot equilibrate. The temperature, where the transition from a liquid equilibrium state to a non-ergodic one, i.e., only partially equilibrated state takes place, is called the **glass transition temperature**, with the general designation T_g .

How can T_g be determined? In principle this can be achieved in various ways. However, two of the methods are of special importance and are used in the majority of cases. These are temperature-dependent measurements of the expansion coefficient or the heat capacity of a sample, carried out during heating or cooling runs. They need only small amounts of material, and standard equipment is commercially available.

Figures 6.25 and 6.26 present as examples the results of a volumetric and a calorimetric measurement on poly(vinylacetate). The glass transition has a characteristic signature that shows up in the curves. As we can see, the transition is associated with steps in the expansion coefficient $d\rho^{-1}/dT$ and the heat capacity $d\mathcal{H}/dT$, i.e., changes in the slope of the functions $\rho^{-1}(T)$ and $\mathcal{H}(T)$. The transition extends over a finite temperature range with typical

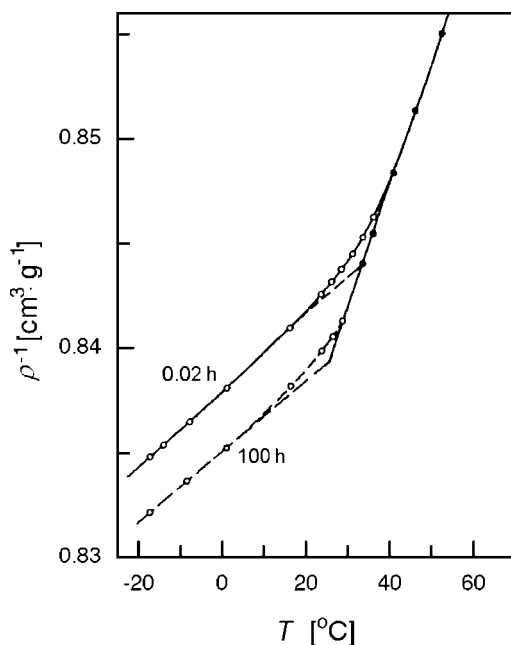


Fig. 6.25. Temperature dependence of the specific volume of PVA, measured during heating. Dilatometric results obtained after a quench to -20°C , followed by 0.02 or 100 h of storage. Data from Kovacs [79]

widths in the order of 10 degrees. The calorimetric experiment also exhibits another characteristic feature. One can see that the location of the step depends on the heating rate \dot{T} , showing a shift to higher temperatures on increasing the rate.

In view of the broadening of the step and the rate effects, it does not seem appropriate to introduce a sharply defined T_g . For practical use as material parameter and for comparisons it is sufficient to conduct the measurements with a standard heating or cooling rate ($|\dot{T}| = (10^{-1} - 1)\text{K s}^{-1}$) and to pick out some temperature near the center of the step, for example, that associated with the maximum slope. The thus obtained values of T_g have a tolerance of some degrees, but this must be accepted regarding the physical nature of the phenomenon.

The cause for the occurrence of the steps in the heat capacity and the expansion coefficient is easily seen. Cooling a sample below T_g results in a freezing of the α -modes. The observations tell us that the α -modes affect not only the shape of a sample, but also its volume and its enthalpy. This is not at all surprising. If segments move, they produce an additional volume in their neighborhoods. In the literature, this is often called a **free volume** in order to stress that it is not occupied by the hard cores of the monomers. The free volume increases with temperature because motions intensify, that

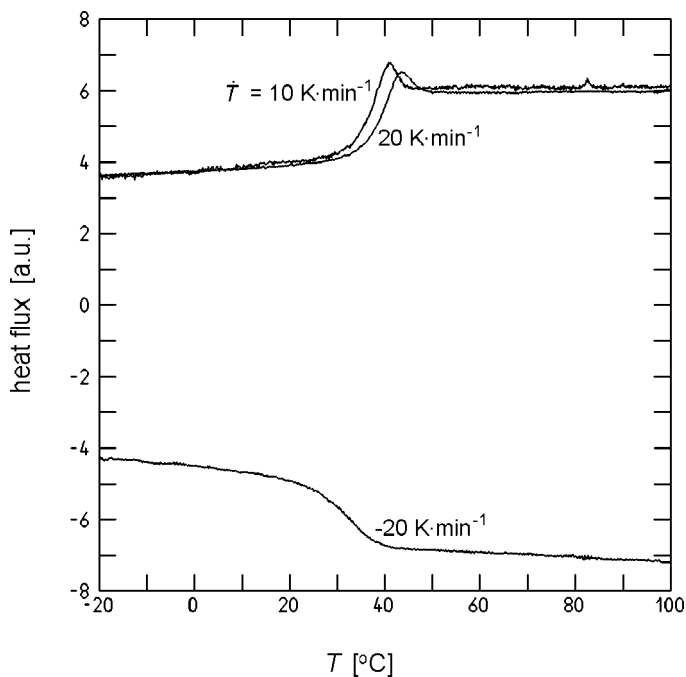


Fig. 6.26. Heat capacity of PVA, as measured in a differential calorimeter during heating (with two different heating rates) and cooling

is to say, the jump rates increase and, more importantly, a growing number of conformational states becomes populated and not all of them allow a dense chain packing. Therefore, when on crossing T_g from low temperatures the α -modes become active, beginning slowly and then steadily increasing in intensity, a growing additional free volume correspondingly arises. Thermal expansion in the glass is due to the anharmonicity of vibrational motions, as in crystalline solids. As we can see, the α -modes contribute another, even larger part to the expansion coefficient and it comes into effect at T_g .

That a corresponding behavior is found for the enthalpy and the heat capacity is conceivable. As the free volume incorporates energy, changes in the volume and in the enthalpy are interrelated and this results in simultaneous steps in the expansion coefficient and the heat capacity.

Being in a non-equilibrium state, liquids below T_g have a tendency further to change the structure in the direction towards the equilibrium. A slow decrease in volume and enthalpy is often observed. Figure 6.25 also exemplifies this behavior. Prolonged storage of the sample of poly(vinylacetate) below T_g for 100 h results in a shrinkage in volume. Note that, as a consequence, T_g , as measured during the subsequent heating, is shifted to lower values. Formally, this may be associated with the shift of the point of intersection of the two lines representing the glassy and liquid state. Physically, it is caused by

a change in the microstructure. **Ageing** is the technical term used in general for these processes and they can produce problems since often the mechanical properties deteriorate.

We have seen that the position of the step in the expansion coefficient or the heat capacity, observed during a cooling run, depends on the cooling rate. It is possible to analyze this dependence in more detail and to derive a criterion for the location of the glass transition. To begin with, recall what happens when cooling a polymeric liquid. In the fluid state, all degrees of freedom equilibrate rapidly so that thermal equilibrium is always maintained. Conditions change on approaching the glass transition since, here, the relaxation times of the α -modes reach values that are too high to further allow for a continuous equilibration. Vibrations and local modes still react immediately to programmed temperature changes but the sluggish α -modes lag behind more and more. Finally, after having crossed the transition range, the energy exchange between the instantaneously reacting modes and the α -modes stops completely.

In an analysis, one has to consider the time dependence of relaxation processes under non-isothermal conditions as imposed during a cooling or heating run. Observations suggest that we represent the sample volume as a sum of two contributions

$$\mathcal{V}(T) = \mathcal{V}_u(T) + \Delta\mathcal{V}_\alpha(T) . \quad (6.136)$$

The first part \mathcal{V}_u describes the volume of a hypothetical system without α -modes, being determined by the hard cores of the molecules, the anharmonicity of the vibrations and possible effects of local relaxation processes. The second term $\Delta\mathcal{V}_\alpha$ accounts for the free volume produced by the α -modes. An analogous description is suggested for the enthalpy and we formulate it correspondingly as

$$\mathcal{H}(T) = \mathcal{H}_u(T) + \Delta\mathcal{H}_\alpha(T) . \quad (6.137)$$

Since $\mathcal{V}_u(T)$ and $\mathcal{H}_u(T)$ pass continuously through the glass transition without any peculiar effects, we may reduce the discussion to the contributions of the α -modes. To keep the equations simple, we disregard the multimode character of the α -process and assume a single relaxation time, τ_α , with a temperature dependence following the Vogel–Fulcher law. Then kinetics can be analyzed by an application of the relaxation equation

$$\frac{d\Delta\mathcal{H}_\alpha}{dt} = -\tau_\alpha^{-1}(T)(\Delta\mathcal{H}_\alpha - \Delta\mathcal{H}_{\alpha,\text{eq}}(T)) , \quad (6.138)$$

which is formulated here for the calorimetric experiment. According to this equation, the change from a non-equilibrium value of the enthalpy associated with the α -modes, $\Delta\mathcal{H}_\alpha$, to the equilibrium value, $\Delta\mathcal{H}_{\alpha,\text{eq}}$, occurs with a temperature-dependent rate τ_α^{-1} .

The experimental heat capacity, c_α , is given by

$$c_\alpha = \frac{d\Delta\mathcal{H}_\alpha}{dT}, \quad (6.139)$$

while the equilibrium value, $c_{\alpha,\text{eq}}$, is represented by

$$c_{\alpha,\text{eq}} = \frac{d\Delta\mathcal{H}_{\alpha,\text{eq}}}{dT}. \quad (6.140)$$

We consider a temperature program based on a constant cooling rate $\dot{T} < 0$,

$$T(t) = T(0) + \dot{T}t. \quad (6.141)$$

Under these conditions the relaxation equation converts into the relation

$$c_\alpha(t)\dot{T} = -\tau_\alpha^{-1}(T)(\Delta\mathcal{H}_\alpha(t) - (\Delta\mathcal{H}_{\alpha,\text{eq}}(0) + \dot{T}c_{\alpha,\text{eq}}t)). \quad (6.142)$$

Differentiation on both sides yields

$$\begin{aligned} \dot{T} \frac{dc_\alpha}{dt} &= -\tau_\alpha^{-1}(T)\dot{T}(c_\alpha - c_{\alpha,\text{eq}}) \\ &\quad - \frac{d\tau_\alpha^{-1}}{dT}\dot{T}(\Delta\mathcal{H}_\alpha(t) - (\Delta\mathcal{H}_{\alpha,\text{eq}}(0) + \dot{T}c_{\alpha,\text{eq}}t)), \end{aligned} \quad (6.143)$$

assuming a constant value for $c_{\alpha,\text{eq}}$. Combination of both differential equations, followed by a division by \dot{T} on both sides, results in

$$\frac{dc_\alpha}{dt} = -\tau_\alpha^{-1}(T)(c_\alpha - c_{\alpha,\text{eq}}) + c_\alpha \frac{d \ln \tau_\alpha^{-1}}{dT} \dot{T}. \quad (6.144)$$

Here we find two terms determining the quantity of interest, dc_α/dt . At temperatures far above T_g , the first term dominates. Here, the relaxation rates are high and change only slowly with temperature. Within this limit, Eq. (6.144) may be replaced by

$$\frac{dc_\alpha}{dt} \approx -\tau_\alpha^{-1}(T)(c_\alpha - c_{\alpha,\text{eq}}). \quad (6.145)$$

To see the consequences, just consider a cooling run starting at a temperature T . Beginning with $c_\alpha = 0$, the equilibrium value $c_{\alpha,\text{eq}}$ will be reached within a time $\tau_\alpha(T)$. From thereon, c_α remains constant and equal to $c_{\alpha,\text{eq}}$.

In the other limit, for temperatures around and below T_g , the relaxation rates are very low and their changes, as described by the Vogel-Fulcher law, are large. Hence, the second term dominates and Eq. (6.144) can be approximated by

$$\frac{dc_\alpha}{dt} \approx c_\alpha \frac{d \ln \tau_\alpha^{-1}}{dT} \dot{T} \quad (6.146)$$

or

$$\frac{d \ln c_\alpha}{dT} \approx \frac{d \ln \tau_\alpha^{-1}}{dT}. \quad (6.147)$$

The solution is

$$c_\alpha \propto \tau_\alpha^{-1}, \quad (6.148)$$

or, using the Vogel–Fulcher law Eq. (6.127),

$$c_\alpha(T) \propto \tau_0^{-1} \exp -\frac{T_A}{T - T_V}. \quad (6.149)$$

We see that in this range, c_α converges rapidly to zero.

The cross-over from one to the other regime and thus the glass transition takes place when both terms have the same order of magnitude. Equating the two terms yields

$$\tau_\alpha^{-1} \simeq \frac{d \ln \tau_\alpha^{-1}}{dT} \dot{T}, \quad (6.150)$$

or

$$\frac{d \ln \tau_\alpha^{-1}}{dt} \tau_\alpha \simeq 1. \quad (6.151)$$

Equation (6.151) formulates a criterion for T_g . It states that T_g is reached during a cooling run when the relative change of the relaxation rate τ_α^{-1} within a time in the order of τ_α is no longer negligible.

It is interesting to calculate the relaxation time at T_g , as it follows from these equations. Using the Vogel–Fulcher law gives

$$\frac{T_A}{(T_g - T_V)^2} \dot{T} \tau_\alpha(T_g) \simeq 1. \quad (6.152)$$

We have typically $T_A \simeq 2000$ K, $T_g - T_V \simeq 50$ K and therefore

$$\frac{T_A}{(T_g - T_V)^2} \simeq 1 \text{ K}^{-1}. \quad (6.153)$$

For a cooling rate $\dot{T} \simeq 10^{-2} \text{ K s}^{-1}$ we thus arrive at

$$\tau_\alpha(T_g) \simeq 10^2 \text{ s}. \quad (6.154)$$

Hence, a calorimetric measurement and a volumetric experiment produce the step at a temperature where the relaxation time of the α -modes is in the order of minutes.

Equation (6.152) correctly describes the effect of the heating or cooling rates. If $|\dot{T}|$ is increased, the step occurs at an even shorter relaxation time τ_α , and therefore at higher temperatures, which is in accordance with the experiment. For illustration and further confirmation, Fig. 6.27 presents the results of numerical solutions of Eq. (6.144), as obtained for three different cooling rates, with typical values chosen for the other parameters. The shifts largely agree with the experimentally observed behavior.

To show some typical values, Table 6.1 collects the T_g 's of several amorphous polymers. One finds two major groups. First the natural and synthetic

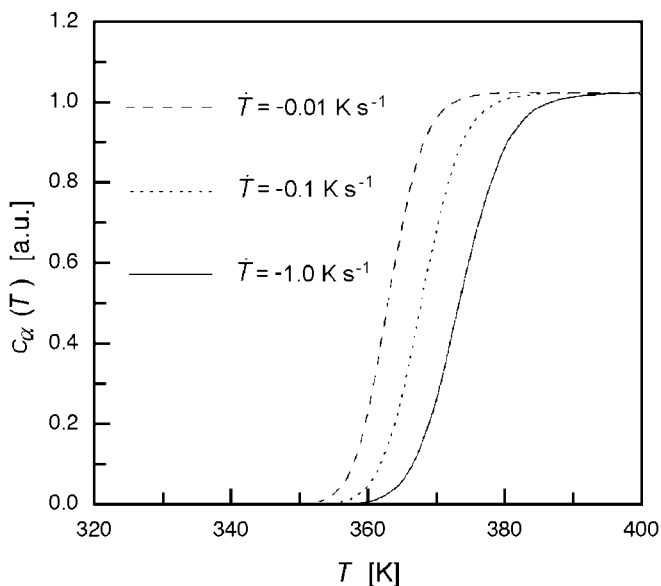


Fig. 6.27. Model calculation on the basis of Eq. (6.144), simulating heat capacity measurements during cooling runs with the indicated rates ($T_A = 2000$ K, $T_V = 300$ K, $\tau_\alpha(\infty) = 10^{-11}$ s, $T(t=0) = 400$ K) [80]

Table 6.1. Glass transition temperatures of some common polymers

Polymer	T_g [K]
poly(dimethyl siloxane)	146
polybutadiene (<i>cis</i>)	164
polyisoprene (<i>cis</i>) (natural rubber)	200
polyisobutylene	200
poly(vinyl methylether)	242
poly(α -methyl styrene)	293
poly(vinyl acetate)	305
polystyrene	373
poly(methyl methacrylate) (atactic)	378
poly(acrylic acid)	379
poly(acrylonitrile)	398
polycarbonate	418

rubbers, together with poly(dimethyl siloxane), which have T_g 's far below ambient temperature, and second polymers, which are glassy at room temperature. The latter mostly have T_g 's located around 100°C .

A concern of practical importance is a knowledge of relations between the chemical constitutions of polymers and their respective glass transition temperatures. A good microscopic understanding is lacking, but there are

a number of empirical rules based on the assumption that different molecular units give separate contributions to T_g . Also quite useful are **mixing rules**, which describe the T_g -values of blends as a function of the T_g 's of the components in pure states and their volume fractions. As it turns out, in many cases a good representation is achieved by the **Fox–Flory equation**, given by

$$\frac{1}{T_g} = \frac{\phi_A}{T_g^A} + \frac{\phi_B}{T_g^B} . \quad (6.155)$$

6.3.4 Relaxation in Partially Crystalline Systems

The relaxation behavior of partially crystalline systems is complex and different from amorphous polymers. Observations give the general impression that, in comparison to amorphous systems, partially crystalline samples are much less uniform in behavior. Many of the systems exhibit peculiarities and these can dominate the viscoelastic properties. This is not the place to explore this large field in the depth it requires, because this would mean that we would have to discuss separately the mechanical behavior of polyethylene, poly(ethylene terephthalate), polypropylene, *i*-polystyrene, poly(tetrafluoroethylene), etc. For illustration purposes we select polyethylene as an instructive example.

We begin with a look at the results of a temperature-dependent measurement of the storage shear modulus and the mechanical loss tangent shown in Fig. 6.28. Data were obtained with the help of a torsion pendulum working with a frequency of about 1 s^{-1} . The figure includes data obtained for two commercial samples, a linear polyethylene with high crystallinity and a low density polyethylene (LDPE) with short-chain branches. Two groups of relaxation processes show up for linear polyethylene, one at low temperatures, designated as γ -process, and another at high temperatures, called the ' α -process'. For the branched polyethylene a third process emerges in addition, the ' β -process' characterized by a loss maximum at around -20°C .

The change in behavior from the highly crystalline linear polyethylene to samples with lower crystallinity occurs continuously, as is demonstrated by the measurement shown in Fig. 6.29. Here chlorination was employed for a controlled reduction of the crystallinity. We observe that decreasing the crystallinity results in a strong increase of the loss signal related to the β -process.

The relaxation behavior of amorphous polymers was dominated by two processes, the glass-rubber transition and the terminal flow region, which are both characterized by a temperature dependence given by the WLF equation. For polyethylene, one cannot expect a flow transition because flow is suppressed by the crystallites in the sample. The fact is that for linear polyethylene, *i.e.*, polyethylene with high crystallinity, there is no WLF-controlled process at all. The numerous measurements in the literature provide clear evidence that the two processes observed in linear polyethylene, α and γ , are both based on activated mechanisms obeying the Arrhenius law. The process

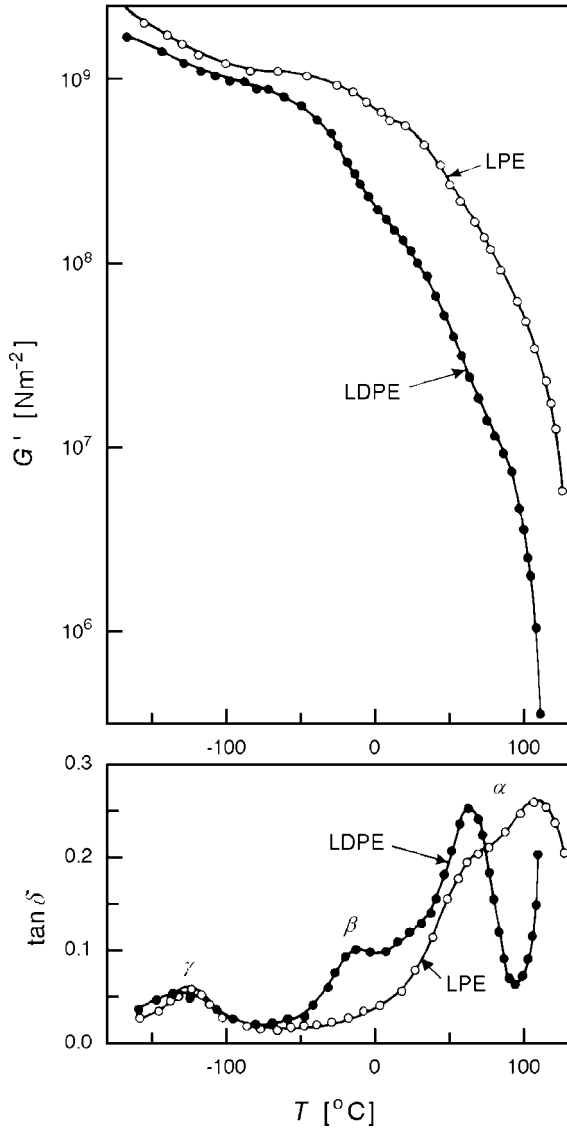


Fig. 6.28. Temperature dependence of the storage shear modulus (*top*) and the loss tangent (*bottom*) of linear (LPE) and branched polyethylene (LDPE). Data obtained by Flocke [81], using a torsion pendulum with frequencies in the order of 1 s^{-1}

that does show a WLF behavior is the β -process. The disappearance of the β -process in polyethylene samples with high crystallinity tells us that the state of order and the molecular dynamics in the disordered regions, which still make up a non-negligible part of the sample volume (typically 20%), differs quali-

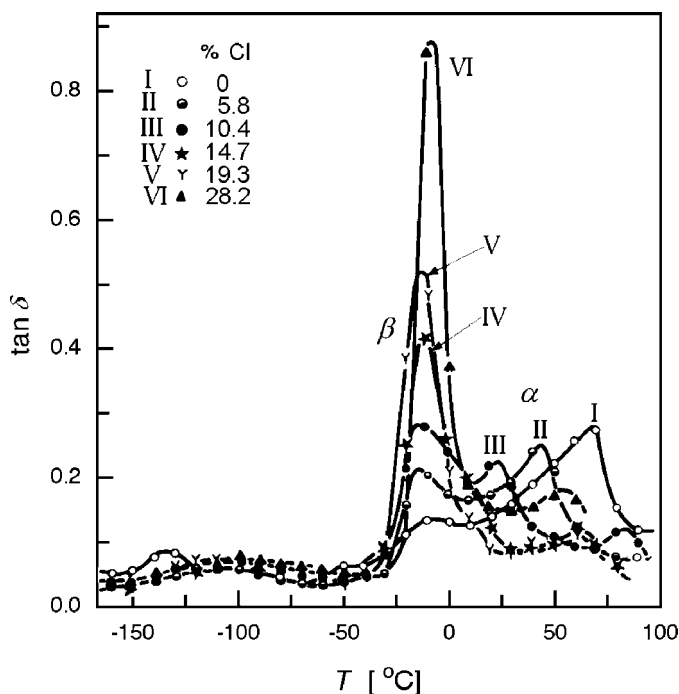


Fig. 6.29. Temperature dependence of the loss tangent of chlorinated PE, obtained for a series of different samples with chlorine contents between 0 and 28.2%. Results of a torsion pendulum measurement by Schmieler and Wolf [82]

tatively from that in an amorphous polymer. On the other hand, increasing the volume fraction of disordered material evidently changes the mobility in these regions towards the usual properties of a melt. The β -process observed for polyethylene with low crystallinity indeed corresponds to the glass-rubber transition in amorphous polymers.

The use of the Greek letters in agreement with the convention of choosing the symbols α , β , γ , etc. for a designation of the processes in the sequence they show up from high temperatures downwards, may produce some confusion in the meaning of the term α -process. While for amorphous polymers, it is identical with the glass-rubber transition, this is not the case for polyethylene. Here, if the glass-rubber transition exists at all, it is called the ' β -process'.

The mobility in the disordered regions of polyethylene shows great variations. The β -process, as observed in dielectric measurements, is unusually broad and changes its shape with temperature. Figure 6.30 presents results obtained for a sample of polyethylene that included vinylacetate groups as co-units in the chains. These co-units are rejected from the crystallites and accumulate in the amorphous regions. Because the groups carry a dipole moment, their dynamics shows up in the dielectric spectrum. The difference in

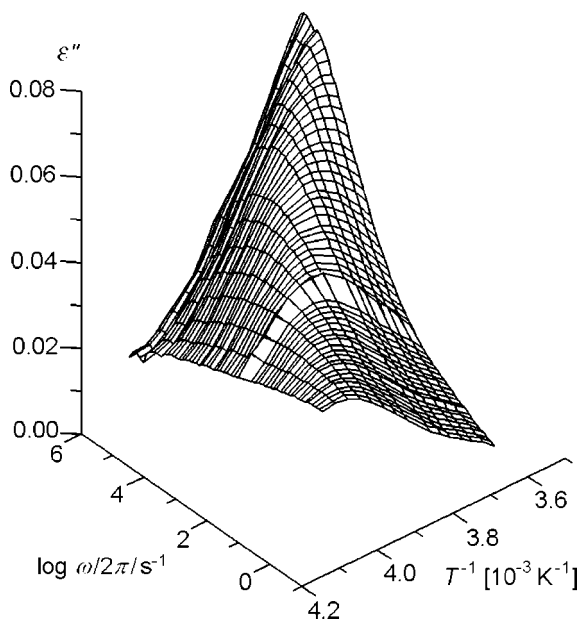


Fig. 6.30. Frequency dependence and temperature dependence of the dielectric loss associated with the β -process in PEcVA with 17% per weight of VA units [83]

behavior between the glass transition in an amorphous polymer and the β -process in a partially crystalline system such as polyethylene becomes very clear when comparing Fig. 6.30 with Fig. 6.18, which shows the α -process for poly(vinylacetate). For the partially crystalline poly(ethylene-*co*-vinylacetate) (PEcVA) loss curves are much broader and also exhibit a pronounced temperature dependence. The observations are indicative of large variations in the segmental mobility in the disordered regions, obviously caused by the restrictions and limitations imposed by the crystallites and the trapped entanglements. The temperature dependence is partly due to the continuous change in crystallinity that we discussed in Sect. 5.4. This, however, is not the whole effect since the structural changes practically end at about 0°C , while the progressive broadening goes on. The β -process has a cooperative character, which implies that segmental motions are correlated up to a certain distance ξ_β . Consequently, hindrances such as crystallite surfaces become effective over a similar range. The observed increase in the variance of the mobilities on approaching T_g may thus be understood as being caused by an increase in ξ_β . Since it appears that, close to T_g , the whole amorphous layer is affected, one concludes that the correlation length then becomes similar to the layer thickness, i.e., is in the order of some nanometers.

The largest changes in the mechanical properties of polyethylenes with moderate to high crystallinity are caused by the α -process. Figures 6.31 and 6.32 present results of frequency-dependent measurements of the tensile mod-

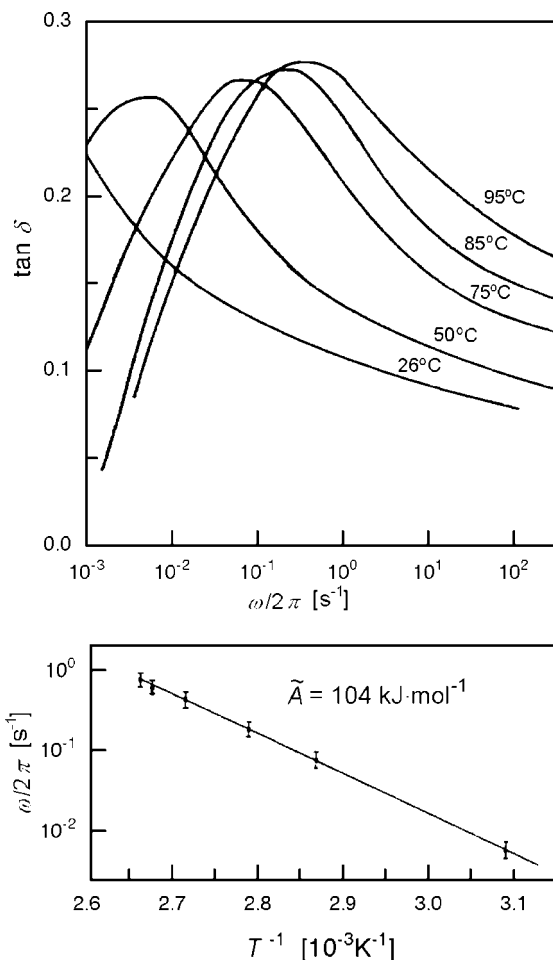


Fig. 6.31. Mechanical α -process in LDPE. Loss tangent (*top*) and temperature dependence of the frequency of the loss peak (*bottom*) [84]

ulus of such a sample, conducted at different temperatures between 26 °C and 95 °C. As can be seen, the loss tangent shows a systematic shift to higher frequencies. The temperature dependence of the loss maximum is indicative of an activated process with an activation energy $\tilde{A} = 104 \text{ kJ mol}^{-1}$. Figure 6.32 shows that the storage tensile modulus decays with both decreasing frequencies and rising temperatures, whereby the latter effect is caused by the continuous melting.

What is the origin of the α -process? Different observations must be included in the considerations. First, remember the results of the NMR experiment presented in Sect. 5.4.2. Here, a longitudinal chain transport through the crystallites was clearly indicated. The chain motion is apparently accom-

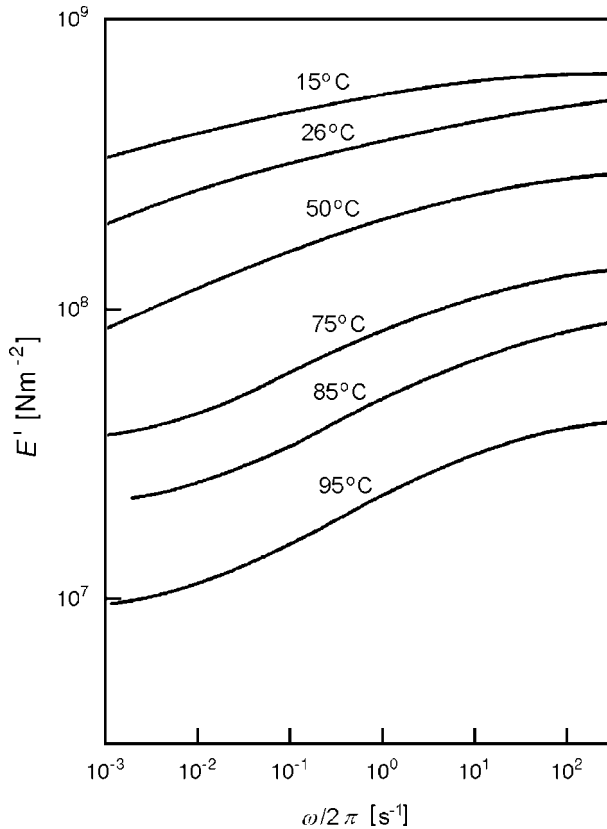


Fig. 6.32. Same system as in Fig. 6.31. Frequency-dependent storage tensile modulus [84]

plished by a 180° -twist defect, which is created at a crystal surface and then moves through the crystallite to the other side. As a result, all monomers of a crystalline sequence are rotated by 180° and shifted over the length of one CH_2 -unit. This screw-motion alone cannot set up the α -process, since it is mechanically inactive. As the crystals remain unchanged, both internally and in their external shape, there is no coupling to a stress field. Furthermore, the high relaxation strength of the α -process suggests a location in the weak amorphous parts of the structure rather than in the crystallites. How can the different observations be cast in one common picture? The answer is that the α -process in polyethylene has a composite nature. The mechanical relaxation indeed originates from an additional shearing of the amorphous regions. However, the prerequisite for this shearing is a chain movement through the crystallites. If such a motion is thermally activated, the pinning of the amorphous sequences onto the crystallite surfaces is no longer permanent. This allows a reorganization of the amorphous regions, which gives rise to a fur-

ther stress decay. Hence, in the α -process, two relaxation processes, one in the crystallites and the other one located in the amorphous zones, are coupled. As indicated by the broadness of the loss curves, the α -process is based on a larger group of relaxatory modes. Since the temperature variation leaves the shape of the loss curves essentially unchanged, we conclude that all modes employ the same elementary process, to be identified with the step-like longitudinal shifts of the crystalline sequences. NMR experiments and dynamic mechanical measurements indeed yield nearly identical activation energies – $\tilde{A} = 105 \text{ kJ mol}^{-1}$ in Fig. 5.53 and $\tilde{A} = 104 \text{ kJ mol}^{-1}$ in Fig. 6.31. Of interest is a comparison of the rate of elementary steps with the mechanical relaxation rate. The difference amounts to four orders of magnitude, telling us that the reorganization of the chains in the amorphous regions is a complex procedure requiring a huge number of elementary steps.

The experiments show the basic effect of the polyethylene crystallites. While in an amorphous polymer the transition from the glassy state to the melt is accomplished by one group of relaxatory modes within 10 to 20 K, the same process extends in a semicrystalline system like polyethylene over a much larger temperature range. Another NMR spectroscopic experiment is suitable for analyzing in detail these continuous mobility changes. The experiment is carried out for deuterated polyethylene. Deuterons (^2H) possess twice the spin of protons ($I = 1$ compared to $I = 1/2$), but the magnetic moment is much smaller so that effects of dipole–dipole interactions are comparatively weak. The peculiar property of ^2H is a large electric quadrupole moment and this interacts with the local electric field gradient tensor. Usually one deals with CH-bonds, where the electrons do indeed produce a strong field gradient at the location of the proton or deuteron. As a result of the interaction, the transitions $I_z = 1 \rightarrow 0$ and $I_z = 0 \rightarrow -1$ become associated with different energy changes. The two lines may be represented as

$$\omega = \omega_0 \pm \omega_Q, \quad (6.156)$$

where ω_0 stands for the Larmor-frequency of an isolated ^2H , and ω_Q represents the quadrupole splitting. ω_Q depends only on the angle θ enclosed by the magnetic field and the CH-bond direction that sets the orientation of the uniaxially symmetric field gradient tensor. For standard magnetic fields the splitting amounts to values in the order $\omega_Q/2\pi \simeq 10^5 \text{ s}^{-1}$. Deuterons thus represent spin labels that are exclusively governed by the local interaction with the electric field gradient.

The line shape of a ^2H NMR absorption spectrum under static conditions directly reflects the orientational distribution of the CH-bonds in the sample. Molecular dynamics modifies the spectral shape in a predictable way. Reorientational motion of individual CH-bonds generally leads to a narrowing of the line. A simple situation arises in the **rapid exchange limit** when the reorientation rate τ_r^{-1} becomes large compared to the inverse of the spectral width,

$$\tau_r^{-1} \gg \omega_Q^{-1}. \quad (6.157)$$

Then the shift $\pm\omega_Q(\theta)$ caused by the quadrupole-field gradient interaction is replaced by the time average $\bar{\omega}_Q^t$. For an isotropic reorientational motion this leads to a complete vanishing of the splitting. If reorientations only include a limited angular range, a certain splitting is retained. Specific motions lead to specific spectra. Theory enables precise predictions to be made and thus to discriminate between different motional processes.

Figure 6.33 depicts results of a corresponding study of linear polyethylene. Spectra of deuterons in the amorphous phase of a perdeuterated sample are shown, as measured at different temperatures between 163 K and 313 K, making use of a large difference in the spin-lattice relaxation time by which they can be separated from the deuterons in the crystallites. The experimental spectra are compared with the results of a model calculation. In agreement with the experimental spectrum at 163 K the model spectrum represents a superposition of a rigid phase (70%) and deuterons incorporated in mobile **kink-defects** (30%); kink-defects correspond to a sequence gauche⁻-trans-gauche⁺ or gauche⁺-trans-gauche⁻ in an otherwise stretched part of the chain. The transition between the two conformers is mechanically active, because it changes the chain contour. This conformational transition is regarded as the probable mechanism of the γ -process; the NMR experiments corroborate the assignment. Analysis of the next NMR spectra shows that the state of motion based on mobile kink-defects pertains up to 200 K, whereby the mobility increases continuously due to a rising defect concentration. Above 200 K the situation changes. In order to reproduce the spectra measured at 213 K and 293 K for part of the deuterons a reorientational motion that covers a larger angular range has to be assumed. Conformational considerations show that such wider motions can be accomplished by correlated rotations of five subsequent bonds in a chain, different from the three-bond motion of a kink-defect. Reproduction of the spectrum at 313 K requires that one assumes an even larger correlation range along the chain, incorporating seven subsequent bonds. Figure 6.34 summarizes all the results. The picture that

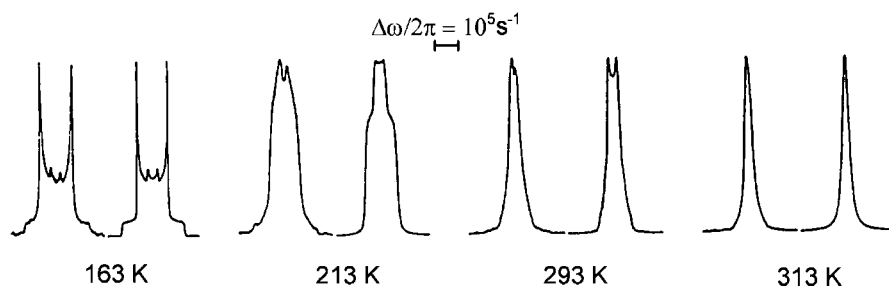


Fig. 6.33. Observed (*left*) and calculated (*right*) pairs of ^2H NMR spectra of the mobile deuterons in the amorphous regions of PE at different temperatures. Work of Spiess et al. [85]

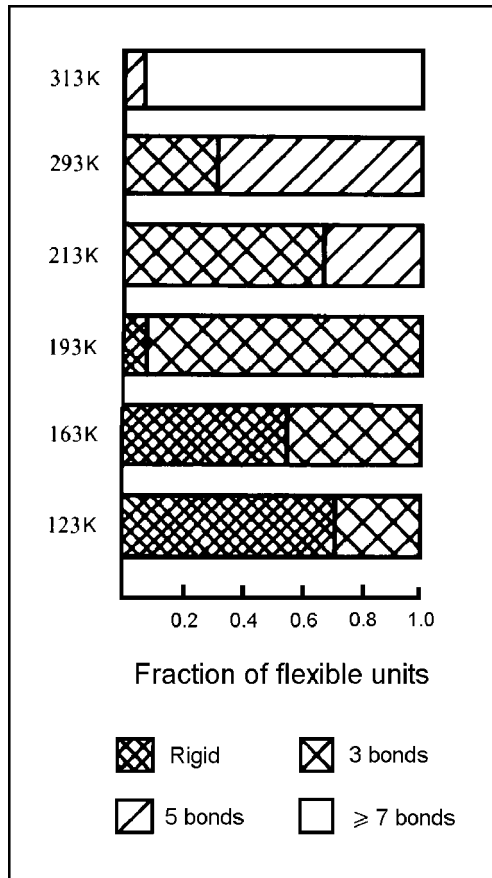


Fig. 6.34. Fractions of flexible units with different lengths in the amorphous regions of PE derived from the analysis of the ^2H NMR line shapes displayed in Fig. 6.33 [85]

thus emerges is that of an amorphous phase that is influenced by the limitations imposed by constraints. The constraints, which originate from the crystallites and trapped entanglements, are weakened upon heating and disappear only at the final melting.

Further Reading

- E.-J. Donth: *Relaxation and Thermodynamics in Polymers: Glass Transition*, Akademie Verlag, 1992
 J.D. Ferry: *Viscoelastic Properties of Polymers*, John Wiley & Sons, 1970
 N.G. McCrum, B.E. Read, G. Williams: *Anelastic and Dielectric Effects in Polymeric Solids*, John Wiley & Sons, 1967

- D.J. Meier (Ed.): *Molecular Basis of Transitions and Relaxations*, Gordon and Breach, 1978
- F.R. Schwarzl: *Polymermechanik*, Springer, 1990
- I.M. Ward: *Mechanical Properties of Solid Polymers*, John Wiley & Sons, 1971
- G. Williams: *Dielectric Properties of Polymers* in R.W. Cahn, P. Haasen, E.J. Kramer, E.L. Thomas (Eds.): *Materials Science and Technology*, Vol. 12 *Structure and Properties of Polymers*, VCH Publishers, 1993

Conjugated Polymers

The large majority of polymers, first of all the broadly used commodity materials polyethylene, polypropylene, poly(ethylene terephthalate) or polystyrene, have similar electrical and optical properties: They are insulators and they are colorless, i.e., they possess no mobile charges and the lowest electronic excitations are in the UV region. There exists a peculiar class of polymers with quite different properties; these are polymers with conjugated double bonds in the main chain. They are semiconductors or conductors and interact with light.

Figures 7.1 and 7.2 depict a characteristic observation. A thin film of poly-(phenylene vinylene) (PPhV) covered with two different electrodes made of an indium-tin oxide alloy (ITO) and calcium, respectively, is placed on a glass substrate and then connected to an external source of current. Nothing happens up to a voltage of 2 V, but then a flow of current sets in and grows with further rising voltage. Simultaneously with the onset of current the PPhV film begins to emit light, with an intensity proportional to the current. The effect is known as **electroluminescence**. A setup with such a performance is called a **light emitting diode**, abbreviated LED. The word ‘diode’ hereby

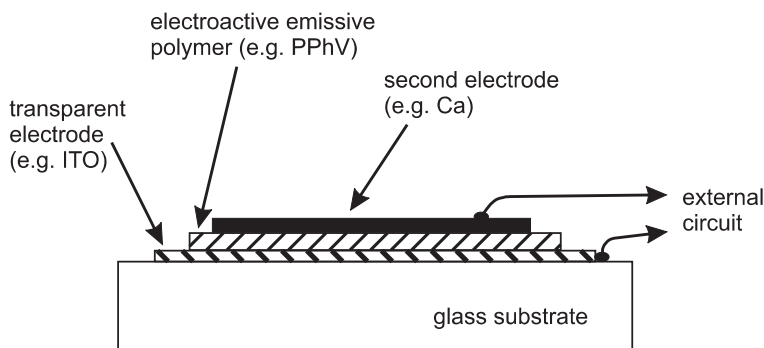


Fig. 7.1. Principal set-up of a polymer LED device

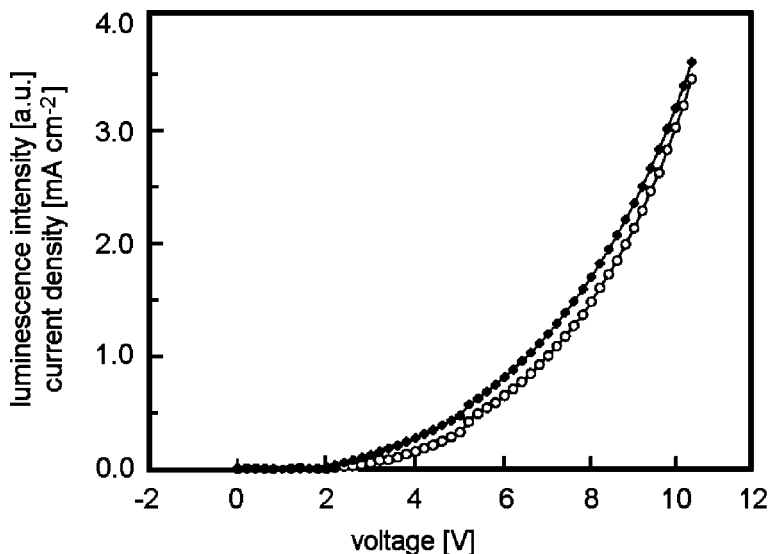


Fig. 7.2. ITO/PPhV/Ca LED: Variation of the current density (*filled symbols*) and the luminescence intensity (*open symbols*) with the applied voltage. From Friend and Greenham [86]

indicates that the current can flow only in one direction; if the voltage direction is reversed, practically no current flows. The active element in this **organic light emitting diode**, shortly OLED, is the **conjugated polymer** poly(phenylene vinylene). All conjugated polymers possess conjugated π electrons, i.e., electrons that are delocalized rather than being part of one valence bond. Excitation energies of conjugated π electrons are usually in the visible range and they are, therefore, addressed as being **optically active**. A selection of prominent examples has already been given in Table 1.3 in Chap. 1.

It was a second, really spectacular property that initiated the interest in conjugated polymers. In 1977 it was found by Shirakawa, Heeger and McDiarmid that films of polyacetylene (PAC) increase their conductivity tremendously when they are exposed to iodine vapor, from a basic value at the lower end of the semiconducting range up to values comparable to metals. Figure 7.3 represents these iodine dopant induced changes in a comparison with other materials. They encompass the enormous range of seventeen orders of magnitude.

It is understandable that these unusual findings triggered intense activities in research and development. The first conjugated polymers under study were all unstable in air and it was very difficult to prepare films. Suitable chemical modifications then succeeded to produce stable materials. They can be processed from solution or even the melt, sometimes via a conversion of short-chain precursors.

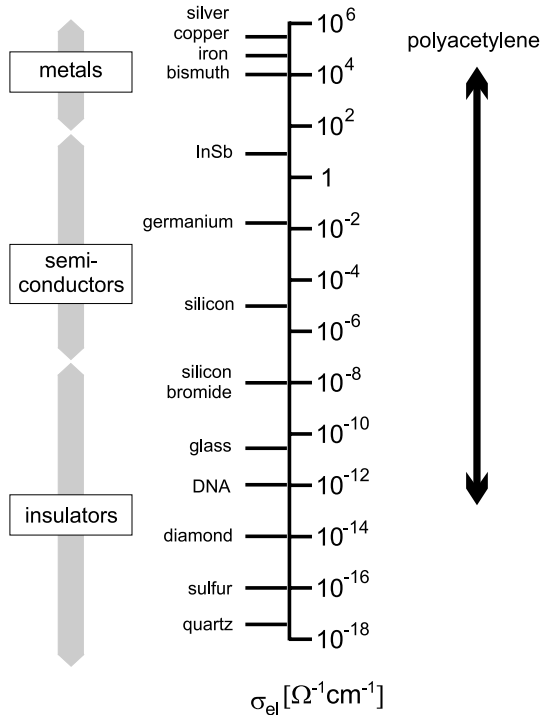


Fig. 7.3. Range of conductivities covered by doped PAc in a comparison with other materials

To provide a brief introduction into this peculiar class of polymer materials, in this chapter we first consider the elementary optical excitations, then discuss the electroluminescence, and finally deal with the conduction properties and the magnetism of doped samples.

7.1 Electrooptic Activity

7.1.1 Excitons and Free Charges

Considering the physical background of the optical and electrical activity of conjugated polymers several questions immediately come up, namely:

- What is the nature of the excited states that are created when photons are absorbed?
- What transitions show up in the subsequent luminescence?
- What levels are used by charge carriers when a current is flowing?

We discuss these in this section.

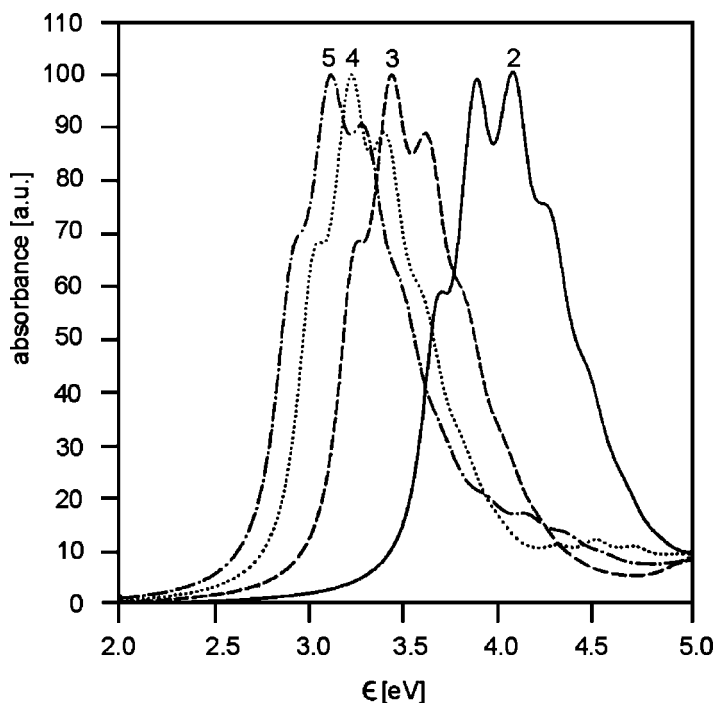


Fig. 7.4. Optical absorption spectra of two-ring, three-ring, four-ring, and five-ring oligomers of phenylene vinylene. A shift to lower energies with increasing length of the molecule is observed. From Cornil et al. [87]

Regarding the first question it is instructive to have a look at the experimental result presented in Fig. 7.4. The figure shows absorption spectra in the visible range, which were obtained for a series of oligomers of phenylene vinylene. The four presented absorption bands all have a similarly fine structure and are shifted against each other; the higher the number of monomers, the lower the frequency. A first conclusion can be drawn from the invariance of the profile of the bands. Since it is independent of the number of coupled monomers it must be a property of the monomer itself. We therefore first ask about the elementary optical excitations of a monomer. Figure 7.5 presents its chemical structure on the left-hand side and on the right-hand side a sketch of the distribution of the π electrons. One bond of each double bonds is set up by two σ electrons, the other is formed from overlapping atomic p_z orbitals oriented perpendicularly to the (xy) -plane of the planar molecular skeleton. The **conjugation**, i.e., the resonance interaction between the π bonds results in delocalized π electron states. Here, these states are occupied by the eight π electrons of a phenylene vinylene unit. There is a highest occupied molecular π orbital abbreviated **HOMO**. Above it there exists a **gap** and it extends up to next level, the lowest unoccupied molecular π orbital, shortly called **LUMO**.

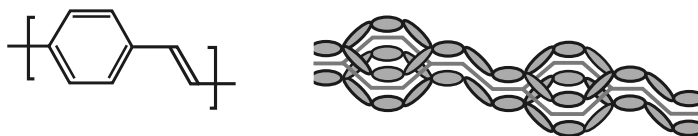


Fig. 7.5. (*left*) Structure unit of PPhV. (*right*) Clouds of π electrons in a unit, placed above and below the plane of the CC backbone. The *lines* connecting the carbon atoms represent the σ bonds

For conjugated polymers the gap energy is in the range of 1.5 eV to 3 eV, i.e., in the range of visible light and the near infrared, similar to anorganic semiconductors. As always in the ground state of a multielectron system with an even number of electrons, the spins compensate each other so that a singlet state, denoted S_0 , results.

The absorption bands in Fig. 7.4 are to be assigned to the lowest possible one-electron excitation. This is accomplished by a transfer of the electron at the HOMO level to the next higher state. One might think at first that this is the LUMO level, but this is incorrect. The LUMO level would indeed be occupied if a ninth electron were added to the monomer. If, however, the electron in the HOMO level is excited, this level is left empty, and the then positively charged monomer exerts an attractive Coulomb force. The force reduces the excitation energy, which now falls below the gap energy. The thus formed state can be thought of as a coupled electron-hole pair and is named an **exciton**. In order to be optically active, the transition must have a non-vanishing transition dipole moment. One requirement for this is an unchanged total spin. Hence, this exciton state is necessarily a singlet state and is denoted S_1 .

The fine structure of the bands follows from the fact that together with an electronic excitation also vibrations of the molecular skeleton are induced. There is a prerequisite for such a common electronic and vibrational excitation: It only happens if the transfer of the electron to a higher level leads to a change in the molecular structure, i.e., some change in bond lengths and bond angles. Figure 7.6 explains this coupling, dealing with two possible situations. The **Franck-Condon principle** states that electronic transitions are very rapid compared to motions of the nuclei setting up the molecular skeleton. Hence, they always take place at constant positions of the nuclei. In the drawings on the left-hand side of Fig. 7.6 transitions are therefore described by an arrow in the vertical direction, starting from the vibrational ground state ($n_v = 0$) in the electronic ground state S_0 . The variable X represents here some displacement coordinate. If the structure were not affected by the electronic excitation, the transition would automatically lead into the vibrational ground state of S_1 , as indicated in the upper left figure. Then, as shown on the right, only one sharp absorption band is expected, which is rarely seen. On the other hand, if the electron transfer also produces a shift

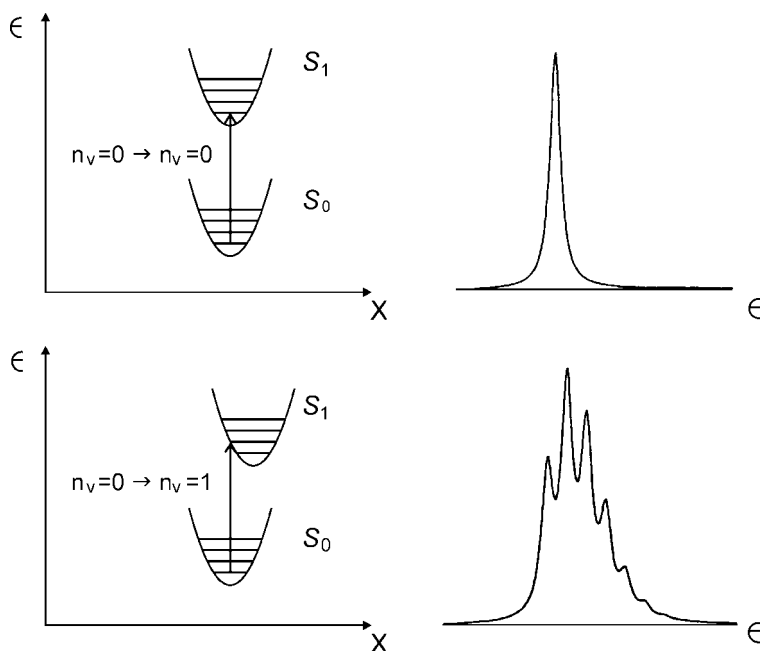


Fig. 7.6. Appearance of the exciton band profile if the excitation leaves the structure of the molecule unchanged (*top right*) and if it leads to some change (*bottom right*). The *left-hand side* explains the difference of the spectra by applying the Franck-Condon principle; X represents a displacement coordinate

in the equilibrium value of the structure coordinate X , the electronic excitation is necessarily coupled to an excitation of a vibrational quantum. This is explained by the lower left figure, where the vertical arrow ends at $n_v = 1$ in the S_1 level. In this case, there also exist non-vanishing probabilities for transitions to even higher and also lower vibrational levels. As a result, a band with a fine structure appears, as shown on the right side, and exactly this is observed in the experiment.

The **red shift** of the bands following from an increase of the molar mass of the oligomer is a well-known phenomenon. The continuing interaction between the π electrons of the coupled monomers extends the conjugation over the whole chain. The interaction further stabilizes all the π electrons, i.e., leads to a drop of all energy levels and a lowering of the energy difference between S_0 and S_1 . There is another important consequence of the interaction: If an exciton is created at some monomer by the absorption of a photon, it will not remain stationary, but propagate. After a short time it can be found on each monomer of the chain with equal probability. An exciton carries energy. To move an exciton, i.e., the energy that it represents, it is not necessary to move the constituting electron-hole pair itself. A shift of the energy can also be achieved by a simultaneous decay-excitation process in two

neighboring monomers. The rate of this transfer depends on the overlap of the associated wave functions, as is described by the **Förster mechanism**. The delocalization of the exciton that extends in the stationary state over the whole oligomer concerns both the excited electron and the created hole. The mean distance between the electron and the hole varies between different materials. For conjugated polymers it lies above the monomer diameter, typically being of the order of a few monomer lengths. Excitons are also a characteristic feature in the excitation spectra of anorganic semiconductors. There, the electron–hole distance is larger, corresponding to many lattice cells. These bound pairs are addressed as **Mott–Wannier excitons**. On the other hand, for excitons found in molecular crystals or ionic solids both the electron and the hole remain within the size of one molecule. These excitons are known as **Frenkel excitons**. The excitons in conjugated oligomers or polymers have an intermediate position, in between the Mott–Wannier and the Frenkel type.

In a perfectly ordered solid or a perfectly ordered macromolecule excitons move according to quantum-mechanical kinetics, i.e., like wave packets. Because this requires strict phase relationships in space and time, this mode of motion, addressed in the literature as **coherent motion** of excitons, is perturbed by all deviations from regularity. Chains of conjugated polymers always include various defects such as kinks and torsions. These break the conjugation. Typically, regular sequences extend only over five to ten repeat units. The results of measurements for a series of oligomers like the ones displayed in Fig. 7.4 can be used for the estimate. The red shift of the exciton frequency ω with increasing monomer number, n , can be described by the equation

$$\omega(n) = \omega_0 + \frac{\Delta\omega}{n} . \quad (7.1)$$

Applying this to the exciton frequency observed for a polymer gives the number of conjugated structure units n . Conjugated polymers are semicrystalline systems, built up of crystalline and amorphous regions, and the crystallites often contain a high amount of defects. As a consequence, the coherent mode of motion is only found within ordered crystalline domains with sizes in the nm range. Long-range energy transfers in such a structure remain possible, but by a much slower **incoherent** kind of exciton motion, to be described as a diffusive **hopping process**. Referring to this rate determining process only, a conjugated polymer in the solid state resembles an **ensemble of domains** of varying size, from ordered assemblies of regular chain sequences down to single monomers incorporated in the coiled chain parts in the amorphous regions. With the size of these sites the excitation energy also varies, the minimum being found for the largest domains. Even under these conditions of a varying excitation energy, excitons can carry out hopping motions between adjacent domains. The highest transfer rates are found for **resonance transitions** between domains with equal excitation energies, but a transition to a domain with a lower or higher energy is also possible, although with a lower rate. The latter moves must be supported by the creation or annihilation of phonons.

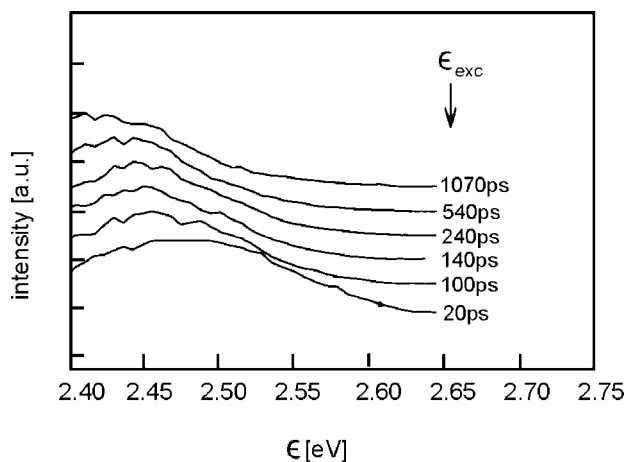


Fig. 7.7. PPhV: Time-dependent change of the fluorescence spectrum after an excitation pulse at 2.65 eV (*arrow*). The waiting times are given. From Bässler [88]

Of course, the time an exciton can use for a motion is limited. At any time an exciton can spontaneously annihilate under the emission of a photon, thus contributing to the luminescence. In addition, there always exist mechanisms of a non-radiative decay. Figure 7.7 shows an experiment that reflects the diffusive motion of excitons within the **energy landscape** associated with the broad **density of states** distribution provided by the ensemble of domains. The figure shows luminescence spectra observed subsequent to a short pulse after a certain waiting time. One finds a time-dependent change of the luminescence spectrum with a shift to lower energy with increasing time. Hence, there is a tendency of the excitons to diffuse to the domains with lower excitation or decay energy. The process can be modeled and the development of the luminescence reproduced.

Due to the coupling of the excited electron to the hole left back on the HOMO level, excitons are non-charged particles that cannot contribute to an electrical current. A current requests the motion of free charges, either electrons or holes. These can indeed exist in conjugated polymers. They are found if

- an exciton dissociates into a free electron and a free hole after an additional energy input,
- rather than creating an exciton, an absorbed photon immediately produces a free electron–free hole pair,
- free holes or electrons are supplied by dopants or injected from the electrodes.

The experiments shown in Figs. 7.8 and 7.9 provide examples for the first two processes.

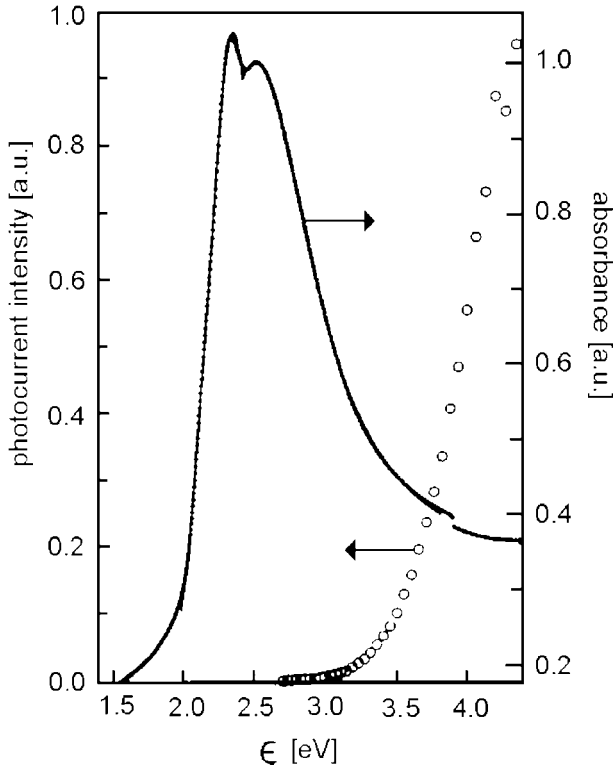


Fig. 7.8. PdAc: Photoconductive spectral response (*circles*) compared to the optical absorption spectrum (*continuous line*). From Pakbaz et al. [89]

The first figure presents the **spectro-photoconductive response** of poly(diacetylene) (PdAc). Some low voltage is applied to the sample, but at first virtually no current is observed. The sample is then illuminated by monochromatic radiation under variation of the frequency. When coming from low frequencies the photon energy of 3 eV is reached, a flow of current sets in and rises with further increasing photon energy. Obviously, if photons with energies above this limit are absorbed they create free carriers in the sample, thus enabling a current to flow under the applied voltage. Interesting is the comparison with the frequency dependence of the absorbance, which is also shown in the figure. Photon absorption begins much earlier, already at 1.5 eV, but is at first not associated with a photocurrent. Hence, in this first frequency range only excitons are created. The energy difference between the peak at 2.4 eV associated with the creation of an exciton and the onset of the photocurrent amounts to about 0.6 eV. Its meaning is clear: It represents the dissociation energy of the exciton, i.e., the electron-hole binding energy.

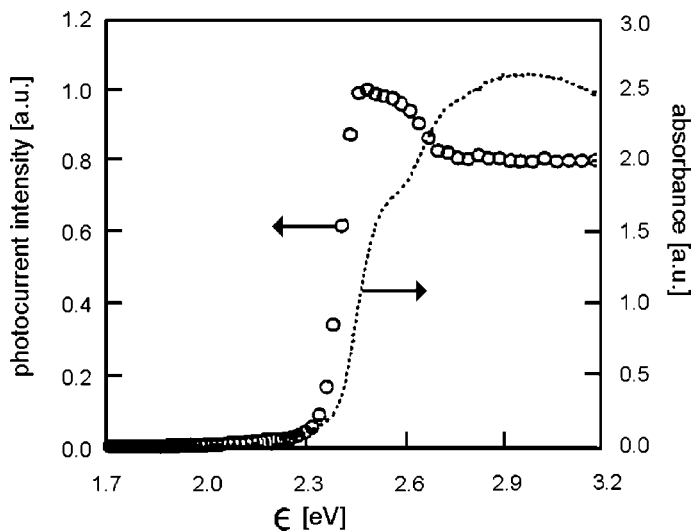


Fig. 7.9. PPhV: Photoconductive spectral response (*circles*) compared to the optical absorption spectrum (*continuous line*). From Lee et al. [90]

The second example, which deals with poly(phenylene vinylene), shows that this difference can also be very small and virtually vanish. Here, the onset of the absorption is practically identical with the onset of the photocurrent. The reason for this peculiar property of poly(phenylene vinylene) is still under discussion. There might exist sites (in particular places located at the film-electrode interface) where the additional energy necessary to dissociate the exciton is spontaneously provided.

As has been mentioned, transferring an electron up to a higher level in general leads to changes in the structure of the molecular skeleton. A structural response is also to be expected for a freely moving electron or hole: It polarizes its surroundings on the chain. This polarization generally leads to an energy decrease. Theoretical estimates for this drop yield a value of the order 0.1 eV and indicate an extension of the polarization over a couple of monomers. The polarization remains localized and moves together with the electron or hole. Many treatments in the literature emphasize this effect, then dealing with negatively or positively charged moving particles named **polarons** instead of just considering the motion of free electrons and holes.

Like excitons, electrons, holes or polarons also carry out a hopping motion between the domains in a conjugated polymer. Each domain provides unoccupied states around the LUMO and HOMO level for electrons and holes, respectively. They are delocalized within the domains and vary, as for the excitons, in their energy with the domain size. The tails of the corresponding density of states distributions act as shallow traps that keep the charges temporarily fixed.

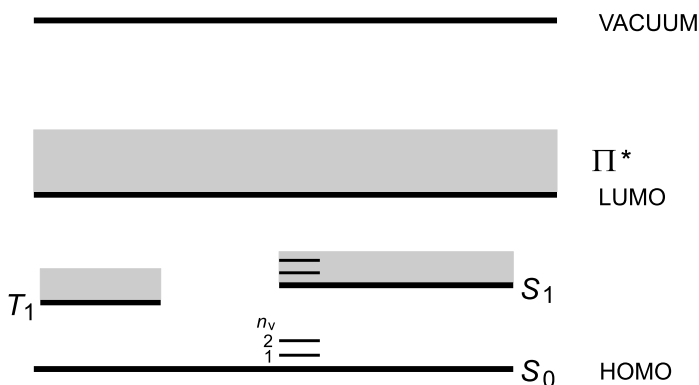


Fig. 7.10. One-electron levels and multielectron states created by excitations of one π electron in an ordered domain of a conjugated polymer. Prior to the excitation, in the ground state S_0 the electron occupies the HOMO level. S_1 denotes a first order singlet exciton with an energy at the lower bound of the associated vibronic band. The creation of an exciton is in general coupled to simultaneous vibrational excitations; n_v are vibrational quantum numbers. T_1 denotes a first order triplet exciton at the lower bound of an associated vibronic band. The LUMO level is at the lower edge of the band Π^* of states with one non-bonded electron. The VACUUM level is that of electrons with vanishing kinetic energy outside the sample

Figure 7.10 summarizes once again the energetic situation, giving a scheme for the energies of all the discussed states, both one electron levels and multielectron states, referring to one domain. One additional feature is included. On the left-hand side a further multielectron state denoted T_1 is shown. It represents a first order **triplet exciton**. It differs from the singlet exciton in the total spin, which here has the quantum number 1. It is not possible to create triplet excitons by a photon absorption starting from the ground state S_0 since it necessitates a change in the spin direction. However, there exists another pathway for the formation of triplet excitons, namely a spontaneous coupling of a free electron and a free hole; they may have been created by an injection from the electrodes or the dissociation of singlet excitons. Spontaneous decays of triplet excitons under the omission of photons are forbidden, strictly speaking, they still remain possible but occur with an extremely low rate. Triplet excitons decrease the efficiency of light emitting diodes, as will be discussed in the next section.

7.1.2 Electroluminescence

In the introduction to this chapter a light-emitting diode was described as being set up of a polymer film (PPhV) and two different electrodes (ITO and Ca) on the surfaces (Fig. 7.1). Figure 7.2 then showed that for voltages above a critical value a current coupled to the emission of light flows. Figure 7.11 now displays the spectrum of the emitted light as well. The curve denoted EL

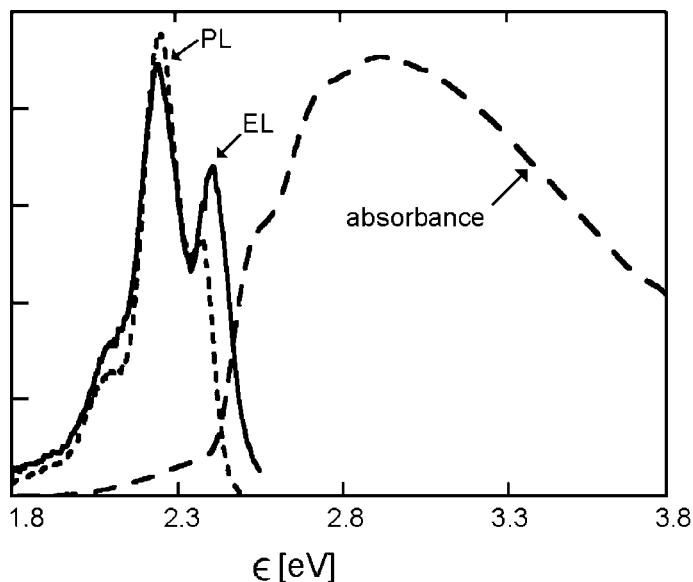


Fig. 7.11. PPhV: Luminescence spectra after an electrical (EL) and a photonic (PL) excitation, shown together with the optical absorption spectrum. From Friend and Greenham [91]

represents this spectrum with a broad band with fine structure. The band is to be assigned to the vibronically broadened annihilation of an exciton. Also included in the figure is the photo luminescence spectrum (PL) observed after an excitation of poly(phenylene vinylene) by photons with energies above 2.6 eV. The two emission bands EL and PL are practically identical. Hence, both an electrical or optical excitation create the same excitons, which then annihilate under the emission of photons. The figure also shows the optical absorbance spectrum of poly(phenylene vinylene). It sets in at the frequency of the exciton and shows a strong rise at 2.4 eV. Here the photon energy reaches the value that is required to excite one electron from the HOMO to the LUMO level, i.e., to create a free electron and a free hole.

A discussion of the functioning of a polymer LED can be based on the energy level scheme given in Fig. 7.12. It deals with the conditions in an LED onto which an external voltage is applied. Polymer LEDs are set up using two different electrodes. One of them, in the ITO example, has a high work function (as given by the energy that has to be supplied to transfer an electron from the Fermi level to the vacuum level). The second one, here calcium, has a low work function. When the electrodes are attached to the polymer film, **electrical double layers** spontaneously form at the interfaces; as always happens when two different conductive materials are brought in contact with each other. The layer on the metal side is very thin, the oppositely charged depletion layer near the surface of the polymer film has some extension. As a consequence, steps

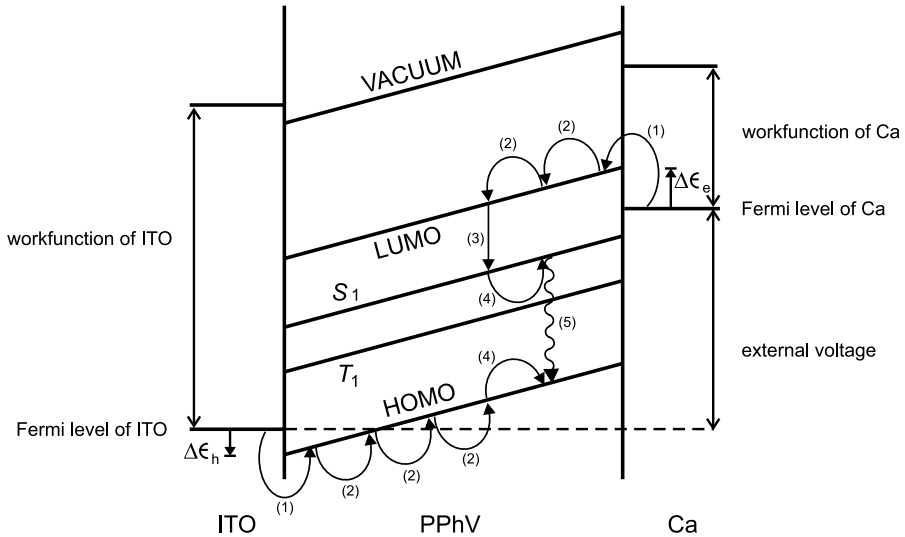


Fig. 7.12. Energy level diagram for a ITO/PPhV/Ca LED under a voltage as given by the difference between the anode and cathode potential. Work functions of the two electrodes. Barriers to the injection of electrons, $\Delta\epsilon_e$, and holes, $\Delta\epsilon_h$

in the electrostatic potential V arise at both metal–polymer interfaces. The step heights have such values that in the initial equilibrium state, i.e., the state established before the application of an external voltage, the chemical potential of the electrons, which now includes also an electrostatic contribution $(-e)V$, becomes identical in all three materials. Applying an external voltage leads to deviations from the current-free equilibrium state, and a current starts to flow. Within the polymer film the electrostatic potential decays. The decay of the potential that determines the electrical field,

$$E = -\frac{dV}{dx}, \quad (7.2)$$

and the current density j are related by

$$j = \sigma_{el}E. \quad (7.3)$$

σ_{el} denotes the **electric conductivity**. For all semiconductors σ_{el} is to be described by

$$\sigma_{el} = ec_e\nu_{el,e} + ec_h\nu_{el,h}. \quad (7.4)$$

c_e or c_h denote the number densities of electrons and holes. The variables ν_{el} represent **electric mobilities**. They give the ratio between the mean velocity \bar{u} of a charged particle and the acting electric field

$$\nu_{el} = \frac{|\bar{u}|}{E}. \quad (7.5)$$

Compared to anorganic semiconductors electric mobilities in conjugated polymers are generally low.

If an LED is activated by an external voltage, from the cathode electrons change into the polymer film to the LUMO level of mobile free electrons and holes are simultaneously ejected by the anode and enter the HOMO levels. The barriers to be surmounted have heights $\Delta\epsilon_h$ and $\Delta\epsilon_e$ and the entrance steps are represented by the curved arrows denoted (1). As is obvious, under the given conditions with electrodes with strongly differing work functions, cathode and anode cannot be exchanged. The then arising high barriers allow for only a low current. The setup thus indeed has rectification properties, i.e., is a diode. Within the polymer layer both the electrons and the holes move by a hopping process from domain to domain, directed by the applied field as indicated by curved arrows (2). Sometimes it happens that an electron and a hole arrive at one site at the same time. Then an exciton can form under a transfer of the binding energy to the lattice (3). The exciton also carries out a diffusive motion between the domains (4). However, being a neutral particle, its hopping motion is random, i.e., non-directed. At some time the exciton will spontaneously annihilate under the emission of a photon (5).

Poly(phenylene vinylene) and also other conjugated polymers have an imbalance in the properties of electrons and holes. The entrance barrier is higher and the mobility is lower for the electrons, and as a result electrons are accumulated near the cathode. As a consequence, the emission region also shifts to the neighborhood of the cathode. Near a metal surface excitons annihilate more frequently in radiationless manner and the luminescence efficiency drops. To avoid this undesired effect modern LEDs are often constructed from two organic layers, one preferentially transporting electrons (ETL), and the other one, the conjugated polymer, transporting holes (HTL) first of all. For such an ITO-HTL-ETL-Ca LED the light emission region moves toward the HTL-ETL interface in the center and the rate of radiationless decays decreases.

If an electron and hole couple within one domain, either a singlet (S_1) or a triplet exciton (T_1) forms. Since triplet excitons have three independent states, corresponding to quantum numbers $S_z = 1, 0, -1$ for the spin component in the z -direction, while only one state exists for the singlet exciton, triplets form with a three times higher rate than singlets. Their existence in a LED can be observed by spectroscopical means. Triplets possess a characteristic absorption band that relates to a transition from T_1 to a higher order triplet state. Figure 7.13 shows this characteristic band for poly(phenylene vinylene). The experiment demonstrates that triplets are generally created when free electrons and holes are present; they may have been produced by either applying a current or an optical excitation with photons of sufficiently high energy.

As has already been mentioned, the existence of the triplet excitons is a disadvantage of polymer LEDs. They do not contribute to the luminescence

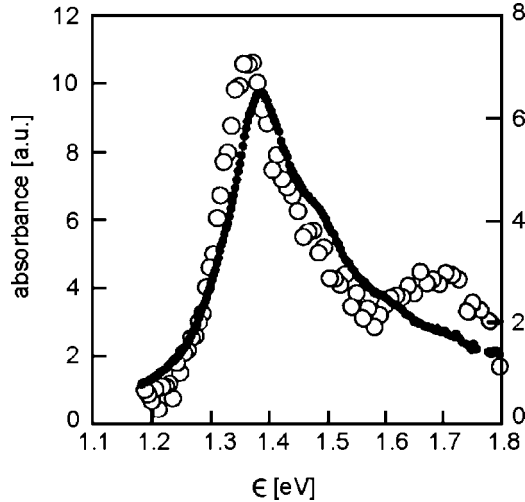


Fig. 7.13. PPhV: Absorption spectrum assigned to triplet excitons demonstrating their presence after an electrical (*open circles*) or optical (*filled symbols*) excitation. Measurements were carried out at 20 K. From Brown et al. [92]

signal of the device and, therefore, reduce its efficiency. Putting all relevant factors together, the electroluminescence efficiency, γ_{EL} , of a polymer LED can be described as

$$\gamma_{\text{EL}} = \phi_{\text{opt}} p_{\text{ex}} \phi_{\text{S}} p_{\text{pl}} \quad (7.6)$$

p_{ex} gives the probability that an electron and a hole entering the organic layers from the external current form an exciton, ϕ_{S} describes the fraction of singlet excitons and p_{pl} denotes the photoluminescent quantum yield. p_{pl} differs from unity due to the presence of **quenching sites** offering non-radioactive decay paths to the excitons. A polymer LED represents a multilayer structure whose optical properties are affected by reflections, refraction and interference phenomena. This is globally expressed by the fourth factor, ϕ_{opt} , dealing with the outcoupling, i.e., giving the fraction of photons emitted from the front surface.

The color of the light emitted by a polymer LED, which is determined by the exciton energy, can be varied by chemical substitutions or by changes in the conjugation length. The conjugation range can be reduced in controlled manner by the introduction of co-units into the chain. Another means is a dissolution of chains of the conjugated polymer in a matrix of a common polymer; Fig. 7.14 gives such an example. A ladder polyphenylene (PPh) was blended with polystyrene (PS). For a concentration of 30% of the conjugated polymer the emission line shows a broad spectral distribution (a). The distribution becomes sharper when decreasing the concentration. In the dilute limit of 1% of ladder polyphenylene one observes a line with a sharp maximum in the blue range (c).

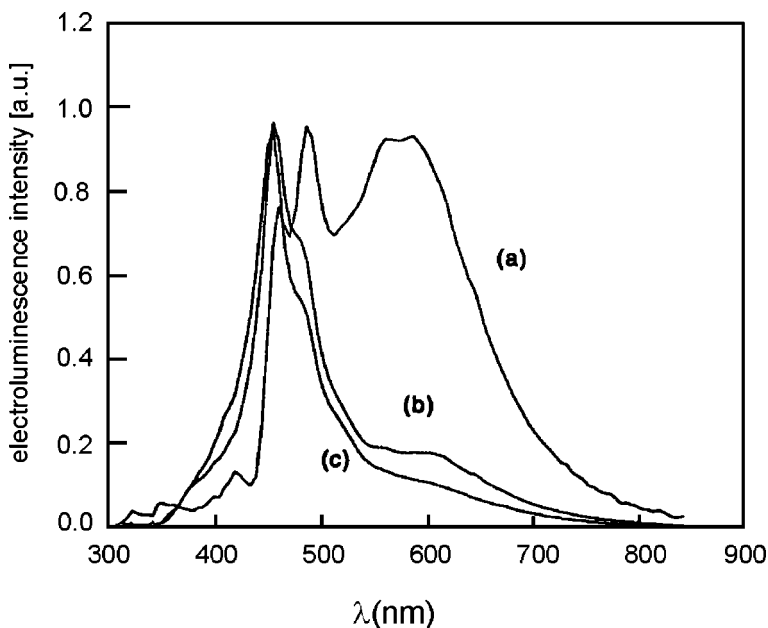


Fig. 7.14. Electroluminescence spectra of a ladder PPhV dissolved in PS (*a*: 30%, *b*: 10%, *c*: 1% PPhV, from Friend and Greenham [93])

7.2 Effects of Doping

7.2.1 Electrical Conductivity

Dealing with the electrical conductivity of polyacetylene (PAC), Fig. 7.3 in the introduction to this chapter described the effect of **doping** with iodine. While pure polyacetylene is a semiconductor as all conjugated polymers, the doping process turns it into a system that finally possesses an electric conductivity comparable to metals with values in the range of 10^4 to $10^5 \Omega^{-1} \text{cm}^{-1}$. ‘Doping’ of a semiconductor means that an oxidizing or reducing agent is introduced into the sample. In the case of conjugated polymers this is usually carried out either by an exposure of the sample to a corresponding gas or the placement in a corresponding liquid. Oxidizing atoms or molecules take up electrons from their surroundings, in a conjugated polymer first π electrons from the HOMO level. They thus act as **electron acceptors**. As a result holes, i.e. positive charge carriers, are created. Reducing agents supply additional electrons and thus function as **electron donators**. These electrons occupy states at and near the LUMO level. With such a supply of electrons or holes the number of free charges increases greatly. As is shown in Fig. 7.3 for polyacetylene, the resulting rise in the conductivity can be tremendous. Polyacetylene is not an exception; doping results for all conjugated polymers to similarly large values of the conductivity.

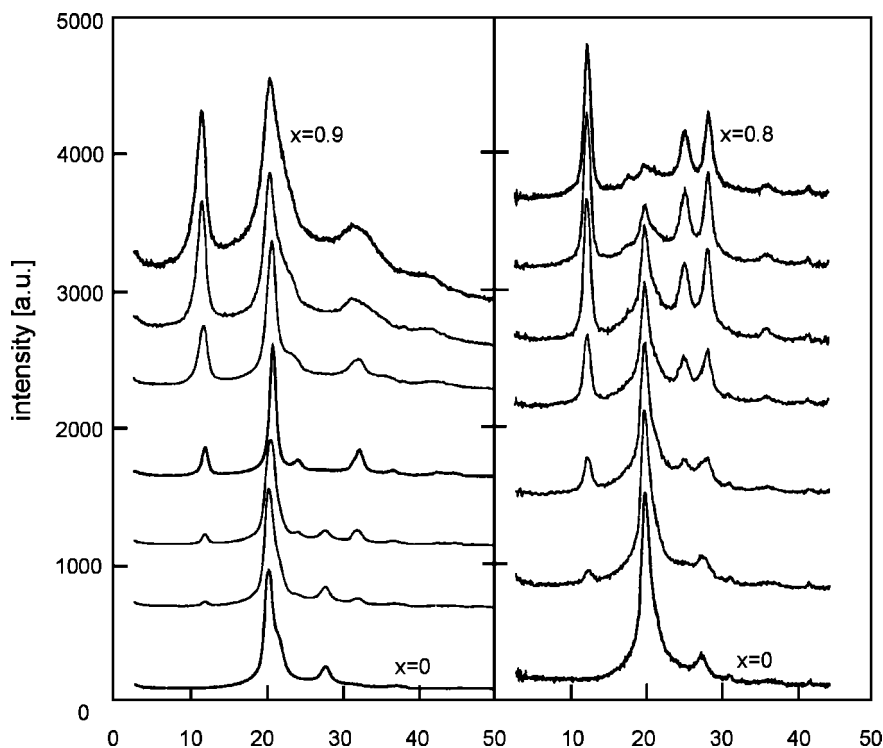


Fig. 7.15. PPhV during a doping with gaseous Na (*left*) and Cs (*right*): X-ray scattering patterns obtained after different times of gas exposure (final concentrations are $x = 0.9$ and 0.8 dopant atoms per monomer). The *scattering curves* show changes of the crystal structure associated with an intercalation of the dopant atoms. From Winokur [94]

The concentration of dopant molecules or atoms in the highly conductive state typically amounts to some percent of the number density of monomers. When becoming dissolved in a sample, dopant atoms may have a preference for the amorphous regions, but they also enter the crystals. Figure 7.15 demonstrates that this even happens in a regular manner. X-ray scattering curves measured during the process of doping of poly(phenylene vinylene) with Na and Cs, respectively, show the disappearance of some Bragg reflections and the appearance of new ones. Obviously, a new structure develops in which the dopant atoms are placed on regular lattice sites.

Figure 7.16 shows the results of temperature-dependent conductivity measurements for samples of polyacetylene doped with various amounts of iodine. The conductivities measured at room temperature for the samples with the highest dopant contents are comparable to those of metals. It is important to note that even if the room temperature values are comparable, there exists a striking difference in the temperature dependence. Whereas for metals

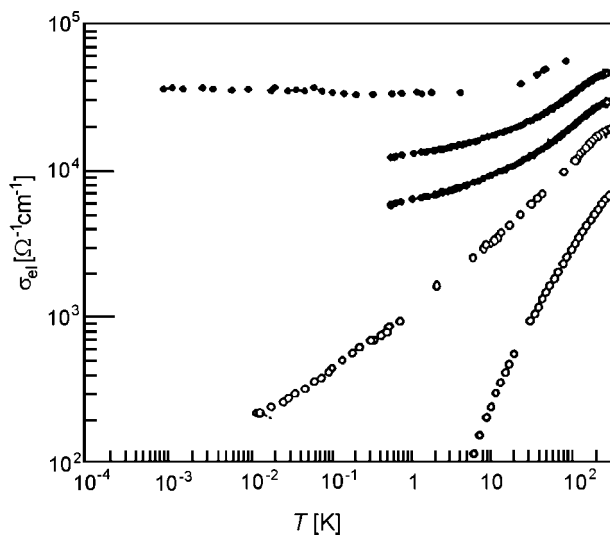


Fig. 7.16. Temperature-dependent conductivities $\sigma_{\text{el}}(T)$ of various iodine doped PAc samples. Conductivities increase with rising iodine content. From Kaneko and Ishiguro [95]

the conductivity always decreases with rising temperature, one here observes here, and this is typical for all doped conjugated polymers, the reverse tendency, i.e., a positive temperature coefficient of the conductivity. For many doped conjugated polymers the conductivity practically vanishes for temperatures near zero, opposite to metals where here the largest values are reached. This qualitative difference is indicative of a difference in the mechanism of motion of the charges. In metals, there are freely moving **ballistic** electrons that are scattered from time to time at perturbations of the lattice; between two successive scattering events the charge carrier becomes accelerated by the electric field. Quite different from the metallic kinetics, charge carriers in doped conjugated polymers carry out a directed **hopping motion** from domain to domain. The largest domains are within the crystalline regions, with sizes up to several ten nanometers. The domains in the amorphous regions are smaller and have sizes in the nanometer range. The quantum-mechanical motion within a domain is much more rapid than the hopping between domains and can be neglected in time considerations. The interdomain jumps have to be activated. Since this needs thermal energy, jump rates and thus the conductivity decrease when the temperature is lowered.

Independent of the mechanism of motion, electrical conductivities can always be described by Eq. (7.4) as

$$\sigma_{\text{el}} = e c_e \nu_{\text{el},e} + e c_h \nu_{\text{el},h} .$$

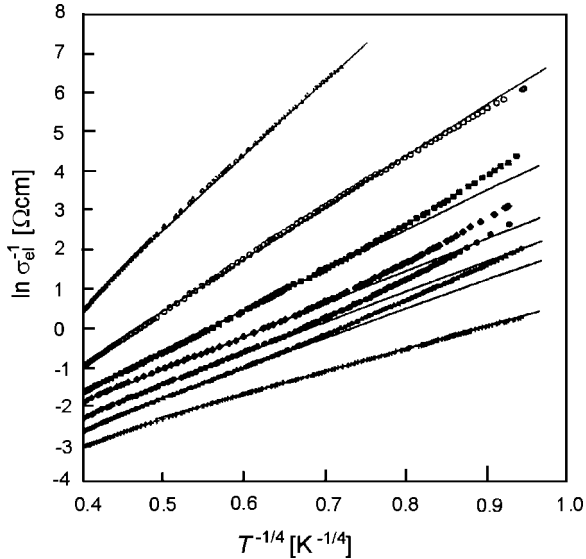


Fig. 7.17. PPy samples doped with increasing amounts of PF_6 (*highest to lowest curve*): Temperature dependence of the resistivity σ_{el}^{-1} indicative of a hopping motion of the charges. From Menon et al. [96]

For given electron and hole densities c_e and c_h as determined by the dopant content, the temperature dependence $\sigma_{\text{el}}(T)$ just reflects the temperature dependence of the electric mobilities $\nu_{\text{el,e}}$ and $\nu_{\text{el,h}}$. For a hopping motion with varying hopping distances theories predict a temperature dependence of the mobility and, thus, of the electric conductivity as given by the equation

$$\sigma_{\text{el}} \propto \exp - \left(\frac{T_A}{T} \right)^{1/4} . \quad (7.7)$$

Such a dependence is indeed found in experiments. Figure 7.17 presents as an example the temperature dependence of the **resistivity** σ_{el}^{-1} of polypyrrol (PPy) doped with PF_6 . In the figure $\ln \sigma_{\text{el}}^{-1}$ is plotted versus $T^{-1/4}$, as suggested by Eq. (7.7). The straight lines indicate agreement with the theory. Resistivities and activation temperatures T_A are lowered when more dopant is introduced.

Although this is the typical behavior, at high dopant contents one sometimes also finds evidence for a closer approach to metallic properties. Figure 7.18, which presents results for polyaniline (PAN), shows a nearly constant conductivity for the lowest temperatures and highest dopant contents. It appears that here the motion no longer has an activated character. According to an explanation offered in the literature, the charges here move from site to site by tunneling processes that require no thermal activation.

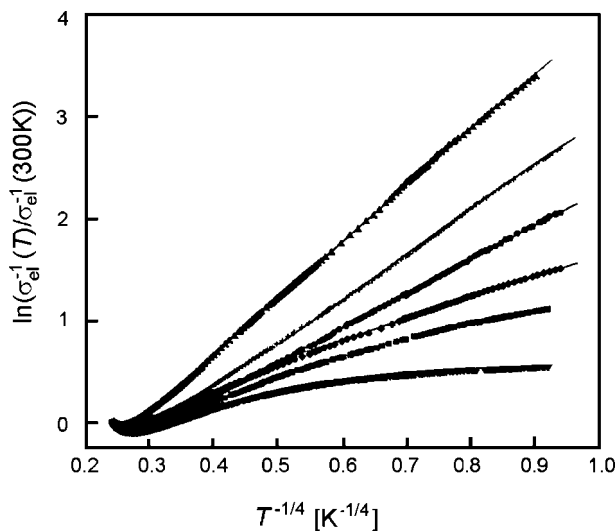


Fig. 7.18. PAN doped with increasing amounts of cresol: Change of the temperature dependence of the resistivity indicative for a transition from a hopping motion of the charges to a quasi-metallic transport mode (*lowest curve*). From Menon et al. [96]

As all semicrystalline polymers, conjugated polymers can be oriented by drawing. Figure 7.19 shows that for such oriented samples the conductivity becomes anisotropic, having much higher values in the drawing direction than perpendicular to it. Such a behavior is to be expected. Since the ordered regions in a sample of a conjugated polymer are more extended in the chain direction, less jumps are required to proceed over a certain distance. The barriers for jumps between sites adjacent in the chain direction might also be lower.

Applying an external pressure lowers the distances between the monomers and thus will, in tendency, raise the interdomain jump rates. One therefore expects an increase in the conductivity; Fig. 7.20 shows that this is indeed found.

7.2.2 Magnetism and Reflectivity

A metal possesses a continuous distribution of energy levels in the conduction band and they are occupied by electrons up to the Fermi energy ϵ_F . Similar conditions are found in each ordered domain of a conjugated polymer, even if the wave functions are spatially restricted. The Π^* band is composed of a quasi-continuous sequence of states beginning at the LUMO level and it can be occupied by the electrons supplied by the dopants. These fill the Π^* band up to a certain level determined by the dopant concentration. Together with their spin electrons have a magnetic moment μ_B , the **Bohr magneton**. Paramagnetic properties are therefore to be expected, however, as in metals, they are peculiar. Magnetic properties of metals have a specific character due to the fact that each level is occupied twice, with one spin-up and one spin-down

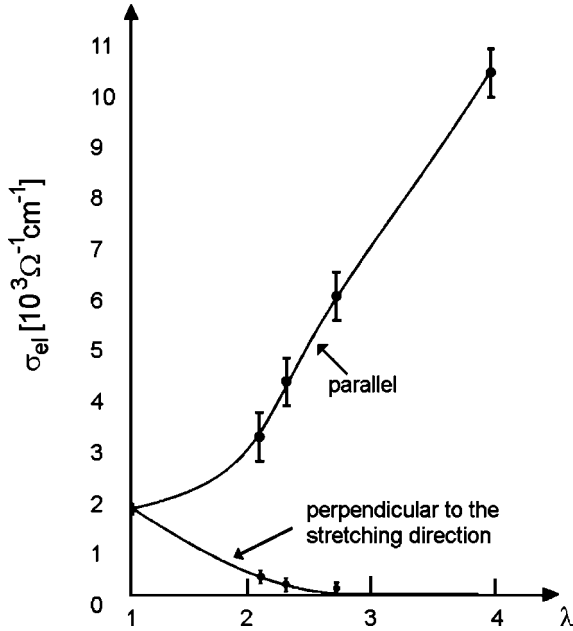


Fig. 7.19. PAc oriented by stretching: Increase of the anisotropy of the conductivity with the stretching ratio $\lambda = L/L_0$. From Naarmann [97]

electron. If a magnetic field is applied, electron spins cannot just reorient but, when doing so, simultaneously have to change the level. Figure 7.21 explains the situation and the response of metallic electrons to an applied magnetic field. The density of energy levels $\mathcal{D}(\epsilon)$ is here shown together with its mirror image, with the right-hand and left-hand sides corresponding to states with spins parallel and anti-parallel to the field direction, respectively. As long as no magnetic field is present, it is found that both parts are filled up to the Fermi surface at ϵ_F . If a magnetic field of strength B is applied, the energy of all parallelly oriented spins is increased by $\mu_B B$, while that of the anti-parallel spins is reduced by the same amount. In the first instance, the situation in the middle of the figure is obtained. This does not, however, correspond to the new equilibrium state, since the spin system can gain energy by a redistribution into the situation shown on the right-hand side of the figure. As shown in many textbooks on solid state physics, this redistribution leads to a magnetization

$$M = 2\mu_B \frac{3c_e}{4\epsilon_F} \mu_B B = \mu_0 c_e \frac{3\mu_B^2}{2\epsilon_F} \frac{B}{\mu_0}, \quad (7.8)$$

hence, to a temperature-independent paramagnetic susceptibility

$$\chi_m = \mu_0 c_e \frac{3\mu_B^2}{2\epsilon_F}. \quad (7.9)$$

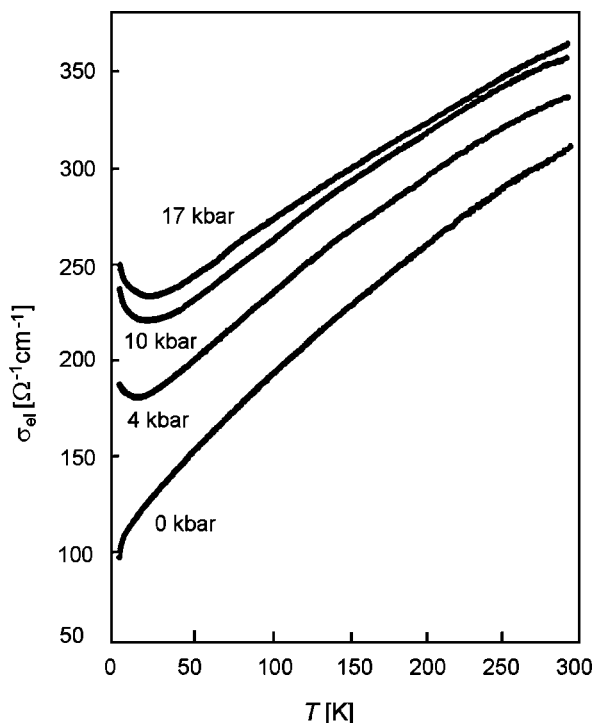


Fig. 7.20. PPy doped with PF_6 : Variation of the temperature-dependent conductivity with the applied pressure. From Menon et al. [98]

This is known as **Pauli paramagnetism**. In view of the energetic situation in the domains of a highly doped conjugated polymer, where the additionally supplied electrons also fill the Π^* band in the manner described by the left drawing in Fig. 7.21, one also expects Pauli paramagnetism here. This is indeed observed. Figure 7.22 shows as an example the magnetic properties of polyacetylene samples with different dopant contents x . For the highest dopant content the paramagnetic susceptibility is temperature-independent, as is characteristic for Pauli paramagnetism. The findings for lower dopant contents or non-doped polyacetylene are different. They indicate a change towards the behavior of isolated electron spins. Isolated electron spins are found in many paramagnetic organic or anorganic materials where radicals are incorporated. They react on an applied field with a simple reorientation and the susceptibility becomes temperature-dependent following the **Curie law**

$$\chi_m = \mu_0 c_e \frac{\mu_B^2}{kT}. \quad (7.10)$$

Obviously, in non-doped or low doped conjugated polymers isolated spins are dominant.

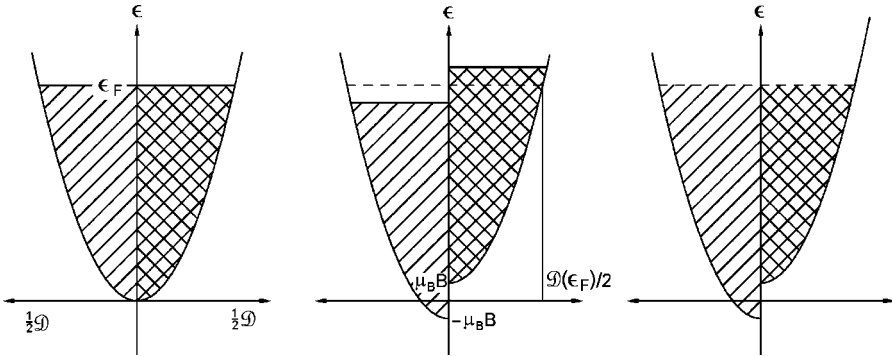


Fig. 7.21. Paramagnetism of metallic electrons at low temperature. *Left:* The starting point in the absence of a field. Occupied energy levels for the two spin orientations are represented separately. \mathcal{D} is the density of states with $\mathcal{D} \sim (\epsilon - \epsilon_F)^{1/2}$. *Middle:* The change in the energies upon switching on a magnetic field. *Right:* Lowering of the energy through a redistribution and a reestablishment of a uniform Fermi surface

Another characteristic property of metals is their total reflection of light. Even more, metals reflect all electromagnetic radiation with frequencies below a critical frequency located in the ultra-violet region. This critical frequency, which is known as the **plasma frequency** ω_{pl} , relates to the fundamental vibration of lowest frequency that the plasma of electrons can carry out in the positively charged lattice. An electromagnetic wave can only propagate in metals if it is carried on by a plasma vibration with the same frequency, hence, only for $\omega > \omega_{\text{pl}}$. The nature of the fundamental plasma oscillation is indicated in the drawing of Fig. 7.23. Imagine, as shown in Fig.7.23, a disc-like metallic sample and consider that all the electrons are shifted upwards by Δx . In this way, a negative and positive layer of charge forms on the upper and lower surfaces, respectively, and thus, as in a capacitor, there is a homogeneous electric field E_x , whose strength is given by

$$\epsilon_0 E_x = ec_e \Delta x . \tag{7.11}$$

The field acts, in turn, on the electrons and leads to an acceleration described by the equation of motion

$$c_e m_e \frac{d^2 \Delta x}{dt^2} = -ec_e E_x = -\frac{1}{\epsilon_0} e^2 c_e^2 \Delta x . \tag{7.12}$$

The solution of this equation is a vibration with eigenfrequency

$$\omega_{\text{pl}}^2 = \frac{c_e e^2}{\epsilon_0 m_e} . \tag{7.13}$$

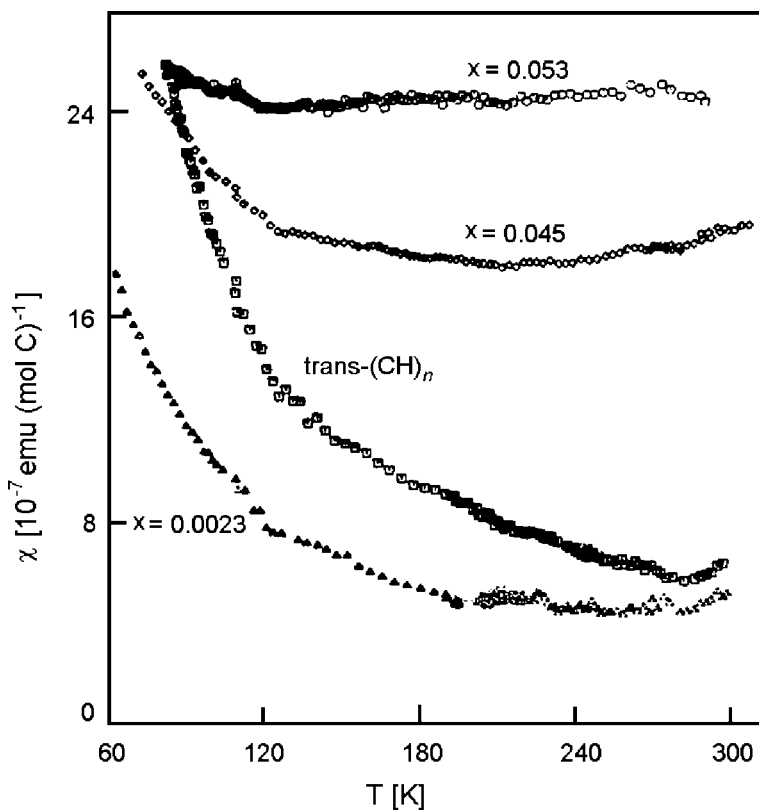


Fig. 7.22. PAc doped with various amounts x of iodine: Temperature dependence of the magnetic susceptibility of spins in the sample. From Epstein et al. [99]

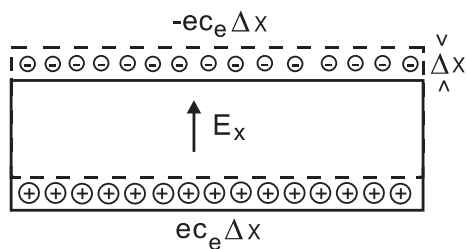


Fig. 7.23. The fundamental mode of the plasma vibrations: The surface charges which form upon a collective displacement of all electrons generate a restoring electric field

Do plasma vibrations also occur in highly doped conjugated polymers? According to the findings, the answer is yes, because these indeed reflect light. Even under the spatial limitations in the domains the free charges occupying

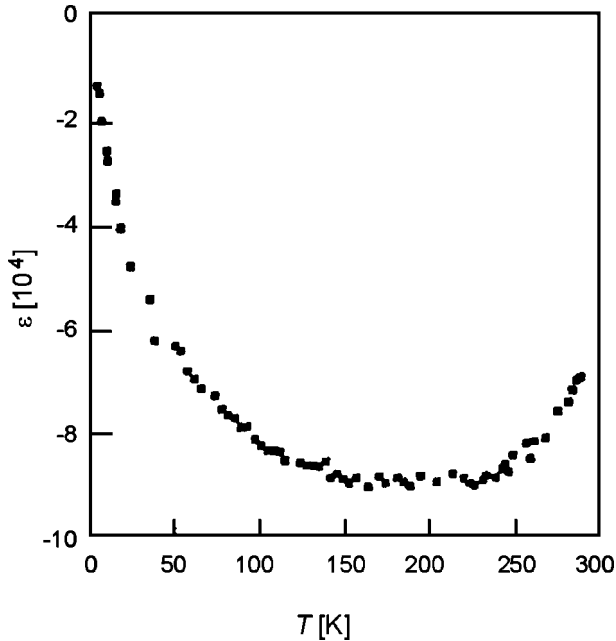


Fig. 7.24. Temperature-dependent negative dielectric constant measured at 6.5×10^9 Hz for PAn doped with cresol. From Joo et al. [100]

the II^* band are able to carry out plasma vibrations, with a fundamental vibration similar to that sketched in Fig. 7.23. For an electron density c_e comparable to metals the basic frequency ω_{p1} is again in the ultra-violet region. Total reflectivity then must also hold for radiation in the infrared and microwave region; Fig. 7.24 provides an example for the latter range. The Maxwell equations relate total reflection of electromagnetic waves with a material possessing a negative dielectric constant. In the figure, the curve dealing with properties of polyaniline shows such a negative dielectric constant, which here implies total reflection of microwave radiation.

Further Reading

- H. Bässler: *Exciton and Charge Carrier Transport in Random Organic Solids* in R. Richert, A. Blumen (Eds.): *Disorder Effects on Relaxation Processes*, Springer, 1994
- A. Blythe, D. Bloor: *Electrical Properties of Polymers*, Cambridge University Press, 2005
- R. Farchioni, G. Grosso (Ed.): *Organic Electronic Materials: Conjugated Polymers and Low Molecular Weight Organic Solids*, Springer, 2001

- N.S. Sariciftci (Ed.): *Primary Photoexcitations in Conjugated Polymers*, World Scientific, 1996
- T.A. Skotheim, J. Reynolds (Eds.): *Conjugated Polymers*, CRC Press, 2006
- J. Shinar (Ed.): *Organic Light-Emitting Devices: A Survey*, Springer, 2004
- G. Strobl: *Condensed Matter Physics – Crystals, Liquids, Liquid Crystals and Polymers*, Ch. 5.1.3, Springer, 2004

Microscopic Dynamics

Chapter 6 provided an overview of the characteristics of the mechanical and dielectric behavior of polymer systems. We discussed the material properties as they are described by the various response functions and were in particular concerned with the pronounced effects of temperature. These macroscopic properties have a microscopic basis. So far, we have addressed this basis only in qualitative terms. This chapter deals with the microscopic dynamics and hereby, in particular, with some models yielding a quantitative description for observed macroscopic properties.

Before we come to these models, we need to introduce a basic law of statistical thermodynamics, which is required for some of the subsequent treatments, namely the **fluctuation-dissipation theorem**. In the previous chapter it was pointed out that the relaxation times showing up in time-dependent or frequency-dependent response functions equal certain characteristic times of the molecular dynamics in thermal equilibrium. This is true in the range of linear responses, where interactions with applied fields are always weak compared to the internal interaction potentials and therefore leave the times of motion unchanged. The fluctuation-dissipation theorem concerns this situation and explicitly describes the relation between the microscopic dynamics in thermal equilibration and macroscopic response functions.

8.1 The Fluctuation-Dissipation Theorem

Imagine that we select within a sample a subsystem contained in a volume v , which is small but still macroscopic in the sense that statistical thermodynamics can be applied. If we could measure the properties of this subsystem we would observe time-dependent fluctuations, for example in the shape of the volume, i.e., the local strain, the internal energy, the total dipole moment, or the local stress. The fluctuation-dissipation theorem relates these spontaneous, thermally driven fluctuations to the response functions of the system. We formulate the relationship for two cases of interest, the fluctuations of the dipole moments in a polar sample and the fluctuations of stress in a melt.

The total dipole moment of a subsystem

$$\mathbf{p}_v = \sum_i \mathbf{p}_i \quad (8.1)$$

is the result of the superposition of the group dipole moments \mathbf{p}_i contained in the subvolume v . Together with the single dipole moments \mathbf{p}_i the total dipole moment varies in time and a characterization can be achieved with the aid of correlation functions. The simplest, but also most important one is the second order time correlation function

$$\langle \mathbf{p}_v(t') \cdot \mathbf{p}_v(t' + t) \rangle = \langle \mathbf{p}_v(0) \cdot \mathbf{p}_v(t) \rangle .$$

This describes the correlation between the results of two observations of \mathbf{p}_v , carried out at t' and $t' + t$. t' is thereby arbitrary since systems in thermal equilibrium are homogeneous in time. Fluctuations occur independently along x, y and z . The correlation function for one of the components, denoted by p_v , is therefore

$$\langle p_v(0)p_v(t) \rangle = \frac{\langle \mathbf{p}_v(0) \cdot \mathbf{p}_v(t) \rangle}{3} . \quad (8.2)$$

In the previous chapter we dealt with the dielectric response. Application of an electric field produces a polarization. If the field is imposed at zero time the polarization develops as described by Eq. (6.16),

$$\mathbf{P}(t) = \varepsilon_0 \Delta \varepsilon(t) \mathbf{E}_0 , \quad (8.3)$$

finally leading to the equilibrium value

$$\mathbf{P}(\infty) = \varepsilon_0 \Delta \varepsilon(\infty) \mathbf{E}_0 . \quad (8.4)$$

If the electric field then is switched off, the polarization returns back to zero, in a time-dependent process described by

$$\mathbf{P}(t) = \varepsilon_0 (\Delta \varepsilon(\infty) - \Delta \varepsilon(t)) \mathbf{E}_0 . \quad (8.5)$$

t here gives the time elapsed since the moment of switching off. The fluctuation-dissipation theorem relates the correlation function of the fluctuations of the component of the total dipole moment along the field direction, p_v , to the decay function of the polarization, by

$$\langle p_v(0)p_v(t) \rangle = vkT\varepsilon_0 (\Delta \varepsilon(\infty) - \Delta \varepsilon(t)) . \quad (8.6)$$

The left-hand side deals with spontaneous fluctuations in thermal equilibrium as they arise from the molecular dynamics, the right-hand side concerns the reaction of a sample to the imposition of an external field. The fluctuation-dissipation theorem thus states that linear responses of macroscopic systems and equilibrium fluctuations are related to each other. More specifically, Eq. (8.6) states that the regression of spontaneous fluctuations,

as they occur in subsystems of mesoscopic size, follows the same law as the relaxation subsequent to an external perturbation of a macroscopic system. The fluctuation-dissipation theorem was first introduced as a hypothesis by Onsager and later, in 1951, proved by Callen and Welton.

As a second example, we formulate the theorem considering the stress fluctuations in quiescent melts with focus on the shear component σ_{zx} . In this case it has the form

$$\langle \sigma_{zx}(0)\sigma_{zx}(t) \rangle = kT \frac{G(t)}{v} . \quad (8.7)$$

The physical background is the same as in the first example. Equation (8.7) states that the regression of the fluctuations of the local shear stress follows the same law as the macroscopic stress relaxation.

The limiting values for $t = 0$ of Eqs. (8.6) and (8.7) provide the variances of the fluctuating variables. We obtain the equations

$$\langle p_v^2 \rangle = v\varepsilon_0 \Delta\varepsilon(\infty)kT \quad (8.8)$$

and

$$\langle \sigma_{zx}^2 \rangle = kT \frac{G(0)}{v} , \quad (8.9)$$

which imply that all fluctuations increase proportionally to T . When comparing the two expressions we also recognize a characteristic difference. The total dipole moment represents an extensive variable, $p_v \propto v$, and here the variance is proportional to the size of the subsystem. On the other hand, for the local stress, an intensive variable, the variance decreases inversely to the subsystem size. The latter behavior needs a comment, since a question may arise: Which value has to be attributed to an intensive variable in a subsystem? The answer is: Intensive variables, here σ_{zx} , have to be identified with the spatial average in v . This average varies between different subsystems in a sample, or, for one given subsystem it varies with time. Equation (8.9) states that the variations decrease if the averaging volume is increased. This, indeed, expresses a basic requirement of thermodynamics. In the thermodynamic limit, i.e., for systems of infinite size, intensive variables must become sharp.

The name ‘fluctuation-dissipation theorem’ actually refers to another version of the relationship, namely the one holding if times are replaced by frequencies. We use general terms and choose the symbol X_v for the extensive variable and the notation ψ_0 for the applied constant field or force. For the linear response, we write in equivalence to Eq. (6.29)

$$X_v(t) = v\alpha(t)\psi_0 \quad (t \geq 0) \quad (8.10)$$

with $\alpha(t)$ as general time-dependent susceptibility. The general form of Eq. (8.6) is

$$\langle X_v(0)X_v(t) \rangle = vkT(\alpha(\infty) - \alpha(t)) . \quad (8.11)$$

Rather than characterizing the dynamics of a fluctuating state variable by the time-dependent correlation function $\langle X_v(0)X_v(t) \rangle$, one can also describe it by the spectral density $\langle X_v(\omega)^2 \rangle$. The **Wiener–Chinchin theorem**, a fundamental theorem of statistical physics, states that these two functions represent a pair of Fourier transforms, i.e.,

$$\langle X_v(0)X_v(t) \rangle = \frac{1}{2\pi} \int_{-\infty}^{\infty} \langle X_v(\omega)^2 \rangle \exp(-i\omega t) d\omega \quad (8.12)$$

and

$$\langle X_v(\omega)^2 \rangle = \int_{-\infty}^{\infty} \langle X_v(0)X_v(t) \rangle \exp(i\omega t) dt . \quad (8.13)$$

The steady state susceptibility, $\alpha(t \rightarrow \infty)$, agrees with the limiting value of the dynamic susceptibility at zero frequency,

$$\alpha(t \rightarrow \infty) = \alpha'(\omega = 0) . \quad (8.14)$$

If we apply Eqs. (8.12) and (8.14) in Eq. (8.11), setting $t = 0$, we obtain

$$\frac{1}{2\pi} \int_{-\infty}^{\infty} \langle X_v(\omega)^2 \rangle d\omega = vkT\alpha'(\omega = 0) \quad (8.15)$$

or, employing the Kramers–Kronig dispersion relation Eq. (6.46),

$$\frac{1}{2\pi} \int_{-\infty}^{\infty} \langle X_v(\omega)^2 \rangle d\omega = vkT \frac{1}{\pi} \int_{-\infty}^{\infty} \frac{\alpha''(\omega)}{\omega} d\omega . \quad (8.16)$$

Equating the integrands on both sides yields the other version of the fluctuation-dissipation theorem

$$\langle X_v(\omega)^2 \rangle = \frac{2vkT}{\omega} \alpha''(\omega) . \quad (8.17)$$

It is this form that is addressed by the name, as the expression relates the spectral density of the fluctuations of X_v to the imaginary part of the associated dynamic susceptibility and, as mentioned earlier, the latter describes the energy dissipation.

An analogous relationship holds for the spectral density of the field fluctuations. The general form of the fluctuation dissipation theorem is here

$$\langle \psi(\omega)^2 \rangle = \frac{2kT}{v\omega} a''(\omega) . \quad (8.18)$$

$a''(\omega)$ represents the imaginary part of the general dynamic modulus defined as

$$a(\omega) = \frac{1}{\alpha(\omega)} . \quad (8.19)$$

Fluctuations arise from all dynamical modes in the system; however, different experiments associate them with different weights. Take, for example, the glass–rubber transition. The transition shows up in measurements of the dynamic compliance, the dynamic modulus and the dielectric function. Even if the shapes $D''(\omega)$, $E''(\omega)$ and $\varepsilon''(\omega)$ differ from each other, the maxima of the absorption curves being located at different frequencies, all experiments yield spectral densities that follow from the dynamics of the same group of motions, namely the α -modes. In the dielectric experiment these are weighted according to the changes of dipole moments, in compliance measurements the weighting factor relates to the changes in the shape of a polymer and in the dynamic modulus curve it depends on the internal stresses or moment transfers along a chain. The relaxation time spectrum of the α -modes is very broad and encompasses more than four orders of magnitude. The main contributions to the moduli originate from modes with short relaxation times, whereas the compliances put the major weight on the long-time part of the spectrum. The dielectric α -process has its maximum usually in between the two mechanical processes and thus appears to put main emphasis on the central part.

The fluctuation-dissipation theorem may be regarded as an interface between the microscopic and the macroscopic properties of a sample. It provides us with a prescription of how to proceed when these two are to be related. On the microscopic side, a theoretical analysis of dynamical models often enables us to calculate equilibrium correlation functions for properties of interest. The fluctuation-dissipation theorem then relates these correlation functions with the results of measurements of corresponding response functions.

In the following, we will discuss some microscopic dynamical models. We begin with the **Rouse model**, which describes the dynamics of chains in a non-entangled polymer melt. The effects of entanglements on the motion can be accounted for by the **reptation model**, which we will treat subsequently. Then we shall be concerned with the motion of polymer chains in a solvent, when the **hydrodynamic interaction** between the segments of a chain plays a prominent role. At the end of this chapter, we briefly discuss the modes of **motion in polyelectrolyte solutions**, which are strongly affected by Coulomb forces.

8.2 The Rouse Model

If a polymer molecule is stretched out by applying forces to the end groups and the forces are removed again it returns to the initial coiled conformation. The reason for this behavior has already been mentioned: The transition back to an isotropic coil increases the number of available rotational isomeric states and thus the entropy. The recoiling effect can also be expressed in mechanistic terms, by stating that, if the two endgroups of a polymer chain are held fixed at a certain distance, a tensile force arises due to the net moment transfer onto the ends. If, rather than keeping hold of the endgroups, two arbitrary points

within a polymer molecule are kept at constant positions, a tensile force also arises between them.

We shall derive this force in the next chapter when dealing with the elasticity of rubbers. If Gaussian properties are assumed the result, as given by Eq. (9.13), is as follows: If a sequence within a chain that has a mean squared end-to-end distance $\langle \Delta \mathbf{r}^2 \rangle$ is chosen and its endpoints are at a distance $\Delta \mathbf{r}$, then the tensile force is

$$\mathbf{f} = b \Delta \mathbf{r} \quad (8.20)$$

with

$$b = \frac{3kT}{\langle \Delta \mathbf{r}^2 \rangle}. \quad (8.21)$$

The result implies that a sequence behaves like a spring, showing a linear dependence of the force on the extension. The force constant b is proportional to the absolute temperature T , as is characteristic for forces of entropic origin. Note furthermore that b decreases on increasing the size of the sequence.

A polymer chain in a melt moves in the surroundings set up by the other chains. At first, this looks like a complicated situation. However, as it turns out, one can employ a simple, approximate treatment. For particles of at least mesoscopic size, the various interactions with adjacent molecules may be represented in summary by one viscous force. This is well-known from treatments of the dynamics of a colloid in a solvent. There it can be assumed that if a colloid moves with a velocity \mathbf{u} , the solvent molecules in contact with its surface create a force that is proportional to \mathbf{u} and the solvent viscosity η_s ,

$$\mathbf{f} = \zeta \mathbf{u} \quad (8.22)$$

with

$$\zeta \propto \eta_s. \quad (8.23)$$

ζ is the **friction coefficient**. We shall utilize this equation also in Sect. 8.4, where more explanations will be provided.

Rouse devised a treatment of the dynamics of polymer chains in a melt, which makes use of this notion of a viscous force and also takes account of the tensile forces arising in stretched parts of the chain. The procedure used in setting up the **Rouse model** is remarkably simple. In a first step the chain is subdivided into N_R **Rouse sequences**, each sequence being sufficiently long to ensure Gaussian properties. Then, in a second step, each Rouse sequence is substituted by a bead and a spring. The springs are the representatives of the elastic tensile forces, while the beads play the role of centers whereon friction forces apply. The thus emerging **Rouse chain** is composed of a series of beads connected by springs, as depicted in Fig. 8.1.

The equations of motion of the Rouse chain are formulated with all inertial effects neglected. Then the velocity $d\mathbf{r}_l/dt$ of bead l is given by

$$\zeta_R \frac{d\mathbf{r}_l}{dt} = b_R(\mathbf{r}_{l+1} - \mathbf{r}_l) + b_R(\mathbf{r}_{l-1} - \mathbf{r}_l). \quad (8.24)$$

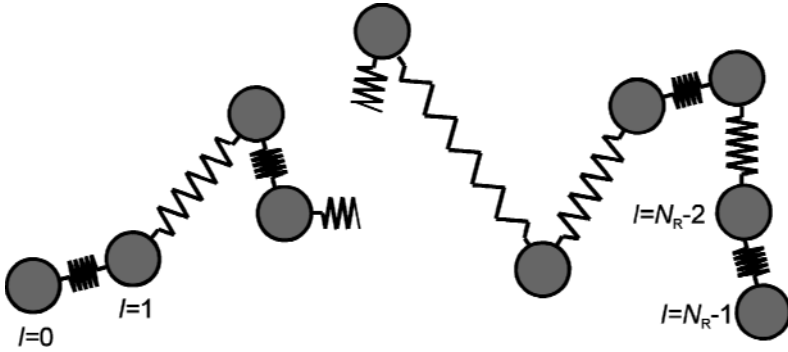


Fig. 8.1. Rouse chain composed of N_R beads connected by springs

The left-hand side represents the viscous force, the parameter ζ_R designating the friction coefficient per bead. On the right-hand side we have the elastic forces originating from the adjacent beads, which are located at the positions \mathbf{r}_{l-1} and \mathbf{r}_{l+1} . The force constant b_R of the springs depends on the mean squared end-to-end distances of the Rouse sequences, a_R^2 and follows from Eq. (8.21) as

$$b_R = \frac{3kT}{a_R^2} . \tag{8.25}$$

It is easy to solve this set of differential equations. Note at the beginning that motions in the three directions of space, x, y, z , decouple and are equivalent. For the treatment we select the z -direction and consider the equations of motion

$$\zeta_R \frac{dz_l}{dt} = b_R(z_{l+1} - z_l) + b_R(z_{l-1} - z_l) . \tag{8.26}$$

First we discuss chains with infinite length. In this case, we have translational symmetry in terms of l . Then there must be wave-like solutions of the form

$$z_l \propto \exp\left(-\frac{t}{\tau}\right) \exp(il\delta) . \tag{8.27}$$

They include an exponential time dependence, as can be anticipated for relaxation processes; δ describes the phase shift between adjacent beads. If we take Eq. (8.27) and introduce it in Eq. (8.26), we obtain the dependence of the relaxation rate τ^{-1} on δ

$$\tau^{-1} = \frac{b_R}{\zeta_R} (2 - 2 \cos \delta) = \frac{4b_R}{\zeta_R} \sin^2\left(\frac{\delta}{2}\right) . \tag{8.28}$$

Figure 8.2 presents this dependence for values of δ between $-\pi$ and $+\pi$. Considerations can be restricted to this range, as other values of δ give nothing new for a discrete chain.

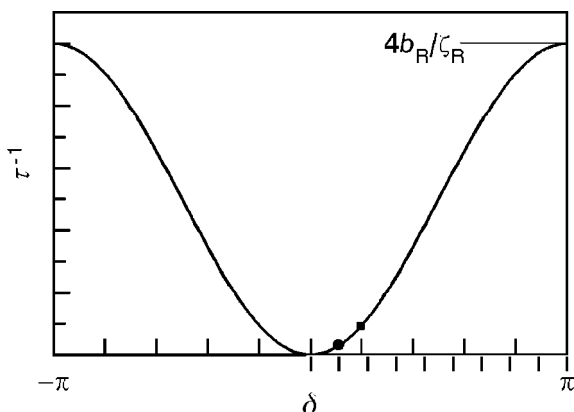


Fig. 8.2. Relaxation rates of Rouse modes as a function of the phase shift δ . *Marks on the inside* of the abscissa show the mode positions for a cyclic chain with $N_R = 10$ beads, the *marks on the outside* give the modes of a linear chain with the same length. The lowest order Rouse modes of the two chains with relaxation rates τ_R^{-1} are especially indicated by a *filled square* and a *filled circle*

A formal means of accounting for the finite size of a chain while maintaining the wave-like solutions is provided by the introduction of cyclic boundary conditions. For a chain with N_R beads, this implies the equality

$$z_l = z_{l+N_R} , \quad (8.29)$$

which is satisfied if

$$N_R \delta = m 2\pi . \quad (8.30)$$

N_R discrete values of the phase shift are thus selected

$$\delta_m = \frac{2\pi}{N_R} m , \quad m = - \left(\frac{N_R}{2} - 1 \right) , \dots , \frac{N_R}{2} . \quad (8.31)$$

Figure 8.2 shows the locations for $N_R = 10$.

Even if for polymers cyclic boundary conditions can be translated into reality, namely by a synthesis of cyclic macromolecules, common polymer systems are composed of linear chains. These linear chains possess free ends where the tensile forces vanish. The boundary conditions then become

$$z_1 - z_0 = z_{N_R-1} - z_{N_R-2} = 0 \quad (8.32)$$

or, in differential form,

$$\frac{dz}{dl}(l=0) = \frac{dz}{dl}(l=N_R-1) = 0 . \quad (8.33)$$

The real and the imaginary part of Eq. (8.27)

$$z_l \propto \cos(l\delta) \exp -\frac{t}{\tau} \tag{8.34}$$

$$z_l \propto \sin(l\delta) \exp -\frac{t}{\tau} \tag{8.35}$$

represent separate solutions of the equation of motion. The boundary condition at $l = 0$ is only fulfilled by the cosine solution. The condition for the upper end, $l = N_R - 1$, then selects the values of δ by

$$\frac{dz_l}{dl}(l = N_R - 1) \propto \sin[(N_R - 1)\delta] = 0 . \tag{8.36}$$

Since this is solved by

$$(N_R - 1)\delta = m\pi , \tag{8.37}$$

we obtain the following eigenvalues for a linear chain with free ends: δ_m :

$$\delta_m = \frac{\pi}{N_R - 1} m , \quad m = 0, 1, 2, \dots, N_R - 1 . \tag{8.38}$$

Hence, we find for the linear chain N_R independent solutions. They are called **Rouse modes** and differentiated by their order m . Figure 8.2 shows the eigenvalues δ_m for a chain with $N_R = 10$, compared to a cyclic Rouse chain.

Figure 8.3 presents the displacement pattern associated with the lowest order Rouse mode with $m = 1$ (the solution for $m = 0$ describes a free

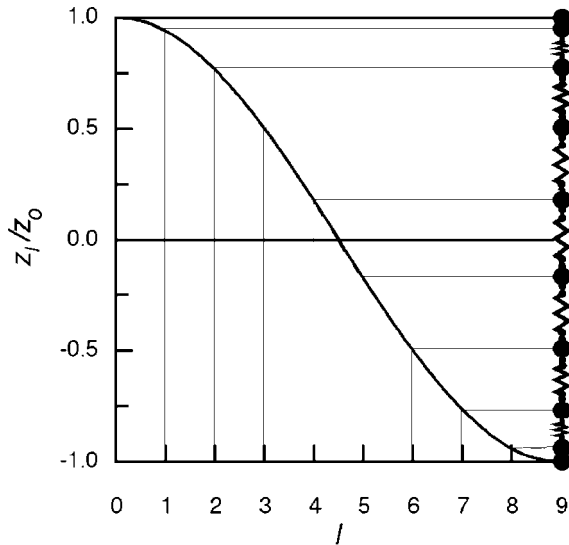


Fig. 8.3. Displacement pattern of the primary Rouse mode

translation). The relaxation rate of this mode, shortly called **Rouse rate** τ_{R}^{-1} , follows from Eq. (8.38) together with Eq. (8.28) as

$$\tau_1^{-1} = \tau_{\text{R}}^{-1} \approx \frac{b_{\text{R}}}{\zeta_{\text{R}}} \frac{\pi^2}{(N_{\text{R}} - 1)^2}, \quad (8.39)$$

or, with Eq. (8.25), as

$$\tau_{\text{R}}^{-1} \approx \frac{3kT\pi^2}{\zeta_{\text{R}} a_{\text{R}}^2 (N_{\text{R}} - 1)^2}. \quad (8.40)$$

The result includes the size a_{R} of the Rouse sequences and, therefore, a quantity with a freedom of choice. This arbitrariness can be removed. Since

$$R_0^2 = a_{\text{R}}^2 (N_{\text{R}} - 1), \quad (8.41)$$

we obtain for the **Rouse time** τ_{R} the expression

$$\tau_{\text{R}} = \frac{1}{3\pi^2} \frac{(\zeta_{\text{R}}/a_{\text{R}}^2)}{kT} R_0^4. \quad (8.42)$$

The result indicates that the ratio $\zeta_{\text{R}}/a_{\text{R}}^2$ should be independent of the choice of the sequence. This is true if the friction coefficient ζ_{R} is proportional to the number of monomer units in the sequence. Strictly speaking, the latter property constitutes a basic requirement for the validity of the Rouse model: The friction coefficient of a sequence *must* to be proportional to the number of monomer units. In fact, this is not trivial and obvious from the very beginning. It seems to be correct in a melt because, as we shall see, here the Rouse model works quite satisfactorily if compared to experimental results. On the other hand, the assumption is definitely wrong for isolated polymer chains in a solvent where hydrodynamic interactions strongly affect the motion; we shall be concerned with this point in a subsequent section.

Equation (8.42) gives the dependence of the Rouse time on the degree of polymerization. Since

$$R_0^2 = a^2 N, \quad (8.43)$$

we obtain

$$\tau_{\text{R}} \propto N^2. \quad (8.44)$$

The shortest relaxation time in the Rouse spectrum depends on the choice of the Rouse sequence and follows, for $m = N_{\text{R}} - 1$, from Eqs. (8.28) and (8.38) as

$$\tau_{N_{\text{R}}-1} = \frac{\zeta_{\text{R}} a_{\text{R}}^2}{12kT} = \frac{(\zeta_{\text{R}}/a_{\text{R}}^2)}{12kT} a_{\text{R}}^4. \quad (8.45)$$

We see that there is a cut-off at the short-time end that depends on a_{R} . Of course, further relaxation modes exist. However, they can no longer be described by the Rouse model as motions become localized in this range

of high relaxation rates and then depend on the chemical composition of a chain.

As we can see, the motion of a polymer chain in a non-entangled melt as represented by the Rouse model can be described as a superposition of $3N_R$ linearly independent Rouse modes, corresponding to N_R modes in x -, y - and z -directions, respectively. In a dynamic equilibrium state all these Rouse modes become thermally excited and it is instructive to calculate their mean-squared amplitudes. The displacement pattern of mode m is given by

$$z_l = Z_m \cos(l\delta_m). \quad (8.46)$$

Z_m denotes a **normal coordinate**, that determines the mode amplitude. Thermal excitations of modes, oscillatory modes as well as the relaxatory modes discussed here, depend on the associated change in free energy. For the bead-and-spring model the change in free energy per polymer chain, Δf_p , is given by

$$\Delta f_p = \frac{b_R}{2} \sum_{l=0}^{N_R-2} (z_{l+1} - z_l)^2 \quad (8.47)$$

$$= \frac{b_R}{2} Z_m^2 \sum_{l=0}^{N_R-2} \{\cos[(l+1)\delta_m] - \cos(l\delta_m)\}^2 \quad (8.48)$$

$$\approx \frac{b_R}{2} Z_m^2 \delta_m^2 \sum_{l=0}^{N_R-2} \sin^2(\delta_m l) = \frac{b_R}{2} \frac{N_R-1}{2} Z_m^2 \delta_m^2. \quad (8.49)$$

The function $\Delta f_p(Z_m)$ determines the probability distribution $p(Z_m)$ for the amplitude Z_m , which follows from Boltzmann statistics as

$$p(Z_m) \propto \exp - \frac{\Delta f_p(Z_m)}{kT}. \quad (8.50)$$

Since

$$\Delta f_p \propto Z_m^2, \quad (8.51)$$

we find a Gaussian distribution for the normal coordinate Z_m . The variance $\langle Z_m^2 \rangle$ may be derived from the property

$$\langle \Delta f_p \rangle = \frac{kT}{2}, \quad (8.52)$$

giving

$$\frac{b_R}{2} \frac{N_R-1}{2} \delta_m^2 \langle Z_m^2 \rangle = \frac{3kT}{2a_R^2} \frac{N_R-1}{2} \delta_m^2 \langle Z_m^2 \rangle = \frac{kT}{2}. \quad (8.53)$$

Note that, as expected for an ideal chain, $\langle Z_m^2 \rangle$ is indeed independent of temperature since

$$\langle Z_m^2 \rangle = \frac{2a_R^2}{3(N_R-1)\delta_m^2}, \quad (8.54)$$

or, using Eq. (8.38),

$$\langle Z_m^2 \rangle = \frac{2}{3\pi^2} \frac{R_0^2}{m^2}. \quad (8.55)$$

According to this result, the amplitudes of the Rouse modes rapidly decrease with increasing mode order m . If we consider the contributions of the different Rouse modes to the known total mean squared end-to-end distance, $\langle R^2 \rangle = R_0^2$, we find that a large part is already provided by the three lowest order Rouse modes. Contributions to the end-to-end distance in the z -direction, $\langle R_z^2 \rangle = R_0^2/3$, all come from z -polarized Rouse modes with odd m 's

$$\langle (z_{N_R-1} - z_0)^2 \rangle = \langle (2Z_1)^2 \rangle + \langle (2Z_3)^2 \rangle + \dots \quad (8.56)$$

which leads to

$$\langle (z_{N_R-1} - z_0)^2 \rangle = \frac{8}{\pi^2} \frac{R_0^2}{3} \left(1 + \frac{1}{9} + \dots \right) = \frac{R_0^2}{3}. \quad (8.57)$$

Hence, 90% of the total mean squared end-to-end distance of a chain originates from the lowest order Rouse modes. In theoretical treatments, polymer chains are sometimes substituted by elastic dumbbells, set up by two beads connected by a spring. The justification for this simplification follows from the dominant role of the primary Rouse modes.

We finish this section with the schematic drawing displayed in Fig. 8.4, which is meant to indicate what the time-dependent fluctuations of the amplitude of a Rouse mode may look like. The interaction of a chain with its surroundings leads to excitations of this mode at random times, which are here represented in an idealized manner by sharp steps. In between, the mode amplitude decreases exponentially with a characteristic relaxation time as described by the equation of motion. These are the only parts in the time-dependent curve that show well-defined temporal properties. We may therefore anticipate that the shape of the time correlation function is solely determined by the repeated periods of exponential decay. Regarding the results

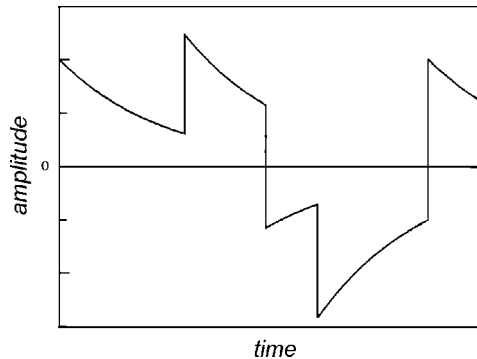


Fig. 8.4. Time dependence of the amplitude Z_m of a Rouse mode (schematic)

of this section, we may thus formulate the time correlation function for the normal coordinate Z_m directly, as

$$\langle Z_m(0)Z_m(t) \rangle = \langle Z_m^2 \rangle \exp -\frac{t}{\tau_m} = \frac{2R_0^2}{3\pi^2 m^2} \exp -\frac{t}{\tau_m}, \quad (8.58)$$

the relaxation time τ_m being given by Eqs. (8.38) and (8.28).

8.2.1 Stress Relaxation

Having discussed the microscopic dynamical properties of a system of Rouse chains, we now inquire about the resulting mechanical behavior and consider as an example the shear stress relaxation modulus, $G(t)$. $G(t)$ can be described with the aid of the fluctuation-dissipation theorem utilizing Eq. (8.7), as

$$\langle \sigma_{zx}(0)\sigma_{zx}(t) \rangle = kT \frac{G(t)}{v}.$$

We have to calculate the fluctuations in the stress field produced by a system of Rouse chains in thermal equilibrium. As explained above, fluctuations of an intensive variable such as the stress depend upon the size of the chosen subsystems. We select subsystems of volume v , having orthogonal edges with lengths l_x, l_y and l_z as displayed in Fig. 8.5. Being concerned with the shear stress σ_{zx} , we recognize that contributions all arise from springs with a non-vanishing component of extension in the x -direction. We choose the symbols $\hat{x}_i, \hat{y}_i, \hat{z}_i$ for the three components of the extension of spring i , which may be incorporated in any chain, and designate by $f_{x,i}$ the associated force component along x . The mean value of σ_{zx} in a subsystem is obtained by a summation over the contributions of all included springs i

$$\sigma_{zx} = \sum_i \frac{1}{l_x l_y l_z} \hat{z}_i f_{x,i}. \quad (8.59)$$

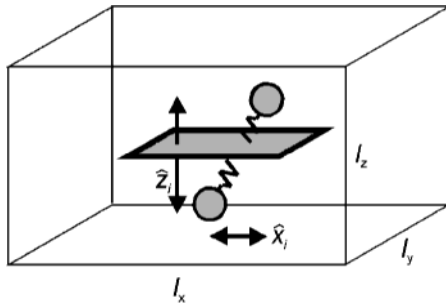


Fig. 8.5. Notions used in the calculation of the tensile stress σ_{zx} associated with a system of Rouse chains: Reference volume $v = l_x l_y l_z$; unit area, crossed by the spring i with extensions \hat{x}_i and \hat{z}_i along x and z

To see the background of this equation, consider a unit area normal to the z -axis, as indicated in Fig. 8.5. Stress on this plane is produced by all springs crossing it. The term

$$\frac{1}{l_x l_y l_z} \hat{z}_i$$

expresses the probability that spring i , with an extension \hat{z}_i along z , crosses the unit area. When crossing this area, the spring contributes a force $f_{x,i}$ to σ_{zx} . We now adopt Eq. (8.20) and write

$$\sigma_{zx} = \frac{1}{l_x l_y l_z} \sum_i \hat{z}_i f_{x,i} = \frac{1}{v} \sum_i \hat{z}_i f_{x,i} = \frac{b_R}{v} \sum_i \hat{z}_i \hat{x}_i . \quad (8.60)$$

σ_{zx} , being defined as the spatial average in a volume v , represents a fluctuating quantity that shows different values in different subsystems or for measurements at different times. The ensemble average vanishes

$$\langle \sigma_{zx} \rangle = 0 , \quad (8.61)$$

since

$$\langle \hat{z}_i \hat{x}_i \rangle = \langle \hat{z}_i \rangle \langle \hat{x}_i \rangle = 0 \quad (8.62)$$

regarding that the movements of Rouse chains along z and x are independent. The time correlation function of the fluctuations of the shear stress, $\langle \sigma_{zx}(0) \sigma_{zx}(t) \rangle$, follows as

$$\langle \sigma_{zx}(0) \sigma_{zx}(t) \rangle = \frac{1}{v^2} b_R^2 \sum_{k,l,k',l'} \langle \hat{x}_{k,l}(0) \hat{z}_{k,l}(0) \hat{x}_{k',l'}(t) \hat{z}_{k',l'}(t) \rangle . \quad (8.63)$$

Here, the extensions along x and z of the spring l on the chain k are denoted $\hat{x}_{k,l}$ and $\hat{z}_{k,l}$ and those of the spring l' on the chain k' correspondingly. The sum includes all chains contained in v . As the extensions of springs in different chains are uncorrelated, we write

$$\langle \sigma_{zx}(0) \sigma_{zx}(t) \rangle = \frac{1}{v^2} c_p v b_R^2 \sum_{l,l'} \langle \hat{x}_l(0) \hat{x}_{l'}(t) \rangle \langle \hat{z}_l(0) \hat{z}_{l'}(t) \rangle , \quad (8.64)$$

where $c_p v$ gives the number of chains in v .

Chain dynamics may be represented as a superposition of independent Rouse modes. The displacements of mode m' , polarized in the z -direction, are given by

$$z_l = Z_{m'} \cos(\delta_{m'} l) . \quad (8.65)$$

The extensions of the springs follow by taking the derivative

$$\hat{z}_l = z_{l+1} - z_l \approx \frac{dz_l}{dl} = -Z_{m'} \delta_{m'} \sin(\delta_{m'} l) . \quad (8.66)$$

Equivalently, the extension associated with mode m , polarized along x , is given by

$$\hat{x}_l = x_{l+1} - x_l \approx \frac{dx_l}{dl} = -X_m \delta_m \sin(\delta_m l) . \quad (8.67)$$

We thus obtain

$$\langle \hat{x}_l(0) \hat{x}_{l'}(t) \rangle = \sum_m \langle X_m(0) X_m(t) \rangle \sin(\delta_m l) \sin(\delta_m l') \delta_m^2 \quad (8.68)$$

and

$$\langle \hat{z}_l(0) \hat{z}_{l'}(t) \rangle = \sum_{m'} \langle Z_{m'}(0) Z_{m'}(t) \rangle \sin(\delta_{m'} l) \sin(\delta_{m'} l') \delta_{m'}^2 . \quad (8.69)$$

Since

$$\sum_l \sin(\delta_m l) \sin(\delta_{m'} l) \sum_{l'} \sin(\delta_m l') \sin(\delta_{m'} l') = \left(\frac{N_R - 1}{2} \right)^2 \delta_{m,m'} \quad (8.70)$$

where $\delta_{m,m'}$ denotes the Kronecker-delta, we find

$$\begin{aligned} \langle \sigma_{zx}(0) \sigma_{zx}(t) \rangle &= \frac{1}{v} c_p b_R^2 \left(\frac{N_R - 1}{2} \right)^2 . \\ &\quad \sum_m \delta_m^4 \langle X_m(0) X_m(t) \rangle \langle Z_m(0) Z_m(t) \rangle . \end{aligned} \quad (8.71)$$

Introducing the mean-squared amplitudes $\langle X_m^2 \rangle$ and $\langle Z_m^2 \rangle$ of the Rouse modes in thermal equilibrium, as given by Eq. (8.53), leads to

$$\langle \sigma_{zx}(0) \sigma_{zx}(t) \rangle = \frac{1}{v} c_p (kT)^2 \sum_m \frac{\langle X_m(0) X_m(t) \rangle}{\langle X_m^2 \rangle} \frac{\langle Z_m(0) Z_m(t) \rangle}{\langle Z_m^2 \rangle} . \quad (8.72)$$

Now we utilize the fluctuation-dissipation theorem, i.e., apply Eq. (8.7) to obtain the shear relaxation modulus

$$G(t) = c_p kT \sum_m \frac{\langle X_m(0) X_m(t) \rangle}{\langle X_m^2 \rangle} \frac{\langle Z_m(0) Z_m(t) \rangle}{\langle Z_m^2 \rangle} . \quad (8.73)$$

Equation (8.73) relates $G(t)$ to the magnitudes and the time dependencies of the fluctuations of the Rouse modes in thermal equilibrium. The time correlation functions are given by Eq. (8.58)

$$\langle Z_m(0) Z_m(t) \rangle = \langle Z_m^2 \rangle \exp -\frac{t}{\tau_m} , \quad (8.74)$$

and equivalently

$$\langle X_m(0) X_m(t) \rangle = \langle X_m^2 \rangle \exp -\frac{t}{\tau_m} . \quad (8.75)$$

Hence, we finally obtain

$$G(t) = c_p kT \sum_{m=1}^{N_R-1} \exp\left(-2 \frac{t}{\tau_m}\right). \quad (8.76)$$

Equation (8.76) describes the shear stress relaxation modulus associated with a system of Rouse chains. The result has a remarkably simple structure, because all Rouse modes contribute to $G(t)$ with the same weight. Note that the relaxation rates are increased by a factor of two with regard to the Rouse mode rates τ_m^{-1} .

Equation (8.76) may be further evaluated by carrying out the summation. If we disregard the short-time range, the discussion may be reduced to the contributions of the low order Rouse modes and we can replace Eqs. (8.28) and (8.38) by the approximate relation

$$\tau_m^{-1} \approx \tau_R^{-1} m^2. \quad (8.77)$$

Introduction into Eq. (8.76) and a change from the summation to an integral gives

$$G(t) \propto \int_{m=1}^{N_R-1} dm \exp(-2\tau_R^{-1} m^2 t) \approx \int_{m=0}^{\infty} dm \exp(-2\tau_R^{-1} m^2 t) \quad (8.78)$$

or, with the substitution

$$u = m \left(\frac{t}{\tau_R}\right)^{1/2}, \quad (8.79)$$

the expression

$$G \propto \left(\frac{\tau_R}{t}\right)^{1/2} \int_{u=0}^{\infty} \exp(-2u^2) du, \quad (8.80)$$

hence

$$G(t) \propto t^{-1/2}. \quad (8.81)$$

The result is a power law that is characteristic for the relaxation of Rouse chains and it may be compared with experiments on polymer melts. Indeed, one finds good agreement for several systems. The center of the glass–rubber transition, as observed in stress relaxation experiments, is often well-described by Eq. (8.81). Figure 8.6 depicts, as an example, the time-dependent shear modulus of poly(vinylchloride) (PVC), presented as a master-curve referred to the glass transition temperature ($T_g = 65^\circ\text{C}$). The slope of the log–log plot corresponds to an exponent $-1/2$.

The power law for the time-dependent modulus can be transformed into a law valid for the frequency domain, either by applying the general relations of linear response or by using the ω -dependent form of the fluctuation-dissipation theorem. The result is

$$G'(\omega) \propto (\eta_0 \omega)^{1/2}. \quad (8.82)$$

The measurement shown in Fig. 6.16 agrees with this prediction.

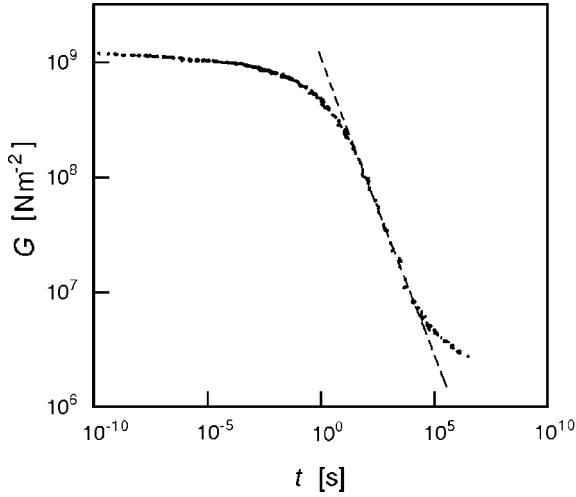


Fig. 8.6. Time-dependent shear modulus of PVC. Master curve set up for $T_g = 65^\circ\text{C}$ as the reference temperature. The *dashed line* indicates the slope predicted by the Rouse model. Data from Eisele [101]

We can also determine the viscosity in the zero shear rate limit by application of Eq. (6.107) as

$$\begin{aligned}
 \eta_0 &= \int_0^\infty G(t) dt \\
 &= kTc_p \sum_{m=1}^{N_R-1} \frac{\tau_m}{2} \\
 &\approx kTc_p \frac{\tau_R}{2} \sum_{m=1}^\infty \frac{1}{m^2} = kTc_p \tau_R \frac{\pi^2}{12}. \quad (8.83)
 \end{aligned}$$

Regarding Eq. (8.44), the result indicates a linear dependence of η_0 on the degree of polymerization,

$$\eta_0 \propto \frac{c_m}{N} N^2 \propto N. \quad (8.84)$$

This is in full agreement with the observations on non-entangled melts displayed in Fig. 6.13.

The Rouse model is also applicable for entangled melts, however, only in a restricted manner. While a description of the motion of the whole polymer chain is not possible it still can be employed for a treatment of the dynamics of the chain parts between entanglements. We will discuss the resulting overall behavior in the next section.

The Rouse model also has intrinsic limitations at short times. According to Eq. (8.76), the unrelaxed modulus is determined by the number density of Rouse sequences, c_R , since we find

$$G(0) = c_p kT (N_R - 1) = c_R kT. \quad (8.85)$$

This dependence on the choice of the sequence associated with an element of the Rouse chain may look strange at first; however, the cause of this apparent arbitrariness and the solution of the problem are easy to see. One has to realize that the internal degrees of freedom of the sequence give further contributions to the shear modulus; the correct value follows only from both parts together. We therefore have to write in general

$$G(t) = \Delta G_{\text{mic}}(t) + G_{\text{Rouse}}(t) \quad (8.86)$$

where the first part, $\Delta G_{\text{mic}}(t)$, accounts for the short-time properties. In contrast to the Rouse modes, the internal modes are finally controlled by the microstructure, i.e., the chemical composition. The point of transition from the Rouse representation to the detailed description has, indeed, a freedom of choice; one has only to stay outside the range where specific microscopic effects appear.

8.2.2 The Dielectric Normal Mode

We return once again to the frequency-dependent and temperature-dependent measurements of the dielectric function of polyisoprene (PI) presented in Sect. 6.3.2. As shown in Figs. 6.20 and 6.21, two relaxation processes exist. The low frequency process, the normal mode, is the one of interest here. As has already been mentioned, it reflects the movements of the end-to-end distance vector \mathbf{R} of the chain. The Rouse model enables these movements to be treated in the case of melts that are not entangled. Earlier, we learned that the motion of the end-to-end distance vector is to a large part due to the superposition of the three lowest order Rouse modes, polarized in the x , y and z -directions. Therefore, the dielectric normal mode, when measured for samples with a molar mass below the entanglement limit, may be identified with these primary modes.

For a Rouse chain built up of N_R polar sequences, each one carrying a dipole moment with a longitudinal component \mathbf{p}_{\parallel}^l , the total dipole moment \mathbf{p}_p is given by

$$\mathbf{p}_p = \sum_{l=0}^{N_R-1} \mathbf{p}_{\parallel}^l. \quad (8.87)$$

Let us refer in the discussion to a representation of the dielectric data in the time domain, as expressed by the time-dependent dielectric function $\varepsilon(t)$. Figure 8.7 depicts its general shape in a schematic drawing. The α -process and the normal mode show up as two subsequent steps located at the

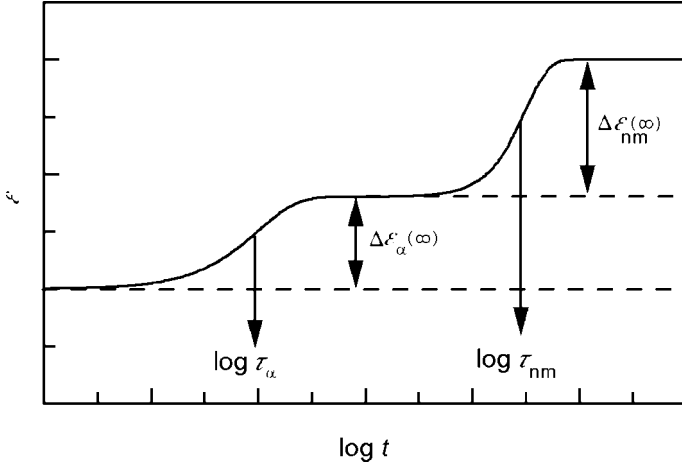


Fig. 8.7. General shape of the time-dependent dielectric function $\varepsilon(t)$ of PI showing the α -process and the dielectric normal mode (schematic drawing)

times τ_α and τ_{nm} , with heights corresponding to the relaxation strengths $\Delta\varepsilon_\alpha$ and $\Delta\varepsilon_{nm}$.

The fluctuation-dissipation theorem provides an exact description of the step $\Delta\varepsilon_{nm}(t)$ associated with the normal mode. Employing Eq. (8.6) in combination with Eq. (8.2) and using the relation

$$\langle \mathbf{p}_v(0)\mathbf{p}_v(t) \rangle = v c_p \langle \mathbf{p}_p(0)\mathbf{p}_p(t) \rangle \tag{8.88}$$

assuming independent motions of different chains, we obtain

$$c_p \langle \mathbf{p}_p(0)\mathbf{p}_p(t) \rangle = 3kT\varepsilon_0(\Delta\varepsilon_{nm}(\infty) - \Delta\varepsilon_{nm}(t)) . \tag{8.89}$$

The relaxation strength, $\Delta\varepsilon_{nm}(\infty)$, follows from

$$c_p \langle \mathbf{p}_p^2 \rangle = 3kT\varepsilon_0 \Delta\varepsilon_{nm}(\infty) . \tag{8.90}$$

Since

$$\langle \mathbf{p}_p^2 \rangle = N_R \left\langle \left(\mathbf{p}_p^l \right)^2 \right\rangle \tag{8.91}$$

and

$$\langle \mathbf{R}^2 \rangle = N_R a_R^2 \tag{8.92}$$

we have

$$\langle \mathbf{p}_p^2 \rangle = \frac{\left\langle \left(\mathbf{p}_p^l \right)^2 \right\rangle}{a_R^2} \langle \mathbf{R}^2 \rangle = \beta^2 \langle \mathbf{R}^2 \rangle . \tag{8.93}$$

Equation (8.93) relates the variance of the dipole moment of the polymer to the mean squared end-to-end distance of the chain. We therefore substitute in Eq. (8.89) \mathbf{p}_p by \mathbf{R} , thus obtaining

$$c_p \beta^2 \langle \mathbf{R}(0) \mathbf{R}(t) \rangle = 3kT \varepsilon_0 (\Delta \varepsilon_{\text{nm}}(\infty) - \Delta \varepsilon_{\text{nm}}(t)). \quad (8.94)$$

Now we employ the Rouse model. As the end-to-end distance vector is essentially determined by the lowest order Rouse modes, we can also represent the time correlation function in good approximation by

$$\langle \mathbf{R}(0) \mathbf{R}(t) \rangle \approx R_0^2 \exp -\frac{t}{\tau_R}. \quad (8.95)$$

Applying Eq. (8.95) in Eq. (8.94) leads to

$$\varepsilon_0 \Delta \varepsilon_{\text{nm}}(t) \simeq \frac{c_p \beta^2 R_0^2}{3kT} \left(1 - \exp -\frac{t}{\tau_R} \right). \quad (8.96)$$

Equation (8.96) provides a description of the normal mode, giving the relaxation strength as well as the relaxation time. Notice in particular that the observed molar mass dependence of τ_{nm} for non-entangled melts as shown in Fig. 6.22,

$$\tau_{\text{nm}} \propto M^2, \quad (8.97)$$

is in full agreement with the prediction of the Rouse theory

$$\tau_R \propto N^2. \quad (8.98)$$

Further contributions with minor weights originate from the subsequent Rouse modes with $m > 1$. They may lead to the observed line-broadening on the high frequency side, as described empirically by the Havriliak–Negami equation.

We finish this discussion with two remarks. Experiments mostly yield the frequency-dependent complex dielectric constant, rather than $\varepsilon(t)$. The conversion is carried out straightforwardly by application of the general relationships Eqs. (6.31) and (6.44). We write

$$\varepsilon_0 \Delta \varepsilon_{\text{nm}}(\omega) = \int_0^\infty \frac{d}{dt} (\varepsilon_0 \Delta \varepsilon_{\text{nm}}(t)) \exp(i\omega t) dt \quad (8.99)$$

$$= \varepsilon_0 \Delta \varepsilon_{\text{nm}}(\infty) \int_0^\infty \frac{1}{\tau_R} \exp\left(-\frac{t}{\tau_R}\right) \exp(i\omega t) dt \quad (8.100)$$

$$= \varepsilon_0 \Delta \varepsilon_{\text{nm}}(\infty) \frac{1}{1 - i\omega \tau_R}, \quad (8.101)$$

thus arriving, as expected, at the expression for a Debye process.

The second remark concerns the use of the order of magnitude symbol in Eq. (8.96). In fact, this result is not exact, because we disregard possible **inner field** effects. Complete treatments of dielectric functions of polar liquids must account for the difference between the externally applied electric field and the local field effective at the position of a dipole. These inner fields may well modify the dynamics of polar chains, but to include this effect theoretically is not a simple task and lies outside our scope.

8.3 Entanglement Effects in Polymer Melts

Entanglements constitute a major feature of the structure in polymer melts and strongly affect the dynamics. Because they interpenetrate each other (the more they interpenetrate, the higher the molar mass), polymer molecules become entangled. Since the chains are linearly connected objects that cannot cross each other, the individual motions become constrained, and it is impossible for the chain to move freely as a whole in all directions.

How can one deal with this situation? It is important to recognize that the restrictions are of peculiar nature in that they mainly concern the lateral chain motion, i.e., the motion perpendicular to the chain contour. It is this property that enables a simple model to be constructed. Grasping this main point, de Gennes and Edwards suggested to envisage the chain dynamics as a motion confined to a **tube**. This tube is set up by those of the adjacent polymers that represent obstacles for the lateral motion. Owing to its simplicity, the tube model allows us to carry out a theoretical analysis. As we will see, it can explain the properties of entangled polymers to a large degree in quantitative terms.

We have already met several manifestations of the entanglements, in particular

- the occurrence of the rubber-elastic plateau in the time-dependent and frequency-dependent mechanical response functions,
- the change in the molar mass dependence of the viscosity when the entanglements become effective, and
- the change in the molar mass dependence of the relaxation time of the dielectric normal mode at the same point.

Hence, the effect of the entanglements is two-fold, since both the elastic and the viscous properties are concerned. The observations all indicate the existence of a critical molar mass, introduced earlier as the critical molar mass at the entanglement limit, denoted by M_c . Polymers with low molar masses, $M < M_c$, exhibit no entanglement effects, but for $M > M_c$ they show up and become dominant. All properties that are founded on motions on length scales corresponding to a molar mass above M_c are affected. This holds, in particular, for the viscosity and the dielectric normal mode since these include the whole polymer chain. On the other hand, Rouse dynamics is maintained within the sequences between the entanglement points, as has already been mentioned.

The change in the dynamics from a free Rouse motion to a movement constrained to a tube, which occurs at a certain sequence length, shows up in quasi-elastic neutron scattering experiments. These experiments have the advantage that they combine a spatial resolution in the 1–10 nm range with a frequency resolution in the GHz-range. In addition, experiments may be conducted on mixtures of deuterated and protonated polymers. Since deuterium and hydrogen have different scattering cross-sections, one can study

directly the individual properties of the minority species. Studies are usually carried out on a dilute solution of protonated chains in a deuterated matrix. Experiments then yield the intermediate scattering law $S(\mathbf{q}, t)$. A Fourier transformation relates $S(\mathbf{q}, t)$ to the time-dependent pair correlation function of the monomers in protonated chains $g(\mathbf{r}, t)$

$$S(\mathbf{q}, t) = \int \exp(-i\mathbf{q}\mathbf{r})(g(\mathbf{r}, t) - \langle c_m \rangle) d^3\mathbf{r} \quad (8.102)$$

(if necessary, for an understanding the explanations to Eq. (A.34) in the Appendix should be checked). For a dilute solution $g(\mathbf{r}, t)$ agrees with the pair correlation function of the monomers of *one* chain. Hence, experiments inform about the motion of individual chains.

If the motion of the chains in the melt is not restricted, the long-time limit of the pair correlation function is given by

$$g(\mathbf{r}, t \rightarrow \infty) = \langle c_m \rangle. \quad (8.103)$$

As a consequence, the intermediate scattering function vanishes for long times

$$S(\mathbf{q}, t \rightarrow \infty) = 0. \quad (8.104)$$

This behavior changes if the motion of the chains remains confined. Under such conditions the pair correlation function differs from $\langle c_m \rangle$ for all times,

$$g(\mathbf{r}, t \rightarrow \infty) \neq \langle c_m \rangle, \quad (8.105)$$

if the distances \mathbf{r} lie within the confinement range. For distances \mathbf{r} outside this zone, $g(\mathbf{r}, t)$ is determined by the contributions of other chains and Eq. (8.104) remains valid.

Figure 8.8 presents the results of quasielastic neutron scattering experiments on melts of poly(ethylene-*co*-propylene). The curves belong to different scattering vectors \mathbf{q} . We can see that decay times decrease with increasing q , as is generally expected for all kinds of diffusive motions.

A straightforward theoretical analysis proves that the intermediate scattering law of a system of Rouse chains may be expressed as a function of one dimensionless variable only, which is defined as

$$u = q^2 a_R^2 \left(\frac{t}{\tau(\delta = \pi)} \right)^{1/2} = q^2 \left(\frac{12kT a_R^2 t}{\zeta_R} \right)^{1/2}. \quad (8.106)$$

$\tau(\pi)$ is the minimum relaxation time of the Rouse chain, as given by Eq. (8.45). When using the variable u , measurements at different q 's coincide, or better, become parts of one common curve. The lower part of Fig. 8.8 displays this reduced representation. The dynamics at short times up to $u = 2$ is indeed Rouse-like. All the curves merge together and correspond to the prediction of the Rouse model. For longer times, however, the situation changes, as curves

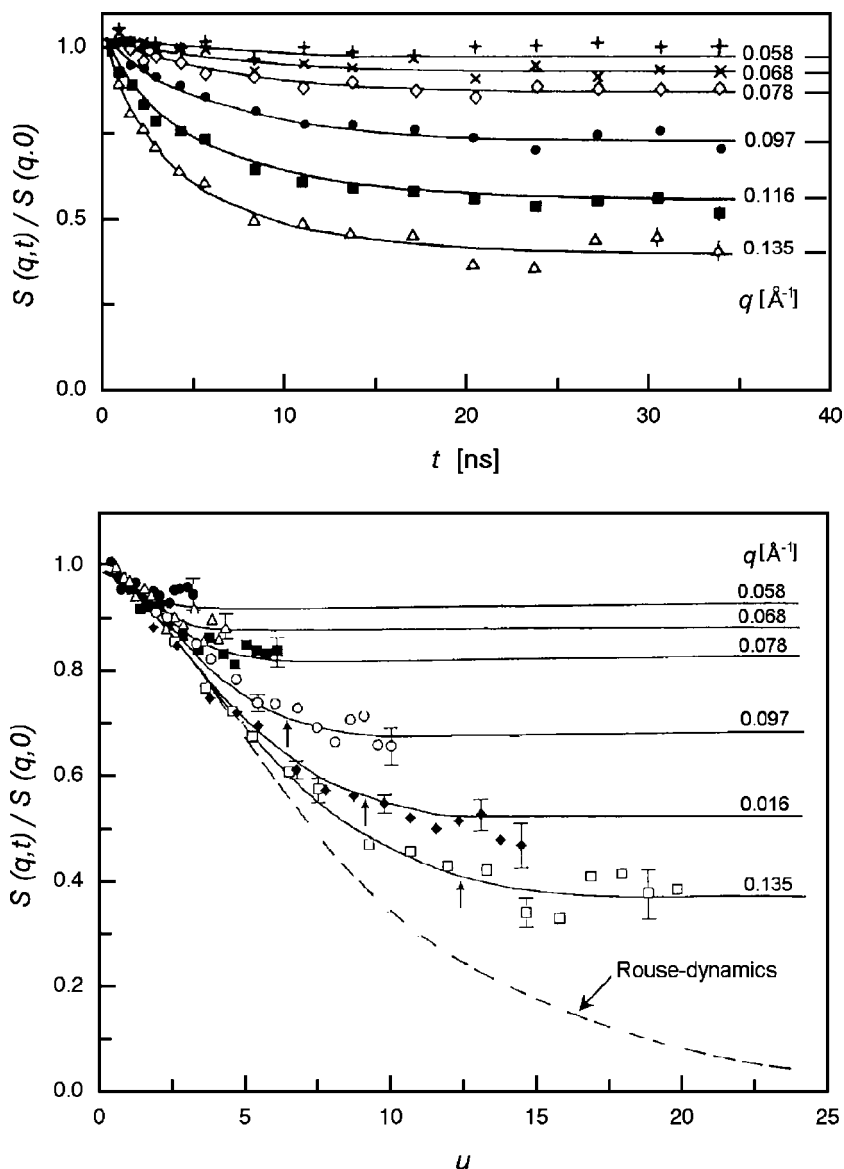


Fig. 8.8. Results of a quasielastic neutron scattering experiment carried out for a melt of poly(ethylene-co-propylene) at 199 °C (10% protonated chains dissolved in a deuterated matrix; $M = 8.6 \times 10^4$ g mol⁻¹). Intermediate scattering laws measured at the indicated scattering vectors (*top*); data representation using the dimensionless variable $u = q^2(12kT a_R^2 t / \zeta_R)^{1/2}$ (*bottom*). From Richter et al. [102]

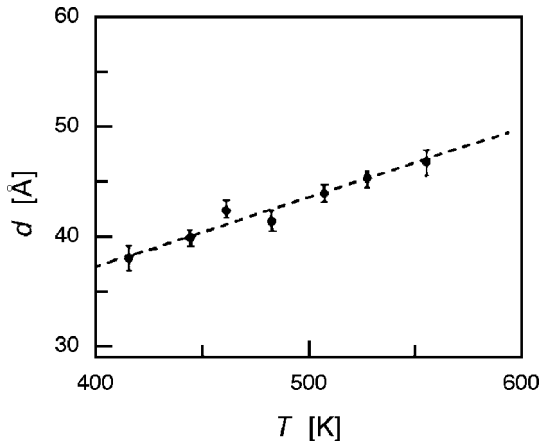


Fig. 8.9. Size d of the confinement range, as derived from the long-time limits of the curves shown in Fig. 8.8 [102]

now deviate from the Rouse scattering law. The measured curves level-off rather than tending to zero. As explained above, exactly this behavior is indicative of a confinement, at least a temporary one in the time range of the experiment. Hence, we find clear evidence for a change from Rouse dynamics to a confined motion.

It is possible to derive from the long-time limiting values the size of the confinement range. $S(q, t \rightarrow \infty)$ actually provides a Fourier analysis of its shape. To see this, just note that $S(q, t \rightarrow \infty)$ is given by

$$S(q, t \rightarrow \infty) = \int \exp(-i\mathbf{q}\mathbf{r})(g(\mathbf{r}, \infty) - \langle c_m \rangle) d^3\mathbf{r} \quad (8.107)$$

and furthermore, that the function

$$g(\mathbf{r}, \infty) - \langle c_m \rangle$$

has non-vanishing values only for distances \mathbf{r} within the confinement range. Consequently, a measurement of the halfwidth Δq of $S(q, \infty)$ yields an estimate of the diameter d of the confinement range, based on the reciprocity relation of Fourier transforms

$$d \simeq \frac{1}{\Delta q}. \quad (8.108)$$

Results, as obtained for different temperatures, are shown in Fig. 8.9. We notice that d increases with rising temperature, i.e., the motional constraints become weaker.

The neutron scattering experiments indicate that the Rouse model remains valid for chain sequences below a critical length. This suggests that we

represent the time-dependent shear modulus of an entangled polymer melt as being composed of three parts

$$G(t) = \Delta G_{\text{mic}}(t) + c_p kT \sum_{m=m^*}^{N_R-1} \exp\left(-2\frac{t}{\tau_m}\right) + c_p kT m^* \Phi\left(\frac{t}{\tau_d}\right) \quad (8.109)$$

As above in Eq. (8.86), $\Delta G_{\text{mic}}(t)$ describes the short-time contributions determined by the chemical microstructure of the chain. The central part is given by the Rouse model. It represents the dynamics for chain sequences that are shorter than the chain parts between entanglements and, on the other side, are still long enough to ensure that Gaussian properties hold. The Rouse mode with the longest relaxation time not yet affected by the entanglements is that with the order m^* given by

$$\delta_{m^*}(N_{R,c} - 1) \simeq \pi, \quad (8.110)$$

where $N_{R,c}$ is the number of Rouse units corresponding to a sequence with the critical molar mass M_c . Using Eq. (8.38) we obtain

$$m^* \frac{\pi}{N_R - 1} (N_{R,c} - 1) \simeq \pi \quad (8.111)$$

or

$$m^* \simeq \frac{N_R - 1}{N_{R,c} - 1}. \quad (8.112)$$

The associated relaxation time is, according to Eq. (8.77),

$$\tau_{m^*} \approx \tau_R \left(\frac{N_{R,c} - 1}{N_R - 1}\right)^2. \quad (8.113)$$

Rouse modes with $m < m^*$ do not exist. They become replaced by other relaxation processes and the third term in Eq. (8.109) describes this contribution. The relaxation strength is identical to that of the replaced Rouse modes, because this part remains unrelaxed after the decay of all modes with $m \geq m^*$. Writing the correlation function for the long-term part in the form $\Phi(t/\tau_d)$ implies the assumption that, similar to the Rouse-modes, also this part is controlled by a single characteristic time, the disentangling time τ_d , only. As introduced here, $\Phi(t/\tau_d)$ is a general function that is normalized, i.e.,

$$\Phi(0) = 1.$$

τ_d may be identified, for example, with the integral width of Φ

$$\int_{t=0}^{\infty} \Phi dt = \tau_d.$$

It is known from the experiments (Figs. 6.13 and 6.14) that τ_d shows a power law dependence on M ,

$$\tau_d \propto M^\nu, \quad \text{with} \quad \nu = 3 - 3.6.$$

A main feature of the behavior expressed by Eq. (8.109) is the formation of a gap in the spectrum of relaxation times, arising between the first two contributions and the long-time part. This gap produces the plateau region, and the extension is determined by the ratio τ_d/τ_{m^*} . For the dependence of this ratio on the molar mass we can write

$$\frac{\tau_d}{\tau_{m^*}} \simeq \frac{M^\nu}{M_c^\nu}, \quad (8.114)$$

considering that $\tau_d \simeq \tau_{m^*}$ for $M \simeq M_c$.

In order to see the effect of the entanglements on the viscosity, we apply Eq. (6.107),

$$\eta_0 = \int_0^\infty G(t) dt, \quad (8.115)$$

to Eq. (8.109). Ignoring the short-time part $\Delta G_{\text{mic}}(t)$, we find that the shear viscosity is given by the relaxation strengths and the mean relaxation times of both the Rouse modes and the disentangling processes, as

$$\eta_0 = c_p kT [(N_R - m^*)\tau_\alpha + m^*\tau_d] \quad (8.116)$$

or

$$\eta_0 = G(0) \left(\frac{G(0) - G_{\text{pl}}}{G(0)} \tau_\alpha + \frac{G_{\text{pl}}}{G(0)} \tau_d \right). \quad (8.117)$$

G_{pl} denotes the plateau modulus and τ_α is the mean relaxation time of the Rouse mode part, agreeing with the mean relaxation time of a Rouse system of chains with N_R equal to $N_{R,c}$. Because the first term on the right-hand side of Eq. (8.117) is constant, for the molar mass dependence of the viscosity of entangled melts we obtain the expression

$$\eta_0 = \beta_1 + \beta_2 \tau_d(M) = \beta_1 + \beta_3 M^\nu. \quad (8.118)$$

In the limit of high molar mass, $M \gg M_c$, we have

$$\eta_0 \propto \tau_d \propto M^\nu. \quad (8.119)$$

8.3.1 The Reptation Model

Starting from the tube concept and considering the motions of the confined chains, Doi and Edwards devised a theory that became well-known as the

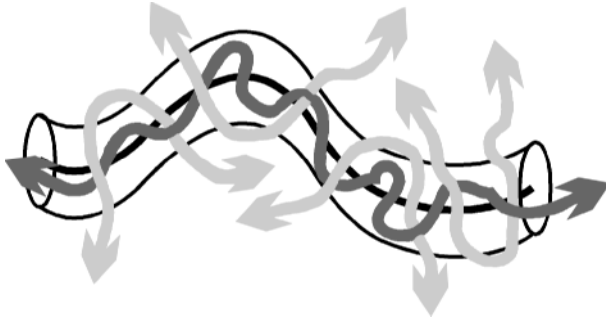


Fig. 8.10. Modeling the lateral constraints on the chain motion imposed by the entanglements by a tube. The average over the rapid wiggling motion within the tube defines the primitive path (*continuous dark line*)

reptation model. The model assumptions are indicated in Fig. 8.10. Under the constraints imposed by the tube, the chain motion may be thought of as being set up of two different components. First, there is a rapid wiggling motion oriented along the tube cross-sections. It corresponds to the Rouse part in the spectrum. Averaging over several cycles of this rapid motion gives the mean positions of the monomers along the tube, represented in the figure by the dark line in the tube center. This line, called the **primitive path**, describes the shortest path connecting the endgroups of the chain, which is compatible with the topology of the entanglements as modeled by the tube. The second component of the motion is the time-dependent evolution of this primitive path and exactly this process leads to the disentangling of the chain. The Doi–Edwards theory focuses on the latter mechanism and thus reduces the problem of the motion of a chain under the constraints in a melt to the problem of the time dependence of the primitive path.

Both the actual chain and the primitive path represent random coils. Since the end-to-end distances are equal, we have

$$R_0^2 = N_R a_R^2 = l_{\text{pr}} a_{\text{pr}} . \quad (8.120)$$

Here, we have introduced the contour length of the primitive path, l_{pr} , and an associated sequence length a_{pr} . a_{pr} characterizes the stiffness of the primitive path and is determined by the topology of the entanglement network.

The process of disentangling, as it is envisaged in the reptation model, is sketched in Fig. 8.11. The motion of the **primitive chain**, the name given to the dynamic object associated with the primitive path, is described as a diffusion along its contour, that is to say, a **reptation**. The associated curvilinear diffusion coefficient can be derived from the **Einstein relation**, which holds generally, independent of the dimension or the topology. Denoting it \hat{D} , we have

$$\hat{D} = \frac{kT}{\zeta_p} . \quad (8.121)$$

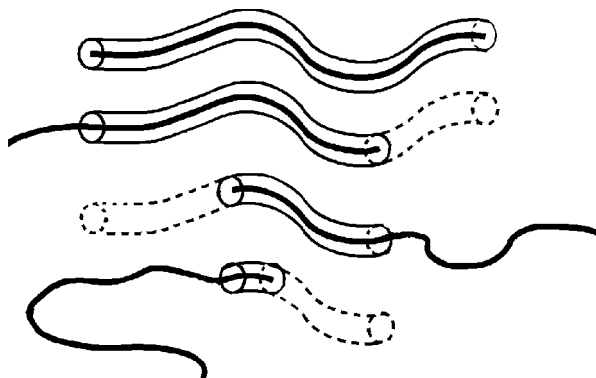


Fig. 8.11. Reptation model: Breakdown of the tube resulting from a reptative motion of the primitive chain. The parts left empty disappear

Here, ζ_p is the friction coefficient of the chain. As there are no entanglements within the tube, ζ_p equals the sum of the friction coefficients of all beads

$$\zeta_p = N_R \zeta_R . \quad (8.122)$$

Hence, \hat{D} is given by

$$\hat{D} = \frac{kT}{N_R \zeta_R} . \quad (8.123)$$

The diffusive motion leads to a continuous disentangling of the chain, as indicated in the figure. When parts of the chain have left the original tube, the empty part of the tube is filled with other chains and disappears. The result of the process is a continuous shortening of the initial tube and simultaneously a continuous increase in the amount of reorientation of the chain. The process of disentangling is finished when the initial tube has vanished.

The time needed to achieve a complete disentangling can be estimated. In order to become disentangled, chains have to diffuse over a distance l_{pr} , i.e., the original length of the primitive path, and this requires a time

$$\tau_d \simeq \frac{l_{pr}^2}{\hat{D}} . \quad (8.124)$$

If we use Eqs. (8.120) and (8.123) we obtain the molar mass dependence of the disentangling time

$$\tau_d \propto \zeta_R N_R^3 . \quad (8.125)$$

Since τ_d determines the viscosity, the reptation model also predicts

$$\eta_0 \propto N_R^3 \propto M^3 , \quad (8.126)$$

which perfectly agrees with the experimental result of Fig. 6.14 in the limit of high molar masses. There are several suggestions for how to explain the

deviations showing up for intermediate molar masses in Figs. 6.14 and 6.13. Generally speaking, they result from the fact that for such molar masses the tube is not yet a stable object. Its contour length as determined by the primitive path fluctuates and the constraints set by the entanglements may be released since the chains involved also diffuse. Both effects accelerate the chain motion.

Doi and Edwards analyzed the described disentangling process of the primitive chain in more detail. As in the case of the Rouse motion, the dynamics of the disentangling process can also be represented as a superposition of independent modes. Again, only one time constant, the disentangling time τ_d , is included, and it sets the time scale for the complete process. In the Doi–Edwards treatment, τ_d is identified with the longest relaxation time. Calculations result in an expression for the time-dependent shear modulus in the terminal flow region. It has the form

$$G = G_{\text{pl}} \Phi \left(\frac{t}{\tau_d} \right) \quad (8.127)$$

with

$$\Phi = \frac{8}{\pi^2} \sum_{\text{odd } m} \frac{1}{m^2} \exp \left(-\frac{m^2}{\tau_d} t \right). \quad (8.128)$$

The Einstein relation, already employed in Eq. (8.121) to write down the curvilinear diffusion coefficient in the tube, also gives us, when used as normally, the diffusion coefficient of a polymer in a melt, provided that there are no entanglements. We call it D and find

$$D = \frac{kT}{\zeta_p} = \frac{kT}{N_R \zeta_R} \propto \frac{1}{M}. \quad (8.129)$$

How does this result change for an entangled melt? The reptation model gives an answer. One only has to realize that the disentangling process is associated with a shift of the center of mass of a polymer molecule over a distance in the order of l_{pr} along the primitive path and, therefore, leads to a mean-squared displacement

$$\langle \Delta r_c^2 \rangle \simeq R_0^2 = l_{\text{pr}} a_{\text{pr}}. \quad (8.130)$$

Since the diffusion coefficient in three dimensions is generally given by

$$D = \frac{\langle \Delta r_c^2 \rangle}{6\Delta t}, \quad (8.131)$$

we obtain

$$D \propto \frac{l_{\text{pr}} a_{\text{pr}}}{\tau_d} \propto \frac{N_R}{N_R^3} \propto \frac{1}{M^2}. \quad (8.132)$$

Hence, according to the reptation model, the transition from a non-entangled to an entangled polymer melt should be accompanied by a change in the

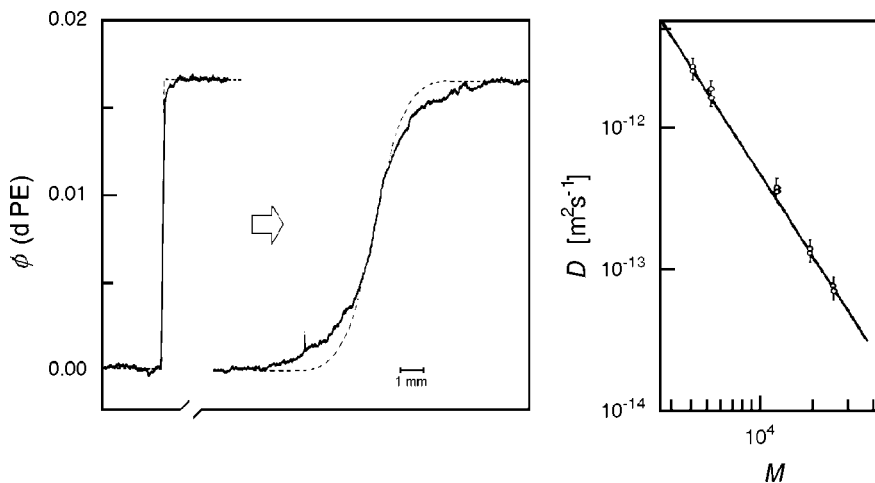


Fig. 8.12. Determination of diffusion coefficients of deuterated PE chains in a PE matrix by infrared absorption measurements in a microscope. Concentration profiles $\phi(x)$ obtained in the separated state at the beginning and at a later stage of diffusive mixing (the *dashed lines* were calculated for monodisperse components; the deviations are due to polydispersity) (*left*). Diffusion coefficients at $T = 176^\circ\text{C}$, derived from measurements on a series of d-PEs of different molar mass (*right*). The *continuous line* corresponds to a power law $D \propto M^2$. Work of Klein [103]

exponent of the power law for the diffusion coefficient, $D \propto M^\nu$, from $\nu = -1$ to $\nu = -2$.

Equation (8.132) is in good agreement with experimental results, as is exemplified by the data presented in Fig. 8.12. Here, diffusion coefficients of deuterated polyethylenes in a matrix of a standard polyethylene were measured in a microscope using infrared radiation. The infrared radiation discriminates between the two components due to the different vibrational properties of the two species. Concentration profiles then can be directly determined by an absorption measurement. Following the time-dependent evolution of the concentration profile, starting with separated components in two films in lateral contact, enables a determination of the diffusion coefficient to be carried out. The left-hand side of Fig. 8.12 depicts two typical concentration profiles, the curve on the left giving the initial profile at the boundary of the two films, the curve on the right referring to a later stage of development. Experiments were conducted for a series of deuterated polyethylenes with different molar masses. The right-hand side shows the diffusion coefficients as obtained for $T = 176^\circ\text{C}$. The slope of the broken line exactly agrees with the theoretical prediction.

There is another beautiful experiment that is even more convincing in its support of the reptation model. Fluorescence microscopy enables the motion of fluorescently stained single chains to be observed directly. The technique was

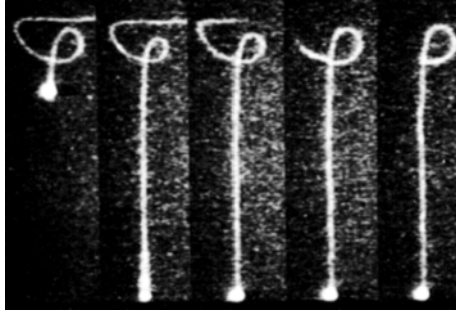


Fig. 8.13. Series of images of a fluorescently stained DNA chain embedded in a concentrated solution of unstained chains: Initial conformation (*left*); partial stretching by a rapid move of the bead at one end (*second from the left*); chain recoil by a reptative motion in the tube (*subsequent pictures to the right*). Reprinted with permission from T. Perkins, D.E. Smith and S. Chu. *Science*, 264:819, 1994. Copyright (1994) American Association for the Advancement of Science

applied to a concentrated solution of monodisperse DNA molecules with an ultra-high molar mass corresponding to a contour length in the 100 μm -range. A coated 1 μm -diameter polystyrene sphere was attached on one end of the chain and it could be manipulated and moved with the aid of optical tweezers. In one experiment the test chain was rapidly pulled at this end; Fig. 8.13 shows the subsequent relaxation. We see that the recoil follows exactly the path formed by the chain in its original conformation, i.e., the drawing back occurs within the tube. We thus have direct evidence that tube-like constraints exist in this system and that they are stable for a long time.

8.4 Solution Viscosities

Having discussed the dynamics of polymer chains in the melt, in this section, we will examine their motion in solution as well as the related viscous properties. As we shall see, here the diffusion coefficient cannot be described by either of the two equations for the melt, but is given by

$$D \propto \frac{kT}{\eta_s R} \propto M^{-\nu} \quad (8.133)$$

with $\nu = 3/5$ for good solvents. The reason for the qualitatively different behavior is the dominant effect of **hydrodynamic interactions**. They turn each chain into a closed object that cannot be penetrated by the solvent. Correspondingly, the viscosity increase produced by dissolved polymers equals that of dispersed colloids. Peculiar effects arise again for polyelectrolytes. Strong electrostatic interchain interactions are found already at very low concentrations. They change the character of the diffusive motions and greatly enhance the viscosity.

8.4.1 Neutral Polymers: Hydrodynamic Interaction

We first consider an internally rigid colloidal particle suspended in a liquid. Application of an external force will cause the particle to move. The motion necessarily affects the surrounding liquid. The enforced replacement of solvent molecules from the front to the back of the moving colloid results in a disturbance that extends over a larger region. For a constant velocity, a flow field that moves in the stationary state together with the particle is created. Figure 8.14 depicts this flow field. It has a major component in the direction of the velocity of the colloid. Since the flow field is inhomogeneous and includes velocity gradients, energy is dissipated. The force acting on the particle provides the power.

We can analyze this force in more detail. To begin with, remember the simple case of a shear flow created if two parallel plates are moved against each other with constant velocity v_x . Here, a linear velocity profile evolves, like that included in Fig. 8.16. The power that has to be supplied is given by

$$\frac{dW}{dt} = fv_x = \eta_s \frac{\partial v_x}{\partial z} L_x L_y \frac{\partial v_x}{\partial z} L_z = \eta_s \mathcal{V} \left(\frac{\partial v_x}{\partial z} \right)^2. \quad (8.134)$$

η_s denotes the viscosity of the fluid, L_z is the thickness of the liquid layer, and the product $L_x L_y$ gives the area of the plates. The expression on the right-hand side states that the power dissipated per unit volume is proportional to η_s and to the square of the velocity gradient. Here, the result was obtained for the particular case of a constant velocity gradient. Theories for the general

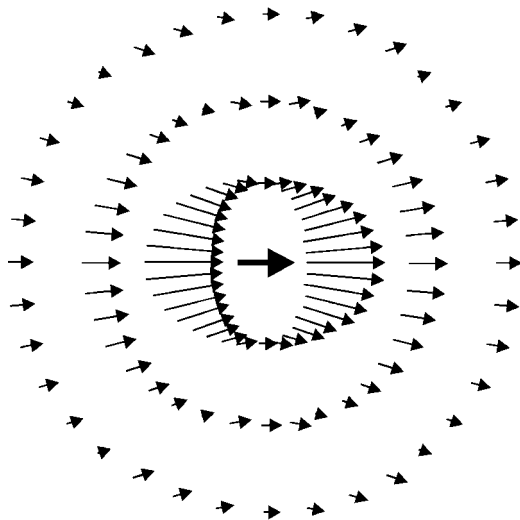


Fig. 8.14. Flow field created in a liquid if a suspended spherical particle is moved by the action of an external force (Eq. (8.147)). The *thicker arrow in the center* represents the force

case of arbitrary flow fields with varying velocity gradients derive the following expression for the dissipated power:

$$\frac{d\mathcal{W}}{dt} = \eta_s \int_{\mathcal{V}} \frac{\partial v_i}{\partial x_j} \frac{\partial v_i}{\partial x_j} d^3\mathbf{r} \quad (8.135)$$

(we adopt the convention of performing a summation on repeated indices).

The flow field $\mathbf{v}(\mathbf{r})$ produced by the particle if it is dragged with a constant velocity \mathbf{u} through the liquid can generally be described as

$$\mathbf{v}(\Delta\mathbf{r}) = \mathbf{H}(\Delta\mathbf{r})\mathbf{u} , \quad (8.136)$$

in component notation

$$v_i(\Delta\mathbf{r}) = H_{ik}(\Delta\mathbf{r})u_k , \quad (8.137)$$

whereby $\Delta\mathbf{r} = \mathbf{r} - \mathbf{r}_c$ denotes the distance between \mathbf{r} and the colloid position \mathbf{r}_c . Employing $\Delta\mathbf{r}$ means that the flow field moves together with the particle, i.e., is stationary in a particle fixed coordinate system. The tensor \mathbf{H} determines, when applied on \mathbf{u} , the velocity field. The velocity gradient tensor included in Eq. (8.135) follows by calculating the derivative

$$\frac{\partial v_i}{\partial r_j} = \frac{\partial}{\partial \Delta r_j} H_{ik}(\Delta\mathbf{r})u_k = h_{ijk}(\Delta\mathbf{r})u_k . \quad (8.138)$$

Here we introduced another tensor, of third rank, with components h_{ijk} . The formulated dependence is of the linear type, therefore, holds for **Newtonian liquids**. All low molar mass liquids behave in Newtonian manner, at least for ordinary velocities. If Eq. (8.138) is inserted into Eq. (8.135), followed by an integration over the whole flow field, the dissipated power is obtained

$$\frac{d\mathcal{W}}{dt} = \eta_s \int_{\mathcal{V}} h_{ijk}h_{ijl}u_k u_l d^3\mathbf{r} = \eta_s u_k \beta_{kl} u_l . \quad (8.139)$$

Here, we introduced yet another tensor, with components β_{kl} . It is specific for the particle and depends on its size and shape.

The power required for dragging the particle is supplied by the force acting on it

$$\frac{d\mathcal{W}}{dt} = \mathbf{f} \cdot \mathbf{u} = f_l u_l . \quad (8.140)$$

Comparing Eqs. (8.139) and (8.140) we obtain

$$f_l = \eta_s u_k \beta_{kl} . \quad (8.141)$$

Hence, \mathbf{u} and \mathbf{f} are linearly related. Force and velocity do not need to be oriented parallel to each other, but for moving spheres they do for symmetry

reasons, and we will discuss only this case. Here the tensor β_{ki} reduces to a scalar parameter, β and one can write

$$\mathbf{f} = \eta_s \beta \mathbf{u} . \quad (8.142)$$

The proportionality constant relating the applied force to the resulting velocity is the **friction coefficient** ζ , and is given by

$$\zeta = \beta \eta_s . \quad (8.143)$$

In order to calculate the friction coefficient of a spherical colloid, the Navier–Stokes equation for liquids has to be solved, with the boundary condition that the liquid layer adjacent to the particle adheres to its surface thus moving with the same velocity. The problem was solved long ago by Stokes. The result is the famous equation

$$\zeta = 6\pi R \eta_s . \quad (8.144)$$

It states that the friction coefficient of a sphere scales linearly with the radius R . When dealing with particles that are isotropic on average but otherwise have an arbitrary structure, it is sometimes convenient to replace them by an **equivalent sphere**. The replacement implies that we assign to the particle a **hydrodynamic radius** R_h , defined by

$$R_h = \frac{\zeta}{6\pi\eta_s} . \quad (8.145)$$

According to the definition, R_h is the radius of a spherical particle that possesses the same friction coefficient as the given colloid.

We return once again to the flow field depicted in Fig. 8.14. Actually it represents the result of a calculation first carried out by Oseen. Oseen derived the field produced by a point-like particle being dragged through the liquid by a force \mathbf{f} . As proved in his treatment, the following analytical expression relates the flow field $\mathbf{v}(\Delta\mathbf{r})$ to \mathbf{f} :

$$\mathbf{v}(\Delta\mathbf{r}) = \frac{1}{8\pi\eta_s} \left(\frac{\mathbf{f}}{\Delta r} + \frac{(\mathbf{f} \cdot \Delta\mathbf{r})\Delta\mathbf{r}}{\Delta r^3} \right) , \quad (8.146)$$

or, using a tensor notation

$$\begin{aligned} v_i &= \frac{1}{8\pi\eta_s \Delta r} \left(\delta_{ij} + \frac{\Delta r_i \Delta r_j}{\Delta r_k \Delta r_k} \right) f_j \\ &= H_{ij}^{\text{Os}} f_j . \end{aligned} \quad (8.147)$$

H_{ij}^{Os} is known as the **Oseen hydrodynamic interaction tensor**. In a common situation there exists a certain flow field, $\mathbf{v}_0(\mathbf{r})$ and a suspended particle moves at first with the liquid. Application of an external force, \mathbf{f} , on the par-

ticle then produces a disturbance, $\mathbf{v}_d(\Delta\mathbf{r})$. It becomes superposed on $\mathbf{v}_0(\mathbf{r})$ so that the flow field changes to

$$\mathbf{v}(\mathbf{r}) = \mathbf{v}_0(\mathbf{r}) + \mathbf{v}_d(\Delta\mathbf{r}) . \quad (8.148)$$

The Oseen tensor provides an accurate description of $\mathbf{v}_d(\Delta\mathbf{r})$.

The central point of Oseen's result is the predicted slow decay of the disturbance with the reciprocal of the distance. This implies that the hydrodynamic interaction is of a long-ranged nature and therefore strong and effective. The consequences for a group of particles are drastic. Since the flow has a major component in the direction of the force, all particles in the group will support each other in the motion. As a result, a group of particles which interact via flow field forces, i.e., are coupled by the **hydrodynamic interaction**, moves faster through the liquid than isolated particles under the same total external force. What happens in the special case of a polymer? The answer is intuitively clear. The monomers of the coil, being confined to a volume with a diameter in the order of R_g , strongly interact via the hydrodynamic forces. Indeed, the coupling becomes so strong that all solvent molecules within the coil region are forced to move together with the chain segments, so that the coil can essentially be considered as impermeable. Therefore, polymers in a solvent actually behave like hard spheres and the hydrodynamic radius R_h attributed to them thus has a real significance.

It is possible to elaborate this intuitive picture in a thorough theory and this task was first carried out by Kirkwood and Risemann. Their result relates the hydrodynamic radius to the radius of gyration, R_g , of the chain, by

$$R_h \approx \frac{2}{3} R_g , \quad (8.149)$$

or the friction coefficient of a polymer molecule, ζ_p , to R_g by

$$\zeta_p = 4\pi\eta_s R_g . \quad (8.150)$$

The Einstein relation relates the friction coefficient of a colloid to its diffusion coefficient. Applying it to Eq. (8.150), we obtain for the diffusion coefficient of a dissolved polymer the expression

$$D = \frac{kT}{4\pi\eta_s R_g} . \quad (8.151)$$

Equation (8.151) opens another route for the determination of the radius of gyration of chains and thus, if the effective length per monomer is known, for the degree of polymerization and the molar mass. A method for measuring D is required for this purpose and there exists a standard technique, namely dynamic light scattering. It generally results in a determination of the intermediate scattering law $S(q, t)$, like the quasielastic neutron scattering experiments discussed earlier, but with different resolutions in space and time.

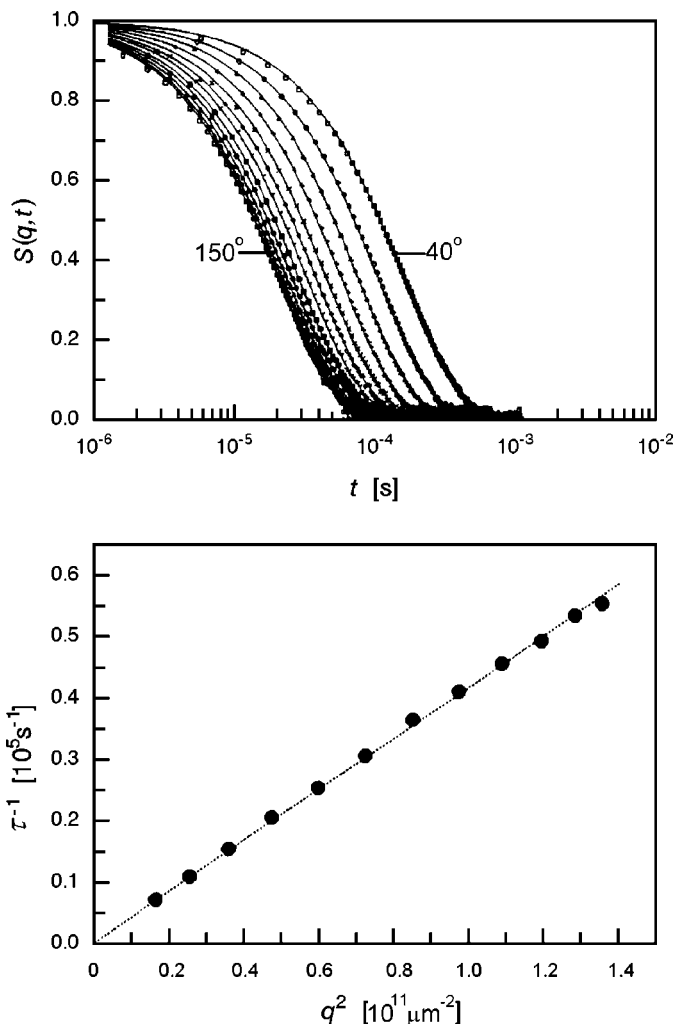


Fig. 8.15. Results of a dynamic light scattering experiment on a solution of PS ($M = 4.9 \times 10^4 \text{ g mol}^{-1}$, $c_w = 0.053 \text{ g cm}^{-3}$) in dioxane: Intermediate scattering law $S(q, t)$ for different values of the scattering angle in the range $2\vartheta_B = 40^\circ$ to 150° (in steps of 10°) (top); derived q -dependence of the rate of decay τ^{-1} (bottom) [104]

Figure 8.15 provides an example. Data were obtained for a dilute solution of polystyrene in toluene.

The result may be explained as follows. First note that for the given spatial resolution, in the order of the wavelength of light, polymers appear point-like. A dilute solution of polymers, therefore, resembles a system of independently moving point-like colloids. The intermediate scattering law then relates to the diffusive motion of the center of mass of a single polymer, as described by the

self-correlation part of the time-dependent pair correlation function, $\hat{g}(\mathbf{r}, t)$ (see Eq. (A.32) in the Appendix). $\hat{g}(\mathbf{r}, t)$ is given for a diffusing colloid by

$$\hat{g} = \frac{1}{(4\pi Dt)^{3/2}} \exp -\frac{r^2}{4Dt}, \quad (8.152)$$

which is the solution of the basic differential equation for diffusive motions,

$$\frac{\partial}{\partial t} \hat{g}(\mathbf{r}, t) = D\Delta \hat{g}(\mathbf{r}, t), \quad (8.153)$$

for the initial condition

$$\hat{g}(\mathbf{r}, t = 0) = \delta(\mathbf{r}). \quad (8.154)$$

The intermediate scattering law therefore has the form

$$\begin{aligned} S(q, t) &= \int_{\mathcal{V}} \exp(-i\mathbf{q}\mathbf{r}) \hat{g}(\mathbf{r}, t) \, d^3\mathbf{r} \\ &= \exp(-Dq^2t). \end{aligned} \quad (8.155)$$

Hence, a simple exponential decay is expected and indeed verified by the experiments, e.g. those presented in Fig. 8.15. The signature of diffusive motions is the predicted linear increase of the relaxation rate with the square of the scattering vector, the diffusion coefficient D representing the proportionality constant. This dependence is also shown in the figure.

Intrinsic Viscosity

A second, even simpler technique for determining the hydrodynamic radius is viscosimetry. Generally, the suspension of colloids or the dissolution of polymers leads to an increase in the measured macroscopic viscosity. It is easy to see the principal reason for this effect when considering the simple shear flow situation depicted in Fig. 8.16. We choose a spherical volume element of the liquid and follow the changes imposed by the flow field. As we can see, it becomes translated, rotated and deformed. If this volume element is now replaced by a rigid spherical colloid, the translation and rotation are still possible; however, the deformation is inhibited. The inability of the rigid sphere to realize the deformation that would be necessary to keep the linear profile of the flow field unperturbed, results in an additional local flow around the sphere. The local flow is associated with high velocity gradients and, therefore, causes an extra energy dissipation. This additional dissipation of energy becomes apparent in an increase in the force required to move the upper plate, when compared to the pure solvent at the same plate velocity. If this force is measured, one can derive an **effective macroscopic viscosity** η , upon utilizing the same equation as for a pure fluid,

$$f = \eta L_x L_y \frac{\partial v_x}{\partial z}. \quad (8.156)$$

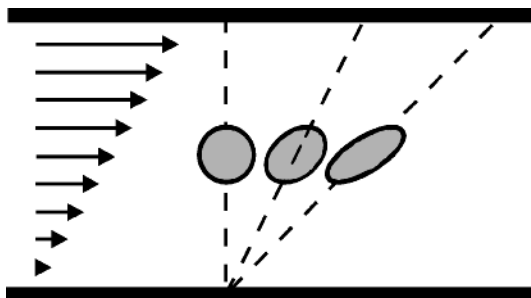


Fig. 8.16. Translation, rotation and deformation of a spherical volume element in a liquid under the conditions of simple shear flow

The quantity of interest is the excess of η over the viscosity of the pure solvent, η_s . It was Einstein who demonstrated that this excess can be directly interpreted when dealing with a suspension of spheres. He derived the following series expansion:

$$\eta = \eta_s(1 + \gamma\phi + \dots) . \quad (8.157)$$

The expansion variable ϕ denotes the volume fraction occupied by spheres, and γ is a numerical factor ($\gamma = 2.5$). The result is remarkably simple, because it implies that the excess viscosity is only dependent on the volume fraction of the spheres, irrespective of whether there are many small spheres or larger spheres in smaller numbers.

Equation (8.157) can be applied to a solution of polymers since the macromolecules behave like hard, impermeable spheres with volumes as given by the hydrodynamic radius. Detailed theoretical treatments suggest a minor correction, because it is found that the hydrodynamic radius to be used in viscosity measurements differs slightly from that applied in the representation of the diffusion coefficient. While the latter is given by Eq. (8.149), viscosity measurements have to be based on the relation

$$R_h \approx \frac{7}{8}R_g . \quad (8.158)$$

ϕ in Eq. (8.157) is then given by

$$\phi = c_p \frac{4\pi}{3} R_h^3 \approx c_p \frac{7\pi}{6} R_g^3 . \quad (8.159)$$

Works on polymer solutions employ a particular quantity in order to specify the excess viscosity. It is known as **intrinsic viscosity** and generally denoted $[\eta]$. $[\eta]$ is defined as

$$[\eta] = \lim_{c_w \rightarrow 0} \frac{\eta_r}{c_w} \quad (8.160)$$

with

$$\eta_r = \frac{\eta - \eta_s}{\eta_s} , \quad (8.161)$$

thus including a passage to the limit of vanishing polymer concentrations. η_r is the **reduced excess viscosity**. Applying Eq. (8.157), the intrinsic viscosity follows as

$$[\eta] = \frac{\gamma\phi}{c_w}. \quad (8.162)$$

Since

$$c_p \propto \frac{c_w}{M} \quad (8.163)$$

and generally

$$R_g \propto aN^\nu \propto a \left(\frac{M}{M_m} \right)^\nu \quad (8.164)$$

with

$$\begin{aligned} a &= a_F, \quad \nu = 3/5 \quad \text{for chains in good solvents and} \\ a &= a_0, \quad \nu = 1/2 \quad \text{for chains in theta solvents,} \end{aligned}$$

the intrinsic viscosity results as

$$[\eta] = \text{const} \frac{a^3}{M} \left(\frac{M}{M_m} \right)^{3\nu}. \quad (8.165)$$

This is usually expressed by the formula

$$[\eta] = KM^\mu \quad (8.166)$$

whereby, as a comparison shows, the prefactor is given by

$$K = \text{const} \left(\frac{a}{M_m^\nu} \right)^3 \quad (8.167)$$

and the exponent by

$$\mu = 3\nu - 1. \quad (8.168)$$

Equation (8.166) is known as the **Mark–Houwink–Sakurada relation**. It generally holds quite well. The data obtained for two different solutions of poly(isobutylene) presented in Fig. 8.17 provide an example.

With the aid of such molar mass-dependent $[\eta]$ measurements one can discriminate between ideal and expanded chains. One finds an exponent $\mu = 0.5$ corresponding to $\nu = 0.5$ for ideal chains and larger values for expanded chains, up to the limit of $\mu = 0.8$ corresponding to $\nu = 0.6$ expected for an expanded chain with ultra-high molar mass. In addition, the prefactor K can be used for determining the chain stiffness as expressed by the effective length per monomer a . Since the constant in Eq. (8.167) is known, a can be derived. In particular, by carrying out measurements of $[\eta]$ in theta solvents, the characteristic ratio, $C_\infty = a^2/a_b^2$ (Eq. (2.32)), can be determined.

Once the value of K and μ have been established for a given polymer-solvent system, and usually μ is found to lie somewhere in between the two

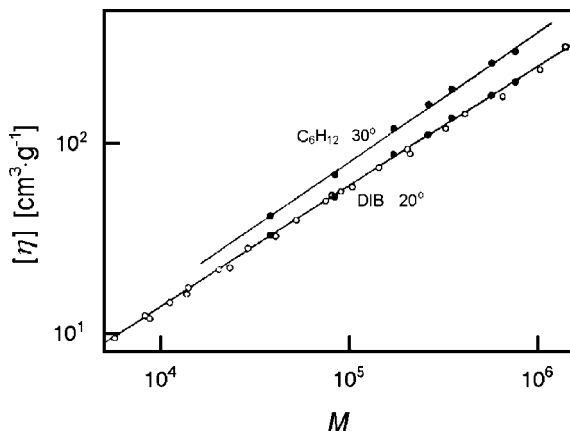


Fig. 8.17. Intrinsic viscosity-molar mass relationship for PI in diisobutylene (DIB) at 20 °C and in cyclohexane at 30 °C. Data collected in Flory's book [105]

limiting cases of an ideal and an expanded chain, molar masses of samples can be derived from measured intrinsic viscosities. Due to these relationships, viscosity measurements have become a standard analytical tool that is simple and therefore frequently applied.

The intrinsic viscosity refers to the limit of a zero polymer concentration and thus deals with the effect of completely separated chains on the solution viscosity only. For finite concentrations the chains partially overlap, which leads to an increase of the reduced excess viscosity. The increase is well-described by

$$\eta_r = [\eta] + \beta_H [\eta]^2 c_w + \dots \quad (8.169)$$

The coefficient β_H is known as the **Huggins constant**.

8.4.2 Polyelectrolytes: Coulomb Interaction

Not surprisingly, the chain stretching and regular interchain ordering generated by the electrostatic forces in polyelectrolyte solutions are also accompanied by a peculiar dynamics. Motions are generally accelerated by the action of the strong Coulomb forces. These are much stronger than the entropic and enthalpic forces controlling the diffusive motion in dilute solutions of neutral polymers. In addition, motions become cooperative, the modes of motion including both the polyions and the mobile counter-ions in coupled manner. Separate concentration fluctuations of polyions and counter-ions would cause charge density fluctuations and therefore decay immediately.

Dynamic light scattering provides a means to observe these fluctuations and Fig. 8.18 gives an example. For each scattering vector \mathbf{q} a decay time τ of the thus selected fluctuation, with wave vector $\mathbf{k} = \mathbf{q}$, was measured. Concentration fluctuations in liquids are always of diffuse nature, since all particles

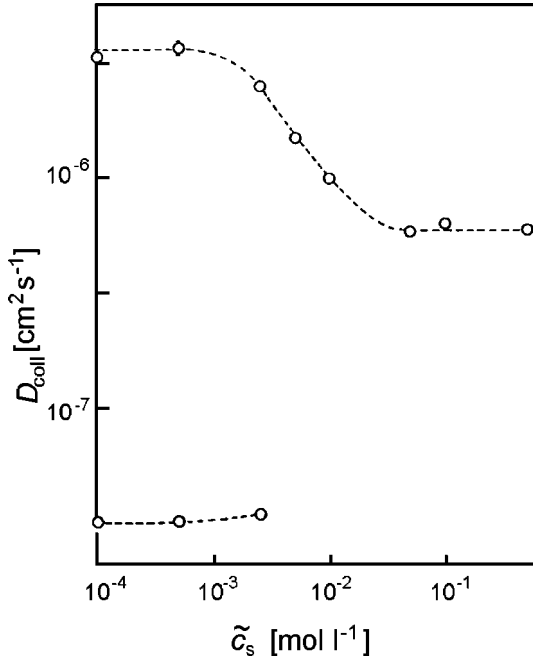


Fig. 8.18. Results of a dynamic light scattering study on aqueous solutions of NaPSS: Variation of the collective diffusion coefficient $D_{\text{coll}} = \tau^{-1}/q^2$ with the concentration of added NaCl. For low values of \tilde{c}_s a second slower mode appears. From Drifford and Dalbietz [106]

carry out diffusive motions, individually and cooperatively. Consequently, the rate of decay shows the proportionality

$$\tau^{-1} \propto q^2$$

or, introducing the collective diffusion coefficient D_{coll} , follows the equation

$$\tau^{-1} = D_{\text{coll}}q^2. \quad (8.170)$$

The experiment investigated the effect of the addition of salt on the dynamics. The initial conditions in the practically salt-free situation are given at the beginning. Here D_{coll} shows a large value of about $3 \times 10^{-6} \text{ cm}^2 \text{ s}^{-1}$. Increasing the salt content \tilde{c}_s leads to a drop of D_{coll} by one order of magnitude, ending up at values typical for solutions of neutral polymers. The change comes as expected considering that the charges on the polyions are increasingly screened by the salt ions. At the end the Coulomb forces have practically disappeared. At low salt concentrations a second fluctuation mode shows up. It indicates the existence of long living associates that perform very slow motions. Indeed, such **slow modes** are often found in highly viscous systems, also in concentrated polymer solutions or polymer melts near to T_g .

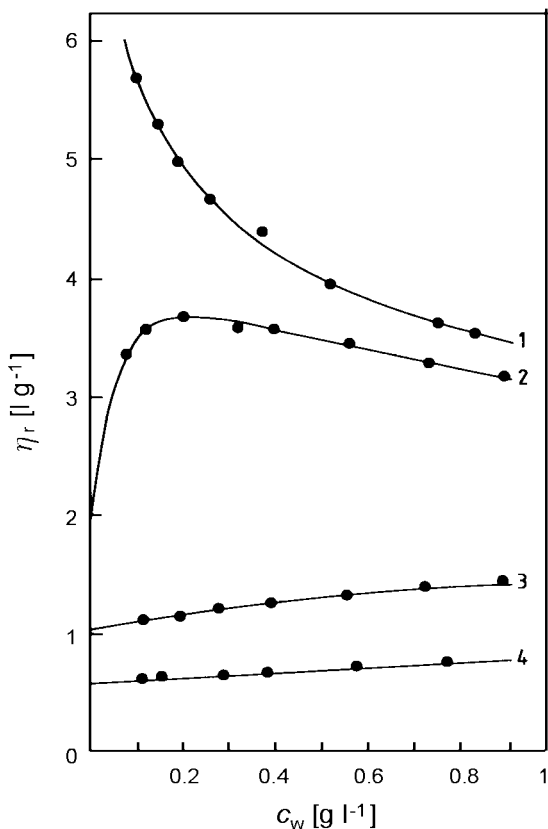


Fig. 8.19. Aqueous solutions of sodium carboxy cellulose with added NaCl: Variation of the reduced viscosity with the polymer concentration for (1) no dissolved NaCl (2) $2.5 \times 10^{-4} \text{ mol l}^{-1}$ (3) $5 \times 10^{-3} \text{ mol l}^{-1}$ and (4) $5 \times 10^{-2} \text{ mol l}^{-1}$ NaCl. From Dautzenberg et al. [107]

The Coulomb forces with the resulting build-up of structures in polyelectrolyte solutions also have drastic consequences for the solution viscosity. Variations in the viscosity with the polymer content are conveniently discussed in terms of the reduced excess viscosity η_r (Eq. (8.161)). For solutions of neutral polymers η_r increases slowly with the polymer concentration c_w , as described by Eq. (8.169). Polyelectrolyte solutions exhibit a quite different behavior. They show very high values of η_r already at very low polymer concentrations and one then often observes a drop rather than an increase with c_w . Curve 1 in Fig. 8.19 gives a typical example of this behavior. The decrease can be empirically described by the **Fuoss–Strauss relation**

$$\eta_r = \frac{\beta_1}{1 + \beta_2 c_w^{1/2}}. \quad (8.171)$$

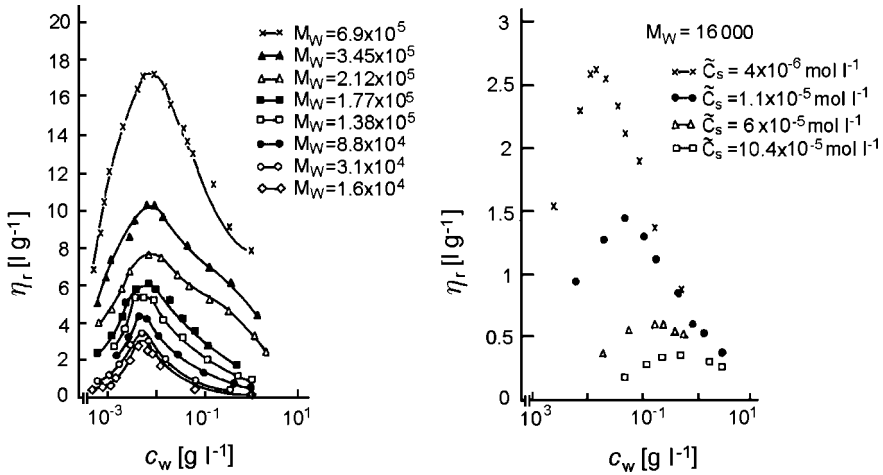


Fig. 8.20. Concentration dependence of the reduced excess viscosity measured for aqueous solutions of NaPSS for (left) various molar masses at a constant salt concentration $\tilde{c}_s = 4 \times 10^{-6} \text{ mol l}^{-1}$ and (right) for a sample with a molar mass $M_w = 1.6 \times 10^4 \text{ g mol}^{-1}$ for different concentrations of NaCl. From Cohen et al. [108]

The further curves given in the figure demonstrate that on the addition of salt, i.e., on weakening the Coulomb forces, the viscosity generally decreases. For high enough salt concentrations, curve 4, one finally arrives at the same behavior as is found for neutral polymer solutions, namely, a slow increase of η_r with c_w . An interesting case is presented by curve 2: Here the viscosity passes over a maximum.

In fact, if curve 1 had been continued by further measurements into the range of very low polymer concentrations, a maximum would also have been found. Figure 8.20 shows thus completed curves obtained in a series of measurements carried out for various molar masses. The occurrence of the maximum in η_r is a general phenomenon found for all polyelectrolytes. As demonstrated by the depicted curves, the location of the maximum is independent of the molar mass. The molar mass only changes the value of η_r in the expected direction, with increasing molar mass to higher viscosities. The figures on the right-hand side again represent the effect of the addition of salt: One observes a general decrease, now together with a shift of the maximum position to higher polymer concentrations when the salt concentration \tilde{c}_s increases. Interestingly, a check shows that the location of the maximum is associated with a constant ratio c_w/\tilde{c}_s .

Obviously, these peculiar properties of the viscosity are a consequence of the structure formation in polyelectrolyte solutions. Imposing a shear flow on a polyelectrolyte solution leads to a constant destruction and reformation of the structure. The force required to keep these processes running depends on

the binding forces that stabilize the structure in a quiescent solution. The increase of η_r observed at very low concentrations of the polymer, which is much larger than the enhancement found for neutral polymers, indicates that at first the binding forces increase. The drop setting in after passing the maximum is indicative for a weakening of the binding forces, following from the decrease of the Debye screening length. It is interesting to note that a similar concentration dependence of the viscosity is found in dispersions of charged colloids. Here, lattices under the action of the Coulomb forces are formed, which also undergo a destruction–reformation process in shear flows. Theories have been developed for this simpler system and describe the reduced excess viscosity by the equation

$$\eta_r \propto c_w \xi_D^3 . \quad (8.172)$$

The first factor accounts for the initial increase and the second factor produces the subsequent decrease of η_r , both originating in changes in the lattice binding force.

Further Reading

- R.B. Bird, R.C. Armstrong, O. Hassager: *Dynamics of Polymeric Liquids, Vol. 2 Kinetic Theory*, John Wiley & Sons, 1977
 H. Dautzenberg, W. Jaeger, J. Kötz, B. Philipp, Ch. Seidel, D. Stscherbina: *Polyelectrolytes*, Hanser, 1994
 M. Doi, S.F. Edwards: *The Theory of Polymer Dynamics*, Clarendon Press, 1986
 P.-G. de Gennes: *Scaling Concepts in Polymer Physics*, Cornell University Press, 1979
 A.Y. Grosberg, A.R. Khokhlov: *Giant Molecules*, Academic Press, 1997

Non-Linear Mechanics

The observations, notions and model calculations presented so far in the discussions of mechanical properties concerned the range of linear responses only. In fact, when applying polymeric materials under realistic conditions one frequently reaches the limits of these treatments, since non-linear effects appear and have to be properly accounted for. In this chapter, we shall deal with three cases of special importance:

- When using rubbers, non-linear mechanical properties are encountered in all situations of practical interest. Rubbers exhibit large deformations even under comparatively weak external forces and thus are mostly found outside the range of small strains.
- Rubbers swell if a solvent penetrates. This isotropic dilatation becomes particularly large if cross-linked polyelectrolytes are swollen by water. The equilibrium state here is controlled by both the osmotic pressure of the mobile counter-ions and the non-linear network properties.
- During processing of polymer melts, strain rates are usually so high that a characterization of the flow properties by a constant viscosity coefficient as for low molar mass Newtonian liquids is no longer adequate.

We begin with a look at three typical examples. The first one is presented in Fig. 9.1 and depicts the **load-extension curve** observed for a sample of natural rubber. The extension is described by the ratio between the lengths in the stressed and the initial natural state, denoted λ , and the load is given in terms of the force per cross-section unit area in the undeformed state, denoted $\hat{\sigma}_{zz}$. The measurement goes up to an extension ratio of about seven, thus demonstrating the unique deformability of rubbers. **Non-linearity** is evident in the curve. It exhibits a sigmoidal shape; a linear law holds only for a small range around the origin.

The other two examples deal with the flow properties of polymer melts as they are encountered under ordinary processing conditions. Figure 9.2 presents results of measurements of the viscosity of a melt of polyethylene, obtained at steady state for simple shear flows under variation of the shear rate. Data

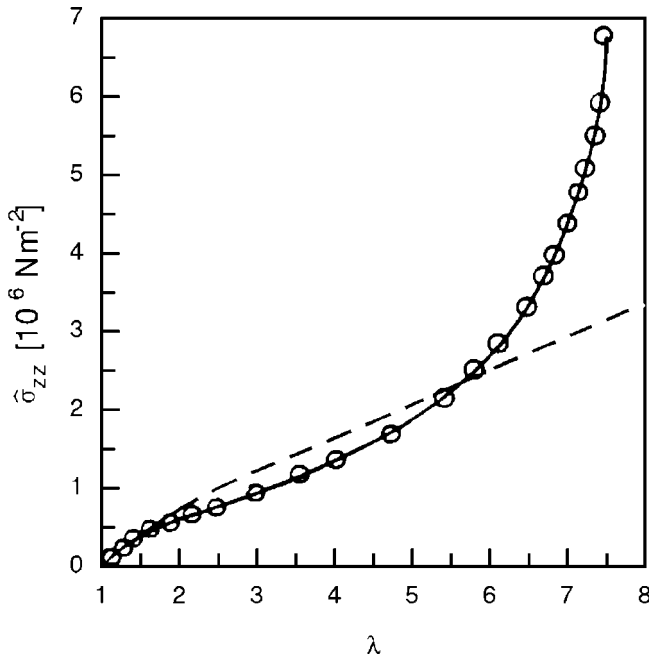


Fig. 9.1. Load-extension curve registered for a sample of natural rubber (λ : extension ratio; $\hat{\sigma}_{zz}$: tensile stress). Comparison with the function Eq. (9.31) derived for an ideal rubber (*broken line*). Results from Treloar [109]

were collected for a series of different temperatures. At low shear rates one finds a constant value for the viscosity coefficient, i.e., a strict proportionality between shear stress and shear rate, but then a decrease sets in. This deviation from linearity is commonly found in polymers and begins already at moderate shear rates. As one observes a decrease in the required shear stress, the effect is commonly addressed as **shear thinning**.

The third example concerns a further characteristic property of flowing polymer melts. If during an extrusion process a polymer melt is forced to flow through a capillary, the extrudate shows a lateral expansion at the exit. Figure 9.3 shows the thickening ratio of a polystyrene melt, i.e., the ratio d/d_0 between the diameter of the extrudate and the diameter of the capillary, as a function of the extrusion rate that is here specified by the shear rate measured at the wall. Again the magnitude of the effect increases with the shear rate. The behavior indicates that shear flow in polymer melts is accompanied by the development of a **normal stress** acting perpendicularly to the shear stress and the direction of the flow. In the interior of the capillary, this pressure is provided by the wall. The thickening takes place at the moment when the end of the wall is reached. The building-up of normal stresses in simple shear flows is a non-linear phenomenon, being absent in Newtonian liquids.

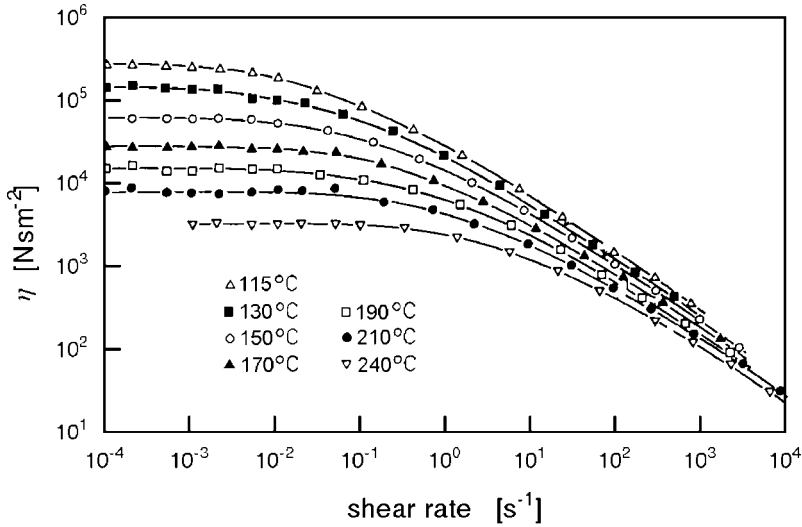


Fig. 9.2. Shear rate dependence of the viscosity η , observed for a melt of PE at various temperatures. Measurements by Meissner [110]

Indeed, if normal stresses are found, they are in lowest order proportional to the square of the shear rate.

A qualitative understanding of the origin of the normal stress phenomenon is not difficult. We learned in the previous chapters that a polymer melt resembles a transient network of entangled polymers. High shear rates, as they are encountered in a capillary, result in a deformation of the chains and, therefore, also of the formed network. As a consequence, tension builds up along the lines of flow and draws the extrudate back when the confinement provided by the walls of the tube terminates. As the tension increases with the strain rate, the chain recoil at the exit increases as well and the extrudate rearranges to a larger diameter.

In this qualitative consideration, we have already addressed a principal point: If strains in a rubber or strain rates in flowing polymer melts are not really small, the chains are displaced significantly from their equilibrium conformations corresponding to isotropic random coils. If structures are altered by external stresses or during flow, then, as has already been emphasized in the previous chapters, we are leaving the range of linear responses and non-linear effects appear. Hence, we have a clear-cut criterion and may judge from the presence of non-linearities whether or not structure changes have been induced.

The two other experiments also exemplify this general relationship. The non-linear sigmoidal stress-strain curve of a rubber under a tensile force shown in Fig. 9.1 is indicative of and caused by the significant changes in the conformational distribution of the chains building up the rubber network. Also

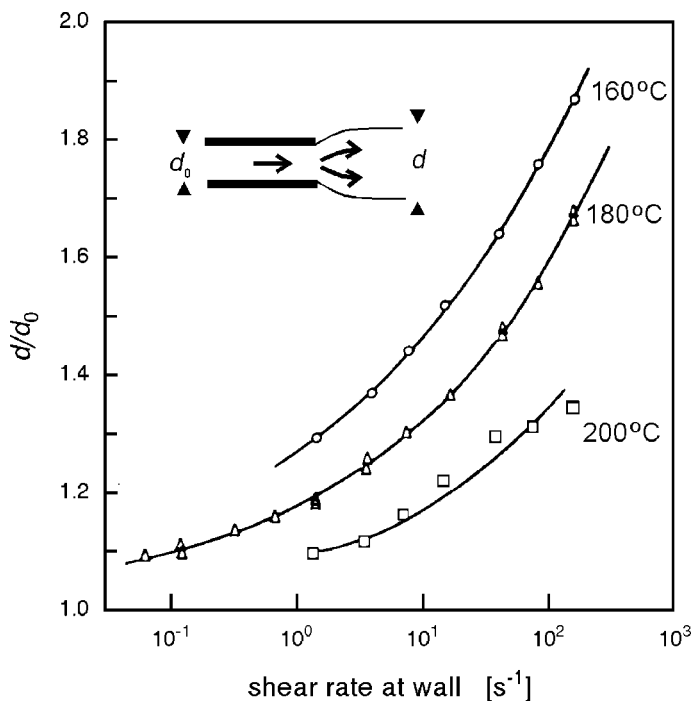


Fig. 9.3. Extrudate thickening observed for a melt of PS for various shear rates and temperatures. Data from Burke and Weiss [111]

the shear thinning demonstrated by the data in Fig. 9.2 originates from induced conformational changes. We learned in the last chapter that, according to Eq. (8.119), the viscosity coefficient is directly related to the time required by the chains for a disentangling. Apparently this time is reduced in flowing melts, as a consequence of a preorientation of chains, which removes some of the entanglements and thus facilitates the disentangling.

That we are considering network mechanics and the non-Newtonian flow properties of melts here in one common chapter is for good reasons: The elastic part in the response of a polymer melt, which is a main cause for its peculiar flow properties, is due to the existing network of entanglements. Understanding the origin of rubber elasticity thus also provides us with a basis for understanding the elastic forces in polymer melts. Some of the microscopic models dealing with the non-Newtonian flow properties of polymer melts actually describe the melt as a network of entanglements that are continuously created and destroyed.

Setting up microscopic models helps in the basic understanding; however, perfect agreement with experimental data is not usually reached. In this situation, a different approach becomes important. One can aim at constructing empirical **constitutive equations** with the objective of having expressions

on hand that can describe the associated stresses for any kind of strain or flow fields. Here, polymer networks and melts can again be treated by the same formalism, which enables finite deformations to be described without the limitations imposed in the linear treatments. This is achieved by the introduction of the **Cauchy strain tensor**, as will be explained in a forthcoming section. Using this tool we will first formulate **Finger's constitutive equation**, which is valid for all isotropic elastic bodies and apply it to rubbers. Then **Lodge's rheological equation of state** of rubber-like liquids will be presented and used for a description of the flow properties of polymer melts.

We begin with a discussion of the physical basis of rubber elasticity.

9.1 Rubber Elasticity

Rubbers find use in a large variety of products such as elastic foams, films, bands, or tires, and possess unique mechanical properties that sets them apart from all other materials. With regard to the microscopic state of order and the local molecular dynamics, rubbers are in the liquid state; their flow properties, however, differ qualitatively from those of fluids. Rubbers are built up of cross-linked polymers, and the cross-links completely suppress any irreversible flow. A piece of rubber can actually be envisaged as one huge polymer molecule of macroscopic size that possesses a high internal flexibility. The cross-links stabilize the shape of a sample, but this shape can be greatly changed by the application of stress. There are opposing forces that balance the external stress; however, compared to the internal forces in crystalline or glassy solids, these are very weak, resulting in elastic moduli four orders of magnitude smaller. As we shall see and discuss in more detail in this chapter, these restoring forces are mainly of entropic nature.

Let us begin by considering a prismatic piece of rubber with orthogonal edges $L_z, L_x = L_y$, and inquire about the force produced by an extension ΔL_z in the z -direction. We will use the extension ratio λ as an independent variable, defined as

$$\lambda = \frac{L_z + \Delta L_z}{L_z} . \quad (9.1)$$

Thermodynamics provides the general tool to be applied in order to obtain the force and we first have to select the appropriate thermodynamic potential. In dealing with a rubber, we choose the Helmholtz free energy, considering that one is usually interested in the force under isothermal conditions and, moreover, that rubbers are practically incompressible. For a piece of rubber that is to be extended in one direction, the Helmholtz free energy \mathcal{F} is a function of λ . Knowing \mathcal{F} , the force f required to obtain an extension λ follows by taking the derivative

$$f = \left(\frac{\partial \mathcal{F}}{\partial \Delta L_z} \right)_{\nu, T} = \frac{1}{L_z} \left(\frac{\partial \mathcal{F}}{\partial \lambda} \right)_{\nu, T} . \quad (9.2)$$

In general, this force is set up of two different contributions

$$f = \frac{1}{L_z} \left(\frac{\partial \mathcal{E}}{\partial \lambda} \right)_{\mathcal{V}, T} - \frac{T}{L_z} \left(\frac{\partial \mathcal{S}}{\partial \lambda} \right)_{\mathcal{V}, T} \quad (9.3)$$

$$= f_{\mathcal{E}} + f_{\mathcal{S}} . \quad (9.4)$$

$f_{\mathcal{E}}$ denotes the energetic contribution and $f_{\mathcal{S}}$ gives the entropic part of the force. Under the condition that the volume \mathcal{V} is not only constant on varying λ , but also on changing T , a temperature-dependent measurement of the force f enables us to make a separate determination of the two parts. The entropic part follows as

$$f_{\mathcal{S}} = -\frac{T}{L_z} \left(\frac{\partial \mathcal{S}}{\partial \lambda} \right)_{\mathcal{V}, T} = \frac{T}{L_z} \left(\frac{\partial^2 \mathcal{F}}{\partial T \partial \lambda} \right)_{\mathcal{V}} = T \left(\frac{\partial f}{\partial T} \right)_{\mathcal{V}, \lambda} \quad (9.5)$$

and the energetic part as

$$f_{\mathcal{E}} = f - T \left(\frac{\partial f}{\partial T} \right)_{\mathcal{V}, \lambda} = -T f \frac{\partial}{\partial T} \ln \left(\frac{f}{T} \right) \Big|_{\mathcal{V}, \lambda} . \quad (9.6)$$

Many kinds of loading experiments have been performed on a large variety of different rubbers and they all agree on the general conclusion that the retractive forces are mainly of entropic origin. This is at least true for the interesting range of moderate to large deformations; at the very beginning of the deformation process, i.e., at low extensions, the energetic part may give more significant contributions. The observations suggest the introduction of the concept of an **ideal rubber**, as a body with the property

$$f_{\mathcal{E}} = 0 ,$$

hence

$$f = f_{\mathcal{S}} .$$

As we shall see, ideal rubbers possess properties that reproduce at least qualitatively the main features in the behavior of real rubbers and thus can provide an approximate first description. Equation (9.6) implies that for an ideal rubber force and temperature are linearly related,

$$f \propto T .$$

Indeed, a strict proportionality to the absolute temperature is the characteristic signature of all forces of entropic origin. Just remember the ideal gas where we find $p \propto T$.

Temperature measurements can be used in order to detect and specify deviations from the ideal case for a given sample. If a piece of rubber is thermally isolated and stretched, its temperature increases. The relation between

an elongational step $d\lambda$ and the induced change dT in temperature follows from

$$d\mathcal{E} = C dT = fL_z d\lambda \tag{9.7}$$

as

$$dT = \frac{fL_z}{C} d\lambda, \tag{9.8}$$

where C denotes the heat capacity. For a non-vanishing energetic contribution to the force, the measured temperature increase becomes smaller. Observed reductions are typically in the order of 10–20%.

One might think at first that the energetic part of the force, $f_{\mathcal{E}}$, can be derived also from a temperature-dependent measurement of the force on the basis of Eq. (9.6). In fact, direct application of this equation is experimentally difficult since the volume does not remain constant under the normally given constant pressure conditions. Indeed, thermal expansion is observed and this is also the reason for the occurrence of a **thermoelastic inversion point**. This shows up in temperature-dependent measurements on rubbers that are kept at a fixed length. Figure 9.4 shows a series of measurements that were performed at different values of λ . For high extensions, we find the signature

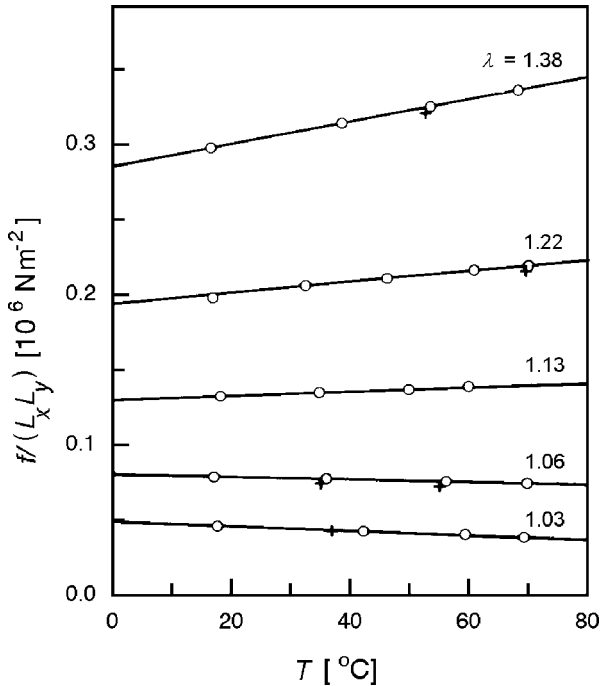


Fig. 9.4. Observation of a thermoelastic inversion point for natural rubber: The temperature dependence of the force at constant extension exhibits a reversal in slope. Measurements by Anthony et al. [112]

of ideal rubbers, i.e., an increase $f \propto T$. For low extensions, on the other hand, thermal expansion overcompensates this effect, and then even leads to a decrease of the force.

Obviously, the entropic forces must originate from the polymer chains that set up the network. It is easy to see the physical basis of the retraction mechanism: When chains are extended on stretching the network, the number of available rotational isomeric states and thus the entropy decreases, and this produces a retractive force. Statistical thermodynamics can describe this effect in more detail, employing model considerations.

9.1.1 The Fixed Junction Model of Ideal Rubbers

Let us first consider a single polymer chain with a mean squared end-to-end distance R_0^2 and inquire about the force that arises if the two ends become separated. As sketched in Fig. 9.5, we assume that one end-group of the chain is located at the origin of a cartesian coordinate system and the second end-group can be moved along the y -axis. In order to keep this second end fixed at a distance y , a non-vanishing force has to be applied. This can be calculated using the same equation as for the macroscopic piece of rubber and follows as

$$f = \frac{\partial f_p}{\partial y} = -T \frac{\partial s_p}{\partial y} . \quad (9.9)$$

Here, f_p and s_p denote the free energy and the entropy of the chain, which, being set up of freely jointed segments, has an invariant internal energy e_p , being associated with the kinetic energy of motion only. Polymer chains in rubbers possess Gaussian properties as in a melt and this can be used for a calculation of the entropy s_p . Applying a basic law of statistical thermodynamics, the entropy can be derived from the partition function, $Z_p(y)$, by

$$s_p = k \ln Z_p(y) . \quad (9.10)$$

In our case, the partition function is determined by the number of conformations available for the chain if the second end is at a distance y . $Z_p(y)$ can be

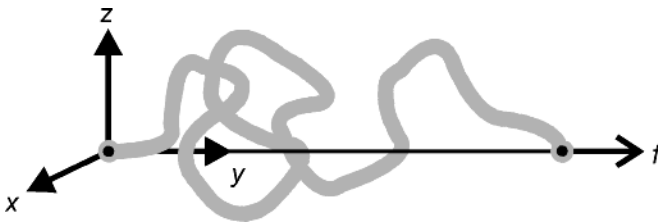


Fig. 9.5. External force f required to keep the ends of a polymer chain at a fixed distance

directly written down. Remember that for a mobile free end the probability distribution in space is given by the Gaussian function (Eq. (2.11))

$$p(x, y, z) = \left(\frac{3}{2\pi R_0^2} \right)^{3/2} \exp - \frac{3(x^2 + y^2 + z^2)}{2R_0^2}$$

with

$$R_0^2 = \langle x^2 + y^2 + z^2 \rangle .$$

This probability distribution just reflects the number of conformations available for the chain if the end-to-end distance vector is kept fixed at (x, y, z) . Therefore, the quantity of interest, $Z_p(y)$, is given by

$$Z_p(y) \propto p(0, y, 0) \propto \exp - \frac{3y^2}{2R_0^2} . \quad (9.11)$$

The entropy follows from Eq. (9.10) as

$$s_p(y) = s_p(0) + k \left(- \frac{3y^2}{2R_0^2} \right) , \quad (9.12)$$

which for the force yields the simple expression

$$f = \frac{3kT}{R_0^2} y = by . \quad (9.13)$$

This is an interesting result. It states that this entropic force increases linearly with the distance between the two end-groups, just as if they were connected by a mechanical spring. The stiffness constant, denoted b , increases with temperature and decreases with increasing size of the chain.

The force disappears only for $y = 0$. This, however, does not imply that the end-groups are coupled together in thermal equilibrium. A harmonic oscillator with a stiffness constant b in contact with a heat bath at a temperature T shows a non-vanishing mean squared displacement $\langle y^2 \rangle$. Straightforward application of Boltzmann statistics yields

$$\langle y^2 \rangle = \frac{kT}{b} . \quad (9.14)$$

Here we obtain correspondingly

$$\langle y^2 \rangle = \frac{R_0^2}{3} , \quad (9.15)$$

which is the result expected for a Gaussian chain.

A rubber represents an ensemble of polymer chains, each one running between two cross-links. The Helmholtz free energy of a sample is related to the distribution function of the conformational states. Since the chains are

not free, the ends being fixed at cross-links, a change in the external shape of a sample necessarily modifies the distribution function. We have to consider this change and calculate the resulting change in free energy.

To keep the treatment simple we include a number of assumptions:

- All the chains composing the network have the same degree of polymerization N , and thus identical values for the stiffness constant $b \propto R_0^{-2} \propto N^{-1}$.
- The conformational distribution in the undeformed state agrees with that of an uncross-linked melt, i.e., is given by an isotropic Gaussian function.
- The cross-link points are fixed within the sample. Any sample deformation becomes directly transferred to the cross-links and changes their positions in an affine manner.

The model so set up is the simplest one to treat and is known as the **fixed junction model** with reference to the last point. Let us refer again to a prismatic piece of rubber, with edges L_x, L_y and L_z , and consider a homogeneous orthogonal deformation, which changes the lengths of the edges as follows:

$$L_x \rightarrow \lambda_1 L_x, \quad (9.16)$$

$$L_y \rightarrow \lambda_2 L_y, \quad (9.17)$$

$$L_z \rightarrow \lambda_3 L_z. \quad (9.18)$$

The extension ratios λ_1, λ_2 and λ_3 also determine the shifts in the locations of all junction points and therefore the changes of the end-to-end distance vectors of all chains. More specifically, the end-to-end distance vector of chain i in the unstrained state

$$\mathbf{r}'_i = \begin{pmatrix} x'_i \\ y'_i \\ z'_i \end{pmatrix}$$

transforms affinely into a vector \mathbf{r}_i in the deformed sample, given by

$$\mathbf{r}_i = \begin{pmatrix} x_i = \lambda_1 x'_i \\ y_i = \lambda_2 y'_i \\ z_i = \lambda_3 z'_i \end{pmatrix}.$$

We wish to calculate the change in entropy resulting from the deformation and first write down the entropy in the stress free state. For a single chain with ends fixed at a distance \mathbf{r}'_i , the entropy is given by Eq. (9.12) replacing y^2 by $r_i'^2$

$$s'_i = s_p(0, 0, 0) - \frac{3k}{2R_0^2} (x_i'^2 + y_i'^2 + z_i'^2). \quad (9.19)$$

To obtain the total entropy of the sample, we include in the summation all chains of a Gaussian ensemble. For a volume \mathcal{V} and a chain density c_p we write

$$\begin{aligned}
 \mathcal{S}' &= \sum_i s'_i = \mathcal{V}c_p \int s_p(x', y', z') p(x', y', z') dx' dy' dz' \\
 &= \mathcal{V}c_p \int \left(s_p(0, 0, 0) - k \frac{3}{2R_0^2} (x'^2 + y'^2 + z'^2) \right) \\
 &\quad \cdot \frac{3}{2R_0^2 \pi} \exp \left[-\frac{3}{2R_0^2} (x'^2 + y'^2 + z'^2) \right] dx' dy' dz' \\
 &= \mathcal{V}c_p \left(s_p(0, 0, 0) - \frac{3k}{2R_0^2} (\langle x'^2 \rangle + \langle y'^2 \rangle + \langle z'^2 \rangle) \right) \\
 &= \mathcal{V}c_p \left(s_p(0, 0, 0) - \frac{3k}{2} \right). \tag{9.20}
 \end{aligned}$$

Next, we derive the entropy in the deformed state, \mathcal{S} . It follows as

$$\begin{aligned}
 \mathcal{S} &= \mathcal{V}c_p \int \left(s_p(0, 0, 0) - k \frac{3}{2R_0^2} (\lambda_1^2 x'^2 + \lambda_2^2 y'^2 + \lambda_3^2 z'^2) \right) \\
 &\quad \cdot \left(\frac{3}{2R_0^2 \pi} \right)^{3/2} \exp \left[-\frac{3}{2R_0^2} (x'^2 + y'^2 + z'^2) \right] dx' dy' dz' \\
 &= \mathcal{V}c_p \left(s_p(0, 0, 0) - \frac{3k}{2R_0^2} (\lambda_1^2 \langle x'^2 \rangle + \lambda_2^2 \langle y'^2 \rangle + \lambda_3^2 \langle z'^2 \rangle) \right) \\
 &= \mathcal{V}c_p \left(s_p(0, 0, 0) - \frac{1}{2} k (\lambda_1^2 + \lambda_2^2 + \lambda_3^2) \right). \tag{9.21}
 \end{aligned}$$

In the calculation of the integral we refer to the distribution function in the initial stress free state and the deformation is accounted for by introducing into the expression for \mathcal{S} the modified single chain entropies. The quantity of interest is the change in entropy, following as

$$\Delta \mathcal{S} = \mathcal{S} - \mathcal{S}' = -\mathcal{V}c_p \frac{k}{2} (\lambda_1^2 + \lambda_2^2 + \lambda_3^2 - 3). \tag{9.22}$$

Consider now the case of an uniaxial extension in z -direction, with an extension ratio λ , i.e.,

$$\lambda_3 = \lambda. \tag{9.23}$$

The induced changes in the two lateral directions are equal to each other,

$$\lambda_1 = \lambda_2. \tag{9.24}$$

Assuming incompressibility, as expressed by

$$\lambda_1 \lambda_2 \lambda_3 = 1, \tag{9.25}$$

we have

$$\lambda_1^2 \lambda = 1. \tag{9.26}$$

Using these relations, we obtain for the change in entropy resulting from an uniaxial extension λ the expression

$$\Delta\mathcal{S} = -\frac{\mathcal{V}c_p k}{2} \left(\frac{2}{\lambda} + \lambda^2 - 3 \right). \quad (9.27)$$

The force follows as above, by taking the derivative of the associated free energy

$$f = -\frac{T}{L_z} \frac{\partial \mathcal{S}}{\partial \lambda} = -\frac{T}{L_z} \frac{\partial \Delta \mathcal{S}}{\partial \lambda} = \frac{\mathcal{V}c_p k T}{L_z} \left(-\frac{1}{\lambda^2} + \lambda \right). \quad (9.28)$$

Replacement of the force by the stress yields a form that is independent of the sample dimensions. The stress in the deformed state is obtained by referring to the actual cross-section

$$\sigma_{zz} = \frac{f}{(L_x L_y / \lambda)}. \quad (9.29)$$

This leads to

$$\sigma_{zz} = c_p k T \left(\lambda^2 - \frac{1}{\lambda} \right). \quad (9.30)$$

Sometimes, for direct comparisons with measured load-extension curves, the **nominal stress**, sometimes also called the **engineering stress** and denoted $\hat{\sigma}_{zz}$ is used. Here the force is referred to the cross-section $L_x L_y$ in the initial state, giving

$$\hat{\sigma}_{zz} = \frac{f}{L_x L_y} = c_p k T \left(\lambda - \frac{1}{\lambda^2} \right). \quad (9.31)$$

As we can see, the model considerations result in a short analytical expression for the stress–strain relationship of an uniaxially deformed ideal rubber. Equations (9.30) and (9.31) are valid for all values of λ , including $\lambda > 1$ and $\lambda < 1$, both extensions and compressions, respectively. It is important to note that apart from T the stress depends on the chain density c_p only. The fact that there is no explicit effect of the degree of polymerization implies that our initial assumption of a uniform value of N for the chains between cross-links is not a necessary prerequisite for the result and can therefore be omitted. As long as c_p is constant, the same elastic force emerges for any distribution of N ; each chain gives in the isotropic average an equal contribution to the stress, which is independent of the length. Figure 9.6 shows the dependence as given by Eq. (9.31). In the limit of large extensions the retractive force increases linearly with λ , while in the compression range the behavior is mostly non-linear. Clearly the pressure must diverge for $\lambda \rightarrow 0$. Per definition, the elastic modulus E is related to small strains only, being determined by the slope at the origin, $\lambda = 1$. One obtains

$$E = \frac{d\sigma_{zz}}{de_{zz}}(e_{zz} = 0) = \frac{d\sigma_{zz}}{d\lambda}(\lambda = 1) = \frac{d\hat{\sigma}_{zz}}{d\lambda}(\lambda = 1) = 3c_p k T. \quad (9.32)$$

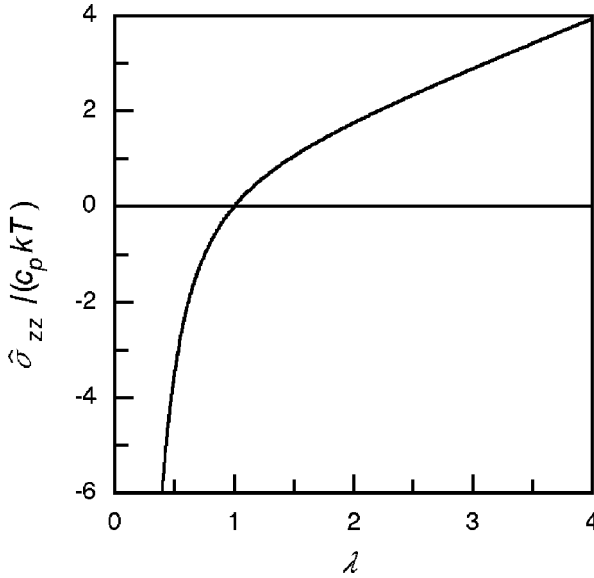


Fig. 9.6. Uniaxially deformed ideal rubber: Dependence of the nominal stress ($\hat{\sigma}_{zz}$) on the extension ratio (λ) according to Eq. (9.31)

We will compare these model predictions with load-deformation curves of real rubbers, but beforehand a remark is necessary. It is clear that there is no basis for a comparison of absolute values. These depend in the model on the density c_p of chains between chemical cross-links, however, in a rubber not only the chemical junction points, but also the entanglements act as cross-links. In a polymer melt, in the region of the rubbery plateau, the latter are indeed the only ones present. Chemical cross-linking stabilizes the topological cross-links, because these become trapped if a permanent network is created. The relative weight of the contribution of the entanglements to the force can be estimated, in the simplest way by comparing the retractive forces before and after the chemical cross-linking of a melt. As it turns out, chain entangling is even dominant for the usual low cross-link densities and accounts for the larger part of the total force. Entanglements differ from the chemical cross-links in that they are not fixed and may slip along chains, which diminishes their efficiency. Actually, a certain reduction in efficiency on similar grounds is also to be anticipated for the chemical cross-links. We have assumed a perfect fixing in space; however, in reality, the junction points fluctuate, performing a restricted Brownian motion around their mean positions (which is, in fact, accounted for in an improved model, known as the ‘phantom network’). Hence, in conclusion, one normally has to relinquish a prediction of absolute stress values and reduce comparisons with models to the shape of measured curves. Values for c_p , as derived from a data fitting, have to be addressed as an **effective density** of active elements. c_p may be formally translated into

a **mean molar mass of chains between junction points**, denoted M_{eff} , through

$$c_p = \frac{\rho}{M_{\text{eff}}} N_L \quad (9.33)$$

but M_{eff} is just another empirical parameter. It depends in an unpredictable manner on the cross-link density, the functionality of the cross-linking groups; they can couple together the ends of three, four or even more chains, the chain stiffness, etc.

We should now look at two sets of data, presented previously in Fig. 9.1 and now in Fig. 9.7. Both figures include adjusted model curves. It is to be noted that the data in Fig. 9.7, which cover the range of moderate extensions together with compression states, are remarkably well-represented. On the other hand, pronounced differences show up in Fig. 9.1, which goes to large extensions. The reason for the discrepancy becomes clear when recalling a basic property of the Gaussian model chain. As pointed out previously (Sect. 2.3.1), the Gaussian description implies an infinite contour length of chains; however, in reality their lengths are finite. Each chain possesses a maximum extension as given by its length in the straight helical conformation. Obviously, this limitation must produce at larger extensions deviations from the Gaussian behavior and this is the cause of the observed increase in stress. In fact, it is possible to account for this effect and so to improve the agreement. One has to replace the Gaussian distribution in Eq. (9.11) by real distribution functions,

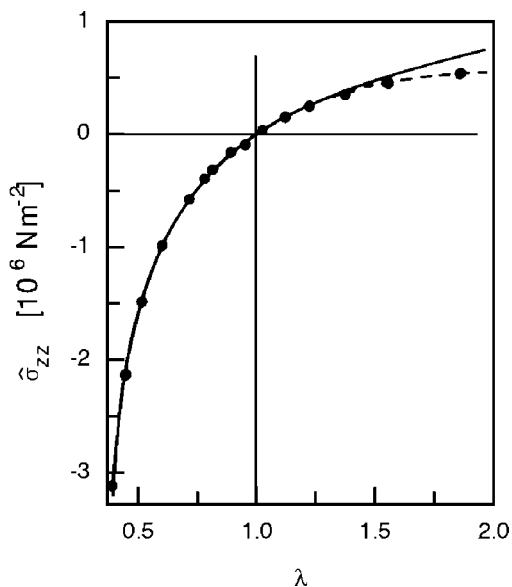


Fig. 9.7. Extension ($\lambda > 1$)-compression ($\lambda < 1$) curve of natural rubber, compared to the theoretical function Eq. (9.31) derived for an ideal rubber (*continuous line*). Data from Treloar [109]

either by the exact distribution function given in Sect. 2.3.1 or a suitable approximation and then modify the entropy calculations correspondingly. Thus corrected curves usually provide a satisfactory representation of measured curves even in the range of larger extensions.

Last but not least, models that assume ideal behavior do not account for the always present energetic effects. Therefore, a comprehensive representation of thermoelastic data encompassing a larger temperature range, like the ones displayed in Fig. 9.4, cannot be achieved with these models alone.

Regarding these complications, one might feel that attempts to account for all the remaining deviations by proper modifications of statistical thermodynamic models of ideal rubbers do not look very promising. In this situation, a certain drawback is to be considered as appropriate. Rather than searching for a detailed microscopic understanding, one can look for phenomenological treatments enabling an empirical representation of the mechanical properties of a given rubbery material. One might think at first that this is a simpler goal to achieve. However, even this is not a trivial task, in particular if one's aim is a comprehensive description of all modes of deformation employing only a small number of material parameters. This is exactly the desire of engineers who need reliable and directly applicable material functions for working with rubbers. Continuum mechanics provides appropriate tools for generally dealing with large deformations, not only those found in rubbers, but also those encountered in flowing polymer melts. In the next section, we will briefly discuss the basis of these concepts.

9.1.2 The Cauchy Strain Tensor

Elasticity theory for solids is formulated with the assumption that strains remain small. One then finds the linear relations between stress and strain as they are described by Hooke's law. For rubbers, deformations are generally large and the linear theory then becomes invalid. We have to ask how strain can be characterized in this general case and how it can be related to the applied stress.

First, let us recall the definition of stress. In deformed rubbers the state of stress can be described in the same manner as in the case of small deformations of solids, by giving the stress tensor $\boldsymbol{\sigma} = (\sigma_{ij})$. The meaning of the components σ_{ij} is indicated in Fig. 9.8. Imagine that we pick out a cubic volume element in the deformed body at the position \mathbf{r} , with edges parallel to the laboratory fixed cartesian coordinate system. Then $\boldsymbol{\sigma}$ specifies the forces that the material outside the cube exerts through the surfaces on the particles in the interior. More specifically, component σ_{ij} denotes the force per unit area acting along the j -axis on the face oriented perpendicular to the i -axis. Knowledge of $\boldsymbol{\sigma}$ also enables us to calculate the force \mathbf{f} acting on any plane with normal vector \mathbf{n} . \mathbf{f} follows as the product

$$\mathbf{f} = \boldsymbol{\sigma} \times \mathbf{n} . \quad (9.34)$$

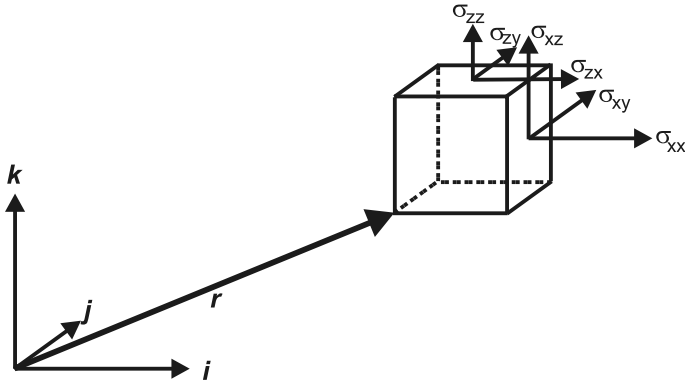


Fig. 9.8. Description of the stress around a material point at \mathbf{r} in a deformed body: Stress tensor components σ_{ij} specifying the forces acting on the faces of a cubic volume element

The stress tensor is symmetric, i.e.,

$$\sigma_{ij} = \sigma_{ji} , \quad (9.35)$$

since static equilibrium is only attained for a vanishing torque on the cube. Sometimes, in special cases, the stress tensor is calculated for the forces being referred to the cross-section in the undeformed state. For rubbers under a large strain, this leads to altered values and these, as mentioned earlier, are called nominal or engineering stresses.

A deformation of a body of rubber displaces all material points in the sample. There is a one-to-one correspondence between the locations of a material point in the deformed and the unstrained body. We again refer to the laboratory-fixed coordinate system and describe the relation between the locations in the deformed state

$$\mathbf{r} = \begin{pmatrix} x \\ y \\ z \end{pmatrix}$$

and the initial natural state

$$\mathbf{r}' = \begin{pmatrix} x' \\ y' \\ z' \end{pmatrix}$$

by the displacement function

$$\mathbf{r}'(\mathbf{r}) .$$

Choosing this function rather than the reverse relation $\mathbf{r}(\mathbf{r}')$ implies that one refers to the deformed body in the description of the strain, in agreement with the description of the stress.

Not all functions $\mathbf{r}'(\mathbf{r})$ result in stress. If a sample is translated or rotated as a rigid body, no stress arises. Clearly, the general prerequisite for stress is a change in internal distances. For a check one can pick out a material point at \mathbf{r} , select a neighboring material point at $\mathbf{r} + d\mathbf{r}$ and inquire about the change in their distance on removing the load. If $d\mathbf{r}$ transforms into $d\mathbf{r}'$, the difference of the squares of the lengths is given by

$$d\mathbf{r}' \cdot d\mathbf{r}' - d\mathbf{r} \cdot d\mathbf{r} . \tag{9.36}$$

As the relation between $d\mathbf{r}'$ and $d\mathbf{r}$ is determined by the vector gradient of the mapping function $\mathbf{r}'(\mathbf{r})$,

$$d\mathbf{r}' = \frac{\partial \mathbf{r}'}{\partial \mathbf{r}} \cdot d\mathbf{r} , \tag{9.37}$$

with

$$\left(\frac{\partial \mathbf{r}'}{\partial \mathbf{r}} \right)_{ij} = \frac{\partial r'_i}{\partial r_j} , \tag{9.38}$$

we can write for the squared lengths difference

$$\begin{aligned} dr'_i dr'_i - dr_i dr_i &= \frac{\partial r'_i}{\partial r_j} dr_j \frac{\partial r'_i}{\partial r_k} dr_k - dr_i dr_i \\ &= dr_j (C_{jk} - \delta_{jk}) dr_k . \end{aligned} \tag{9.39}$$

Here, we have introduced a tensor \mathbf{C} , defined as

$$C_{jk} = \frac{\partial r'_i}{\partial r_j} \frac{\partial r'_i}{\partial r_k} . \tag{9.40}$$

\mathbf{C} is called the **Cauchy strain tensor**. Any deformation, it may be large or small, homogeneous or non-uniform, can be characterized by a space-dependent function $\mathbf{C}(\mathbf{r})$. Knowing $\mathbf{C}(\mathbf{r})$, the local extensions in all directions can be obtained for each material point of a deformed body just by a calculation of the two-fold product Eq. (9.39). Recall that we have introduced the Cauchy strain tensor by a two-step procedure based on the complete description of the deformation by the displacement function $\mathbf{r}'(\mathbf{r})$, going first to the deformation gradient function $\partial \mathbf{r}' / \partial \mathbf{r}$ and then proceeding to $\mathbf{C}(\mathbf{r})$. The first step eliminated rigid translations and the second step the rotations, overall as well as local ones. $\mathbf{C}(\mathbf{r})$ therefore does indeed include only those parts of the body motion that are true deformations giving rise to the development of stress. For homogeneous states of strain, $\mathbf{C}(\mathbf{r})$ reduces to one unique tensor and, in the following, we will deal with this simpler case only.

It is easy to see the significance of the various components of the Cauchy strain tensor and we refer here to Fig. 9.9. First consider the infinitesimal

differential vector $d\mathbf{r}_1$ parallel to the x -axis. On unloading it transforms into $d\mathbf{r}'_1$, which has the squared length

$$d\mathbf{r}'_1 \cdot d\mathbf{r}'_1 = \left(\left(\frac{\partial x'}{\partial x} \right)^2 + \left(\frac{\partial y'}{\partial x} \right)^2 + \left(\frac{\partial z'}{\partial x} \right)^2 \right) dx^2. \quad (9.41)$$

The right-hand side equals the product $C_{11} dx^2$. Hence, generalizing this result, the diagonal elements C_{ii} describe the length changes of the edges of a cubic volume element, oriented parallel to the axes of the laboratory fixed cartesian coordinate system, the changes being expressed in terms of the squared length ratios.

Second, consider the angle θ'_{13} enclosed by $d\mathbf{r}'_1$ and $d\mathbf{r}'_3$, the transforms of $d\mathbf{r}_1 = i dx$, $d\mathbf{r}_3 = j dy$. Its cosine follows from

$$|d\mathbf{r}'_1| |d\mathbf{r}'_3| \cos \theta'_{13} = d\mathbf{r}'_1 \cdot d\mathbf{r}'_3. \quad (9.42)$$

The right-hand side agrees with the product $C_{13} dx dy$. Hence, we obtain

$$\cos \theta'_{13} = \frac{C_{13}}{(C_{11} C_{33})^{1/2}} \quad (9.43)$$

and learn from this example that the non-diagonal elements of the Cauchy strain tensor describe the changes of the three rectangular angles of the cube.

The Cauchy strain tensor is symmetric by definition. Therefore, it can be converted into a diagonal form by an appropriate rotation of the coordinate system. We deal with these conditions as indicated in Fig. 9.9, by attaching, to each selected material point, a triple of orthogonal infinitesimal distance

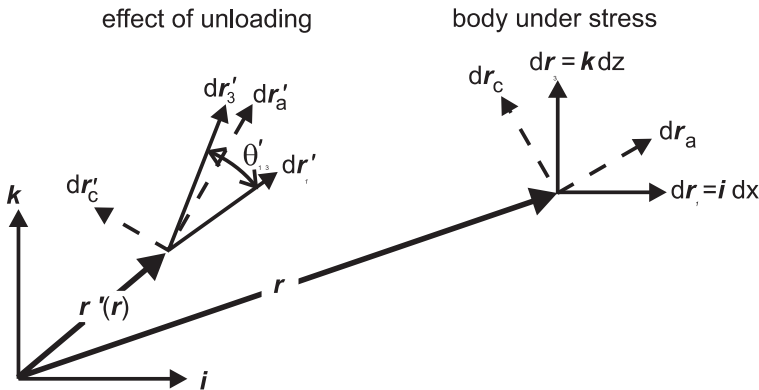


Fig. 9.9. Notions used in the definition of the Cauchy strain tensor: The material point at r in the deformed body with its neighborhood shifts on unloading to the position r' . The orthogonal infinitesimal vectors $d\mathbf{r}_1$ and $d\mathbf{r}_3$ in the deformed state transform into the oblique pair of vectors $d\mathbf{r}'_1$ and $d\mathbf{r}'_3$. Orthogonality is preserved for the vectors $d\mathbf{r}_a$, $d\mathbf{r}_c$ oriented along the principal axes

vectors $d\mathbf{r}_a, d\mathbf{r}_b$ and $d\mathbf{r}_c$, oriented parallel to the **principal axes**, which diagonalize the Cauchy tensor. The zero non-diagonal elements of the Cauchy tensor in the principal axes system imply that all angles θ'_{ij} , enclosed by the transforms of the infinitesimal distance vectors, designated as $d\mathbf{r}'_a, d\mathbf{r}'_b$ and $d\mathbf{r}'_c$, are 90° . Hence, on unloading the orthogonal triple $d\mathbf{r}_a, d\mathbf{r}_b, d\mathbf{r}_c$ may become rotated and the three vectors may change their lengths; orthogonality, however, is preserved. Previously we introduced factors λ_i as denoting the extension ratios in orthogonal deformations, with reference to the natural unstrained state (Eqs. (9.16)–(9.18)). The Cauchy strain tensor in diagonal form includes the reciprocal values λ_i^{-1} as

$$C_{ij} = \delta_{ij} \lambda_i^{-2} . \tag{9.44}$$

Instead of employing the Cauchy strain tensor one can also utilize the **Eulerian strain tensor** defined as

$$2E_{ij} = \delta_{ij} - C_{ij} . \tag{9.45}$$

In the limit of infinitesimal deformations the Eulerian strain tensor becomes identical with the strain tensor used in the linear elasticity theory, as can be easily shown. The components e_{ij} of the linear strain tensor are defined as

$$e_{ij} = \frac{1}{2} \left(\frac{\partial s_i}{\partial r'_j} + \frac{\partial s_j}{\partial r'_i} \right) , \tag{9.46}$$

whereby \mathbf{s} denotes the shift of the material point \mathbf{r}' in the undeformed state induced by the load, i.e.,

$$\mathbf{s} = \mathbf{r} - \mathbf{r}' . \tag{9.47}$$

For small deformations it makes no difference, whether the undeformed or the deformed body is chosen as the reference frame. We can therefore also write

$$e_{ij} = \frac{1}{2} \left(\frac{\partial s_i}{\partial r_j} + \frac{\partial s_j}{\partial r_i} \right) . \tag{9.48}$$

E_{ij} may be rewritten as

$$\begin{aligned} E_{ij} &= \frac{1}{2} \left(\delta_{ij} - \frac{\partial(r_k - s_k)}{\partial r_i} \frac{\partial(r_k - s_k)}{\partial r_j} \right) \\ &= \frac{1}{2} \left(\delta_{ij} - \left(\delta_{ki} - \frac{\partial s_k}{\partial r_i} \right) \left(\delta_{kj} - \frac{\partial s_k}{\partial r_j} \right) \right) \\ &= \frac{1}{2} \left(\frac{\partial s_i}{\partial r_j} + \frac{\partial s_j}{\partial r_i} - \frac{\partial s_k}{\partial r_i} \frac{\partial s_k}{\partial r_j} \right) . \end{aligned} \tag{9.49}$$

Hence, in linear approximation, neglecting in the limit of infinitesimal deformations the second order term, we do indeed obtain

$$E_{ij} = e_{ij} . \tag{9.50}$$

9.1.3 Finger's Constitutive Equation

We are now in the position to formulate empirical stress-strain relations in the form of **constitutive equations**. The Cauchy strain tensor focuses on those parts in the deformation of a body that produce stress. We can therefore assume that the stress, $\boldsymbol{\sigma}$, is a function of the Cauchy strain tensor, \mathbf{C} , only. As this basic assumption alone is certainly too general for a promising approach, one may wonder if there are any restrictions with regard to the possible form of the functional dependence. In fact, theoretical analysis has led to the conclusion that such restrictions do exist. The problem aroused much interest as early as at the end of the last century and a main result was due to Finger. He succeeded in deriving a constitutive equation that is generally valid for all elastic isotropic bodies. The term 'elastic' is here used in the general sense, implying that the body reacts in a well-defined way to an externally applied force and returns completely to its natural state upon unloading. Finger arrived at the conclusion that the stress-strain relation for this kind of general elastic or, as they are sometimes called, **hyperelastic** bodies depends on one scalar function only, namely the relation between the free energy density and the state of strain as characterized by the **strain invariants**.

As any second rank tensor, the Cauchy strain tensor possesses three invariants. These are expressions in terms of the tensor components C_{ij} , which remain invariant under all rotations of the coordinate system. The three invariants of the Cauchy strain tensor are given by the following expressions:

$$I_C = C_{11} + C_{22} + C_{33} , \quad (9.51)$$

$$II_C = C_{11}C_{22} + C_{22}C_{33} + C_{33}C_{11} , \\ - C_{12}C_{21} - C_{13}C_{31} - C_{23}C_{32} , \quad (9.52)$$

$$III_C = \text{Det } \mathbf{C} . \quad (9.53)$$

For the diagonal form Eq. (9.44), they reduce to

$$I_C = \lambda_1^{-2} + \lambda_2^{-2} + \lambda_3^{-2} , \quad (9.54)$$

$$II_C = \lambda_1^{-2}\lambda_2^{-2} + \lambda_2^{-2}\lambda_3^{-2} + \lambda_3^{-2}\lambda_1^{-2} , \quad (9.55)$$

$$III_C = \lambda_1^{-2}\lambda_2^{-2}\lambda_3^{-2} . \quad (9.56)$$

There are different choices for the invariants since any combination gives new invariant expressions, but the most common is the one cited here. As the free energy density depends on the local strain only and, being a scalar quantity, must be invariant under all rotations of the coordinate system, one can readily assume for the free energy density a functional dependence

$$f(I_C, II_C, III_C) . \quad (9.57)$$

With these ingredients **Finger's constitutive equation** can be formulated. It relates the Cauchy strain tensor to the stress tensor as

$$\boldsymbol{\sigma} = c_{-1}\mathbf{C}^{-1} + c_0\mathbf{1} + c_1\mathbf{C} . \quad (9.58)$$

\mathbf{C}^{-1} denotes the inverse of the Cauchy tensor, $\mathbf{1}$ is the unit tensor. c_{-1}, c_0, c_1 describe functions of the three invariants and these are directly related to the free energy density. The relations are

$$c_{-1} = 2III_C^{3/2} \frac{\partial f}{\partial III_C}, \tag{9.59}$$

$$c_0 = -2III_C^{1/2} \left(II_C \frac{\partial f}{\partial II_C} + III_C \frac{\partial f}{\partial III_C} \right), \tag{9.60}$$

$$c_1 = -2III_C^{1/2} \frac{\partial f}{\partial I_C}. \tag{9.61}$$

Finger derived this equation on the basis of general arguments. As we can see, it provides us with a powerful tool: Once one succeeds in determining the strain dependence of the free energy of a body, the stresses produced in all kinds of deformations can be predicted.

There is an alternative form of Finger’s equation, which gives us a choice and is, indeed, to be preferred when dealing with rubbers. We introduce the **Finger strain tensor** \mathbf{B} , being defined as the reciprocal of the Cauchy strain tensor

$$\mathbf{B} = \mathbf{C}^{-1}. \tag{9.62}$$

The substitution of \mathbf{C} by \mathbf{B} implies, as the main point, that one is now choosing the invariants of \mathbf{B} as independent variables, rather than those associated with \mathbf{C} . The second form of Finger’s constitutive equation is

$$\boldsymbol{\sigma} = b_1 \mathbf{B} + b_0 \mathbf{1} + b_{-1} \mathbf{B}^{-1} \tag{9.63}$$

with

$$b_1 = \frac{2}{III_B^{1/2}} \frac{\partial f}{\partial I_B}, \tag{9.64}$$

$$b_0 = \frac{2}{III_B^{1/2}} \left(II_B \frac{\partial f}{\partial II_B} + III_B \frac{\partial f}{\partial III_B} \right), \tag{9.65}$$

$$b_{-1} = -2 \cdot III_B^{1/2} \frac{\partial f}{\partial II_B}. \tag{9.66}$$

Because the directions of the principal axes of \mathbf{B} and \mathbf{C} must coincide, the diagonal form of the Finger strain tensor is simply

$$B_{ij} = \lambda_i^2 \delta_{ij}. \tag{9.67}$$

The invariants then follow as

$$I_B = \lambda_1^2 + \lambda_2^2 + \lambda_3^2, \tag{9.68}$$

$$II_B = \lambda_1^2 \lambda_2^2 + \lambda_2^2 \lambda_3^2 + \lambda_3^2 \lambda_1^2, \tag{9.69}$$

$$III_B = \text{Det } \mathbf{B}. \tag{9.70}$$

Whether to use the first or the second form of Finger's constitutive equation is just a matter of convenience, depending on the expression obtained for the free energy density in terms of the one or the other set of invariants. For the system under discussion, a body of rubbery material, the choice is clear: The free energy density of an ideal rubber is most simply expressed when using the invariants of the Finger strain tensor. Equation (9.22), giving the result of the statistical mechanical treatment of the fixed junction model, exactly corresponds to

$$f = \frac{G}{2}(I_B - 3) . \quad (9.71)$$

As we can see, the second and third invariants, II_B and III_B , are not included. The third invariant relates generally to the relative volume change. For incompressible bodies it is equal to unity,

$$III_B = \lambda_1^2 \lambda_2^2 \lambda_3^2 = 1 , \quad (9.72)$$

and can, therefore, be omitted in the further treatments. When writing down Eq. (9.71) we introduced a parameter G . As it will turn out, G denotes the shear modulus.

Knowing f , we can formulate the constitutive equation of an ideal rubber. Since only b_1 gives a contribution, we simply obtain

$$\boldsymbol{\sigma} = G\mathbf{B} . \quad (9.73)$$

This result, however, is not yet complete. For an incompressible solid like a rubber, superposition of a hydrostatic pressure onto the other applied external forces leaves the shape of the sample and thus the state of strain unchanged. We can account for this arbitrariness by including the undetermined hydrostatic pressure, denoted p , as a further component in the equation and rewrite it as

$$\boldsymbol{\sigma} = G\mathbf{B} - p\mathbf{1} . \quad (9.74)$$

The constitutive equation thus yields stresses that are indeterminate to the extent of an arbitrary hydrostatic pressure.

The same modification is necessary when dealing in general with incompressible hyperelastic bodies. Introducing the additional term in Finger's constitutive equation, Eq. (9.63), and regarding the absence of III_B , we obtain

$$\boldsymbol{\sigma} = 2\frac{\partial f}{\partial I_B}\mathbf{B} - 2\frac{\partial f}{\partial II_B}\mathbf{B}^{-1} - p\mathbf{1} . \quad (9.75)$$

This is now a constitutive equation, which looks appropriate for our purposes. Being generally valid for all incompressible elastic bodies, it can be applied in particular for the treatment of real rubbers.

So far, we have been concerned with uniaxial deformations of rubbers only. Utilizing Eq. (9.75) we can analyze any kind of deformation in a straightforward manner and, in particular, the important case of a simple shear. To

begin with, we check once again for the results obtained for the known case of uniaxial strain or compression of an ideal rubber. Here, the transformation equations are

$$z' = \lambda^{-1}z, \tag{9.76}$$

$$x' = \lambda^{1/2}x, \tag{9.77}$$

$$y' = \lambda^{1/2}y. \tag{9.78}$$

The Cauchy strain tensor follows from Eq. (9.40) as

$$\mathbf{C} = \begin{pmatrix} \lambda & 0 & 0 \\ 0 & \lambda & 0 \\ 0 & 0 & \lambda^{-2} \end{pmatrix} \tag{9.79}$$

and the Finger tensor therefore as

$$\mathbf{B} = \begin{pmatrix} \lambda^{-1} & 0 & 0 \\ 0 & \lambda^{-1} & 0 \\ 0 & 0 & \lambda^2 \end{pmatrix}. \tag{9.80}$$

The inversion of the Cauchy tensor, which is necessary when deriving the Finger tensor, is trivial in this case. For non-orthogonal deformations this is more complicated. Here one can make use of a direct expression for the components of \mathbf{B} , which has the form

$$B_{ij} = \frac{\partial r_i}{\partial r'_k} \frac{\partial r_j}{\partial r'_k}. \tag{9.81}$$

The proof of Eq. (9.81) is straightforward. We have

$$B_{ij}C_{jk} = \frac{\partial r_i}{\partial r'_l} \frac{\partial r_j}{\partial r'_l} \frac{\partial r'_m}{\partial r_j} \frac{\partial r'_m}{\partial r_k}. \tag{9.82}$$

Since

$$\frac{\partial r'_m}{\partial r_j} \frac{\partial r_j}{\partial r'_l} = \frac{\partial r'_m}{\partial r'_l} = \delta_{ml} \tag{9.83}$$

we indeed obtain

$$B_{ij}C_{jk} = \frac{\partial r_i}{\partial r'_l} \frac{\partial r'_l}{\partial r_k} = \delta_{ik}. \tag{9.84}$$

Due to the unknown hydrostatic pressure, p , the individual normal stresses σ_{ii} are indeterminate. However, the normal stress differences are well-defined. Consider the difference between σ_{zz} and σ_{xx} . Insertion of the Finger strain tensor associated with uniaxial deformations, Eq. (9.80), in the constitutive equation (9.74) yields

$$\sigma_{zz} - \sigma_{xx} = G(\lambda^2 - \lambda^{-1}). \tag{9.85}$$

As σ_{xx} vanishes, the result is in agreement with the previous Eq. (9.30). A comparison reveals the equality

$$G = c_p kT . \quad (9.86)$$

In the uniaxial deformation mode both lateral dimensions change. Other types of strain are obtained if one of the lateral edges is kept fixed. **Shear** is the general name used for this group of deformations. We first consider an orthogonal deformation known as **pure shear**, which corresponds to the following transformation relations:

$$z' = \lambda^{-1} z , \quad (9.87)$$

$$x' = \lambda x , \quad (9.88)$$

$$y' = y . \quad (9.89)$$

Figure 9.10 schematically depicts this deformation, together with the two other modes considered here, uniaxial loading and simple shear. For all modes the drawings indicate the changes in shape of a cubic volume element cut out in the stressed state, resulting from an unloading. The Finger strain tensor associated with pure shear has the form

$$\mathbf{B} = \begin{pmatrix} \lambda^{-2} & 0 & 0 \\ 0 & 1 & 0 \\ 0 & 0 & \lambda^2 \end{pmatrix} . \quad (9.90)$$

Insertion of \mathbf{B} in Eq. (9.74) results in the following expressions for the normal stress differences:

$$\sigma_{zz} - \sigma_{xx} = G(\lambda^2 - \lambda^{-2}) , \quad (9.91)$$

$$\sigma_{zz} - \sigma_{yy} = G(\lambda^2 - 1) , \quad (9.92)$$

$$\sigma_{yy} - \sigma_{xx} = G(1 - \lambda^{-2}) . \quad (9.93)$$

Hence, for this mode we find non-vanishing values for all three normal stress differences.

As our third example we consider the important case of **simple shear**, in the form indicated in Fig. 9.10. The transformation relations are

$$x' = -\gamma \cdot z + x , \quad (9.94)$$

$$y' = y , \quad (9.95)$$

$$z' = z . \quad (9.96)$$

Here, the symbol γ stands for the shear strain, defined as

$$\gamma = \tan \left(\theta'_{xz} - \frac{\pi}{2} \right) \quad (9.97)$$

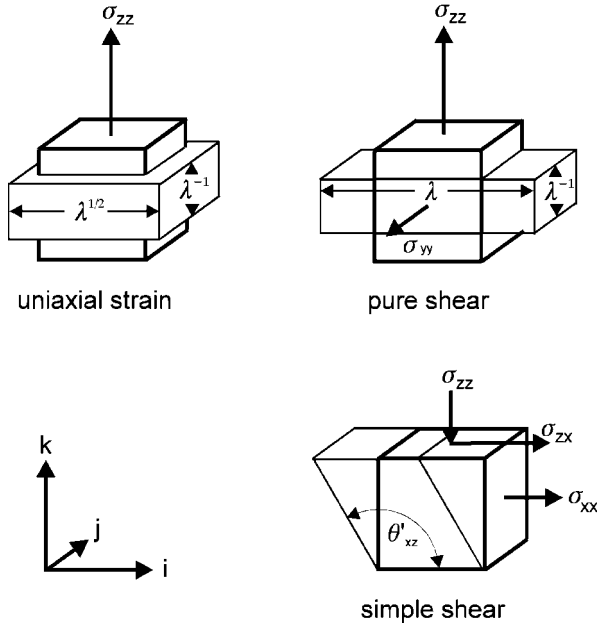


Fig. 9.10. Several modes of deformation of a rubber. Changes in shape of a cubic volume element picked out in the stressed state, as it results from the unloading. Acting components of stress are indicated

(γ is identical with the component e_{zx} of the linear strain tensor). Application of Eq. (9.81) yields the associated Finger strain tensor

$$\mathbf{B} = \begin{pmatrix} 1 + \gamma^2 & 0 & \gamma \\ 0 & 1 & 0 \\ \gamma & 0 & 1 \end{pmatrix}. \tag{9.98}$$

Use in Eq. (9.74) gives

$$\sigma_{zx} = G\gamma, \tag{9.99}$$

$$\sigma_{xx} - \sigma_{zz} = G\gamma^2, \tag{9.100}$$

$$\sigma_{yy} - \sigma_{zz} = 0. \tag{9.101}$$

These are noteworthy results. First, we find a linear relation between the shear stress σ_{zx} and the shear strain γ , which is unlimited. Thus, for this special kind of load, linearity is retained up to arbitrarily large deformations. We can also identify G , introduced at first as an empirical constant, as indeed representing the shear modulus. The predicted linearity is largely corroborated by the experimental findings. Figure 9.11 depicts the dependence $\sigma_{zx}(\gamma)$ as measured for a sample of natural rubber. A steady increase in shear strain is observed, which is essentially linear, apart from a slight curvature at moderate deformations.

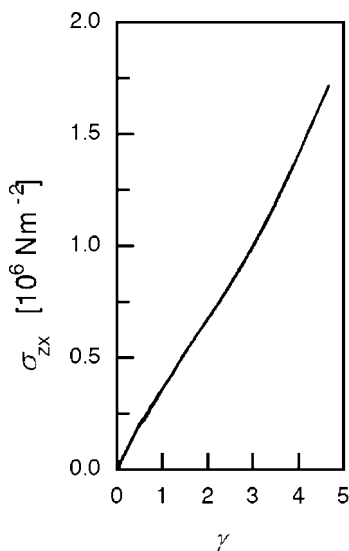


Fig. 9.11. Shear stress–shear strain curve observed for a sample of natural rubber during simple shear. Data of Treloar [109]

Non-linearity shows up in the second finding. We observe that simple shear is accompanied by the development of a non-vanishing normal stress difference $\sigma_{xx} - \sigma_{zz}$. The effect is non-linear since it is proportional to the square of γ . The result tells us that in order to establish a simple shear deformation in a rubber, application of shear stress alone is insufficient. One has to apply in addition either pressure onto the shear plane ($\sigma_{zz} < 0$) or a tensile force onto the plane normal to the x -axis ($\sigma_{xx} > 0$), or an appropriate combination of both. The difference $\sigma_{xx} - \sigma_{zz}$ is called the primary normal stress difference; likewise $\sigma_{yy} - \sigma_{zz}$ is commonly designated as the secondary normal stress difference. As we can see, the latter vanishes for an ideal rubber.

Having found such a simple description for ideal rubbers, enabling us to make predictions of the stress for all kinds of deformations in a straightforward way, one might presume that the modifications in behavior, as they are observed for real rubbers, can be accounted for by suitable alterations performed in the framework of the general equation for incompressible solids Eq. (9.75). In a first step one may consider the effects of an inclusion of the second term proportional to \mathbf{B}^{-1} in the simplest possible form, by assuming constant values for both, the derivative $\partial f / \partial I_B$ and the derivative $\partial f / \partial II_B$. Such a choice is equivalent to a free energy function

$$f = \beta_1(I_B - 3) + \beta_2(II_B - 3), \quad (9.102)$$

where β_1 and β_2 denote the two constants. The resulting constitutive equation is

$$\boldsymbol{\sigma} = -p\mathbf{1} + 2\beta_1\mathbf{B} - 2\beta_2\mathbf{B}^{-1}. \quad (9.103)$$

In the consideration of uniaxial extensions we can proceed in analogous manner as above, and we are led to the result

$$\sigma_{zz} - \sigma_{xx} = 2\beta_1(\lambda^2 - \lambda^{-1}) - 2\beta_2(\lambda^{-2} - \lambda) \tag{9.104}$$

$$= (2\beta_1\lambda + 2\beta_2)(\lambda - \lambda^{-2}) . \tag{9.105}$$

For a derivation of the state of stress under simple shear, we need the form of $\mathbf{B}^{-1} = \mathbf{C}$. It follows by applying Eq. (9.40) to Eqs. (9.94) to (9.96). The result is

$$\mathbf{B}^{-1} = \begin{pmatrix} 1 & 0 & -\gamma \\ 0 & 1 & 0 \\ -\gamma & 0 & 1 + \gamma^2 \end{pmatrix} . \tag{9.106}$$

Equation (9.103) then yields

$$\sigma_{zx} = (2\beta_1 + 2\beta_2)\gamma , \tag{9.107}$$

$$\sigma_{xx} - \sigma_{zz} = (2\beta_1 + 2\beta_2)\gamma^2 , \tag{9.108}$$

$$\sigma_{yy} - \sigma_{zz} = 2\beta_2\gamma^2 . \tag{9.109}$$

For simple shear, we have thus again obtained linearity for σ_{zx} , as for ideal rubbers, but now with non-vanishing values for both the primary and the secondary normal stress difference.

The suggestion to expand the treatment in this way is due to Mooney. It was readily accepted and applied with success for the description of tensile stress–strain curves. Figure 9.12 presents an example, which also reveals, however, a major deficiency. Data are shown in the form of a **Mooney plot**, which is based on Eq. (9.105) written as

$$\frac{\hat{\sigma}_{zz}}{\lambda - \lambda^{-2}} = 2\beta_1 + \frac{2\beta_2}{\lambda} \tag{9.110}$$

employing the nominal tensile stress and setting $\hat{\sigma}_{xx} = 0$. Results encompass both the extension and the compression range. We notice that the Mooney equation yields a satisfactory data representation for the extension range, with

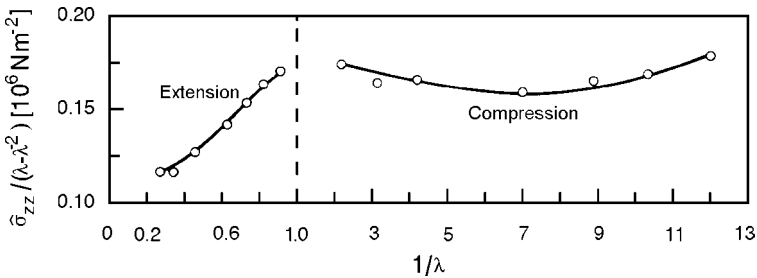


Fig. 9.12. Mooney plot of compression and extension data obtained for natural rubber. Results from Rivlin and Saunders [113]

a value $\beta_2 > 0$ as determined by the slope; however, there is no continuation into the range of compressions, where we find $\beta_2 \approx 0$. Hence, the simple modification of the free energy function as expressed by Eq. (9.102) is actually inadequate for the desired general representation of real rubber behavior.

There are various suggestions for a better choice, however, they are all rather complicated and their discussion is outside our scope. It appears today that a short analytical expression for the free energy density of a real rubber in the form of a simple extension of the free energy density of an ideal rubber does not exist. Even so, the general constitutive equation, Eq. (9.75), certainly provides us with a sound basis for treatment. Once the functional dependence of the free energy density, $f(I_B, II_B)$, has been mapped by a suitable set of experiments, and one succeeds in representing the data by an empirical expression, one can predict the stresses for any kind of deformation.

9.2 Swelling of Neutral and Electrolytic Gels

When a cross-linked polymer sample is placed in a solvent, the solvent molecules penetrate into the network and swell it. After a certain time an equilibrium state becomes established where network forces and osmotic pressure balance each other. While the degrees of swelling thus reached for common elastomers remain moderate, depending on the solvent quality and the cross-link density, one observes a spectacularly large swelling when putting a cross-linked polyelectrolyte in a good solvent as represented by water; the widely employed **superabsorbers** make use of this property. In the following we will discuss both cases.

The take-up of solvent molecules from the surroundings transfers a network from its initial dry state with volume \mathcal{V}_{g0} to a swollen state with a larger value \mathcal{V}_g . The equilibrium is associated with a certain **swelling ratio**

$$Q = \frac{\mathcal{V}_g}{\mathcal{V}_{g0}} = \frac{1}{\phi_p}, \quad (9.111)$$

where ϕ_p describes the polymer volume fraction in the swollen state. Q , or ϕ_p , are determined by the equality of two pressures, the osmotic pressure acting towards an expansion and the contra-acting stress of the isotropically dilated network.

How is this equilibrium state of the gel determined; solvent filled networks are generally addressed as **gels**, water filled networks often also more specifically as **hydrogels**? Equilibrium conditions have to be established for the solvent molecules, because they can move freely from one part of the system, the gel, to the other part, the surroundings with the pure solvent. The requirement is the equality of the (molar) chemical potential of the solvent (subscript s) in the two phases (superscripts g and 0)

$$\tilde{g}_s^g = \tilde{g}_s^0. \quad (9.112)$$

Since the solvent concentration is reduced in the gel and thus the chemical potential under normal pressure, an equal chemical potential can only be achieved for an enhanced pressure in the gel, i.e., $p_g > p_0$. The pressure difference is the osmotic pressure

$$\Pi = p_g - p_0 . \quad (9.113)$$

Π depends on the properties of the gel in the swollen state, as given by the (molar) concentration \tilde{c}_m of monomeric units, the interaction between solvent and network chains as expressed by the Flory–Huggins parameter χ , and for a polyelectrolyte network, the fraction ϕ_{io} of ionized monomers. How is the pressure difference generated? The simple answer is: It is provided by the isotropic stress of the swollen network, σ . Hence, the equilibrium condition is

$$\Pi = \sigma . \quad (9.114)$$

In order to determine the equilibrium we need expressions for the dependence of both Π and σ on the swelling ratio Q .

An expression for the isotropic network stress is obtained using Eq. (9.22) in the case of an isotropic dilatation

$$\lambda_x = \lambda_y = \lambda_z = \lambda . \quad (9.115)$$

This leads to the increase of the Helmholtz free energy; we here still use $\Delta\mathcal{F}$ rather than $\Delta\mathcal{G}$, i.e., we neglect the atmospheric pressure contribution $p_{\text{atm}}\Delta\mathcal{V}$ – to

$$\Delta\mathcal{F} = -T\Delta S = \nu_{g0}\tilde{c}_{p0}\frac{\tilde{R}T}{2}(3\lambda^2 - 3) . \quad (9.116)$$

Here, \tilde{c}_{p0} denotes the (molar) concentration of chain segments between cross-links in the dry state. With

$$\frac{\nu_g}{\nu_{g0}} = \lambda^3 = Q \quad (9.117)$$

one obtains

$$\Delta\mathcal{F} = \frac{3}{2}\nu_{g0}\tilde{c}_{p0}\tilde{R}T(Q^{2/3} - 1) . \quad (9.118)$$

The isotropic stress follows from

$$\sigma = \frac{d\Delta\mathcal{F}}{d\nu_g} \quad (9.119)$$

and is therefore given by

$$\sigma = \frac{1}{\nu_{g0}}\frac{d\Delta\mathcal{F}}{dQ} = \tilde{c}_{p0}\tilde{R}TQ^{-1/3} . \quad (9.120)$$

Equation (9.120) is obviously incomplete, as it would give a non-vanishing stress in the initial state, i.e., for $Q = 1$. In fact, in the dry state the network

forces, which always act towards a volume shrinkage, are counter-balanced by repulsive monomer–monomer interaction forces. The total external stress σ thus includes a second contribution, p_{rep} , so that we have

$$\sigma = \tilde{c}_{p0} \tilde{R}T Q^{-1/3} + p_{\text{rep}} , \quad (9.121)$$

with

$$p_{\text{rep}}(Q = 1) = -\tilde{c}_{p0} \tilde{R}T . \quad (9.122)$$

However, since there is obviously

$$p_{\text{rep}}(Q \gg 1) \approx 0 , \quad (9.123)$$

this second contribution can be neglected when calculating the gel equilibrium state.

Dealing with the osmotic pressure we first consider the case of an electrically neutral network in a good solvent. We refer here to the Flory–Huggins treatment of A/B-polymer mixtures (Sect. 4.1) and use it for a network(A)–solvent(B) system, by just setting

$$\begin{aligned} N_A &\rightarrow \infty , \\ N_B &= 1 , \\ \tilde{n}_B &= \tilde{n}_s , \\ \tilde{v}_c &= \tilde{v}_s = \tilde{v}_m , \end{aligned}$$

\tilde{v}_s and \tilde{v}_m denoting the equally chosen molar volumes of the solvent and the monomeric units respectively. Application of the Flory–Huggins theory in this case is certainly not a fully legitimate step, because polymer solutions cannot be treated satisfactorily by a mean field theory, but the general tendencies still show up. The difference $\tilde{g}_s^g - \tilde{g}_s^0$, which would evolve for a uniform normal pressure follows from

$$\tilde{g}_s^g - \tilde{g}_s^0 = \frac{\partial \Delta \mathcal{G}_{\text{mix}}}{\partial \tilde{n}_s} \quad (9.124)$$

with

$$\Delta \mathcal{G}_{\text{mix}} = \tilde{R}T (\tilde{n}_s \ln \phi_s + \chi \tilde{n}_s \phi_p) . \quad (9.125)$$

Expression (9.125) is obtained from Eq. (4.10) by the above setting. The osmotic pressure compensates the drop in the chemical potential, i.e.,

$$\Pi \tilde{v}_s = - (\tilde{g}_s^g - \tilde{g}_s^0) . \quad (9.126)$$

Performing the calculation we start from

$$\tilde{g}_s^g - \tilde{g}_s^0 = \tilde{R}T \left(\ln \phi_s + \frac{\tilde{n}_s}{\phi_s} \frac{d\phi_s}{d\tilde{n}_s} + \chi \phi_p + \chi \tilde{n}_s \frac{d}{d\tilde{n}_s} (1 - \phi_s) \right) \quad (9.127)$$

with

$$\phi_s = \frac{\tilde{n}_s \tilde{v}_s}{\tilde{n}_s \tilde{v}_s + \mathcal{V}_p} = \frac{\tilde{n}_s \tilde{v}_s}{\mathcal{V}} \quad (9.128)$$

and

$$\frac{d\phi_s}{d\tilde{n}_s} = \frac{d}{d\tilde{n}_s} \frac{\tilde{n}_s \tilde{v}_s}{\mathcal{V}} = \frac{\mathcal{V} \tilde{v}_s - \tilde{n}_s \tilde{v}_s^2}{\mathcal{V}^2} = \frac{\tilde{n}_s \tilde{v}_s}{\tilde{n}_s \mathcal{V}} (1 - \phi_s) = \frac{\phi_s}{\tilde{n}_s} (1 - \phi_s). \quad (9.129)$$

We obtain with

$$\phi_p = 1 - \phi_s \quad (9.130)$$

the result

$$\tilde{g}_s^g - \tilde{g}_s^0 = \tilde{R}T (\ln(1 - \phi_p) + \phi_p + \chi \phi_p^2) = -\Pi \tilde{v}_s. \quad (9.131)$$

A simple expression for the equilibrium degree of swelling is obtained for a high dilution of the network in the gel, i.e., $\phi_p \ll 1$. Then the osmotic pressure is

$$\Pi \approx \frac{\tilde{R}T}{\tilde{v}_s} \phi_p^2 \left(\frac{1}{2} - \chi \right), \quad (9.132)$$

and the equilibrium is reached, according to Eq. (9.114), for

$$\tilde{c}_{p0} Q^{-1/3} = \frac{(\frac{1}{2} - \chi)}{\tilde{v}_s} \frac{1}{Q^2} \quad (9.133)$$

or

$$Q^{5/3} = \frac{1}{\tilde{c}_{p0}} \frac{\frac{1}{2} - \chi}{\tilde{v}_s}. \quad (9.134)$$

As expected, swelling increases with the solvent quality ($\chi < 0$) and a decrease in the degree of cross-linking. Figure 9.13 gives an example of the latter factor. According to the stress-strain law for ideal rubbers, Eq. (9.30), we have for the tensile stress at a fixed extension the proportionality

$$\sigma_{zz} \propto \tilde{c}_{p0}. \quad (9.135)$$

In a comparison of tensile stresses in the dry state and swelling ratios in a solvent for networks with different cross-link densities one therefore expects a relationship

$$Q^{5/3} \propto \sigma_{zz}. \quad (9.136)$$

The result of such a comparison, conducted for poly(ε -caproamide) networks in *m*-cresol, is shown in the figure, and it agrees with the expectation.

Next, we consider the situation in a salt free polyelectrolyte network. Since charge neutrality is preserved within the gel due to the strong Coulomb forces, the counter-ions cannot leave this phase and, therefore, produce their full osmotic pressure. It depends on their concentration $\phi_{io} \tilde{c}_m$ as

$$\frac{\Pi}{\tilde{R}T} = \phi_{io} \tilde{c}_m = \frac{\phi_{io} \tilde{c}_{m0}}{Q}. \quad (9.137)$$

Here, \tilde{c}_{m0} denotes the molar concentration of monomers in the dry state, which equals the molar concentration of the counter-ions. The contributions of the

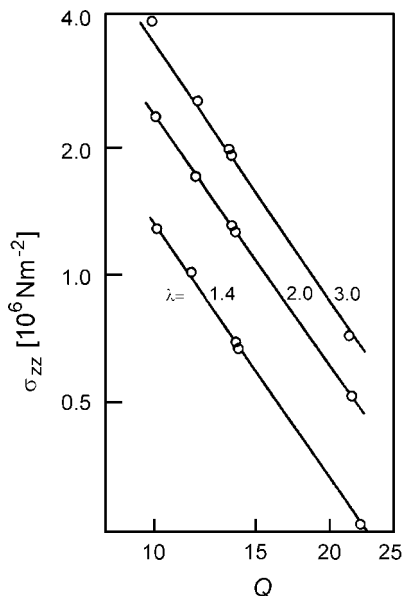


Fig. 9.13. Poly(ϵ -caproamide)s with various cross-link densities: Relationship between swelling ratios Q in m -cresol and tensile stresses σ_{zz} in the dry state at three extensions λ . From Schaeffgen and Flory [114]

network chains and the interaction between solvent molecules and monomers to II are small compared to the effect of the counter-ions and can usually be neglected.

To obtain the swelling equilibrium for the electrolyte gel we use Eq. (9.120) together with Eq. (9.137) on the basis of Eq. (9.114)

$$\frac{\phi_{\text{io}} \tilde{c}_{\text{m}0}}{Q} = \tilde{c}_{\text{p}0} Q^{-1/3}. \quad (9.138)$$

This leads to

$$Q = \left(\frac{\phi_{\text{io}} \tilde{c}_{\text{m}0}}{\tilde{c}_{\text{p}0}} \right)^{3/2}. \quad (9.139)$$

The expression on the right-hand side depends on the molar mass M_{eff} of the chains between cross-links, since

$$\frac{\tilde{c}_{\text{m}0}}{\tilde{c}_{\text{p}0}} = \frac{M_{\text{eff}}}{M_{\text{m}}} \quad (9.140)$$

with M_{m} denoting the molar mass of the monomeric units. If the ratio $M_{\text{eff}}/M_{\text{m}}$ is large, the degree of swelling Q is large as well. Figure 9.14 shows as an example the swelling properties of a poly(acrylic acid) (PAA) hydrogel. For pure water Q is in the order of 10^2 .

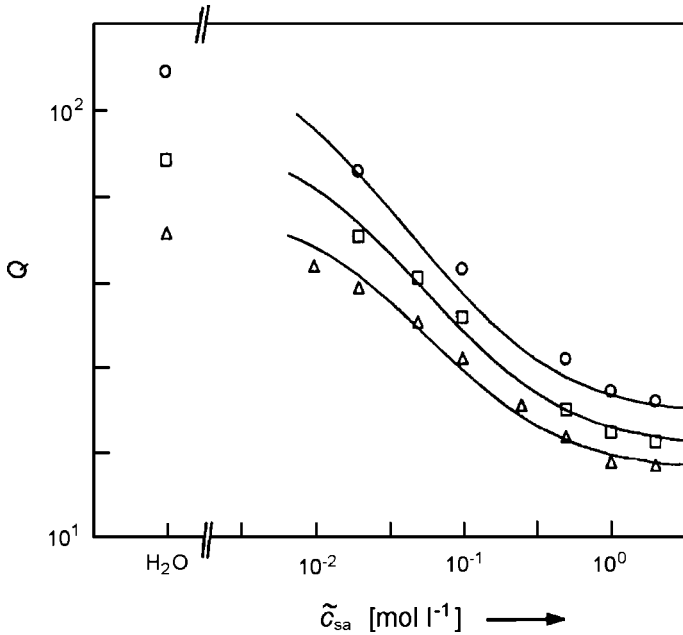


Fig. 9.14. PAA gels with different cross-link densities (260, 433 and 606 mol m⁻³): Equilibrium degree of swelling by water as a function of the NaCl concentration outside the gel. From Schröder and Oppermann [115]

One can again ask how Q changes in the presence of salt. As was discussed earlier (Sect. 3.3.3) salt reduces the osmotic pressure. The swelling ratio will also drop, which is shown by the experiment. Here, the reduction amounts to more than one order of magnitude. On the other hand, water is usually a good solvent for polyelectrolytes, i.e., one with a negative χ -parameter. Obviously, this favorable interaction further promotes the entrance of water into the gel and thus increases the swelling ratio. Both effects can be dealt with theoretically. In Sect. 3.3.3 we derived the Donnan equation, which gives the osmotic pressure in a polyelectrolyte for a higher salt concentration in the surroundings (Eq. (3.136) under neglect of the first term)

$$\Pi = \tilde{R}T \frac{\phi_{\text{io}}^2 \tilde{c}_{\text{m}}^2}{4\tilde{c}_{\text{sa}}} . \tag{9.141}$$

With

$$\phi_{\text{p}} = \tilde{c}_{\text{m}} \tilde{v}_{\text{m}} \tag{9.142}$$

the equilibrium condition here reads

$$\tilde{c}_{\text{p}0} Q^{-1/3} = \frac{\phi_{\text{io}}^2}{4\tilde{c}_{\text{sa}} \tilde{v}_{\text{m}}^2} \frac{1}{Q^2} , \tag{9.143}$$

or

$$Q^{5/3} = \frac{\phi_{\text{io}}^2}{4\tilde{c}_{\text{p0}}\tilde{v}_{\text{m}}^2\tilde{c}_{\text{sa}}} . \quad (9.144)$$

If in the case of a high negative χ -parameter, the solvent quality must also be accounted for, the swelling equilibrium is given by

$$Q^{5/3} = \frac{1}{\tilde{c}_{\text{p0}}} \left[\frac{\phi_{\text{io}}^2}{4\tilde{v}_{\text{m}}^2\tilde{c}_{\text{sa}}} + \frac{\frac{1}{2} - \chi}{\tilde{v}_{\text{s}}} \right] . \quad (9.145)$$

The Donnan contribution to the osmotic pressure vanishes in the limit of very high salt concentration, and we then end up again at the swelling properties of an electrically neutral network, i.e., at Eq. (9.134).

9.3 Non-Newtonian Melt Flow

Polymers owe their attractiveness as materials for a wide range of applications to a large extent to their ease of processing. Manufacturing processes such as injection molding, fiber spinning or film formation are mainly conducted in the melt and it is a great advantage of polymers that their melting temperatures are comparatively low. On the other hand, the flow properties of polymer melts are complicated and process control requires a broad knowledge. To deal with simple Newtonian liquids, one needs just one parameter, namely the viscosity η . In principle, knowing it allows us to calculate stresses for any given flow pattern. Polymeric liquids are more complex in behavior. From the very beginning, i.e., even at low frequencies or low shear rates, one has to employ two coefficients for a characterization. As we have already seen in the discussion of linear responses, in addition to the shear viscosity one needs to know the recoverable shear compliance that relates to the always present elastic forces. At higher strain rates more complications arise. There, η and J_e are no longer constants but change with the shear rate. In this section, we will briefly discuss these phenomena.

The problem that has to be solved in order to set the processing of polymer melts on a solid basis is the formulation of rheological equations of state. The rheologists' approach in treating the problems of melt flow is generally a purely empirical one. The objective is to find analytical expressions correctly describing the relationships between the time-dependent strains or velocities in a given fluid and the emerging stresses. Ideally, equations should be generally applicable, i.e., hold for all possible strain histories, and at the same time be analytically simple, to facilitate their use. As we will see, for polymer melts this aim amounts to a difficult task. We can enter into this field only in a very restricted manner and will present solely the simplest model, known as the **Lodge fluid**. The main purpose of this section is to introduce and discuss some standard experiments commonly employed for a characterization of polymer flow behavior. They refer to situations frequently encountered under practical conditions.

9.3.1 Rheological Material Functions

Two of the various flow patterns realized in polymer melts during processing are of particular importance. First, there is the flow through a tube. Here, all volume elements move along straight lines parallel to the axis. The velocities are non-uniform, the maximum velocity being found at the center and the minimum at the wall where the fluid particles are fixed. The consequence of the varying velocities are frictional forces acting between the volume elements incorporated in adjacent stream lines. Obviously, flow through tubes is locally equivalent to shear flows. Similarly to simple shear, layers of liquid slide over each other without changing their form. A different kind of deformation is found in **extensional flows**. These are encountered, for example, during melt spinning in the fiber production. The dominant feature now is the stretching of all volume elements, which means a great change in form; the sliding of adjacent layers against each other, giving the main effect in shear flow, is less important. Hence, we have, at least, two different classes of deformations, which both have to be analyzed. As a minimum, for a first rheological characterization of a given polymer one needs two kinds of experimental arrangements, and we discuss them one after the other.

Simple shear flow is identical with the pattern depicted in Fig. 9.15. The velocity field is given by

$$v_x = \dot{\gamma}z , \quad (9.146)$$

$$v_y = v_z = 0 . \quad (9.147)$$

The only parameter included is the shear rate $\dot{\gamma}$. There is an instrument that is widely used because it realizes simple shear flow conditions in a manner convenient for experiments. This is the **cone-and-plate rheometer** sketched on the left-hand side of Fig. 9.16. The polymer melt is placed in the gap and, if the gap angle is kept small, then the shear rate is the same everywhere. With the aid of this apparatus, various experiments may be carried out, as for example,

- determinations of the steady state properties at constant shear rates,
- measurements under oscillatory shear,

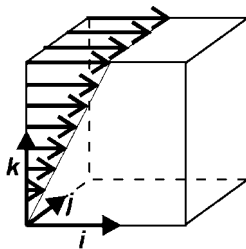


Fig. 9.15. Pattern of simple shear flow. *Arrows* indicate the velocity field

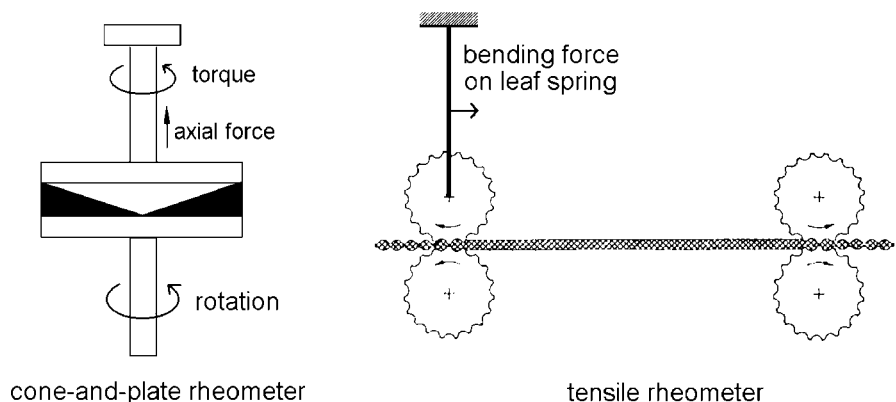


Fig. 9.16. Standard arrangements used for the characterization of shear flows (*left*) and extensional flows (*right*). Shear viscosities can be derived from the torque measured in a cone-and-plate rheometer; the primary normal stress difference is deduced from the axial force. Elongational viscosities follow from the tensile force required for the drawing of a molten fibre in the tensile rheometer, as monitored by a leaf spring

- observations of the stress growth for linearly increasing shear,
- detection of the shear, stress relaxation after a sudden deformation of the melt, and
- studies of the elastic recovery after unloading.

The two material parameters characterizing polymeric fluids at low strain rates, the viscosity, η , and the recoverable shear compliance, J_e , can be directly determined. η follows from the measurement of the torque under steady state conditions, J_e shows up in the reverse angular displacement subsequent to an unloading, caused by the retraction of the melt. From the discussion of the properties of rubbers we already know that simple shear is associated with the building-up of normal stresses. More specifically, one finds a non-vanishing value of the first normal stress difference. We may anticipate, therefore, that the deformation of the entanglement network in a shear-deformed polymer melt likewise results in the emergence of normal stresses. The cone-and-plate rheometer permits us to make a direct determination, because this causes a thrusting axial force. Being proportional to the square of the shear in rubbers and equivalently, as we shall learn, to the square of the shear rate in polymer melts, normal stresses constitute a non-linear phenomenon. Although they can be small for low shear rates, they are present from the very beginning.

The properties of melts under extensional flows can be studied with the aid of a **tensile rheometer**. The basic experimental arrangement is sketched on the right-hand side of Fig. 9.16. A cylindrical rod of polymer melt, usually floating on a liquid substrate, is drawn by two pairs of ribbed rollers. One of the rollers is mounted on a leaf spring, so that the force required for the

drawing process can be monitored by the deflection. It is important to recognize the conditions imposed if the rollers circulate with a constant frequency. Obviously, the procedure realizes a constant rate of elongation relative to the momentary length, i.e., a constant value for the relative length change per second. Expressed in terms of the stretching ratio, λ , we have

$$\frac{1}{\lambda(t)} \frac{d\lambda}{dt} = \text{const} \quad (9.148)$$

The process thus differs from a drawing where clamps attached to the two ends of a sample move with a constant relative speed, as this leads to

$$\frac{d\lambda}{dt} = \text{const} \quad (9.149)$$

The constant in Eq. (9.148) is known as the **Hencky rate of extension** and we choose for it the symbol $\dot{\epsilon}_H$

$$\dot{\epsilon}_H = \frac{d \ln \lambda}{dt} . \quad (9.150)$$

Whereas experiments conducted with a constant rate of elongation yield a linear extension with time, those carried out with a constant Hencky rate result in an exponential time dependence of λ ,

$$\lambda(t) = \exp(\dot{\epsilon}_H t) . \quad (9.151)$$

For solids one may choose either of the two drawing processes. For liquids a drawing with a constant Hencky rate of extension is to be preferred, because the original length included in λ then becomes irrelevant, as is desired.

We now introduce the major rheological material functions, with illustrations provided by typical experimental results. Figure 9.17 depicts data obtained for low density polyethylene under steady shear flow conditions, employing a cone-and-plate rheometer. Curves display both the shear rate dependence of the viscosity, with similar results as in Fig. 9.1, and the shear rate dependence of the first normal stress difference. The stresses arising for simple shear flows may be generally expressed by the following set of equations:

$$\sigma_{zx} = \eta(\dot{\gamma})\dot{\gamma} , \quad (9.152)$$

$$\sigma_{xx} - \sigma_{zz} = \Psi_1(\dot{\gamma})\dot{\gamma}^2 , \quad (9.153)$$

$$\sigma_{yy} - \sigma_{zz} = \Psi_2(\dot{\gamma})\dot{\gamma}^2 . \quad (9.154)$$

Equations include and thus define three rheological material functions:

- the shear viscosity η ,
- the primary normal stress coefficient Ψ_1 , and
- the secondary normal stress coefficient Ψ_2 .

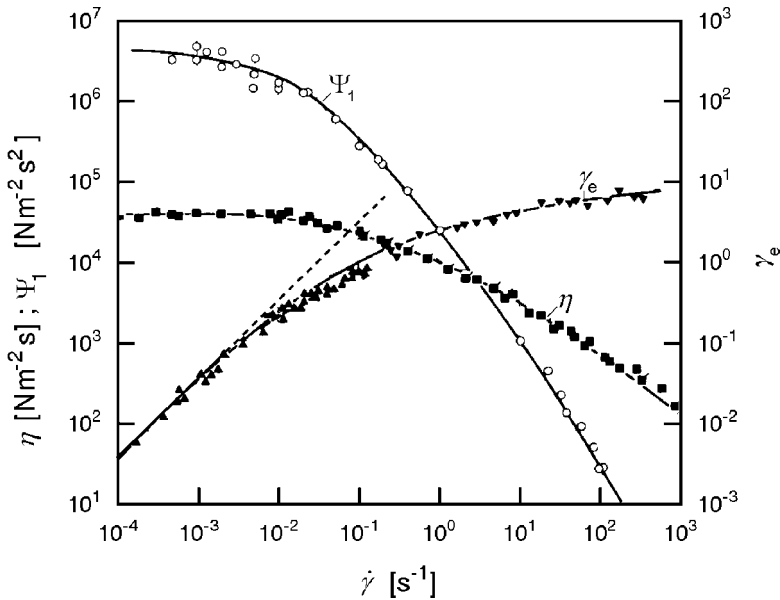


Fig. 9.17. PE under steady state shear flow at 150 °C: Strain rate dependencies of the viscosity η , the primary normal stress coefficient Ψ_1 and the recoverable shear strain γ_e . The *dotted line* represents Eq. (9.157). Results obtained by Laun [116]

All three functions are dependent on the shear rate $\dot{\gamma}$. Ψ_2 does not appear in the figure, because it is difficult to deduce it from measurements in a cone-and-plate rheometer. It can be obtained using other devices and results indicate that Ψ_2 is usually much smaller than Ψ_1 , thus having only a minor effect on the flow behavior. The important property showing up in the measurements is the shear thinning, observed for both η and Ψ_1 and setting in for strain rates above $\dot{\gamma} \simeq 10^{-2} \text{ s}^{-1}$.

The third curve in the figure, denoted γ_e , gives the amount of shear strain recovery subsequent to a removal of the external torque. There is an interesting observation. The linear increase of γ_e with $\dot{\gamma}$ at low shear rates is exactly determined by the zero shear rate values of the viscosity and the primary normal stress coefficient, η_0 and $\Psi_{1,0}$. This is revealed by the coincidence of the limiting curve $\gamma_e(\dot{\gamma} \rightarrow 0)$ with the dotted line representing the linear function

$$\frac{\Psi_{1,0}}{2\eta_0} \dot{\gamma} = \frac{\sigma_{xx} - \sigma_{zz}}{2\sigma_{zx}} . \tag{9.155}$$

The agreement implies a relationship between the zero shear rate value of the recoverable shear compliance, following from γ_e as

$$J_e^0 = \lim_{\dot{\gamma} \rightarrow 0} \frac{\gamma_e}{\sigma_{zx}} \tag{9.156}$$

and the zero shear values of the viscosity and the primary normal stress coefficient. It has the following form:

$$J_e^0 = \frac{\Psi_{1,0}}{2\eta_0^2}. \tag{9.157}$$

The relationship implies that, in the limit of low shear rates, we still have only two independent parameters. The primary normal stress coefficient does not represent an independent property, but is deducible from the two parameters controlling the linear response, J_e^0 and η_0 .

Figure 9.18 refers to two other standard experiments. It depicts the results of **stress growth experiments**, conducted again on a polyethylene melt. The figure includes both measurements probing shear and tensile properties, thus facilitating a direct comparison. Curves show the building-up of shear stress upon inception of a steady state shear flow at zero time and the development of tensile stress upon inception of a steady state extensional flow. Measurements were carried out for various values of the shear rate $\dot{\gamma}$ or the Hencky rate of extension $\dot{\epsilon}_H$.

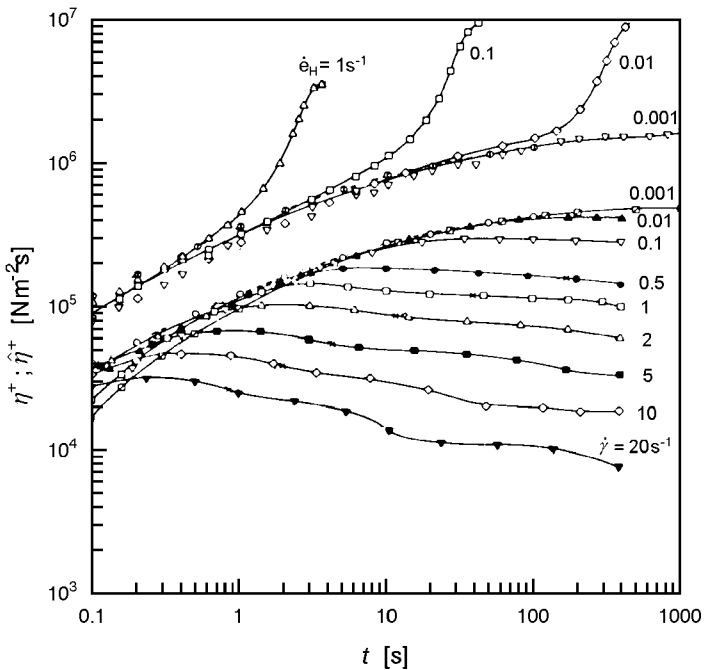


Fig. 9.18. Results of stress growth experiments in shear, $\eta^+(t)$, and extension, $\hat{\eta}^+(t)$, at different deformation rates $\dot{\gamma}$ and $\dot{\epsilon}_H$, respectively, carried out for PE at 150 °C. Measurements by Meissner [117]

The results of the shear experiments are described with the aid of the **time-dependent viscosity** defined as

$$\eta^+(t, \dot{\gamma}) = \frac{\sigma_{zx}(t)}{\dot{\gamma}}. \quad (9.158)$$

In analogous manner the **time-dependent extensional viscosity**, defined as

$$\hat{\eta}^+(t) = \frac{\sigma_{zz}(t)}{\dot{\epsilon}_H}, \quad (9.159)$$

is employed for a description of the properties of extensional flow. The steady state value reached after the period of growth

$$\hat{\eta} = \hat{\eta}^+(t \rightarrow \infty) = \frac{\sigma_{zz}}{\dot{\epsilon}_H} \quad (9.160)$$

is known as the **extensional viscosity** or **Trouton viscosity**. A look at the results is instructive and shows us characteristic differences between shear and tensile deformations. First consider the limit of low strain rates. We find here a simple result, as both curves agree in shape, only differing by a factor of three. As we shall see below, the two curves can be deduced from the flow properties in the linear regime, by application of Lodge's equation of state for rubber-like liquids. The reason for the difference and the fact that the larger forces arise in the extensional flow is obvious. For equal values of $\dot{\gamma}$ and $\dot{\epsilon}_H$, the tensile strains produce much larger deformations. Of particular interest is the comparison of the behavior at larger strain rates. In both cases one observes characteristic deviations from the low strain rate curves. The shear stressing leads to deviations to lower values, i.e., to a shear thinning. The asymptotic values reached at long duration give the steady state shear viscosities shown in Fig. 9.17. An opposite behavior appears in the tensile deformation mode, where we find deviations to higher values, indicating a **strain hardening**. In the latter experiments it is often difficult to reach the steady state, as this is frequently preceded by a fracture of the melt fibre. Sometimes one is successful and then curves like the one shown in Fig. 9.19 are observed. The shape in the range before the steady state plateau is reached reminds one of stress-strain curves of rubbers under uniaxial load, like that shown in Fig. 9.1. The similarity might suggest that, like the rubber, here in the melt a strain hardening again arises from the limited extensibility of the mobile chain sequences. As it turns out, however, this is not the primary cause. As will be shown in the next section, an increase in stress is also predicted for the Lodge liquid if strain rates become large compared to intrachain relaxation rates.

A further typical result is shown in Fig. 9.20, giving the plateau values of the extensional viscosity at steady state as a function of the associated drawing stress σ_{zz} . Measurements were carried out for various low density polyethylenes (PE-LD) and one linear polyethylene (PE-HD). For the majority of samples, in the non-linear range one first observes an increase and then

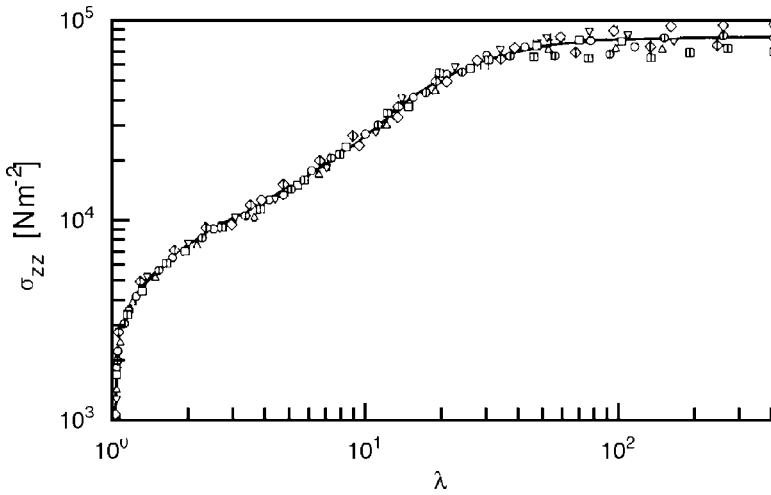


Fig. 9.19. Tensile stress growth curves observed for PE at 150 °C, obtained for a constant Hencky strain rate $\dot{\epsilon}_H = 0.1 \text{ s}^{-1}$. Data from Laun and Münstedt [118]

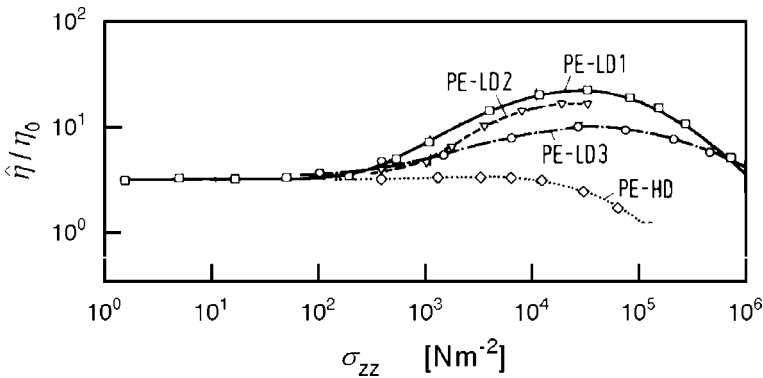


Fig. 9.20. Steady state extensional viscosities $\hat{\eta}$ as a function of the applied tensile stress, as observed for various samples of PE. Data are given in reduced form, with reference to the respective zero shear rate viscosities η_0 . From Münstedt and Laun [119]

for higher strain rates and stresses, after passing over a maximum, a decrease. We may understand this behavior as being the result of competition between two effects. After the first period of strain hardening there follows a viscosity reduction on further increasing the strain rates, owing to a decrease in the entanglement density in the oriented fiber occurring for similar reasons as in the case of shear thinning.

9.3.2 The Lodge Liquid

Treatments of flows of polymer melts require a rheological equation of state that allows a calculation of the stress tensor for all points \mathbf{r} of a given flow field. We have a complete description of the flow kinetics if we specify for each material point, located at \mathbf{r} at time t , the full trajectory in the past. The latter may be expressed by the function

$$\mathbf{r}'(\mathbf{r}, t, t'), \quad (9.161)$$

which describes the positions \mathbf{r}' at the previous times t' . Clearly we may start from the assumption that the stress field at time t , $\boldsymbol{\sigma}(\mathbf{r}, t)$, is a functional of the trajectories of all material points. This statement, however, is obviously too general to be useful for applications. We have learned in the discussion of finite deformations of rubbers how the problem can be reduced. An essential reduction was achieved by the introduction of the Cauchy tensor \mathbf{C} , or alternatively, the Finger tensor \mathbf{B} . As we have seen, the state of stress of a hyperelastic body may be described by functions $\boldsymbol{\sigma}(\mathbf{C})$ or $\boldsymbol{\sigma}(\mathbf{B})$. This notion can be extended and generalized to treat the time-dependent deformations occurring in polymer melts. Referring to the Finger tensor, we introduce a function

$$\mathbf{B}(\mathbf{r}, t, t')$$

depending on the present time t and a previous time t' , with components B_{ij} being given by

$$B_{ij}(t, t') = \frac{\partial r_i}{\partial r'_k} \frac{\partial r_j}{\partial r'_k}. \quad (9.162)$$

This is analogous to the previous definition, Eq. (9.81), which is now applied to the state of the melt at time t' , given by the displacement function $\mathbf{r}'(\mathbf{r}, t, t')$, rather than to the natural state of a rubber. According to the definition, the **time-dependent Finger strain tensor**, $\mathbf{B}(\mathbf{r}, t, t')$, characterizes the deformation of the neighborhood of the material point at \mathbf{r} that has taken place between the past time t' and the present time t . With the aid of the Finger tensor, we have formulated a general equation of state valid for all hyperelastic bodies. Likewise, we now assume that the stress in a flowing melt can be expressed as a functional of the tensors $\mathbf{B}(\mathbf{r}, t, t')$:

$$\boldsymbol{\sigma}(\mathbf{r}, t) = \boldsymbol{\sigma}(\mathbf{B}(\mathbf{r}, t, t')), \quad \text{with } t' < t. \quad (9.163)$$

This general expression first accounts for the principle of causality by stating that the state of stress at a time t is dependent on the strains in the past only. Second, by using the time dependent Finger tensor \mathbf{B} , one extracts from the flow fields only those properties that produce stress and eliminates motions like translations or rotations of the whole body that leave the stress invariant. Equation (9.163) thus provides us with a suitable and sound basis for further considerations.

The problem is to find expressions that can describe the experimental observations. We have a perfect solution if we succeed in constructing an equation of state that correctly formulates the stresses for an arbitrary strain history. To reach this final goal is certainly very difficult. It might appear, however, that we have a suitable starting point. Polymer fluids have much in common with rubbery materials. In a simplified view, we find, as the only difference, that cross-links are permanent in rubbers whereas, in fluids, they are only temporary with lifetimes that are still large compared to all the internal equilibration processes. Hence, it makes sense to search for a formula that includes, from the very beginning, the properties of rubbers as expressed by the equation of state of ideal rubbers, Eq. (9.74).

Lodge was the first to formulate such an equation by a combination of Eq. (9.74) with the Boltzmann superposition principle as expressed by Eq. (6.111). Explicitly, the **Lodge equation of state of rubber-like liquids**, when written for homogeneous deformations, has the following form

$$\boldsymbol{\sigma}(t) = - \int_{t'=-\infty}^t G(t-t') \frac{d\mathbf{B}(t,t')}{dt'} dt'. \quad (9.164)$$

The Boltzmann superposition principle represents the stress as a result of changes in the state of strain at previous times. In the linear theory that is valid for small strains, these can be represented by the linear strain tensor. In Lodge's equation the changes in the latter are substituted by changes in the time dependent Finger tensor

$$-d\mathbf{B}(t,t'),$$

thus enabling us to describe finite strains. The meaning of the function G remains unchanged. It still represents the stress relaxation modulus.

To see the consequences implied by this equation of state, it is instructive to consider at first simple shear flow conditions. We may write down the time-dependent Finger tensor immediately, just by replacing in Eq. (9.98), derived for a deformed rubber, γ by the increment $\gamma(t) - \gamma(t')$. This results in

$$\mathbf{B}(t,t') = \begin{pmatrix} 1 + (\gamma(t) - \gamma(t'))^2 & 0 & \gamma(t) - \gamma(t') \\ 0 & 1 & 0 \\ \gamma(t) - \gamma(t') & 0 & 1 \end{pmatrix}. \quad (9.165)$$

Next, we introduce \mathbf{B} into Lodge's equation of state, calculate the derivatives and thus obtain all stress components. The result for the shear stress is

$$\sigma_{zx}(t) = \int_{t'=-\infty}^t G(t-t') \frac{d\gamma}{dt'} dt', \quad (9.166)$$

and for the primary normal stress difference we obtain

$$(\sigma_{xx} - \sigma_{zz})(t) = 2 \int_{t'=-\infty}^t G(t-t')(\gamma(t) - \gamma(t')) \frac{d\gamma}{dt'} dt' . \quad (9.167)$$

The secondary normal stress difference vanishes, as was the case for an ideal rubber

$$\sigma_{yy} - \sigma_{zz} = 0 . \quad (9.168)$$

Representing a combination of the equation of state of ideal rubbers and Boltzmann's superposition principle, Lodge's equation provides an interpolation between the properties of rubbers and viscous liquids. The limiting cases of an elastic rubber and the Newtonian liquid are represented by

$$G = \text{const} \quad (9.169)$$

and

$$G(t-t') = \eta \delta(t-t') , \quad (9.170)$$

respectively. Insertion of a constant G in Lodge's equation reproduces the elastic properties of a rubber under simple shear deformation, as we find

$$\sigma_{zx}(t) = G\gamma(t) , \quad (9.171)$$

$$\begin{aligned} (\sigma_{xx} - \sigma_{zz})(t) &= 2G \int_{t'=0}^t (\gamma(t) - \gamma(t')) \frac{d\gamma}{dt'} dt' \\ &= G\gamma^2(t) . \end{aligned} \quad (9.172)$$

If we take Eq. (9.170), we obtain

$$\sigma_{zx}(t) = \eta \frac{d\gamma}{dt} \quad (9.173)$$

$$(\sigma_{xx} - \sigma_{zz})(t) = 0 , \quad (9.174)$$

i.e., the flow properties of a Newtonian liquid.

Next, let us consider the predictions for a shear stress growth experiment. In a stress growth experiment, a linearly increasing shear is imposed, i.e.,

$$\gamma(t) = \dot{\gamma}t \text{ for } t > 0 . \quad (9.175)$$

Applying Eq. (9.166), we obtain for the time-dependent shear stress

$$\sigma_{zx}(t) = \dot{\gamma} \int_{t'=0}^t G(t-t') dt' , \quad (9.176)$$

and for the primary normal stress difference

$$\begin{aligned}
 (\sigma_{xx} - \sigma_{zz})(t) &= 2\dot{\gamma}^2 \int_{t'=0}^t G(t-t')(t-t') dt' \\
 &= 2\dot{\gamma}^2 \int_0^t G(t'')t'' dt'' .
 \end{aligned}
 \tag{9.177}$$

The results give us the following expressions for the material functions $\eta^+(t)$ and $\Psi_1^+(t)$:

$$\eta^+(t) = \int_0^t G(t'') dt''
 \tag{9.178}$$

and

$$\Psi_1^+(t) = 2 \int_0^t G(t'')t'' dt'' .
 \tag{9.179}$$

The steady state values reached after passing through the period of stress growth equal the asymptotic limits for $t \rightarrow \infty$, i.e.,

$$\eta = \eta^+(t \rightarrow \infty)
 \tag{9.180}$$

$$\Psi_1 = \Psi_1^+(t \rightarrow \infty) .
 \tag{9.181}$$

We thus obtain, for the steady state viscosity and the steady state primary normal stress coefficient, the expressions

$$\eta = \int_0^\infty G(t'') dt''
 \tag{9.182}$$

$$\Psi_1 = 2 \int_0^\infty G(t'')t'' dt'' .
 \tag{9.183}$$

As we can see, both are independent of the strain rate $\dot{\gamma}$. Hence, as a first conclusion, Lodge's equation of state cannot describe the shear thinning phenomenon. Equation (9.182) is in fact identical with Eq. (6.107) derived in the framework of linear response theory. The new result contributed by Lodge's formula is the expression Eq. (9.183) for the primary normal stress difference. It is interesting to note that the right-hand side of this equation already appeared in Eq. (6.108) of the linear theory, formulating the relationship between $G(t)$ and the recoverable shear compliance J_e^0 . If we take the latter equation, we realize that the three basic parameters of the Lodge rubber-like liquid, η_0 , J_e^0 and $\Psi_{1,0}$, are indeed related, by

$$\Psi_{1,0} = 2J_e^0\eta_0^2 .
 \tag{9.184}$$

The result exactly reproduces the experimental observations in the limit of low shear rates as presented in Fig. 9.17; the straight dotted line is based on this relation. We may conclude, therefore, that Lodge's equation correctly describes the development of normal stresses in the initial period of shear-stressed polymeric liquids.

Next, we consider the second class of experiments and check the predictions of the Lodge model with regard to extensional flows. Using again an equation from the ideal rubbers we can directly write down the time-dependent Finger tensor $\mathbf{B}(t, t')$. It has the form

$$\mathbf{B}(t, t') = \begin{pmatrix} \left(\frac{\lambda(t)}{\lambda(t')}\right)^{-1} & 0 & 0 \\ 0 & \left(\frac{\lambda(t)}{\lambda(t')}\right)^{-1} & 0 \\ 0 & 0 & \left(\frac{\lambda(t)}{\lambda(t')}\right)^2 \end{pmatrix} \quad (9.185)$$

and follows from Eq. (9.80) by a substitution of the stretching ratio λ referring to the natural state by the relative length change between times t' and t as given by the ratio $\lambda(t)/\lambda(t')$. Tensile stress growth experiments are conducted with a constant Hencky rate of extension, starting the drawing process at zero time. This leads to an exponential time dependence of λ as expressed by Eq. (9.151) and therefore to the following expression for the time-dependent Finger tensor:

$$\mathbf{B}(t, t') = \begin{pmatrix} \exp[-\dot{\epsilon}_H(t-t')] & 0 & 0 \\ 0 & \exp[-\dot{\epsilon}_H(t-t')] & 0 \\ 0 & 0 & \exp[2\dot{\epsilon}_H(t-t')] \end{pmatrix}. \quad (9.186)$$

Insertion of $\mathbf{B}(t, t')$ in the equation of state for rubber-like liquids yields the normal stress difference

$$\begin{aligned} (\sigma_{zz} - \sigma_{xx})(t) &= - \int_{t'=0}^t G(t-t') \frac{d}{dt'} (\exp[2\dot{\epsilon}_H(t-t')] \\ &\quad - \exp[-\dot{\epsilon}_H(t-t')]) dt' \\ &= \dot{\epsilon}_H \int_{t'=0}^t G(t-t') (2 \exp[2\dot{\epsilon}_H(t-t')] \\ &\quad + \exp[-\dot{\epsilon}_H(t-t')]) dt'. \end{aligned} \quad (9.187)$$

In the absence of lateral pressures, i.e.,

$$\sigma_{xx} = 0,$$

we can formulate the result as

$$\sigma_{zz}(t) = \dot{\epsilon}_H \hat{\eta}^+(t, \dot{\epsilon}_H) \quad (9.188)$$

with

$$\hat{\eta}^+(t, \dot{\epsilon}_H) = \int_{t''=0}^t G(t'')(2 \exp(2\dot{\epsilon}_H t'') + \exp(-\dot{\epsilon}_H t'')) dt'' . \quad (9.189)$$

Figure 9.21 shows the time-dependent viscosities derived from Eqs. (9.178) and (9.189) for both simple shear and extensional flow. For simplicity a single exponential relaxation with a relaxation time τ is assumed for $G(t'')$. The dotted line represents the time-dependent viscosity for simple shear, $\eta^+(t)$, which is independent of $\dot{\gamma}$. A qualitatively different result is found for the extensional flow. As we can see, the time-dependent extensional viscosity $\hat{\eta}^+(t)$ increases with $\dot{\epsilon}_H$ and for $\dot{\epsilon}_H > 0.5\tau^{-1}$ a strain hardening arises.

It is interesting to compare these calculations with the experimental results presented in Fig. 9.18. Indeed, there is perfect agreement in the limit of low deformation rates, $\dot{\gamma} \rightarrow 0$ and $\dot{\epsilon}_H \rightarrow 0$. In both the model and the experiment, we find two parallel curves for $\eta(t)$ and $\hat{\eta}(t)$ that are separated by a factor 3. Notice that the factor 3 also emerges for a rubber under static conditions, where we found $E = 3G$ (Eqs. (9.32) and (9.86)). There is no agreement at all for the shear flow at finite strain rates since shear thinning phenomena are not accounted for. Similarly, the agreement is lacking for the tensile stress growth experiments at higher strain rates. Although the Lodge model predicts an

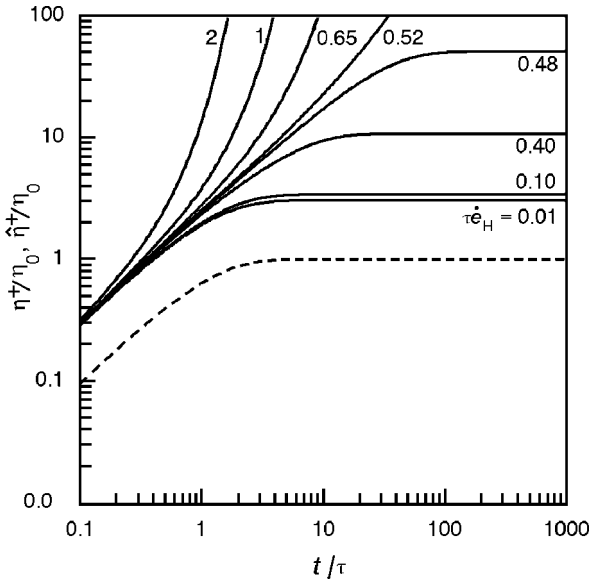


Fig. 9.21. Time-dependent viscosities for shear and extensional flow, η^+ and $\hat{\eta}^+$, as predicted by Lodge's equation of state. Calculations are performed for different Hencky strain rates $\dot{\epsilon}_H$, assuming a single exponential relaxation modulus $G(t) \propto \exp(-t/\tau)$

increase with the strain rate, the experimental curves differ from the calculated data. In particular, the viscosity reduction at high strain rates indicated by the final values is not accounted for by the model. Hence, we have to conclude that the capacity of the Lodge model is limited when compared to the behavior of real polymer melts. What it provides is a correct prediction of the normal stress phenomena at low strain rates and it also describes part of the stress enhancement observed in extensional flows.

As it is obviously necessary to alter the assumptions, one might check at first whether moderate modifications of the Lodge model can lead to an improvement of the agreement with the experiment. Still, the Lodge model can be regarded as a good starting point, as it furnishes a perfect representation of data for low strain rates, independent of the total deformation. There are various proposals in the literature on how an improvement could be achieved; however, a fully satisfactory equation of state in the sense of providing all material functions in quantitative terms for a given polymer, using a small number of adjustable parameters, has not been found so far. Rather than giving an overview, which definitely lies outside our scopes, we will just cite, for illustration, one of the better known approaches. One generalization of Eq. (9.164) has the following form:

$$\boldsymbol{\sigma} = - \int_{t'=-\infty}^t G(t-t') \frac{d\Phi(\mathbf{B}(t,t'))}{dt'} dt' . \quad (9.190)$$

Here, while retaining the relaxation function $G(t-t')$, the Finger tensor is replaced by a functional Φ depending on $\mathbf{B}(t,t')$ and its invariants $I_B(t,t')$ and $II_B(t,t')$. The modification makes it possible to account for the viscosity reduction effects. As an example, one can factorize Φ and write

$$\Phi(\mathbf{B}(t,t')) = \exp[-\beta(I_B(t,t') - 3)] \mathbf{B}(t,t') . \quad (9.191)$$

The exponential acts like a damping function and causes stress reductions if the deformations become large, as is desired.

9.3.3 The Stress-Optical Rule

Figures 9.22 and 9.23 present experimental results that at first glance may look quite astonishing. Flowing polymer melts are birefringent, for obvious reasons and the experiment compares for a stretched polystyrene the time dependence of the birefringence

$$\Delta n = n_c - n_a \quad (9.192)$$

(n_c and n_a are the indices of refraction along and normal to the stretching direction) with that of the tensile stress. The time dependencies shown in Fig. 9.22 have a similar appearance and indeed, as proved by the plot of Δn

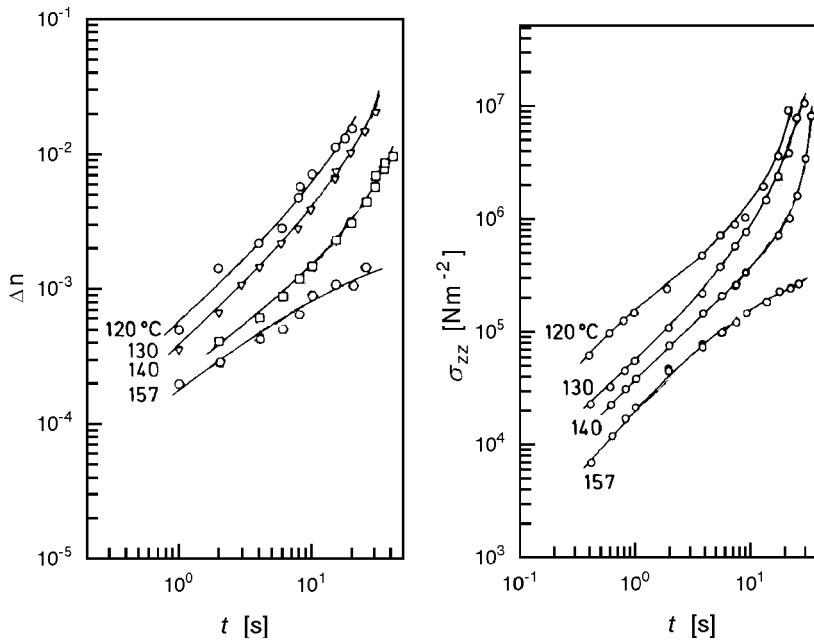


Fig. 9.22. Time dependence of tensile stress observed in stretching experiments ($\dot{\epsilon}_H = 0.075 \text{ s}^{-1}$) carried out on PS at the indicated temperature (*right*). Simultaneous measurement of the birefringence as a function of time (*left*). Data of Matsumoto and Bogue [120]

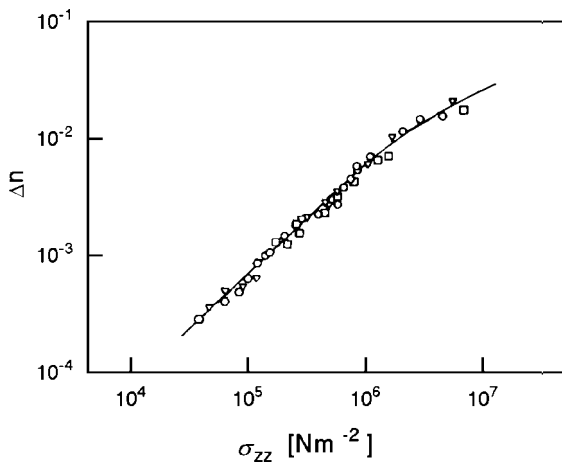


Fig. 9.23. Relation between birefringence and tensile stress deduced from the data of Fig. 9.22 after an elimination of the time [120]

versus σ_{zz} in Fig. 9.23, obtained by elimination of t from all curves, there is a strict relationship, even common to all temperatures. Moreover, over a wide range of stresses a linear relationship

$$\Delta n = \text{const } \sigma_{zz} \quad (9.193)$$

is found. As only differences between normal stresses are well-defined, we write more accurately

$$\Delta n = C_{\text{opt}}(\sigma_{zz} - \sigma_{xx}) . \quad (9.194)$$

Equation (9.194) is known as the **linear stress-optical rule** and is generally valid for polymer melts. The proportionality constant C_{opt} is called the **stress-optical coefficient**, and its value is a characteristic property for each polymer.

The linear stress-optical rule also holds under the conditions of simple shear flow. Observed data comply with the scenario depicted schematically in Fig. 9.24. The drawings show the principal axes of the stress tensor and of the optical indicatrix, for different shear rates. Data evaluation proves that the orientations of the two triples of principal axes always coincide, as is indicated in the sketches. The inclination angle of the primary axis, θ_c , is 45° for infinitesimally small shear rates and then decreases towards zero on increasing $\dot{\gamma}$. The stress optical rule here reads

$$\Delta n = n_c - n_a = C_{\text{opt}}(\sigma_c - \sigma_a) . \quad (9.195)$$

It can be verified by simultaneous measurements of the birefringence $n_c - n_a$, the inclination angle θ_c and the shear stress σ_{zx} . Straightforward calculations yield the following relation between the principal stresses σ_a , σ_c and the shear stress σ_{zx} in the laboratory-fixed coordinate system:

$$2\sigma_{zx} = (\sigma_c - \sigma_a) \sin(2\theta_c) . \quad (9.196)$$

Combination of Eqs. (9.195) and (9.196) gives

$$\frac{\Delta n \sin(2\theta_c)}{2\sigma_{zx}} = C_{\text{opt}} . \quad (9.197)$$

Figure 9.25 shows the results of measurements of C_{opt} based on this equation, carried out for two different samples of polyethylene over a wide range of shear rates $\dot{\gamma}$. As we note, C_{opt} is strictly constant, in striking contrast to the shear viscosities η , which are included in the figure for comparison. Here we find a linear relation that is valid within the range of non-linear mechanical behavior. Surely we are in the non-linear range: Birefringence is indicative of changes in the conformational distribution of the chains and this, in turn, leads to the non-linearity.

Validity of the linear stress-optical rule is a key observation with regard to the physical nature of the stresses created in flowing polymer melts. Generally speaking, stress in a polymer fluid arises from all forces acting between

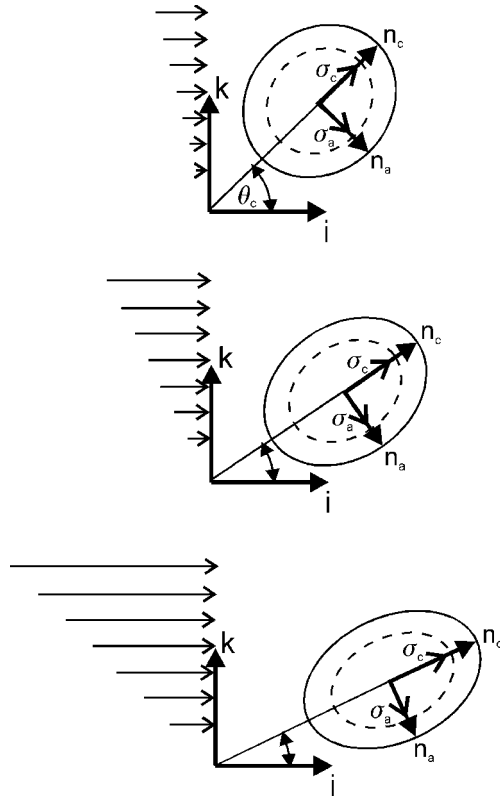


Fig. 9.24. Stress-optical relation as observed in polymer melts under simple shear flow: Optical indicatrix (*ellipsoids drawn with continuous lines*) and stress tensor (*ellipsoids drawn with broken lines*) show equal orientations of the principal axes and proportionality between the birefringence $n_c - n_a$ and the principal stress difference $\sigma_c - \sigma_a$. The inclination angle θ_c decreases with increasing shear rate

monomers on alternate sides of a reference plane. In polymers, we may divide them into two parts. We first have the strong valence bond forces, which are effective along a polymer chain, and second the non-bonded interactions active between all monomers on adjacent positions; they may belong to the same or to different chains. Having two contributions to the stress, the question arises as to how this can be accommodated with the validity of the stress-optical rule. Because only intrachain deformations produce optical effects we must conclude that the intramolecular forces dominate the situation in flowing polymer melts, the effects of the non-bonded interactions being negligible.

Indeed, under this assumption the stress-optical rule can be verified and interpreted. We describe a chain in the spirit of the Rouse model, as sketched in Fig. 9.26. Each polymer is subdivided into sequences of equal size, long

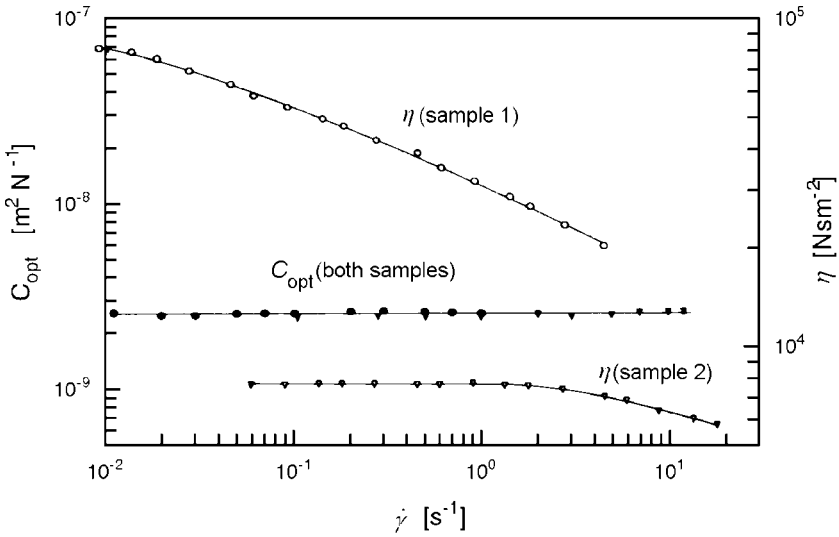


Fig. 9.25. Steady state shear viscosities and the stress optical coefficient observed for two samples of PE with different molar mass distributions at 150 °C. Measurements by Wales [121]

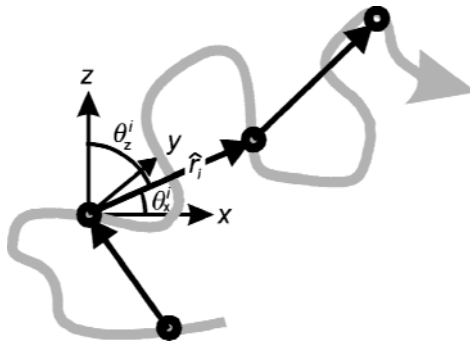


Fig. 9.26. Representation of a polymer chain as a series of freely jointed springs with extensions \hat{r}_i and orientation angles $\theta_x^i, \theta_y^i, \theta_z^i$

enough to ensure that they behave like elastic springs, with a force constant b_R given by Eq. (8.18),

$$b_R = \frac{3kT}{a_R^2} . \tag{9.198}$$

Using this representation of the chains in a melt, which may or may not be entangled, we can deduce the linear stress-optical rule. Previously, in Eq. (8.60)

we formulated an expression for the contribution of stretched springs to the shear stress σ_{zx}

$$\sigma_{zx} = \frac{b_R}{v} \sum_i \hat{x}_i \hat{z}_i .$$

The summation included all springs i in the volume v , with extensions \hat{x}_i and \hat{z}_i along the x and z -directions. Because all springs behave equivalently we can also write

$$\sigma_{zx} = b_R c_{\text{spr}} \langle \hat{x}_i \hat{z}_i \rangle \quad (9.199)$$

where c_{spr} is the number density of springs. The same arguments can be used in order to find an expression for the tensile stress. In full analogy to Eq. (9.199) it reads

$$\sigma_{zz} = b_R c_{\text{spr}} \langle \hat{z}_i \hat{z}_i \rangle . \quad (9.200)$$

For the normal stress difference we obtain correspondingly

$$\sigma_{zz} - \sigma_{xx} = c_{\text{spr}} b_R (\langle \hat{z}_i^2 \rangle - \langle \hat{x}_i^2 \rangle) . \quad (9.201)$$

The averaging carried out on the right-hand sides involves two steps, a time average over the fluctuations of each spring and subsequently the average over all springs. $\langle \hat{z}_i^2 \rangle$ and $\langle \hat{x}_i^2 \rangle$ describe the resulting mean squared extensions along z (the unique axis) and x .

Introducing the total extension \hat{r}_i and the orientation angles θ_z^i and θ_x^i as described in Fig. 9.26, we may write for each spring i

$$\hat{z}_i = \hat{r}_i \cos \theta_z^i , \quad (9.202)$$

$$\hat{x}_i = \hat{r}_i \cos \theta_x^i . \quad (9.203)$$

We also insert the above expression for b_R and obtain

$$\sigma_{zz} - \sigma_{xx} = c_{\text{spr}} \frac{3kT}{a_R^2} (\langle \cos^2 \theta_z^i \rangle - \langle \cos^2 \theta_x^i \rangle) \langle \hat{r}_i^2 \rangle \quad (9.204)$$

with the assumption of independent fluctuations of \hat{r}_i and the orientation angles. Since for each spring i we have

$$\cos^2 \theta_x^i + \cos^2 \theta_y^i + \cos^2 \theta_z^i = 1 , \quad (9.205)$$

for the average over all springs correspondingly

$$\langle \cos^2 \theta_x^i \rangle + \langle \cos^2 \theta_y^i \rangle + \langle \cos^2 \theta_z^i \rangle = 1 , \quad (9.206)$$

furthermore, due to the overall uniaxial symmetry

$$\langle \cos^2 \theta_x^i \rangle = \langle \cos^2 \theta_y^i \rangle \quad (9.207)$$

and therefore

$$\langle \cos^2 \theta_x^i \rangle = \frac{1}{2} (1 - \langle \cos^2 \theta_z^i \rangle) , \quad (9.208)$$

for the normal stress difference we obtain

$$\sigma_{zz} - \sigma_{xx} = c_{\text{spr}} \frac{3kT}{a_{\text{R}}^2} \left(\frac{3\langle \cos^2 \theta_z^i \rangle - 1}{2} \right) \langle \hat{r}_i^2 \rangle . \quad (9.209)$$

The expression in parentheses on the right-hand side characterizes the degree of orientation of the springs in the sample and is known as the **orientational order parameter**. We denote it $S_{\text{or}}^{\text{spr}}$ and write shortly

$$\sigma_{zz} - \sigma_{xx} = c_{\text{spr}} \frac{3kT}{a_{\text{R}}^2} \langle \hat{r}_i^2 \rangle S_{\text{or}}^{\text{spr}} . \quad (9.210)$$

Next, we consider the optical properties of a spring. A stretched spring is an optically anisotropic object and we may write down a general expression for the associated polarizability tensor, denoted β_{spr} . It must have the form

$$\beta_{\text{spr}} = n_{\text{m}} \beta F(f) . \quad (9.211)$$

Here, β stands for the polarizability tensor of one monomer unit in a perfect orientation parallel to the stretching direction of the spring and n_{m} is the number of monomers per spring. $F(f)$ is a certain function of the tensile force in the spring, of even character

$$F(f) = F(-f) \quad (9.212)$$

and with the limiting values

$$F(f \rightarrow 0) \rightarrow 0 \quad (9.213)$$

$$F(f \rightarrow \infty) \rightarrow 1 . \quad (9.214)$$

There are good arguments in support of Eq. (9.211). The application of a force f simultaneously with the stretching of the spring also causes an orientation of the incorporated segments. The degree of orientation must be an unambiguous function of f only, not dependent on n_{m} . The latter point becomes clear when we consider the change in β_{spr} resulting from a coupling in series of n_{spr} springs with equal forces. One expects, of course,

$$\beta_{\text{spr}} \propto n_{\text{spr}} \quad (9.215)$$

and this is only fulfilled by the form Eq. (9.211). The even symmetry of $F(f)$ and the limits $F(f \rightarrow 0, \infty)$ are due to obvious reasons.

We may also formulate an expansion in powers of f valid for small forces. In the absence of linear terms we have

$$\beta_{\text{spr}} = n_{\text{m}} \beta F_2 f^2 \quad (9.216)$$

with

$$F_2 = \frac{1}{2} \frac{d^2 F}{df^2}. \quad (9.217)$$

In the next chapter we will again discuss the birefringence of uniaxially deformed samples. As will be shown, one can relate Δn to the degree of orientation of the monomers in a sample, as expressed by the associated orientational order parameter, S_{or}^m , and the anisotropy of the polarizability per monomer, $\Delta\beta$, using

$$\Delta n = \frac{\bar{n}^2 + 2}{\bar{n}} \frac{1}{6\varepsilon_0} c_m \Delta\beta S_{\text{or}}^m \quad (9.218)$$

(see Eqs. (10.50) and (10.28)). We use the same equation to formulate Δn for an ensemble of springs instead of the monomers and obtain

$$\Delta n = \frac{\bar{n}^2 + 2}{\bar{n}} \frac{1}{6\varepsilon_0} c_{\text{spr}} \Delta\beta_{\text{spr}} S_{\text{or}}^{\text{spr}}. \quad (9.219)$$

As the spring extensions and, thus the forces, fluctuate, we write for the anisotropy, $\Delta\beta_{\text{spr}}$, of the polarizability of a spring

$$\Delta\beta_{\text{spr}} = n_m \Delta\beta \langle F(f) \rangle. \quad (9.220)$$

Now we can express the stress-optical ratio. Adopting the series expansion Eq. (9.216) and using Eqs. (9.210), (9.219), and (9.220), we obtain

$$\frac{\Delta n}{\sigma_{zz} - \sigma_{xx}} = \frac{\bar{n}^2 + 2}{\bar{n}} \frac{1}{6\varepsilon_0} \frac{n_m \Delta\beta a_{\text{R}}^2}{3kT} \frac{\langle f^2 \rangle}{\langle \hat{r}_i^2 \rangle} F_2. \quad (9.221)$$

Since

$$\mathbf{f} = \frac{3kT}{a_{\text{R}}^2} \hat{\mathbf{r}}_i \quad (9.222)$$

and for an ideal chain

$$a_{\text{R}}^2 = n_m a_0^2,$$

there finally results

$$\frac{\Delta n}{\sigma_{zz} - \sigma_{xx}} = C_{\text{opt}} = \frac{1}{2\varepsilon_0} \frac{\bar{n}^2 + 2}{\bar{n}} \frac{kT}{a_0^2} F_2 \Delta\beta. \quad (9.223)$$

With this we have found an expression for C_{opt} that is, indeed, constant for a given polymer. We conclude that the stress-optical coefficient includes three microscopic parameters, the size a_0 of a monomer, expressing the chain stiffness, the optical anisotropy per monomer, $\Delta\beta$, and the coefficient F_2 , which relates to the elastic restoring forces.

Here we have presented the linear stress-optical rule as a basic property of polymer melts but, of course, it also holds for rubbers, with unchanged stress-optical coefficients. This must be the case, since stresses arise from a network

of chains in both melts and rubbers, so that the arguments presented above apply for both systems equally. Figure 9.27 shows as an example the relation between birefringence and tensile stress as observed for a sample of natural rubber.

Validity of the linear stress-optical rule points at the dominant role of the network forces in polymer melts. The Lodge equation of state can be interpreted on this basis. We introduced the equation empirically, as an appropriate combination of properties of rubbers with those of viscous liquids. It is possible to associate the equation with a microscopic model. Since the entanglement network, although temporary in its microscopic structure, leads under steady state conditions to stationary viscoelastic properties, we have to assume a continuous destruction and creation of stress-bearing chain sequences. This implies that at any time the network will consist of sequences of different ages. As long as a sequence exists, it can follow all imposed deformations.

To describe this situation, one may proceed as follows. Let $n(t, t')dt'$ be the number of stress-bearing sequences per unit volume, created during an interval dt' at a past time t' and persisting up to the present time t . Their contribution to the stress at t can be expressed as

$$n(t, t')kTB(t, t') dt' \quad (9.224)$$

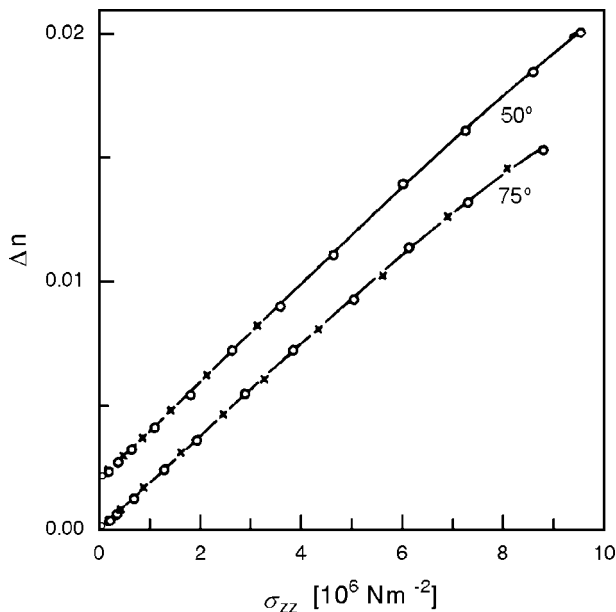


Fig. 9.27. Relation between birefringence and tensile stress for natural rubber. The upper curve is shifted in the vertical direction. Work of Treloar [109]

if we adopt ideal rubber behavior (Eqs. (9.74) and (9.86)). An equation in agreement with the Lodge equation of state is obtained when writing

$$(\boldsymbol{\sigma} + p\mathbf{1})(t) = \int_{t'=-\infty}^t n(t, t') kT \mathbf{B}(t, t') dt' . \quad (9.225)$$

Here the contributions of all active chain sequences with different ages are superimposed. To show the agreement, we rewrite the Lodge equation

$$(\boldsymbol{\sigma} + p\mathbf{1})(t) = - \int_{t'=-\infty}^t G(t-t') \frac{d\mathbf{B}(t, t')}{dt'} dt' \quad (9.226)$$

by carrying out an integration by parts

$$(\boldsymbol{\sigma} + p\mathbf{1})(t) = -\mathbf{B}(t, t' = t) \frac{dG}{dt'}(t' = t) + \int_{t'=-\infty}^t \frac{dG(t-t')}{dt'} \mathbf{B}(t, t') dt' . \quad (9.227)$$

Since

$$\mathbf{B}(t, t) = \mathbf{1} \quad (9.228)$$

we may incorporate the first term on the right-hand side in $p\mathbf{1}$ and write

$$(\boldsymbol{\sigma} + p\mathbf{1})(t) = \int_{t'=-\infty}^t m(t-t') \mathbf{B}(t, t') dt' \quad (9.229)$$

with

$$m(t-t') = \frac{dG(t-t')}{dt'} . \quad (9.230)$$

This is a second form for the equation of state of rubber-like liquids. $m(t-t')$ is called a **memory function**, because it characterizes the fading of the memory of the past. Since Eqs. (9.225) and (9.229) have equal forms we find here

$$m(t-t') = kTn(t, t') . \quad (9.231)$$

The model of appearing and disappearing load-bearing chain sequences thus provides us with a possible interpretation of the memory function of the Lodge liquid.

Further Reading

R.B. Bird, R.C. Armstrong, O. Hassager: *Dynamics of Polymeric Liquids*, Vol. 1 *Fluid Mechanics*, John Wiley & Sons, 1977

- R.B. Bird, R.C. Armstrong, O. Hassager: *Dynamics of Polymeric Liquids*, Vol. 2 *Kinetic Theory*, John Wiley & Sons, 1977
- P.J. Flory: *Principles of Polymer Chemistry*, Cornell University Press, 1953
- W.W. Graessley: *Viscoelasticity and Flow in Polymer Melts and Concentrated Solutions* in J.E. Mark, A. Eisenberg, W.W. Graessley, L. Mandelkern, J.L. Koenig: *Physical Properties of Polymers*, Am. Chem. Soc., 1984
- H. Janeschitz-Kriegl: *Polymer Melt Rheology and Flow Birefringence*, Springer, 1983
- R.G. Larson: *Constitutive Equations for Polymer Melts and Solutions*, Butterworths, 1988
- W. Retting, H.M. Laun: *Kunststoff-Physik*, Carl Hanser, 1991
- M. Rubinstein, R.H. Colby: *Polymer Physics*, Oxford University Press, 2003
- L.R.G. Treloar: *The Physics of Rubber Elasticity*, Clarendon Press, 1975

Deformation, Yielding and Fracture

A prerequisite for the use of polymeric materials in daily life is their mechanical stability. Goods made of plastics must keep their form under the permitted loads and one has to be sure that they will not break under ordinary conditions. Therefore, a good knowledge of the limits of mechanical stability is of utmost importance. This chapter deals with these **ultimate properties**. We will discuss the mechanisms and laws controlling deformation in polymeric solids and also present some of the generally used basic concepts of fracture mechanics. From the long experience in polymer manufacturing there exists a wealth of knowledge. It is far too broad to treat it here in a survey. So we will just consider some of the main observations.

Deformations of a polymeric solid always include, in addition to the reversible part, an irreversible flow. Usually this plastic flow sets in immediately when a sample is stretched and becomes very intensified when the **yield point** is reached. Upon further drawing this **strain softening** is often followed by a **strain hardening**, which stabilizes the sample again. Temperature plays a big role and there are also effects from the environment when fluids or gases that permeate into the polymer are present. From all the observations on various polymeric solids, it has become clear that there are two routes for the yielding. They have a different appearance and are easily discriminated. The first type is known as **shear yielding**. Figure 10.1 gives an example and depicts the behavior of a polyethylene with high crystallinity. Stretching a sample with a constant drawing rate results in the load-extension curve shown. The force increases at first but then, reaching the yield point, it passes over a maximum and somewhere a **neck** appears. Continuing the drawing, the neck extends up to the full length of the sample. This **cold-drawing** takes place under a constant tensile force and finally elongates the sample by several times its original length. If the stretching is continued further, the force increases again, up to the point of breaking. The sketches included in the figure illustrate all these changes. Shear yielding can also occur without necking and then leads to a continuously growing homogeneous plastic deformation of the sample. In the next section, this simpler case exemplified by a polyethylene

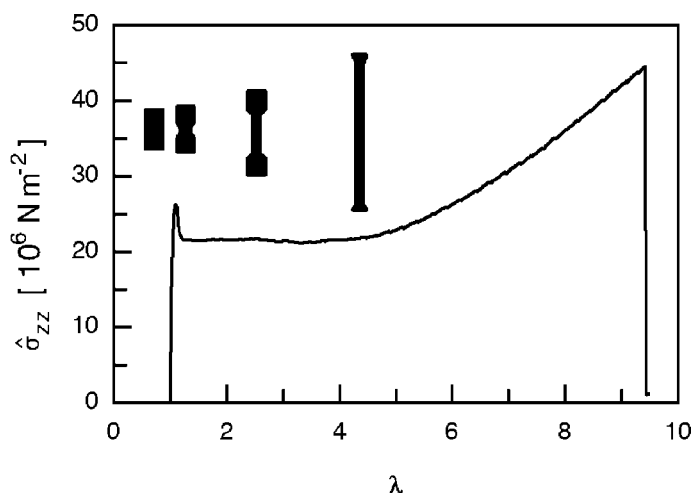


Fig. 10.1. Load (nominal tensile stress $\hat{\sigma}_{zz}$)-extension (ratio λ) curve of a sample of PE ($M = 3.6 \times 10^5 \text{ g mol}^{-1}$, $\phi_c = 0.8$, drawing rate $d\lambda/dt = 2.4 \times 10^{-2} \text{ s}^{-1}$). The changes in the shape of the sample are schematically indicated

with low crystallinity will be presented in detail. Shear yielding is typical for all semicrystalline polymers, but it is also found for a few amorphous polymers. Polycarbonate (PC) is an example. Figure 10.2 presents a photograph of a stretched polycarbonate developing a neck. The image explains the origin of the name ‘shear yielding’: Here we observe **shear bands** and they are preferentially oriented along the directions of maximum shear stress.

The second route of yielding is observed, for example, for polystyrene. Figure 10.3 depicts again a load-extension curve. The force increases at first linearly but then, after a slight bending, the sample breaks before a maximum is reached. In the bending range just before fracture, a whitening is observed, as shown by the photograph. Closer inspection reveals the formation of many void containing microdeformation zones. These localized zones of plastic flow are called **crazes**, and **crazing** is the term used to address this other mech-

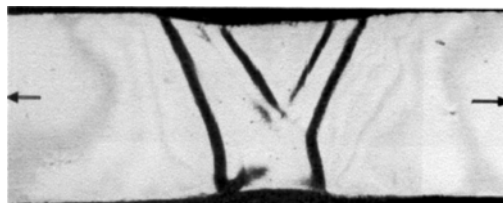


Fig. 10.2. Formation of shear bands at the beginning of necking, observed for a sample of PC. The *arrows* indicate the direction of the applied tensile stress. Micrograph obtained by Morbitzer [122]

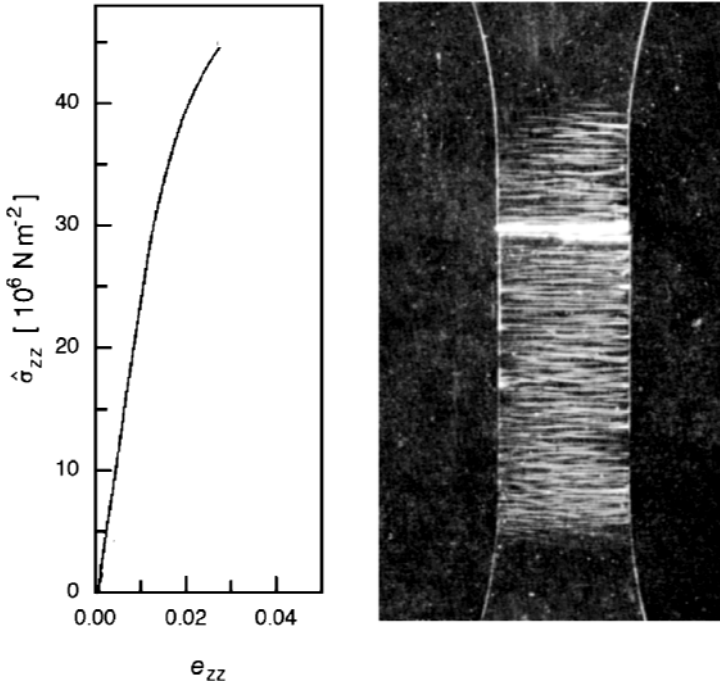


Fig. 10.3. Stress-strain curve of a sample of PS and photograph showing crazes

anism. Shear yielding and crazing are not alternative processes that exclude each other. Often both show up together, or one follows the other. Which one is dominant depends on the stress conditions and the temperature.

The amount of flow before fracture determines the **ductility** of a polymer sample. In **tough** materials, a considerable amount of energy is dissipated by yield processes prior to fracture. In contrast, **brittle** samples break without showing much preceding flow. The difference becomes apparent in the fracture energy, which is much lower for brittle samples than for tough compounds. The fracture energy, as determined by the area under the load-extension curve, is the appropriate measure for the ductility of a given sample. Therefore, regarding our examples, polyethylene is to be considered as tough and polystyrene as brittle.

The ductility changes with temperature. This is demonstrated by Fig. 10.4, showing measurements on poly(vinylchloride) (PVC) at different temperatures. Second, a series of load-extension curves obtained at one temperature for various strain rates is presented. Poly(vinylchloride) is always brittle when compared to polyethylene and the brittleness of the sample increases upon lowering the temperature and on increasing the strain rate. These tendencies, which are generally found, are due to obvious reasons. Yielding is based on specific relaxation processes and thus depends on the ratio of strain rates to

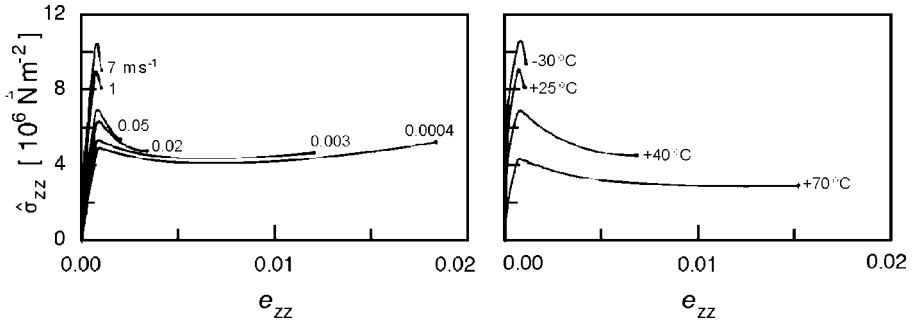


Fig. 10.4. Stress–strain curves of PVC measured at room temperature for the indicated strain rates (*left*) and at different temperatures for a constant strain rate ($\dot{e}_{zz} = 10^{-3} \text{ s}^{-1}$) (*right*). From Retting [123]

the respective relaxation rates. Large values of this ratio imply that plastic flow cannot take place and this results in brittle behavior. Sometimes, an early break at high strain rates is also caused by adiabatic heating effects. If the heat is not conducted away rapidly enough, crystallites may melt and the sample fails by a kind of melt fracture. Toughness is a property that is appreciated in many applications. The desire for high-performance polymer materials is to have, simultaneously, a high stress at the yield point, high values of the elastic modulus and a high ductility. To achieve this synergism is a difficult task and a main goal of industrial research.

10.1 Shear Deformation in Semicrystalline Polymers

If forces are applied to a semicrystalline polymer in the way of a tension, a compression or a simple shear, deformations take place under a constant volume. Hence, they are always composed of a reversible elastic shear and an irreversible shear yielding. In this section, we discuss the properties of **tensile deformations**. As it is found, here deformation mechanisms change at three critical strains associated with a strain softening, a strain hardening and a loss of memory of the initial sample shape. The drawing stress is set up of contributions from the amorphous network, the skeleton of crystallites and viscous forces, and experiments enable a separation to be carried out.

10.1.1 Critical Strains

A number of different experiments are necessary for a characterization of the tensile deformation properties of a sample. Measurements carried out for a poly(ethylene-*co*-vinylacetate) (PEVA12, 12% vinylacetate units, $\phi_c = 0.33$) provide an instructive, typical example.

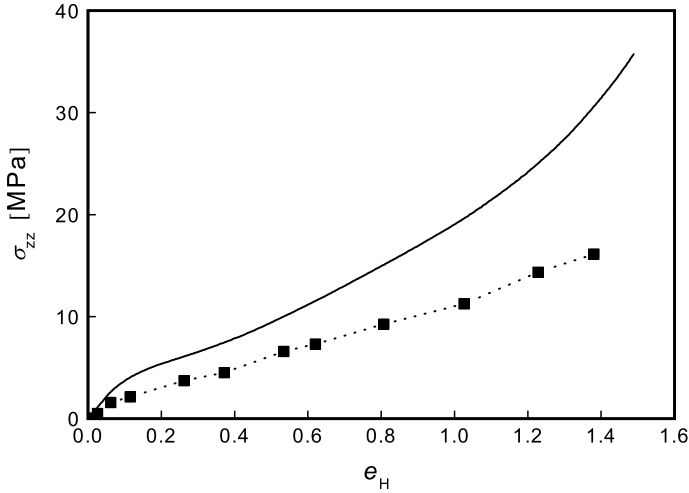


Fig. 10.5. Stretching curve measured for PEVA12 with a strain rate $\dot{e}_H = 0.005 \text{ s}^{-1}$ (continuous line). Quasi-static stress-strain relationship (squares) [124]

Tensile stress deforms PEVA12 homogeneously, i.e., without a necking. Figure 10.5 shows the **stretching curve** describing the relationship between the tensile stress

$$\sigma_{zz} = \frac{f}{A} \quad (f: \text{force, } A: \text{varying cross-section}) \quad (10.1)$$

and the **true strain** or **Hencky strain**

$$e_H = \ln \lambda . \quad (10.2)$$

The stretching curve was measured with a fixed Hencky strain rate $\dot{e}_H = 0.005 \text{ s}^{-1}$. The shape of the curve is highly non-linear. It indicates a strain softening at a yield point, located at $e_H \approx 0.1$. Later there follows a strain hardening, setting in at $e_H \approx 0.6$.

The true strain is always composed of a recoverable elastic part, $e_{H,e}$, and a non-recoverable plastic part, $e_{H,p}$, as

$$e_H = e_{H,e} + e_{H,p} . \quad (10.3)$$

A decomposition is provided by a **step-cycle test** like the one presented in Fig. 10.6. In this test mode the stretching is performed stepwise, being interrupted after each step by an unloading-loading cycle. The cycle amplitude gives the elastic part, the strain remaining at zero load the plastic part. The continuous run of Fig. 10.5 is also included and it coincides with the series of steps. The results of a decomposition at various strains are given in Fig. 10.7. They show some remarkable features typical for semicrystalline polymers:

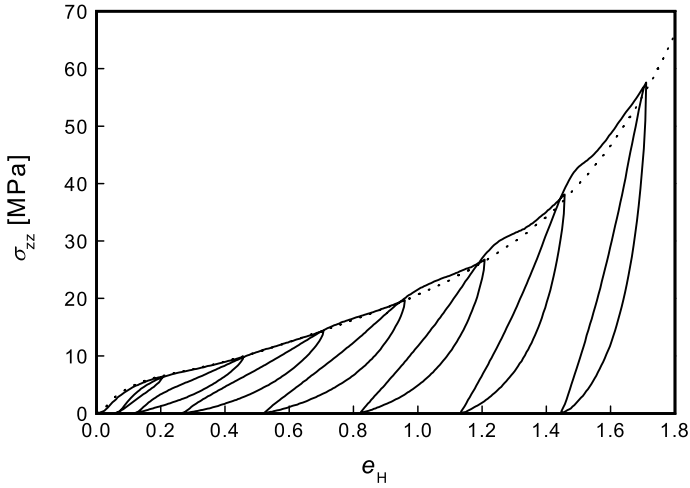


Fig. 10.6. Step-cycle test carried out for PEVA12 ($\dot{e}_H = 0.005 \text{ s}^{-1}$) [124]

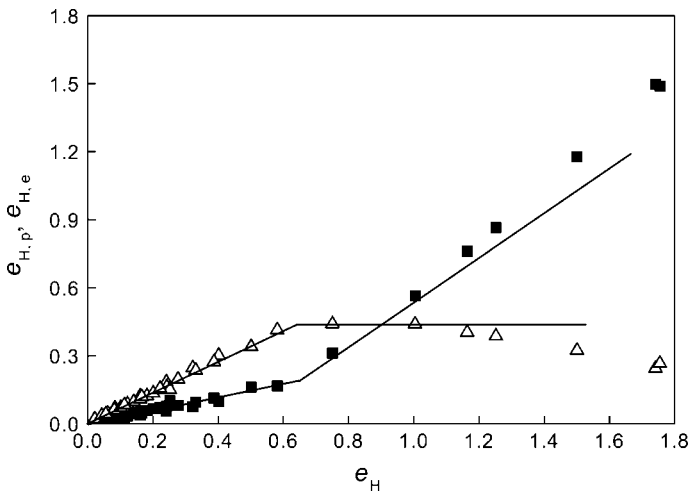


Fig. 10.7. Elastic (*triangles*) and plastic (*squares*) parts of the strain derived from the step-cycle test shown in Fig. 10.6 [124]

- The elastic strain reaches a maximum value on a plateau. This occurs at that strain where strain hardening sets in, in PEVA12 for $e_H \approx 0.6$.
- A plastic strain develops from the very beginning of the deformation process and not, as in metals, only for strains above a yield point.
- The plateau has a limited extension and the elastic strain then decreases again.

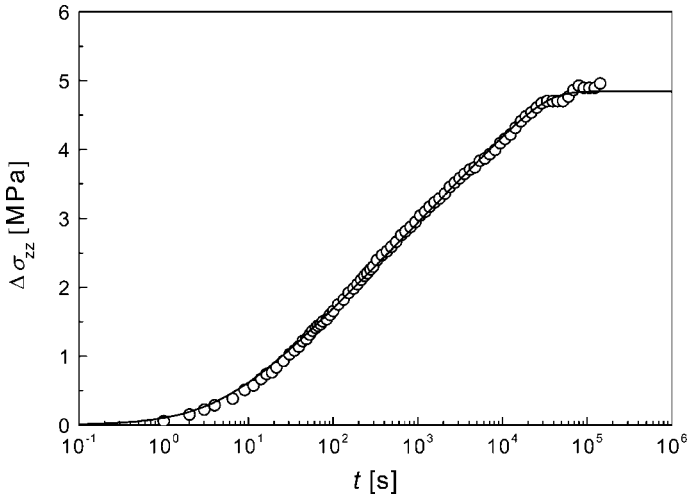


Fig. 10.8. PEVA12: Stress relaxation after a stretching to $e_H = 0.8$ (*open spheres*). Comparison with a theoretical calculation (*continuous line*) [124]

If a semicrystalline polymer is stretched to a certain strain and then arrested, the stress decays. Figure 10.8 shows the time dependence of the stress decay

$$\Delta\sigma_{zz} = \sigma_{zz}(0) - \sigma_{zz}(t) \quad (10.4)$$

for PEVA12 after a stretching to $e_H = 0.8$ in a $\Delta\sigma_{zz}$ vs. $\log t$ plot. In the experiment more characteristic features show up:

- The decay follows a logarithmic law over a large time range, $\Delta\sigma_{zz} \propto \log t + \text{const.}$
- This range is limited and finally an end value is approached.

A subtraction of the total amount of stress decay, $\Delta\sigma_{zz}(t \rightarrow \infty)$, from the respective initial stresses measured along the stretching curve gives the stress-strue strain relationship associated with the limit of zero strain rates, i.e., under quasi-state conditions. The **quasi-static stress-strain relationship** obtained in this manner for PEVA12 is included in Fig. 10.5.

Figures 10.9 to 10.11 illustrate how stretching curves and critical strains vary with temperature, again with results for PEVA12, and with the crystallinity; here polyethylenes with different crystallinities are compared. Curves demonstrate a further general property of semicrystalline polymers. While the stresses vary in systematic manner, there is no effect on the **critical strains** for softening ($e_H \approx 0.1$) and hardening ($e_H \approx 0.6$) and virtually no change in the elastic-plastic composition of the strains. Hence, tensile deformation of semicrystalline polymers is **strain-controlled** and changes the mechanism at two critical strains that are temperature and crystallinity invariant.

What is the background of these peculiar deformation properties? A first insight is provided by the stretching curves in Fig. 10.11, when considering

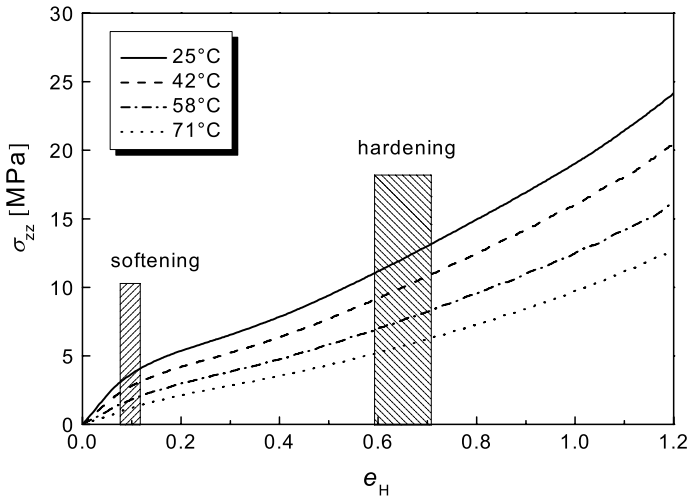


Fig. 10.9. PEVA12: Stretching curves measured at the indicated temperatures ($\dot{e}_H = 0.005 \text{ s}^{-1}$) [125]

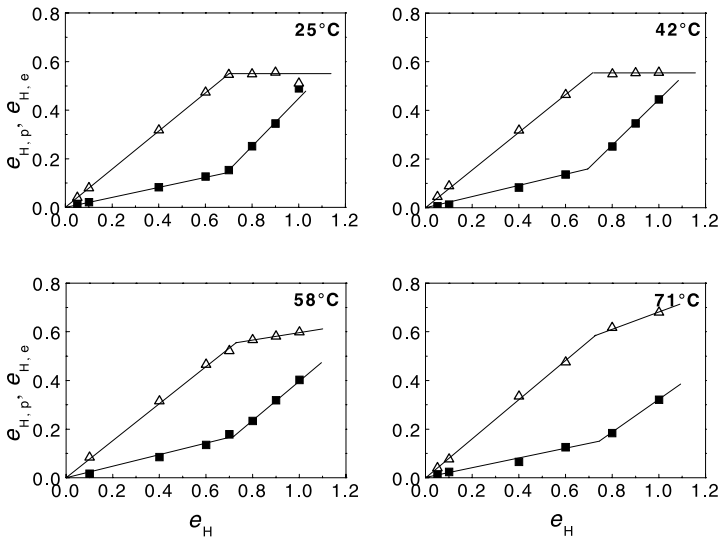


Fig. 10.10. PEVA12: Plastic (*squares*) and elastic (*triangles*) parts of the strain deduced from step-cycle tests at different temperatures [125]

the similarity in shape of the curves of the high crystallinity sample PE27 with that of PEVA27, which is a rubber-like material. It indicates that, even if PE27 is a solid from the external appearance, the tensile deformation properties are still those of a rubber. They are only modified by a high effective inner viscosity. The rubber-like forces originate from the amorphous regions,

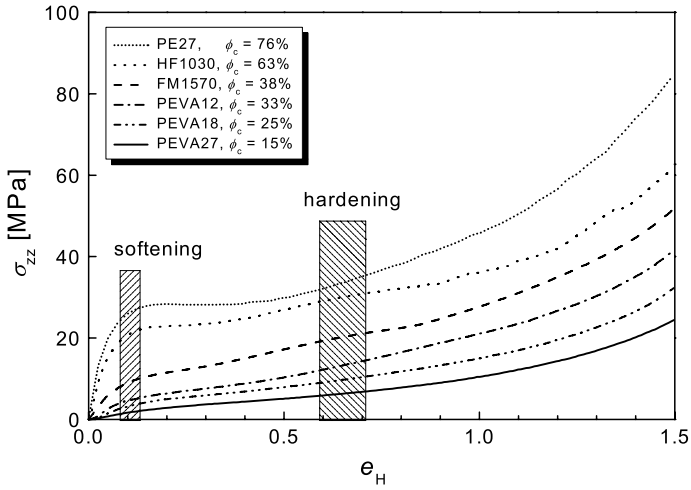


Fig. 10.11. Stretching curves obtained at room temperature for various PE samples with different crystallinities ($\dot{e}_H = 0.005 \text{ s}^{-1}$) [125]

cross-links being given not only by the crystallites but also by the locked-in entanglements. Crystallization from the melt does not remove the entanglements, but just shifts them into the remaining fluid-like regions. That the original entanglement network is globally preserved up to rather high deformations is demonstrated by findings such as those presented in Fig. 10.12.

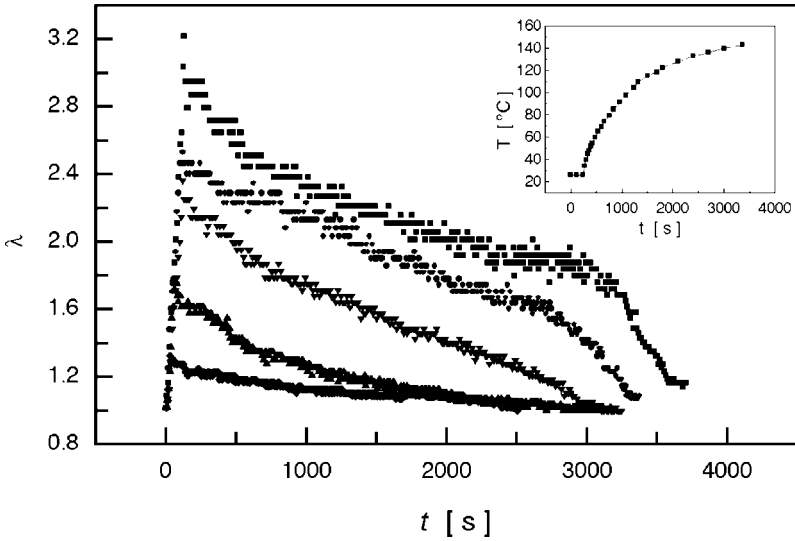


Fig. 10.12. Shrinkage of a stretched PE sample upon heating. Observations for various initial extensions. The heating program is given in the *insert* [126]

A polyethylene with high crystallinity was stretched to different extensions λ , then one clamp of the stretching device was opened and the shrinkage observed. The opening led to a rapid first contraction as given by the elastic part of the strain. When the sample was subsequently heated the shrinkage continued. For $\lambda < 2.5$ it shrank back to its original length when the temperature of complete crystal melting was reached. The entanglement network then returned to its initial isotropic state. A memory of the original shape was preserved in this manner. For $\lambda > 2.5$ the recovery was no longer complete. Now the drawing was accompanied by disentangling processes. Figure 10.7 indicates that the elasticity plateau ends at a certain strain. As comparisons show, exactly at this strain chains begin to disentangle.

Strain control of the deformation properties implies that the strain is homogeneous in the semicrystalline sample. The crystal lamellae possess a granular substructure; nm-sized **crystal blocks** are the basic morphological elements. The **sliding motions** of the blocks against each other provide sufficient degrees of freedom to accommodate any imposed strain. Figure 10.13 is a sketch of the given situation and Fig. 10.14 shows an image, as obtained in an electron microscope for a drawn poly(1-butene)(P1B) sample. In addition to the sliding, blocks can be sheared or can experience a solid–solid phase transition, from the stable modification to another modification, which is preferred in a stress field. Block sliding sets in at the beginning of drawing as a local process and then, at the yield point, it turns into a collective motion. The block movements are partially reversible, partially irreversible.

The subsequent strain hardening relates to another mechanism, namely a morphological transformation. Drawing an initially isotropic sample at first deforms the spherulites, but then destroys them and creates a fibrillar structure. Figure 10.15 presents micrographs obtained in a polarizing microscope before and after drawing a film of polyethylene. The morphology in the extended state is set up of fibrillar elements. Optical microscopy cannot resolve the fibrils. These show up in an atomic force microscope, as for example, in the picture of Fig. 10.16. Why does fibrillation start at a certain critical strain? The answer is that the network always exerts a stress on the crystal blocks. At

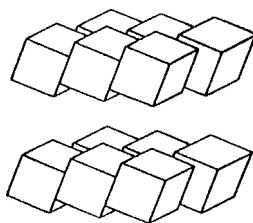


Fig. 10.13. Arrangement of crystal blocks within a lamella. Imposing an external strain leads to sliding motions

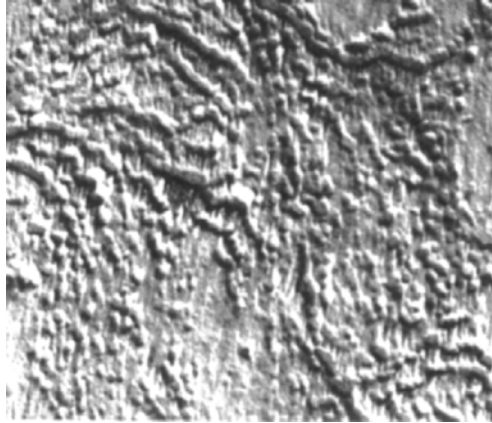


Fig. 10.14. Electron micrograph of a drawn sample of P1B showing a splitting-up of the crystal lamellae into blocky elements. From Yang and Geil [127]

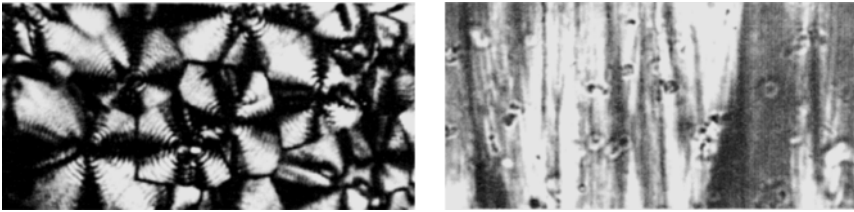


Fig. 10.15. Morphological changes on cold-drawing, observed for a film of PE in a polarizing optical microscope. Micrographs obtained by Hay and Keller [128]

a certain external strain, which is transferred without changes to the network, it reaches a value where blocks, first the oblique oriented ones experiencing the highest resolved shear stress, are no longer stable, disassociate and transform into fibrils.

All structural changes may also be followed by X-ray scattering, by registration of scattering patterns during drawing, or for necking samples at various positions in the shoulder. This is exemplified by Fig. 10.17, which in addition to the isotropic pattern of the original structure of a polyethylene and the final pattern measured in the neck center also includes a pattern obtained somewhere in the shoulder region. The two latter patterns are typical fiber diagrams showing cylindrical symmetry around the drawing direction. The sliding and shearing of crystal blocks and a transformation of a certain fraction into the triclinic modification produces the pattern in the middle. Fibril formation is indicated by the appearance of sharp Bragg reflections on the equator. They show up for the first time when the plateau in the elastic strain is reached and the region of strain hardening is entered.

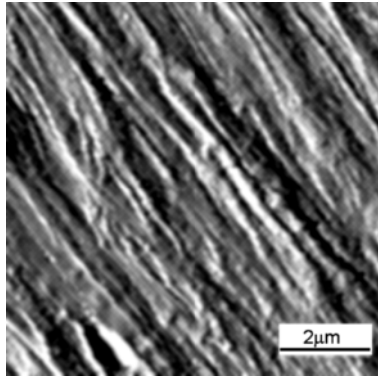


Fig. 10.16. Surface structure of a cold-drawn PE film registered with an atomic force microscope, using the deflection mode [126]



Fig. 10.17. X-ray scattering patterns of PE, as registered for the isotropic part (*left*), the center of the shoulder (*center*) and the neck (*right*) of a cold-drawn sample. The two reflections in the isotropic pattern are to be assigned to the 110-lattice and the 200-lattice planes of orthorhombic PE. The third reflection with a larger lattice plane spacing emerging in the textured patterns is due to a triclinic crystalline phase that forms during drawing [126]

10.1.2 Constituents of the Drawing Stress

The stress arising during stretching a semicrystalline polymer thus is set up of three contributions:

- rubber-like forces originating from the stretched network of entangled amorphous chain sequences,
- forces transmitted by the skeleton of crystallites, and
- forces arising from the viscosity.

An evaluation of experimental data on the basis of the rheomechanical model depicted in Fig. 10.18 allows their determination. In the zero strain rate limit, where all viscous forces vanish, one finds a superposition of the network force with a force that is transmitted by the crystal skeleton. The model describes

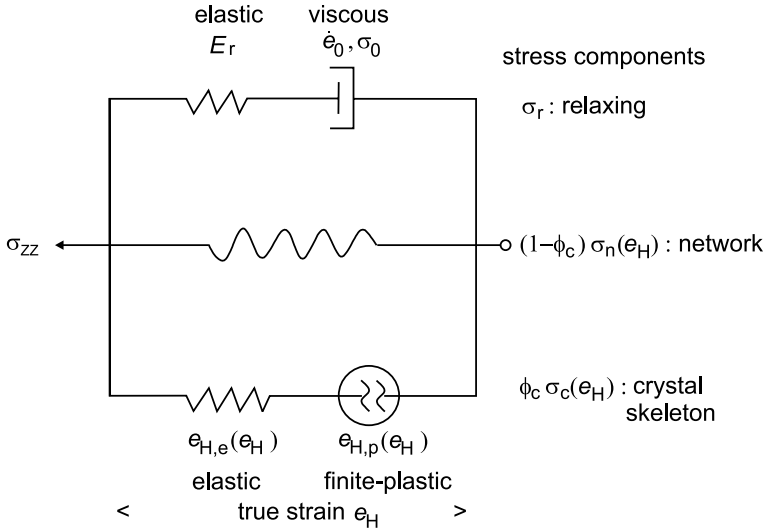


Fig. 10.18. A three-component model treating the tensile deformation properties of semicrystalline polymers

this quasi-static stress by the lower two branches with stresses $(1 - \phi_c)\sigma_n$ and $\phi_c\sigma_c$. The third branch represents the relaxing viscous stress σ_r . As shown later in this section (Fig. 10.22), drawing stresses increase with the strain rate according to the relation

$$\sigma_y = \sigma_0 \ln \dot{\epsilon}_H + \text{const} . \tag{10.5}$$

This suggests describing the viscous force σ_r by the **Eyring law of viscosities** as

$$\frac{\sigma_r}{\sigma_0} = a \sinh \frac{\dot{\epsilon}_H}{\dot{\epsilon}_0} \tag{10.6}$$

$$\approx \ln \frac{\dot{\epsilon}_H}{\dot{\epsilon}_0} \left(\text{for } \frac{\dot{\epsilon}_H}{\dot{\epsilon}_0} \gg 1 \right) . \tag{10.7}$$

In the limit $\dot{\epsilon}_H \rightarrow 0$ the Eyring law turns into the Newton law, with

$$\sigma_r \approx \frac{\sigma_0}{\dot{\epsilon}_0} \dot{\epsilon}_H . \tag{10.8}$$

The Eyring law of viscosity uses two parameters, the reference stress σ_0 and the reference strain rate $\dot{\epsilon}_0$, rather than one viscosity coefficient η_0 only. According to Eq. (10.8) η_0 , σ_0 and $\dot{\epsilon}_0$ are related by

$$\frac{\sigma_0}{\dot{\epsilon}_0} = \eta_0 . \tag{10.9}$$

The relaxing stress branch includes also an elastic element, with a Young's modulus E_r .

The stress transmitted by the crystal skeleton, $\phi_c \sigma_c$, is of peculiar nature. In principal, the block sliding could lead to a complete decay of the force acting within the skeleton, but this is not found; after a sufficiently long time a stationary value of the crystal transmitted stress is reached. Therefore, the skeleton of the blocks does not resemble a purely viscous system. It cannot be treated like an ideal elasto-plastic body either. The latter system remains elastic until a certain yield point where a permanent flow at a constant stress sets in, but semicrystalline polymers behave differently. There exists a plastic flow from the very beginning, down to smallest strains and stresses. Even more importantly, this flow is limited and remains finite at every imposed strain or applied stress. Hence, the crystal skeleton shows a behavior to be addressed as **finite plasticity**. This plasticity arises together with an elasticity that can be high, being represented by the elastic strain $e_{H,e}$. What is the background of this behavior? The answer is that the plastic deformation remains finite because the sample hardens during the flow, in a manner that finally brings all flow processes to an end.

All parameters of the rheomechanical model can be derived from a set of experiments like the ones for PEVA12 presented here. The properties of the relaxing stress branch follow from the stress relaxation experiments. σ_r obeys the differential equation

$$\dot{e}_H = \frac{\dot{\sigma}_r}{E_r} + \dot{e}_0 \sinh \frac{\sigma_r}{\sigma_0} = 0 \quad (10.10)$$

or

$$\frac{d}{dt} \frac{\sigma_r}{\sigma_0} = -\frac{1}{\tau_r} \sinh \frac{\sigma_r}{\sigma_0} \quad (10.11)$$

with

$$\tau_r^{-1} = \frac{\dot{e}_0 E_r}{\sigma_0} = \frac{E_r}{\eta_0} . \quad (10.12)$$

τ_r denotes the relaxation time in the Newtonian limit of low stresses. The differential equation can be solved by a separation of the variables σ_r/σ_0 and t/τ_r . The result is

$$\frac{\sigma_r(t)}{\sigma_0} = 2 \operatorname{atanh} \left(\tanh \frac{\sigma_r(0)}{2\sigma_0} \exp -\frac{t}{\tau_r} \right) . \quad (10.13)$$

Using

$$\operatorname{atanh} x = \frac{1}{2} \ln \frac{1+x}{1-x} \quad (\text{valid for } |x| < 1) \quad (10.14)$$

for times in the range

$$\frac{t}{\tau_r} \ll 1 \quad (10.15)$$

leads to the observed logarithmic time dependence

$$\frac{\sigma_r(t)}{\sigma_0} \approx \ln \frac{t}{\tau_r} + \text{const} \quad (10.16)$$

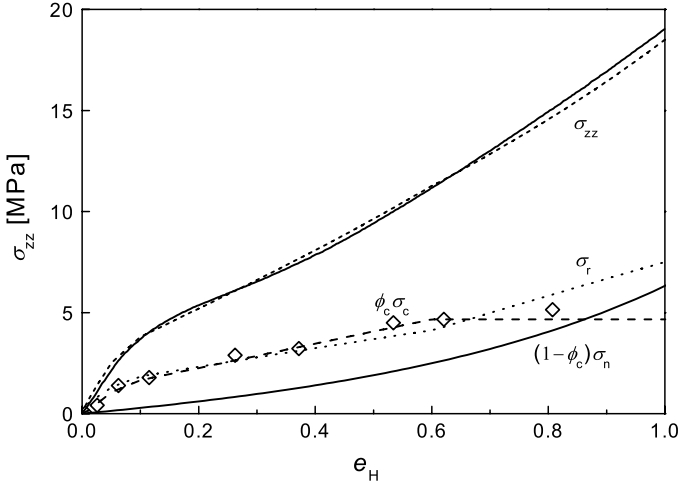


Fig. 10.19. Decomposition of the stretching curve shown in Fig. 10.5 in the three components of the model in Fig. 10.18: Quasi-static elasto-plastic contribution of the crystal skeleton ($\phi_c \sigma_c$), elastic stress of the entanglement network ($(1 - \phi_c) \sigma_n$) and relaxing viscous stress (σ_r) [124]

As can be seen, the curve slope gives the reference stress σ_0 . A fit of stress relaxation data by Eq. (10.13), as exemplified in Fig. 10.8, yields the total amount of stress relaxation $\Delta\sigma_{zz}(t \rightarrow \infty) = \sigma_r$.

For the splitting of the quasi-static stress – obtained after the subtraction of σ_r from the measured stress σ – into its two components, the asymptotic behavior at large strains can be used. It is dominated by the network forces and thus determined by the associated network shear modulus. The properties of the crystallite branch, i.e., the associated elasticity and finite plasticity, follow from step-cycle tests.

Figure 10.19 shows the decomposition of the stress into its three parts for the stretching curve of Fig. 10.5. For this polyethylene with low crystallinity skeleton force and viscous stresses are of similar magnitude. The network stress is at first negligible, but finally dominates. The plateau observed for σ_c is conceivable. From the onset of fibril formation a further elongation of the crystal skeleton can be achieved by a morphological transition, namely the transformation of blocks into fibrils. This takes place at a constant or only slowly increasing stress.

10.1.3 The Mechanics of Neck Formation

Figure 10.1 showed the drawing properties of a polyethylene with high crystallinity at room temperature. Having reached the yield point, visible flow sets in at some point of the sample and is accompanied by a drop in the load. The lateral dimensions narrow and finally a neck is formed, with a smaller, but

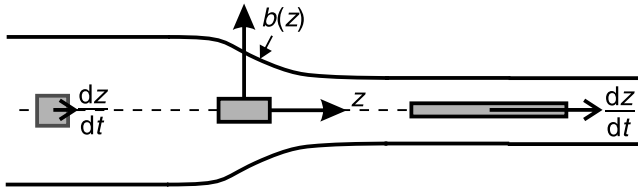


Fig. 10.20. States of deformation of a volume element passed over by a shoulder with the profile $b(z)$, and the velocity dz/dt relative to the shoulder

again stable cross-section area. A shoulder with a continuous profile develops between the original parts and the neck. Further extension of the sample is achieved by an increase of the neck length, i.e., a move of the two shoulders over the sample. The external force that has to be applied for this cold-drawing remains constant as long as the neck length increases.

It is instructive to analyze in detail the deformation process arising from the passage of the shoulder over some point in the sample. We select a sample with cylindrical shape, consider a volume element at the centerline and follow the changes in its shape from the original state into the final extended state. The states of deformation imposed on the volume element if the shoulder is moved over its position are well-defined. Since shear flow occurs without a volume change, the sequence of deformation states can be directly derived from the profile of the shoulder. We choose a moving coordinate system fixed at the center of the shoulder and describe the profile of the shoulder by the function $b(z)$, giving the radius b of the sample as a function of the coordinate z , as indicated in Fig. 10.20. For a volume element at the centerline, with radius l_ρ and length l_z , we have due to its incompressibility

$$l_z(z)\pi l_\rho^2(z) = \text{const} \quad (10.17)$$

Its extension, λ depends on z only, being given by

$$\lambda(z) = \frac{l_z(z)}{l_z(-\infty)} = \frac{l_\rho^2(-\infty)}{l_\rho^2(z)} = \frac{b^2(-\infty)}{b^2(z)}. \quad (10.18)$$

The profile also determines the strain rate, being given by

$$\frac{d\lambda}{dt} = \frac{d\lambda}{dz} \frac{dz}{dt} = -\frac{2b^2(-\infty)}{b^3(z)} \frac{db}{dz} \frac{dz}{dt}. \quad (10.19)$$

Here, dz/dt denotes the velocity of the volume element relative to the shoulder as measured in the moving coordinate system. Since the material flow through the shoulder is a constant, we write

$$\pi b^2(z) \frac{dz}{dt} = \text{const},$$

and therefore obtain

$$\frac{d\lambda}{dt} \propto -\frac{1}{b^5(z)} \frac{db}{dz} \quad (10.20)$$

or, in terms of the Hencky strain rate,

$$\dot{\epsilon}_H = \frac{1}{\lambda} \frac{d\lambda}{dt} \propto -\frac{1}{b^3} \frac{db}{dz} . \quad (10.21)$$

Equation (10.21) states that the extension rate of the volume element is not a constant but strongly time-dependent. It starts from zero, then increases, passes over a maximum near the position of the largest slope in the profile and finally returns to zero.

This peculiar time dependence of the deformation rate is associated with a simple law for the evolution of stress. Since the external force during cold-drawing is constant, the tensile stress acting on the volume element follows from

$$\sigma_{zz}(z)\pi b^2(z) = \text{const} \quad (10.22)$$

if we assume a uniform distribution over the cross-section. As a consequence stress and extension become linearly related,

$$\sigma_{zz}(z) \propto \lambda(z) . \quad (10.23)$$

Equation (10.23) is imposed by the conditions of the drawing experiment. Indeed, it is exactly this requirement by which the time-dependent deformation $\lambda(t)$ is selected and thus the profile determined.

In order to understand how this selection mechanism works we need to know the variation of the stretching curves with the applied Hencky strain rate. Figure 10.21 presents a series of curves $\sigma_{zz}(\lambda)$ obtained for a polyethylene with high crystallinity, for Hencky strain rates in the range $\dot{\epsilon}_H = (0.35 - 10) \times 10^{-2} \text{ s}^{-1}$. With increasing strain rate, the stress increases throughout the whole range. Figure 10.22 shows the relation between the stress at the yield point, σ_y , and the strain rate. It is well-described by the expression

$$\sigma_y = \sigma_0 \ln \dot{\epsilon}_H + \text{const} , \quad (10.24)$$

indicating validity of the Eyring law of viscosities, Eq. (10.7).

Let us for the moment forget about the strain rate effects and assume a rate-independent stress-strain curve of the same type as the experimental curves. We may ask for the expected result of an experiment where the externally applied tensile stress increases linearly with the extension, $\sigma_{zz} \propto \lambda$, which is the condition experienced by each volume element during cold-drawing. Figure 10.23 depicts the situation. If the load reaches the yield point, here at $\lambda_A \approx 1.1$, the stress will from thereon follow the straight line included in the figure. Obviously, equilibrium cannot be established over a large range of deformations up to the point where the line and the stress-extension curve cross each other again. At this point, λ_B , an equilibrium is again established.

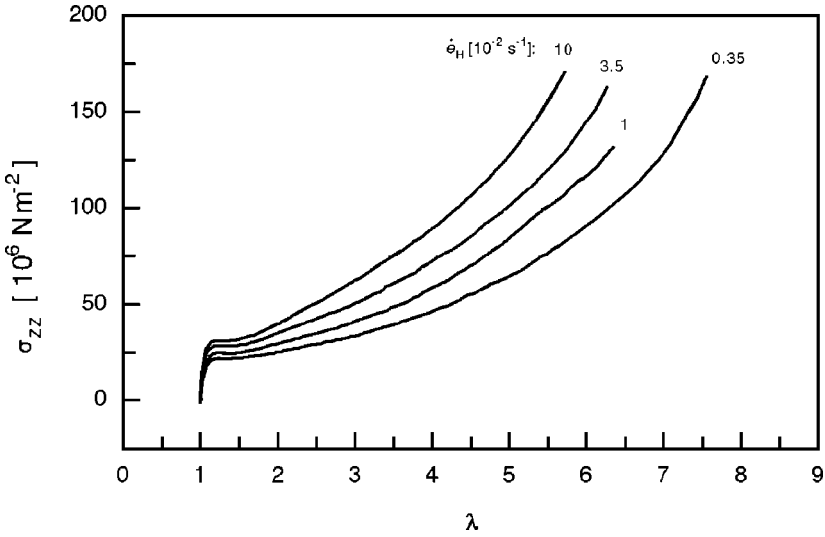


Fig. 10.21. Stress-extension curves measured under video control for a sample of PE ($M = 3.6 \times 10^5 \text{ g mol}^{-1}$, $\phi_c = 0.8$) at the indicated Hencky strain rates. Constant strain rates were accomplished by a registration of the strain in the center of the developing neck and a continuous readjustment of the applied tensile force [126]

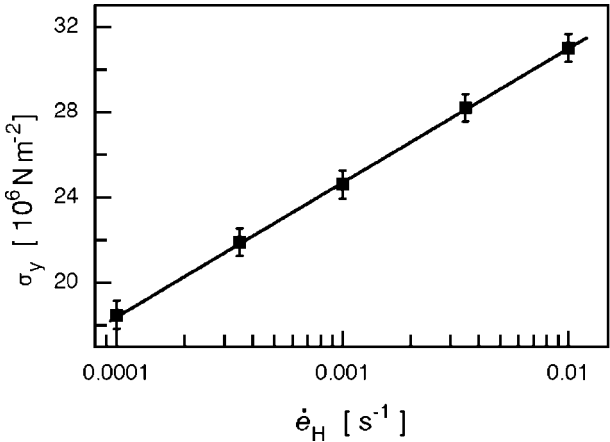


Fig. 10.22. Dependence of the stress at the plateau, σ_y , on the Hencky strain rate, deduced from the data in Fig. 10.21 [126]

Between λ_A and λ_B , there exists a gap in the sequence of accessible states of deformation, which is a consequence of the non-linearity of the stress-extension curve.

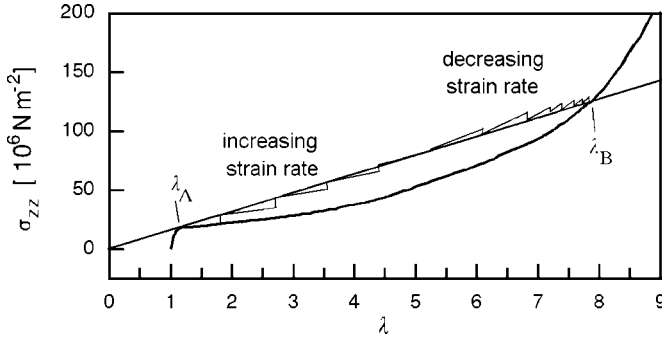


Fig. 10.23. Mechanical response of a volume element in a fiber with the shown $\sigma_{zz}(\lambda)$ dependence, if subjected to a linearly increasing stress as represented by the *straight line*. For a hypothetical sample without internal friction there is no equilibrium between λ_A and λ_B . In the real sample, a balance is achieved by the strain rate-dependent viscous forces (*thin line with steps*)

Absence of deformation states between λ_A and λ_B is the ideal case. The observation of a shoulder with finite extension in cold-drawn polymer samples indicates that reality is different, as this implies a continuous transition from λ_A to λ_B . The establishment of force-balanced states also in the transition region is accomplished by the strain rate effects. Quite generally, stresses grow and decay with increasing and decreasing strain rates, respectively, thus allowing for a continuous readjustment of the internal forces to the linear relation $\sigma_{zz} \propto \lambda$ imposed by the drawing-experiment. According to Eq. (10.21), the shoulder profile determines the strain rate at each point, and it possesses exactly that shape necessary for the balance.

Is there a criterion that allows us to predict whether or not necking occurs on stretching a sample with a constant speed? Our discussion of the factors determining the shoulder profile has already focussed on the main point giving the answer. Necking is a direct consequence of the occurrence of a gap in the sequence of accessible states. Figure 10.24 may help to further explain the situation. Being concerned about the equilibrium properties of an incompressible fiber with a sigmoidal $\sigma_{zz}(\lambda)$ dependence, we also should have a look at the shape of the associated force-extension curve given by $f(\lambda) \propto \sigma_{zz}/\lambda$. As we can see, in contrast to $\sigma_{zz}(\lambda)$, which possesses a plateau, $f(\lambda)$ exhibits a maximum and a minimum. The extrema are located at the positions where

$$\frac{d}{d\lambda} \frac{\sigma_{zz}}{\lambda} = 0 \tag{10.25}$$

or

$$\frac{d\sigma_{zz}}{d\lambda} = \frac{\sigma_{zz}}{\lambda}, \tag{10.26}$$

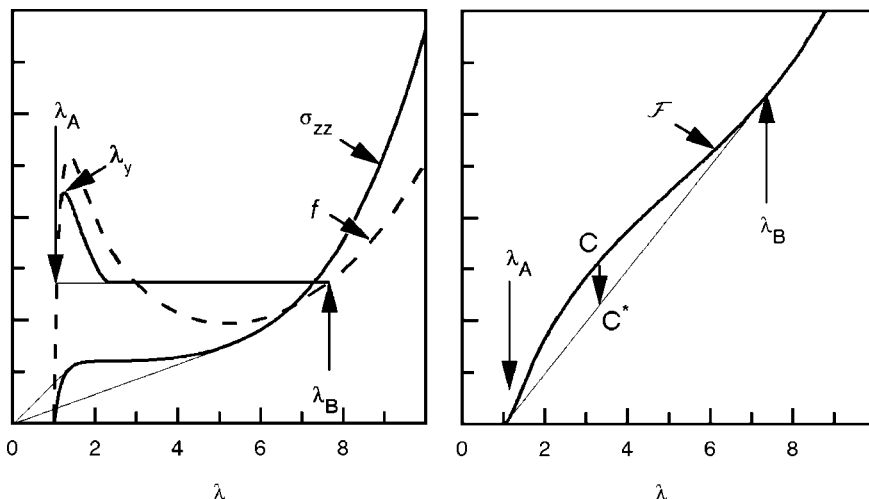


Fig. 10.24. λ -dependence of the retracting force f (left, broken line) and the free energy \mathcal{F} (right) of an elastic fiber with a sigmoidal stress-extension relation $\sigma_{zz}(\lambda)$ (left, continuous line). The locations of the extrema in $f(\lambda)$ follow from the Considère tangent construction, as indicated on the left

and these can be determined by the tangent construction shown in the figure. The procedure is known as the **Considère construction**. We may calculate the free energy of the fiber in dependence on λ . It follows as

$$\mathcal{F}(\lambda) = \int_1^{\lambda} f d\lambda' \quad (10.27)$$

and the result is also included in the figure. Importantly, the shape of $\mathcal{F}(\lambda)$ indicates that we have three ranges that differ in the mechanical stability, namely

$$\begin{aligned} \lambda < \lambda_A: & \text{ a (small) stable range ,} \\ \lambda_A < \lambda < \lambda_B: & \text{ an instable intermediate zone ,} \\ \lambda > \lambda_B: & \text{ a final stablerange .} \end{aligned}$$

λ_A and λ_B are determined by the common tangent on two points of $\mathcal{F}(\lambda)$, as is shown in the drawing. The cause of the instability and the consequences are evident. A transition from the homogeneous state C to a mixture of states A and B, as represented by the point C* on the connecting line, results in a decrease of \mathcal{F} and will therefore take place spontaneously. The situation is perfectly analogous to the transition to a two-phase state found for a binary mixture within the miscibility gap discussed earlier (see Fig. 4.5 and the related explanations). Now we have a gap in the sequence of accessible states of

deformation. Hence, a hyperelastic fiber with a sigmoidal $\sigma_{zz}(\lambda)$ -curve, which leads to a maximum and minimum in the load-extension curve, must disintegrate within a certain range of λ 's into a two-phase structure, with parts extended to λ_A and other parts extended to λ_B . The equilibrium phases either follow from the common tangent construction applied on $\mathcal{F}(\lambda)$, or equivalently by searching for the **Maxwell line** solution for $f(\lambda)$ (equal values for the integral between λ_A and λ_B , independent of whether it is calculated for the horizontal Maxwell line or along the curve $f(\lambda)$). If these conditions are given, an experimental load-extension curve might look like the one indicated in the figure: After the first increase, the load drops at some point $\lambda_y > \lambda_A$ and decays to the horizontal line. λ_y may be identified with the technical yield point. The load drop is accompanied by the first formation of the second phase, with elongation λ_B , i.e., the appearance of the neck. A move along the horizontal line, i.e., the drawing at constant load, is accomplished by the neck extension. After having reached $\lambda = \lambda_B$, the second phase extends further.

Of course, a cold-drawing of a polymeric solid with an amorphous or semicrystalline structure does not exactly agree with the drawing of this hypothetical hyperelastic fiber, since there are large contributions of friction by internal forces and also irreversible structural changes. As mentioned above in the discussion of the shoulder profile, this produces strain rate effects, which in the drawing process lead to the occurrence of transition states with deformations intermediate between the two coexisting states. However, a qualitative change in the stability criteria is not to be expected and one can therefore use the criterion: Necking is to be anticipated if the Considère construction applied to the true stress-extension curves, $\sigma_{zz}(\lambda)$, finds two points with $d\sigma_{zz}/d\lambda = \sigma_{zz}/\lambda$.

10.1.4 Fibrillar State of Order

Cold-drawing converts an initially isotropic semicrystalline sample into the oriented fibrillar state. At room temperature this is a stable structure; the skeleton of fibrillar crystallites built up during the drawing prevents the oriented amorphous network from retracting again. How can this quasi-stable structure be experimentally characterized? The parameter that is now additionally needed in a global description is the degree of orientation. It can be measured optically, spectroscopically or by scattering methods. Here, we briefly discuss

- measurements of the optical birefringence,
- evaluations of orientation-dependent deuteron NMR spectra, and
- analyses of X-ray fiber patterns.

Small angle X-ray scattering experiments provide insight into the crystalline-amorphous structure of the fibrils and the changes following from annealing processes. Of importance is also the question of the drawability of semicrystalline polymers. It is controlled by the properties of the entanglement net-

work in the initial state and greatly enhanced when the entanglement density is reduced by special preparation techniques.

Relation Between Birefringence and Orientational Order

An appropriate measure for the degree of orientation in an uniaxially drawn sample is the orientational order parameter of the monomeric units, S_{or}^{m} , defined as the average

$$S_{\text{or}}^{\text{m}} = \left\langle \frac{3 \cos^2 \theta - 1}{2} \right\rangle. \quad (10.28)$$

Here θ denotes the angle between the long axis of a monomer and the unique axis, i.e., the direction of drawing. For an isotropic sample we have

$$S_{\text{or}}^{\text{m}} = 0. \quad (10.29)$$

The maximum value reached for a perfectly oriented sample where all monomers, they can be incorporated in crystallites or part of sequences in the amorphous regions, are aligned with their long axes in drawing direction is

$$S_{\text{or}}^{\text{m}} = 1. \quad (10.30)$$

Favorable conditions are met for a cold-drawn fiber or film when its birefringence $\Delta n = n_{\parallel} - n_{\perp}$ can be determined (n_{\parallel} and n_{\perp} denote the refractive indices along and perpendicular to the drawing direction). Here, S_{or}^{m} can be directly deduced from Δn , using the relation

$$S_{\text{or}}^{\text{m}} = \frac{\Delta n}{\Delta n_{\text{max}}}. \quad (10.31)$$

Δn_{max} denotes the maximum birefringence realized in the ideal case of a perfectly oriented sample.

In order to derive Eq. (10.31), two coordinate systems are introduced. The first one, with coordinates x, y, z , is fixed on the sample, with the z -axis oriented in the drawing direction. The second, with coordinates x', y', z' , is anchored on a monomer unit and varies in orientation between different monomers. We choose the latter local coordinate system in such a way that the polarizability tensor per monomer, β' , has a diagonal form

$$\beta' = \begin{pmatrix} \beta_{\perp} & 0 & 0 \\ 0 & \beta_{\perp} & 0 \\ 0 & 0 & \beta_{\perp} + \Delta\beta \end{pmatrix}. \quad (10.32)$$

Hereby, we assume an uniaxial local symmetry with the symmetry axis in the chain direction, which is a good approximation for many polymers. β' can be transformed into the sample-fixed coordinate system by

$$\beta = \Omega^{-1} \cdot \beta' \cdot \Omega. \quad (10.33)$$

Ω is the rotation matrix that accomplishes the transformation. We calculate the diagonal elements of β . β_{xx} follows as

$$\begin{aligned}\beta_{xx} &= \sum_l \Omega_{xl}^{-1} \beta'_{ll} \Omega_{lx} \\ &= \beta_{\perp} \cos^2 \theta_{x',x} + \beta_{\perp} \cos^2 \theta_{y',x} + (\beta_{\perp} + \Delta\beta) \cos^2 \theta_{z',x} \\ &= \beta_{\perp} + \Delta\beta \cos^2 \theta_{z',x},\end{aligned}\quad (10.34)$$

where $\theta_{i',j}$ denotes the angle between the axes i' and j . The results for β_{yy} and β_{zz} are correspondingly

$$\beta_{yy} = \beta_{\perp} + \Delta\beta \cos^2 \theta_{z',y}, \quad (10.35)$$

$$\beta_{zz} = \beta_{\perp} + \Delta\beta \cos^2 \theta_{z',z}. \quad (10.36)$$

Because the monomer orientations vary, we take the averages

$$\langle \beta_{xx} \rangle = \langle \beta_{yy} \rangle = \beta_{\perp} + \Delta\beta \langle \cos^2 \theta_{z',x} \rangle, \quad (10.37)$$

$$\langle \beta_{zz} \rangle = \beta_{\perp} + \Delta\beta \langle \cos^2 \theta_{z',z} \rangle. \quad (10.38)$$

The mean values of all non-diagonal elements, $\langle \beta_{i \neq j} \rangle$, vanish due to the uniaxial symmetry of the sample. Since

$$\cos^2 \theta_{z',x} + \cos^2 \theta_{z',y} + \cos^2 \theta_{z',z} = 1, \quad (10.39)$$

hence

$$2\langle \cos^2 \theta_{z',x} \rangle = 1 - \langle \cos^2 \theta_{z',z} \rangle, \quad (10.40)$$

we have

$$\langle \beta_{zz} \rangle - \langle \beta_{xx} \rangle = \Delta\beta \frac{3\langle \cos^2 \theta_{z',z} \rangle - 1}{2} \quad (10.41)$$

or in short, introducing the orientational order parameter defined by Eq. (10.28)

$$\langle \beta_{zz} \rangle - \langle \beta_{xx} \rangle = \Delta\beta S_{\text{or}}^{\text{m}}. \quad (10.42)$$

Next we search for an expression for the dielectric tensor

$$\epsilon = \begin{pmatrix} \epsilon_{\perp} & 0 & 0 \\ 0 & \epsilon_{\perp} & 0 \\ 0 & 0 & \epsilon_{\parallel} \end{pmatrix}. \quad (10.43)$$

Application of the Clausius–Mosotti equation yields

$$\epsilon_{\parallel} - 1 = (\epsilon_{\parallel} + 2) \frac{1}{3\epsilon_0} c_{\text{m}} \langle \beta_{zz} \rangle \approx (\bar{\epsilon} + 2) \frac{1}{3\epsilon_0} c_{\text{m}} \langle \beta_{zz} \rangle \quad (10.44)$$

and

$$\epsilon_{\perp} - 1 \approx (\bar{\epsilon} + 2) \frac{1}{3\epsilon_0} c_{\text{m}} \langle \beta_{xx} \rangle, \quad (10.45)$$

with

$$\bar{\varepsilon} = (2\varepsilon_{\perp} + \varepsilon_{\parallel})/3. \quad (10.46)$$

The anisotropy of the dielectric constant

$$\Delta\varepsilon = \varepsilon_{\parallel} - \varepsilon_{\perp} \quad (10.47)$$

follows as

$$\begin{aligned} \Delta\varepsilon &= (\bar{\varepsilon} + 2) \frac{1}{3\varepsilon_0} c_m (\langle \beta_{zz} \rangle - \langle \beta_{xx} \rangle) \\ &= (\bar{\varepsilon} + 2) \frac{1}{3\varepsilon_0} c_m \Delta\beta S_{\text{or}}^m. \end{aligned} \quad (10.48)$$

Finally, the birefringence Δn is obtained using

$$\Delta\varepsilon = \Delta(n^2) \approx 2\bar{n}\Delta n, \quad (10.49)$$

which results in

$$\Delta n = \frac{\bar{n}^2 + 2}{\bar{n}} \frac{1}{6\varepsilon_0} c_m \Delta\beta S_{\text{or}}^m \quad (10.50)$$

$$= \Delta n_{\text{max}} S_{\text{or}}^m. \quad (10.51)$$

Hence, measurements of the birefringence indeed yield the orientational order parameter S_{or}^m of the monomers.

Even if the derivation is straightforward, application of Eq. (10.50) has some restrictions. First, samples have to be transparent, but fibers and oriented film often contain voids that scatter the light and thus perturb the determination of Δn . Second, an accurate knowledge of Δn_{max} is more the exception than the rule. For example, the value for amorphous polyethylene is still unknown. One cannot just use the known birefringence of n-alkane crystallites, accounting only for the lower density. The birefringence in polyethylene systems is strongly affected by the inner field, which varies with the chain conformation and the packing density. Oriented polyethylenes would have a negative birefringence, i.e., $n_{\parallel} < n_{\perp}$, without the inner field. Hence, the inner field plays a decisive role and it is difficult to calculate the magnitude of the birefringence for the different states of order.

Orientation Dependence of NMR Spectra

Alternatively, for characterizing the state of orientation one can also employ NMR spectroscopy, with the best conditions being found for deuterated samples. The general procedure was sketched previously, at the end of Sect. 6.3.4: As ^2H spectra depend on the orientational distribution of the C–H bonds relative to the external magnetic field, they may be evaluated by model calculations under variation of the orientational distribution function of the

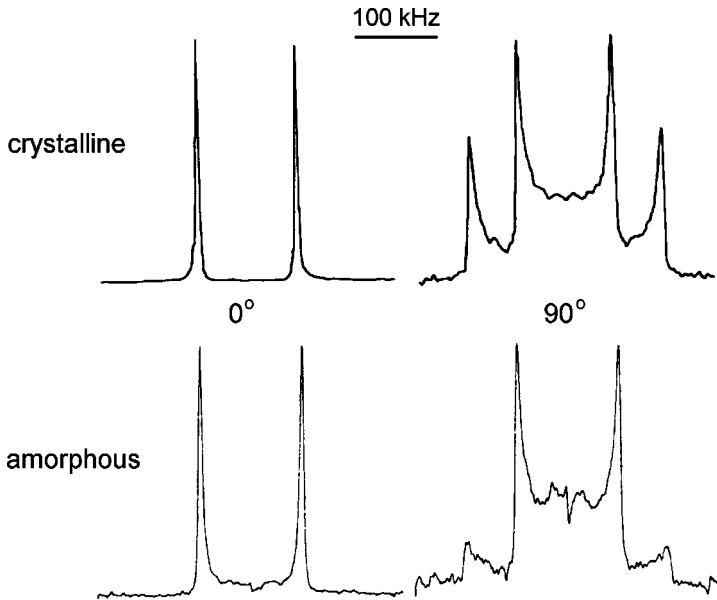


Fig. 10.25. ^2H NMR spectra registered for the crystalline and the amorphous phase of cold-drawn PE. Spectra were obtained for orientations of the unique axis of the samples parallel (0°) and perpendicular (90°) to the magnetic field. From Spiess et al. [129]

monomers. NMR can discriminate between deuterons in crystallites and amorphous regions on the basis of the different mobilities. These result in different spin-lattice relaxation times, which enables the degrees of orientation in both phases of a semicrystalline sample to be separately determined. Figure 10.25 gives an example and presents NMR spectra obtained for the crystalline and amorphous regions of a cold-drawn polyethylene registered for two different sample orientations relative to the magnetic field. Data evaluation is carried out by a comparison with model calculations. Here the results indicate a substantially lower degree of orientational order in the amorphous regions than for the crystallites; spectra can be reproduced when assuming Gaussian orientational distribution functions with half widths of about 3 degrees for the crystallites and 24 degrees for the monomers in the amorphous regions.

X-Ray Fiber Patterns

Figure 10.17 demonstrated that the development of orientational order during a cold-drawing process can be followed by the registration of X-ray scattering patterns. These contain information about both the orientational texture of the crystallites and the orientational distribution of the chain axes in the amorphous regions. These orientational distributions show up in the azimuthal

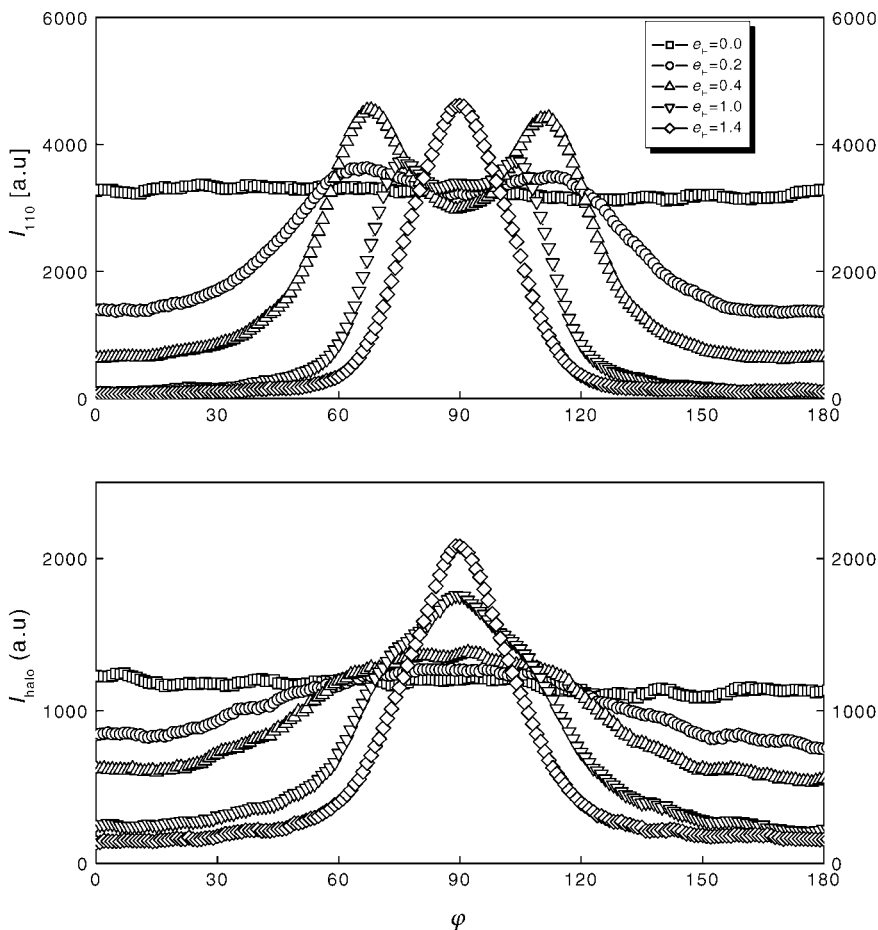


Fig. 10.26. PEVA12: Azimuthal variation of the 110 reflection intensity $I_{110}(\varphi)$ (top) and of the intensity at the halo maximum $I_{\text{halo}}(\varphi)$ (bottom), deduced from X-ray scattering patterns obtained at different stages of the cold-drawing process [125]

variation of the intensities of Bragg reflections and the amorphous **halo**, respectively. Figure 10.26 presents such intensity variations in quantitative form, as observed on drawing the polyethylene sample of Fig. 10.5 to the indicated strains. At the end, the fibrillar state is reached. A data evaluation yielded the variations of the order parameters S_{110} and S_{halo} and they are depicted in Fig. 10.27. They are again defined as the average

$$\left\langle \frac{3 \cos^2 \theta - 1}{2} \right\rangle$$

but, different from Eq. (10.28), θ now denotes the angle between the drawing direction and the *normal* on the chain direction. A perfect orientation along

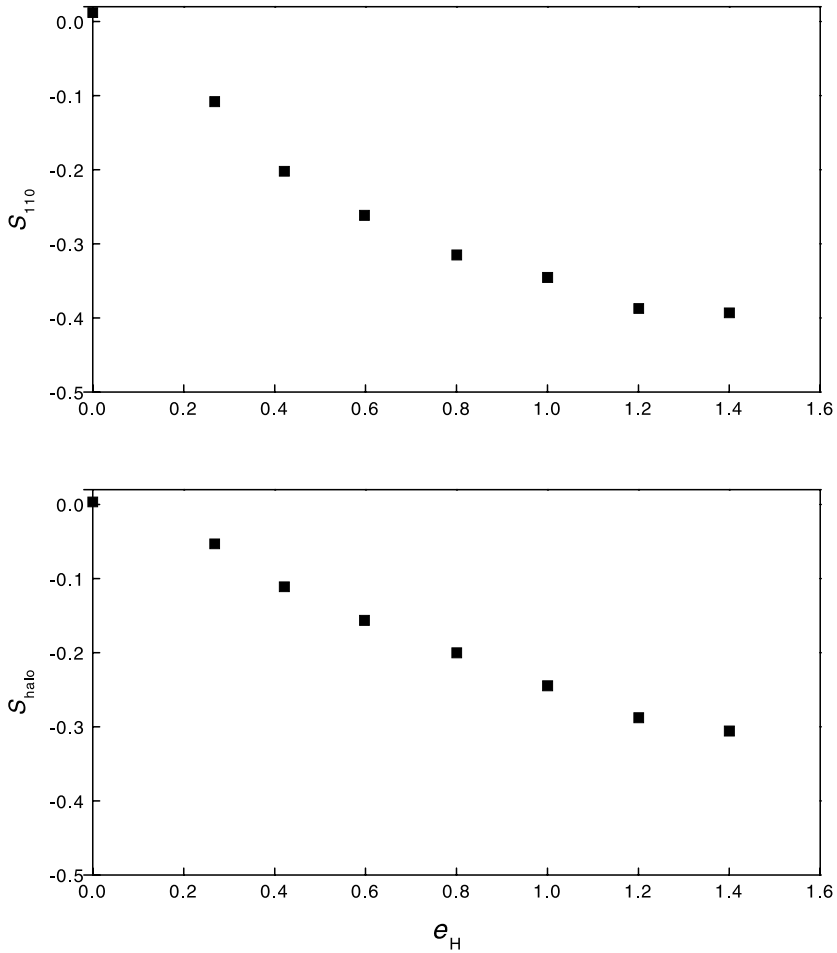


Fig. 10.27. Order parameters S_{110} , S_{halo} associated with the orientational distributions of the normals on the chain direction within the crystalline and the amorphous regions. The final values refer to the fibrillar state [125]

the drawing direction would lead to the value $S_{110} = S_{\text{halo}} = -0.5$. For the PEVA12 sample this perfect order is not reached in the fibrils, whereby a difference exists between the better oriented crystalline and the less oriented amorphous chain sequences.

The Inner Fiber Structure

As was discussed in detail in Sect. 5.1, X-ray scattering experiments in the small-angle range (SAXS) can be used for an investigation of crystalline-amorphous superstructures. The conversion of the spherulitic structure com-

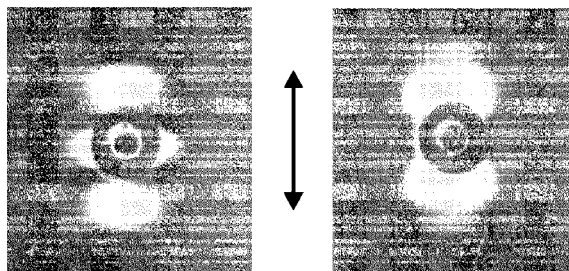


Fig. 10.28. SAXS diagrams registered for PE drawn in the solid state at 70°C directly after the drawing (*left*) and after a subsequent heat treatment at 120°C (*right*). The *arrow* displays the drawing direction. Experiment by Fischer et al. [130]

posed of isotropically distributed stacks of crystallites with quasi-periodic order into an oriented state that is still partially crystalline, the degree of crystallinity remains largely unchanged, leads to a scattering pattern like the one shown on the left-hand side of Fig. 10.28. This **two-point diagram** obtained for a cold-drawn polyethylene, with two intensity maxima on the **meridian** parallel to the direction of drawing was registered on an X-ray film using a high resolution camera. The maxima indicate a quasi-periodic density fluctuation along the oriented fibrils. An interesting effect is observed when samples that were cold-drawn in the solid state are annealed at temperatures that are elevated but still below the temperature of final melting. As shown by the scattering pattern on the right-hand side of Fig. 10.28, this leads to a disappearance of the streaks along the **equator** and an increase in the intensities of the two meridional reflections. The disappearance of the streaks indicates a fusion of neighboring fibrils and the intensity increase is indicative of an improvement in the crystalline-amorphous ordering. The structural reorganization corresponds to a process of defect clustering, which assembles all entanglements that cannot be incorporated into a crystal, in laterally extended layer-like disordered regions. Figure 10.29 suggested by Fischer illustrates this view.

Fiber Drawability

The **drawability** of polymer samples as given by the maximum **draw ratio** before fracture determines the achievable maximum degree of orientation; the higher the drawability, the higher the degree of orientation. Since the degree of chain orientation in a fiber determines the fiber stiffness, it is of interest to have preparation procedures that lead to a high draw ratio. It is found that the primary factor affecting the drawability is the entanglement density. If the number of entanglements is reduced, the drawability increases.

A procedure of technical importance leading to a reduction is **gel-spinning**. A high molar mass polymer is dissolved in a solvent and the solution

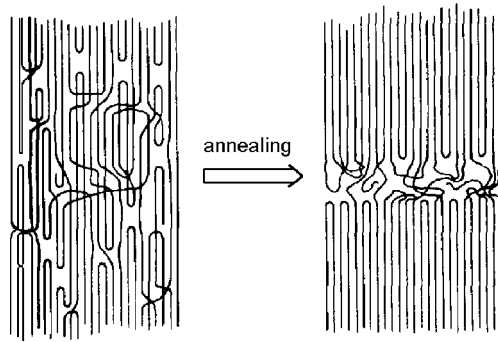


Fig. 10.29. Improvement of the ordering between crystalline and amorphous regions resulting from a heat treatment of a cold-drawn sample. From Fischer et al. [130]

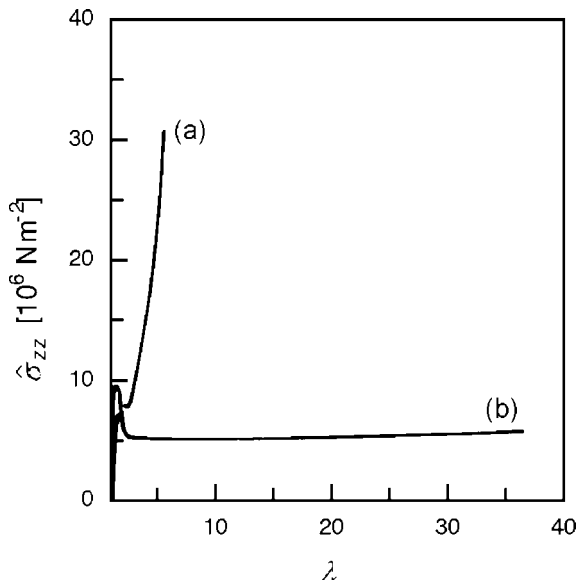


Fig. 10.30. Load-extension curves observed on drawing at 90°C a melt crystallized sample of PE (a) and a gel-spun PE fiber (b). From Lemstra et al. [131]

is spun through a die into a cooling bath, thus producing a gel. Then the solvent is removed by drying or extraction and the fiber is drawn again. Figure 10.30 shows a load-extension curve obtained for polyethylene prepared in this way, in comparison with its usual cold-drawing behavior. We can see that the drawability has increased tremendously. The reason for the drastic change is the reduction of the number of entanglements by the dissolution process and the transfer of this lowered number to the gel and the dried fiber. One expects an inverse relation between the polymer concentration in the solution and the drawability of the fiber and this is indeed observed. Figure 10.31 depicts the

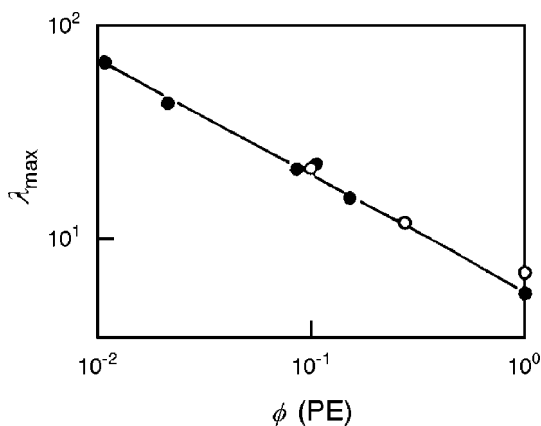


Fig. 10.31. Relation between the maximum draw ratio of a gel-spun PE fiber ($M > 10^6 \text{ g mol}^{-1}$) and the concentration in the solution. Data from Iguchi and Kyotani [132]

dependence of the maximum draw ratio, λ_{\max} , on the volume fraction ϕ of polyethylene in the solution, it corresponds to a function $\lambda_{\max} \propto \phi^{-1/2}$.

Gel-spinning has gained technical importance because the subsequent **ultra-drawing** yields particularly high stiffness values. Elastic moduli up to $2 \times 10^{11} \text{ N m}^{-2}$ have been obtained for polyethylene for draw ratios of about 100, which comes rather near the theoretical limit given by the stiffness of a bundle of *all-trans* polyethylene chains $E = 3 \times 10^{11} \text{ N m}^{-2}$.

10.2 Crazing

Electron microscopy can be used to have a direct look on the structure of a craze. Figure 10.32 presents a micrograph obtained from a microtomed ultra-thin slice cutting through a craze in polystyrene. In addition, for further clarification, Fig. 10.33 gives a sketch of a craze, drawn for a location on an edge. Craze are found both at the surface and in the interior of samples, and represent, as shown by the figures, localized zones of deformation. As indicated by the sketch, they have the form of a lens containing fibrils in a void matrix. The micrograph shows these fibrils connecting the two surfaces of the craze. The fibrils have diameters in the order of 10 nm and fill the craze volume to about 50%. The resulting large density difference to the matrix is the cause of the strong light scattering by the crazes and leads to the stress whitening. Diameters of crazes when they become visible in an optical microscope are in the order of μm , but then they can grow up to macroscopic dimensions, up to the cross-section of the whole sample.

For which polymers and under which conditions do crazes occur? Craze form primarily in amorphous polymers, for molar masses above the entan-

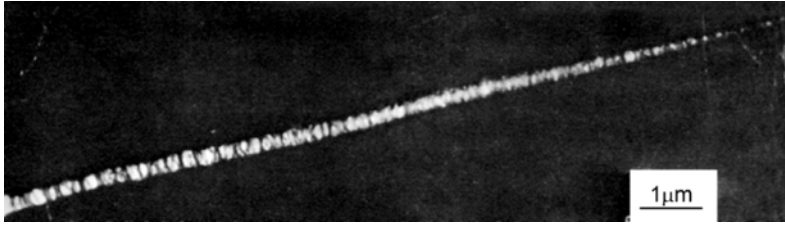


Fig. 10.32. Electron micrograph of a craze in PS, obtained by Kambour [133]

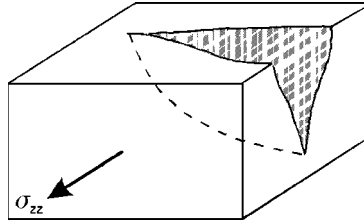


Fig. 10.33. Edge-located craze. The surfaces of the deformation zone are connected by fibrils that only partially fill the craze

glement limit. There is no craze formation under compression or under pure shear. The typical situation leading to craze initiation is the imposition of an uniaxial or biaxial tensile stress. If such stresses are applied and fulfill certain threshold conditions, crazes form statistically, preferentially at first at the sample surface. The initiation rate depends on the applied stress, as is shown in Fig. 10.34. The higher the stress imposed, the shorter the time for the observation of the first crazes. After the initial increase with time, the craze density saturates. Removing the stress, the crazes close their openings somewhat, but survive. They disappear only if the sample is annealed at temperatures above the glass transition.

Regarding the statistical nature of their appearance, craze formation looks like an activated process. Although the details of the initiation step are not yet clarified, it is generally assumed that cavitation, i.e., the development of microvoids, must play a primary role. As the creation of pores in a homogeneous material is exceedingly difficult, it also seems clear that local heterogeneities, resulting in a stress intensification, are a necessary prerequisite. Hence, the activation energy of the process may be related to the formation of pores, at locations where tensile stresses are sufficiently magnified.

Figure 10.35 presents a nice experiment, where a planar stress field ($\sigma_3 = 0$) with varying values of the two in-plane principal stresses, σ_1 and σ_2 , was produced by a tensile force on a plate of poly(methylmethacrylate), into which a circular hole had been cut. One observes regions without any crazes and other regions where crazes occur, showing a systematically varying density. Observations of this kind suggest the formulation of a **criterion**

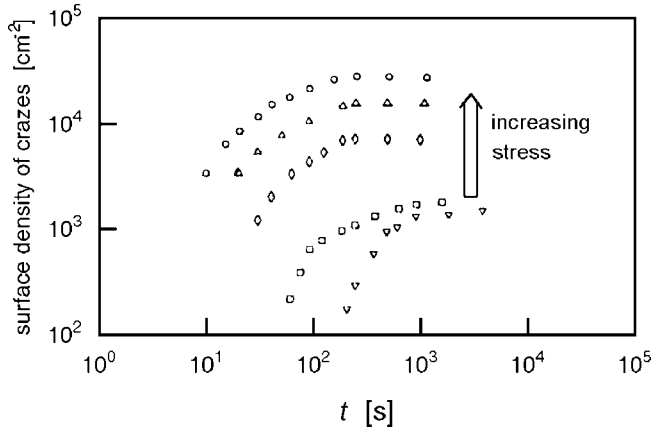


Fig. 10.34. Increase of the number of crazes with time, observed for a sample of PS subject to various states of tensile stress. Work of Argon and Hannoosh [134]

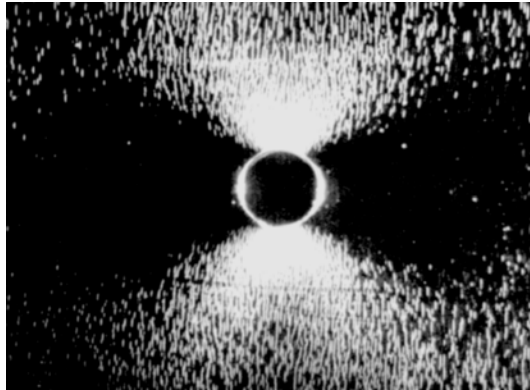


Fig. 10.35. Craze pattern in the vicinity of a hole in a plate of PMMA subjected to a tensile stress in horizontal direction. Micrograph from Sternstein et al. [135]

for crazing, giving the boundary line between planar stress states that lead to crazing and those that do not. For the experiment presented here, which referred to surface crazes only, the condition for crazing may be written as

$$|\sigma_1 - \sigma_2| \geq A + \frac{B}{\sigma_1 + \sigma_2} \quad (10.52)$$

with $A < 0$ and $B > 0$. A and B are material parameters that depend on temperature. The major point expressed by the criterion is that both shear, as given by the difference $\sigma_1 - \sigma_2$, and a dilatational component, as described by the sum $\sigma_1 + \sigma_2$, are necessary prerequisites for the formation of crazes.

Crazes under a constant stress are not stable and grow in length and thickness with a constant rate. The direction of growth is well-defined with

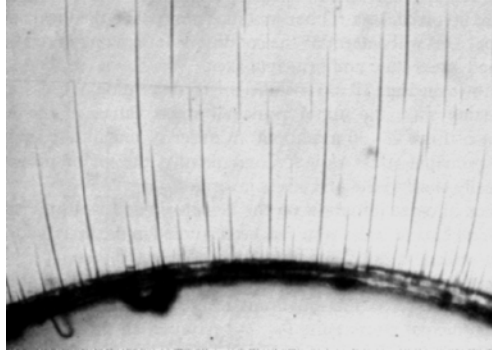


Fig. 10.36. Curvilinear crazes developed in the high stress region near a hole in a plate of PMMA, following lines perpendicular to the maximum principal stress. From Sternstein et al. [135]

the craze tip moving perpendicularly to the maximum principal stress. If the direction of the maximum stress changes, the direction of the craze changes accordingly. This is demonstrated by the photograph presented in Fig. 10.36. The crazes start at the points of largest stress enhancement at the edge of the hole and then proceed perpendicularly to the maximum principal stress.

Simultaneously with the lateral dimensions, the thickness increases. This is accompanied by an equivalent increase in the length of the fibrils connecting the craze surfaces. Since observations indicate a constant thickness of the fibrils subsequent to a short initial period, their growth obviously occurs by a drawing-in of fresh material from the surfaces. It thus appears that the fibril drawing process is equivalent to the macroscopic cold-drawing by neck extension, now taking place in mesoscopic dimensions, with the shoulders being fixed onto and moving together with the craze surfaces. Indeed, the extension ratios found for the microfibrils, which can be directly derived from the volume fraction of material within the craze, essentially agree with the draw ratios associated with neck formation.

It is possible to provide an estimate for the draw ratio reached. It may be identified with the point where strain hardening sets in and, as for an entangled polymer melt, the hardening is caused by the approach of the chain sequences between entanglements to their limits of extensibility. First we need the knowledge of the molar mass of these sequences. This molar mass, denoted M_e , can be obtained with the aid of Eq. (9.86),

$$G = c_p kT ,$$

which gives the shear modulus of an ideal rubber. M_e may be calculated if we identify G with the plateau value of the dynamic shear modulus of the melt, G_{pl} , and write for the density of active chains

$$c_p = \frac{\rho}{M_e} N_L . \quad (10.53)$$

M_e then follows as

$$M_e = \frac{N_L k T \rho}{G_{pl}} . \quad (10.54)$$

The degree of polymerization N_e and the contour length $l_{ct,e}$ of chains with molecular weight M_e are

$$N_e = \frac{M_e}{M_m} \quad (10.55)$$

and

$$l_{ct,e} = a_m N_e , \quad (10.56)$$

where a_m and M_m stand for the length and the molecular weight per monomer, respectively. Chains with an end-to-end distance vector oriented along the drawing direction experience the highest draw ratios. Their average end-to-end distance in the isotropic state, R_e , according to Eq. (2.35) is

$$R_e = a_0 N_e^{1/2} . \quad (10.57)$$

With the knowledge of $l_{ct,e}$ and R_e the draw ratio at the onset of strain hardening can be estimated. Calling it λ_{max} , we write

$$\lambda_{max} \simeq \frac{l_{ct,e}}{R_e} = \frac{a_m}{a_0} N_e^{1/2} . \quad (10.58)$$

Figure 10.37 shows a comparison between experimentally determined draw ratios of craze fibrils and values of λ_{max} . The agreement is not perfect, but the general tendency of the data is satisfactory. The analysis shows that the crazes are stabilized by strain hardened fibrils bearing the imposed load. Without the strain hardening effect, stable crazes would not exist.

An appealing model explaining the mechanism of lateral craze growth was suggested by Argon. It is indicated in Fig. 10.38 with a schematic drawing of the edge of a craze and its development with time. The main point in the model is an assumed instability of the air–polymer interface, which may arise under the conditions of the sharply decaying dilatational stress effective at the craze tip. The phenomenon is known from fluids, where **menisci** advance under the action of a suction gradient. There the surface becomes unstable with regard to wave-like perturbations above a critical wavelength. The same instability may arise in a growing craze. As indicated in the drawing, here fibrils may be repeatedly produced near the advancing craze tip, by the break-up of the interface after a transverse corrugation. The wavelength of the corrugation determines the distance and, thus, the thickness of the fibrils. A prerequisite for the process is plastic flow in a limited zone in front of the moving edge, as may readily occur for the given high stress values. Material enters this plastic zone at the outer end, then advances through the zone under increasing strain and finally becomes included in the interface convolution process forming the fibrillar craze matter.

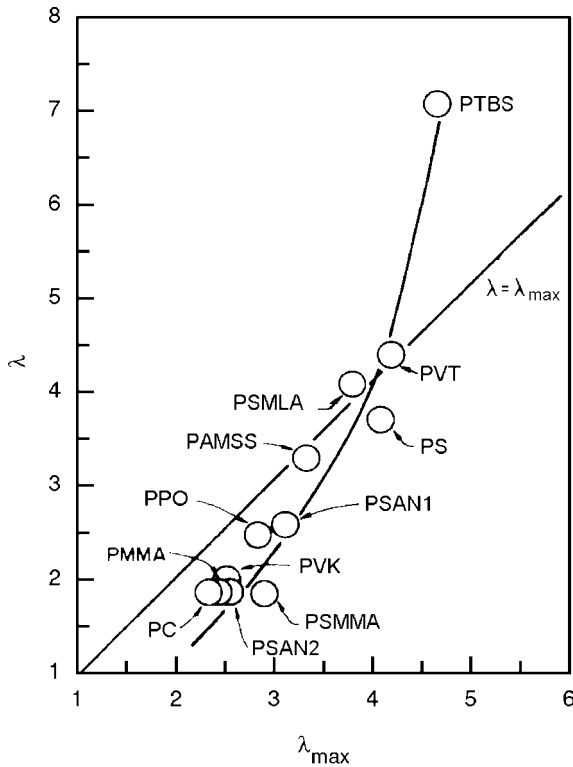


Fig. 10.37. Extension ratios λ of craze fibrils observed for various compounds, plotted against the draw ratio at the onset of strain hardening, λ_{\max} , as derived from the plateau modulus. From Kramer [136]

We finish this chapter with a look at the structure of **high impact polystyrene**, abbreviated HIPS, which is a widely-used product belonging to the larger class of **rubber toughened thermoplastics**. Mixing polystyrene with an elastomer like polybutadiene results in a two-phase structure. Figure 10.39 displays the structural details as they appear in an electron micrograph. Embedded in the polystyrene matrix are spherical inclusions of polybutadiene and the picture shows that the structure is even more complex, since there are again polystyrene inclusions within the inclusion. High impact polystyrene is a tough material and owes this toughness to the initiation of crazes in large numbers. These are observed in the picture. If stress is applied, crazes are generated at the surfaces of the inclusions, which produce a stress intensification. One might think at first that for the given high density of crazes the material would also fracture more easily. However, since each craze only runs to an adjacent rubber particle and there becomes arrested, this is not the case.

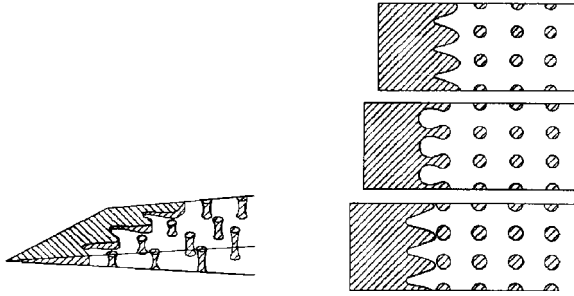


Fig. 10.38. Argon's model of lateral craze growth based on the phenomenon known as 'meniscus instability'. Side view of the corrugated polymer-air interface (*left*). Advances of the craze front by a repeated break-up of the interface (view in fibril direction, *right*) [137]

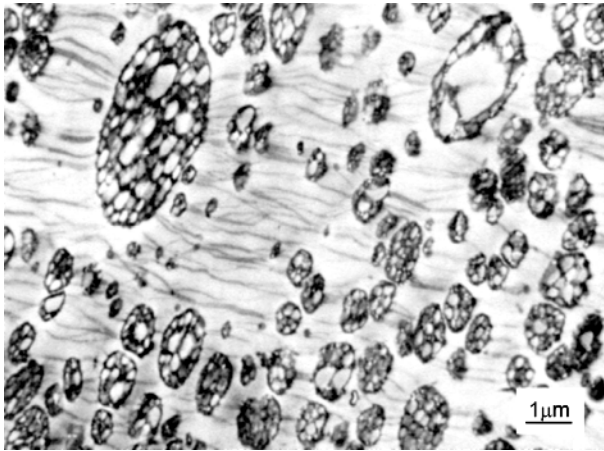


Fig. 10.39. Electron micrograph of a stained microtomed section of HIPS, showing crazes running between the elastomeric precipitates. From Kambour [133]

10.3 Brittle Fracture

If the stress applied to a polymeric solid is sufficiently high to initiate a pronounced yielding and is then further enhanced, the point of break is finally reached. In tough samples there is extensive plastic flow before fracture, which results in a large amount of energy being dissipated, whereas, in brittle compounds, failure occurs much earlier, immediately after the begin of strain softening. Samples of polystyrene or poly(methylmethacrylate) break after the first observation of crazes and thus exemplify brittleness. In the last section of this chapter we will consider this process of **brittle fracture** in more detail.

It is a general observation for all kinds of solid materials – metals, ceramics or polymers – that they never reach their theoretical limits of strength. How is this **theoretical limit** determined? For a low molar mass crystal this is easy to see when considering, for example, the change of the free energy associated with a homogeneous dilatation. Basically, the free energy is determined by the pair interactions between the atoms or molecules in the crystal and this function, $u(r)$, has a general shape as sketched in Fig. 10.40. Enlarging the volume by applying an external isotropic dilatational stress, σ , first requires an increasing stress, but then σ passes over a maximum and a region of mechanical instability is entered where crystals spontaneously disintegrate. The location of the maximum thus determines the theoretical limit of strength. It follows from $u(r)$, the condition being

$$\frac{d\sigma}{dV} = \frac{d^2\mathcal{F}}{dV^2} \sim \frac{d^2u}{dr^2} = 0. \quad (10.59)$$

We obtain this result for a hypothetical isotropic dilatational stress. Using similar arguments, one could also deduce the theoretical limits for other kinds of stress.

In a polymeric solid conditions are more complex. There are both intermolecular van der Waals forces and intramolecular covalent forces and, furthermore, the microscopic structure is amorphous or only partially crystalline. Microscopic fracture mechanisms are, therefore, more involved and also include chain slippage and chain scission. The latter process can occur in fully extended sequences that are anchored with their ends in crystallites or immobile entanglements, by a combined effect of mechanical stress and thermal fluctuations. Even if the situation is complicated, based on some rough knowledge of the bond energies and intermolecular forces one can still obtain some estimate of the theoretical limits of strength. Comparing it to measured

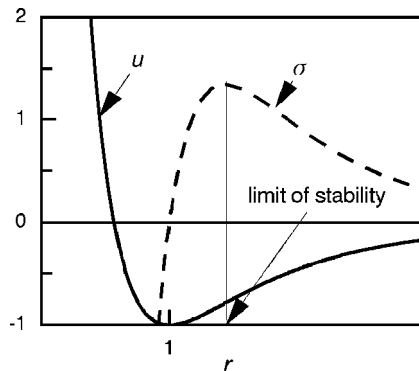


Fig. 10.40. Theoretical limit for the mechanical stability under an isotropic tensile stress σ . $u(r)$ is the pair potential in a low molar mass crystal

fracture strengths, it is found that the theoretical limits are far from being reached for polymeric solids.

What is the cause of the large difference? This is easily revealed. The lack of agreement is due to the presence of flaws in solid bulk matter. Near flaws, which may be microvoids, microcracks, inclusions of foreign particles or other structural heterogeneities, stresses become greatly intensified. As a consequence, when applying stress, the limits of stability are locally exceeded and fracture is then initiated.

Being controlled by the flaws in a sample, fracture strength is not a well-defined bulk property like the parameters and functions describing viscoelasticity. This has consequences for the characterization of strength by measurements. As different samples never possess an equal distribution of flaws, an exact reproducibility cannot be expected and large variations are the rule. Predictions with regard to the strength of bulk samples can, therefore, only be of statistical nature, based on series of measurements and the deduction of probabilities that fracture occurs under given conditions of stress. A peculiar feature is the volume dependence. Since fracture can start at any flaw, the increase in the total number with increasing volume reduces the mechanical stability of a sample correspondingly. Hence, dealing with the property **strength** is not a conventional task and requires special measures.

An obvious way to overcome some of the difficulties and to have a frame for reproducible measurements is the preparation of special samples that have a macroscopic flaw where fracture is initiated, followed by a propagation of the crack in controlled manner. Although this procedure cannot remove the principal difficulty encountered in the assessment of the fracture behavior of a given sample, it can provide true material parameters for use in comparisons of different compounds. Figure 10.41 depicts a standard configuration, with

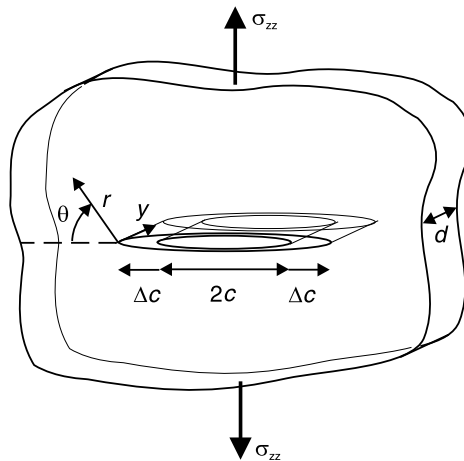


Fig. 10.41. Standard configuration (opening mode I) considered in linear fracture mechanics: Infinite plate containing a crack of length $2c$ subject to a tensile stress σ_{zz}

a sharp crack introduced in a plate. Applying stress, the fracture starts at the two edges. **Linear fracture mechanics** deals with these conditions and describes the behavior of sharp cracks cut into an elastic body.

10.3.1 Linear Fracture Mechanics

The analysis was first carried out by Griffith in a treatment of the brittle fracture of metals. Its transfer to polymeric solids may look questionable at first, as these are neither ideally elastic nor linear in the response at strains near to failure. Actually, Griffith's considerations are of general nature and can also be applied to polymers, after introducing some physically important but formally simple modifications.

We consider the plate shown in Fig. 10.41, which contains a crack of length $2c$. The plate has a thickness d , a Young's modulus E , and its surface area is assumed as infinite. If a tensile force is applied perpendicular to the crack direction, one finds a uniform uniaxial stress far from the crack, denoted σ_{zz} . It is possible to calculate the drop of the elastic free energy of the plate, which results if the length of the crack is increased by $\Delta 2c$. The solution of the problem is given by the expression

$$\Delta \mathcal{F} = \frac{\pi c \sigma_{zz}^2}{E} d \Delta 2c. \quad (10.60)$$

The increase of the crack length produces additional surfaces on both sides and this requires a work $\Delta \mathcal{W}$, which is proportional to their area

$$\Delta \mathcal{W} = 2wd\Delta 2c. \quad (10.61)$$

The equation includes w as proportionality constant. Treating perfectly brittle solids, Griffith identified w with the surface free energy. For polymers, the meaning of w has to be modified. As will be discussed, other contributions appear and even take control. The condition for fracture follows from a comparison of the two quantities $\Delta \mathcal{F}$ and $\Delta \mathcal{W}$, which independent of the contributions to w . A crack grows if the **strain energy release rate** G_I , given by

$$G_I = \frac{1}{d} \frac{\Delta \mathcal{F}}{\Delta 2c} = \frac{\pi c \sigma_{zz}^2}{E}, \quad (10.62)$$

can provide the work needed to create the new surface. This is the case for

$$G_I \geq 2w = G_{Ic}. \quad (10.63)$$

Equation (10.63) is known as **Griffith's fracture criterion**. It includes a critical value of the strain energy release rate, denoted G_{Ic} and the latter is determined by the surface parameter w . The subscript 'I' is used in the literature to indicate reference to the **opening mode I** of Fig. 10.42 and to

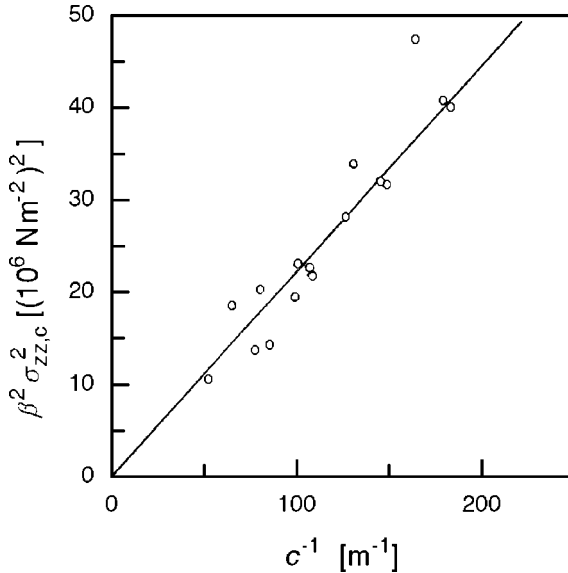


Fig. 10.42. Values of the tensile stress $\sigma_{zz,c}$ at the beginning of crack growth in samples of PMMA containing a crack of length $2c$. β^2 is a geometrical constant, equal to π for infinite plates and with slightly different values for finite bodies. Data from Williams [138]

discriminate it from other possible modes of loading. From Eqs. (10.62) and (10.63) the critical value of the tensile stress follows as

$$\sigma_{zz,c} = \left(\frac{2Ew}{\pi c} \right)^{1/2}. \tag{10.64}$$

$\sigma_{zz,c}$ sets the stability limit for the crack. For tensile stresses below the limit, the crack just opens maintaining a constant length $2c$. If the tensile load exceeds $\sigma_{zz,c}$, the crack starts growing, until it has crossed the sample cross-section, i.e., until it has completed the fracture. Note that only two material coefficients enter into the fracture criterion Eq. (10.64), namely the Young’s modulus E and the surface parameter w .

One result of the treatment is the predicted dependence of $\sigma_{zz,c}$ on the crack length c . One expects $\sigma_{zz,c} \propto 1/\sqrt{c}$, and this is indeed verified by experimental observations. Figure 10.42 depicts, as an example, fracture data obtained for poly(methylmethacrylate) at room temperature, represented in a plot of $\sigma_{zz,c}^2$ versus c^{-1} .

There is a second, equivalent form of the fracture criterion. It is possible to calculate the stress field near to the tip of the crack in the plate of Fig. 10.41. The result is given by the expression

$$\sigma_{ij}(r, \theta) = \frac{K_I}{(2\pi r)^{1/2}} \Phi_{ij}(\theta) \tag{10.65}$$

when employing the coordinates r, θ and y introduced in the figure. According to this expression, the stress tensor with components σ_{ij} depends on the distance r from the tip and the angle θ only and not on y . We have here a state of plane stress, with $\sigma_{yy} = 0$ and non-vanishing values of the stress only parallel to the plate surfaces. The stress distribution is given by a certain angular-dependent tensor function $\Phi_{ij}(\theta)$ and the r -dependent factor $1/(2\pi r)^{1/2}$. The result implies that the relative stress distribution around the crack tip does not vary with the external load, which just affects the magnitude. The effect of the load is completely accounted for by the parameter K_I , known as the **stress intensity factor**. The stress intensity factor can be calculated with the result

$$K_I = \sigma_{zz}(\pi c)^{1/2} . \quad (10.66)$$

Equation (10.65) predicts a singularity for the stress at the crack tip, as $\sigma_{ij} \rightarrow \infty$ for $r \rightarrow 0$. Therefore, the local stresses, as described by this expression, cannot be utilized in the formulation of a fracture criterion. Instead, the stress intensity factor can be employed and the condition to be fulfilled for a stable crack formulated as

$$K_I \leq K_{Ic} \quad (10.67)$$

Here K_{Ic} denotes the critical value of the stress intensity factor. The approach is conceivable because theoretical analysis proves that, in spite of the divergence of the stress at the tip, the total elastically stored energy remains finite. K_I can be directly related to the stored energy and, thus, to the strain energy release rate G_I . As the comparison of Eq. (10.66) with Eq. (10.62) shows, the relationship reads

$$K_I^2 = EG_I . \quad (10.68)$$

As it turns out, the relation holds not only for the configuration of Fig. 10.41, but also for plates with a finite surface area, or for a semi-infinite plate with a notch at the edge. The critical value of the stress intensity factor K_{Ic} follows from a combination of Eqs. (10.68) and (10.63), as

$$K_{Ic}^2 = 2wE . \quad (10.69)$$

It is determined by two material coefficients only, as is the case for G_{Ic} .

In conclusion, Griffith's analysis of the crack stability provides two true material parameters, the critical values at failure of the strain energy release rate, G_{Ic} , and of the stress intensity factor, K_{Ic} . Either of them can be used for a description of the fracture properties of common, i.e., not precracked samples, in the sense that higher values of G_{Ic} or K_{Ic} indicate a higher resistance to failure.

10.3.2 The Slow Mode of Crack Growth

Griffith's analysis predicts a stable crack for stresses below the critical limit of failure and an uncontrolled accelerated growth above the limit, due to

the permanent excess of the released strain energy over the required surface free energy. Polymer behavior is different, as is exemplified by the results of fracture experiments conducted on poly(methylmethacrylate) depicted in Fig. 10.43. Studies were carried out under variation of the external load, i.e., of K_I , with crack velocities being registered with the aid of a high speed camera. Cracks are stable up to a certain value of the stress intensity factor or the strain energy release rate, and we denote the latter G_{II} . At this point crack growth sets in, however, not in an accelerated manner but with a slow stationary growth rate (in order to establish a constant stress intensity factor for growing cracks, the tensile load has to be permanently readjusted to fulfill Eq. (10.66)). The growth rate increases with K_I until a second point is reached where a transition takes place, leading to a non-stationary, i.e., accelerated mode of growth. This second transition is called the **critical transition**, and its location in terms of the stress intensity factor and the strain energy release rate is denoted K_{IC} and G_{IC} , respectively. Crack velocities \dot{c} after the critical transition are determined by inertial forces and the velocity of elastic waves.

The polymer specific feature is the existence of a range of stationary slow growth preceding the uncontrollable rapid mode of failure, i.e., the occurrence of the **subcritical crack growth** in the range $G_{II} < G_I < G_{IC}$. Its origin becomes basically clear if we look at Fig. 10.43 from the other perspective, as giving the strain energy release rate G_I as a function of an imposed crack velocity \dot{c} . Under stationary conditions, G_I must equal the work suspended to form new surfaces as expressed by the parameter $2w$. According to the curves w increases with \dot{c} for subcritical growths. In Griffith's original treatment of brittle

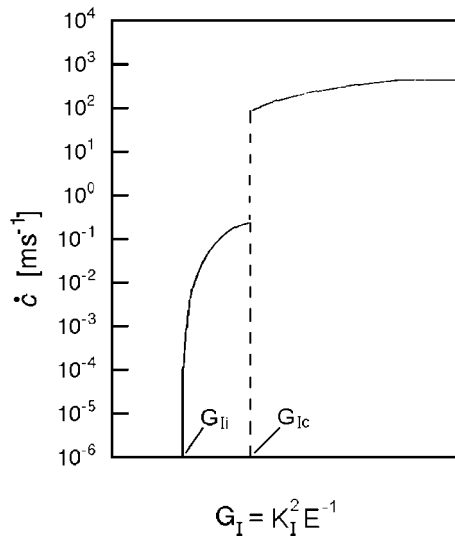


Fig. 10.43. Crack growth as a function of G_I , as observed for PMMA ($M = 2 \times 10^6 \text{ g mol}^{-1}$) at room temperature. From Döll [139]

fracture w corresponded to the surface free energy only, which just relates to the absence of binding forces in one direction. In the case under discussion, the fracture of polymers, the situation is qualitatively different. The work required for the formation of a surface during fracture is here dominated by a preceding plastic flow. The observed rate dependence of w is a property of the flow processes. Indeed, the values of w deduced from Griffith's fracture criterion for polymers are much larger than the surface free energy alone. For example, for poly(methylmethacrylate) one finds $G_{Ic} \simeq 100-1000 \text{ J m}^{-2}$, compared to a surface free energy $2w_s \simeq 0.1 \text{ J m}^{-2}$. Hence, although the fracture of materials like polystyrene and poly(methylmethacrylate) is still called brittle, it does not comply with this name in the strict sense.

The growth rate dependence of the work suspended in plastic flows is conceivable if we recall, for example, the strain rate dependence of the force applied for the shear yielding during cold-drawing. In the range of subcritical growth one finds a power law for the relation between K_I and \dot{c} ,

$$K_I \propto \dot{c}^\mu \quad (10.70)$$

with a small exponent μ ($\approx 1/25$).

There is a detailed picture of the flow processes controlling the slow growth of cracks and it directly relates to crazing. Insight again comes from electron microscopy. Figure 10.44 presents micrographs of the region around a crack tip showing a plastically deformed zone in front of the tip. The image with higher resolution on the right-hand side indicates that this zone is filled with fibrils as is found in the interior of a craze. From such observations a picture of crack growth emerges as it is indicated schematically in the upper part of Fig. 10.45. If a tensile load is applied, the high stresses in the immediate neighborhood of the crack tip result in a crossing of the yield point and the formation of a zone with plastic deformation. In polymers, the pertinent mode of local

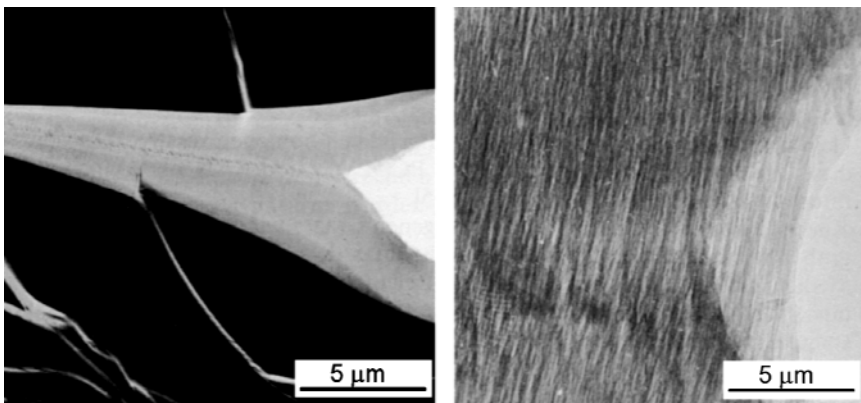


Fig. 10.44. Crack tip (*bright sections on the right in both pictures*) within a craze in PS. Electron micrographs obtained by Michler [140]

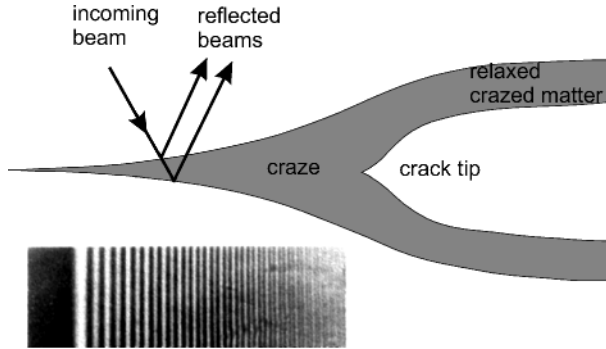


Fig. 10.45. Crack propagation behind a simultaneously moving zone with crazed matter. The profile of the preceding craze tip can be derived from the interference pattern produced by the two reflected beams. The fringe pattern presented here was obtained for PMMA by Doyle [141]

plastic flow is crazing. Hence, fibrils form in the plastic zone, being separated by voids. If the applied stress is further enhanced, the fibrils elongate and reach at a certain point their limit of internal stability at which they break. At this moment, a crack has formed within the craze and subcritical crack growth starts. Under the applied stress the craze grows being followed by the crack tip within the craze. For a fixed value of K_I stationary conditions are established, with a constant cusp-like shape of the zone with crazed matter in front of the tip and a constant crack velocity. Failure is completed when the crack has expanded over the sample cross-section.

Additional evidence for a crack growth behind a growing craze provides the surface structure of fractured samples. Images obtained by scanning electron microscopy show a thin film formed of collapsed fibrils on the fracture surface. Figure 10.46 presents as an example such an image, here of a fracture surface of poly(methylmethacrylate).

The cusp-like profile of the craze zone in front of the crack may be deduced from another experiment on poly(methylmethacrylate), presented in the lower part of Fig. 10.45. The displayed fringe pattern is observed in a microscope, when the region around the crack tip is illuminated by a light beam from above. As a result of the interference of two light beams, one reflected at the upper and the other at the lower surface of the craze with crack, an interference pattern emerges. Analysis enables the profile of the craze in front of the crack to be determined. The profiles thus measured are cusp-like, as in the schematic drawing.

With the knowledge of the structure of the plastic zone in front of the crack tip one can write down a simple equation for the surface parameter $2w$, known also as **material resistance**. The total expended work equals that consumed on drawing the fibrils in the craze up to their maximum length at the point of break. As was discussed in the previous section, fibrils elongate

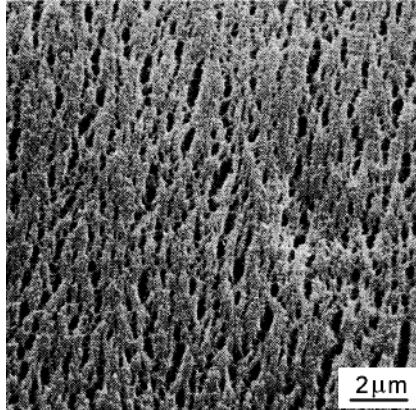


Fig. 10.46. Fracture surface of PMMA as observed in a scanning electron microscope. The structure originates from collapsed crazed matter. Micrograph obtained by Döll and Könczöl [142]

by an incorporation of fresh material at the craze surface, which takes place under a constant tensile stress. Hence, we write

$$2w \approx \sigma_y \Delta z_b, \quad (10.71)$$

where σ_y stands for the tensile stress effective at the craze surface and Δz_b denotes the maximum fibril length, reached at the point of break. This leads to an expression for the stress intensity factor that can be used to deal with the slow crack growth regime. Stationary growth implies equality of G_I with $2w$, hence

$$K_I = EG_I = E\sigma_y \Delta z_b. \quad (10.72)$$

One may ask for the cause of the fibril rupture. Ideally, for a fibril with constant width, elongation by the incorporation of additional material at both ends could continue infinitely. Reality is different, since the fibril diameter is not truly stable but narrows due to an ongoing creep. Away from the crack tip this is a slow process, but adjacent to the tip it becomes accelerated by the intensification of stress. Rather than breaking somewhere in the central part, fibrils often fail at the craze surface, for example, if an obstacle prevents a further material supply. Generally, the stability of the fibrils against rupture increases with the molar mass, as the necessary chain disentangling requires more and more time, and both σ_y and Δz_b go to higher values. As a consequence, the strength of samples also increases with the molar mass; this is shown by the data in Fig. 10.47. They were obtained from measurements on fractions of polystyrene. In addition to the critical stress at break, the figure includes also the minimum stresses for the observation of crazes. Opposite to the stresses at failure the latter ones are M -independent; craze initiation is a local event, depending primarily on the interaction between neighboring chain sequences.

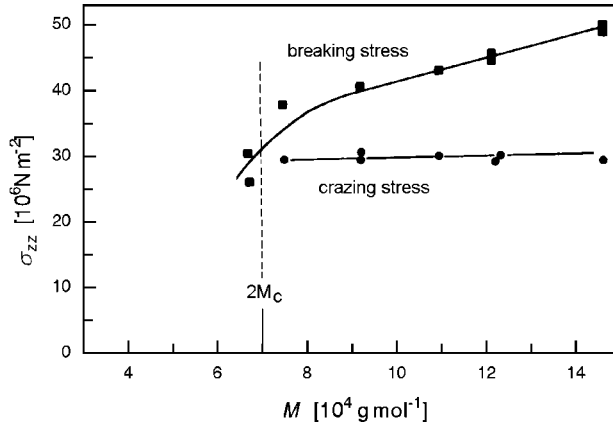


Fig. 10.47. Fractions of PS, subject to uniaxial stress. Molar mass dependencies of the minimum stress for the observation of crazes and the stress at failure. Data from Fellers and Kee [143]

On the basis of Eq. (10.72) we can understand how the balance between the released strain energy and the energy consumption in work of plastic deformation is realized over a finite range of crack velocities. This becomes accomplished by the rate dependence of the drawing stress σ_y , which goes up with \dot{c} , and that of Δz_b . By the increase of $2w = \sigma_y \Delta z_b$ with \dot{c} , a new equilibrium with G_I can be established following any upward change in G_I or K_I . The limit of stationary slow growth is reached when $2w$ is no longer rate sensitive enough to compensate for the increase in G_I . Then growth is no longer stationary and the crack expands in an uncontrolled manner.

We finish this last chapter with a short remark on **environmental effects**. Indeed, the influences of environmental gases or liquids on crazing and failure of polymeric materials can be rather strong and have to be properly accounted for in experiments. The primary action of active agents involves absorption and thus swelling of the material, with the result of plastification, i.e., a decrease of T_g , and a reduction of surface energies. Both effects obviously facilitate craze initiation, since cavitation processes are involved and the chain mobility is increased. Craze growth is promoted as well, for the same reasons, and so is the tendency for failure, since the load carrying capacity of the fibrils may be diminished. The presence of agents that diffuse into the polymer may therefore greatly reduce the barriers for crazing and fracture. In extreme cases, bodies may even break spontaneously on coming into contact with an absorbing agent, since then frozen strains are released and produce internal stresses. It is obvious that these are technically important influences and they have to be carefully considered to be sure that materials are safe under all possible environmental conditions.

Further Reading

- E.H. Andrews, P.E. Reed, J.G. Williams, C.B. Bucknall: *Advances in Polymer Science*, Vol. 27 *Failure in Polymers*, Springer, 1978
- H.H. Kausch: *Polymer Fracture*, Springer, 1978
- H.H. Kausch (Ed.): *Advances in Polymer Science* Vol. 91/92 *Crazing in Polymers*, Springer, 1990
- G.H. Michler: *Kunststoff-Mikromechanik*, Carl Hanser, 1992
- I.M. Ward: *Mechanical Properties of Solid Polymers*, John Wiley & Sons, 1971

A

Scattering Experiments

A.1 Fundamentals

As for bulk condensed matter in general, analysis of the microscopic structure of polymer systems is mostly carried out by scattering experiments. This Appendix is meant to provide the reader with a summary of results of scattering theory, including both general and specific equations, in a selection suggested by the needs of the considerations in this book.

Depending on the system under study and the desired resolution, photons in the X-ray and light scattering range or neutrons are used. The general set-up of a scattering experiment is indicated schematically in Fig. A.1. We have an incident beam of monochromatic radiation with wavelength λ and an intensity I_0 . It becomes scattered by a sample and the intensity I of the scattered waves is registered by a detector (D) at a distance A , under variation of the direction of observation. Employing the **scattering vector** \mathbf{q} , defined as

$$\mathbf{q} = \mathbf{k}_f - \mathbf{k}_i , \quad (\text{A.1})$$

where \mathbf{k}_f and \mathbf{k}_i denote the wave vectors of the incident and the scattered plane waves, respectively, the result of a scattering experiment is usually expressed by giving the **intensity distribution in \mathbf{q} -space**, $I(\mathbf{q})$. In the majority of scattering experiments on polymers the radiation frequency remains practically unchanged. Then we have

$$|\mathbf{k}_f| \approx |\mathbf{k}_i| = \frac{2\pi}{\lambda} \quad (\text{A.2})$$

and $|\mathbf{q}|$ is related to the **Bragg scattering angle** ϑ_B by

$$|\mathbf{q}| = \frac{4\pi}{\lambda} \sin \vartheta_B \quad (\text{A.3})$$

(ϑ_B is identical to half of the angle enclosed by \mathbf{k}_i and \mathbf{k}_f).

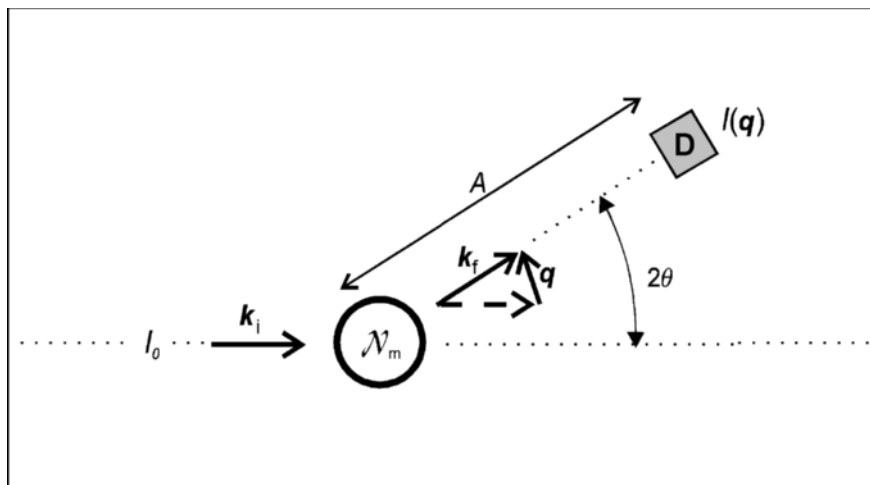


Fig. A.1. General set-up of a scattering experiment

A.1.1 Basic Equations

Two different functions can be used for representing scattering data in reduced forms. The first one, denoted $\Sigma(\mathbf{q})$, is the **differential scattering cross-section per unit volume**

$$\Sigma(\mathbf{q}) = \frac{1}{V} \frac{d\sigma}{d\Omega} = \frac{1}{V} \frac{I(\mathbf{q})A^2}{I_0}. \quad (\text{A.4})$$

In light scattering experiments this function is called the **Rayleigh ratio**. While the effect of the volume is removed, $\Sigma(\mathbf{q})$ remains dependent on the scattering power of the particles in the sample, which varies with the applied radiation. For X-rays, the scattering power is related to the electron densities, for light scattering to the associated refractive indices and for neutron scattering to the scattering length densities.

This dependence on the applied radiation is eliminated in the second function which, however, can only be employed if the scattering can be treated as being due to just one class of particles. In polymer systems these can be identified with the monomeric units. For equal particles the scattering properties can be described by the **interference function** $S(\mathbf{q})$, also called **scattering function** or **scattering law**, which is defined as

$$S(\mathbf{q}) = \frac{I(\mathbf{q})}{I_m N_m}. \quad (\text{A.5})$$

Here N_m represents the total number of particles/monomers in the sample and I_m is the scattering intensity produced by one particle, if placed in the same incident beam. The interference function expresses the ratio between the

actual intensity and the intensity that would be measured, if all particles in the sample were to scatter incoherently. It thus indeed describes the interference effect.

As may be directly verified, $\Sigma(\mathbf{q})$ and $S(\mathbf{q})$ are related by the equation

$$\Sigma(\mathbf{q}) = \langle c_m \rangle \left(\frac{d\sigma}{d\Omega} \right)_m S(\mathbf{q}). \quad (\text{A.6})$$

Here $(d\sigma/d\Omega)_m$ denotes the scattering cross section per particle or monomer and $\langle c_m \rangle$ stands for their mean density

$$\langle c_m \rangle = \frac{\mathcal{N}_m}{\mathcal{V}}. \quad (\text{A.7})$$

Scattering diagrams generally emerge from the superposition and interference of the scattered waves emanating from all the particles in the sample. If we describe the amplitudes of single scattered waves at the point of registration by the detector in normalized form, by complex numbers of modulus unity and phases φ_i , the total scattering amplitude is obtained as

$$C = \sum_{i=1}^{\mathcal{N}_m} \exp(i\varphi_i). \quad (\text{A.8})$$

Simple geometrical considerations presented in all textbooks dealing with scattering theory show that the phases φ_i are determined by the particle positions \mathbf{r}_i and the scattering vector \mathbf{q} only, being given by

$$\varphi_i = -\mathbf{q}\mathbf{r}_i. \quad (\text{A.9})$$

Hence, the scattering amplitude produced by a set of particles at locations \mathbf{r}_i may be formulated as a \mathbf{q} -dependent function

$$C(\mathbf{q}) = \sum_{i=1}^{\mathcal{N}_m} \exp(-i\mathbf{q}\mathbf{r}_i). \quad (\text{A.10})$$

The scattering intensity is proportional to the squared modulus of C . Since measurements require a certain time, average values are generally obtained and we write

$$I(\mathbf{q}) \propto \langle |C(\mathbf{q})|^2 \rangle. \quad (\text{A.11})$$

The brackets indicate an ensemble average that involves, as always in statistical treatments of physical systems, all microscopic states of the sample. For ergodic systems the time average carried out by the detector equals the theoretical ensemble average.

As the normalization of the amplitudes of the single scattered waves is already implied in the definition of the interference function Eq. (A.5), Eq. (A.11) may be completed as

$$S(\mathbf{q}) = \frac{1}{\mathcal{N}_m} \langle |C(\mathbf{q})|^2 \rangle. \quad (\text{A.12})$$

This is a basic equation of general validity and it may serve as starting point for the derivation of other forms of scattering equations.

Our task is the calculation of the above average of the squared scattering amplitude. A first formula follows directly by use of Eq. (A.10), leading to

$$S(\mathbf{q}) = \frac{1}{\mathcal{N}_m} \sum_{i,j=1}^{\mathcal{N}_m} \langle \exp[-i\mathbf{q}(\mathbf{r}_i - \mathbf{r}_j)] \rangle. \quad (\text{A.13})$$

Instead of specifying the discrete positions \mathbf{r}_i of all particles, one can also use a continuum description and introduce the particle density distribution $c_m(\mathbf{r})$. First we write down the scattering amplitude for a single microstate, as represented by the associated density distribution

$$C(\mathbf{q}) = \int_{\mathcal{V}} \exp(-i\mathbf{q}\mathbf{r})(c_m(\mathbf{r}) - \langle c_m \rangle) d^3\mathbf{r}. \quad (\text{A.14})$$

As scattering occurs only if c_m varies within the sample, we here subtract the mean value $\langle c_m \rangle$, thus relating the scattering directly to the fluctuations. As we can see, $C(\mathbf{q})$ equals the Fourier transform of the fluctuations in the particle density. Insertion of Eq. (A.14) into Eq. (A.12) and carrying out the ensemble average yields

$$S = \frac{1}{\mathcal{N}_m} \int_{\mathcal{V}} \int_{\mathcal{V}} \exp[-i\mathbf{q}(\mathbf{r}' - \mathbf{r}'')] \langle [c_m(\mathbf{r}') - \langle c_m \rangle][c_m(\mathbf{r}'') - \langle c_m \rangle] \rangle d^3\mathbf{r}' d^3\mathbf{r}'' . \quad (\text{A.15})$$

For all macroscopically homogeneous systems, where

$$\langle c_m(\mathbf{r}')c_m(\mathbf{r}'') \rangle = \langle c_m(\mathbf{r}' - \mathbf{r}'')c_m(0) \rangle, \quad (\text{A.16})$$

this equation reduces to a single integral. Substitution of $\mathbf{r}' - \mathbf{r}''$ by \mathbf{r} yields

$$S(\mathbf{q}) = \frac{1}{\langle c_m \rangle} \int_{\mathcal{V}} \exp(-i\mathbf{q}\mathbf{r})(\langle c_m(\mathbf{r})c_m(0) \rangle - \langle c_m \rangle^2) d^3\mathbf{r}. \quad (\text{A.17})$$

Equation (A.17) expresses $S(\mathbf{q})$ as the Fourier transform of the space dependent correlation function of the particle density.

A third form of the basic scattering equation is obtained if structures are characterized with the aid of the **pair distribution function** $g(\mathbf{r})$. Per definition, the product

$$g(\mathbf{r}) d^3\mathbf{r}$$

gives the probability that, starting from a given particle, the particle itself or some other particle is found in the volume element $d^3\mathbf{r}$ at a distance \mathbf{r} . The pair distribution function $g(\mathbf{r})$ is composed of two parts,

$$g(\mathbf{r}) = \delta(\mathbf{r}) + g'(\mathbf{r}), \quad (\text{A.18})$$

the delta function giving the self-contribution and the second part, g' , the contributions of the other particles. For fluid systems with short-range order, the limiting value of the pair distribution function at large distances equals the mean density

$$g(|\mathbf{r}| \rightarrow \infty) \rightarrow \langle c_m \rangle. \quad (\text{A.19})$$

As follows directly from the definitions, the density distribution and the pair distribution function are related by

$$\langle c_m(\mathbf{r})c_m(0) \rangle = \langle c_m \rangle g(\mathbf{r}). \quad (\text{A.20})$$

Insertion of Eq. (A.20) into Eq. (A.17) gives

$$S(\mathbf{q}) = \int_{\mathcal{V}} \exp(-i\mathbf{q}\mathbf{r})(g(\mathbf{r}) - \langle c_m \rangle) d^3\mathbf{r}. \quad (\text{A.21})$$

As we notice, the scattering function once again equals a Fourier transform, now of the pair distribution function.

From Eq. (A.21) there follows the asymptotic value of S for large values of \mathbf{q} . In the limit $\mathbf{q} \rightarrow \infty$ only the contribution of the self-correlation part, $\delta(\mathbf{r})$, is left and we find

$$S(\mathbf{q} \rightarrow \infty) \rightarrow 1. \quad (\text{A.22})$$

We conclude that, for large \mathbf{q} , there are neither constructive nor destructive interferences between the particles so that they behave like incoherent scatterers.

For isotropic systems with

$$g(\mathbf{r}) = g(r = |\mathbf{r}|) \quad (\text{A.23})$$

the scattering function is also isotropic

$$S(\mathbf{q}) = S(q = |\mathbf{q}|). \quad (\text{A.24})$$

The Fourier relation between $g(r)$ and $S(q)$ then has the form

$$S(q) = \int_{r=0}^{\infty} \frac{\sin(qr)}{qr} 4\pi r^2 (g(r) - \langle c_m \rangle) dr. \quad (\text{A.25})$$

We have formulated three equivalent relations, Eqs. (A.13), (A.17) and (A.21), which can all be employed in the evaluation of scattering data. All three equations express a Fourier relation between $S(\mathbf{q})$ and functions that describe properties of the microscopic structure in statistical terms. To put special emphasis on this well-defined structural background, $S(\mathbf{q})$, firstly introduced as the ‘scattering function’, is often also addressed as the **structure function** or **structure factor**. We will use all these different names, chosen freely.

A.1.2 Time-Resolved Scattering Experiments

Since the particles in a sample are moving, the interference pattern fluctuates in time. The fluctuations can be included in the treatment, by representing the scattering amplitude as a function with a statistical time dependence, $C(\mathbf{q}, t)$. So far we have dealt with the case of **static scattering experiments**, where the fluctuations are not registered and the detector only provides the mean value of the scattering intensity. It is also possible to conduct scattering experiments with neutrons or light in such a way that the time-dependent fluctuations are monitored. These time-resolved measurements provide information on the internal dynamics in a sample and thus can considerably expand the information content of a scattering experiment.

Here we give a summary of the main results as they follow from a purely classical treatment. These are applicable for **quasielastic scattering experiments**, i.e., experiments where the amount of energy exchange between the neutrons or photons and the sample remains small compared to both the initial energy of the scattered particles and the thermal energy kT of the particles in the sample. In studies of relaxation processes in polymer systems these requirements are generally fulfilled.

If the particles in the sample are mobile, their positions or, in the continuum description, the density distribution become functions of time, $\mathbf{r}_i(t)$ or $c_m(\mathbf{r}, t)$. As a consequence the scattering amplitude C fluctuates, and we may write either

$$C(\mathbf{q}, t) = \sum_{i=1}^{\mathcal{N}_m} \exp[-i\mathbf{q}\mathbf{r}_i(t)] \quad (\text{A.26})$$

or

$$C(\mathbf{q}, t) = \int_{\mathcal{V}} \exp(-i\mathbf{q}\mathbf{r}) [c_m(\mathbf{r}, t) - \langle c_m \rangle] d^3\mathbf{r} . \quad (\text{A.27})$$

There are techniques that provide a statistical analysis of these time-dependent fluctuations. The main result of the analysis is a determination of the **time correlation function** of the scattering amplitude, defined as

$$S(\mathbf{q}, t) = \frac{1}{\mathcal{N}_m} \langle C(\mathbf{q}, t' + t) C^*(\mathbf{q}, t') \rangle . \quad (\text{A.28})$$

The chosen form relates to the previous Eq. (A.12) and expands it by an inclusion of the time dependence. $S(\mathbf{q}, t)$ expresses the correlation in time of the scattering amplitudes measured at two times separated by t . The stationary character of thermal equilibrium states implies that the right-hand side is independent of t' . In **dynamic light scattering experiments** the determination of $S(\mathbf{q}, t)$ is accomplished by the photon correlation technique. In **dynamic neutron scattering experiments**, **spin-echo measurements** can be used in order to obtain the correlation function.

$S(\mathbf{q}, t)$ is called **intermediate scattering function** or **intermediate scattering law**, and plays a central role in the analysis of dynamic scattering

experiments. The importance is due to $S(\mathbf{q}, t)$ being related in a well-defined way to the equilibrium dynamics in the system. The relation can be directly established, by insertion of the time-dependent scattering amplitudes, as described by Eq. (A.26) or Eq. (A.27), in Eq. (A.28). This results in

$$S(\mathbf{q}, t) = \frac{1}{\mathcal{N}_m} \sum_{i,j=1}^{\mathcal{N}_m} \langle \exp[-i\mathbf{q}(\mathbf{r}_i(t) - \mathbf{r}_j(0))] \rangle \quad (\text{A.29})$$

and

$$S(\mathbf{q}, t) = \frac{1}{\mathcal{N}_m} \int_{\mathcal{V}} \int_{\mathcal{V}} \exp[-i\mathbf{q}(\mathbf{r}' - \mathbf{r}'')] \langle (c_m(\mathbf{r}', t)c_m(\mathbf{r}'', 0)) - \langle c_m \rangle^2 \rangle d^3\mathbf{r}' d^3\mathbf{r}'' . \quad (\text{A.30})$$

For a macroscopically homogeneous system the latter equation reduces to

$$S(\mathbf{q}, t) = \frac{1}{\langle c_m \rangle} \int_{\mathcal{V}} \exp(-i\mathbf{q}\mathbf{r}) (\langle c_m(\mathbf{r}, t)c_m(0, 0) \rangle - \langle c_m \rangle^2) d^3\mathbf{r} . \quad (\text{A.31})$$

In the discussion of the structure of samples we employed the pair distribution function $g(\mathbf{r})$. This notion can be generalized to include also the dynamics, by introducing the **time-dependent pair distribution function** $g(\mathbf{r}, t)$. Per definition, the product

$$g(\mathbf{r}, t) d^3\mathbf{r}$$

describes the probability that, starting from a given particle at zero time, the same or another particle is found in the volume element $d^3\mathbf{r}$ at a distance \mathbf{r} , if the check is performed after a time delay t . As in the case of the static Eq. (A.18), one finds two contributions

$$g(\mathbf{r}, t) = \hat{g}(\mathbf{r}, t) + g'(\mathbf{r}, t) . \quad (\text{A.32})$$

The first one, \hat{g} , gives the probability that a particle will become displaced by \mathbf{r} during the time t ; the second contribution, g' , is furnished by the other particles.

As follows directly from the definitions, $g(\mathbf{r}, t)$ is proportional to the space-dependent and time-dependent density correlation function

$$\langle c_m(\mathbf{r}, t)c_m(0, 0) \rangle = \langle c_m \rangle g(\mathbf{r}, t) . \quad (\text{A.33})$$

Consequently, Eq. (A.31) is equivalent to

$$S(\mathbf{q}, t) = \int_{\mathcal{V}} \exp(-i\mathbf{q}\mathbf{r}) (g(\mathbf{r}, t) - \langle c_m \rangle) d^3\mathbf{r} . \quad (\text{A.34})$$

Equation (A.34) is the generalization Eq. (A.21).

Rather than measuring the time correlation function of the scattering amplitude, one can also use a monochromator and determine the spectral density. As stated by the Wiener–Chinchin theorem, the spectral density of a fluctuating quantity and its time correlation function are related by Fourier transformations. In our case, we have

$$S(\mathbf{q}, \omega) = \int_{t=-\infty}^{\infty} \exp(i\omega t) S(\mathbf{q}, t) dt \quad (\text{A.35})$$

and reversely

$$S(\mathbf{q}, t) = \frac{1}{2\pi} \int_{\omega=-\infty}^{\infty} \exp(-i\omega t) S(\mathbf{q}, \omega) d\omega . \quad (\text{A.36})$$

$S(\mathbf{q}, \omega)$ is known as the **dynamic scattering law** or, emphasizing the structural background, as the **dynamic structure factor**. Using Eq. (A.34) we obtain

$$S(\mathbf{q}, \omega) = \int_{\mathcal{V}} \int_{t=-\infty}^{\infty} \exp[-i(\mathbf{q}\mathbf{r} - \omega t)] (g(\mathbf{r}, t) - \langle c_m \rangle) d^3\mathbf{r} dt . \quad (\text{A.37})$$

As we can see, dynamic scattering experiments carried out under variation of the scattering vector and the frequency yield a Fourier analysis of the time-dependent pair distribution function.

Usually, experiments give the partial differential cross-section per unit volume

$$\Sigma(\mathbf{q}, \omega) = \frac{1}{\mathcal{V}} \frac{d^2\sigma}{d\omega d\Omega} . \quad (\text{A.38})$$

It is related to the dynamic scattering law by

$$\Sigma(\mathbf{q}, \omega) = \langle c_m \rangle \left(\frac{d\sigma}{d\Omega} \right)_m S(\mathbf{q}, \omega) \quad (\text{A.39})$$

in full analogy to Eq. (A.6).

Finally, we formulate relations between static and dynamic scattering functions. According to the definitions, the static scattering law is identical with the dynamic scattering law at zero time

$$S(\mathbf{q}) = S(\mathbf{q}, t = 0) . \quad (\text{A.40})$$

Applying Eq. (A.36) we can introduce $S(\mathbf{q}, \omega)$ and obtain

$$S(\mathbf{q}) = \frac{1}{2\pi} \int_{\omega=-\infty}^{\infty} S(\mathbf{q}, \omega) d\omega . \quad (\text{A.41})$$

For the differential cross-section we find correspondingly

$$\Sigma(\mathbf{q}) = \frac{1}{2\pi} \int_{\omega=-\infty}^{\infty} \Sigma(\mathbf{q}, \omega) d\omega. \quad (\text{A.42})$$

A.2 Absolute Intensities in Light-, X-ray- and Neutron-Scattering Experiments

In standard light scattering experiments on polymer solutions, absolute scattering intensities are usually determined since this is necessary for the determination of molar masses. Measurements of absolute intensities also provide additional information in X-ray or neutron diffraction studies on multicomponent and multiphase polymer systems. In the following, we will give the equations to be used.

For a complete evaluation of absolute scattering intensities one requires a knowledge of the differential cross-section per monomer, as this is included in Eq. (A.6). Let us first deal with light scattering experiments on dilute polymer solutions. The quantity of interest here is the effective differential cross-section of the dissolved monomers. Clearly it must be related to the difference in the polarizabilities of the solute and the solvent, as no scattering at all would arise for equal polarizabilities. Since a dilute solution scatters light like a gas, we can use Rayleigh's scattering equation, thereby substituting the polarizability of the gas atoms by the difference in the polarizabilities between solute and solvent molecules, denoted $\delta\beta$

$$\left(\frac{d\sigma}{d\Omega} \right)_m = \frac{\pi^2 \delta\beta^2}{\varepsilon_0^2 \lambda_0^4}. \quad (\text{A.43})$$

More accurately, $\delta\beta$ expresses the difference between the polarizability of a monomer and the total polarizability of all displaced solvent molecules that together occupy an equal volume. λ_0 denotes the wavelength of the light in vacuum. Equation (A.43) is valid for the scattering of isotropic particles if both the incoming and the scattered beam are polarized perpendicular to the scattering plane.

For dilute systems, $\delta\beta$ can be related to the difference between the indices of refraction of the solution, n , and the pure solvent, n_s , by

$$c_m \delta\beta = \varepsilon_0 (n^2 - n_s^2). \quad (\text{A.44})$$

We apply this relation in Eq. (A.43) and obtain

$$\left(\frac{d\sigma}{d\Omega} \right)_m = \frac{\pi^2 (n^2 - n_s^2)^2}{\lambda_0^4 c_m^2}. \quad (\text{A.45})$$

Use of the approximation

$$n^2 - n_s^2 \approx \frac{dn^2}{dc_m} c_m = 2n_s \frac{dn}{dc_m} c_m \quad (\text{A.46})$$

yields

$$\left(\frac{d\sigma}{d\Omega} \right)_m = \frac{4\pi^2 n_s^2}{\lambda_0^4} \left(\frac{dn}{dc_m} \right)^2. \quad (\text{A.47})$$

The Rayleigh ratio follows from Eq. (A.6) as

$$\Sigma(\mathbf{q}) = \frac{4\pi^2 n_s^2}{\lambda_0^4} c_m \left(\frac{dn}{dc_m} \right)^2 S(\mathbf{q}). \quad (\text{A.48})$$

Replacement of the number density of monomers, c_m , by their concentration by weight, c_w , using

$$c_m = c_w N_L / M_m, \quad (\text{A.49})$$

finally yields

$$\Sigma(\mathbf{q}) = K_1 M_m c_w S(\mathbf{q}) \quad (\text{A.50})$$

with the **contrast factor for light**, K_1 , given by

$$K_1 = \frac{4\pi^2 n_s^2}{\lambda_0^4 N_L} \left(\frac{dn}{dc_w} \right)^2. \quad (\text{A.51})$$

Light scattering experiments are usually evaluated on the basis of this equation.

Next, the respective relations for X-ray scattering experiments are given. In the small angle range, which is of special interest for polymer studies, the effective differential cross-section per monomer is

$$\left(\frac{d\sigma}{d\Omega} \right)_m = r_e^2 (\Delta z)^2. \quad (\text{A.52})$$

Here r_e denotes the classical electron radius

$$r_e = 2.81 \times 10^{-15} \text{ m}. \quad (\text{A.53})$$

Δz again describes a difference between monomer and displaced solvent molecules, now the difference in the total number of electrons. Δz may be deduced from the electron densities of the single components, the electron density of the monomeric unit, $c_{e,m}$, and the electron density of the solvent, $c_{e,s}$. We may write

$$(\Delta z)^2 = (c_{e,m} - c_{e,s})^2 v_m^2 \quad (\text{A.54})$$

(v_m stands for the monomer volume). If we now take Eqs. (A.52) and (A.54), introduce them into Eq. (A.6) and also exchange c_m for c_w with the aid of Eq. (A.49) we obtain a result analogous to Eq. (A.50),

$$\Sigma(\mathbf{q}) = K_x M_m c_w S(\mathbf{q}). \quad (\text{A.55})$$

The contrast factor K_x now relates to X-ray scattering and is given by

$$K_x = r_e^2 (c_{e,m} - c_{e,s})^2 v_m^2 \frac{N_L}{M_m^2}. \quad (\text{A.56})$$

For the evaluation of X-ray scattering experiments on multicomponent and multiphase systems such as polymer blends or partially crystalline polymer systems, a fourth form of scattering equations is often appropriate. We first refer to a one component system composed of particles with z_m electrons, corresponding to a differential cross-section

$$\left(\frac{d\sigma}{d\Omega} \right)_m = z_m^2 r_e^2. \quad (\text{A.57})$$

We now introduce the spatially varying electron density $c_e(\mathbf{r})$. It is given by

$$z_m c_m(\mathbf{r}) = c_e(\mathbf{r}). \quad (\text{A.58})$$

Replacing $c_m(\mathbf{r})$ by $c_e(\mathbf{r})$ in Eq. (A.17) and applying Eq. (A.6) results in

$$\Sigma(\mathbf{q}) = r_e^2 \int_V \exp(-i\mathbf{q}\mathbf{r}) (\langle c_e(\mathbf{r})c_e(0) \rangle - \langle c_e \rangle^2) d^3\mathbf{r}. \quad (\text{A.59})$$

Considerations on a more general basis show that Eq. (A.59) not only holds for one component systems but is generally valid in X-ray scattering experiments. It describes Σ as the Fourier transform of the space-dependent electron density correlation function. Equation (A.59) is equivalent to Eqs. (A.13), (A.17) and (A.21), when used together with Eq. (A.6).

Finally, we turn to neutron scattering experiments and directly write down the corresponding equations. The cross-section per monomer or per solvent molecule follows from the sum over the **scattering lengths** b_i of the respective constituent atoms, when calculating the square

$$\left(\frac{d\sigma}{d\Omega} \right)_m = \left(\sum_i b_i \right)^2. \quad (\text{A.60})$$

It is obvious that neutron scattering experiments on dilute solutions can also be described by an equation with the form of Eqs. (A.50), (A.55)

$$\Sigma(\mathbf{q}) = K_n M_m c_w S(\mathbf{q}). \quad (\text{A.61})$$

Now we have to use the contrast factor for neutron scattering, denoted K_n . It is given by

$$K_n = \left(\sum_i b_i - \sum_j b_j \right)^2 \frac{N_L}{M_m^2}. \quad (\text{A.62})$$

There are two sums on the right-hand side. The first one with running index i refers to the monomer, the second one, with index j , is meant to represent the total scattering length of the displaced solvent molecules. Clearly, for neutron scattering, similarly to the scattering of photons, it is the difference in scattering power between monomers and solvent molecules that determines the absolute scattering intensity.

We can also formulate a general equation for neutron scattering in analogy to Eq. (A.59) valid for X-rays. This is achieved by substituting the product $r_e c_e$ by the **scattering length density** c_n , resulting in

$$\Sigma(\mathbf{q}) = \int_{\mathcal{V}} \exp(-i\mathbf{q}\mathbf{r}) (\langle c_n(\mathbf{r})c_n(0) \rangle - \langle c_n \rangle^2) d^3\mathbf{r}. \quad (\text{A.63})$$

All these equations concern a coherent process of neutron scattering, since they all express interferences, and these can only arise for well-defined phase relations between the scattered waves emanating from the different particles. In fact, in neutron scattering experiments, one encounters a complication since there always exists an additional contribution of incoherent scattering processes. The latter take place without a regular phase relation between different particles. Although this second part cannot contain any information on the structure, it is nevertheless important since it can be used in quasielastic scattering experiments for the study of single particle motions. Complete treatments and experiments show that one can measure an intermediate scattering law associated with the incoherent part only and that this directly relates to the Fourier transform of the **self-correlation function** of a moving particle, denoted $\hat{g}(\mathbf{r}, t)$ in Eq. (A.32). Explicitly, the relation has the form

$$S^{\text{inc}}(\mathbf{q}, t) = \int_{\mathcal{V}} \exp(-i\mathbf{q}\mathbf{r}) (\hat{g}(\mathbf{r}, t) - \hat{g}(\mathbf{r}, t \rightarrow \infty)) d^3\mathbf{r}. \quad (\text{A.64})$$

The relative weights of the coherent and the incoherent process in a neutron scattering experiment vary greatly between different atoms. For hydrogen atoms, for example, the incoherent scattering is dominant, and dynamic neutron scattering experiments on organic materials therefore frequently focus on the dynamics of the single particles. For deuterium we find the reverse situation, with a dominance of the coherent process, which opens the way for investigations of the structure and of collective dynamical processes.

A.3 Low Angle Scattering Properties

A.3.1 Guinier's Law

Scattering experiments at low angles on dilute colloidal systems, polymer solutions included, can be applied for a determination of the molar mass and the size of colloids or polymers. The relation may be explained as follows.

We start from Eq. (A.13) and consider a dilute system of polymers or, more general, colloids, each one composed of N monomeric units. For \mathcal{N}_p colloids in the sample we have

$$\mathcal{N}_m = N\mathcal{N}_p . \quad (\text{A.65})$$

For a dilute system we neglect all interferences between different colloids. Equation (A.13) can then be rewritten as

$$\begin{aligned} S(\mathbf{q}) &= \frac{1}{\mathcal{N}_m} \sum_{i,j=1}^{\mathcal{N}_m} \langle \exp[-i\mathbf{q}(\mathbf{r}_i - \mathbf{r}_j)] \rangle \\ &= \frac{1}{\mathcal{N}_p N} \mathcal{N}_p \sum_{i,j=1}^N \langle \exp[-i\mathbf{q}(\mathbf{r}_i - \mathbf{r}_j)] \rangle . \end{aligned} \quad (\text{A.66})$$

In the low angle range close to the origin we may use a series expansion up to second order, giving

$$S(\mathbf{q}) \approx \frac{1}{N} \sum_{i,j=1}^N \left\langle 1 - i\mathbf{q}(\mathbf{r}_i - \mathbf{r}_j) + \frac{1}{2}[\mathbf{q}(\mathbf{r}_i - \mathbf{r}_j)]^2 \right\rangle . \quad (\text{A.67})$$

For isotropic systems the linear term vanishes and the quadratic term transforms into

$$\langle [\mathbf{q}(\mathbf{r}_i - \mathbf{r}_j)]^2 \rangle = \frac{1}{3} q^2 \langle |\mathbf{r}_i - \mathbf{r}_j|^2 \rangle . \quad (\text{A.68})$$

This leads to

$$S(\mathbf{q}) \approx \frac{1}{N} \left(N^2 - \frac{q^2}{6} \sum_{i,j=1}^N |\mathbf{r}_i - \mathbf{r}_j|^2 \right) . \quad (\text{A.69})$$

If we introduce the **radius of gyration**, defined by

$$R_g^2 = \frac{1}{2N^2} \sum_{i,j=1}^N |\mathbf{r}_i - \mathbf{r}_j|^2 , \quad (\text{A.70})$$

we obtain an expression for the structure factor in the limit of low \mathbf{q} 's

$$S(\mathbf{q}) \approx N \left(1 - \frac{q^2 R_g^2}{3} + \dots \right) . \quad (\text{A.71})$$

The equation, often addressed as **Guinier's law**, tells us that measurements in the low angle range can be used for a determination of the size of a colloid, as characterized by R_g , and the mass, as given by N .

An equivalent, probably better known definition of R_g is

$$R_g = \frac{1}{N} \sum_{i=1}^N \langle |\mathbf{r}_i - \mathbf{r}_c|^2 \rangle \quad (\text{A.72})$$

whereby \mathbf{r}_c denotes the center of mass of the colloid, given by

$$\mathbf{r}_c = \frac{1}{N} \sum_{i=1}^N \mathbf{r}_i . \quad (\text{A.73})$$

The equivalence follows by noting that

$$\begin{aligned} \sum_{i,j=1}^N (\mathbf{r}_i - \mathbf{r}_j)^2 &= \sum_{i,j=1}^N [(\mathbf{r}_i - \mathbf{r}_c) - (\mathbf{r}_j - \mathbf{r}_c)]^2 \\ &= N \left(\sum_i^N (\mathbf{r}_i - \mathbf{r}_c)^2 + \sum_j^N (\mathbf{r}_j - \mathbf{r}_c)^2 \right) \\ &\quad - 2 \sum_i^N (\mathbf{r}_i - \mathbf{r}_c) \sum_j^N (\mathbf{r}_j - \mathbf{r}_c) \\ &= 2N \sum_i^N (\mathbf{r}_i - \mathbf{r}_c)^2 , \end{aligned} \quad (\text{A.74})$$

thereby taking into account that

$$\sum_i^N (\mathbf{r}_i - \mathbf{r}_c) = 0 . \quad (\text{A.75})$$

A.3.2 Forward Scattering

A general relation associates the limiting value of the structure factor in the forward direction, $S(\mathbf{q} \rightarrow 0)$, with the fluctuation of the number of particles in a given volume \mathcal{V} and, furthermore, based on thermodynamics, with the isothermal compressibility of the sample.

The relation follows directly from an application of Eq. (A.15)

$$\begin{aligned} S(\mathbf{q} \rightarrow 0) &= \frac{1}{\langle \mathcal{N}_m \rangle} \left\langle \left(\int_{\mathcal{V}} (c_m(\mathbf{r}) - \langle c_m \rangle) d^3\mathbf{r} \right)^2 \right\rangle \\ &= \frac{1}{\langle \mathcal{N}_m \rangle} \langle (\mathcal{N}_m - \langle \mathcal{N}_m \rangle)^2 \rangle . \end{aligned} \quad (\text{A.76})$$

The ratio

$$\frac{\langle (\mathcal{N}_m - \langle \mathcal{N}_m \rangle)^2 \rangle}{\langle \mathcal{N}_m \rangle} = \frac{\langle \mathcal{N}_m^2 \rangle - \langle \mathcal{N}_m \rangle^2}{\langle \mathcal{N}_m \rangle} \quad (\text{A.77})$$

is independent of the chosen volume. This must be the case, since the left-hand side of the equation, i.e., $S(\mathbf{q})$, does not depend on \mathcal{V} , and it also follows from the treatment of fluctuations in statistical thermodynamics. Fluctuation

theory relates the particle number fluctuation to the isothermal compressibility

$$\kappa_T = \left(\frac{\partial \langle c_m \rangle}{\partial p} \right)_T, \quad (\text{A.78})$$

by

$$\frac{\langle \mathcal{N}_m^2 \rangle - \langle \mathcal{N}_m \rangle^2}{\langle \mathcal{N}_m \rangle} = kT \kappa_T. \quad (\text{A.79})$$

Combination of Eqs. (A.76) and (A.79) yields

$$S(\mathbf{q} \rightarrow 0) = kT \kappa_T. \quad (\text{A.80})$$

Equation (A.80) is generally valid for all one-component systems, independent of the state of order, which may be gaseous, liquid-like or crystalline.

An equation that is fully equivalent to Eq. (A.80) can be applied in studies of polymer solutions. The limiting value for $\mathbf{q} \rightarrow 0$ of the structure factor of a solution is given by

$$S(\mathbf{q} \rightarrow 0) = kT \kappa_{\text{osm}} \quad (\text{A.81})$$

as it follows by a replacement of κ_T in Eq. (A.80) by the osmotic compressibility

$$\kappa_{\text{osm}} = \left(\frac{\partial \langle c_m \rangle}{\partial \Pi} \right)_T. \quad (\text{A.82})$$

Π denotes the osmotic pressure and $\langle c_m \rangle$ gives the mean monomer density in the solution. The replacement is justified by fluctuation theory, which derives for the fluctuation of the number of colloids in a fixed volume of a solution an equation equivalent to Eq. (A.79), substituting κ_T by κ_{osm} .

A.4 Special Polymer Systems

A.4.1 Binary Mixtures and Block Copolymers

Scattering experiments play a prominent role in the analysis of structures of polymer mixtures and block copolymers. Scattering curves of the homogeneous fluid state can be evaluated quantitatively by a comparison with theoretical scattering functions. We derive the theoretical functions in this section using general relations between fluctuations and response functions.

In the discussion of concentration fluctuations in polymer blends in Sect. 4.3, we obtained Eq. (4.74) for the increase in the Gibbs free energy associated with the formation of a concentration wave of the A -chains. It shows that the excitation of a wave with wave vector \mathbf{k} to an amplitude $\phi_{\mathbf{k}}$ leads to an energy increase $\delta\mathcal{G}$ given by the quadratic form

$$\delta\mathcal{G} = \frac{1}{2} a_{\mathbf{k}} |\phi_{\mathbf{k}}|^2. \quad (\text{A.83})$$

While Eq. (4.74) contained an expression for $a_{\mathbf{k}}$ based on the Flory–Huggins theory of polymer mixtures, in a more general view $a_{\mathbf{k}}$ can be considered as representing a general modulus. Equation (A.83) can also be presented in the form

$$\delta\mathcal{G} = \frac{1}{2}\psi_{\mathbf{k}}\phi_{\mathbf{k}}^* , \quad (\text{A.84})$$

thereby introducing with

$$\psi_{\mathbf{k}} = a_{\mathbf{k}}\phi_{\mathbf{k}} \quad (\text{A.85})$$

a field that is the energetic conjugate to $\phi_{\mathbf{k}}$. The linear relation between $\psi_{\mathbf{k}}$ and $\phi_{\mathbf{k}}$ can alternatively be expressed as

$$\phi_{\mathbf{k}} = \alpha_{\mathbf{k}}\psi_{\mathbf{k}} , \quad (\text{A.86})$$

employing a response coefficient $\alpha_{\mathbf{k}}$. $\alpha_{\mathbf{k}}$ is the reciprocal of $a_{\mathbf{k}}$

$$\alpha_{\mathbf{k}} = \frac{1}{a_{\mathbf{k}}} . \quad (\text{A.87})$$

The mean squared fluctuations of $\phi_{\mathbf{k}}$ in thermal equilibrium follow by applying Boltzmann statistics. The probability distribution is

$$p(\phi_{\mathbf{k}}) \propto \exp - \frac{a_{\mathbf{k}}|\phi_{\mathbf{k}}|^2}{2kT} \quad (\text{A.88})$$

which yields

$$\langle |\phi_{\mathbf{k}}|^2 \rangle = \frac{kT}{a_{\mathbf{k}}} = kT\alpha_{\mathbf{k}} . \quad (\text{A.89})$$

The fluctuation $\langle |\phi_{\mathbf{k}}|^2 \rangle$ shows up in a scattering experiment as determining the scattering intensity at $\mathbf{q} = \mathbf{k}$. In Sect. 4.3 we used a lattice model and introduced the scattering function per cell, $S_c(\mathbf{q})$ (Eq. (4.79)). A separate calculation presented at the end of this section will demonstrate that $S_c(\mathbf{q})$ and $\langle |\phi_{\mathbf{k}=\mathbf{q}}|^2 \rangle$ are related by

$$v_c S_c(\mathbf{q}) = \langle |\phi_{\mathbf{k}=\mathbf{q}}|^2 \rangle \quad (\text{A.90})$$

(v_c denotes the cell volume). Using this equation we find the following relationship between the scattering function $S_c(\mathbf{q})$ and the response coefficients $\alpha_{\mathbf{k}}$:

$$v_c S_c(\mathbf{q}) = kT\alpha_{\mathbf{k}=\mathbf{q}} . \quad (\text{A.91})$$

This is an important result. It says that the problem of calculating the structure factor of a mixture of polymer chains is equivalent to the problem of calculating response functions. De Gennes was the first to use this equivalence in polymer theories. The procedure is usually addressed as **random phase approximation**, abbreviated RPA, adopting a name firstly chosen by Bohm, Pines and Nozieres in a work on electron properties in metals. Equation (A.91) can be applied in two directions. If response coefficients are known,

scattering functions can be calculated, and, vice versa, if structure factors are known, the knowledge may be used for the derivation of response coefficients. In the following, both ways will be combined.

We first inquire about the scattering function of an athermal mixture of A- and B-chains, assuming that the mixture is densely packed and incompressible. Under this condition we may choose either the A- or the B-monomers as the representative particles responsible for the scattering, and we select the monomers A.

We approach the problem with a calculation of the response coefficient associated with an excitation of a concentration wave with wave vector \mathbf{k} . Imagine that this excitation is due to the action of a sinusoidally varying potential field which interacts exclusively with the A's. If this potential has the strength $\psi_{\mathbf{k}}$, the response is described by

$$\phi_{\mathbf{k}} = \alpha_{\mathbf{k}}^0 \psi_{\mathbf{k}} . \quad (\text{A.92})$$

Although the field only interacts directly with the A's, there are, as we shall see, more effects contributing to $\alpha_{\mathbf{k}}^0$; $\alpha_{\mathbf{k}}^0$ represents a **collective response coefficient**. The upper index '0' is meant to indicate that here we are treating an athermal system with $\chi = 0$.

Owing to the incompressibility, an excitation of a concentration wave of the A's with amplitude $\phi_{\mathbf{k}}$ is necessarily associated with a simultaneous excitation of a concentration wave of the B's. The latter has an amplitude in opposite direction

$$\phi_{\mathbf{k}}^{\text{B}} = -\phi_{\mathbf{k}}^{\text{A}} = -\phi_{\mathbf{k}} . \quad (\text{A.93})$$

Formally, the induced displacement of the B's may be regarded as a result of the action of a second potential, an **internal field** with amplitude $\hat{\psi}_{\mathbf{k}}$. Since this internal field arises from the requirement of a constant total monomer density, it cannot discriminate between A- and B-monomers, but must act on both species equally. The external potential $\psi_{\mathbf{k}}$ and the induced internal field $\hat{\psi}_{\mathbf{k}}$ together produce the following responses:

$$\phi_{\mathbf{k}} = \alpha_{\mathbf{k}}^{\text{AA}} (\psi_{\mathbf{k}} + \hat{\psi}_{\mathbf{k}}) , \quad (\text{A.94})$$

$$\phi_{\mathbf{k}}^{\text{B}} = -\phi_{\mathbf{k}} = \alpha_{\mathbf{k}}^{\text{BB}} \hat{\psi}_{\mathbf{k}} \quad (\text{A.95})$$

The A-chains interact with both the external potential and the induced internal field, whereas the B-chains interact with the internal field only. We have introduced here two further response coefficients, $\alpha_{\mathbf{k}}^{\text{AA}}$ and $\alpha_{\mathbf{k}}^{\text{BB}}$. According to the equations they represent response coefficients for the A- and B-chains separately, expressing how chains of both types respond to the acting fields. As all many-chain effects that ensure the constant total density are included in $\hat{\psi}_{\mathbf{k}}$, $\alpha_{\mathbf{k}}^{\text{AA}}$ and $\alpha_{\mathbf{k}}^{\text{BB}}$ represent true single chain response coefficients. This fact is important, as one now has to ask about the responses of non-interacting single chains only, and the answer is simple. Recall that chains are ideal in a melt, so that we have to inquire about the response coefficients of Gaussian

chains. These, however, are known, since response coefficients are proportional to structure factors, and the structure factors of ideal chains are given by the Debye equation Eq. (2.61). It can be applied separately for the A- and B-chains, thus yielding $\alpha_{\mathbf{k}}^{\text{AA}}$ and $\alpha_{\mathbf{k}}^{\text{BB}}$.

For a calculation of $S_c(\mathbf{q})$ we have to compute the collective response coefficient $\alpha_{\mathbf{k}}^0$. First we eliminate the induced field $\hat{\psi}_{\mathbf{k}}$. Addition of Eqs. (A.94) and (A.95) leads to

$$\hat{\psi}_{\mathbf{k}} = -\frac{\alpha_{\mathbf{k}}^{\text{AA}}}{\alpha_{\mathbf{k}}^{\text{AA}} + \alpha_{\mathbf{k}}^{\text{BB}}} \psi_{\mathbf{k}}. \quad (\text{A.96})$$

Insertion of Eq. (A.96) into Eq. (A.94) gives

$$\phi_{\mathbf{k}} = \frac{\alpha_{\mathbf{k}}^{\text{AA}} \alpha_{\mathbf{k}}^{\text{BB}}}{\alpha_{\mathbf{k}}^{\text{AA}} + \alpha_{\mathbf{k}}^{\text{BB}}} \psi_{\mathbf{k}}. \quad (\text{A.97})$$

Comparison of this equation with Eq. (A.92) yields

$$\frac{1}{\alpha_{\mathbf{k}}^0} = \frac{1}{\alpha_{\mathbf{k}}^{\text{AA}}} + \frac{1}{\alpha_{\mathbf{k}}^{\text{BB}}} \quad (\text{A.98})$$

We thus obtain an explicit expression for the collective response coefficient $\alpha_{\mathbf{k}}^0$, in terms of the known single chain response coefficients $\alpha_{\mathbf{k}}^{\text{AA}}$ and $\alpha_{\mathbf{k}}^{\text{BB}}$. With this we have essentially solved our first problem.

Next, we turn to a non-athermal mixture. The difference in the interaction between like and unlike chains is accounted for in the spirit of the Flory-Huggins treatment by introduction of the χ parameter. This is achieved by changing Eq. (A.92) into

$$\phi_{\mathbf{k}} = \alpha_{\mathbf{k}}^0 (\psi_{\mathbf{k}} + \chi' \phi_{\mathbf{k}}) \quad (\text{A.99})$$

with

$$\chi' = \frac{2\chi kT}{v_c}. \quad (\text{A.100})$$

On the other hand, we shall retain the representation of the single chain responses by ideal chain response coefficients, assuming that this is still a good approximation. The idea behind Eq. (A.99) is easy to see, as it corresponds to a sequence of two steps. If an external potential $\psi_{\mathbf{k}}$ initiates a concentration wave, this wave in turn produces a molecular field $\chi' \phi_{\mathbf{k}}$, which for $\chi' > 0$ further reinforces and for $\chi' < 0$ weakens the external potential. Equation (A.99) is identical in form with the well-known mean field equation of ferromagnets, where the Weiss-field λM produced by the magnetization M reinforces the primary magnetic field H

$$M = \alpha_H (H + \lambda M) \quad (\text{A.101})$$

(α_H is the magnetic susceptibility). Equation (A.99) gives

$$\phi_{\mathbf{k}} = \frac{\alpha_{\mathbf{k}}^0}{1 - \chi' \alpha_{\mathbf{k}}^0} \psi_{\mathbf{k}} \quad (\text{A.102})$$

hence

$$\alpha_{\mathbf{k}} = \frac{\phi_{\mathbf{k}}}{\psi_{\mathbf{k}}} = \frac{\alpha_{\mathbf{k}}^0}{1 - \chi' \alpha_{\mathbf{k}}^0} . \quad (\text{A.103})$$

Taking the reciprocals on both sides yields

$$\frac{1}{\alpha_{\mathbf{k}}} = \frac{1}{\alpha_{\mathbf{k}}^0} - \chi' . \quad (\text{A.104})$$

Equation (A.104) relates the collective response coefficient $\alpha_{\mathbf{k}}^0$ of an athermal polymer mixture to that of a mixture with a non-vanishing χ parameter.

We can now combine Eqs. (A.98), (A.100) and (A.104) to obtain the final result of the RPA treatment, which has the form

$$\frac{1}{\alpha_{\mathbf{k}}} = \frac{1}{\alpha_{\mathbf{k}}^{\text{AA}}} + \frac{1}{\alpha_{\mathbf{k}}^{\text{BB}}} - \frac{2\chi kT}{v_c} . \quad (\text{A.105})$$

Block copolymers constitute a second system that has been successfully treated in the RPA framework. We remark at the beginning that we have only to discuss the athermal situation since the effect of a non-vanishing χ parameter can then be treated in the same manner as for the polymer mixtures. The response equations for a block copolymer melt in the homogeneous phase can be directly formulated, writing

$$\phi_{\mathbf{k}} = \alpha_{\mathbf{k}}^{\text{AA}}(\psi_{\mathbf{k}} + \hat{\psi}_{\mathbf{k}}) + \alpha_{\mathbf{k}}^{\text{AB}}\hat{\psi}_{\mathbf{k}} \quad (\text{A.106})$$

$$\phi_{\mathbf{k}}^{\text{B}} = -\phi_{\mathbf{k}} = \alpha_{\mathbf{k}}^{\text{BA}}(\psi_{\mathbf{k}} + \hat{\psi}_{\mathbf{k}}) + \alpha_{\mathbf{k}}^{\text{BB}}\hat{\psi}_{\mathbf{k}} . \quad (\text{A.107})$$

Incompressibility is accounted for in the same way as for polymer mixtures, by the introduction of the internal field $\hat{\psi}_{\mathbf{k}}$. The new feature in the block copolymer system is the occurrence of the coefficients $\alpha_{\mathbf{k}}^{\text{AB}}$ and $\alpha_{\mathbf{k}}^{\text{BA}}$. They describe cross-responses given by the reaction of the A-chains to a force that acts on the B-chains and vice-versa. As is obvious, cross-responses are generated by the chemical coupling of the A- and B-chains. It is exactly this coupling that sets block copolymers apart from binary mixtures and it changes the response conditions.

The two coupled equations can be evaluated. First note that the ratio between ψ and $\hat{\psi}_{\mathbf{k}}$ is fixed by the assumed incompressibility

$$0 = \psi_{\mathbf{k}} (\alpha_{\mathbf{k}}^{\text{AA}} + \alpha_{\mathbf{k}}^{\text{BA}}) + \hat{\psi}_{\mathbf{k}} (\alpha_{\mathbf{k}}^{\text{AB}} + \alpha_{\mathbf{k}}^{\text{AA}} + \alpha_{\mathbf{k}}^{\text{AA}} + \alpha_{\mathbf{k}}^{\text{BB}}) . \quad (\text{A.108})$$

$\hat{\psi}_{\mathbf{k}}$ can be eliminated from Eqs. (A.106) and (A.108). We thus obtain the collective response coefficient of the A-blocks

$$\alpha_{\mathbf{k}}^0 = \frac{\phi_{\mathbf{k}}^{\text{A}}}{\psi_{\mathbf{k}}} = \frac{\alpha_{\mathbf{k}}^{\text{AA}} \alpha_{\mathbf{k}}^{\text{BB}} - \alpha_{\mathbf{k}}^{\text{AB}} \alpha_{\mathbf{k}}^{\text{BA}}}{\alpha_{\mathbf{k}}^{\text{AB}} + \alpha_{\mathbf{k}}^{\text{BA}} + \alpha_{\mathbf{k}}^{\text{AA}} + \alpha_{\mathbf{k}}^{\text{BB}}} . \quad (\text{A.109})$$

Equation (A.109) represents the RPA result for athermal block copolymers. The effect of a non-vanishing χ parameter can be accounted for as above in Eq. (A.104) by writing

$$\frac{1}{\alpha_{\mathbf{k}}} = \frac{1}{\alpha_{\mathbf{k}}^0} - \frac{2\chi kT}{v_c}. \quad (\text{A.110})$$

$\alpha_{\mathbf{k}}^0$ is now given by Eq. (A.109).

In order to obtain the full expressions for the scattering functions of polymer mixtures and block copolymers, we have to substitute the collective and single chain response coefficients by the corresponding scattering laws. Response coefficients and scattering functions are related by Eq. (A.91). The single chain AA- and BB-response coefficients are thus given by the corresponding Debye scattering functions

$$\frac{kT}{v_c} \alpha_{\mathbf{k}=\mathbf{q}}^{\text{AA}} = \phi N_A S_D(R_A q) \quad (\text{A.111})$$

$$\frac{kT}{v_c} \alpha_{\mathbf{k}=\mathbf{q}}^{\text{BB}} = (1 - \phi) N_B S_D(R_B q). \quad (\text{A.112})$$

N_A , N_B and R_A , R_B are the degrees of polymerization and the mean squared end-to-end distances of the two polymers. The factors ϕ and $1 - \phi$ account for the dilution of the respective chains in the mixture or the block copolymer.

An expression for the cross-response coefficients is still needed. The Debye-structure functions $S_D(R_A q)$ and $S_D(R_B q)$ are the Fourier transforms of the pair distribution functions $g_{\text{AA}}(\mathbf{r})$ and $g_{\text{BB}}(\mathbf{r})$ for the A- and B-monomers within their blocks. Considering this definition, it is clear how the coefficients for the cross responses $\alpha_{\mathbf{k}}^{\text{AB}}$ and $\alpha_{\mathbf{k}}^{\text{BA}}$ are to be calculated. They correspond to the Fourier transforms of the pair distribution functions $g_{\text{AB}}(\mathbf{r})$ and $g_{\text{BA}}(\mathbf{r})$ describing the probability of finding a B- or A-monomer at a distance \mathbf{r} from a A- or B-monomer, respectively. Actually, both are identical

$$g_{\text{AB}}(\mathbf{r}) = g_{\text{BA}}(\mathbf{r}). \quad (\text{A.113})$$

We do not present the calculation here. It is straightforward and leads to

$$\frac{1}{2} [N_{\text{AB}} S_D(R_0 q) - \phi N_A S_D(R_A q) - (1 - \phi) N_B S_D(R_B q)] = \frac{kT}{v_c} \alpha_{\mathbf{k}=\mathbf{q}}^{\text{AB}} \quad (\text{A.114})$$

with

$$N_{\text{AB}} = N_A + N_B \quad \text{and} \quad R_0^2 = R_A^2 + R_B^2. \quad (\text{A.115})$$

Introduction of Eqs. (A.111)–(A.114) into Eqs. (A.98) and (A.109), respectively, together with the use of Eq. (A.104), yields the RPA scattering functions given in Sects. 4.3 and 4.4.2.

For completion, at the end of this section we derive Eq. (A.90),

$$S_c(\mathbf{q}) = \frac{\langle |\phi_{\mathbf{k}=\mathbf{q}}|^2 \rangle}{v_c}.$$

We start from Eq. (A.14),

$$C(\mathbf{q}) = \int_{\mathcal{V}} \exp(-i\mathbf{q}\mathbf{r})(c_{\mathbf{m}}(\mathbf{r}) - \langle c_{\mathbf{m}} \rangle) d^3\mathbf{r} ,$$

which relates the scattering amplitude $C(\mathbf{q})$ to the density distribution $c_{\mathbf{m}}(\mathbf{r})$ of A-monomers. The density fluctuation in polymer mixtures can be described as a superposition of waves with wave vector \mathbf{k} and amplitude $c_{\mathbf{k}}$

$$c_{\mathbf{m}}(\mathbf{r}) - \langle c_{\mathbf{m}} \rangle = \mathcal{V}^{-1/2} \sum_{\mathbf{k}} c_{\mathbf{k}} \exp(i\mathbf{k}\mathbf{r}) \quad (\text{A.116})$$

with

$$c_{\mathbf{k}=0} = 0 .$$

If we choose periodic boundary conditions in a box with equal side lengths L , the sum includes the wave vectors

$$\mathbf{k} = \frac{2\pi}{L} \begin{pmatrix} n_1 \\ n_2 \\ n_3 \end{pmatrix} , \quad (\text{A.117})$$

where the n_i 's are integer numbers. The density of the wave vectors in the \mathbf{k} -space is given by

$$L^3/(2\pi)^3 = \mathcal{V}/(2\pi)^3 . \quad (\text{A.118})$$

Since $c_{\mathbf{m}}(\mathbf{r})$ is a real function, we have

$$c_{\mathbf{k}} = c_{-\mathbf{k}}^* . \quad (\text{A.119})$$

Scattering intensities are proportional to mean squared scattering amplitudes

$$\langle |C(\mathbf{q})|^2 \rangle = \frac{1}{\mathcal{V}} \sum_{\mathbf{k}, \mathbf{k}'} \langle c_{\mathbf{k}} c_{\mathbf{k}'}^* \rangle \cdot \int_{\mathcal{V}} \int_{\mathcal{V}} \exp[-i(\mathbf{q} - \mathbf{k})\mathbf{r}] \exp[i(\mathbf{q} - \mathbf{k}')\mathbf{r}'] d^3\mathbf{r} d^3\mathbf{r}' . \quad (\text{A.120})$$

Waves with different wave vectors, with the exception of pairs $\mathbf{k}' = -\mathbf{k}$, are statistically independent, i.e.,

$$\langle c_{\mathbf{k}} c_{\mathbf{k}'}^* \rangle = \langle |c_{\mathbf{k}}|^2 \rangle \delta_{\mathbf{k}, \mathbf{k}'} + \langle c_{\mathbf{k}}^2 \rangle \delta_{\mathbf{k}, -\mathbf{k}'} . \quad (\text{A.121})$$

Since $c_{\mathbf{k}}^2$ includes a random phase, the second term on the right-hand side vanishes

$$\langle c_{\mathbf{k}}^2 \rangle = 0 . \quad (\text{A.122})$$

We use the Fourier representation of the δ -function and write

$$\begin{aligned} \int_{\mathcal{V}} \int_{\mathcal{V}} \exp[-i(\mathbf{q} - \mathbf{k})(\mathbf{r} - \mathbf{r}')] d^3\mathbf{r} d^3\mathbf{r}' &= \mathcal{V} \int_{\mathcal{V}} \exp(-i\mathbf{q}\Delta\mathbf{r}) d\Delta\mathbf{r} \\ &= \mathcal{V}(2\pi)^3 \delta(\mathbf{q} - \mathbf{k}) . \end{aligned} \quad (\text{A.123})$$

This transforms Eq.(A.120) into

$$\langle |C(\mathbf{q})|^2 \rangle = \sum_{\mathbf{k}} \langle |c_{\mathbf{k}}|^2 \rangle (2\pi)^3 \delta(\mathbf{q} - \mathbf{k}) . \quad (\text{A.124})$$

Scattering experiments do not detect the individual values of \mathbf{k} and \mathbf{q} as described by Eq. (A.117) but integrate over finite ranges $\Delta\mathbf{q}^3$. Therefore, applying Eq. (A.118), we obtain

$$\langle |C(\mathbf{q})|^2 \rangle = \mathcal{V} \langle |c_{\mathbf{k}=\mathbf{q}}|^2 \rangle . \quad (\text{A.125})$$

Now we introduce the scattering function of the lattice model, defined by Eq. (4.79):

$$\begin{aligned} S_c(\mathbf{q}) &= \frac{1}{\mathcal{N}_c} \langle |C(\mathbf{q})|^2 \rangle \\ &= v_c \langle |c_{\mathbf{k}=\mathbf{q}}|^2 \rangle . \end{aligned} \quad (\text{A.126})$$

Replacement of the fluctuations in the monomer density by fluctuations in the volume fraction occupied by the A-chains, using

$$\delta\phi = v_c \delta c_m , \quad (\text{A.127})$$

which implies

$$\langle |\phi_{\mathbf{k}}|^2 \rangle = v_c^2 \langle |c_{\mathbf{k}}|^2 \rangle , \quad (\text{A.128})$$

finally leading to

$$S_c(\mathbf{q}) = \frac{\langle |\phi_{\mathbf{k}=\mathbf{q}}|^2 \rangle}{v_c} ,$$

which is the relationship to be derived.

A.4.2 Two-Phase Layer Systems

Isotropic samples of a semicrystalline polymer essentially correspond to an ensemble of densely packed, isotropically distributed stacks of parallel lamellar crystallites. If the extensions of the stacks parallel and normal to the lamellar surfaces are large compared to the interlamellar distance, the scattering behavior can be related to the electron density distribution $c_e(z)$ measured along a trajectory normal to the surfaces. This trajectory will pass through amorphous regions with density $c_{e,a}$ and crystallites with a core density $c_{e,c}$. The average density $\langle c_e \rangle$ lies between these two limits.

We calculate the scattering cross-section per unit volume by application of Eq. (A.59) and consider at first an ensemble of equally oriented stacks. If we choose the orientation of the surface normals parallel to the z -axis, the electron density distribution depends on z only and we can write

$$\Sigma(\mathbf{q}) = r_e^2 \int_{x,y,z} \exp[-i(q_x x + q_y y + q_z z)] (\langle c_e(z) c_e(0) \rangle - \langle c_e \rangle^2) dx dy dz . \quad (\text{A.129})$$

Carrying out the integrations for x and y , we obtain

$$\Sigma(\mathbf{q}) = r_e^2 (2\pi)^2 \delta(q_x) \delta(q_y) \int_{-\infty}^{\infty} \exp(-iq_z z) K(z) dz \quad (\text{A.130})$$

where $K(z)$ designates the **one-dimensional electron density correlation function**

$$\begin{aligned} K(z) &= \langle (c_e(z) - \langle c_e \rangle)(c_e(0) - \langle c_e \rangle) \rangle \\ &= \langle c_e(z) c_e(0) \rangle - \langle c_e \rangle^2 . \end{aligned} \quad (\text{A.131})$$

The scattering of an isotropic ensemble of stacks of lamellae, as is found in melt crystallized samples, follows from Eq. (A.130) by calculation of the isotropic average, i.e., by distributing the intensity at $\pm q_z$ equally over the surface of a sphere with the same radius. The resulting isotropic intensity distribution, $\Sigma(q)$, is given by

$$\Sigma(q) = \frac{2}{4\pi q^2} r_e^2 (2\pi)^2 \int_{-\infty}^{\infty} \exp(-iqz) K(z) dz . \quad (\text{A.132})$$

The reverse Fourier relation is

$$\begin{aligned} K(z) &= \frac{1}{2r_e^2} \frac{1}{(2\pi)^3} \int_{-\infty}^{\infty} \exp(iqz) 4\pi q^2 \Sigma(q) dq \\ &= \frac{1}{r_e^2} \frac{1}{(2\pi)^3} \int_0^{\infty} \cos(qz) 4\pi q^2 \Sigma(q) dq . \end{aligned} \quad (\text{A.133})$$

Equation (A.133) enables $K(z)$ to be determined if $\Sigma(q)$ is known.

$K(z)$ has a characteristic shape, allowing an evaluation that leads directly to the main parameters of the stack structure. In order to explain the procedure, we first establish the shape of $K(z)$ for a strictly periodic two-phase system and then proceed by a considering the modifications introduced by a stepwise perturbation of the system. Figure A.2 provides an illustration and sketches all the steps.

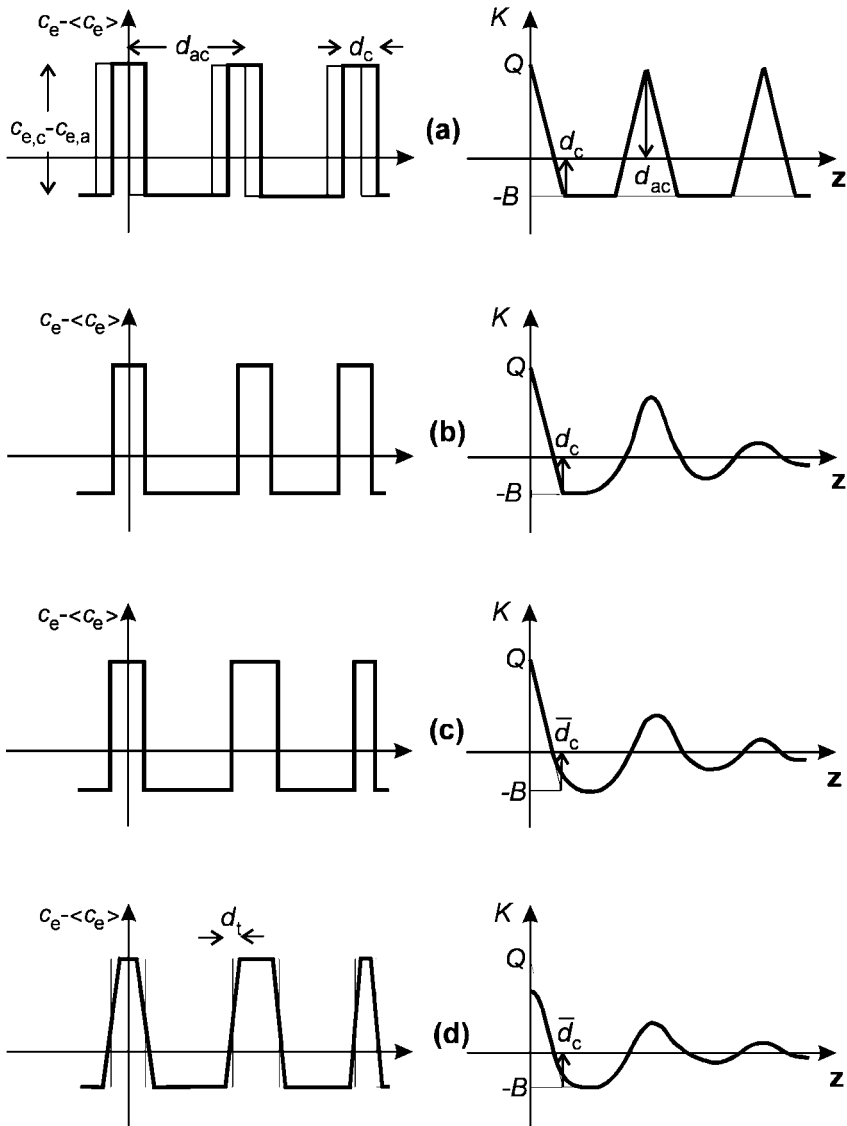


Fig. A.2. Two phase-layer system representative for a semicrystalline polymer. Electron density distribution $c_e(z) - \langle c_e \rangle$ and the associated one-dimensional correlation function $K(z)$ for a perfectly ordered system (a). Effects of varying intercrystalline spacings (b), varying crystallite thicknesses (c) and diffuse interfaces (d)

The periodic structure shows an electron density distribution $c_e(z)$ as indicated on the left of part (a). It can be described by specifying the **long period** d_{ac} , the crystallite thickness d_c and the electron density difference $c_{e,c} - c_{e,a}$. The crystallinity $\phi_c = d_c/d_{ac}$ in this example lies below 50%. We first calculate a special correlation function, denoted $K_a(z)$, defined as

$$K_a(z) = \langle (c_e(z) - c_{e,a})(c_e(0) - c_{e,a}) \rangle. \quad (\text{A.134})$$

When using K_a , all electron densities refer to the electron density of the amorphous regions. Since the ensemble average is identical with an average over all points z' in a stack, $K_a(z)$ may be obtained by an evaluation of the integral

$$K_a(z) = \frac{1}{\Delta} \int_{-\Delta/2}^{\Delta/2} [c_e(z') - c_{e,a}][c_e(z + z') - c_{e,a}] dz'. \quad (\text{A.135})$$

The integration range Δ has to be sufficiently large. The functions $c_e(z)$ and $c_e(z + z')$ are square distributions, and contributions to the integral arise only if two crystalline regions overlap. Consequently, $K_a(z)$ is proportional to the length of the overlap region and given by

$$K_a(z) = \begin{cases} (c_{e,c} - c_{e,a})^2(d_c - z)/d_{ac} & \text{if } |z| < d_c \\ 0 & \text{if } d_c < |z| < d_{ac} - d_c \end{cases} \quad (\text{A.136})$$

and being periodic by

$$K_a(z + d_{ac}) = K_a(z). \quad (\text{A.137})$$

Having determined K_a , one obtains $K(z)$ by

$$K(z) = K_a(z) - \langle (c_e) - c_{e,a} \rangle^2. \quad (\text{A.138})$$

The result is shown on the right of part (a). There is a regular sequence of triangles, centered at $z = 0, d_{ac}, 2d_{ac}$, etc., which reflect the correlations within one crystallite, between next neighbors, second neighbors, etc. The **self-correlation triangle** centered at the origin exhibits some characteristic properties. The value at $z = 0$, denoted Q , is

$$K(z = 0) = Q = \phi_c(1 - \phi_c)(c_{e,c} - c_{e,a})^2. \quad (\text{A.139})$$

The slope dK/dz is

$$\frac{dK}{dz} = \frac{dK_a}{dz} = -\frac{O_{ac}}{2}(c_{e,c} - c_{e,a})^2. \quad (\text{A.140})$$

Here, O_{ac} denotes the **specific internal surface** given by the area per unit volume of the interface separating crystalline and amorphous regions. For the periodic stack it is related to the long period by

$$O_{ac} = \frac{2}{d_{ac}} . \quad (\text{A.141})$$

The horizontal **baseline** between the triangles is located at

$$K = -B = -(\langle c_e \rangle - c_{e,a})^2 \quad (\text{A.142})$$

$$= -\phi_c^2 (c_{e,c} - c_{e,a})^2 . \quad (\text{A.143})$$

$K(z)$ reaches the base-line at

$$z_1 = d_c . \quad (\text{A.144})$$

It is to be recognized that application of these relations is not restricted to the ordered periodic system but can be extended, with slight modifications, to real systems that may show variations in the thicknesses of the crystalline and amorphous regions, and may also possess diffuse phase boundaries. The changes in $K(z)$ resulting from a successive perturbation of the initial system are schematically indicated in Figs. A.2(b)–(d). All structures in this sequence are understood as having equal crystallinities and equal specific internal surfaces.

First, as indicated in part (b), fluctuations in the intercrystalline spacings are introduced. Since the self-correlation part remains unchanged, the only consequence is a broadening of the peak attributed to next-neighbor correlations. There is a maximum at the position of the most probable distance between neighboring crystallites, and it determines the long spacing.

Second, as shown in part (c), we superpose variations in the crystallite thickness. Since ϕ_c and O_{ac} are assumed to be constant, the value of the correlation function at the origin, Q , the initial slope $dK/dz(z=0)$ and the base-line coordinate B are not affected. A modification occurs near the base of the triangle where $K(z)$ becomes curved. If we extrapolate the straight part of $K(z)$, it intercepts the base-line at

$$z_1 = \frac{Q + B}{dK/dz} = \frac{\phi_c}{O_{ac}/2} . \quad (\text{A.145})$$

The number average of the crystallite thickness, \bar{d}_c , is given by

$$\frac{O_{ac}}{2} \bar{d}_c = \phi_c . \quad (\text{A.146})$$

Therefore, we have

$$z_1 = \bar{d}_c . \quad (\text{A.147})$$

Finally, in the last step, we associate the crystallite surfaces with transition zones (part (d)). We do it under the condition that for each crystallite i with thickness d_c^i the total number of electrons remains unchanged, i.e.,

$$\int [c_e(z') - c_{e,a}] dz' = (c_{e,c} - c_{e,a}) d_c^i . \quad (\text{A.148})$$

Using this equation reversely, one may attribute to each crystallite with a diffuse surface a corresponding lamella with sharp boundaries and thickness \bar{d}_c^i . If this replacement is carried out for all crystallites, one returns to a two-phase structure, which we address as the **corresponding two-phase system**. For a transition zone with an extension d_t there results a change in the shape of the correlation function around the origin within the range $z < d_t$. If d_t is small compared to the thicknesses of all crystallites, there still remains a linear portion in the center of the right-hand side of the self-correlation triangle. This allows us to derive directly the parameters of the corresponding two-phase system. Extrapolation of the linear section to $z = 0$ gives Q , and a continuation down to the base-line at $K = -B$ yields \bar{d}_c . The crystallinity ϕ_c , the specific internal surface O_{ac} and the electron density difference then follow by

$$\phi_c = \frac{B}{B + Q}, \quad (\text{A.149})$$

$$O_{ac} = \frac{2\phi_c}{\bar{d}_c}, \quad (\text{A.150})$$

$$(c_{e,c} - c_{e,a})^2 = \frac{Q}{\phi_c(1 - \phi_c)}. \quad (\text{A.151})$$

So far, we have discussed the case $\phi_c < 0.5$. If we wish to investigate samples with $\phi_c > 0.5$, we have to substitute ϕ_c against the volume fraction of the amorphous phase

$$\phi_a = 1 - \phi_c \quad (\text{A.152})$$

and \bar{d}_c against the number average of the thickness of the amorphous layers, \bar{d}_a . The substitution rule follows from **Babinet's reciprocity theorem**, which declares that an exchange of the densities in a two-phase structure leaves the scattering function unchanged.

A crucial point of the analysis lies in the knowledge required of the baseline coordinate B . For samples of low or high crystallinity ($\phi_c < 0.3$ or $\phi_c > 0.7$), the base-line usually shows up. The intermediate region is problematic, as here the base-line may not be observed. Then X-ray scattering experiments have to be complemented by other data such as, for example, the density.

In this discussion of the scattering properties of a polymeric layer system, we have dealt with a special two-phase system. Some of the properties are not specific but generally valid for all two-phase systems, independent of their structure. Here we give three equations of particular importance.

First, we come back to Eq. (A.139). Use of Eq. (A.133) yields

$$Q = (c_{e,c} - c_{e,a})^2 \phi_c(1 - \phi_c) = \frac{1}{r_e^2(2\pi)^3} \int_{q=0}^{\infty} 4\pi q^2 \Sigma(q) dq. \quad (\text{A.153})$$

Q is often called the **invariant**, for obvious reasons. The total integral, as obtained by an integration over all the reciprocal space, only depends on the

volume fractions of the two phases and the electron density difference, hence, it is invariant with regard to the detailed structure. Equation (A.153) is not a specific property of layered systems, but generally valid. The proof is simple. One has to formulate the Fourier transformation reverse to Eq. (A.59), expressing the three-dimensional electron density correlation function as a function of $\Sigma(\mathbf{q})$

$$\langle c_e(\mathbf{r})c_e(0) \rangle - \langle c_e \rangle^2 = \frac{1}{r_e^2(2\pi)^3} \int \exp(i\mathbf{q}\mathbf{r})\Sigma(\mathbf{q})d^3\mathbf{q} \quad (\text{A.154})$$

and consider the limit $\mathbf{r} \rightarrow 0$

$$\langle c_e^2 \rangle - \langle c_e \rangle^2 = \frac{1}{r_e^2(2\pi)^3} \int \Sigma(\mathbf{q})d^3\mathbf{q} . \quad (\text{A.155})$$

Direct calculation shows that for a two-phase system the left-hand sides of Eqs. (A.153) and (A.155) agree.

Secondly, we consider the asymptotic behavior $\Sigma(q \rightarrow \infty)$, looking first at the layer system. Due to the reciprocity property of Fourier transforms, $\Sigma(q \rightarrow \infty)$ relates to the limiting behavior $K(z \rightarrow 0)$. Therefore, using Eqs. (A.132), (A.139) and (A.140) in a series expansion, we can write

$$\Sigma(q \rightarrow \infty) = \frac{1}{2\pi q^2} r_e^2 (2\pi)^2 \lim_{q \rightarrow \infty} \int_{-\infty}^{\infty} \cos(qz) \left(Q - \frac{O_{ac}}{2} (c_{e,c} - c_{e,a})^2 z \right) dz . \quad (\text{A.156})$$

For the purpose of a derivation of the asymptotic properties, we employ the following special representation of K valid for small values of z :

$$Q - \frac{O_{ac}}{2} (c_{e,c} - c_{e,a})^2 z \approx Q \exp \left(- \frac{O_{ac}(c_{e,c} - c_{e,a})^2}{2Q} z \right) . \quad (\text{A.157})$$

With this, the integral can be evaluated

$$\Sigma(q \rightarrow \infty) = \frac{2\pi r_e^2}{q^2} \lim_{q \rightarrow \infty} \int_{-\infty}^{\infty} \cos(qz) Q \exp \left(- \frac{O_{ac}(c_{e,c} - c_{e,a})^2 z}{2Q} \right) dz , \quad (\text{A.158})$$

which yields

$$\Sigma(q \rightarrow \infty) = \frac{2\pi r_e^2}{q^4} O_{ac} (c_{e,c} - c_{e,a})^2 , \quad (\text{A.159})$$

or, in an often used form

$$\Sigma(q \rightarrow \infty) = r_e^2 \frac{P}{(q/2\pi)^4} \text{ with } P = \frac{O_{ac}\Delta c_e^2}{8\pi^3} . \quad (\text{A.160})$$

Equation (A.160), known as **Porod's law** with P as the **Porod coefficient** is generally valid for arbitrary two-phase systems. Indeed, an asymptotic law

$\Sigma(q) \propto 1/q^4$ is the characteristic signature of two-phase systems with sharp boundaries. According to Eq. (A.159), the asymptotic behavior depends only on the interface area per unit volume, multiplied by the square of the density difference.

A third interesting parameter, l_c , follows from a combination of Q and O_{ac} in the same manner as appears in Eq. (A.157) in the exponent

$$l_c = \frac{2Q}{O_{ac}(c_{e,c} - c_{e,a})^2} = \frac{2\phi_c(1 - \phi_c)}{O_{ac}}. \quad (\text{A.161})$$

l_c characterizes the length scale of the two-phase structure. Equation (A.161) is a generalization of Eq. (A.146), which concerns \bar{d}_c and, thus, also a characteristic length. The determination of l_c has an advantage. As the electron density difference is eliminated, there is no need for intensity measurements in absolute units.

Further Reading

- L.E. Alexander: *X-Ray Diffraction Methods in Polymer Science*, John Wiley & Sons, 1969
- B.J. Berne, R. Pecora: *Dynamic Light Scattering*, John Wiley & Sons, 1976
- B. Chu: *Laser Light Scattering* Academic Press, 1991
- O. Glatter, O. Kratky: *Small Angle X-ray Scattering*, Academic Press, 1982
- A. Guinier: *X-Ray Diffraction in Crystals, Imperfect Crystals and Amorphous Bodies*, W.H. Freeman & Co, 1963
- J.S. Higgins, H.C. Benoit: *Polymers and Neutron Scattering*, Clarendon Press, 1994
- S.W. Lovesey: *Theory of Neutron Scattering from Condensed Matter, Vol. 1, Nuclear Scattering*, Clarendon Press, 1984
- R.J. Roe: *Methods of X-Ray and Neutron Scattering in Polymer Science*, Oxford University Press, 2000

B

Glossary of Symbols

a_0	: effective length per monomer for an ideal chain (Eq. (2.35))
a_b	: bond length (Eq. (2.33))
a_F	: effective length per monomer for an expanded chain (Eq. (2.83))
a_K	: Kuhn length (Eq. (2.31))
a_m	: length per monomer in the crystalline state
a_{pr}	: segment length of a primitive chain (Eq. (8.120))
a_R	: size of the Rouse segment
a_l	: element of a freely jointed chain
a_s	: length of segments of a freely jointed chain (Eq. (2.17))
$a(t)$: general time-dependent modulus (Eq. (6.33))
$a(\omega)$: general dynamic modulus (Eq. (8.19))
a_T	: WLF reduction factor (Eq. (6.122))
A_2	: second virial coefficient (Eq. (2.77))
\tilde{A}_2	: modified second virial coefficient (Eq. (3.13))
b_i	: neutron scattering length of atoms i
b_R	: force constant of springs in the Rouse chain (Eq. (8.25))
$\mathbf{B}, (B_{ij})$: Finger strain tensor (Eq. (9.81))
$\mathbf{B}(t, t')$: time-dependent Finger strain tensor (Eq. (9.162))
B	: magnetic field strength
$c_e(\mathbf{r})$: number density of electrons
$c_h(\mathbf{r})$: number density of holes
$c_{e,i}$: number density of electrons in region i
$c_m(\mathbf{r})$: number density of monomers (or other particles)
c_m^*	: number density of monomers at the overlap limit (Eq. (3.2))
c_p	: number density of polymers
c_s	: number density of salt molecules
c_w	: density by weight of a polymer in solution
$c_+(\mathbf{r})$: number density of kations

$c_-(\mathbf{r})$: number density of anions
$c_{\mathbf{k}}$: Fourier component of $c_m(\mathbf{r})$
$c(\omega)$: dynamic specific heat
C	: heat capacity
C_∞	: characteristic ratio (Eq. (2.32))
$C(\mathbf{q})$: scattering amplitude (Eq. (A.14))
C_1, C_2	: WLF parameters (Eq. (6.129))
$\mathbf{C}, (C_{ij})$: Cauchy strain tensor (Eq. (9.40))
C_{opt}	: stress-optical coefficient (Eq. (9.194))
d	: fractal dimension of a polymer chain
d_i	: thickness of the i -layer
d_{ac}	: long period of partially crystalline structure
d_{AB}	: long period of block copolymers with layer structure
d_t	: thickness of transition layer
D	: self-diffusion coefficient of chains (Eq. (8.131))
\hat{D}	: curvilinear diffusion coefficient of reptating chains
D_{coll}	: collective diffusion coefficient (Eq. (4.112))
$D(t)$: time-dependent tensile compliance (Eq. (6.1))
$D(\omega)$: dynamic tensile compliance (Eq. (6.6))
D_{hkl}	: coherence length along the direction hkl
\mathbf{D}	: dielectric displacement vector
e	: elementary charge
\tilde{e}	: internal energy per mole of monomers
e_p	: internal energy of a polymer chain
\mathbf{e}	: unit vector
\mathcal{E}	: internal energy of a sample
\mathbf{E}, E	: electric field strength
$E(t)$: time-dependent tensile modulus (Eq. (6.3))
$E(\omega)$: dynamic tensile modulus (Eq. (6.7))
E_b	: bending modulus of persistent chain (Eq. (2.131))
$\mathbf{e}, (e_{ij})$: linear strain tensor (Eq. (9.46))
$\mathbf{E}, (E_{ij})$: Eulerian strain tensor (Eq. (9.45))
e_H	: Hencky strain (Eq. (10.2))
\dot{e}_H	: Hencky strain rate (Eq. (9.150))
\mathbf{f}, f	: force
f	: Helmholtz free energy density
\tilde{f}	: Helmholtz free energy per mole of monomers
f_p	: Helmholtz free energy of a polymer chain
f_p^e	: electrostatic energy included in a polyion
f_p^{ev}	: excluded volume interaction energy in a polymer chain

f_{pp}^{ev}	: interaction energy between two polymer chains
f_p^s	: rubber-elastic energy of an expanded chain
\mathcal{F}	: Helmholtz free energy of a sample
F_i	: universal functions ($i = II$: Eq. (3.21); $i = \xi$: Eq. (3.63); $i = R$: Eq. (3.69))
$g(\mathbf{r})$: pair distribution function
$g_s(\mathbf{r})$: pair distribution function of chain segments
$\hat{g}(\mathbf{r})$: intramolecular part of the pair distribution function
$g(\mathbf{r}, t)$: time-dependent pair distribution function
$\hat{g}(\mathbf{r}, t)$: self-correlation part of $g(\mathbf{r}, t)$
$G(t)$: time-dependent shear modulus
$G(\omega)$: dynamic shear modulus
G_{pl}	: plateau modulus in polymer melts
G_I	: strain energy release rate (Eq. (10.62))
G_{Ic}	: critical value of G_I at the onset of crack growth (Eq. (10.63))
g	: Gibbs free energy density
$g_{A/B}$: Gibbs free energy density of the phase of A/B-chains
g_p	: Gibbs free energy of a polymer chain
g_a	: chemical potential of a monomer in the melt
g_c	: chemical potential of a monomer in an infinite crystal
Δg_{ij}	: difference in the chemical potential between phases i and j (= $g_j - g_i$)
\mathcal{G}	: Gibbs free energy of a sample
$\Delta \mathcal{G}_b$: activation barrier (Eq. (4.51))
$\Delta \mathcal{G}_{loc}$: local part of $\Delta \mathcal{G}_{mix}$
$\Delta \mathcal{G}_{mix}$: Gibbs free energy of mixing
$h(z)$: osmotic pressure coefficient (Eq. (3.27))
Δh_f	: heat of fusion per monomer
Δh_{ij}	: enthalpy change per monomer in a transition from phase i to phase j
h_p	: enthalpy of a polymer chain
$\Delta \mathcal{H}_f$: heat of fusion
$\Delta \mathcal{H}_{mix}$: heat of mixing
$H(\log \hat{\tau})$: relaxation time spectrum (Eq. (6.84))
(H_{ij}^{Os})	: Oseen tensor (Eq. (8.147))
I	: scattering intensity
I_B	: Bragg reflection intensity
I_i, II_i, III_i	: invariants of tensor i (Eq. (9.53))
I_{io}	: ionic strength (Eq. (3.102))
j	: electric current density

$J(t)$: time-dependent shear compliance
$J(\omega)$: dynamic shear compliance
J_e^0	: recoverable shear compliance (Eq. (6.103))
k	: Boltzmann constant
\mathbf{k}	: wave vector
$K(z)$: one-dimensional electron density correlation function (Eq. (A.131))
$K_{\text{or}}(l)$: orientational correlation function (Eq. (2.5))
K_i	: contrast factors for light, X-rays and neutrons (Eqs. (A.51), (A.56) and (A.62))
K_I	: stress intensity factor (Eq. (10.65))
K_{Ic}	: critical value of K_I at the onset of crack growth (Eq. (10.69))
l_c	: characteristic length of a non-periodic two-phase system (Eq. (A.161))
l_{io}	: distance of ionic charges along the chain
l_{ps}	: persistence length (Fig. 2.6)
l_{ct}	: contour length of a chain
l_{pr}	: contour length of primitive path (Eq. (8.120))
$L(\log \tau)$: retardation time spectrum (Eq. (6.73))
$m(t - t')$: memory function (Eq. (9.229))
M	: molar mass of polymer
\overline{M}_n	: number average molar mass
\overline{M}_w	: weight average molar mass
M_c	: critical molar mass at the entanglement limit (Eq. (6.96))
M_e	: average molar mass of the sequences between entanglement points (Eq. (10.54))
M_m	: molar mass of a monomeric unit
M	: magnetization
n_i	: principal indices of refraction
Δn	: birefringence coefficient
n	: number of monomers in a crystalline stem
n_i	: number of particles in cell i
\tilde{n}_i	: moles of polymer i in a sample
\tilde{n}_c	: moles of units (lattice cells) in a binary mixture
N_b	: number of backbone bonds in a chain
N_i	: degree of polymerization (number of monomers) of polymer i
N_R	: number of Rouse segments in a chain
$N_{R,c}$: critical number of Rouse segments at the entanglement limit
N_s	: number of segments in a chain
N_{su}	: number of ideal subunits in an expanded chain

N_L	: Avogadro–Loschmidt number
\mathcal{N}_c	: number of cells in a binary mixture
\mathcal{N}_m	: number of monomers (or particles) in a sample
\mathcal{N}_p	: number of polymers (colloids) in a sample
σ_p	: interface area per junction point
O_{ij}	: interface area per unit volume (between phases i, j)
p	: pressure
p	: distribution function (for \mathbf{R} , \mathbf{r}_{ij} , M etc.)
P	: Porod coefficient (Eq. (A.160))
\mathbf{p}	: dipole moment
\mathbf{P}	: polarization
\mathbf{q}	: scattering vector ($q = \mathbf{q} = 4\pi \sin \vartheta_B / \lambda$)
Q	: heat
Q	: gel swelling ratio
Q	: SAXS invariant for two phase system (Eq. (A.153))
r_e	: classical electron radius (Eq. (A.53))
\mathbf{r}_{ij}	: vector connecting the junction points i, j in a freely jointed chain
\mathbf{R}	: end-to-end distance vector of a polymer chain
R	: size ($(\mathbf{R} ^2)^{1/2}$) of a polymer chain
R_0	: size of an ideal chain
R_F	: size of an expanded chain
R_g	: radius of gyration of a polymer or colloid
R_h	: hydrodynamic radius (Eq. (8.145))
\tilde{R}	: perfect gas constant
$S(\mathbf{q})$: scattering function (scattering law), referred to one monomer (Eq. (A.5))
$S(\mathbf{q}, t)$: intermediate scattering law (Eq. (A.28))
$S_c(\mathbf{q})$: scattering law, referred to one lattice cell (Eq. (4.79))
$S_D(R_0q)$: Debye structure function (Eq. (2.61))
S_{or}^m	: orientational order parameter of monomers (Eq. (10.28))
$s_p(T)$: entropy of a polymer chain
$\mathcal{S}(T)$: entropy of a sample
Δs_f	: entropy of fusion per monomer
Δs_{ij}	: entropy change per monomer in a transition from phase i to phase j
$\Delta \mathcal{S}_{mix}$: entropy of mixing
$\Delta \mathcal{S}_t$: increase in the translational entropy
T_c	: critical temperature (binary mixtures)
T_c^∞	: temperature controlling the crystal thickness (Eq. (5.18))
T_f	: melting temperature

T_i^∞	: melting temperature of an infinite crystal
T_g	: glass transition temperature
T_{ij}^∞	: transition temperature for phases i and j
T_{sp}	: temperature on spinodal
T_A	: activation temperature (Eq. (6.126))
T_V	: Vogel temperature (Eq. (6.126))
$\mathbf{T}, (t_{ij})$: statistical weight matrix in RIS model (Eq. (2.147))
u	: growth rate of a spherulite
\mathbf{u}	: velocity of a particle
$\tilde{u}(\varphi)$: rotational potential of a backbone bond (per mol)
v	: specific volume
v_c	: volume of a structure unit in a binary mixture
v_e	: excluded volume parameter (Eq. (2.78))
v_m	: volume of a monomer
\tilde{v}_i	: molar volume of species i
$V(\mathbf{r})$: electrostatic potential
\mathcal{V}	: sample volume
$\mathbf{v}(\mathbf{r})$: flow field
w	: surface parameter in fracture mechanics (Eq. (10.61))
\mathcal{W}	: work
$\hat{x}_i, \hat{y}_i, \hat{z}_i$: extension of Rouse segment i (Eq. (8.66))
X_m, Y_m, Z_m	: normal coordinates of Rouse modes m (Eq. (8.46))
x	: overlap ratio (Eq. (3.16))
z	: number of electrons in a molecule
z_{eff}	: effective coordination number (Eq. (4.7))
z	: parameter determining f_p^e and N_{su} (Eqs. (2.90) and (2.118))
Z	: partition function
$\alpha(t)$: time-dependent susceptibility (Eq. (6.29))
$\alpha(\omega)$: dynamic susceptibility (Eq. (6.42))
β	: mean monomer polarizability
$\Delta\beta$: anisotropy of the monomer polarizability
γ	: shear strain
γ_e	: recoverable shear strain
γ_{EL}	: electroluminescence efficiency (Eq. (7.6))
Γ	: relaxation rate
δ	: phase shift
$\varepsilon(t)$: time-dependent dielectric function (Eq. (6.16))
$\varepsilon(\omega)$: complex dielectric function
ε_0	: electric constant
ϵ_F	: Fermi energy

ζ	: friction coefficient of spherical colloid (Eq. (8.143))
ζ_{R}	: friction coefficient of a Rouse segment (Eq. (8.24))
η	: steady state shear viscosity
η_0	: zero shear rate viscosity
$\hat{\eta}$: extensional viscosity (Eq. (9.160))
$\eta^+(t)$: time-dependent shear viscosity (Eq. (9.158))
$\hat{\eta}^+(t)$: time-dependent extensional viscosity (Eq. (9.159))
η_{r}	: reduced excess viscosity (Eq. (8.161))
η_{s}	: solvent viscosity
$[\eta]$: intrinsic viscosity of a dissolved polymer (Eq. (8.160))
ϑ_{B}	: Bragg scattering angle
θ	: orientation angle
κ_{osm}	: osmotic compressibility (Eq. (A.82))
λ	: extension ratio (Eq. (9.1))
$\Lambda(\phi)$: effective interaction parameter (Eq. (4.57))
$\mu(t-t')$: primary response function (Eq. (6.27))
μ_{B}	: Bohr magneton
μ_0	: magnetic constant
ν_{el}	: electric mobility (Eq. (7.5))
ν_{nuc}	: nucleation rate
ξ_{B}	: Bjerrum length (Eq. (3.88))
ξ_{D}	: Debye screening length (Eq. (3.92))
ξ_{s}	: screening length in semidilute solutions (Fig. 3.8)
ξ_{t}	: thermic correlation length (Eq. (2.117))
ξ_{ϕ}	: correlation length of concentration fluctuations (Eq. (4.101))
Π	: osmotic pressure
ρ	: mass density
ρ_{a}	: mass density of amorphous regions
ρ_{c}	: mass density of crystallites
$\rho_{\text{e}}(\mathbf{r})$: charge density distribution
$\rho_{\text{n}}(\mathbf{r})$: varying neutron scattering length density
σ	: isotropic dilatational stress
$\sigma_1, \sigma_2, \sigma_3$: principal stresses
$\boldsymbol{\sigma}, (\sigma_{ij})$: stress tensor
$\hat{\sigma}_{ij}$: nominal stresses
σ_{el}	: electric conductivity
σ_{e}	: excess free energy of monomers at the fold surface
σ_{if}	: excess free energy per unit area of interface
σ_{ij}	: excess free energy of monomers at the i, j -interface
$\Sigma(\mathbf{q})$: scattering cross section per unit volume

τ_d	: disentangling time
τ_i	: characteristic time of a relaxation process i
τ_{nuc}	: nucleation time
τ_R	: Rouse time (Eq. (8.42))
φ_i	: rotation angle of bond i
ϕ_i	: fraction of a component i
ϕ_l	: linear crystallinity (Eq. (5.21))
$\phi_{\mathbf{k}}$: Fourier component of a concentration fluctuation $\delta\phi(\mathbf{r})$
χ	: Flory–Huggins parameter (Eq. (4.6))
χ_c	: critical value of χ (Eq. (4.35))
χ_{sp}	: value of χ along the spinodal (Eq. (4.56))
χ_m	: magnetic susceptibility
ψ	: general potential
ψ_m^{ev}	: potential of excluded volume forces (Eq. (2.78))
Ψ_1	: primary normal stress coefficient (Eq. (9.153))
$\Psi_{1,0}$: primary normal stress coefficient at zero shear rate
Ψ_2	: secondary normal stress coefficient (Eq. (9.154))
ω	: frequency
Ω	: rotation matrix

C

Bibliography

There follows a bibliography for supplementary studies, which collects and further extends the suggestions for reading in the text. Especially included is a selection of treatises on methods and experimental techniques that are of importance for all those actually working in the field.

Textbooks

- F.W. Billmeyer: *Textbook on Polymer Science*, John Wiley & Sons, 1984
R.H. Boyd, P.J. Phillips: *The Science of Polymer Molecules*, Cambridge University Press, 1993
M.M. Coleman, P.P. Painter: *Fundamentals of Polymer Science*, Technomic Publishing Co, 1997
J.M.G. Cowie: *Polymers: Chemistry and Physics of Modern Materials*, International Textbook Co, 1973
U. Eisele: *Introduction to Polymer Physics*, Springer, 1990
P.J. Flory: *Principles of Polymer Chemistry*, Cornell University Press, 1953
U.W. Gedde: *Polymer Physics*, Chapman & Hall, 1995
A.Y. Grosberg, A.R. Khokhlov: *Giant Molecules*, Academic Press, 1997
P. Munk: *Introduction to Macromolecular Science*, John Wiley & Sons, 1989
M. Rubinstein, R.H. Colby: *Polymer Physics*, Oxford University Press, 2003
L.H. Sperling: *Introduction to Physical Polymer Science*, John Wiley & Sons, 1992
R.S. Stein, J. Powers: *Topics in Polymer Physics*, Imperial College Press, 2006

Comprehensive Treatments and Books with Broader Coverage

- G. Allen (Ed.): *Comprehensive Polymer Science Vol. 1, Polymer Characterization*, Pergamon Press, 1989
G. Allen (Ed.): *Comprehensive Polymer Science Vol. 2, Polymer Properties*, Pergamon Press, 1989
R.W. Cahn, P. Haasen, E.J. Kramer, E.L. Thomas (Eds.): *Materials Science and Technology Vol. 12, Structure and Properties of Polymers*, VCH Publishers, 1993
H.F. Mark (Ed.): *Encyclopedia of Polymer Science and Engineering Vols. 1–17*, John Wiley & Sons, 1985–89

- J.E. Mark, A. Eisenberg, W.W. Graessley, L. Mandelkern, J.L. Koenig: *Physical Properties of Polymers*, Am. Chem. Soc., 1984
- J.C. Salamone: *Polymeric Materials Encyclopedia*, CRC press, 1996
- J.M. Schultz (Ed.): *Treatise on Materials Science and Technology Vol. 10, Properties of Solid Polymeric Materials*, Academic Press, 1977

Theoretically Oriented Treatments

- H. Baur: *Thermophysics of Polymers*, Springer, 1999
- R.B. Bird, R.C. Armstrong, O. Hassager: *Dynamics of Polymeric Liquids Vol. 1 Fluid Mechanics*, John Wiley & Sons, 1977
- R.B. Bird, R.C. Armstrong, O. Hassager: *Dynamics of Polymeric Liquids Vol. 2 Kinetic Theory*, John Wiley & Sons, 1977
- J. des Cloizeaux, G. Jannink: *Polymers in Solution: Their Modelling and Structure*, Oxford Science Publishers, 1990
- M. Doi, S.F. Edwards: *The Theory of Polymer Dynamics*, Clarendon Press, 1986
- P.J. Flory: *Statistical Mechanics of Chain Molecules*, John Wiley & Sons, 1969
- G.H. Frederickson: *The Equilibrium Theory of Inhomogeneous Polymers*, Oxford University Press, 2006
- K.F. Freed: *Renormalization Group Theory of Macromolecules*, John Wiley & Sons, 1987
- P.-G. de Gennes: *Scaling Concepts in Polymer Physics*, Cornell University Press, 1979
- A.Y. Grosberg, A.R. Khokhlov: *Statistical Physics of Macromolecules*, AIP Press, 1994
- R.G. Larson: *Constitutive Equations for Polymer Melts and Solutions*, Butterworths, 1988
- W.L. Mattice, U.W. Suter: *Conformational Theory of Large Molecules – The Rotational Isomeric State Model in Macromolecular Systems*, John Wiley & Sons, 1994

Specialized Treatments

- J.F. Agassant, P. Avenas, J.P. Sergent, P.J. Carreau: *Polymer Processing*, Hanser, 1991
- E.H. Andrews, P.E. Reed, J.G. Williams, C.B. Bucknall: *Advances in Polymer Science Vol. 27, Failure in Polymers*, Springer, 1978
- D.C. Bassett: *Principles of Polymer Morphology*, Cambridge University Press, 1981
- A.W. Birley, B. Haworth, J. Batchelor: *Physics of Plastics*, Hanser, 1992
- A. Blythe, D. Bloor: *Electrical Properties of Polymers*, Cambridge University Press, 2005
- W. Brostow, R. Corneliussen: *Failure of Plastics*, Oxford University Press, 1989
- R.M. Christensen: *Mechanics of Composite Materials*, John Wiley & Sons, 1979
- H. Dautzenberg, W. Jaeger, J. Kötz, B. Philipp, Ch. Seidel, D. Stscherbina: *Polyelectrolytes*, Hanser, 1994
- E.J. Donth: *The Glass Transition*, Springer, 2001

- J. Ferguson, Z. Kumbowski: *Applied Fluid Rheology*, Elsevier, 1991
- J.D. Ferry: *Viscoelastic Properties of Polymers*, John Wiley & Sons, 1970
- H. Janeschitz-Kriegl: *Polymer Melt Rheology and Flow Birefringence*, Springer, 1983
- H.H. Kausch: *Polymer Fracture*, Springer, 1978
- H.H. Kausch (Ed.): *Advances in Polymer Science Vols. 91/91, Cracking in Polymers*, Springer, 1990
- A.J. Kinloch, R.J. Young: *Fracture Behaviour of Polymers*, Applied Science Publishers, 1983
- S. Matsuoka: *Relaxation Phenomena in Polymers*, Hanser, 1992
- N.G. McCrum, B.E. Read, G. Williams: *Anelastic and Dielectric Effects in Polymeric Solids*, John Wiley & Sons, 1967
- N.G. McCrum, C.P. Buckley, C.B. Bucknall: *Principles of Polymer Engineering*, Oxford University Press, 1997
- D.J. Meier (Ed.): *Molecular Basis of Transitions and Relaxations*, Gordon and Breach, 1978
- T.Q. Nguyen, H.H. Krausch (Eds.): *Flexible Polymer Chains in Elongational Flow*, Springer, 1999
- L.E. Nielsen: *Polymer Rheology*, Marcel Dekker, 1977
- L.E. Nielsen: *Mechanical Properties of Polymers and Composites Vols. 1/2*, Marcel Dekker, 1974
- D.R. Paul, S. Newman (Eds.): *Polymer Blends Vols. 1/2*, Academic Press, 1978
- T. Skotheim, J. Reynolds: *Conjugated Polymers*, CRC Press, 2006
- H. Tadokoro: *Structure of Crystalline Polymers*, John Wiley & Sons, 1979
- L.R.G. Treloar: *The Physics of Rubber Elasticity*, Clarendon Press, 1975
- I.M. Ward: *Mechanical Properties of Solid Polymers*, John Wiley & Sons, 1971
- I.M. Ward: *Structure and Properties of Oriented Polymers*, Applied Science Publishers, 1975
- I.M. Ward (Ed.): *Structure and Properties of Oriented Polymers*, Chapman & Hall, 1997
- A.E. Woodward: *Atlas of Polymer Morphology*, Hanser, 1989
- J.G. Williams: *Fracture Mechanics of Polymers*, Ellis Horwood Publishers, 1984
- B. Wunderlich: *Macromolecular Physics Vol. 1 Crystal Structure, Morphology, Defects*, Academic Press, 1973
- B. Wunderlich: *Macromolecular Physics Vol. 2 Crystal Nucleation, Growth, Annealing*, Academic Press, 1976
- B. Wunderlich: *Macromolecular Physics Vol. 3 Crystal Melting*, Academic Press, 1980

Methodically Oriented Treatments

- L.E. Alexander: *X-Ray Diffraction Methods in Polymer Science*, John Wiley & Sons, 1969
- B.J. Berne, R. Pecora: *Dynamic Light Scattering*, John Wiley & Sons, 1976
- D.I. Bower, W.F. Maddams: *The Vibrational Spectroscopy of Polymers*, Cambridge University Press, 1989
- P. Cebe, B.S. Hsiao, D.J. Lohse: *Scattering from Polymers. Characterization by X-rays, Neutrons and Light*, ACS Symposium Series 739, 2000

- B. Chu: *Laser Light Scattering*, Academic Press, 1991
- O. Glatter, O. Kratky: *Small Angle X-ray Scattering*, Academic Press, 1982
- J.S. Higgins, H.C. Benot: *Polymers and Neutron Scattering*, Clarendon Press, 1994
- L. Marton, C. Marton (Ed.): *Methods of Experimental Physics Vol. 16, Polymers Part A: Molecular Structure and Dynamics*, Academic Press, 1980
- L. Marton, C. Marton (Ed.): *Methods of Experimental Physics Vol. 16, Polymers Part B: Crystal Structure and Morphology*, Academic Press, 1980
- L. Marton, C. Marton (Ed.): *Methods of Experimental Physics Vol. 16, Polymers Part C: Physical Properties*, Academic Press, 1980
- V.J. McBrierty, K.J. Packer: *Cambridge Solid State Science Series, Nuclear Magnetic Resonance in Solid Polymers*, Cambridge University Press, 1993
- P.C. Painter, M.M. Coleman, J.L. Koenig: *The Theory of Vibrational Spectroscopy and its Application to Polymeric Materials*, John Wiley & Sons, 1982
- R.J. Roe: *Methods of X-Ray and Neutron Scattering in Polymer Science*, Oxford University Press, 2000
- A.C. Roulin-Moloney (Ed.): *Fractography and Failure Mechanisms of Polymers and Composites*, Elsevier, 1989
- K. Schmidt-Rohr, H.W. Spiess: *Multidimensional Solid-State NMR and Polymers*, Academic Press, 1994
- H.W. Siesler, K. Holland-Moritz: *Infrared and Raman Spectroscopy of Polymers*, Marcel Dekker, 1980
- S.J. Spells (Ed.): *Characterization of Solid Polymers*, Chapman & Hall, 1994
- B.K. Vainshtein: *Diffraction of X-Rays by Chain Molecules*, Elsevier, 1966
- B. Wunderlich: *Thermal Analysis of Polymeric Materials*, Springer, 2005

Development Reports

- D.C. Bassett (Ed.): *Developments in Crystalline Polymers Vol. 1*, Applied Science Publishers, 1982
- D.C. Bassett (Ed.): *Developments in Crystalline Polymers Vol. 2*, Elsevier, 1988
- I. Goodman: *Developments in Block Copolymers Vol. 1*, Applied Science Publishers, 1982
- I. Goodman: *Developments in Block Copolymers Vol. 2*, Applied Science Publishers, 1985
- L.A. Kleintjens, P.J. Leemstra: *Integration of Fundamental Polymer Science and Technology*, Elsevier, 1886
- R.M. Ottenbrite, L.A. Utracki, S. Inoue (Eds.): *Current Topics in Polymer Science Vol. 2*, Hanser, 1987
- I.M. Ward (Ed.): *Developments in Oriented Polymers Vol. 1*, Applied Science Publishers, 1982
- I.M. Ward (Ed.): *Development in Oriented Polymers Vol. 2*, Elsevier, 1987

Handbooks and Data Sources

- J. Brandrup, E.H. Immergut: *Polymer Handbook*, John Wiley & Sons, 2005
- D.W. Van Krevelen: *Properties of Polymers*, Elsevier, 1972
- L.A. Utracki (Ed.): *Polymer Blends Handbook*, Kluwer Academic Publishers, 2003

References

1. P.J. Flory. *Statistical Mechanics of Chain Molecules*, page 40. Wiley-Interscience, 1969.
2. J. Des Cloiseaux and G. Jannink. *Polymers in Solution*, page 650. Oxford Science, 1990.
3. Y. Miyaki, Y. Einaga, and H. Fujita. *Macromolecules*, 11:1180, 1978.
4. R. Kirste, W.A. Kruse, and K. Ibel. *Polymer*, 16:120, 1975.
5. M. Wintermantel, M. Antonietti, and M. Schmidt. *J. Appl. Polym. Sci.*, 52:91, 1993.
6. B. Farnoux. *Ann. Fr. Phys.*, 1:73, 1976.
7. B. Farnoux, F. Bou, J.P. Cotton, M. Daoud, G. Jannink, M. Nierlich, and P.G. de Gennes. *J. Physique*, 39:77, 1978.
8. W. Gawrisch, M.G. Brereton, and E.W. Fischer. *Polymer Bulletin*, 4:687, 1981.
9. I. Noda, N. Kato, T. Kitano, and M. Nagesowa. *Macromolecules*, 14:668, 1981.
10. J.P. Cotton. *J. Physique Lett.*, 41:L-231, 1980.
11. M.D. Lechner, K. Gehrke, and E.H. Nordmeier. *Makromolekulare Chemie*, page 238. Birkhäuser, 1993.
12. T. Koch, G.R. Strobl, and B. Stühn. *Macromolecules*, 25:6258, 1992.
13. F. Hamada, S. Kinugasa, H. Hayashi, and A. Nakajima. *Macromolecules*, 18:2290, 1985.
14. M. Daoud, J.P. Cotton, B. Farnoux, G. Jannink, G. Sarma, H. Benoit, R. Duplessix, C. Picot, and P.G. de Gennes. *Macromolecules*, 8:804, 1975.
15. N. Volk, D. Vollmer, M. Schmidt, W. Oppermann, and K. Huber. In M. Schmidt, editor, *Polyelectrolytes with defined molecular architecture II*, page 37. Springer, 2004.
16. M. Nierlich, C.E. Williams, F. Boue, J.P. Cotton, M. Daoud, B. Farnoux, G. Jannink, C. Picot, M. Moan, C. Wolff, M. Rinaudo, and P.G. de Gennes. *J. Phys.*, 40:701, 1979.
17. S. Förster and M. Schmidt. *Advances in Polymer Science*, 120:51, 1995.
18. L. Wang and V.A. Bloomfield. *Macromolecules*, 23:804, 1990.
19. R.J. Roe and W.C. Zin. *Macromolecules*, 13:1221, 1980.
20. T. Hashimoto, M. Itakura, and H. Hasegawa. *J. Chem. Phys.*, 85:6118, 1986.
21. G.R. Strobl, J.T. Bendler, R.P. Kambour, and A.R. Shultz. *Macromolecules*, 19:2683, 1986.
22. D. Schwahn, S. Janssen, and T. Springer. *J. Chem. Phys.*, 97:8775, 1992.

23. T. Hashimoto, J. Kumaki, and H. Kawai. *Macromolecules*, 16:641, 1983.
24. T. Koch and G.R. Strobl. *J. Polym. Sci., Polym. Phys. Ed.*, 28:343, 1990.
25. A. Sariban and K. Binder. *Macromolecules*, 21:711, 1988.
26. C.C. Han, B.J. Bauer, J.C. Clark, Y. Muroga, Y. Matsushita, M. Okada, T. Qui, T. Chang, and I.C. Sanchez. *Polymer*, 29:2002, 1988.
27. G.R. Strobl. *Macromolecules*, 18:558, 1985.
28. M. Takenaka and T. Hashimoto. *J. Chem. Phys.*, 96:6177, 1992.
29. F.S. Bates and G.H. Frederickson. *Ann. Rev. Phys. Chem.*, 41:525, 1990.
30. T. Hashimoto, M. Shibayama, and H. Kawai. *Macromolecules*, 13:1237, 1980.
31. A. Lehmann. *Diplomarbeit*, Physikalisches Institut, Universität Freiburg, 1989.
32. B. Stühn, R. Mutter, and T. Albrecht. *Europhys. Lett.*, 18:427, 1992.
33. M. Schwab and B. Stühn. *Phys. Rev. Lett.*, 76:924, 1996.
34. R. Eppe, E.W. Fischer, and H.A. Stuart. *J. Polym. Sci.*, 34:721, 1959.
35. B. Kanig. *Progr. Colloid Polym. Sci.*, 57:176, 1975.
36. A.S. Vaughan and D.C. Bassett. *Comprehensive Polymer Science, Vol.2*, page 415. Pergamon Press, 1989.
37. G.H. Michler. *Kunststoff-Mikromechanik*, page 187. Hanser, 1992.
38. S. Magonov and Y. Godovsky. *American Laboratory*, 31:52, 1999.
39. C.W. Bunn. *Trans. Farad. Soc.*, 35:482, 1939.
40. M. Kimmig, G. Strobl, and B. Stühn. *Macromolecules*, 27:2481, 1994.
41. T. Albrecht and G.R. Strobl. *Macromolecules*, 28:5827, 1995.
42. T. Albrecht. *Dissertation*, Universität Freiburg, 1994.
43. R. Mutter, W. Stille, and G. Strobl. *J. Polym. Sci., Polym. Phys. Ed.*, 31:99, 1993.
44. C. Hertlein, K. Saalwaechter, and G. Strobl. *Polymer*, 47:7216, 2006.
45. G.S. Ross and L.J. Frolen. *Methods of Experimental Physics, Vol.16B*, page 363. Academic Press, 1980.
46. Y.G. Lei, C.M. Chan, J.X. Li, K.M. Ng, Y. Wang, Y. Jiang, and L. Lin. *Macromolecules*, 35:6751, 2002.
47. M. Massa and K. Dalnoki-Veress. *Phys. Rev. Lett.*, 92:255509, 2004.
48. Y.G. Lei, C.M. Chan, Y. Wang, K.M. Ng, Y. Jiang, and L. Lin. *Polymer*, 44:4673, 2003.
49. J.K. Hobbs. *Chinese J. Polym. Sci.*, 21:135, 2003.
50. P. Kohn. *Diplomarbeit*. Physikalisches Institut, Universität Freiburg, 2004.
51. A. Häfele, B. Heck, T. Kawai, P. Kohn, and G. Strobl. *Eur. Phys. J.-E*, 16:207, 2005.
52. G. Hauser, J. Schmidtke, and G. Strobl. *Macromolecules*, 31:6250, 1998.
53. B. Heck, S. Siegenführ, and G. Strobl. *Polymer*, in press, 2007.
54. B. Heck, T. Hugel, M. Iijima, E. Sadiku, and G. Strobl. *New J. Physics*, 1:17.1, 1999.
55. C. Fougnyes, M. Dosiére, M.H.J. Koch, and J. Roovers. *Macromolecules*, 18:6266, 1998.
56. T. Hippler, S. Jiang, and G. Strobl. *Macromolecules*, 38:9396, 2005.
57. T.Y. Cho, W. Stille, and G. Strobl. *Colloid Polym. Sci.*, in press, 2007.
58. G.R. Strobl, T. Engelke, H. Meier, and G. Urban. *Colloid Polym. Sci.*, 260:394, 1982.
59. G.R. Strobl, M.J. Schneider, and I.G. Voigt-Martin. *J. Polym. Sci.*, 18:1361, 1980.
60. K. Schmidt-Rohr and H.W. Spiëß. *Macromolecules*, 24:5288, 1991.

61. T. Albrecht, S. Armbruster, S. Keller, and G. Strobl. *Macromolecules*, 34:8456, 2001.
62. G. Kumaraswamy, A.M. Issaian, and J.A. Kornfield. *Macromolecules*, 32:7537, 1999.
63. H. Janeschitz-Kriegl. *Macromolecules*, 39:4448, 2006.
64. J.K. Hobbs, A.D.L. Humphris, and M.J. Miles. *Macromolecules*, 34:5508, 2001.
65. J. Petermann and H. Gleiter. *J. Polym. Sci., Polym. Lett. Ed.*, 15:649, 1977.
66. J. Petermann, M. Miles, and H. Gleiter. *J. Polym. Sci., Polym. Phys. Ed.*, 17:55, 1979.
67. H. Seiberle, W. Stille, and G. Strobl. *Macromolecules*, 23:2008, 1990.
68. J. Heijboer. *Kolloid Z.*, 148:36, 1956.
69. J. Heijboer. In *Molecular Basis of Transitions and Relaxations (Midland Macromolecular Monographs, Vol. 4)*, page 75. Gordon & Breach, 1978.
70. F.R. Schwarzl. *Polymermechanik*. Springer, 1990.
71. G.C. Berry and T.G. Fox. *Adv. Polym. Sci.*, 5:261, 1968.
72. M. Abdel-Goad, W. Pyckhout-Hintzen, S. Kahle, J. Allgaier, D. Richter, and L.J. Fetters. *Macromolecules*, 37:8135, 2004.
73. E. Castiff and T.S. Tobolsky. *J. Colloid Sci.*, 10:375, 1955.
74. S. Onogi, T. Masuda, and K. Kitagawa. *Macromolecules*, 3:109, 1970.
75. D.J. Plazek, X.D. Zheng, and K.L. Ngai. *Macromolecules*, 25:4920, 1992.
76. Y. Ishida, M. Matsuo, and K. Yamafuji. *Kolloid Z.*, 180:108, 1962.
77. N.G. McCrum, B.E. Read, and G. Williams. *Anelastic and Dielectric Effects in Polymeric Solids*, page 305. Wiley & Sons, 1967.
78. D. Boese and F. Kremer. *Macromolecules*, 23:829, 1990.
79. A.J. Kovacs. *Fortschr. Hochpolym. Forsch.*, 3:394, 1966.
80. M. Heckmeier. *Diplomarbeit*, Physikalisches Institut, Universität Freiburg, 1995.
81. H.A. Flocke. *Kolloid Z. u. Z. Polym.*, 180:118, 1962.
82. K. Schmieder and K. Wolf. *Kolloid Z.*, 134:149, 1953.
83. B. Holzer and G.R. Strobl. *Acta Polym.*, 47:40, 1996.
84. H. Meier. *Diplomarbeit*, Institut für Physikalische Chemie, Universität Mainz, 1981.
85. H.W. Spiess. *Colloid Polym. Sci.*, 261:193, 1983.
86. R.H. Friend and N.C. Greenham. In T.A. Skotheim, R.L. Elsenbaumer, and J.R. Reynolds, editors, *Handbook of Conducting Polymers*, page 830. Marcel Dekker, 1998.
87. J. Cornil, D. Beljonne, Z. Shuai, T. Hagler, I. Campbell, D.D.C. Bradley, J.L. Bredas, C.W. Spangler, and K. Müllen. *Chem. Phys. Lett.*, 247:425, 1995.
88. H. Bässler. In R. Richert and A. Blumen, editors, *Disorder Effects on Relaxational Processes*, page 485. Springer, 1994.
89. K. Pakbaz, C.H. Lee, A.J. Heeger, T.W. Hagler, and D. McBranch. *Synth. Met.*, 64:295, 1994.
90. C.H. Lee, G. Yu, D. Moses, and A.J. Heeger. *Phys. Rev. B*, 49:2396, 1994.
91. R.H. Friend and N.C. Greenham. In T.A. Skotheim, R.L. Elsenbaumer, and J.R. Reynolds, editors, *Handbook of Conducting Polymers*, page 824. Marcel Dekker, 1998.
92. A.R. Brown, K. Pichler, N.C. Greenham, D.D.C. Bradley, R.H. Friend, and A.B. Holmes. *Chem. Phys. Lett.*, 210:61, 1993.

93. R.H. Friend and N.C. Greenham. In T.A. Skotheim, R.L. Elsenbaumer, and J.R. Reynolds, editors, *Handbook of Conducting Polymers*, page 835. Marcel Dekker, 1998.
94. M.J. Winokur. In T.A. Skotheim, R.L. Elsenbaumer, and J.R. Reynolds, editors, *Handbook of Conducting Polymers*, page 714. Marcel Dekker, 1998.
95. H. Kaneko and T. Ishiguro. *Synth. Met.*, 65:141, 1994.
96. R. Menon, C.O. Yoo, D. Moses, and A.J. Heeger. In T.A. Skotheim, R.L. Elsenbaumer, and J.R. Reynolds, editors, *Handbook of Conducting Polymers*, page 66. Marcel Dekker, 1998.
97. H. Naarmann. In H. Schaumburg, editor, *Polymere*, page 423. Teubner, 1997.
98. R. Menon, C.O. Yoo, D. Moses, and A.J. Heeger. In T.A. Skotheim, R.L. Elsenbaumer, and J.R. Reynolds, editors, *Handbook of Conducting Polymers*, page 55. Marcel Dekker, 1998.
99. A.J. Epstein, H. Rommelmann, M.A. Druy, A.J. Heeger, and A.G. MacDiarmid. *Solid State Comm.*, 38:683, 1981.
100. J. Joo, G. Oblakowski, G. Du, J.P. Pouget, E.J. Oh, J.M. Wiesinger, Y. Min, A.G. MacDiarmid, and J. Epstein, A. *Phys. Rev. B*, 49:2977, 1994.
101. U. Eisele. *Introduction to Polymer Physics*. Springer, 1990.
102. D. Richter, B. Farago, L.J. Fetters, J.S. Huang, B. Ewen, and C. Lartigue. *Phys. Rev. Lett.*, 64:1389, 1990.
103. J. Klein. *Nature*, 271:143, 1978.
104. T. Koch. *Dissertation*, Universität Freiburg, 1991.
105. P.J. Flory. *Principles of Polymer Chemistry*, page 311. Cornell University Press, 1953.
106. M. Drifford and J.P. Dalbietz. *Biophysics*, 24:1501, 1985.
107. H. Dautzenberg, W. Jaeger, J. Kötz, B. Philipp, Ch. Seidel, and D. Stscherbina. *Polyelectrolytes*, page 5. Carl Hanser, 1994.
108. J. Cohen, Z. Priel, and Y. Rabin. *J. Chem. Phys.*, 88:7111, 1988.
109. L.R.G. Treloar. *The Physics of Rubber Elasticity*. Clarendon Press, 1975.
110. J. Meissner. *Kunststoffe*, 61:576, 1971.
111. J.J. Burke and V. Weiss. *Characterisation of Materials in Research*. Syracuse University Press, 1975.
112. R.L. Anthony, R.H. Caston, and E. Guth. *J. Phys. Chem.*, 46:826, 1942.
113. R.S. Rivlin and D.W. Saunders. *Phil. Trans. R. Soc.*, A243:251, 1951.
114. J.R. Schaefgen and P.J. Flory. *J. Am. Chem. Soc.*, 72:689, 1950.
115. U.P. Schröder and W. Oppermann. In J.P. Cohen Addad, editor, *Physical properties of polymeric gels*, page 34. Wiley, 1996.
116. H.M. Laun. *Rheol. Acta*, 21:464, 1982.
117. J. Meissner. *J. Appl. Polym. Sci.*, 16:2877, 1972.
118. H.M. Laun and H. Münstedt. *Rheol. Acta*, 15:517, 1976.
119. H. Münstedt and H.M. Laun. *Rheol. Acta*, 20:211, 1981.
120. T. Matsumoto and D.C. Bogue. *J. Polym. Sci., Polym. Phys. Ed.*, 15:1663, 1977.
121. C. Wales in H. Janeschitz-Kriegl. *Polymer Melt Rheology and Flow Birefringence*, page 115. Springer, 1983.
122. R. Morbitzer in U. Eisele. *Introduction to Polymer Physics*, page 104. Springer, 1990.
123. W. Retting. *Rheol. Acta*, 8:259, 1969.
124. K. Hong, A. Rastogi, and G. Strobl. *Macromolecules*, 37:10165, 2004.

125. K. Hong. *Dissertation*, Universität Freiburg, 2005.
126. R. Hiss. *Dissertation*, Universität Freiburg, 1996.
127. P.H. Geil and Y. Yang. *Makromol. Chem.*, 186:1961, 1985.
128. I.L. Hay and A. Keller. *Kolloid Z. u. Z. Polym.*, 204:43, 1965.
129. H.W. Spiess. In I.M. Ward, editor, *Developments in Oriented Polymers - 1*, page 47. Applied Science, 1982.
130. E.W. Fischer, H. Goddar, and G.F. Schmidt. *Makromol. Chem.*, 118:144, 1968.
131. P.J. Lemstra, R. Kirschbaum, T. Ohta, and H. Yasuda. In I.M. Ward, editor, *Developments in Oriented Polymers - 2*, page 39. Elsevier, 1987.
132. M. Iguchi and H. Kyotani. *Sen-i Gakkaishi*, 46:471, 1990.
133. R.P. Kambour. *Macromol. Rev.*, 7:1, 1973.
134. A.S. Argon and J.G. Hannoosh. *Phil. Mag.*, 36:1195, 1977.
135. S.S. Sternstein. In J.M. Schultz, editor, *Treatise on Materials Science and Technology*, volume 10, page 541. Academic Press, 1977.
136. E.J. Kramer. *Adv. Polym. Sci.*, 52:1, 1983.
137. A.S. Argon and M.M. Salama. *Phil. Mag.*, 36:1217, 1977.
138. J.G. Williams. *Polym. Engn. Sci.*, 17:144, 1977.
139. W. Döll. In H.H. Kausch, editor, *Polymer Fracture*, page 267. Springer, 1978.
140. G.H. Michler. *Kunststoff-Mikromechanik*, page 100. Carl Hanser, 1992.
141. M.J. Doyle. *J. Polym. Sci., Polym. Phys. Ed.*, 13:2429, 1975.
142. W. Döll. In A.C. Roulin-Moloney, editor, *Fractography and Failure Mechanisms of Polymers and Composites*, pages 405, 416. Elsevier, 1989.
143. J.F. Fellers and B.F. Kee. *J. Appl. Polym. Sci.*, 18:2355, 1974.

Index

- α -modes 269
- α -process
 - in amorphous systems 250
 - dielectric 263
 - relaxation strength 267
- γ -process
 - mechanical 246
- AFM
 - tapping technique 168
- anelasticity 223
- average viscoelastic relaxation time 260
- Avrami equation 186
- Bjerrum length 90, 92
- block copolymers 10
 - microphase separation 152
 - critical properties 159
 - order of transition 162
 - strong and weak segregation 155
 - microphases 152
 - gyroid structure 152
 - phase diagram 154
 - structure function
 - RPA result 159, 481
- Boltzmann superposition principle 233
- Bragg scattering angle 463
- branched polymers 11
- brittle fracture 450
 - environmental effects 460
- brittle materials 417
- Brownian chain 33
- Cauchy strain tensor 373
 - invariants of 376
 - principal axes 375
- chain scission 451
- characteristic ratio 29
 - from intrinsic viscosity 351
- charge screening
 - in polyelectrolyte solutions 95
- chemical structures 1
- classical electron radius 472
- cloud point 121
- coils
 - in semidilute solutions 84, 87
 - persistence length 23
 - universality classes 25
- cold-drawing 415, 430
 - applied stress
 - rate dependence 431
- Cole–Cole function 242
- Cole–Cole plot 240
- complex dielectric function 229
- computer simulations 110, 173
- cone-and-plate rheometer 391
- conformational transition
 - localized 237, 246
- conjugated polymers 2, 288
 - effect of doping 302
 - electrical conductivity 299
 - red shift of bands 292, 293
- conjugation of bonds 290
- Considère construction 434
- constitutive equation 360
- contrast factor

- for light 472
- for neutrons 473
- for X-rays 473
- copolymerization 10
- correlation function
 - of scattering amplitude 468
 - of concentr. fluctuations 142
 - of electron density 177, 473
 - one-dimensional 485
 - of moving particle 474
 - of particle density 466
 - orientational 23
 - self-correlation 206
- crack growth
 - critical stress for 454
 - critical transition 456
 - subcritical mode 456
- crazes
 - direction of growth 446
 - growth mechanism 448
 - initiation 445
 - internal structure 444
- crazing 416
 - and fracture 458
 - criterion 446
- creep experiment 224, 238
- creep recovery 225
- critical molar mass 253
- crystal blocks 424
 - sliding motion 424
- crystal growth
 - activation barrier 188, 203
 - branching 170, 183
 - growth rate
 - T -dependence 181, 198
 - pathway 200
- crystallinity 174
 - from density 175
 - from heat of fusion 176
 - invariance 195
- crystallites
 - fold surface 173
 - granular substructure 171, 197
 - lamellar structure 168
 - nucleation 182
 - stability 188
 - surface free energy 191
- crystallization
 - by nucleation and growth 167
 - dominant and subsidiary lamellae 184, 187
 - effect of co-units 189
 - in flowing melts 216
 - role of transient phase 200
 - thermodynamic scheme 201
- crystallization isotherms 184
- crystallization line 192, 195, 203
- crystallization time
 - temperature dependence 187
- Debye length 90, 93
 - and ionic strength 95
- Debye process 239, 248
- Debye structure function 34
 - Kratky plot 38
- Debye-Hückel theory 93, 94
- defect clustering 442
- degree of polymerization 1
- dielectric normal mode 266
 - and Rouse model 330
- differential cross-section 464
 - partial 470
- differential scanning calorimetry 188
- diffusion coefficient
 - collective 146, 353
 - of chains in melt 342
 - of dissolved polymer 347
 - from DLS 347
- dilute solutions 71
- disentangling time 337, 360
 - M -dependence 253, 340
- dissipated energy
 - in dynamic experiments 235
- doped conjugated polymers
 - electrical conductivity 302, 304
 - anisotropy 306
 - temperature dependence 303
 - paramagnetism 306
 - plasma vibrations 310
 - reflectivity 310
- drawability 443
- drawing stress 426
- ductility 417
 - and fracture energy 417
- duromers 12
- dynamic light scattering 468
- dynamic shear compliance 228
- dynamic shear modulus 228

- dynamic specific heat 215
dynamic tensile compliance 226, 227
dynamic-mechanical experiment 226,
239
- Einstein relation 339, 341, 347
elastic dumbbell 324
electric mobility 299
electrical resistivity 305
electroluminescence
in conjugated polymers 297
electron acceptor 302
electron donator 302
electron-hole pairs
in conjugated polymers 291
energy conjugated variables 229
energy gap
in conjugated polymers 290
engineering stress 372
entanglement limit
critical molar mass 252, 333
entanglement network 252, 333
mobility constraints 333
entanglements
effect of crystallization 423
effect on crystallization 166
equilibrium melting point 192
Eulerian strain tensor 375
exciton band
vibronic fine structure 291
excitons 291
annihilation 300
coherent motion 293
incoherent motion 293
luminescence 294
excluded volume 25
excluded volume forces
in dilute solutions
chain repulsion 76
in semidilute solutions 75
mean field potential 42
screening in a melt 44
expanded chains 25
 R -distribution function 46
Kuhnian limit 75
pair distribution function 50
extensional flow 391
extensional viscosity 396
time-dependent 396
- extrudate thickening 358
Eyring law of viscosities 427, 431
- Förster mechanism 293
fiber diagram 174, 425
fibers 12
fibril rupture 459
fibrillar state 435
fibrillar structure 424
fibrillation
critical strain 424
Finger strain tensor 377
invariants of 378
time-dependent 398
Finger's constitutive equations 376,
377
Flory radius 47
Flory-Huggins equation 110
Flory-Huggins parameter 107
 T -dependencies 117
compatibility criterion 112
concentration dependence 120, 138
critical value 114
enthalpic part 111
entropic part 111
in structure function 137, 480
Flory-Huggins treatment 106
local interactions 107
translational entropy 107
fluctuation-dissipation theorem 313
for dipole fluctuations 314
for stress fluctuations 315
general form 316
Fox-Flory equation 277
fractal dimension
of expanded chains 50
of ideal chains 28
fracture criterion 453, 454
surface parameter 453, 457
fracture surface 458
Franck-Condon principle 291
free volume 271
freely jointed segments model 26
Frenkel excitons 293
friction coefficient
of dissolved polymer 347
of suspended colloid 346
Fuoss-Strauss relation 354

- gauche-conformation 16
- gel-spinning 442
- gels 384
- general dynamic modulus 316
- general dynamic susceptibility 233
- general time-dependent modulus 232
- general time-dependent susceptibility 232
- Gibbs free energy of mixing 106
 - for asymmetric blend 116
 - for symmetric blend 113
- Gibbs–Thomson equation 191
- Ginzburg–Landau functional 133
- glass transition temperature 270
 - from expansion coefficient 270
 - from heat capacity freezing criterion 275
 - from heat capacity 270
- glass–rubber transition 250, 254
 - T -dependence 260
- grafted chains 11
- Guinier’s law 475

- Havriliak–Negami equation 269
- heat wave spectroscopy 214
- helix
 - external parameters 21
 - internal parameters 21
 - irrational 22
 - of type m/n 21
- Hencky rate of extension 393
- Hencky strain 419
- HOMO 290
- homogeneous nucleation 182
- hopping motion
 - of charge carriers 296, 300, 304
 - of excitons 293
- Huggins constant 352
- hydrodynamic interaction 347
- hydrodynamic radius
 - and friction coefficient 346
 - of dissolved polymer 347
- hydrogels 384
- hyperelastic bodies 376
 - constitutive equation 378

- ideal chains 25
 - R -distribution function 26
 - exact treatment 30
 - pair distribution function 35
 - self-similarity 28
- ideal rubber 362
 - constitutive equation 378
 - elastic modulus 368
 - free energy density 378
 - simple shear
 - normal stress difference 382
 - stress–strain relationship 368
- intrinsic viscosity 350
- ionic strength 95
- Ising chain 59

- kinetical criterion 166
- Kramers–Kronig relations 234
- Kuhn length 29
- Kuhnian chain 55
- KWW function 255
 - and α -process 256

- LCST 120
- light emitting diode 287, 298
 - color variation 301
 - efficiency 301
 - electrical double layers 298
 - electron transport layer 300
 - hole transport layer 300
 - triplet exciton formation 300
- linear crystallinity 196
- linear fracture mechanics 453
- linear response
 - in general 229
 - superposition principle 231
- linear viscoelasticity 224, 225
- Lodge liquid
 - constitutive equation 399
- loss tangent 236
- LUMO 290

- Maltese cross 168
- Mark–Houwink–Sakurada relation 351
- master curve 248
 - shift factor 255, 260
- material resistance 458
- mean field 42, 108
- melt flow
 - primary normal stress difference 394, 395

- secondary normal stress difference 394
- melting line 192, 202
- memory function 413
- mesomorphic layer 200, 201, 205
- miscibility gap 114
 - upper and lower 118
- mixtures
 - binodal 115, 119
 - tangent construction 116
 - coil sizes 137
 - concentration fluctuations
 - and scattering function 129, 136
 - correlation length 141
 - stability criterion 125, 135
 - wave-like modes 134, 135
 - critical point 129
 - lattice model 109
 - computer simulations 138
 - phase diagram
 - for symmetric blend 115
 - phase separation
 - characteristic patterns 122
 - interfacial free energy 127
 - nucleation and growth 123, 125, 126
 - nucleation rate 127
 - structure function
 - RPA result 137, 481
- molar mass
 - distribution function 2, 8
 - number average 6
 - Poisson 9
 - polydispersity index 6
 - Schulz-Zimm 9
 - weight average 6
 - from Zimm plot 80
 - of sequences between entanglement points 447
- molecular field 94, 108
- monomeric unit 1
- Mooney equation 383
- Mooney plot 383
- Mott-Wannier excitons 293

- neck formation 415, 429
 - prerequisites for 433, 435
 - shoulder 430
 - profile 433
- neutron scattering
 - coherent 474
 - dynamic 468
 - incoherent 474
 - quasielastic 468
 - scattering length 473
 - scattering length density 474
- Newtonian liquid 257, 345
- NMR
 - crystallization studies 180
- nominal stress 372
- non-linear behavior
 - criterion for 359
- normal stresses
 - in melt flow 358
- nucleating agents 184
- nucleation density
 - enhancement in flowing melts 217
- nucleation time 182

- oligomers 165
 - crystal structure 165
- orientational order parameter 410, 436
 - from birefringence 436
 - from NMR 438
 - from X-ray scattering 439
- orientational polarization 236
- Oseen tensor 346
- osmotic compressibility
 - and forward scattering 477
- osmotic modulus 79
- osmotic pressure
 - general equation 76
 - second virial coefficient 41, 76
 - M -dependence 77
 - from Zimm plot 80
 - virial expansion 41, 71
 - in dilute solutions 72
- overlap limit 70
- overlap ratio 73, 75

- pair distribution function 466
 - time-dependent 469
- partially crystalline state 166
- Pauli paramagnetism 308
- PB/PI mixture 148
- pentane effect 59
- persistence length 56
 - change with temperature 57

- relation with Kuhn length 57
 - persistent chain 55
 - bending modulus 57
 - orientational correlation function 56
 - photocurrent
 - in conjugated polymers 295
 - photoluminescence
 - quantum yield 301
 - Poisson–Boltzmann equation 94
 - polarons 296
 - poly(α -methylstyrene) 72
 - poly(ϵ -caprolactone) 193, 205
 - poly(diacetylene) 295
 - poly(ethylene oxide) 182
 - poly(ethylene-*co*-propylene) 334
 - poly(L-lactic acid) 167, 168
 - poly(methacrylate) 246
 - poly(methyl methacrylate) 44, 445, 454, 456, 458
 - poly(oxymethylene) 20
 - poly(phenylene vinylene) 287, 296, 297, 300
 - poly(tetrafluoroethylene) 20, 174
 - poly(vinylacetate) 263, 270
 - poly(vinylchloride) 417, 458
 - polyacetylene 288
 - polyaniline 305
 - polycarbonate 66
 - polyelectrolyte gels
 - equilibrium degree of swelling 387
 - polyelectrolyte solutions
 - chain ordering 98
 - cooperative motions 352
 - effect of salt 97, 353
 - osmotic pressure 101
 - Donnan contribution 103, 389
 - reduced excess viscosity 354, 356
 - polyelectrolytes 2, 89
 - solution properties 89
 - polyethylene 1, 16, 63, 168, 171, 178, 208, 213, 218, 342, 357, 395, 415, 424, 425, 431, 439, 442, 444
 - α -process 277, 280
 - α -process
 - from NMR 213
 - low density polyethylene 11, 172, 393, 396
 - β -process 277, 279
 - mechanical relaxation 277
 - mechanical relaxation 277
 - SAXS curve 176
 - segmental mobility
 - from NMR 283
 - unit cell 173
 - polyisobutylene 254, 262
 - polyisoprene 263
 - polymer crystal
 - basic structure 165
 - structure analysis 173
 - polymorphism 20
 - polypropylene 172
 - polypyrrrol 305
 - polystyrene 1, 41, 42, 50–52, 78, 83, 86, 170, 181, 250, 256, 348, 358, 444
 - high impact polystyrene 449
 - polystyrene-*block*-polyisoprene 153, 158
 - Porod coefficient 185
 - Porod's law 150, 490
 - primary response function 230
 - PS/PB mixture 121
 - PS/PBrS mixture 138, 148
 - PS/PVME mixture 121, 129, 130, 141
 - pure shear 380
- quasi-static stress-strain relation 421
- radius of gyration 475
 - random phase approximation 478
 - Raoult's law 192
 - Rayleigh ratio 464, 472
 - recoverable shear compliance 257, 258
 - recrystallization line 193, 195, 203
 - recrystallization processes 189
 - reduced excess viscosity 351, 352
 - reduced osmotic pressure 74
 - relaxation equation 238
 - relaxation processes
 - in general 237
 - nomenclature 246
 - relaxation strength 238
 - relaxation time 238
 - relaxation time spectrum 244
 - relaxatory modes 236, 246
 - in mechanics 237
 - reptation model 339
 - primitive path 339
 - resonance transition 293

- response functions
 - general relationships 229
- retardation time spectrum 242
- RIS model 59
 - free energy of a chain 63
 - partition function 60
 - statistical weights 61
- rotational diffusion 236
- rotational isomeric states 18
- rotational potential 16
- Rouse chains 318
 - stress field 325
- Rouse model 318
 - equation of motion 319
 - stress relaxation modulus 328
 - power law 328
 - viscosity
 - M -dependence 329
- Rouse modes 321, 323
 - normal coordinates 323
 - amplitude 324
 - time correlation function 325
 - of lowest order 321
- Rouse rate 322
- Rouse sequence 318
- Rouse time 322
 - M -dependence 322
- rubber toughened thermoplastics 449
- rubber-elastic plateau 251, 254
 - width of 252, 256
- rubber-elastic plateau 338
- rubbers 12
 - elastomers 12
 - fixed junction model 366
 - mechanical properties 361
 - retracting force 364
 - entropic origin 365
- scaling law 30
 - size of an ideal chains 30
 - size of expanded chains 47
- scattering experiment
 - general set-up 463
 - time-resolved 468
- scattering function 464
- scattering law 464
 - dynamic 470
 - for lattice model 478
 - intermediate 468
- Scherrer equation 197
- second order phase transitions
 - critical fluctuations 129
- secondary crystallization 205
 - crystal thinning 212
 - from Raman spectra 205
 - from SAXS 206
 - insertion mode 206, 208, 215
 - surface crystallization 207, 212, 215
- self-diffusion coefficient 146
- semicrystalline state 166
 - amorphous regions 166, 212
 - with reduced mobility 181
- chain flux 173
- mechanical relaxation 277
- Raman spectra 178
 - decomposition 180
- reversible structure changes 214
- SAXS 177
- structural parameters
 - temperature dependence 190
- transition zones 178
 - from NMR 214
- two phase layer structure
 - long spacing 488
- two-phase layer structure 166, 169, 484
 - inner surface 177, 487
 - long spacing 176
- semidilute solutions 71
 - mesh size 85
 - osmotic modulus
 - and forward scattering 81
 - pair distribution function 85
 - intramolecular 82
 - screening effects 82
 - screening length 83
 - concentration dependence 86
 - from SAXS 85
- shear bands 416
- shear compliance 227
- shear strain recovery 394
- shear stress growth experiment 400
- shear thinning 358, 394
- shear yielding 415
- shish kebab 220
 - self-supported growth 221
- simple shear 380
- simple shear flow 391

- single-time relaxation process 237, 238
- slow modes 353
- spectro-photoconductive response
 - by conjugated polymers 295
- spherulites 167
 - banded type 171
 - internal texture 170
- spinodal 128, 129
 - determination 141
- spinodal decomposition 123, 125
 - critical slowing down 146
 - similarity property 148
 - transient structure factor 130, 143
 - virtual structure factor 144
- statistical copolymers 10
- step-cycle test 419
- Stokes' law 346
- strain energy release rate 453
- strain hardening 396, 415
- strain softening 415
- strength
 - role of flaws 452
 - theoretical limits 451
- stress decay 421
 - logarithmic law 421, 429
- stress growth experiment 395, 402
- stress intensity factor 455
 - critical value 455
- stress relaxation experiment 226
- stress tensor 371
- stress whitening 416
- stress-optical coefficient 406, 411
- stress-optical rule 406
- stretching curve 419
- structure factor 467
 - dynamic 470
- superabsorbers 384
- swelling 384
- swelling ratio 384
- switchboard model 173

- tacticity 10
- temperature modulated DSC 214
- tensile creep compliance 225
- tensile deformation 418
 - critical strains 418, 421
 - finite plasticity 428
 - strain control 421
- tensile rheometer 392
- terminal flow region 251
 - T -dependence 260
- thermic correlation length 53
- thermoelastic inversion 363
- thermoplasts 12
- theta conditions 39
- time dependent dielectric function 228
- time dependent shear modulus 227
- time-temperature superposition 248
- time-dependent tensile modulus 226
- time-dependent viscosity 396
- time-temperature superposition
 - in amorphous polymers 250
- tough materials 417
- trans-conformation 16
- triplet excitons 297
- true strain 419
- tube flow 391
- tube model 254, 333, 338
 - constraints release 341

- UCST 119
- ultimate properties 415
- ultra-drawing 444

- virial coefficients 72
- viscoelasticity 223
- viscosity
 - and disentangling time 338
 - at zero shear rate 257, 258
 - of a polymer solution 349
- Vogel temperature 199, 261
- Vogel-Fulcher law 199, 261, 267
- vulcanization 12

- whitening 416
- Wiener-Chinchin theorem 316
- WLF equation 263
- worm-like chain 55

- yield point 415, 419
- yielding mechanisms 415

- zero growth rate temperature 198, 203
- Zimm plot 79, 80